JAEA-Review
2014-050

JAEA-Review

JAEA Takasaki Annual Report 2013

(Ed.) Takuji KOJIMA

Takasaki Advanced Radiation Research Institute
Sector of Nuclear Science Research

March 2015

Japan Atomic Energy Agency

日本原子力研究開発機構

本レポートは独立行政法人日本原子力研究開発機構が不定期に発行する成果報告書です。
本レポートの入手並びに著作権利用に関するお問い合わせは、下記あてにお問い合わせ下さい。
なお、本レポートの全文は日本原子力研究開発機構ホームページ（http://www.jaea.go.jp）
より発信されています。

独立行政法人日本原子力研究開発機構 研究連携成果展開部 研究成果管理課
〒319-1195 茨城県那珂郡東海村白方白根2 番地4
電話 029-282-6387, Fax 029-282-5920, E-mail:ird-support@jaea.go.jp

This report is issued irregularly by Japan Atomic Energy Agency.
Inquiries about availability and/or copyright of this report should be addressed to
Institutional Repository Section,
Intellectual Resources Management and R&D Collaboration Department,
Japan Atomic Energy Agency.
2-4 Shirakata Shirane, Tokai-mura, Naka-gun, Ibaraki-ken 319-1195 Japan
Tel +81-29-282-6387, Fax +81-29-282-5920, E-mail:ird-support@jaea.go.jp

JAEA-Review 2014-050

JAEA Takasaki Annual Report 2013

(Ed.) Takuji KOJIMA

Takasaki Advanced Radiation Research Institute

Sector of Nuclear Science Research

Japan Atomic Energy Agency

Watanuki-machi, Takasaki-shi, Gunma-ken

(Received November 28, 2014)

JAEA Takasaki annual report 2013 describes research and development activities performed from April 1, 2013 to March 31, 2014 mainly with Takasaki Ion Accelerators for Advanced Radiation Application (TIARA, four ion accelerators), and electron/gamma-ray irradiation facilities (an electron accelerator and three ^{60}Co gamma-ray irradiation facilities) at Takasaki Advanced Radiation Research Institute, Japan Atomic Energy Agency (JAEA Takasaki). These activities are classified into four research fields: 1) Space, Nuclear and Energy Engineering, 2) Environmental Conservation and Resource Exploitation, 3) Medical and Biotechnological Application, and 4) Advanced Materials, Analysis and Novel Technology.

This annual report contains 169 reports consisting of 160 research papers and 9 status reports on operation/maintenance of the irradiation facilities described above, a list of publications, patents, related press-releases, television broadcasting, and the type of research collaborations as appendices.

Keywords: TIARA, Ion Accelerator, Electron Accelerator, Gamma-ray Facility, Nuclear and Energy Engineering, Environmental Conservation, Resource Exploitation, Medical Application, Biotechnological Application, Advanced Materials, Novel Technology, Materials for Space, Semiconductors, Inorganic Materials, Organic Materials, Functional Materials, Radiation Chemistry, Radiation Biology, Radioisotope Production, Material Analysis, Solid State Physics, Beam Technology, Accelerator Technology, Facility Operation, Safety Control

高崎量子応用研究所研究年報 2013

日本原子力研究開発機構 原子力科学研究部門 高崎量子応用研究所
（編） 小嶋 拓治

（2014 年 11 月 28 日受理）

高崎量子応用研究所研究年報 2013 は、同研究所にある TIARA 施設（イオン加速器 4 基）及び電子・ガンマ線照射施設（電子加速器 1 基、^{60}Co ガンマ線照射施設 3 棟）等を利用して 2013 年 4 月 1 日から 2014 年 3 月 31 日までの間に行われた研究・技術開発成果をまとめたものである。この研究年報には、1）宇宙・原子力・エネルギー、2）環境保全・資源利用、3）医療・バイオ技術応用、4）先端材料・分析・基盤技術の 4 分野に分類した 160 編の論文及び 9 編の施設の運転・管理状況報告からなる合計 169 編を収録する。また、論文リスト、出願特許、新聞発表、テレビ放映及び研究実施形態・利用施設の一覧表を付録として含む。

高崎量子応用研究所：〒370-1292 群馬県高崎市綿貫町 1233
編集委員：（著者代表）小嶋 拓治、前川 康成、小林 泰彦、横田 渉、箱田 照幸、
春山 保幸、中村 義輝

PREFACE

This annual report covers the activities of research and development using the irradiation facilities of TIARA (Takasaki Ion Accelerators for Advanced Radiation Application), an electron accelerator and Co-60 gamma-ray source in Takasaki Advanced Radiation Research Institute, JAEA, from April 2013 to March 2014.

The present report is composed of 169 papers in the following research fields:

1) Space, Nuclear and Energy Engineering,
2) Environmental Conservation and Resource Exploitation,
3) Medical and Biotechnological Application,
4) Advanced Materials, Analysis and Novel Technology,
5) Status of Irradiation Facilities.

In the field of Space Engineering, radiation tolerance of solar cell components and various types of electronic devices has been examined in connection with their space applications. R&Ds of new functional devices such as single photon sources have been also performed by using irradiation techniques. For Nuclear Engineering, practically available results were obtained for radiation stability of Cs or Sr adsorbents, radiation effects on zeolite, cement solidification form, and sludge used for radioactive waste treatment, and radiation resistance of polymer materials and optical devices applied for nuclear facilities. As for structural materials used in light water, fast and fusion reactors, radiation induced microstructural change has been intensively studied using ion beams for pressure vessel steels, fuel claddings and blanket materials at TIARA. For Energy Engineering, high performance polymer electrolyte membranes and electrode catalysts, being suitable for fuel cell application and fluorinated polymer membranes used for hydrogen production and separation filters have been developed by radiation grafting and crosslinking technique.

In the field of Environmental Conservation and Resource Exploitation, radiation grafting technique using γ-rays and electron beams was used to develop fibrous catalysts producing biodiesel fuels as well as adsorbents removing radioactive Cs ions in water. Using the latter material, water purifier was fabricated and its high performance on Cs removal was demonstrated. Improvement of thermal and mechanical properties of various biodegradable polymers has been studied with radiation crosslinking technique for their industrial applications. Hydro-gels produced by crosslinking of hydroxypropyl cellulose were

investigated for denitrification and for the preparation of polymer gel dosimeters, being applied for medical utilization.

In the field of Medical and Biotechnological Application, radiation-induced DNA damage has been investigated and new knowledge was provided. The study on the extent of localization of abasic (AP) sites in solid DNA using Förster resonance energy transfer (FRET) revealed that the level of AP clustering for $^{12}C^{5+}$ were much higher than those for $^{4}He^{2+}$ and ^{60}Co γ-rays, indicating that the clustering of DNA damage depends on LET. To investigate the molecular mechanisms of radiation-induced bystander cell killing, 20-μM of a specific nitric oxide (NO) scavenger "c-PTIO" was added to the culture medium of irradiated normal human lung fibroblasts and non-irradiated cells during irradiation and co-culture. C-PTIO treatment prevented the reduction in survival rates of bystander cells co-cultured with the cells that had been irradiated with 0.5 Gy of γ-rays or carbon ions. This clearly indicates that NO has an important role in the bystander cell-killing effect. On the other hand, the ion microbeam analysis with particle-induced X-ray/Gamma-ray emission (micro-PIXE/PIGE) system for elemental mapping of bio-medical samples was widely utilized to study about a targeted anticancer drug delivery system, pathogenesis of lung injury by inhaled silica, a demineralization preventing effect on a tooth, a method for Cs distribution measurement in plants' cells and so on. Antibodies and peptides labeled with radiometals have great potential for anticancer drug showing high efficacy and low side effects and useful diagnostic drug, because of their high and specific accumulation in cancer. Production of Lu-177 for labeling to antibodies, synthesis of Cu-64 labeled peptides with high affinity to Her2 for PET imaging, and new production methods of radiometals such as Cu-67 and Y-90 by using accelerator neutrons were conducted. The radionuclides are also applied to plant studies on the function of nutrient/pollutant acquisition from the environment, which is crucial for all humanity. A new imaging technology for radiocesium utilizing Cerenkov light was developed. A new analytical algorithm was programmed for estimation of photoassimilate flow speed. Effects of the outer nutrient condition on cadmium uptake by a hyper-accumulator fern were elucidated. The ion beam breeding has been conducted to improve many plants and microorganisms such as chrysanthemums, rice, poplars, yeasts, and fungi. Thermotolerant mutants of entomopathogenic fungi are successfully obtained by the ion-beam and gamma ray-induced mutagenesis. Complex structural changes of DNA are suggested by genetic analyses of high-LET ion beam-induced Arabidopsis mutant lines

showing altered segregation ratios.

In the field of Advanced Materials and Analysis, various materials were developed by applying effects of single-ion, cluster-ions, electrons and gamma-ray irradiations: dehydrogenation catalysis based on Pd/Pt epitaxial film, polyvinylpyrrolidone nanowire/fiber with Au or Pt nanoparticles, polycarbosilane or Sodalite Zeolite membrane respectively for gas or water permeation, SiC nanotubes and PDMS MZ waveguides film for electronic/optical devices, low-impurity charge stripper foils for RCS at J-PARC, hydrogen storage alloy, KMPR resist for proton-beam lithography, and hardness modified AL-Mg-SI alloy. Analyses of characteristics of various materials with and without irradiation were performed using photospectrometry (PL, CL, IL, and Laser-induced breakdown spectroscopy), microscopy (TEM, AFM, SEM), ESR and radiation-applied analysis, e.g. PIXE/PIGE, ILUMIS, IBIC, EELS, AXIC, SXRD, positron annihilation spectroscopy used for current-induced spin polarization, and SPM.

As for the Novel Technology, radiation chemistry studies on radiolysis in water or organic solution and copolymerization of gel were carried out using pulsed and continuous MeV ion beams, respectively. Different kinds of radiation measurements were also studied on a neutron detector based on TOF measurement, wall-less TE proportional counter, fluorescent plate, and a neutrino detector based on Radar reflection/simulation. Characteristics of alanine dosimeter, ionizing chamber, Gafchromic films (HD-V2, EBT3), CVD diamond film, Li-glass and Al_2O_3:C scintillators were examined as new detectors. The fundamental studies on the interaction between MeV/atom cluster ions, e.g. C_2-C_{60}, and target materials were performed on the basis of the measurement of secondary ions/electrons emitted from thin foil targets, and the theoretical simulation of their particle behavior. Technical developments were also in progress on negative-ion source and charge exchange process for getting higher intensity of C_{60} beams, and beam transmission control using nanoporous film or curved insulating channel. Some trial-base applications of cluster ions were also performed on nanowire fabrication, magnetic property change of FeRh, and biomedical molecular imaging for phenylalanine. Developments/improvements of common technology at AVF cyclotron for focusing microbeam irradiation and wide uniform irradiation were in progress besides emittance/acceptance control technique for higher intensity beams. Development of compact focused gaseous MeV ion beam system for 3D printer application was also in progress as off-line experiment.

About the Status of Irradiation Facilities, all the accelerators in TIARA, the AVF cyclotron, the 3-MV tandem accelerator, the 3-MV single ended accelerator and the 400-kV ion implanter, were operated steadily and safely as well as MeV-electron and Co-60 gamma-ray irradiation facilities. Total operation times of the tandem accelerator, the single-ended accelerator and the ion implanter were 40,733, 46,383 and 36,170 hours, respectively, since the beginning of their operation. The total number of experiments made by various users using the AVF cyclotron was 10,336 from the first beam extraction in 1991 to March 2014, as a result of continuous efforts such as regular maintenance and trouble shooting.

Masao Tamada,
Director General
Takasaki Advanced Radiation Research Institute
Sector of Nuclear Science Research
Japan Atomic Energy Agency

1. Space, Nuclear and Energy Engineering

This is a blank page.

1 - 01

Study on Radiation Resistance of Next Generation Space Solar Cells

T. Nakamura [a)], T. Sumita [a)], M. Imaizumi [a)],
S.-i. Sato [b)], H. Abe [b)] and T. Ohshima [b)]

[a)] Aerospace Research and Development Directorate, JAXA,
[b)] Environment and Industrial Materials Research Division, QuBS, JAEA

The space power systems group in JAXA is studying ways to enhance the reliability and performance of power generating solar paddles for space application by reducing their size and weight. There are two important parameters for reducing size, that are conversion efficiency at the beginning of life (BOL) and radiation resistance for bear the severe radiological environment in space. Multi-junction (MJ) solar cells are currently standard power generators for space use since it is high conversion efficiency compared with single-junction (1J) solar cells. Inverted metamorphic triple-junction (IMM3J) solar cells, which attract our great attention as next-generation space solar cells. They have InGaAs bottom subcell instead of Ge in conventional InGaP/(In)GaAs/Ge Triple-junction (3J) solar cells. We aim to develop IMM3J solar cells for space use in order to further enhance conversion efficiency, radiation hardness, and weight saving of solar paddles. In this study, we prepared bare type (no coverglass) InGaP/GaAs/InGaAs prototyped IMM3J and conventional 3J solar cells to compare the radiation hardness. These cells were irradiated with protons and electrons at TARRI, JAEA. Figure 1 shows the performance degradation due to 1 MeV electron irradiation. Closed and open symbols denote the experimental data of IMM3J and conventional 3J solar cells, respectively. The solid and dashed lines depict the fitting results using the following equation: *Remaining factor = (EOL/BOL) = 1- A*log(1+Φ/B)*. The remaining factor (normalized value) of maximum power (Pmax) of IMM3J was slightly inferior to the conventional 3J owing to the degradation of fill-factor (FF). On the other hand, the radiation resistance of IMM3J was superior in terms of short-circuit current (Isc). Therefore, the degradation mechanism of FF in IMM3J should be clarified in order to improve the radiation resistance of IMM3J cells.

We also investigate radiation effects on quantum dot (QD) solar cells, which are considered as the third generation solar cell. Solar cells with QD structure are expected to have extremely high conversion efficiency even in the 1J device [1)]. Also, the development of MJ solar cells with quantum structure is carried out in order to improve the radiation resistance [2)]. We fabricated GaAs PiN solar cells, of which i-layers contain self-organized $In_{0.4}Ga_{0.6}As$ QD layers, and investigated the degradation behavior due to 150 keV proton irradiation. The degradation of GaAs PiN solar cell without QD structure (non-QD) was also investigated for comparison. Protons with energies of 150 keV damage seriously to the interface between QD and base layers, according to SRIM simulation. Figure 2 shows the degradations of FF due to 150 keV proton irradiation. Closed and open symbols denote the experimental data of QD and non-QD solar cells, respectively. The degradations of FF were more remarkable in QD cell than non-QD cell. Since the serious degradation of FF has been similarly found in solar cells with quantum well (QW) structure, it might be due to the introduction of quantum structure. Further investigation is necessary to clarify the cause of the FF degradation.

References

1) A. Luque & A. Marti, Phys. Rev. Lett. 78 (1997) 5014-16.
2) C. Kerestes et al., IEEE J. Photovoltaics 4 (2014) 224-33.

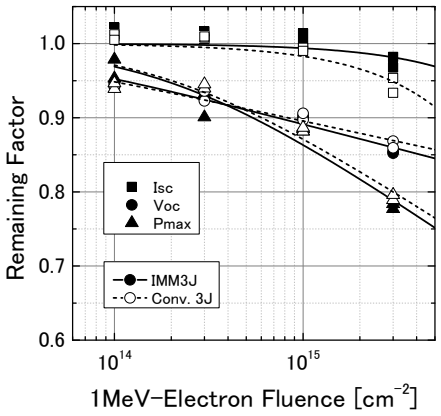

Fig. 1 Degradation curves of Isc, Voc, and Pmax for the IMM3J and conventional 3J cells.

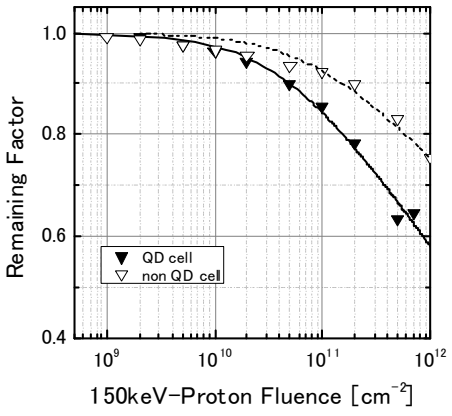

Fig. 2 Comparison of degradation between QD and non-QD cells about FF.

1 - 02 Proton Induced Degradation of GaAs Solar Cells with InGaAs Quantum Dot Layers

S.-i. Sato [a)], T. Ohshima [a)], T. Nakamura [b)], M. Imaizumi [b)], T. Sugaya [c)], K. Matsubara [c)], S. Niki [c)], A. Takeda [d)] and Y. Okano [d)]

[a)] Environment and Industrial Materials Research Division, QuBS, JAEA,
[b)] Aerospace Research and Development Directorate, JAXA,
[c)] Research Center for Photovoltaic Technology, AIST, [d)] Tokyo City University

I. Introduction

The amount of solar array panels mounted on satellites is limited and the required electric power increases day by day. Solar cells with highly stacked layers containing well-aligned quantum dots (QDs) are regarded as promising candidates for space applications as well as terrestrial applications owing to the potential of extremely high efficiency. For example, it was reported that the highest power conversion efficiency for QD solar cells was estimated to be above 60%, if the intermediate band or miniband structures can be formed [1)]. Contrary to the terrestrial use, however, the electrical performance at the end of mission is more important than that at the begging of mission for space use because energetic particles such as electrons and protons in space induce the significant degradation. Therefore, the radiation response of electrical performance should be clarified for space applications.

II. Experimental

Figure 1 shows the schematic cross-section of sample. The solar cells used in this study were GaAs PiN structures, of which i-layers contain self-organized $In_{0.4}Ga_{0.6}As$ QD layers, grown on Si-doped GaAs (001) by Molecular Beam Epitaxy (MBE). The active area of the solar cells was 0.38 $\times$ 0.38 cm^2. Since 50 stacked 2 nm QD layers were grown with 20 nm thick GaAs buffer layer, the thickness of i-layer for the 50 QD solar cell was 1.1 μm. For comparison, GaAs PiN solar cells with an i-layer at a thickness of 1.1 μm were fabricated under the same process without the fabrication of the QD layers (non-QD).

Both solar cells were irradiated with 150 keV and 3 MeV protons under dark conditions. Protons with energy of 150 keV create damage mainly in i-layer (QD layers) whereas protons with energy of 3 MeV create damage mainly in n-type substrate. The electrical characteristics were measured *in-situ* under Air Mass Zero light illumination.

III. Results

Compared to non-QD solar cells, QD solar cells showed higher short-circuit current (Isc) but lower open-circuit voltage (Voc) before irradiation. As a result, the values of output maximum (Pmax) for both solar cells were comparable (12.9-13.8 mW/cm^2). Figure 2 shows degradation of Pmax due to 3 MeV and 150 keV protons. The values of Pmax were normalized the values before irradiation. In the case of 3 MeV protons, the degradation of QD solar cell was slightly smaller than that of non-QD solar cell at the fluence up to 5×10^{12} cm^{-2}. However, the QD solar cell was degraded rapidly at the fluence above 5×10^{12} cm^{-2}, and the non-QD solar cell kept higher value at above 1×10^{13} cm^{-2}. In the case of 150 keV-proton irradiation, the larger degradation was observed since larger damage was expected to be created in i-layer (drift region) compared to 3 MeV protons. However, the degradation behavior of both solar cells due to 150 keV-proton irradiation was similar to that due to 3 MeV proton irradiation.

In this study, we investigated the degradation behavior of QD solar cells due to proton irradiation and compare the radiation resistance to solar cells without QD structure. The obtained results provide the information necessary to clarify the mechanism of radiation degradation and to improve the radiation resistance of QD solar cells.

Reference

1) A. Luque et al., Phys. Rev. Lett. 78 (1997) 5014-16.

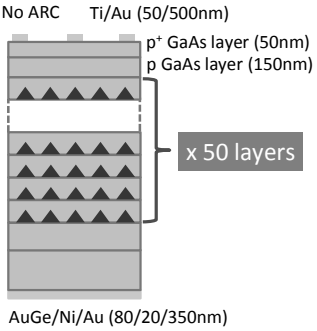

Fig. 1 Schematic cross-section of GaAs PiN solar cells with self-organized $In_{0.4}Ga_{0.6}As$ QD layers.

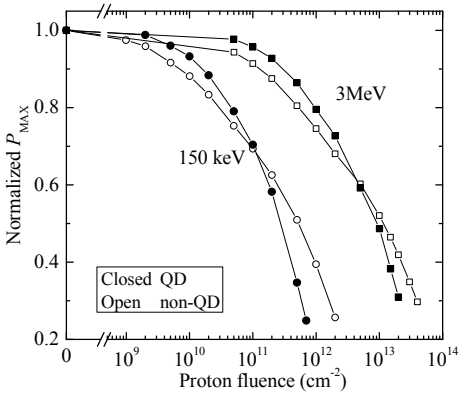

Fig. 2 Degradation of output maximum for QD (closed) and non-QD (open) solar cells irradiated with 150 keV and 3 MeV protons.

1 - 03 Advanced Rad-Hard DICE Circuit for Angled Irradiation on 65nm Bulk CMOS Process

A. Maru[a)], H. Shindou[a)], S. Kuboyama[a)], T. Tamura[a)], H. Abe[b)] and T. Ohshima[b)]

[a)]Aerospace Research and Development Directorate, Japan Aerospace Exploration Agency (JAXA),
[b)]Environment and Industrial Materials Research Division, QuBS, JAEA

Due to the demands for higher density integration and device downsizing, transistors which are used in the logical circuits have been fabricating with less than 100 nm CMOS process. Single-Event Upset (SEU) and Single-Event Transient (SET) phenomena are considered serious problems for those integrated circuits, because their supply voltage and the threshold to the phenomena are also decreasing. It was reported that Dual Interlocked Storage Cell (DICE) circuit is the hardened topology against SEU [1, 2]. However, in highly integrated circuits, it was reported that two neighboring transistors were simultaneously inverted by an incident particle due to the charge sharing mechanism[3]. In such situation, the SEU tolerance of DICE circuits may be invalidated. Therefore, it is important for the design of highly integrated DICE circuits used in space to estimate the extent of the charge sharing.

In the past study[4], we evaluated the effectiveness of the Radiation Hardness By Design (RHBD) approach for 90 nm CMOS process, by using heavy ions from AVF cyclotron at JAEA. The original DICE memory test circuit was fabricated by using 90 nm bulk CMOS process and the angled irradiation testing was performed with this circuit. As a result, SEUs were observed in the original DICE memory circuit when heavy ions were irradiated with grazing angles. This result can be explained by the simultaneous inversion of a critical transistor pair which triggers SEU in the original DICE memory. Due to the penetration of a single heavy ion into the critical transistor pair, SEUs were observed in the previous experiments. To mitigate this we proposed new topology of DICE circuits. In our latest work, we fabricated the new type of DICE circuit named “Hyper DICE” on the 65 nm bulk CMOS process. The test samples were fabricated by Taiwan Semiconductor Manufacturing Company (TSMC). Figure 1 (b) shows the Hyper DICE design concept for mitigating SEUs due to multiple transistor inversion. As shown in Fig. 1 (a), the original DICE is composed by eight transistors and keeps its memory state by two memory nodes.

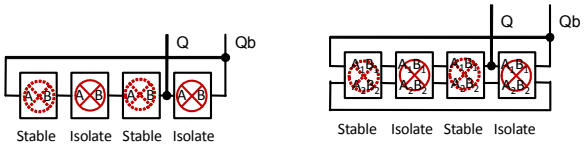

(a) Original DICE circuit (b) Hyper DICE circuit

Fig. 1 Design concept of original DICE and Hyper DICE circuit.

Therefore if two critical transistors of this two memory nodes invert simultaneously, the original DICE memory state upsets. On the other hand, Hyper DICE circuit has four memory nodes to keep its memory state as shown in Fig. 1 (b). Since the Hyper DICE circuit have double memory node than the original DICE circuit, SEUs have never observed by single ion irradiation.

The test samples were evaluated by using heavy ions with LET of 40.3 ~ 68.8 MeV/(mg/cm^2). For the angle irradiation experiments, the test chip was tilted 60 degrees and rotated 0 ~ 360 degrees. Figure 2 shows the angled irradiation test results of the Hyper DICE circuit. The results indicated that sensitive angle exists around the angle of 90 degrees. When the angle is 90 degrees, the irradiated single ion penetrated along the Vdd-Gnd line in the Hyper DICE circuit. Therefore, it is estimated that the critical transistors are making a line along the Vdd-Gnd line. There is the possibility to improve SEU tolerance by modifying transistor layout. We continue evaluating newly developed DICE circuits, and will modify the transistor layout in next stage.

References

1) M. P. Baze et al., IEEE Trans. Nucl. Sci. 55 (2008) 3295.
2) K. Wang et al., Can. Conf. Electron. Comput. Eng. (2009) 1076.
3) A. Amusan et al., IEEE Trans. Nucl. Sci. 53 (2006) 3253.
4) A. Maru et al., IEEE Trans. Nucl. Sci. 57 (2010) 3602.

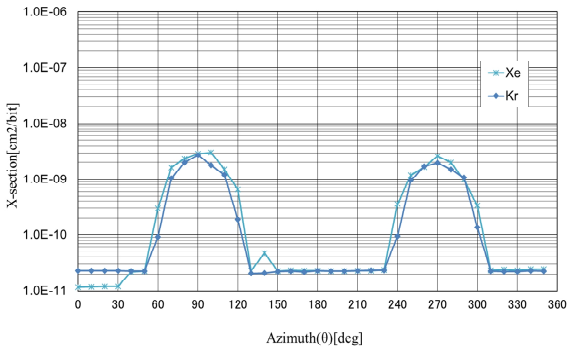

Fig. 2 X-section as a function of the azimuth angle with the tilt angle of 60 degrees in the Hyper DICE circuit.

1 - 04 Gate Oxide Thickness Dependence of Single Event Gate Rupture in SiC MOS Capacitors

M. Deki [a], T. Makino [b], K. Kojima [c], T. Tomita [a] and T. Ohshima [b]

[a] The University of Tokushima, [b] Environment and Industrial Materials Research Division, QuBS, JAEA, [c] National Institute of Advanced Industrial Science and Technology

The catastrophic failure in Metal-Oxide-Semiconductor (MOS) devices induced by the incidence of ions is known as Single Event Gate Rupture (SEGR). The issue of SEGR arises in MOS power devices for not only space but also terrestrial applications led by neutrons created by cosmic rays even on the ground. Silicon Carbide (SiC) is a promising wide-band-gap semiconductor for electronic devices. However, SEGR in SiC MOS devices has not yet been fully understood. It is expected that the provability of SEGR might increase with the electric field applied to devices. Since the electric field in SiC devices must be higher than Si devices, it is very important for development of radiation hardness SiC devices to understand the responses of SEGR. We investigated Linear Energy Transfer (*LET*) dependence of critical electric field (E_{cr}) at which SEGR occurs in SiC MOS capacitors.

The MOS capacitors used in this study were fabricated on an n-type 4H-SiC epitaxial layer either 4.9 or 20 μm thick grown on an n-type 4H-SiC substrate (8° off, Si-face). The gate oxides with two different thicknesses were formed by the pyrogenic oxidation. The thicknesses of the gate oxides were estimated from capacitance-voltage (*C-V*) measurements to be 16.8 ± 2.0 nm and 72.5 ± 12.5 nm. Samples were irradiated with nickel ions at 9 and 18 MeV, krypton ions at 322 MeV, xenon ions at 454 MeV, and osmium ions at 490 MeV. The *LET* of heavy ions was ranged from 14.6 to 94.2 MeV•cm^2/mg. During the ion irradiation the current through the gate oxide of the MOS capacitors was monitored under direct current (DC) biases. They were biased from 1.0 to 14 MV/cm toward the accumulation condition. Because we observed destruction of the gate oxide when the current density was 1 A/cm^2 using optical microscope, we defined the E_{cr} as the electric field at which the current density exceeded 1 A/cm^2.

The currents density through the gate oxide of the 4H-SiC MOS capacitors with and without ion irradiation is shown in Fig. 1 as a function of the electric field applied to the gate oxides. For no-irradiation samples, the current densities below 8 MV/cm are under 10^{-8} A/cm^2. This indicates that the quality of the gate oxides is sufficient with regard to the current density. After increasing gradually, the current density increases sharply to 1 A/cm^2. Although the electric field dependence of the current density is qualitatively similar to all samples, the E_{cr} for an irradiated sample is smaller than that for a sample without irradiation (E_{cr0}) and decreases with increasing *LETs*. This results indicates that SEGR occurs at a lower electric field when ions with a higher *LET* penetrate SiC MOS devices.

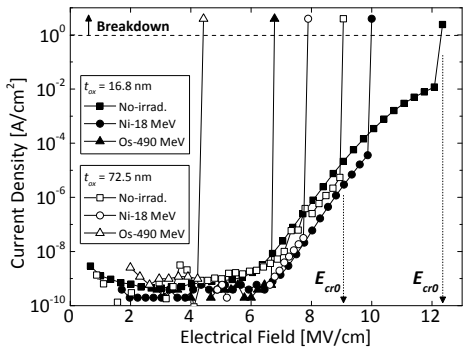

Fig. 1 Leakage current densities of SiC MOS capacitors with and without heavy ion irradiation.

Figure 2 shows the *LET* dependence of the reciprocal of E_{cr} ($1/E_{cr}$) for SiC MOS capacitors with thin and thick gate oxides. The E_{cr} values reported for Si MOS capacitors with 18-nm-thick gate oxide are also plotted in the figure for comparison[1]. For both SiC MOS capacitors with thin and thick oxide, the values of $1/E_{cr}$ increased linearly with increasing *LET*. A linear relation between *LET* and $1/E_{cr}$ has been reported for Si MOS capacitors[1]. However, the slopes of the *LET*-$1/E_{cr}$ lines for Si MOS capacitors was larger than those of the *LET*-$1/E_{cr}$ lines for SiC MOS capacitors. This result suggests that SiC MOS devices are less susceptible to SEGR than Si MOS capacitors, especially in high *LET* regions. For oxide thickness dependence, SiC MOS capacitors with thin oxide showed lower $1/E_{cr}$ values than those with thick oxide at each *LET* value. Thus, this indicate SiC MOS capacitors with thin oxide have higher SEGR resistance than those with thick oxide.

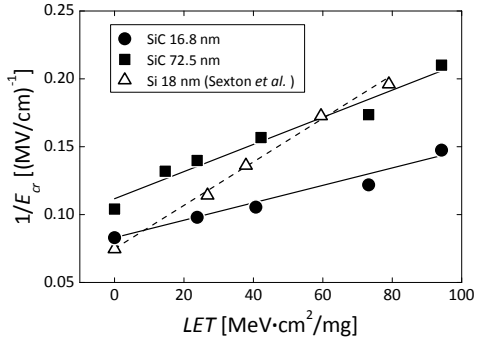

Fig. 2 *LET* dependence of SEGR electric field in SiC and Si MOS capacitors.

Reference

1) F. W. Sexton et al., IEEE Trans. Nucl. Sci. 44 (1997) 2345-52.

1 - 05 Enhancement of Charge Collection by Single Ion in Gallium Nitride (GaN) High Electron Mobility Transistors

S. Onoda [a)], A. Hasuike [b)], Y. Nabeshima [b)], H. Sasaki [b)], K. Yajima [b)] and T. Ohshima [a)]

[a)] Environment and Industrial Materials Research Division, QuBS, JAEA,
[b)] Mitsubishi Electric Corporation

Gallium Nitride (GaN) High Electron Mobility Transistor (HEMTs) is one of the most promising candidates for a high-frequency and high-power Solid-State Power Amplifier (SSPA). The benefit of GaN is that compact, lightweight, and energy-efficient devices operating at high temperature can be developed. Moreover, GaN is known to be resistant to radiation damage owing to its high displacement energy. To use GaN HEMTs in a space radiation environment, it is necessary to perform a reliability test with gamma rays, electrons, protons, neutrons, and heavy ions. In this study, we evaluate the enhanced charge collection in GaN HEMTs by measuring the transient currents induced by a heavy ion.

The high-speed transient currents generated by incident ions are measured with the Transient Ion Beam Induced Current (TIBIC) system at Japan Atomic Energy Agency (JAEA), Takasaki. Figures 1 (a), (b), (c) show the averaged transient gate, drain, and source currents when 18 MeV-Ni ions strike the gate electrode in the off state (V_g= -10 V), pinch-off state (V_g= -2.5 V), and on state (V_g= -1 V). As shown, the positive gate and source currents and the negative drain current are observed for all biases. The absolute drain current is found to be equivalent to the sum of the source and gate currents because of charge neutrality. Figure 1 (d) shows the drain currents as a function of time at various drain biases. It is found that the transient currents increase with increase in applied bias.

The largest charge enhancement is found when 18 MeV-Ni ions strike the center of gate electrode in the pinch-off bias condition as shown in Fig. 1 (b). The collected charges in the pinch-off and on states are several orders of magnitude higher than that in the off state. Similar enhanced charge collection has been observed in other HEMTs and MESFETs. We suggest that the bipolar and the back-channel effects, which are found in other HEMTs and MESFETs [1,2], are associated with an enhanced charge collection. The experimental results suggest that the back-channel effect is a significant enhanced charge collection mechanism in GaN HEMTs [3]. The key point of the back-channel effect is the positive charge accumulation in the GaN layer under the gate. The positive charges reduce the potential barrier between the source and the channel, resulting in the current from the source to the drain. In addition to this, we suggest that the positive fixed charges in the AlGaN layer contribute to the enhanced charge collection. The reason for the largest enhancement at the gate electrode is due to positive charges in both the AlGaN and the GaN layers. To confirm these assumptions, the numerical simulation is required.

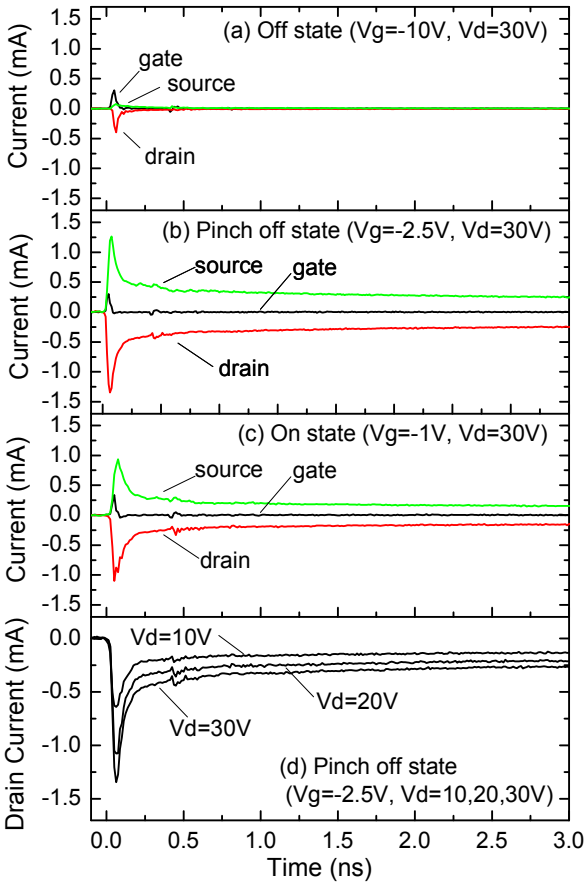

Fig. 1 Averaged transient gate, drain and source currents when 18 MeV Ni ions strike the gate electrode at the following bias configuration; (a) the off state, (b) pinch off state, and (c) the on state. For all cases the drain is biased at +30 V and the source is grounded. (d) the averaged transient drain currents at drain biases of +10, +20, and +30 V, respectively.

References

1) D. McMorrow et al., IEEE Trans. Nucl. Sci. 51 (2004) 2857.
2) S. Onoda et al., IEEE Trans. Nucl. Sci. 59 (2012) 742.
3) S. Onoda et al., IEEE Trans. Nucl. Sci. 60 (2013) 4446.

1 - 06 Assessment of Single Event Effects on H8 Microprocessor and Virtex-5 FPGA at 65 MeV Proton Irradiation

H. Masui, M. Ibrahim, Y. Okumura, T. Tomioka and M. Cho

Laboratory of Spacecraft Environment Interaction Engineering, Kyushu Institute of Technology

1. Introduction

Nano satellite development, typically less than 50 kg has been active in Japanese universities and companies for quite a while. On Board Computers (OBCs) which are used in nano satellites consist of commercial off the shelf (COTS) components. They are usually exposed to Total Ionization Dose (TID) test. Single Event Effect (SEE) test is rarely performed because of the test difficulty, costs and scarcity of available test facilities. However, to ultimately ensure the safe and correct operation of nano satellite, SEE test is necessary to be performed. Actually, SEE occurring on some nano satellites, including Kyutech's satellite "Horyu-2", was reported [1]. The following are the purposes of this fiscal year tests: 1) Establishment of the irradiation test method, 2) Observation of SEE and 3) Checking the SEE mitigation technique and reset system. The tested components were the H8-(36057) and the (Virtex 5-LX50) FPGA.

2. Experimental setup

Figure 1 shows experimental setup schematic. H8 and the FPGA, Device-Under-Test (DUT), were mounted on a PCB plate. A cupper plate covered most of the DUT's surface. The cupper plate had a small aperture (ø7 mm) to pass the proton beam to the DUT. The proton beam condition as energy and flux were: 65 MeV and 1×10^6 to 5×10^7 particles/cm^2/s. The flux was adjusted by an equipped shutter. It was measured by a pico ammeter (Keithley 6485). DUTs were controlled by PCs through serial communication links and remotely monitored over LAN connections. DAQ based on LabVIEW was used to collect voltage and current measurements. DC relay was used to implement a reset system to recover from latch ups and upsets.

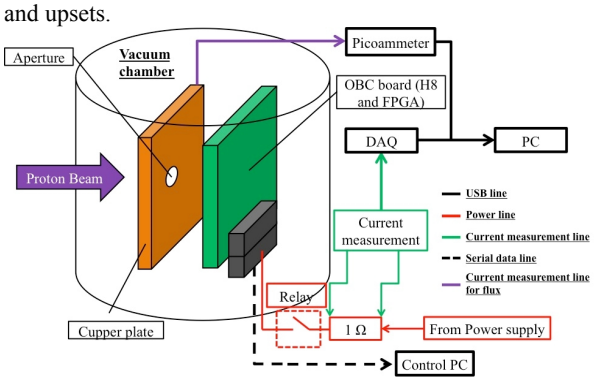

Fig. 1 Schematic of setup.

3. Experimental Results

3.1 H8 microprocessors

With respect to H8 processor, we checked the latch up current and probability of SEE. Table 1 shows the summary of H8. Averaged time to SEL decreased with increasing of flux. However, the latch up current was the same for each flux. From the device cross-section, we could estimate the number of SEE in LEO orbit. Since the nominal flux of proton in LEO is the order of 10^3 particles/cm^2/s [2], the estimated occurrence of SEL is 39.6 times/year for the H8. In Horyu-2 case, it was expected that SEL occurred at least 3 times/year [1]. The difference between experimental results and orbit data seems to be caused by the structure of satellite as aluminum because the OBC mounted on Horyu-2 was not directly exposed to the space.

Table 1 Summary of H8 processor.

Beam Flux [-/cm^2/s]	Averaged time to SEL [s]	Averaged latch up current [A]	Device cross-section [cm^2/device]
4.98×10^7	18.07	0.18	1.11×10^{-9}
1.11×10^7	93.9	0.18	9.56×10^{-10}

3.2 FPGA

SEL was not observed during the tests. SEUs were recorded and used to calculate the average proton static cross section at 65 MeV. Figure 2 shows the count of frame errors versus irradiation time at 2 flux levels. From these results, the average static cross section, based on the upset-bit-cross-section and event-bit-cross-section of the MBUs count, is estimated as 7.13×10^{-14} cm^2/bit and NASA value is 6.37×10^{-14} cm^2/bit [3].

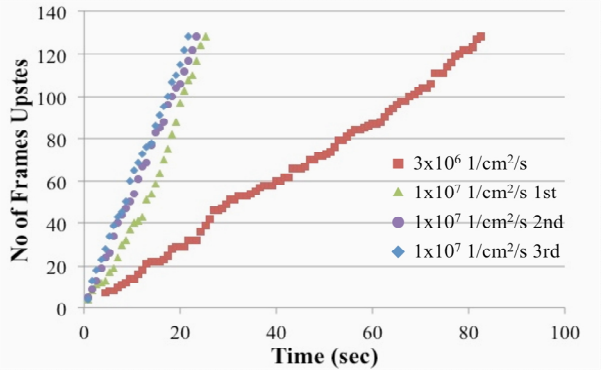

Fig. 2 The count of frame errors versus irradiation time.

References

1) M. Cho et al., Aerospace Technol. 12 (2013)17-24.
2) SPEVIS(URL: https://www.spenvis.oma.be/intro.php).
3) H. Quinn et al., Radiat. Eff. Data Workshop, 2007 IEEE July (2007)177-84.

1 - 07 Characterization of Electrical Properties of Proton Irradiated GaN-based Light Emitting Diode

H. Okada [a)], Y. Okada [a)], H. Sekiguchi [a)], A. Wakahara [a)], S.-i. Sato [b)] and T. Ohshima [b)]

[a)] Department of Electrical and Electronic Information Engineering ,Toyohashi University of Technology, [b)] Environment and Industrial Materials Research Division, QuBS, JAEA

We clarified electrical properties of 380 keV proton irradiated GaN-based light emitting diode (LED). Degradation of electrical and luminescence characteristics were investigated after the proton irradiation of 1×10^{15} cm^{-2}, where the two-terminal resistance of p-type layer of LED showed considerable increase. Lower initial carrier density in p-GaN is a key to explain the properties of proton irradiated GaN-based LEDs.

窒化ガリウム（GaN）に代表される窒化物半導体は、材料系の特徴として機械的、化学的安定性や、広いバンドギャップを有するなどが挙げられ、過酷な環境でも動作する半導体デバイスの実現が可能である。窒化物半導体の発光ダイオード（LED）や窒化アルミニウムガリウム（AlGaN）とのヘテロ構造（AlGaN/GaN)を用いた高電子移動度トランジスタ（HEMT）は、窒化物半導体材料の特長を生かしたデバイスとして活発に研究開発が行われており、前述の特徴と相まって宇宙空間や高温環境下など、シリコンデバイスではカバーできない領域での活躍が期待されている。宇宙空間での利用においては、放射線照射効果の特性を明らかにすることが重要であり、例えば Pearton らは放射線照射した GaN のキャリア密度変化や深い準位の評価などの基礎データをレビューしている[1)]。しかし、特に p-GaN における知見が不足しており、放射線照射による素子特性劣化のメカニズムの包括的な理解には至っていない。我々は、劣化メカニズムの解明に向け、GaN 系 LED 構造の n 型層および p 型層それぞれの陽子線照射効果を調査した。

Figure 1 に本研究に用いた試料の断面図を示す。今回は、市販されている窒化インジウムガリウム（InGaN）量子井戸（MQW）を発光層にもつ GaN LED（発光ピーク波長 λ= 450 nm)を用いて、陽子線照射が電気的特性に及ぼす影響を検討した。LED としての特性を評価するために、リソグラフィー工程によりウェハの一部を誘導性結合反応性エッチング（ICP-RIE）によりエッチングして n 型層を露出させ、p 型層および n 型層にオーミック電極を形成した。ここでは p 型層のオーミック電極には Ag、n 型層のオーミック電極には Ti/Al/Ti/Au を蒸着し、熱処理によりオーミック特性を得た。それぞれの蒸着金属の厚さは 200-300 nm であった。p-GaN 層の厚さは断面 SEM 観察から 250 nm 程度と見積もられた。作製した試料では、p 型および n 型層それぞれの電気的特性変化を評価するために、p 型および n 型層の 2 端子抵抗素子も作製した。デバイス作製後、高崎量子応用研究所 TIARA のイオン注入装置を用いて、真空中、室温にて 380 keV 陽子線を照射した。SRIM を用いたシミュレーションから見込まれる 380 keV 陽子線の飛程は 2-3 μm であり、p 型の電極の上からでも LED の活性層を横切り、n 型層にも十分到達すると予測される。照射量は 1×10^{14} cm^{-2} および 1×10^{15} cm^{-2} とし、熱処理などは施さず、室温での電流-電圧特性を評価した。

Figure 2 に LED の電流-電圧特性をプロットしたものを示す。照射前に比べ, 1×10^{14} cm^{-2} 照射後の特性では、1 V 弱の低順バイアス領域に電流の増加がみられた。これは、陽子線傷照射よる欠陥を介した再結合電流が増加したと考えられる。1×10^{14} cm^{-2} 照射後では、4 V 付近の特性から見積もった直列抵抗に若干の増加が見られるものの、発光強度については大幅な変化はみられなかった。一方、陽子線を 1×10^{15} cm^{-2} 照射した試料では、大幅な電流低下と発光強度の著しい低下が生じた。p 型層および n 型層の 2 端子抵抗の測定から、陽子線照射量に対して特に p 型層が敏感に高抵抗化する振る舞いが見られた。これは p-GaN に添加されているマグネシウム（Mg）の活性化エネルギーが 210 meV[2)]と高く、n-GaN に比べて初期のキャリア濃度を高く出来ないことが大きく影響していると考えられる[3)]。

References

1) S. J. Pearton et al., J. Vac. Sci. Tech. A 31 (2013) 050801.
2) C. G. van de Walle, J. Appl. Phys. 95 (2004) 3851.
3) H. Okada et al., IEICE Trans. Electron. E97-C (5) (2014) 409.

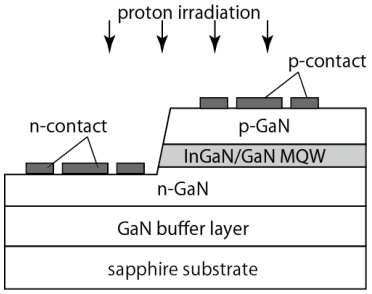

Fig. 1 Sample structure for characterization of proton irradiation effects on GaN-based LED.

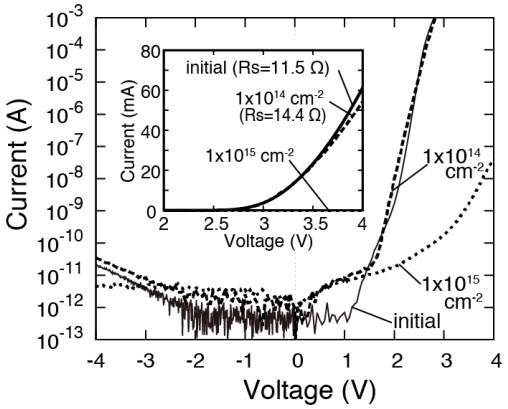

Fig. 2 I-V characteristics of proton irradiated GaN LED in logarithmic plot. Inset shows its linear plot.

1 - 08 Fabrication of Single NV Centers by Low-dose Electron Irradiation of High Purity Diamond

J. Isoya [a], T. Umeda [b], S. Onoda [c], H. Abe [c] and T. Ohshima [c]

[a] Research Center for Knowledge Communities, University of Tsukuba,
[b] Faculty of Pure and Applied Science, University of Tsukuba,
[c] Environment and Industrial Materials Research Division, QuBS, JAEA

NV (nitrogen-vacancy) center in diamond is a pair of substitutional nitrogen and adjacent vacancy. The negatively charged state (NV^-, S=1) has unique properties as solid-state spin qubit such as optical initialization, optical readout, and long coherence time, all at room temperature (RT). NV centers are observable as single centers at RT by confocal microscopy (CFM).

NV centers are fabricated as radiation damages by electron irradiation and subsequent annealing (800 °C to 1,000 °C). Among nitrogen impurity (N_s^0) in a crystal, a part contributes to form NV by trapping vacancy created by electron irradiation, while the rest plays a role of donors to stabilize the negative charge state (NV^-). The NV centers ($[NV^-]$ = ~3 ppm) produced in a type-Ib synthetic high-pressure high-temperature (HPHT) crystal have been utilized as hybrid system of superconducting qubit and ensemble of electron spins [1]. We have extended the method of fabrication of NV to high purity diamond crystal by using 2 MeV electron irradiation of low dose (1×10^{11} to 5×10^{12} cm^{-2}).

(1) Nitrogen distribution in high purity HPHT crystal

The distribution of nitrogen in a HPHT crystal is non-uniform depending strongly on the growth sectors. We have created single NV centers in high purity ($[N_s^0]$=4 ppb measured by electron spin resonance) type-IIa HPHT crystal. The NV centers are observed in {100} growth sectors ($[NV^-]$~0.001 ppb) but not in {111} growth sectors by CFM. Thus, the original non-uniform distribution of N_s^0 has been revealed by the distribution of NV centers formed from N_s^0, even in the low nitrogen concentration.

(2) QEC (quantum error correction) using hybrid quantum register

ODMR (optically detected magnetic resonance) of individual NV centers have been taken for the NV centers formed by electron irradiation and annealing of ^{12}C 99.8% enriched high purity ($[Ns^0]$<1 ppb) CVD (chemical vapor deposition) single crystal diamond. A center exhibiting resolved hyperfine spectrum of two ^{13}C nuclei located at ~0.4 and ~0.6 nm away from the electron spin in addition to ^{14}N has been selected from ~3,000 NV centers. The NV center has been utilized as hybrid quantum register of three nuclear spin qubits and an ancillary electron spin for demonstrating QEC. Quantum information of qubits is easily lost by unavoidable environmental noise. Thus, QEC is essential for scale-up of quantum-computing, otherwise the number of gate operations is severely limited by the coherence time. Nuclear spins are qubits of extraordinary long coherence time at RT. However, two-qubit and three-qubit gates are slow due to weak interaction between nuclear spins. Here, three nuclear spins are coupled to electron spin. This ancillary electron spin has been utilized not only to attain fast two-qubit CNOT and three-qubit CCNOT gates but also to initialize with high fidelity (99%) and readout, in single-shot, nuclear spin qubits, individually. As a reliable three-qubit quantum register, experimental implementation of three-qubit QEC code, first time for solid-state spin qubits at RT, has been achieved (Fig. 1)[2].

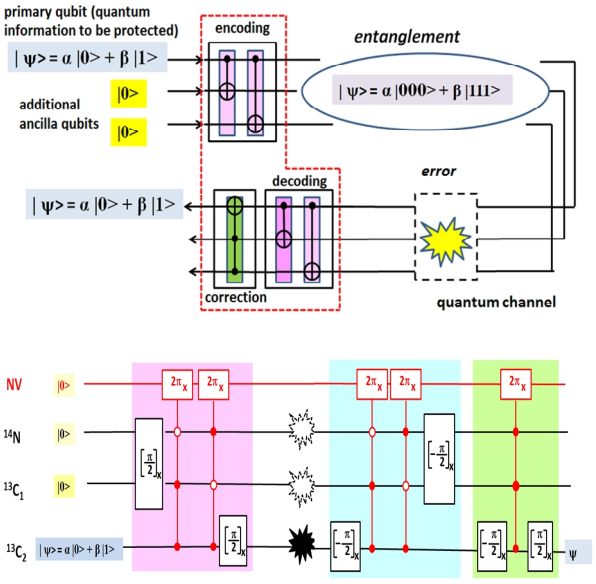

Fig. 1 Three-qubit QEC code and quantum circuit implemented in the experiment.

Acknowledgements

The present work has been carried out as collaboration with Prof. F. Jelezko (University of Ulm) and Prof. J. Wrachtrup (University of Stuttgart).

References

1) K. Kubo et al., Phys. Rev. Lett. 107 (2011) 220501.
2) G. Waldherr et al., Nature 506 (2014) 204.

1 - 09 Development of a Time Projection Chamber for Heavy Ion Tracking Using QPIX Device

M. M. Tanaka [a)], T. Fusayasu [b)], T. Hasegawa [a)], T. Makino [c)], A. Matsuzawa [d)], K. Miuchi [e)], M. Miyahara [d)], R. Miyashita [b)], T. Ohshima [c)], S. Onoda [c)] and A. Sugiyama [b)]

[a)] Institute of Particle and Nuclear Studies, KEK, [b)] Graduate School of Science and Engineering, Saga University, [c)] Environment and Industrial Materials Research Division, QuBS, JAEA, [d)] Graduate School of Engineering, Tokyo Institute of Technology, [e)] Graduate School of Science, Kobe University

We have been developing a CMOS pixel device (QPIX) using 0.18 μm process as shown in Fig. 1. The pixel size is 200 μm^2, and 20 times 20 pixels are implemented on a silicon chip. Each pixel is composed of two main blocks: the analog block consisting of the amplifier, the integrator, the comparator and the Successive Approximation Analog-Digital Converter (ADC); and the digital block mainly consisting of the pixel control logic, the 14-bit Time-of-Flight (TOF) counter, the 10-bit ADC resister and the 8-*b*it Time-over-Threshold (TOT) register. The system clock of 100 MHz determines the timing resolution of TOF and TOT. The pixel size is 200 μm × 200 μm, and the size of active circuit area is 130 μm times 140 μm. The QPIX measures a charged particle track by the x-y position of the pixel and the z position by TOF, and the energy deposit (Q) is measured by ADC [1,2].

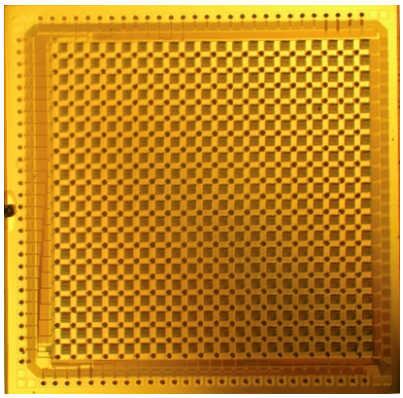

Fig. 1 Micrograph of QPIX chip. The size is 25 mm^2.

The TOT scheme is employed for dE/dx measurement in other ASIC developments, but TOT depends on the particle incidence angle to QPIX (e.g. TOT of a perpendicular track is smaller than that of a parallel track to the Time Projection Chamber:TPC electric field). Therefore we employ ADC for dE/dx measurement.

We developed a TPC shown in Fig. 2. The length of the drift region is 28 mm. The beam is injected in the drift region, and electrons generated by heavy ion drift to the Gas Electron Multipliers (GEM). After electron amplification by GEM, electrons generate mirror charge on the electrode on QPIX.

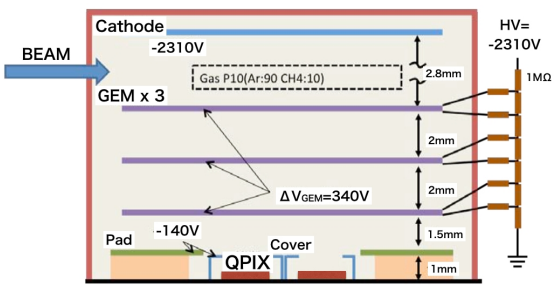

Fig. 2 Cross section of the time projection chamber for heavy ion beam test at TIARA.

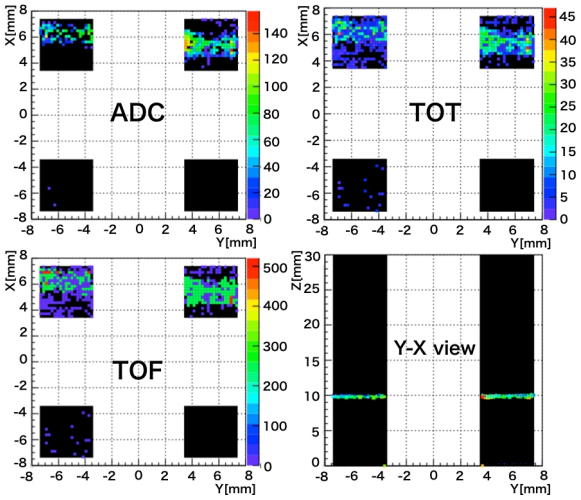

Fig. 3 Event display of the QPIX-TPC beam test. The color indicates ADC, TOF and TOT count.

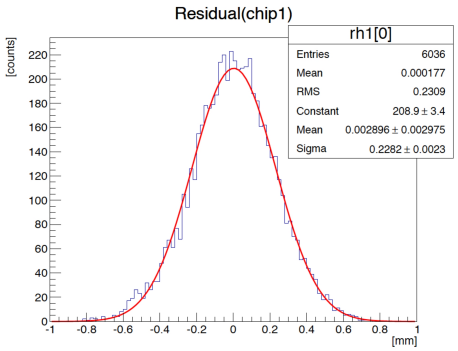

Fig. 4 Residual distribution from fitted tracks. The resolution is 230 μm, because non uniformity of electric field affects the resolution due to the cover at the edge of QPIX and the hole pitch on the GEMs.

We used 335 MeV O^{7+} beam. As shown in Fig. 3 and Fig. 4, QPIX-TPC successfully observed three dimensional ion tracks and its dE/dx.

References

1) A. Matsuzawa et al., Nucl. Instrum. Meth. Phys. Res. A 623 (2010) 477-79.
2) Fei Li, Doctor thesis (2012) Tokyo Institute of Technology.

1 – 10 Radiolytic Stability of Metal Hexacyanoferrate Film as Adsorbent for Recovery of Cesium Ion

M. Arisaka [a)], M. Watanabe [a)], M. Ishizaki [b)], M. Kurihara [b)], R. Chen [c)] and H. Tanaka [c)]

[a)] Division of Chemistry for Nuclear Engineering, NSED, JAEA,
[b)] Department of Material and Biological Chemistry, Faculty of Science, Yamagata University,
[c)] Nanosystem Research Institute, National Institute of Advanced Industrial Science and Technology

Introduction

Metal hexacyanoferrate, MHCF, is known as an adsorbent for selective adsorption of cesium (Cs) ion in solutions. In nuclear industry, applications of MHCF to recovery of Cs from high level radioactive wastes have been studied. Recently, we reported an electrochemical application of MHCF (M = Fe, Cu or Ni) film for Cs recovery from nitric acid (HNO_3) solutions. It was found that Cs loading and unloading can be easily controlled by modulating the film potential[1,2)]. Although it was revealed that radiolytic decomposition of MHCF powder in HNO_3 solution can be ignored[3)] in the adsorbed dose range from 50 - 300 kGy, the stability of MHCF film is not investigated.

In this study, the influence of irradiation with gamma-rays to MHCF films on stability in HNO_3 solutions was investigated.

Experimental

Irradiated sample is a SUS316L plate coated by MHCF film soaked into 0.5 and 1.0 mol/dm^3 HNO_3 solution. MHCF used in this study is as follows; $Fe^{III}_4[Fe^{II}(CN)_6]_3$ (FeHCF), $Cu^{II}_3[Fe^{III}(CN)_6]_2$ (CuHCF), $Ni^{II}_3[Fe^{III}(CN)_6]_2$ (NiHCF).

Irradiation with gamma-rays was done at the Co-60 gamma ray irradiation facilities in Takasaki Advanced Radiation Research Institute of JAEA. Samples in glass tubes were intermittently irradiated with gamma-rays from 1.0×10^{16} Bq ^{60}Co source at an absorbed dose rate of 10 kGy h^{-1} in air at room temperature for a maximum of 27 hours. A dose absorbed by each sample was corrected for an electron density. Absorbed doses were calibrated by a cellulose triacetate film dosimeter.

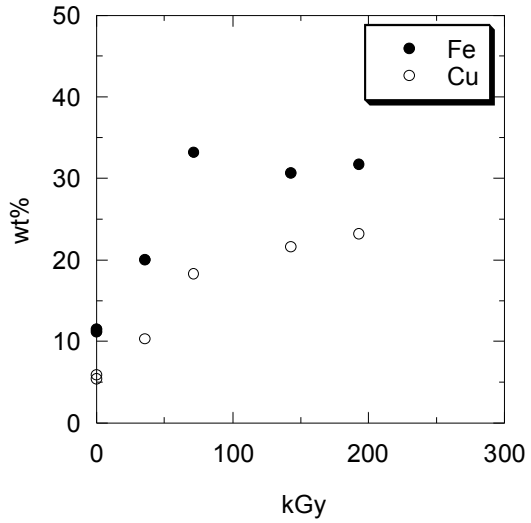

Fig. 1 Weight percents (wt%) of Fe and Cu dissolved into 1.0 mol/dm^3 HNO_3 to initial weight of CuHCF.

For evaluation of radiolytic stability of MHCF film, HNO_3 solutions were separated from the sample by filtration after the irradiation, and amounts of M were determined by ICP-MS.

Results and Discussion

The weight percent (wt%) of M (M = Fe, Cu or Ni) dissolved into 0.5 and 1.0 mol/dm^3 HNO_3 to initial weight of MHCF was determined. As an example, the result for CuHCF film soaked into 1.0 mol/dm^3 HNO_3 is shown in Fig. 1. It was found that the wt% of M increased gradually until 70 kGy, and then kept constant independent of further adsorbed dose. Similar dissolution behaviors were observed for FeHCF and NiHCF. The result under 0.5 mol/dm^3 HNO_3 condition was almost equivalent to that under 1.0 mol/dm^3 HNO_3 condition for three MHCF examined in this study. This indicates that HNO_3 would not participate in the radiolytic decomposition of MHCF film in this system.

The evaluation for electrochemical Cs adsorption ability using the irradiated MHCF films is in progress now. On the other hand, take the stability of MHCF film into account, it is necessary to develop the fixation method of MHCF because the stability of MHCF powder is high under same experimental condition, i.e., the wt% of dissolved M; 0.05% at 300 kGy[3)].

Acknowledgement

Present study includes the result of "Compact and reusable cesium recovery system by electrochemical adsorption/desorption" entrusted to JAEA and AIST by Japan Science and Technology Agency (JST).

References

1) R. Chen et al., Electrochem. Commun. **25** (2012) 23.
2) R. Chen et al., Electrochim. Acta **87** (2013) 119.
3) M. Arisaka et al., JAEA Takasaki Annu. Rep. 2012 JAEA-Review 2013-059 (2014) 19.

1 - 11 Cyanide Generation from Adsorbents Containing Ferrocyanides and Polyacrylonitrile by Gamma Irradiation

Y. Itoh, Y. Saitoh and J. Kojima

Tokai Reprocessing Technology Development Center, NFCEL, JAEA

Treatment of low-level radioactive liquid wastes (LLW) generated from Tokai reprocessing plant are planned in Low-level radioactive Waste Treatment Facility (LWTF).

By treatment of co-precipitation and ultra-filtration in the LWTF, the LLW consist of highly concentrated sodium nitrate containing radioactive nuclide (137Cs and 90Sr).

NiFC-SG and READ-Sr are known as adsorbents for selective adsorption of 137Cs or 90Sr from solutions [1]. Here, NiFC-SG is made from nickel ferrocyanides ($Ni_2Fe(CN)_6$) -loaded silica gels. READ-Sr is made from sodium titanate and polyacrylonitrile (PAN, $[CH_2CH(CN)]_n$), the PAN is used as binder.

However it is necessary to confirm cyanide generation by radiolysis of the ferrocyanides and the PAN contained in these adsorbents, because the cyanide is hazardous substance for its disposal.

In this study, each NiFC-SG and READ-Sr adsorbents were contacting with simulated LLW (5 M $NaNO_3$ solution) or demineralized water in a vial at room temperature, and were irradiated with Co-60 gamma-rays at a dose rate of around 3 kGy/h. The maximum accumulated dose of each adsorbent was around 2.2 MGy.

After the gamma irradiation, the adsorbents were separated from the contacted solution, and the remained solution was centrifuged to provide for analysis. The cyanide concentration was determined by colorimetry with pyridine-pyrazolone.

Figure 1 shows the cyanide concentration generated by the NiFC-SG and READ-Sr adsorbents contacting with the simulated LLW or the demineralized water.

In the NiFC-SG adsorbents, the cyanide concentration in the simulated LLW increased with the absorbed dose, but the cyanide concentration in the demineralized water was less than 0.3 mg/L and independent on the absorbed dose.

On the other hand, in the READ-Sr adsorbents, the cyanide concentration increased with the absorbed dose in the both cases. And also, in the simulated LLW, it was found that the cyanide concentration in the case of the READ-Sr adsorbents was higher than the NiFC-SG adsorbents. Thus PAN is likely to generate cyanide by gamma irradiation compared with ferrocyanides.

Nitrous acid ion was generated in the simulated LLW by radiolysis of nitrate ion. We investigated the correlation between the cyanide concentration and the nitrous acid ion. As shown in Fig. 2, it was confirmed that the cyanide concentration from the NiFC-SG adsorbents linearly increased with the nitrous acid ion concentration.

Therefore it was considered that the cyanide generated from the ferrocyanides in the simulated LLW was due to the influence of the nitrous acid generated by gamma radiation.

In future studies, we are planning to apply inorganic adsorbents without ferrocyanides and PAN.

Acknowledgements

We would like to thank Professor Dr. Hitoshi Mimura, Mr. Shunsuke Susa of Tohoku University and Mr. R. Yamagata at Irradiation Service Section in TARRI for their advice and assistance on the experiment.

Reference

1) H. Mimura, S. Susa et al., ICONE22 Conference, No. 30329, July 7-14 (2014) Prague, Czech.

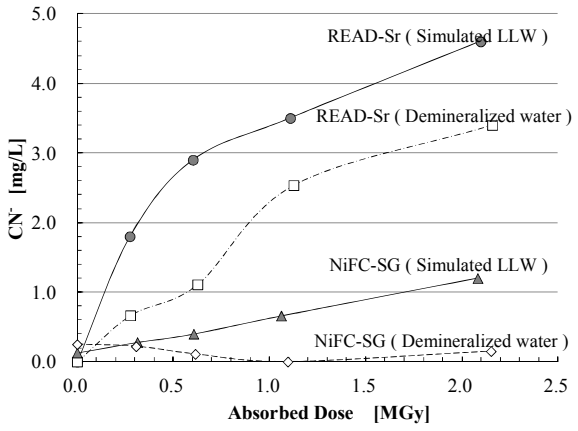

Fig. 1 Cyanide(CN^-) generation from NiFC-SG and READ-Sr in the simulated LLW or demineralized water.

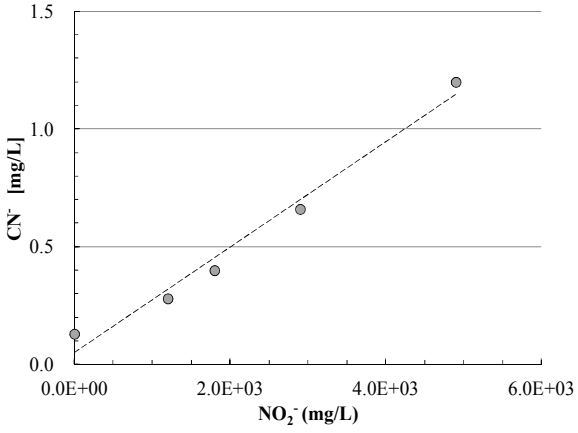

Fig. 2 Relationship between cyanide(CN^-) concentration and nitrous acid concentration generated by the NiFC-SG contacting with simulated LLW.

1 - 12 Electron Beam Irradiation on the Titanate Adsorbent for Sr Recovery

S. Watanabe, M. Nakamura, A. Shibata, K. Nomura and Y. Nakajima

Department of Fukushima Technology Development, NFCEL, JAEA

A titanium oxide based compound (titanate salt) is one of candidates for radioactive Sr recovery from liquid waste generated in the nuclear facility. ^{90}Sr is one of the most important nuclides, which should be removed from the waste before releasing it into the environment due to its strong beta-ray decay energy. The titanate is well known to show excellent ion exchange performance on a divalent cation adsorption, and is employed in the Advanced Liquid Processing System (ALPS) for radioactive Sr decontamination[1]. The spent adsorbents are planned to be filled in the waste storage container (HIC) and stored in the temporary storage facility. However, their resistance to radiations from radioactive elements adsorbed is not widely investigated so far, and the durability against radiations is necessary to be investigated for the safe storage. In this study, we synthesized a hydrous titanic acid ion exchanger according to an article[2], and Sr adsorption performances of irradiated adsorbent and resistance to beta-ray irradiation were evaluated.

The beta-ray emission from ^{90}Sr was simulated by electron beam from 1st accelerator. One g of the cation exchanger initially kept Sr in it and 10 mL of water were put in stainless dish and sealed by kapton film. Then they were irradiated by 1 mA of the electron beam for 30-60 min. Incident energy of the electron was parametrically changed. The dose rate of the incident beam with contribution of backscattered electron from the dish was measured by cellulose triacetate dosimeters. Durability of the cation exchanger against electron beam irradiation was evaluated through changes in Sr concentration of the water and in local structure by batch wise adsorption experiments and Sr and K-edge Extended X-ray Absorption Fine Structure (EXAFS) measurements, respectively. The EXAFS measurements were carried out at BL27B beamline of Photon Factory in High Energy Accelerator Research Organization (KEK), Japan.

As shown in Fig. 1, appearance of the color change of adsorbent changed from white to yellow after the electron beam irradiation. The change in the appearance was not observed during heating up to 373 K though weight of the adsorbent decreased in 67%, therefore the electron irradiation possibly influenced on structure of the titanate.

The irradiation conditions and the concentration of Sr eluted are shown in Table 1. Some part of Sr initially kept in the cation exchanger was eluted after the irradiation. Amount of the eluted Sr after 30 min irradiation with 1 MeV electron was about 1% of the initially absorbed, and the amount increased with increasing the dose. However, the elution of Sr was suppressed when the incident energy was changed during the irradiation. Therefore, interaction between electrons and the titanate is considered to depend on the incident energy of the electron.

Sr-K EXAFS analysis revealed that the number of the nearest O around Sr decreased by the irradiation while the nearest Sr-O distance did not changed. It is reasonable to consider that the elution of Sr was attributed to defects of O in the titanate caused by the electron irradiation.

Fig. 1 Titanete adsorbent (left; before the irradiation, right; after the irradiation).

References

1) Tokyo Electric Power Company, Handouts at press conference 2012, June 25 (2012).
2) T. Fujiwara, JAEA-Testing 2012-004 (2012).

Table 1 Composition of the supernatant solution at before and after the irradiation.

Irradiation conditions	Dose rate (kGy/s)	Irradiation Dose (MGy)	Sr eluted (mg/L)
1 MeV, 1 mA × 30 min	0.75	1.4	21
1 MeV, 1mA × 60 min	0.75	2.7	25
0. 5 MeV, 1mA × 10 min	0.45	1.4*	11
1 MeV, 1mA × 10 min	0.75		
2 MeV, 1mA × 10 min	1.05		

*The dose rate was changed during the irradiation, and the irradiation dose was total value.

1 - 13 Characterization of Composite Adsorbent for Minor Actinides by Micro-PIXE Method (2) Internal Distribution of Metallic Cation

Y. Takahatake [a)], S. Watanabe [a)], Y. Nakajima [a)], Y. Koma [a)], K. Sano [b)], T. Arai [b)], T. Satoh [c)] and M. Koka [c)]

[a)]Department of Fukushima Technology Development, NFCEL, JAEA, [b)]Shibaura Institute of Technology, [c)]Department of Advanced Radiation Technology, TARRI, JAEA

We have been developing the extraction chromatography technology to recover minor actinides (MA; Am and Cm) from spent fast reactor fuels at JAEA. The adsorbent is prepared by impregnating an extractant into the SiO_2-P which is a porous silica particle (ca. 50 μm in its diameter) coated with styrene-divinylbenzene polymer as a binder. In some cases, the recovery rate of the target metals was found to be insufficient, and it suggests that a part of the target metals was retained in the adsorbents. Analyzing the distribution of metallic cation which is adsorbed inside the particle will bring us the indication to optimize the adsorbent structure for better separation. The micro-PIXE analysis was applied to the MA adsorbent to obtain the information about distribution of adsorbed elements in the particle. It was found that the count ratio of the adsorbed element (Nd) to Si of SiO_2-P was available for the index of amount of remaining metal element inside the adsorbent particle. In adition, it was observed that the count ratios of the particles after certain elution time varied widely[1)]. In this study, the Nd/Si count ratios were obtained considering relations among elution time and its relative standard deviation (RSD) with using model adsorbents prepared by the simulated process of the chromatography.

A series of the adsorbents were analyzed by the micro-PIXE at TIARA. The extractant was *N,N,N',N'*-tetra-*n*-octyl- diglycolamide (TODGA), and its mass fraction in the adsorbent was 33.3%. Neodymium, as a simulant of minor actinides, was adsorbed into the adsorbent from the neodymium nitrate solution ([Nd] = 0.01 M, $[H^+]$ = 5 M), and eluted with the 0.01 M nitric acid solution for 10, 60 minutes, and 24 hours by batchwise experiment at room temperature. Particles of the adsorbent were fixed on a polycarbonate film and then each particle was irradiated with proton beam to obtain images of 128×128 pixels. Six to twelve adsorbent particles for each elution time (refer to Table 1) were analyzed to obtain their Nd/Si ratio. Figure 1 shows the obtained spectra. The count ratio of Nd to Si was calculated by dividing the integrated count of Nd peak at 459 ch in the high-energy spectrum by that of Si peak at 176 ch in the low-energy spectrum.

Table 1 shows values of the average Nd/Si count ratio and RSD. The dispersion of the Nd/Si count ratio on condition of no elution suggests that spatial distribution of the extractant on the particle was not uniform. Decrease of the Nd/Si count ratio from 0 to 10 minutes was larger than that from 10 to 1,440 minutes. This phenomenon indicates that Nd which was adsorbed in the near-surface area of the particle was easily eluted, while elution of Nd adsorbed around the center of particle was slow. And Nd was retained in the particle after 24 hours elution. The slow elution of Nd suggests that an eluent hardly reaches the deep part of the particle. The dispersion of the Nd/Si count ratio for 24 hours elution suggests that the shape of pore of the silica particle was not uniform. Therefore, the particle structure should be improved for better elution by enhanced diffusion of an eluent.

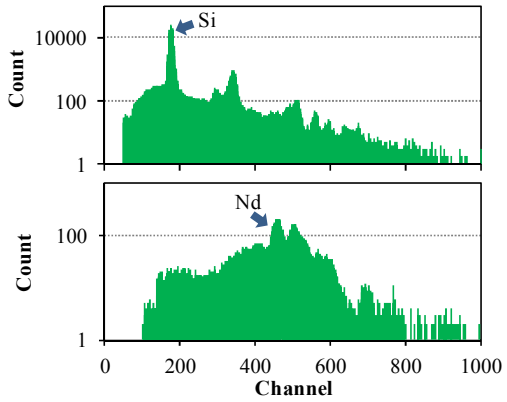

Fig. 1 Characteristic X-ray spectra of the particle of MA adsorbent obtained by micro-PIXE analysis before elution. The upper and lower spectra were obtained by the independent detectors for low and high-energy X-rays, respectively.

Table 1 Mean values of Nd/Si count ratio and their RSD for each elution time.

Elution time (min)	Number of particles analyzed	Mean value of the count ratio of Nd to Si	RSD (%)
0 (no elution)	12	0.67	50
10	7	0.35	26
60	6	0.38	50
1440	8	0.25	67

Reference

1) Y. Takahatake et al., JAEA Takasaki Annu. Rep. 2012 JAEA-Review 2013-059 (2014) 18.

1 - 14 Effect of Gamma Radiolysis on Pit Initiation of Zircaloy-2 in Artificial Seawater

T. Motooka, A. Komatsu, T. Tsukada and M. Yamamoto

Division of Fuels and Materials Engineering, NSED, JAEA

In the Fukushima Daiichi Nuclear Power Station (1F), seawater was injected into spent fuel pools (SFPs) in March 2011. The maximum chloride concentration in the water of the SFPs was estimated to be approximately 2,500 ppm and the concentration had decreased to less than 20 ppm as a result of desalination[1].

Zircaloy-2 (Zry-2) is adopted for the fuel cladding alloy at 1F. Zirconium alloys including Zry-2 are susceptible to pitting corrosion in aqueous chloride solutions with oxidizing ions, such as Fe^{3+} or Cu^{2+}[2]. Spent fuels stored in the SFP were highly radioactive and capable of causing water to decompose into highly oxidizing species (e.g., H_2O_2). It is believed that these radiolysis products might affect the pitting corrosion behavior of the Zry-2 cladding. However, the effect of the radiolysis products in seawater on the pitting corrosion of the Zry-2 cladding is not well known. Therefore, we evaluated the effect of the radiolysis products of seawater on the pitting corrosion of the Zry-2 cladding in this study.

The pitting potentials, which are the least positive potential at which pits can form, of the Zry-2 cladding were measured as a function of chloride concentration with and without gamma-rays radiated from Co-60 source. Test solutions were prepared by artificial seawater (ASW) and distilled water. Figure 1 shows the relationship between chloride concentration and the pitting potential of the Zry-2 cladding obtained in ASW and diluted ASWs at room temperature with and without gamma-ray irradiation. The measurements were carried out at least five times where the scattering of the data was taken into account, and the minimum value was plotted. The figure shows that pitting potential increased with decreasing chloride concentrations in both irradiated and non-irradiated cases. Chloride is the main aggressive anion responsible for pitting corrosion of the Zry-2 cladding, and pitting potential depends linearly on the logarithm of the chloride concentration. In the case of 1/1,000ASW (the ratio of ASW to distilled water is 1 to 999), the pitting potential of the Zry-2 cladding under gamma-ray irradiation was obviously higher than that under non-irradiation. This shows the pit initiation was difficult under gamma-ray irradiation in the diluted seawater.

Closed glass tubes filled with ASW and ASW diluted by water were irradiated at dose rates of 5 kGy/h at room temperature for up to 100 h. One of highly oxidizing species H_2O_2 was detected in both the solutions. The concentration of H_2O_2 was increased with irradiation time. The final concentration of H_2O_2 was 3 ppm in non-diluted ASW and was 5 ppm in 1/1,000ASW.

The thickness of the resultant oxide films formed on the Zry-2 cladding were investigated by X-ray photoelectron spectroscopy (XPS) for samples immersed in 1/1,000ASW for 100 and 720 h with irradiation at a dose rate of 5 kGy/h and without irradiation. The oxide film was composed of zirconium oxide. Thicker oxide films were formed during the irradiation as given in Table 1. Considering the results of the irradiation test of ASW and ASW diluted by water, the oxide film would have been thickened by H_2O_2 under the irradiation. The higher pitting potential in diluted ASW under irradiation, as seen in Fig. 1, is explained by the thicker oxide formation by H_2O_2 production.

Accordingly, the surface of the Zry-2 cladding was found to have higher resistance to pitting corrosion under gamma irradiation.

References

1) http://www.tepco.co.jp/en/nu/ fukushima-np/images/ handouts 121012 05-e.pdf.
2) ASM Handbook Volume 13 Corrosion, ASM International (1996) 717.

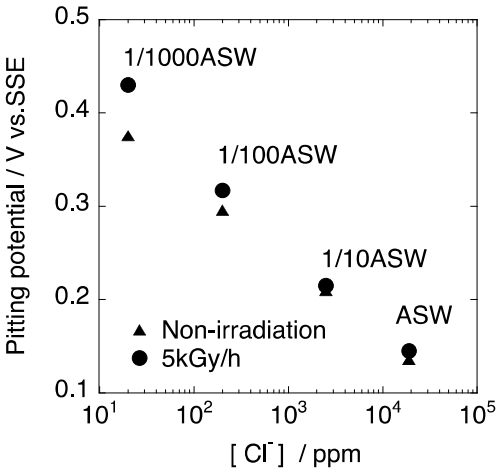

Fig. 1 Pitting potential of the Zircaloy-2 cladding at room temperature with and without gamma-ray irradiation. SSE: Sat. KCl-Ag/AgCl electrode. 1/1,000ASW: ASW/distilled water = 1/999. 1/100ASW:ASW/distilled water = 1/99. 1/10ASW:ASW/distilled water = 1/9.

Table 1 Oxide film thickness by XPS analysis (nm).

Non-irradiation		Irradiation at 5 kGy/h	
100 h	720 h	100 h	720 h
9.6	11.0	12.6	14.4

1 - 15 Electrochemical Properties of Stainless Steel in Zeolites Containing Diluted Artificial Seawater under Gamma-ray Irradiation

C. Kato, T. Satoh and U. Nakano

Fukushima Project Team, NSRI, JAEA

As a part of consideration for long-term storage of spent zeolite adsorption vessels in the Fukushima Daiichi nuclear power station, corrosion of vessel material is one of the important issues. Because seawater was used to cool the reactor core, type 316L stainless steel (316L SS), structural material of the spent zeolite adsorption vessel is exposed to residual chloride and adsorbed radioactive isotopes. However, combined effect of chloride and irradiation on corrosion behavior of the 316L SS has not been fully studied. In this study we performed electrochemical tests of 316L SS in the zeolite containing artificial seawater under gamma-ray irradiation.

Figure 1 shows a schematic diagram of electrochemical cell under gamma-ray irradiation. Herschelite (used in the actual adsorption system), and Natural Mordenite (obtain in Ayashi, for reference) were used as zeolite materials. 316L SS was packed in the zeolites as shown in Fig. 1. Solution was air-saturated diluted artificial seawater (Cl^-=2,000 ppm). Temperature was set at 60 °C taking decay heat of the adsorbed RIs in the vessel into consideration. Co-60 was used for gamma-ray source and dose rate was set at 5 k and 400 Gy/h. Steady corrosion potential, E_{sp}, and pitting potential ,V'_{C100}, of 316L SS were measured. The V'_{C100} was determined on anodic polarization curve at which current density reaches at 100 $\mu A \cdot cm^{-1}$.

Figure 2 shows anodic polarization curves of type 316L SS. There was no difference in V'_{C100} between non-irradiation and 400 Gy/h irradiation. At a dose rate of 5 kGy/h, passive state of stainless steel disappeared because corrosion potential exceeded V'_{C100}, and so, V'_{C100} was not obtained. It was understood that the anodic polarization curve of type 316L didn't depend on gamma-ray irradiation.

Figure 3 shows change in open circuit potential (E_{ocp}) of 316L SS under gamma-ray irradiation (at dose rate of 400 Gy/h). The E_{ocp} was shifted to nobler direction when irradiation was started, while degree of the shift was suppressed by coexistence with zeolite. E_{ocp} was saturated after 500 ks and the saturated E_{ocp} was defined as E_{sp}.

It was found that a risk of local corrosion on stainless steel increased under gamma-ray irradiation because of increasing E_{sp} of stainless steel under irradiation. On the one hand, the increasing E_{sp} was suppressed by coexistence with zeolite. It is important to know change in the environmental factors such as temperature, Cl^- concentration of stagnant water and dose rate with time in the vessels for long-term storage of spent zeolite adsorption.

Reference

1) I. Yamagishi et al., J. Nucl. Sci. Tech. 51 (7-8) (2014) 1044-1053.

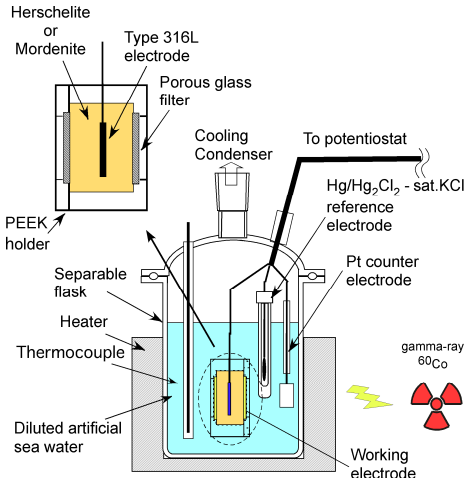

Fig. 1 A schematic diagram of electrochemical cell under gamma-ray irradiation.

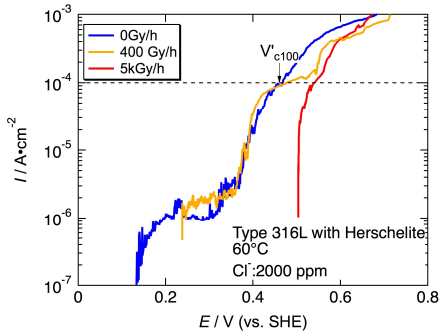

Fig. 2 Anodic polarization curves of type 316L stainless steel contacted with Herschelite containing diluted artificial seawater (Cl^-: 2,000 ppm).

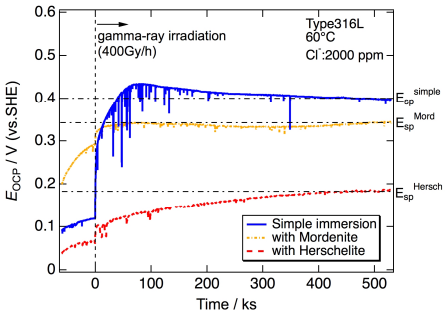

Fig. 3 Change in open circuit potential (E_{OCP}) of type 316L stainless steel after gamma-ray irradiation (at dose rate of 400 Gy/h).

1 - 16 Corrosion Tests of Steels Used for Primary Containment Vessel and Reactor Pressure Vessel in Diluted Seawater under Gamma-ray Irradiation

J. Nakano, T. Tsukada, F. Ueno and M. Yamamoto

Fundamental Decommissioning Technology Development Unit, NSEC, JAEA

In the Fukushima Daiichi Nuclear Power Station (1F), the seawater was injected into the reactor cores in the Unit 1, Unit 2 and Unit 3. The high dose of radiation has been continuing in the primary containment vessel (PCV) because of the molten fuel debris and the fission products. It is well known that H_2, hydrogen peroxide (H_2O_2), free radicals, etc., are produced by water radiolysis[1]. The produced species are chemically active and it is considered that corrosion of the PCV and the reactor pressure vessel (RPV) is influenced by gamma-ray irradiation. To evaluate the durability of the PCV and the RPV, therefore, corrosion tests of the steels for the vessels were conducted in diluted seawater under gamma-ray.

Sheet type specimens of 40 mm × 10 mm × 2 mm were machined from SGV480 (JIS G3118) for the PCV and SQV2A (JIS G3120) for the RPV, and immersed in diluted artificial seawater with chloride concentration of 100 ppm at 323 K (50 °C). Subsequently, the specimens were irradiated with gamma-ray from ^{60}Co source. Figure 1 shows corrosion tests under gamma-ray irradiation at the Takasaki advanced radiation research institute. Two flasks were arranged close to the ^{60}Co sources and two flasks were put at distances of 1.6 m from the ^{60}Co sources. The dose rates were estimated as 4.4 and 0.2 kGy/h, respectively. Ten and 100 mg/L hydrazine (N_2H_4) were added to diluted seawater, to evaluate the effect of N_2H_4 as an oxygen scavenger in water irradiated with gamma-ray. Gas phases in flask were air or N_2.

Figure 2 shows weight loss in the specimens in diluted seawater under gamma-ray irradiation. When gas phase in flask was air, weight loss in the specimens irradiated with a 0.2 kGy/h dose rate was comparable with that in the specimens without irradiation while weight loss in the specimens irradiated with a 4.4 kGy/h dose rate was approximately 1.7 times that of the specimens without irradiation[2].

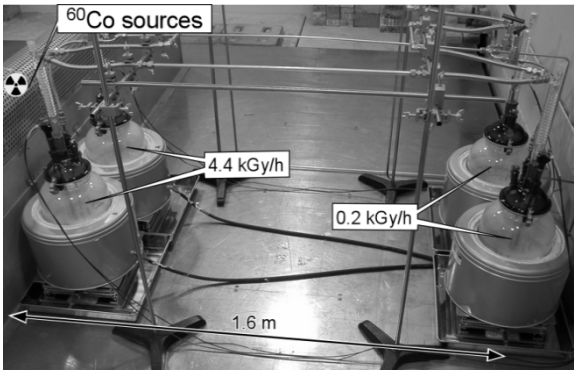

Fig. 1 Corrosion tests under gamma ray irradiation at the Takasaki advanced radiation research institute.

Figure 3 shows average weight loss in the SGV480 in diluted seawater with N_2H_4. Weight loss in the irradiated specimens without N_2H_4 was similar to that with N_2H_4 in air. When gas phase was replaced with N_2 in the flask, weight loss in the specimens decreased[3].

The dose at the PCV in the 1F unit 2 was calculated as 0.2 kGy approximately, much smaller in comparison with dose tested in this study. After the 1F accident, moreover, N_2 gas has been injected into the PCVs to prevent hydrogen explosion. It is inferred that water irradiated with gamma-ray in N_2 atmosphere would hardly accelerate corrosion of the PCV steel in the 1F.

References

1) Caër SL, Water (2011) 235-53.
2) J. Nakano et al., Trans. Atom. Ener. Soc. Jpn. 13 (2014) 1-6. (Japanese).
3) J. Nakano et al., J. Nucl. Sci. Tech. 51 (7-8) (2014) 977-86.

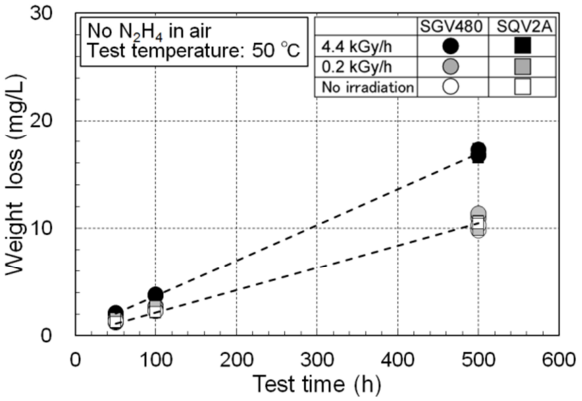

Fig. 2 Weight loss in the specimens in diluted seawater under gamma-ray irradiation.

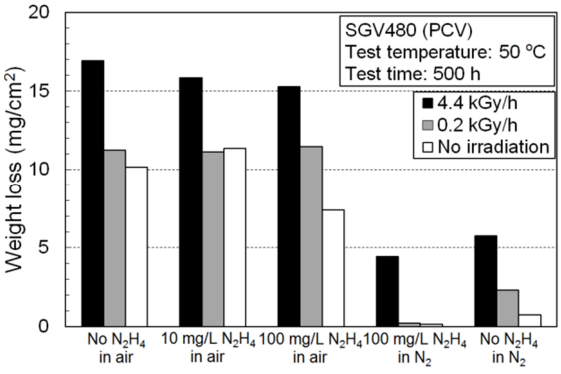

Fig. 3 Average weight loss in SGV480 specimens in diluted seawater after irradiation for 500 h.

1 - 17 Corrosion Resistance of Tank Material Used for Flock Storage - (2) Corrosion Behavior in Fluid Flow Condition by Air Agitation

H. Ambai, Y. Sano, M. Takeuchi and Y. Koma

Department of Fukushima Technology Development, NFCEL, JAEA

Introduction

For the flock, which was generated in the coagulation process for radioactive contaminated water from the Fukushima Daiich nuclear power plant, temporary storage in carbon steel tanks is under planning [1]. In these tanks, agitation by air will be applied, and the corrosion promotion is a concern due to fluid flow and increasing of dissolved oxygen. In this study, following the previous evaluation in the settling condition [2], we investigated the corrosion behavior of SS400 in the condition of fluid flow with air agitation, and considered the corrosion prevention.

Experimental

Based on the TEPCO information on the flock storage condition [1], immersion tests were carried out with SS400 at 46.3 °C with air agitation. During tests, γ-ray of ^{60}Co was irradiated to flock solution at 0.1 kGy/h. Corrosion rates were evaluated by weight loss of SS400 coupons. In order to understand the corrosion mechanism, electrochemical tests were carried out in the same conditions. Potentiodynamic scan rates of 20 mV/min were utilized. Electrochemical cells were composed of Pt counter electrodes and Ag|AgCl reference electrodes. In all of these tests, the flock purchased from AREVA NC JAPAN PROJECTS CO.,LTD. as a surrogate and artificial seawater (Aquamarine supplied from Yashima Chemical Co.) were used.

Results and discussion

The corrosion rates increased with flow rate in the all conditions, but this effect was reduced by the presence of flock and especially significant when the coupon was buried in the flock (Fig. 1). Under γ-ray irradiation, no remarkable change was observed. Flow of inactive gas decreased the corrosion rates (Fig. 2). In particular, Ar gas agitation was more effective under γ-ray irradiation than N_2 gas which brought HNO_3 as radiolysis products (Table 1).

Figure 3 shows the polarization curves in several flow rates. The cathodic current densities and the corrosion potentials increased with the flow rate. The results showed the increasing of corrosion rates with the flow rate in the immersion tests was caused by the promotion of the O_2 reduction reaction. It was considered that the decreasing of corrosion rates in the presence of flock and inactive gas flow in the immersion tests was due to the reducing of this reaction (block against O_2 diffusion and O_2 concentration decreasing).

Our study indicates that the selection of appropriate fluid flow conditions by air agitation (lower flow rate, intermittent agitation, etc.) is important to suppress the corrosion progress. Furthermore, it is more effective for decreasing the corrosion rate to apply the agitation with the inactive gas.

References

1) TEPCO, "Report on our facility management plan for Units 1-4 of Fukushima Daiichi Nuclear Power Station based on the "Policy on the Mid-term Security"" (2012).
2) Y. Sano et al., JAEA Takasaki Annu. Rep. 2012 JAEA-Review 2013-059 (2014) 38.

Table 1 The analysis of irradiated solutions

Solution	NO_3^-[ppm]
Seawater (Air 500ml/min)	0.169
Seawater＋Flock (Air 500ml/min)	0.557
Seawater＋Flock (Ar 100ml/min)	N.D.
Seawater＋Flock (N_2 100ml/min)	0.139

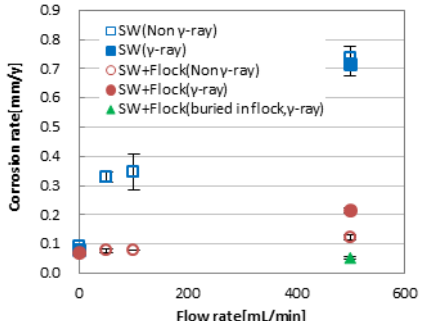

Fig. 1 The effect of fluid flow condition by air agitation to corrosion rates (SW = seawater).

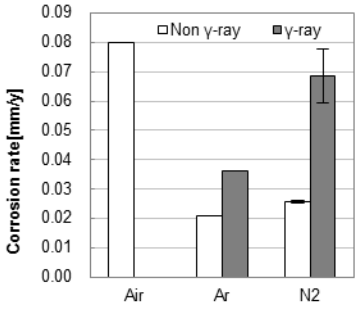

Fig. 2 The effect of gas type (seawater + flock, 100 mL/min).

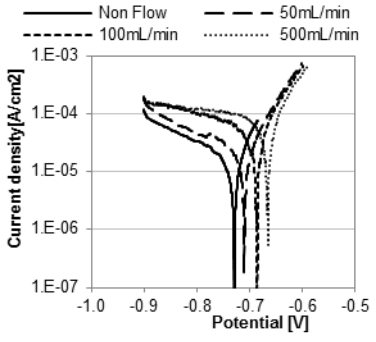

Fig. 3 The effect of fluid flow by air to polarization curves (seawater , non γ-ray).

1 - 18 Effect of Chloride and Bromide Ion on the Concentration of Hydrogen Peroxide Produced from Seawater Radiolysis

K. Hata [a,b], S. Hanawa [a], T. Motooka [b] and T. Tsukada [b]

[a] LWR Long-term Reliability Research Unit, NSRC, JAEA,
[b] Fukushima Project Team, NSRI, JAEA

The Fukushima Daiichi nuclear power plant experienced seawater injection into the cores as an emergent measure for a short period after the accident. As a result of the seawater injection, structural materials in the cores were exposed to unexpected corrosive environment. Radiolytic species were produced in the seawater by the radiation from the core materials. Especially, hydrogen peroxide (H_2O_2) is known as a radiolytic oxidant which dominantly affects corrosion of metallic materials. In this study, to identify important factors which contribute to the H_2O_2 generation in seawater radiolysis, the concentrations of H_2O_2 in gamma-ray irradiated artificial seawater (ASW) were measured and compared with the result of radiolysis calculation conducted by the authors [1]. Measurements were also performed with solutions of some constituents of seawater to identify which ion has the greatest effect on the H_2O_2 production.

Nine milliliter of the aerated ASW and three kinds of solutions were prepared in 10 mL glass bials sealed with polypropylene caps. Composition of the three solutions are shown in Table 1. AQ1 is a solution which contains 29,000 ppm NaCl, 82 ppm NaBr and 193 ppm $NaHCO_3$. This solution is considered as a mimetic seawater in our previous study [1]. These solutions were irradiated by gamma-rays (1 Gy/s) from ^{60}Co. After the irradiation, the concentrations of H_2O_2 in the solutions were measured by Ghormley method which is based on the oxidation of iodide ion to triiodide ion [2].

The concentrations of H_2O_2 in aerated ASW, AQ1, 29,000 ppm NaCl solution, and 82 ppm NaBr solution after irradiation are shown in Fig. 1 with the calculation results [1]. The experimental results showed similar trends to the calculation results. The concentrations of H_2O_2 in ASW are approximately in agreement with that in AQ1. It indicates that Cl^-, Br^- and HCO_3^- have the dominant roles in the H_2O_2 production in seawater radiolysis, though many other ions are dissolved in ASW. However, further calculations by the authors showed that HCO_3^- does not affect the H_2O_2 production [3].

It is known that H_2O_2 is scavenged by hydroxyl radical ($^{\bullet}OH$) and hydrated electron in homogeneous state under irradiation, and halide ions are generally highly reactive with $^{\bullet}OH$ [4]. The high concentration of H_2O_2 in the NaBr solution seen in Fig. 1 is possibly due to the high reactivity of Br^- with $^{\bullet}OH$. However, the concentration of H_2O_2 in AQ1, ASW and the NaCl solution is lower than that in the NaBr solution, though a high amount of halide ions is dissolved in all the solutions. It has been reported that the primary yield of H_2O_2 decreases with increasing the concentration of Cl^- [5]. The authors made the radiolysis calculation and it was shown that the steady-state concentration of H_2O_2 decreases as the primary yield of H_2O_2 is low [3]. Therefore, the lower H_2O_2 concentrations in AQ1, ASW and the NaCl solution is caused by the high concentration of Cl^-.

In conclusion, it is considered that the H_2O_2 generation in seawater radiolysis is mainly controlled by Cl^- and Br^-.

Table 1 Chemical compositions of gamma-ray irradiated solutions (Unit: ppm).

Solutions	NaCl	NaBr	$NaHCO_3$
AQ1	29,000	82	193
NaCl sol.	29,000	-	-
NaBr sol.	-	82	-

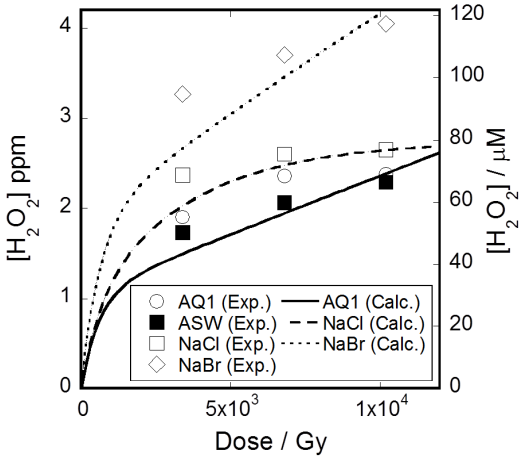

Fig. 1 Experimental and calculation results of H_2O_2 concetration resulted by gamma radiolysis of aerated ASW, AQ1, 29,000 ppm NaCl solution, and 82 ppm NaBr solution.

References

1) K. Hata et al., Proc. Nucl. Plant Chem. Conf. (NPC2012) Sep. (2012) Paris, France.
2) J. A. Ghormley et al., J. Am. Chem. Soc. 78 (1956) 2934.
3) K. Hata et al., Proc. Water Chem. Corrosion Nucl. Power Plants in Asia, Oct. (2013) Taichung, Taiwan.
4) O. Roth et al., J. Phys. Chem. A 115 (2011) 700.
5) J. Pucheault et al., J. Phys. Chem. 83 (1979) 330.

1 - 19 Radiolytic Hydrogen Absorption Behavior of Zirconium in Nitric Acid Solution under Gamma-ray Irradiation

Y. Ishijima, T. Motooka, F. Ueno and M. Yamamoto

Division of Fuels and Materials Engineering, NSED, JAEA

In Japan, a commercial reprocessing plant is being test operated in Rokkasho reprocessing plant. Purex process which used nitric acid and dodecane with tributhyl phosphate for solvent has been adopted in the plant. In some cases, stainless steels have been severely corroded. This appears to be intergranular corrosion in those solutions. In order to avoid corrosion in such severe environment, some equipments in the plant have been made of zirconium (Zr).

However, it is well known that Zr has susceptibility of hydrogen embrittleent by hydride formation. In used nuclear fuel solution, hydrogen atoms are always generated by radiolysis under alpha-ray irradiation. And it is considered that radiolytic hydrogen can diffuse into Zr and generate zirconium hydride. Therefore, there is a concern about the degradation of nuclear fuel reprocessing plant by hydrogen embrittlement in long term operation.

In this study, we conducted radiolytic hydrogen absorption tests and constant load tensile tests under gamma-ray irradiation.

Commercial grade pure Zr plate (ASTM R60702) was used for test material. Table 1 shows the chemical composition of test material. Disk type specimens ($\phi 8 \times$ 5 mm) were used for radiolytic hydrogen absorption tests. Rod shape specimens were used for constant load tensile tests. Schematic illustration of tensile test specimen is shown in Fig. 1.

Radiolytic hydrogen absoption tests were carried out in 1, 3, and 7 mol/L nitric acid solutions. Dose rates from ^{60}Co source were chosen 3 and 5 kGy/h. Irradiation time was 1,000 h. After irradiation, thermal desorption spectrometry (TDS) was carried out to evaluate the hydrogen absorption value with quadrupole mass spectrometer (QMS). Temperature range of TDS was from room temperature to 1,073 K. Heating rate of TDS was 100 K/h.

Constant load tensile tests were carried out in pure water. Dose rate was 3 kGy/h. Applied load was 144 kgf. Constant load tensile tests were stopped after 1,000 h. Figure 2 shows appearance of constant load tensile test machine.

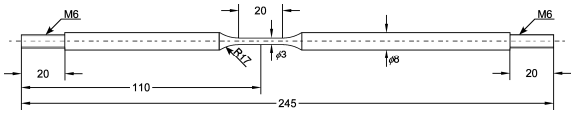

Fig. 1 Schematic illustration of test specimen.

Table 1 Chemical composition of test sample (wt%).

	H	C	N	O	Ni	Fe+Cr	Hf	Zr
Sample	<0.002	0.02	0.003	0.14	0.029	0.2	0.39	>99.2
ASTM R60702	<0.005	<0.05	<0.025	<0.16	-	0.2	4.5	>99.2

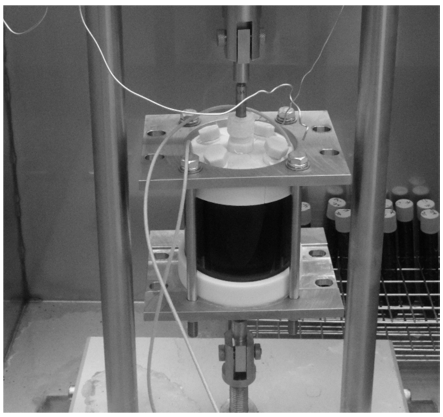

Fig. 2 Appearance of constant load tensile test machine.

Effect of dose rate for radiolytic hydrogen absorption in 3 mol/L nitric acid solution is shown in Fig. 3. From TDS analysis, absorbed hydrogen generated zirconium hydride in metal. These results suggest that radiolytic hydrogen by alpha-ray irradiation can generate hydride in Zr. Absorb value increases with dose rate. From this result, it is considered that absorbed value increases with concentration of Pultonium in used nuclear fuel solutions.

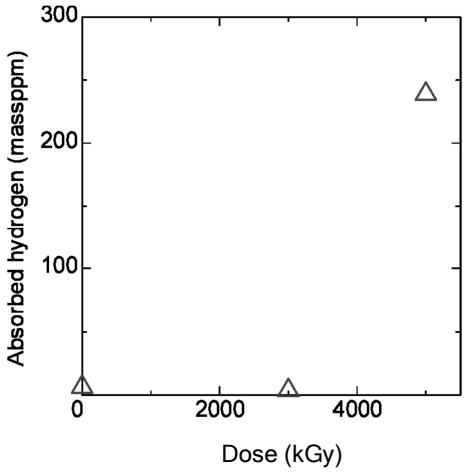

Fig. 3 Effect of dose rate for hydrogen absorption in 3 mol/L nitric acid solution.

Specimen did not fail in constant load tensile test under gamma-ray irradiation until 1,000 h. From this result, it is considered that hydride generation rate is very slow in Zr. Therefore, it was diffcult to show hydrogen embrittlement in this test condition.

1 - 20 Evaluation of Hydrogen Gas Generation from Cement Solidification Form by Gamma-ray Irradiation III

T. Nakayama, K. Hanada, S. Suzuki, Y. Kawato and Y. Meguro

Nuclear Cycle Backend Technology Development Unit, NCBD, JAEA

Radioactive combustible wastes generated in Japan Atomic Energy Agency are incinerated and the ash obtained will be solidified with cement. After conditioning, the cement solidification form will continuously generate hydrogen gas by water radiolysis in the form. Therefore the amount of generated hydrogen gas should be understood in order to evaluate the safety of the form during its storage. It is thought that the hydrogen gas generation is strongly influenced by the condition of water and its amount in the form. In a previous study, it was found that hydrogen gas generation from a cement solidification form of incinerated ash was larger than that from a cement paste form without incinerated ash [1]. Much amount of water was used for mixing of the incinerated ash with cement than for cement itself due to reactions of water with the ash, and then much free water remaining in the solidification form would result in increase of the amount of hydrogen gas. Moreover, it was found that the amount of hydrogen gas generation from the thermally dried sample greatly decreased [2]. That is water amount in the form is one of the important factors to determine the hydrogen gas generation. In this study, we investigated influence of water cement ratio, cement material, absorbed dose rate, and absorbed dose on the hydrogen gas generation to understand the hydrogen gas generation mechanism.

A bottom ash of nonradioactive waste, ordinary portland cement, blast furnace slag cement and high-range water-reducing admixture that added 1% of cement weight were employed to make several cement solidification forms of ca. 12 mm diameter and 50 mm high and the mixing conditions are summarized in Table 1. The No.2 was dried sample obtained by heating No.1 at 383 K for 24 h. The No.3 was also dried sample obtained by vacuuming No.1. The solidified sample was sealed in a 50 mL vial and irradiated by ^{60}Co γ-rays at 3 kGy/h for 1 h in the Gamma-ray irradiation facility. The No.11, No.12, and No.13 samples were irradiated at 1 kGy/h for 3 h, 1.5 kGy/h for 2 h, and 3 kGy/h for 3 h, respectively. The hydrogen gas in the vial was determined by gas chromatography. The free water in the form was determined from the difference of the sample weight before and after thermal dry at 383 K for 24 h after irradiation. The G-value was calculated for the free water weight in the form instead of the sample weight.

Results of irradiation test are summarized in Table 1. The amount of hydrogen gas is normalized into the value for 1 g of the sample and 1 kGy of the absorbed dose. The amount of hydrogen gas generation increased with an increase of the free water ratio (No. 1, 2, 3) and the G-values were different. Especially the value for the thermal dry sample, in which the free water ratio was too low, was large. This fact suggests that the G-value, i.e., hydrogen gas generation mechanism would be influenced by physicochemical nature of water and its environment. Remarkable relationship between hydrogen gas amount and the ash filling rate (No.1, 4, 5), water cement ratio (No.1, 6, 7), cement material (No.1, 6, 7 - 8, 9, 10), absorbed dose rate (No.1, 11, 12), or absorbed dose (No.1, 13) was not observed. The G-values for the free water were calculated and also shown in Table 1. The G-value seems to be scattered between 1 and 2 molecule/100 eV except No. 2. It is hard to find remarkable relationship between the G-value and the parameters such as the ash filling rate, the cement material, and the dose, but there is a week relationship between the G-value and the free water ratio, in which the G-value decreased with an increase of the free water ratio. The G-values were over 1 molecule/100 eV for all samples examined in this study and this was much larger than that of pure water (No.14). The G-value of pure water was 0.5 ± 0.0 molecule/100 eV. It concluded that the radiolysis of water in the solidified form with ash was different from that in pure water.

References

1) T. Nakayama et al., JAEA Takasaki Annu. Rep. 2011 JAEA-Review 2012-046 (2013) 20.
2) T. Nakayama et al., JAEA Takasaki Annu. Rep. 2012 JAEA-Review 2013-059 (2014) 20.

Table 1 Conditions of samples and results of hydrogen gas yield and G-value.

Sample	Condition				Results			
	Ash /wt%	water / wt%	cement / wt%	Irradiation time / h	Radiation does rate / kGy h^{-1}	H_2 yield / mL g^{-1} kGy^{-1}	Free water ratio / %	G-value / molecule 100 eV^{-1}
No.1	30	45	25	1	2.5	(4.6±1.3)x10^{-4}	13.5	1.43
No.2 thermal dry	30	45	25	1	2.5	(0.8±0.3)x10^{-4}	0.3	10.59
No.3 vacuum dry	30	45	25	1	2.4	(2.3±0.1)x10^{-4}	4.8	1.99
No.4	10	30	60	1	2.4	(4.2±0.1)x10^{-4}	14.6	1.19
No.5	40	45	15	1	2.5	(5.2±0.2)x10^{-4}	20.2	1.05
No.6	30	41	29	1	2.4	(3.5±0.1)x10^{-4}	12.8	1.11
No.7	30	48	22	1	2.4	(3.5±0.0)x10^{-4}	7.7	1.84
No.8 **	30	41	29	1	2.5	(3.6±0.1)x10^{-4}	12.4	1.20
No.9 **	30	45	25	1	2.5	(3.1±0.1)x10^{-4}	6.4	1.94
No.10 **	30	48	22	1	2.5	(4.0±0.3)x10^{-4}	8.5	1.98
No.11	30	45	25	3	0.9	(3.7±0.1)x10^{-4}	10.0	1.50
No.12	30	45	25	2	1.2	(4.4±0.5)x10^{-4}	11.7	1.59
No.13	30	45	25	3	2.8	(3.8±0.2)x10^{-4}	12.0	1.30
No.14 Water	0	100	0	1	2.8	(12.4±0.5)x10^{-4}	100.0	0.50

*High-range water-reducing admixture added 1 wt% of cement weight.
**These samples were solidified using blast furnace slag cement.

1 - 21 Effect of Salt Content in Bituminized Waste on Radiolysis Gas Generation

K. Irisawa and Y. Meguro

Nuclear Cycle Backend Technology Development Unit, NCBD, JAEA

Low-level radioactive concentrate, which was generated by the reprocessing of spent nuclear fuels, was solidified as bituminized waste product (BWP) in the Tokai reprocessing plant from 1982 to 1997. The Tokai BWP mainly consists of ca. 55 wt.% Blown Bitumen AD Compound (Showa Shell Sekiyu K.K.), which has the same physical properties as the Blown Bitumen R85/40, and ca. 45 wt.% salts, which consist of $NaNO_3$, $NaNO_2$, Na_3PO_4, AgI, (Ba, Sr)SO_4, $NiCs_2[Fe(CN)_6]$ etc[1]. There are, however, a certain amount of BWPs with different salt contents and salt compositions depending on campaigns of the liquid waste treatment.

It is generally known that H_2 is generated by radiolysis degradation of bitumen. In the light of disposal of the Tokai BWPs, it would be necessary to evaluate radiolysis H_2 generated from the BWPs. It is considered that salt contents in the Tokai BWP influence on radiolysis H_2 generation. In this study, we acquired basic data regarding radiolysis H_2 generated from the BWPs with various salt contents (5, 15, 30 and 45 wt.%) by ^{60}Co γ-ray irradiation.

Approximately 5 g of the samples in Pyrex glass vessels are irradiated by 3 - 94 kGy. In order to evaluate effect of dose rate on radiolysis, 0.006, 0.6 and 6 kGy/h of γ-ray irradiation were conducted in 500, 5 and 0.5 h, respectively. Absorbed dose was measured using alanine dosimeters, and H_2 in the vessel was measured by gas chromatography.

Effects of the dose rates in 3 kGy γ-ray irradiation on the H_2 amount for the samples were not observed. The amounts of generated H_2 from the synthetic BWP with 45 wt.% of salt content by 0.006, 0.6 and 6 kGy/h of the dose rates were 2.2, 2.0 and 2.4 × 10^{-8} mol/g kGy, respectively. This indicates that the dose rates did not influence on the amount of generated H_2. Figure 1 indicates relationships between absorbed dose and H_2 amount per unit weight. The H_2 amount increased in proportion to the absorbed dose in each sample. The lines were derived by the least-squares regression using the H_2 generation amount in each sample and a good correlation (i.e. $R^2 > 0.99$) was observed. In contrast, H_2 amount decreased with increasing the salt contents in the samples. Figure 2 shows relationships between the salt content and the G(H_2) value. The G(H_2) value of the AD compound was 0.49 ± 0.6 molecule/100 eV (n=3) and was in a good agreement with the previous data for the Blown Bitumen R85/40 (G(H_2) = 0.52)[2]. The G(H_2) value of synthetic BWP decreased with increasing the salt content. This result means that the G(H_2) value of the synthetic BWP varied by the salt content, and that the variation of the G(H_2) value occurred due to the fact that the salt content in the sample was influenced on H_2 generation by γ-ray irradiation.

In order to evaluate effects of the salt content on the G(H_2) value, the G(H_2) value of only the bitumen component in each synthetic BWP was calculated, and was also plotted in Fig. 2. The G(H_2) value normalized by the bitumen component almost agreed with each sample and that of the AD Compound. The agreement of the G(H_2) values of the bitumen component in the BWPs with various salt contents means that the salts embedded in the sample did not influence on H_2 generated from the BWPs. Consequently, when the H_2 generation by γ-ray irradiation is evaluated, only the bitumen component in the BWP should be taken into account. In order to evaluate radiolysis H_2 generated from the Tokai BWP in more detail, it is also necessary to investigate radiolysis H_2 generation by α-ray and β-ray irradiations.

References

1) K. Yoshinaka et al., JAEA-Technology 2008-063, (2008).
2) D. C. Phillips et al., Harwell (1983) AERE-R 10925.

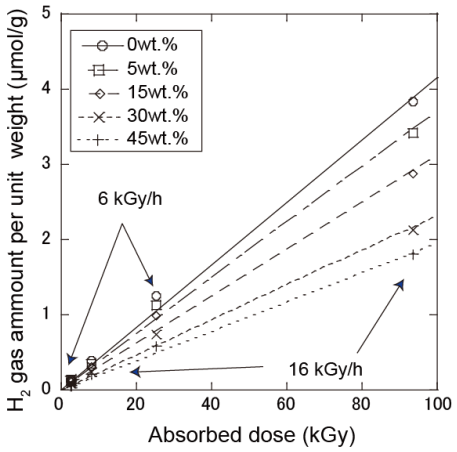

Fig. 1 Relationships between absorbed dose and H_2 gas amount per unit weight.

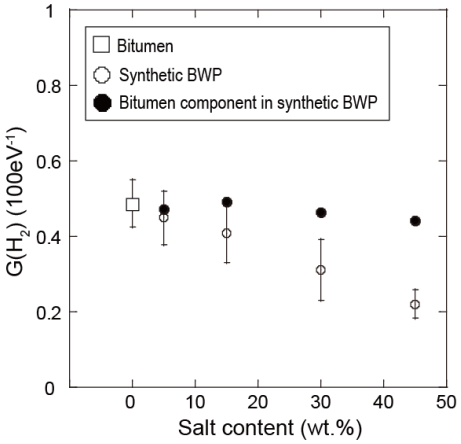

Fig. 2 Relationships between salt content in the samples and G(H_2) value.

1 - 22 Evaluation of Radiation Resistance of Inorganic Materials for Solidification of Sludge from Water Treatment in Fukushima Daiichi

J. Sato , T. Nakayama, Y. Kawato and Y. Meguro

Nuclear Cycle Backend Technology Development Unit, NCBD, JAEA

A radioactive sludge was generated from contaminated water treatment system in Fukushima Daiichi. Because major substances of the sludge were identified as barium sulfate, nickel ferrocyanide and ferric hydroxide, the sludge contains large amount of radioactive nuclides. Therefore the influence of radiation on its waste form is one of the most important concerns. The study to solidify the sludge using four inorganic solidified materials; Ordinary Portland Cement (OPC), Portland Blast-Furnace Slag Cement Type-B(BB), Cement Glass(CG) and Geopolymer(GP) was started. Some water was needed for kneading in each material, therefore it is considered that hydrogen gas is generated by radiolysis of water. In addition it is necessary to investigate the degradation behavior of ferrocyanide in terms of release of cyanide by radiolysis. In this study, we determined the G-value of the generation of hydrogen gas and measured the amount of cyanide generation by irradiation with gamma rays to the simulated sludge solidified. And we investigated the influence of irradiation on the sludge and solidified materials.

The simulated sludge was produced in a similar equipment of the waste treatment system in Fukushima Daiichi by AREVA. The 80% of supernatant was removed from the sludge, and the residue was dried at 110 °C for 3 days. The solidified samples were produced at 40 or 50 wt% filling ratio of sludge by using inorganic materials with changing of the water-powder ratio; 0.8, 1.0, 1.2 for cement solidification, 0.4, 0.6, 0.8 for CG, and 1.4 for GP. Only cement samples were added 2% high-range water-reducing admixture. The conditions of the solidified samples are shown in Table 1. The mixture after mixing filled in a cylindrical container (φ13 mm × 50 mm). The samples cured at room temperature for 28 days, then put into a glass ampoule (φ18 mm × 150 mm). The samples were irradiated by ^{60}Co γ-rays at 34 Gy/h for 160 h in gamma-ray irradiation facility. The total absorbed dose was adjusted to be 4.6 kGy. Hydrogen gas concentration was determined by gas chromatography and the cyanide concentration was determined by a gas detector tube. After gas analysis, the amount of free water in the samples ware determined by measuring weight change of the samples after heating at 110 °C for 72 h. The G-value was calculated for the free water weight in the sample instead of the sample weight.

The G-value of hydrogen gas and the ratio of free water were shown in Table 2. For the solidified samples using cements (OPC and BB), the G-value, especially for No. 2, 3 5 & 6, showed the similar value in the previous study[1] (G-value: 0.21 molecule/100 eV, ratio of free water : 0.23), and the G-value increased with the increase of the free water. This suggests that the free water in the solidified form is one of the important factors to determine the G-value. The G-value of CG samples indicated higher than other samples in spite of almost same ratio of free water. The G-value of the GP samples was as same as that of the cement samples, although the ratio of free water was the highest in all materials. As the results, it was presumed that the hydrogen gas generation was influenced from not only the free water but also the solidified material. The cyanide was not detected (< 2.0 ppm) after the irradiation examined in this study (Table 2), and it is lower than the maximum allowable concentration for workers (5.0 ppm). In this study, the total absorbed dose was equivalent to that of about 30 years' irradiation in the waste form solidified the actual sludge on the basis of the radioactivity of sludge. Therefore it was predicted that risk to release cyanide is low by degradation of ferrocyanide in the sludge.

Reference

1) R. E. Barletta et al., NUREG CR 2969 (1982).

Table 1 Conditions of solidified samples.

Sample		Composition		
		Material	Sludge (wt%)	Water/Powder ratio
No. 1	OPC-1 50/0.8	OPC	50	0.8
No. 2	OPC-2 50/1.0	OPC	50	1.0
No. 3	OPC-3 50/1.2	OPC	50	1.2
No. 4	BB-1 50/0.8	BB	50	0.8
No. 5	BB-2 50/1.0	BB	50	1.0
No. 6	BB-3 50/1.2	BB	50	1.2
No. 7	CG-1 50/0.4	CG	50	0.4
No. 8	CG-2 50/0.6	CG	50	0.6
No. 9	CG-3 50/0.8	CG	50	0.8
No. 10	GP-1 40/1.4	GP	40	1.4

Table 2 Result of the irradiation test.

Sample	G-value(H_2) (/100 eV)	Ratio of free watar (g/g sample)	Conc. of CN^- (ppm)
No. 1	0.16 ±0.034	0.17 ±0.003	< 2.0
No. 2	0.21 ±0.022	0.20 ±0.003	-
No. 3	0.24 ±0.002	0.22 ±0.001	-
No. 4	0.20 ±0.026	0.18 ±0.002	< 2.0
No. 5	0.21 ±0.011	0.21 ±0.002	-
No. 6	0.23 ±0.005	0.23 ±0.001	-
No. 7	0.32 ±0.027	0.17 ±0.001	< 2.0
No. 8	0.28 ±0.003	0.21 ±0.006	-
No. 9	0.28 ±0.009	0.23 ±0.004	-
No. 10	0.26 ±0.029	0.24 ±0.024	< 2.0

1 - 23 Alpha-ray Durability of Co-precipitation Sludge Generated by Radioactive Water Treatment

S. Watanabe, M. Nakamura, A. Shibata, K. Nomura and Y. Nakajima

Department of Fukushima Technology Development, NFCEL, JAEA

Precipitation technology is widely applied water purification process and is also effective for decontamination of radioactive liquid waste generated in nuclear power plants [1]. Co-precipitation with iron hydroxide treatment is employed as one of preprocesses of Advanced Liquid Processing System (ALPS) for decontamination of radioactive water released from Fukushima Daiichi Nuclear Power Plant[2]. Alpha emission nuclides, ^{60}Co, ^{54}Mn, etc. are aimed to be decontaminated in this process. The sludge produced by this process is planned to be stored until an appropriate disposal methods is selected officially, thus it is necessary to investigate the durability of the sludge against radiations from those nuclides for safety management of the radioactive waste. In this study, durability of the sludge produced by co-precipitation of target elements with iron hydroxide against alpha-ray irradiation was evaluated through the He^{2+} ion irradiation experiments.

The simulated sludge was prepared by adding $FeCl_3$ and NaOH solutions into simulated contaminated water containing Ce^{3+}, Co^{2+}, Mn^{2+}, Ru^{3+}, Sr^{2+}, Mg^{2+}, Ca^{2+}, Cs^{+} ions and by mixing the solution at pH＝8. Co-precipitated sludge shown in Fig. 1 was sampled and the composition was evaluated through the concentration changes of ions in the supernatant solution. Approximately 50 mL of the sludge was obtained from 1 L of the feed solution. The sludge was put in stainless steel container with 50 mm diameter and 2 mm thickness and then the container was sealed with a kapton film. The surface of the sample was uniformly irradiated with He^{2+} ions passing through the kapton film. He^{2+} ions accelerated by 3 MV tandem accelerator of TIARA to be 9 MeV were reduced by the kapton film and atmosphere to be 5.0 MeV when the beam reached at the surface of the sample. Thickness of the sample was larger than penetration range of the He ion with 5.0 MeV, therefore we assumed that all incident energy of the ions was transferred to the sample. Irradiation does was calculated from size and weight of the sample, incident energy of He ions and the beam current.

Compositions of the feed solution for the co-precipitation and of supernatant solutions before and after the irradiation are shown in Table 1. In the co-precipitation process, Co, Mn, Ru were successfully decontaminated. However, Ce, which was added to the feed solution as an analogue of actinides, did not accompany with the sludge but remained in the solution. Therefore trivalent lanthanides and actinides are suspected to stay in the waste water at the co-precipitation process. However detail behaviors of trivalent cations should be further investigated since the concentration of Ce increased after the co-precipitation treatment. As well as trivalent cations, decontamination performance for the othervalent metal ions also have be investigated to predict the precise behaviors of actinides.

The composition of the solution did not show distinct change after the irradiation. According to alpha radioactivity reported by TEPCO [2], 66 kGy irradiation means more than a hundred years storage even if all alpha nuclides are trapped in the sludge. Therefore influence of alpha nuclides on stability of the sludge during the long term storage is not serious if the concentration of them in the contaminated water are about a few Bq/L.

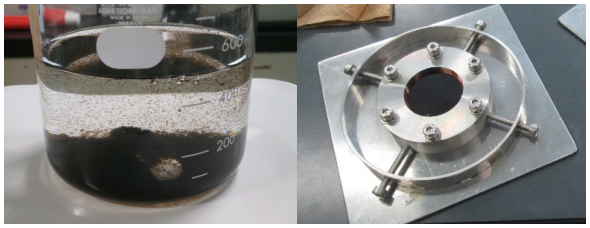

Fig. 1 Simulated sludge (left; after preparation, right; inside the container for the irradiation).

References

1) V. Pacary et al., Chem. Eng. Res. Des. 88(9) (2010) 1142-47.
2) Tokyo Electric Power Company, Handouts at press conference 2013, Mar. 29 (2013).

Table 1 Composition of the supernatant solution at before and after the irradiation.

	Composition of the supernatant solution (mg/L)							
	Ce	Co	Mn	Ru	Sr	Mg	Ca	Cs
Feed solution	4.8×10^{0}	4.7×10^{2}	3.2×10^{1}	1.4×10^{2}	1.1×10^{3}	1.3×10^{3}	1.4×10^{4}	3.5×10^{2}
After the co-precipitation	9.0×10^{0}	2.3×10^{2}	2.8×10^{0}	0.7×10^{0}	1.1×10^{3}	1.3×10^{3}	1.4×10^{4}	3.5×10^{2}
After 66 kGy irradiation	8.1×10^{0}	2.1×10^{2}	0.7×10^{0}	0.4×10^{0}	1.0×10^{3}	1.4×10^{3}	1.3×10^{4}	3.1×10^{2}
After 132 kGy irradiation	7.7×10^{0}	2.1×10^{2}	0.6×10^{0}	0.5×10^{0}	1.0×10^{3}	1.4×10^{3}	1.3×10^{4}	3.1×10^{2}

1 - 24 Experimental Study of Irradiation Effects on Supported Precious Metal Catalyst for Passive Autocatalytic Recombiner

Y. Kamiji, R. Nagaishi, M. Inoue and R. Hino

Nuclear Engineering Research Collaboration Center, JAEA

Hydrogen gas is generated at nuclear power plant (NPP) by various chemical reactions such as water radiolysis during normal operation or accidents, metal-steam reaction and molten-core concrete interaction during accidents. Flammability control systems (FCS) are installed in the NPPs in order to prevent explosion. Especially passive autocatalytic recombiner (PAR) is effective even in station black out (SBO), since it can be operated without electricity. Although PARs are installed in some of NPPs, the existing PAR has two problems; one is its heaviness, and another is a potential to become ignition source by excess temperature rise at catalyst. We have been developing new PAR to solve the above two problems. In this study, degradation of supported precious metal catalyst included in the PAR under gamma-ray irradiation was examined, which is necessary for the practical installation of PAR into the NPPs.

The dimension of catalyst sample was approximately 90 mm O.D. and 90 mm height. These samples were reduced at 800 °C for an hour before irradiation. The four samples were irradiated by ^{60}Co γ-rays from gamma-ray irradiation facility of Takasaki Advanced Radiation Research Institute. Table 1 shows the test conditions for (a) irradiation and (b) reaction test. These samples were irradiated up to 1.0 MGy in each desiccator at room temperature (RT). The irradiation dose was decided to include the value of 5.7×10^5 Gy which is estimated as total of cumulative dose after 30 days of loss of coolant accident at BWR and cumulative dose during 40-years-normal-operation[1]. In order to clarify the influence of humidity during the irradiation, two ambient conditions focusing on humidity were pre-conditioned. Those are ambient air which is approximately 20% RH and humid air with sodium chloride saturated solution (SCSS) which is conditioned about 75% RH [2] as shown in Table 1 (a). After the irradiation, the reaction tests were performed to confirm the catalytic activity of sample by the test apparatus in Oarai R&D center. Hydrogen mixed standard gas (1.30%-H_2, 0.65%-O_2, Balance-Ar) was supplied at 1 L/min into the sample, and then hydrogen concentration of outlet gas was measured by gas-chromatograph. In this test, dependences of temperature and humidity are examined, especially in test case "D", the samples are immersed to distilled water before the test as a severe humid condition.

After the irradiation, no degradation was observed from the test results in case of A, B and C, in which supplied hydrogen was reacted entirely. On the other hands, clear differences were seen in the result of case D as shown in Fig. 1. Only sample 5 which was irradiated at 1.0 MGy with high humidity reacted almost all hydrogen right after start up. In addition, the surface area of precious metal was larger than the non-irradiated sample from result of CO adsorption measurement. This means reduction of particle size of precious metal occurred. These results suggest that precious metal is easily reduced by irradiation, and that catalyst activity is not degraded but is improved as the result. Further experiments and analyses for each precious metal and support material are in progress.

References

1) Nuclear Power Licensing Division, Nuclear and Industrial Safety Agency, 07-東通新- A-03-02 (2008).
2) L. Greenspan, Journal of Research of the National Bureau of Standards – A. Physics and Chemistry Vol. 81A, No. 1, January-February (1977).

Table 1 Test conditions for (a) irradiation and (b) reaction test.

(a) Irradiation	
CAT	Condition
1	Non-irradiated
2	0.5 MGy,w/o SCSS
3	0.5 MGy, w/SCSS
4	1.0 MGy,w/o SCSS
5	1.0 MGy, w/SCSS

(b) Reaction test	
Test	Condition
A	RT/Non-humidified
B	RT/Humidified
C	80 °C/Humidified
D	80 °C/Humidified *

*Catalysts are immersed to distilled water before each test.

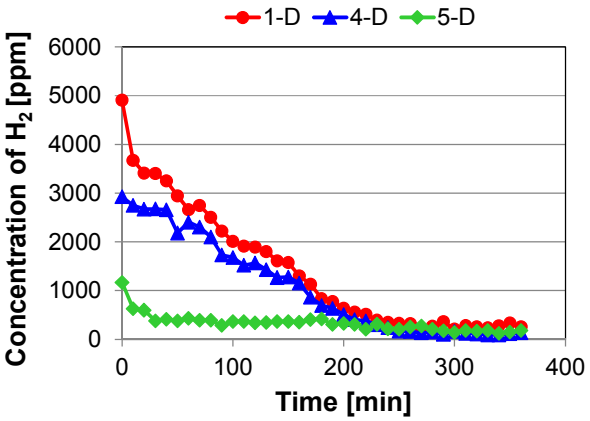

Fig. 1 Results of time histories of hydrogen concentration in reaction test case "D" for representative catalyst sample 1, 4 and 5.

1 - 25 Irradiation Effect of Gamma Rays on Cyanate Ester/Epoxy Resins (3)

A. Idesaki [a)], H. Uechi [b)], Y. Hakura [b)] and H. Kishi [b)]

[a)] Environment and Industrial Materials Research Division, QuBS, JAEA
[b)] Graduate School of Engineering, University of Hyogo

Cyanate ester/epoxy resins, which show excellent radiation resistance of several tens MGy, have been expected to be applied for an electrical insulator of superconducting magnet systems in ITER, muon beamline at J-PARC, and so on. While radiation resistance of cyanate ester/epoxy resins has been studied mainly from the view point of changes in mechanical properties, there are few reports on irradiation effects on the resin from the view point of changes in physicochemical properties such as gas evolution behavior, change in chemical structure, and so on. We have studied about effects of γ-ray irradiation on cyanate ester/epoxy resins and obtained results as following[1,2]:

(1) Hydrogen (H_2), carbon dioxide (CO_2) and carbon monoxide (CO) gases were main gaseous components evolved after the irradiation.

(2) Glass transition temperature (T_g) decreased after the irradiation that means network structure is decomposed by the irradiation.

In this work, solid state ^{13}C nuclear magnetic resonance spectroscopy (NMR) spectra were obtained in order to discuss what kind of chemical structure is decomposed by the irradiation.

Dicyanate ester of bisphenol A (DCBA) and diglycidyl ether of bisphenol A (DGEBA) were mixed by 50/50 in weight and cured at 230 °C as a final curing temperature. DCBA/DGEBA resin was irradiated by ^{60}Co γ-rays up to a dose of 100 MGy at ambient temperature under vacuum. After the irradiation, ^{13}C NMR spectra were obtained and peaks were assigned according to some literatures. The ^{13}C NMR spectrum of unirradiated DCBA/DGEBA showed that the resin includes structures of isopropylidene (No.1-6), ether linkage (No.7-10), cyanurate (No.11-13), isocyanurate (No.14-16) and oxazolidinone (No.17-19) (Fig. 1). After 100 MGy irradiation, the relative peak intensity of No. 1 and 2 decreased by 7 and 21% indicating decomposition of isopropylidene structure. For the peaks from 65 ppm to 83 ppm, especially for the peak No. 9, the relative peak intensity decreased by 33% that indicates ether linkages are decomposed. Such structural decomposition causes the change in surroundings of benzene ring. The relative peak intensity of No. 3, 6 and 10 decreased slightly (5-13%) after the irradiation. On the other hand, peak intensity of No.11 did not change. This means that cyclic -N=C-(O)-N= in cyanurate structure was not decomposed by the irradiation. This is considered to be caused by relatively high bond-dissociation energy of C-N bond (745 kJ/mol) in comparison with C-H (335 kJ/mol), C-O (530 kJ/mol) and C-C (599 kJ/mol) bonds. Such cyclic C-N-(O) structure is also included in isocyanurate and oxazolidinone structures, therefore, it can be inferred that cyclic C-N-(O) bonds included in cyanurate, isocyanurate and oxazolidinone structures are hardly affected by the irradiation and that isopropylidene structure and ether linkages are rather decomposed by the irradiation.

As a conclusion, it was revealed that ether linkages are mainly decomposed by the γ-ray irradiation with evolving gases of H_2, CO_2 and CO and decreasing in T_g. In this work, DCBA and DGEBA were used, however, there are several kinds of different chemical structure like bisphenol B, E, F type for both of cyanate ester and epoxy. Since their combination and compounding ratio may influence on initial properties of obtained resin and radiation resistance, it is important to clarify effect of their combination and compounding ratio on the radiation resistance of cyanate ester/epoxy resins in order to realize their application for the electrical insulator of superconducting magnet systems.

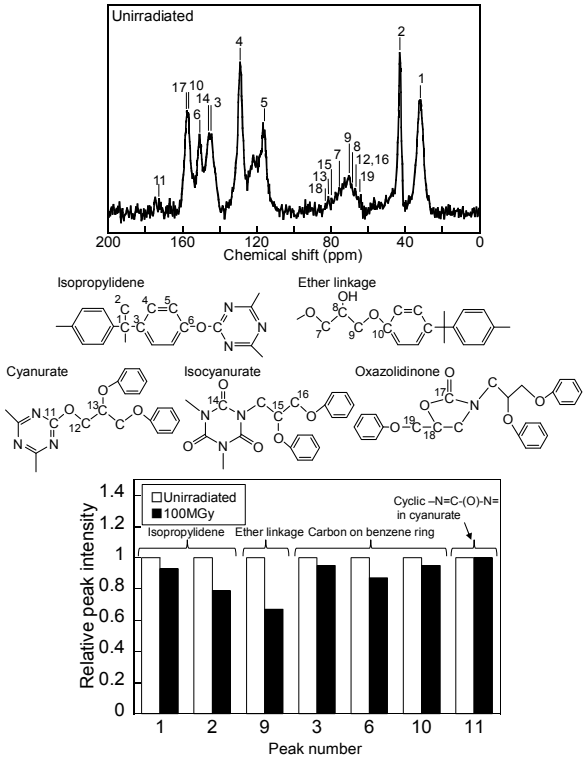

Fig. 1 Result of solid state ^{13}C NMR measurement.

References

1) A. Idesaki et al., JAEA Takasaki Annu. Rep. 2009 JAEA-Review 2010-065 (2011) 21.
2) A. Idesaki et al., JAEA Takasaki Annu. Rep. 2010 JAEA-Review 2011-043 (2012) 20.

1 - 26 Observation of Oxidized Region in Gamma-ray Irradiated Polyethylene with KOH Treatment and SEM-EDS

A. Shimada, M. Sugimoto and M. Yoshikawa

Environment and Industrial Materials Research Division, QuBS, JAEA

Degradation behavior of polymer cable insulation should be investigated before installation in the atomic energy-related facilities in order to realize safe and stable operation. In the insulation degradation, a radiation induced oxidation reaction is one of the most important factors. Therefore, it is necessary to confirm the extent of the oxidation reaction in the insulation. Oxygen penetrates into the insulation from the surface to deeper region during the oxidation reaction. A method for observation of the oxidized region with KOH treatment and SEM-EDS (Scanning Electron Microscopy - Energy Dispersive x-ray Spectroscopy) was established for ethylene propylene rubber (EPR) [1]. Carboxyl groups (-COOH) are produced by oxidation of EPR after irradiation with gamma-rays in air. By soaking this oxidized EPR in the KOH solution, hydrogen atoms in the carboxyl groups are replaced with potassium atoms (-COOK). Potassium can be detected by EDS, and therefore, the oxidized region is observed by SEM-EDS. SEM-EDS has the merit of the observation and element analysis simultaneously. SEM-EDS has not been adopted to observe the oxidized region of polymer other than EPR. In this study, we examined observation of the oxidized region of polyethylene.

A polyethylene sheet (size: 5 cm square and 2 mm thickness) was irradiated by ^{60}Co gamma-rays at room temperature with a dose rate of 2 kGy/h for 400 h. Irradiation was conducted at JAEA Takasaki Food Irradiation Facility. A piece of irradiated polyethylene was picked up by utility knife as shown in Fig. 1. Two mL of 0.1 N of KOH solution and 2 mL of isopropanol were poured in a glass vial. That piece was added to the glass vial. The solution was kept at 70 °C for 24 h. Next, the piece was picked up and washed with distilled water. Then the piece was dried at room temperature in vacuum for 1 night. The piece was coated by carbon to improve conductivity. Potassium of the cross section of the piece was observed by SEM-EDS. The accelerated voltage of SEM was 25 kV.

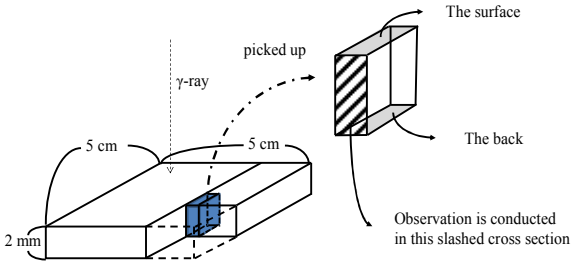

Fig. 1 The way to pick up a sample and its definition for observation by SEM-EDS.

As shown in Fig. 2, potassium was observed near the surface in the cross-section of the polyethylene sheet. The intensity of potassium is higher at the region within several tens micro meters from the surface and the back than the other region. The result means that oxidation occurs at these regions. It is shown that the oxidized region of not only EPR but also polyethylene can be observed with KOH treatment and SEM-EDS. So, SEM-EDS is effective for the analysis of the oxidation of the materials.

Reference

1) Y. Morita et al., ACS Symposium, Series 475 (1991) 485-99.

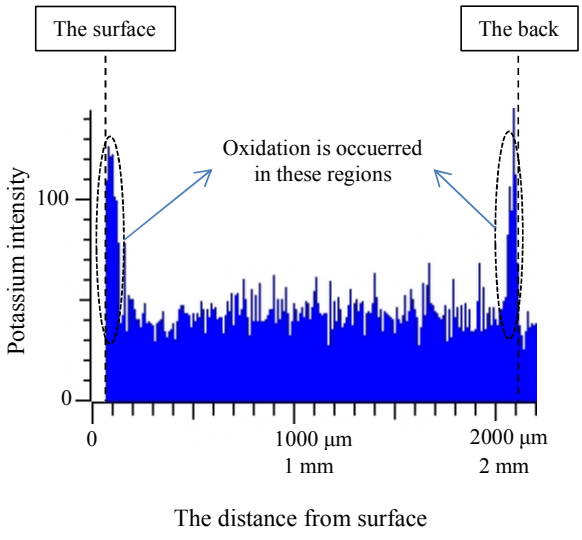

Fig. 2 Potassium distribution in a polyethylene sheet irradiated with at a dose rate of 2 kGy/h for 400 h.

1 - 27 Radiation Resistance Test of Insulation for JT-60SA In-vessel Coil

H. Murakami, A. Sukegawa, G. Matsunaga and K. Yoshida

Department of Tokamak System Technology, FRDD, JAEA

The modifying of the JT-60U magnet system to the superconducting coils (JT-60SA) is progressing as a satellite facility for ITER by both parties of Japanese government (JA) and European Union (EU) in the Broader Approach agreement [1]. The in-vessel coils are located inside the vacuum vessel for error field correction and fast plasma control. The in-vessel coils are made of copper conductor and glass-resin insulation. The radiation dose of in-vessel coil is much higher than superconducting magnet located outside of vacuum vessel because the vacuum vessel works as a radiation shield. The total radiation dose of in-vessel components and out-vessel components are predicted to be 9 MGy and 20 kGy, respectively. Therefore the insulation materials of in-vessel coils are required more than 9 MGy of radiation resistance.

BT (Bismaleimide Triazine) resin, CE (Cyanate Ester) resin and epoxy resin were selected as the candidates of the insulation material. BT resin and CE resin are well known as high radiation resistant material. BT resin and CE resin withstand more than 50 MGy of radiation dose[2,3]. On the other hand, the epoxy resin has advantage on the cost because of lower material cost and easy manufacturing.

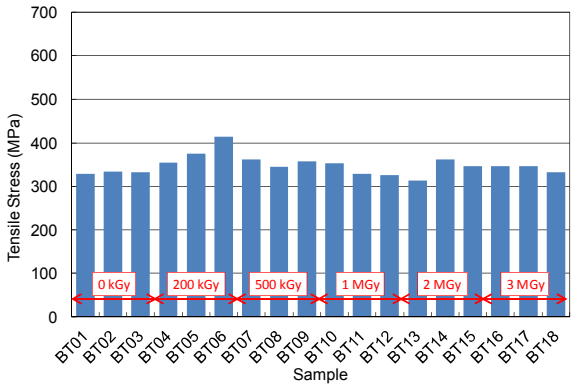

Fig. 1 Tensile test results (BT resin).

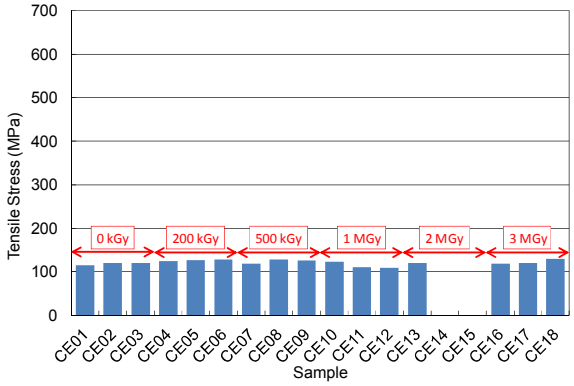

Fig. 2 Tensile test results (CE resin).
(*)CE14,CE15 were not measured due to machine trouble.

The radiation resistance tests are being conducted to select the insulation material for in-vessel coil. The model number of BT resin, CE resin and epoxy resin are "GXA-67N, Hitachi Chemical", "LVT-50, Lonza" and "Duralco 4460, Cotronics", respectively. The tensile tests are performed using samples irradiated up to 3 MGy at the Cobalt 60 irradiation facility at JAEA Takasaki Institute as a radiation resistance test. The acceptance criterion is more than 50% of tensile strength of non-irradiated samples.

The test results of BT resin (Fig.1) and CE resin (Fig. 2) indicate that the tensile strength of irradiated samples is almost same as the tensile strength of non-irradiated samples. The test results of epoxy resin (Fig. 3) show that two type of tensile strength, around 290 MPa and 500 MPa, were measured. This difference is derived from sample direction as shown in Fig. 4. Considering the sample direction, the tensile strength of epoxy resin is not degraded up to 3 MGy.

The radiation resistance test for insulation materials of in-vessel coil was conducted and all materials can be used up to 3 MGy. The higher irradiated samples up to 9 MGy of rated dose for in-vessel coil will be tested soon to decide the insulation material.

References

1) S. Ishida et al., Nucl. Fusion 51, (2011) 094018.
2) Center for Proton Accelerator Facilities Planing Groupe, JAERI-Data/Code 2003-015 (2003).
3) K. Bittner et al., Fusion Eng. Des. 66-68 (2003) 1209-13.

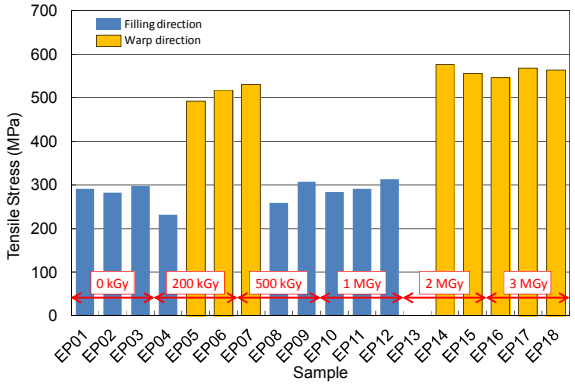

Fig. 3 Tensile test results (epoxy resin).
(*)EP13 was not measured due to machine trouble.

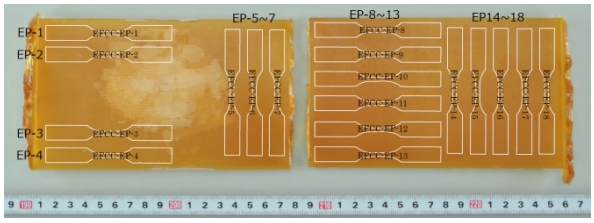

Fig. 4 Sample direction of epoxy resin.

1 - 28 Development of Remote Imaging and Radiation Measurement Technique under High Radiation Dose

H. Naito, T. Ishikawa, T. Saikawa, K. Ito, C. Ito and T. Sekine

Experimental Fast Reactor Department, ORDC, JAEA

Introduction

A new probing technique using optical fiber is under development to inspect the damaged boiled water reactors of the Fukushima Daiichi Nuclear Power Station [1]. The proposed probing system consists of a fiberscope for observation, a fiber-coupled laser-induced breakdown spectroscopy system, and scintillators with optical fibers for gamma-ray monitoring. In this report, (1) the irradiation result of high radiation resistant image fiber and (2) the gamma-ray detection tests of scintillators were described.

Radiation resistance of image fiber

To be high radiation resistant, we have developed the image fiber which was made of pure silica core with 1,000 ppm hydroxyl and fluorine doped silica cladding[2]. In addition, we have planned the observation using infrared region, in which is no large absorption by radiation. In the past irradiation tests, we measured the radiation induced loss of the image fiber using low picture elements image fiber[1,2], then we examined transmission capability of image in high radiation environment. Long wavelength light is easy to leak from the core of optical fiber. We increased cladding thickness for an infrared imaging to avoid light leakage to the neighbor core. An image fiber which was 10 m long and had 4.4 μm thick cladding and 22,000 picture elements was irradiated with ^{60}Co gamma-rays over 1 MGy at TARRI. The transmission images of the test chart are shown in Fig. 1. Infrared imaging can be useful although the resolution of infrared image was a little worse than that of visible image. After the irradiation, for visible light, the center of image was darkened a bit but we could observe.

High-dose rate gamma-ray measurement system

For measuring high-dose rate gamma-rays, we have adopted optical instrumentation system using fiber and ruby scintillator. Experiments were carried out using ^{60}Co gamma-ray at TARRI. The optical fiber has improved radiation resistance by the addition of fluorine to pure silica. The ruby scintillator made from Al_2O_3 with a Cr_2O_3 content of 0.4%. Figure 2 shows the wavelength spectra. There is a peak emission of Cr^{3+} in ruby scintillator at 693 nm, and there is a peak emission of optical fiber to 300～500 nm. It is expected measurable selectively emitting ruby scintillator by performing wavelength discrimination.

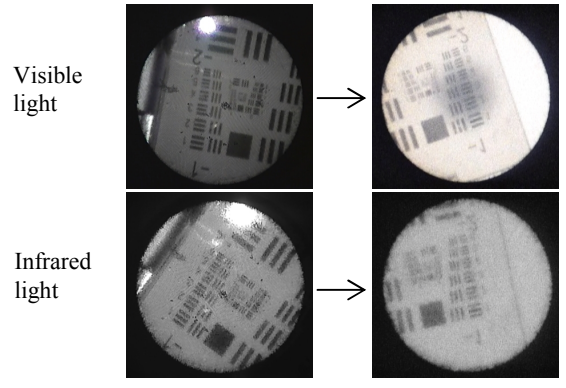

Fig. 1 Transmission images of the test chart: (Top) visible light (Bottom) infrared light, (Left) before irradiation (Right) after 1 MGy irradiation. Picture elements of image fiber were 22,000.

Figure 3 shows the results of the radiation resistance experiment. We got the applicable prospect of this measurement system since there is no reduction of the transmission and the amount of light emission in both ruby scintillators, optical fiber after the irradiation of 1 MGy.

Summary

We confirmed that the optical fibers have enough radiation resistance and have a prospect of the application for ruby scintillator as a high-dose gamma-ray measurement system. We are preparing a prototype probing system and make steady progress on a practical application for the remote inspection in RPV/PCV.

References

1) H. Naito et al., JAEA Takasaki Annu. Rep. 2012 JAEA-Review 2013-059 (2014) 27.
2) H. Naito et al., JAEA Takasaki Annu. Rep. 2010 JAEA-Review 2011-043 (2012) 23.

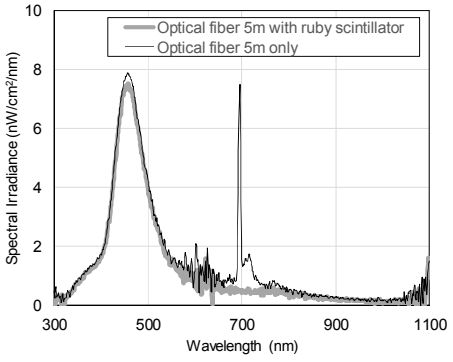

Fig. 2 Wavelength spectra under gamma-rays of 4 kGy/h.

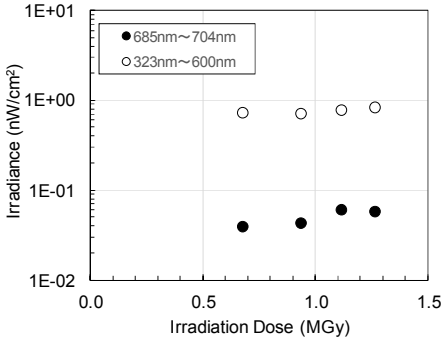

Fig. 3 Relationship between irradiance intensity and irradiation dose.

1 - 29 Degradation Behavior of LED and Photo Diode by Gamma Irradiation

T. Takeuchi, H. Hanakawa, H. Shibata, T. Uehara, S. Ueno,
H. Kumahara and K. Tsuchiya

Neutron Irradiation and Testing Reactor Center, ORDC, JAEA

As a part of research and development for restarting of JMTR, advanced measuring systems are desired under neutron irradiation. Previously, in-situ measurements of the temperature, neutron flux and so on had been performed with instrumented capsules. However, after the restart, many users will not be able to obtain satisfying irradiation data because over 90 percent of the instrumented capsules are already booked in irradiation schedule. Therefore, development of remote sensing techniques, which enable us to obtain the data from un-instrumented capsules during irradiation, has been started from 2012. In this study, gamma irradiation effects on LEDs and photo diodes (PDs) were evaluated for the development of a radiation-resistant in-water wireless transmission system using visible light.

The three types of LEDs and the two types of PDs were irradiated at the ^{60}Co gamma-ray irradiation facility[1]. The irradiation condition is shown in Table 1. The LEDs were encapsulated in a bullet-shaped epoxy resin package and each had 575, 609 and 635 nm of peak emission wavelengths, respectively. One of the PDs had a light window composed of a borosilicate glass and a silicone resin, and the other a quartz glass. The current-voltage property and total luminous flux of the LEDs and the dark current and light sensitivity of the PDs were measured before and after the irradiation.

The dose dependence of the total luminous flux of the LEDs is shown in Fig. 1. The total luminous flux rapidly decreased at the low dose and then slowly at the high dose for all LEDs. The shorter wavelength the LED emitted, the greater the total luminous flux decreased. After the irradiation, the resin lenses turned oxblood and their coloring became dark with the irradiation dose. Meanwhile, the current-voltage characteristics hardly changed.

The dose dependence of the light sensitivity of the PDs is shown in Fig. 2. For the PD with the resin light window, the light sensitivity rapidly decreased at the low dose and then slowly at the high dose. The shorter wavelength the PD received, the greater the light sensitivity decreased. These tendency are almost the same as in the case of the LED. For the other one with the quartz glass window, which has good irradiation resistance[2], the light sensitivity did not changed significantly except for the wavelength of 450 nm. After the irradiation, only the resin window turned oxblood and their coloring became dark with the irradiation dose while the dark currents were at most 10 nA for both the PDs. These results indicated that the decreases of the total luminous flux of the LEDs and the light sensitivity of the PDs were caused by not the degradation of the semiconductor parts but the coloring of the resin parts by the irradiation.

In the future, the irradiation experiments with applying voltage on the devices will be performed as the actual condition in use. Irradiation effects on other components, e.g. electric sources and optical filters, will also be investigated.

Table 1 Gamma irradiation condition of the LEDs and PDs.

Dose [kGy]	Dose rate [kGy/h]	Temperature [°C]
10, 20, 50, 100, 1000	10	～20

Acknowledgement

The authors would like to thank to R. Yamagata at the irradiation facility in JAEA for supporting the experiments.

References

1) H. Saito et al., JAEA-Technology 2008-071 (2008).
2) E. J. Friebele et al., J. Non-Crust. Solids, 38 & 39 (1980) 245.

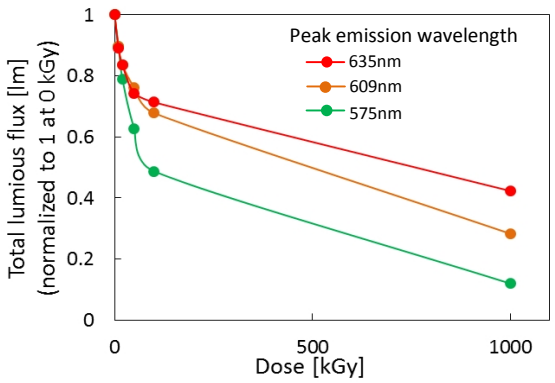

Fig. 1 Dose dependence of the total luminous flux of the LEDs.

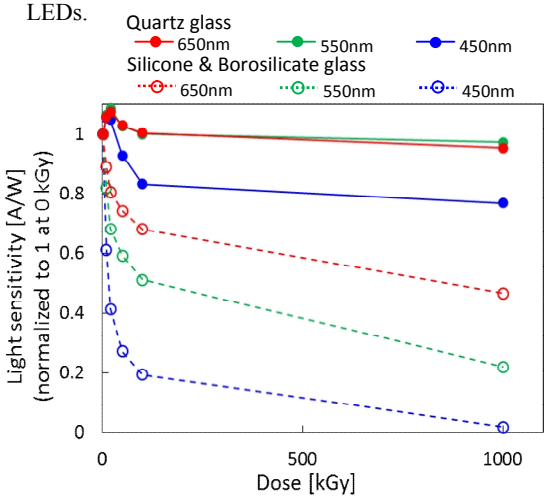

Fig. 2 Dose dependence of the light sensitivity of the PDs.

1 - 30 Development of Radiation-resistant LED Lighting

M. Kamikawa [a)], K. Oka [b)], R. Yamagata [c)], K. Izumi [a)], J. Takemoto [a)] and M. Kawasaki [a)]

[a)] Kandenko Co., Ltd.,
[b)] Laser Application Technology Division, QuBS, JAEA,
[c)] Department of Advanced Radiation Technology, TARRI, JAEA

We had performed the gamma-ray irradiation tests on the equipments of ready-made LED lighting. As a result, we had obtained base data for radiation-resistant of the equipments. And we developed radiation-resistant LED lighting by the data. This paper reports on the examination of the gamma-ray irradiation for “Development of the Radiation-resistant LED lighting”.

加速器施設・核融合施設・原子炉施設・核燃料再処理施設等は、高放射線環境下になるエリアを有する。高放射線環境下では、電気設備の多くは寿命が著しく短くなり、照明器具も例外ではない。これまでに、筆者らは既製品 LED 照明のガンマ線照射試験を行い、基礎データを測定してきた [1)]。本研究では、これらの基礎データを基に開発した、「耐放射線性 LED 照明器具の開発」とガンマ線照射試験について報告する。

炉心周辺 [2)] は、放射線環境のほかに、高温多湿の環境であることが想定されるため、IP [3)]（塵埃・水の浸入に対する保護）性能を有する器具の設計・製作を行った。器具の外観と概要を Fig. 1 に示す。

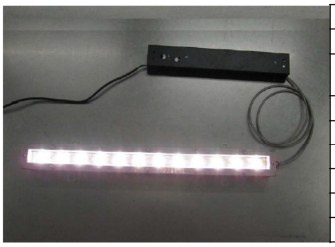

luminous flux	1800lm（more than）
Input Voltage	AC 100-242V
Output Current	DC 300mA（Constant current）
Output Voltage	DC 115V
Output Power	35W
IP	IP65
SIZE （mm）	W800×H80×D80
Weight （kg）	About 5kg
Others	Outside of Converter

Fig. 1 Radiation-resistant LED lighting and its specification.

耐放射線性試験は、高崎量子応用研究所内のコバルト 60 照射施設第 1 照射室を利用し、ガンマ線照射により実施した。試験は、吸収線量 5 MGy となるまで照射した。ガンマ線吸収線量と照度の変化率の関係を Fig. 2 に示す。

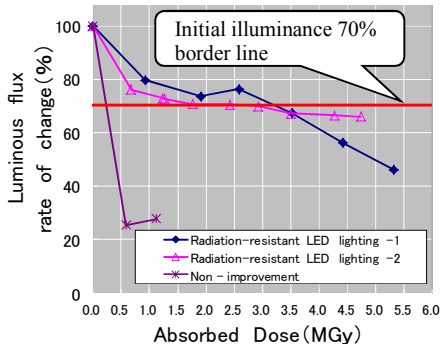

Fig. 2 Luminous flux rate of change.

今回開発した耐放射線性 LED 照明器具は、耐放射線性の優れた材料・素材を選定した事により、ガンマ線吸収線量約 2 MGy 以上でも初期照度の 70%以上の照度を維持できることを確認した。この結果は約 2 MGy においても JIS-C-8150-3 [4)]に記載する初期光束の 70%を満足できたと考える。未照射時の光源の様子とガンマ線吸収線量の違いによる光源の様子を Fig. 3 に示す。またガンマ線照射時の各電気的特性（入出力電流・電圧）の変化率は、±1%程度で安定して点灯していることが確認できた。

本器具は、器具製作時に IP 試験（IP 65）を実施しこの仕様を満足している。しかし、放射線環境下では、絶縁物の物性劣化などでこの性能が維持しないことが考えられる。そこで、ガンマ線照射後もこの性能を有しているかの確認を行った。その結果、ガンマ線照射（吸収線量 3.3 MGy）後でも IP 65 を満足していることを確認した。

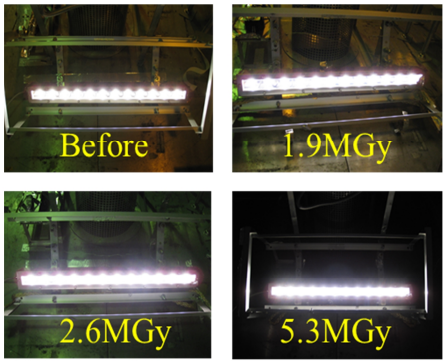

Fig. 3 Luminous flux state of gamma-ray irradiation.

本研究で開発した LED 照明器具の耐放射線性に関する実証試験を実施し、耐放射線性 LED 照明器具を開発することができた。今回開発した「耐放射線性 LED 照明器具」は、炉心周辺部のような線量率が高く、高温多湿のような特殊環境に耐え、省エネルギー、長寿命の照明器具である。

本研究における開発から、廃炉作業等高放射線環境下における照明器具のメンテナンス頻度の低減による被ばくの低減及び放射線廃棄物の減容化に貢献できるものと考える。今後は、経済性・耐放射線性の向上を考察して製作した、改良器具のガンマ線照射試験を実施する。

放射線環境下への適用や、早期の福島復興支援にも貢献できるものと考える。

References

1) M. Kamikawa et al., JAEA Takasaki Annu. Rep. 2012 JAEA-Review 2013-059 (2014) 28.
2) Ministry of Economy, Trade and Industry, Home Page Technical catalogue WG, “Development of the containment vessel in-house investigation technology”, (Feb. 2012).
3) JIS C 0920: 2003 Degrees of protection provided by enclosures (IP Code).
4) JIS C 8105-3: 2011 Luminaires-Part3: General requirements for performance.

1 - 31 Irradiation Hardening of Extra High Purity Ni-base Superalloy under External Stress

I. Ioka [a)], G. H. Kim [b)] and T. Inoue [c)]

[a)] Division of fuels and Materials Engineering, NSED, JAEA, [b)] Tokamak Eng. Dept, National Fusion Research Institute, ITER Korea, [c)] Division of Fuels and Materials Development, ANSRD, JAEA

An extra high purity (EHP) Ni-base superalloy has been developed as MA doped MOX fuel claddings for sodium cooled fast reactors. In EHP alloys, impurities, such as C, O, N, P and S were reduced to less than 100 ppm in total to improve workability, irradiation embrittlement and intergranular corrosion resistance. The cladding materials suffer from stress (external pressure, thermal stress) under the operation. There have been many irradiation experiments done under external stress to investigate stress effects on microstructural evolution of 300 series austenitic stainless steels. It is reported that the total nucleation rate of Frank loops increased with increasing external stress [1)]. However, there are few studies on the effect of external stress on microstructural evolution of Ni-base superalloy under irradiation. The purpose of this study is to evaluate the effect of external stress on irradiation hardening of EHP Ni-base superalloy.

The material used in this study was W-rich silicide phase strengthened EHP Ni-base alloy, so called EHP(WSi) alloy. The EHP(WSi) alloy was manufactured by the multiple refined melting processes. The ingot was solution-treated at 1,498 K for 1 h and then aged at 1,123 K for 24 h. The chemical composition of the alloy is given in Table 1. The materials were cut to small coupon type specimens ($20 \times 5 \times 0.5$ mm^3). Specimens were plastically deformed by mean of a special bending holder during the irradiation as shown in Fig. 1. Tensile strain on the surface of bent specimens was calculated to be about 2%, so that the initial stress was over 0.2% offset stress level. Both deformed and undeformed specimens were simultaneously irradiated using the holder. Irradiation was performed under triple (Ni^{3+}+He^{+}+H^{+}) ion beams at 673 K in the TIARA facility at JAEA. Ions of 12 MeV Ni^{3+}, 1.05 MeV He^{2+} and 380 keV H^{+} were injected to simulate a FaCT core irradiation environment. The peak depth of displacement damage was calculated to be 2 μm by SRIM-2000. The mean displacement damage at depth of 1.5 μm was changed from 1 to 27 dpa. The injection rates for He and H were 1 appmHe/dpa and 15 appmH/dpa, respectively. The surface temperature of the both specimens was measured by two-dimensional infrared pyrometer and kept to be constant under irradiation. The microhardness was measured by using a nanoindenter. The hardening behaviour of the irradiated specimens was evaluated by indentation depth of 400 nm in consideration of the damage depth. The microhardness was calculated from mean values of 10 points per each specimen.

The dependence of microhardness on irradiation was evaluated for EHP(WSi) alloy with and without bending deformation. Figure 2 shows the change in irradiation hardening at 823 K as a function of dose. The vertical axis of Fig. 2 denotes the microhardness of irradiated specimen normalized by that of unirradiated. In both of deformed and undeformed specimens, the microhardness increased immediately up to 5 dpa and was saturated. Although variation of data for deformed specimen was large, the normalized microhardness of deformed specimens was slightly lower than that of undeformed ones from initial condition. The same tendency that irradiation hardening of SUS316L bent specimen was suppressed at about 10 dpa in comparing with that of un-bent specimen for the irradiation at 673 K has been reported by Okubo et al [2)]. The difference between the deformed and undeformed specimens was not clear, so the microstructural evaluation by TEM is essential issue for interpreting the difference.

References

1) H. Tanigawa et al., Nucl. Instrum. Meth. Phys. Res. B 102 (1995) 151.
2) N. Okubo et al., J. Nucl. Mater. 386-388 (2009) 290.

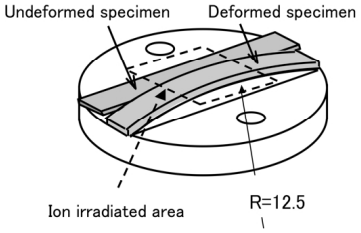

Fig. 1 Special bending holder for ion irradiation.

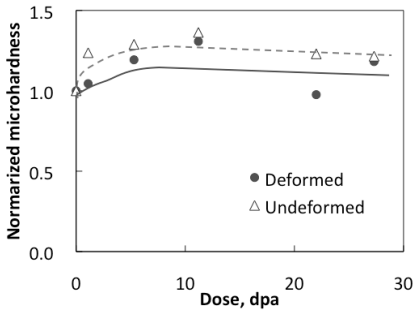

Fig. 2 Dependence of microhardness on irradiation damage at 823 K for EHP(WSi) alloy.

Table 1 Chemical composition of EHP(WSi) alloy (wt%).

Fe	Ni	Cr	W	Si	C	P	S	O	N
bal.	42.8	25.35	10.24	2.75	0.004	0.0005	<0.0005	<0.0005	0.0006

1 - 32 Precipitate Stability and Swelling Resistance of High-Nickel Alloy during Irradiation

T. Inoue [a,b], S. Yamashita [a,b,c], Y. Sekio [b], I. Yamagata [a,b], T. Kaito [a,b] and I. Ioka [d]

[a] Fast Reactor Fuels and Materials Technology Development Unit, ANSRD, JAEA, [b] Fukushima Fuels and Materials Department, ORDC, JAEA, [c] Fukushima Project Team, ORDC, JAEA, [d] Division of Fuels and Materials Engineering, NSED, JAEA

1. Introduction

Precipitation-strengthened high-nickel alloys have been developed for fuel cladding material in advanced reactor because of their intrinsic superior swelling property. In most cases, these alloys are strengthened by an intermetallic compound such as ordered phase γ' [Ni_3(Ti, Al)] formed in the matrix. The most important issue in development of high-nickel alloy is considered to be the improvement of mechanical properties at elevated temperature; the significant ductility is lost due to irradiation at high temperature. The cause of this problem was believed to be the re-distribution of ordered phase γ' and solute segregation to defect sink sites, such as grain boundary, dislocation and void surface, during irradiation [1]. In this study, several types of precipitation-strengthened high-nickel alloys were developed and then the phase stability (precipitate stability and swelling resistance) in these alloys during irradiation was evaluated by utilizing TIARA facility.

2. Experimental

The materials used in this study were two types of high nickel alloys and an austenitic stainless steel for the comparison; carbo-nitride phase strengthened high-nickel alloy (8NK_A), γ'/γ'' [Ni_3Nb] phase strengthened high-nickel alloy (1543G) and Ti-modified SUS316 stainless steel (PNC316).

Specimens were irradiated at the TIARA facility by 12.0 MeV Ni^{3+} ions with 1.05 MeV He^+ ions and 0.38 MeV H^+ ions. The irradiation was mainly performed to 100 dpa at the depth of 1.0 μm and the damage rate was about 1.0×10^{-3} dpa/s at this depth. The implantation rates for He and H were 1 appmHe/dpa and 15 appmH/dpa, respectively.

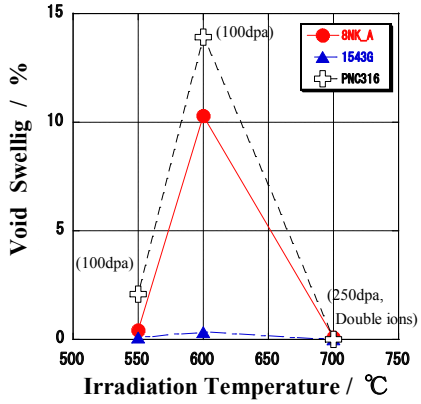

Fig. 1 Irradiation temperature dependence of void swelling in triple ($Ni^{3+}+He^{+}+H^{+}$) and double ($Ni^{3+}+He^{+}$) beam ion-irradiated high-nickel alloys.

Thin foils for transmission electron microscopy (TEM) were fabricated using a focused ion beam (FIB) instrument. TEM observations for phase stability evaluation of ion-irradiated high-nickel alloys were carried out with a JEM-4000FX operated at 400 kV.

3. Results and Discussion

Figure 1 shows irradiation temperature dependence of void swelling of 8NK_A, 1543G and PNC316. This result indicates that swelling peak temperature is around 600 °C and that 1543G has superior swelling resistant property to the other alloys [2].

TEM images of typical void and precipitate structures observed in 1543G, 8NK_A and PNC316 at 550 and 600 °C are shown in Fig. 2. It is considered that void formation and growth of all specimens were suppressed due to fine precipitation distribution at 550 °C and that void coarsening was accompanied when the existing massive shape of precipitates coarsened at 600 °C. This result indicates that swelling resistance of these precipitation-hardening alloys is closely related to the precipitate morphology and stability during irradiation.

References

1) W. J. S. Yang et al., J. Nucl. Mater. 132 (1985) 249.
2) S. Yamashita et al., JAEA Takasaki Annu. Rep. 2012 JAEA-Review 2013-059 (2014) 35.

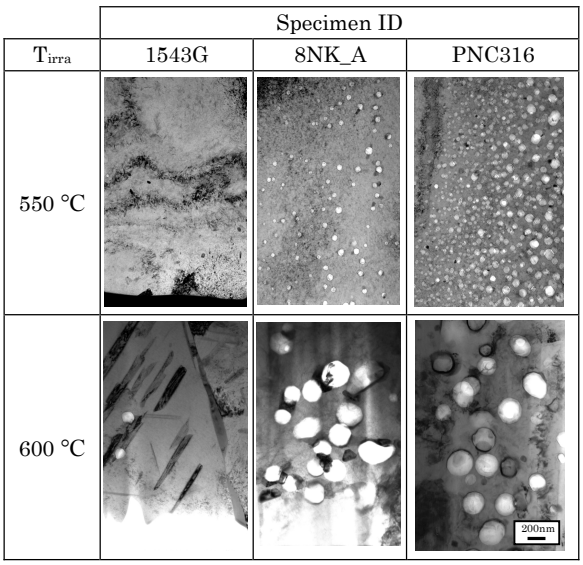

Fig. 2 TEM micrographs showing voids in 1543G, 8NK_A and PNC316 irradiated with triple ions up to 100 dpa at 550 and 600 °C.

1 - 33 Irradiation Hardening of G-Phase Strengthened Ni-base Alloy under Multi-ion Irradiation

I. Ioka [a)], G. H. Kim [b)] and T. Inoue [c)]

[a)] Division of Fuels and Materials Engineering, NSED, JAEA, [b)] Tokamak Eng. Dept., National Fusion Research Institute, ITER Korea, [c)] Division of Fuels and Materials Development, ANSRD, JAEA

1. Introduction

Precipitation-strengthened Ni-base alloys have been considered for fuel cladding in advanced reactors. Because these alloys have not only excellent properties at high temperature, but also very good performance with respect to swelling and creep resistance during irradiation. The main factor of high temperature strength in these alloys is the formation of ordered phase γ' [Ni_3(Ti, Al)] or γ'/γ'' [Ni_3Nb] in the matrix [1)]. However, many studies reported that these alloys exhibited the significant ductility loss due to irradiation at high temperature [1-3)]. The reasons of poor ductility were believed to be the re-distribution of ordered phase γ' and solute segregation during irradiation at defect sink sites, such as grain boundary, void surface and dislocation.

From this viewpoint, we have developed an alternative Ni-base alloy strengthened by W-rich silicide (G phase), which has a good stability at high temperature. The aim of this work is to evaluate the ductility of the G phase strengthened Ni-base alloy irradiated at various temperatures. The ductility is evaluated from microhardness of ion-irradiated material. The microhardness of G phase strengthened Ni-base alloy is compared with that of ordered phase γ' in Nimonic PE16, which is a representative commercial alloy of precipitation-strengthened Ni-base alloys.

2. Experimental

G phase strengthened Ni-base alloy (Fe-43Ni-25Cr-10W-2.7Si) under extra high purity grade so-called EHP(WSi) alloy was used for the ion-beam irradiation experiments. To estimate irradiation hardening, ion-irradiation were performed under triple (Ni^{3+} + He^{+} + H^{+}) ion beams at 100 dpa and at temperatures ranging from 673 K to 973 K, which was the range of operation temperature for cladding material of JSFR. Twelve MeV Ni^{3+} was injected to produce radiation damage and ions of 1.05 MeV He^{2+} and 380 keV H^{+} were implanted through Al degrader foils to simulate a FaCT core irradiation environment. The peak depth of displacement damage was calculated to be 2 μm by SRIM-2000. The mean displacement damage at depth of 1.5 μm was selected to be 100 dpa. The injection rates for He and H were 1 appm/dpa and 15 appm/dpa, respectively.

The surface temperature of the specimens was measured by two-dimensional infrared pyrometer and kept to be constant under irradiation. The microhardness was measured by using a nanoindenter. The hardening behaviour of the irradiated specimens was evaluated by indentation depth of 400 nm in consideration of the damage depth.

3. Results and discussion

The dependence of microhardness on irradiation temperature was evaluated for EHP(WSi) and Nimonic PE16. The change in microhardness is shown in Fig. 1. The vertical axis of Fig. 1 denotes the microhardness of irradiated specimen normalized by that of unirradiated. The unirradiated specimens have received the same heat history as the irradiated specimens. In both specimens, the microhardness decreased with the increase of irradiation temperature. It seems that the decrease in microhardness is attributed to thermal recovery of irradiation defects. EHP(WSi) showed a bigger irradiation hardening within the range from 673 K to 823 K compared with PE16. It is considered that it is based on the difference in the stability of radiation defects. The detailed microstructural evaluation with TEM is essential issue for interpreting the difference.

References

1) W. J. S. Yang et al., J. Nucl. Mater. 132 (1985) 249.
2) W. J. S. Yang, J. Nucl. Mater. 108&109 (1982) 339.
3) D. J. Mazey et al., J. Nucl. Mater. 160 (1988) 153.

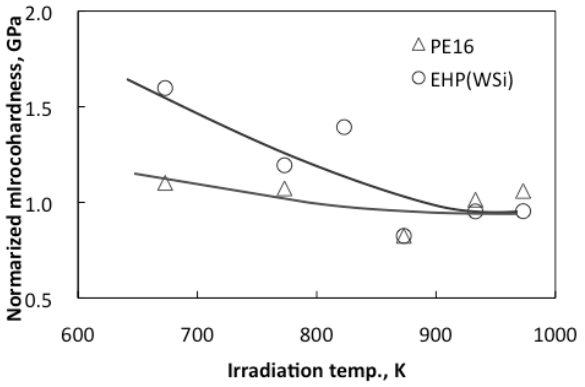

Fig. 1 Change in microhardness of Nimonic PE16 and EHP.(WSi) irradiated at 100 dpa as a function of irradiation temperature.

1 - 34 Helium Effects on Hardening Behaviors of Ferritic/Martensitic and Austenitic Steels in High Irradiation Fields

N. Okubo [a)], N. Ishikawa [a)] and S. Ohnuki [b)]

[a)] Division of Fuels and Materials Engineering, NSED, JAEA,
[b)] Faculty of Engineering, Hokkaido University

Ferritic/martensitic steels F82H and austenitic stainless steels SUS316L were irradiated with aiming at considerably high damage level and high concentration of helium by means of dual ion irradiations in this period. The hardening behavior of the irradiated SUS316L steels indicated that the hardness was saturated and was kept constant at higher dose of irradiation. There was almost no difference on radiation hardening behaviors between single irradiation and dual irradiation. In the case of F82H, however, no saturation of hardening behavior was observed even at high fluence of 250 dpa. Also, the hardening behavior of F82H showed extra hardening in dual irradiation comparing with single irradiation.

In future commercial fusion system and ADS target components, the structural materials will be heavily irradiated under severe conditions, where displacement damage, high concentration of He and H atom accumulations will simultaneously occur by high energy neutron irradiations. Degradation of mechanical properties after irradiation should be suppressed within a range permissible for the system design. High fluence neutron irradiation experiments over a few hundred dpa are practically difficult due to long time irradiation and high cost. Especially, nuclear transmutation gas concentration in present experimental reactor irradiation is not sufficient for estimating He effects. Simultaneous ion irradiation experiments are powerful techniques for simulating fusion and ADS irradiation fields.

In this report, we address irradiation hardening behaviors of SUS316L and F82H steels in the case of simultaneous irradiation of helium at considerably high damage levels.

Ion irradiations of 10 MeV-Fe^{3+} and 1.05 MeV-He^{+}, which depth distribution was extended by energy degrader made of 800 nm Al foil, was conducted for SUS316L (solution annealed) and F82H (IEA Heat, normal heat treatment) at 300 °C. Achieved damage level was 250 and 200 dpa in single and dual irradiation, respectively. The irradiation rate was 1.2×10^{-3} dpa/s and Helium rate was about 100 appmHe/dpa. After the irradiation, the micro-hardness was measured by using nanoindentation technique. To suppress the variation of surface morphology among the specimens, the identical specimen was irradiated for SUS316L and F82H after intermittent hardness measurements over 100 dpa in both cases of single and dual irraditions.

Dependence of single and dual irradiation hardening on the displacement damage to SUS316L and F82H is shown in Fig. 1. In the case of single irradiation to SUS316L, the irradiation hardening increased gradually as increasing the damage up to 50 dpa and was subsequently saturated. The dual irradiation showed almost the same hardening behavior as that for SUS316L. Then, He effect did not appear in this experiment for SUS316L. In the case of F82H, however, different hardening behavior appeared in both single and dual irradiations. The radiation hardening was not saturated even at considerably high fluence of 250 dpa in single irradiation. In the case of dual irradiation, extra hardening appeared obviously from 50 to 200 dpa. The extra increment was about 9% at maximum.

In ferritic steels, the radiation hardening is correlative with DBTT (ductile-brittle transition temperature) shift [1)]. This means that materials used in future ADS and fusion system should be modified in case of high irradiation at relative low temperature around 300 °C. Optimization of heat treatments is one of the promising techniques [2)] to suppress the radiation degradation.

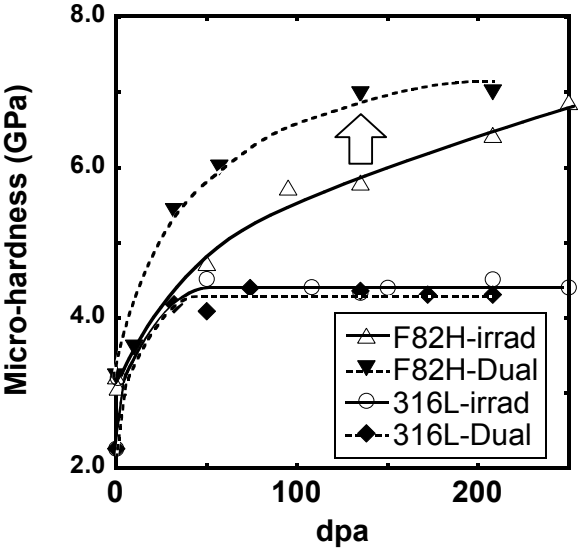

Fig. 1 Hardening behaviors of F82H and SUS316L steels.

References

1) T. Yamamoto et al., J. Nucl. Mater. 356 (2012) 27-49.
2) N. Okubo et al., J. Nucl. Mater. 417 (2011) 112-14.

1 - 35 Evaluation of Irradiation Resistance of ODS Ferritic Steel for Fast Reactor Application

T. Tanno [a)], S. Ohtsuka [a)], Y. Yano [a)], T. Kaito [a)] and N. Ohkubo [b)]

[a)] Fast Reactor Fuels and Materials Technology Development Unit, ANSRD, JAEA,
[b)] Division of Fuels and Materials Engineering, NSED, JAEA

Because fuel cladding having long life and fracture resistance is a key technology for the practical application of fast reactor, R&D of it is being carried out. Japan Atomic Energy Agency (JAEA) chooses oxide dispersion strengthened (ODS) steel as the advanced fuel cladding material for fast reactors.

The 9Cr and 11Cr-ODS steels are prioritized in JAEA. The stability of the dispersed oxide under irradiation at high temperature should be evaluated, because the dispersion strengthening is dominant in high temperature strength of ODS steels. In case of 11Cr-ODS steel, ductility loss due to irradiation at lower temperature (< 450 °C) is a concern similar to other conventional high-Cr ferritic steels. A lot of irradiation data are necessary to evaluate irradiation resistivity, whereas the data are limited. There are many difficulties to conduct neutron irradiation, such as limited irradiation field, long irradiation time, human resource, activation, etc. Heavy ion irradiation is beneficial as alternative irradiation, because it can provide high dose in short time, and activation is negligible if injection energy is lower than threshold energy. The purpose of this study is to obtain the dose dependence of irradiation behavior of JAEA-ODS steels in short period by ion irradiation.

The irradiated materials are JAEA-9Cr and 11Cr-ODS steel, and the chemical compositions of them are 9 wt%Cr-0.13C-2W-0.2Ti-0.35Y_2O_3 and 11Cr-0.14C-1.4W-0.4Ni-0.3Ti-0.35Y_2O_3, respectively. For each steel, two types of heat treatments were adopted: normalizing-and-tempering (NT; 1050 °C × 1 h, AC → 800 °C × 1 h, AC), and furnace-cooling (FC; 1,050 °C × 1 h → furnace-cooling at 30 °C/h). The specimens, which had been cut from the ODS steels and polished to optical grade with colloidal silica, were irradiated up to 120 dpa with 10.5-MeV Fe^{3+} ions from the 3-MV tandem ion accelerator of TIARA. The irradiation temperatures were 400 and 700 °C, which are the bottom and top temperatures of fuel cladding in fast reactor normal operation.

Nano-indentation tests were carried out to monitor the indication of oxide dispersion condition change under high temperature irradiation and irradiation hardening at low temperature.

Figure 1 shows the irradiation hardening ΔH_{IT} at 400 °C. The FC specimens were hardened over 1 GPa by 40 dpa irradiation, and the hardening was saturated. The values of ΔH_{IT} for NT specimens at 40 dpa were smaller than those for FC specimens and were not saturated. The increase of ΔH_{IT} continued up to 120 dpa, and the values of ΔH_{IT} at 120 dpa were almost the same as those for FC specimens. As the matrix of NT specimens is tempered martensite containing dense dislocation which is the sink site of irradiation defects, the concentration of irradiation defects decreased, and the irradiation hardening rate would decrease in NT specimens. The irradiation hardening behaviors of 9Cr and 11Cr-ODS steels are similar. Therefore, in this test, increasing Cr content from 9 to 11 wt% did not enhance irradiation hardening.

Figure 2 shows the irradiation hardening at 700 °C. The FC specimens were hardened to 0.7 - 1 GPa by 40 dpa irradiation, whereas the irradiation hardening of NT specimens was not significant up to 80 dpa. At 700 °C, the mobility of defects increases, and most of defects cannot form clusters, because they can reach the sink, such as the dislocations, then disappear in NT specimens. However, irradiation defects could accumulate in FC specimens, because of less of the sink in FC specimens. This difference might be cause of the difference between the irradiation hardening behavior of NT and FC specimens. In addition, the fact that irradiation softening was not significant, suggests that the dispersed oxide particles were stable under high-dose irradiation.

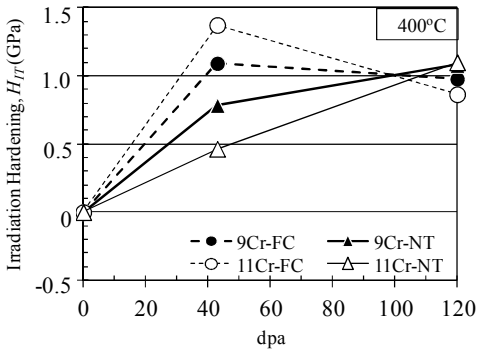

Fig. 1 Irradiation hardening due to ion irradiation at 400 °C.

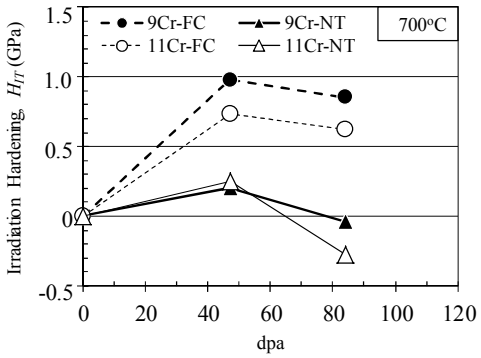

Fig. 2 Irradiation hardening due to ion irradiation at 700 °C.

1 - 36 Effects of Displacement Damage and Gas Atoms on Radiation Hardening and Microstructure in F82H Weldment

M. Ando, H. Tanigawa and K. Ozawa

Division of Rokkasyo BA Project, FRDD, JAEA

Reduced activation ferritic/martensitic steel (RAFs) is the most promising candidate for the blanket structural material in fusion reactor[1]. This blanket contains many joints of F82H plates using tungsten inert gas (TIG) welding, electron beam (EB) welding, hot isostatic pressing (HIP) and so on. These joints are also exposed to high neutron flux irradiation in fusion reactor. Neutron irradiation experiments are being performed at HFIR, JMTR and so on. Some data of modified F82H and welded F82H are also obtained from post irradiation experiment. On the other hand, the effect of transmutation helium on mechanical properties and void swelling in RAFs is also an important subject. Multi ion irradiation method contributed to this subject in F82H base metal because this method can easily simulate the ratio of displacement damage and helium/hydrogen production[2]. However study of helium/hydrogen gas effect with F82H welded joints is not enough.

The objective of this study is to evaluate radiation hardening and void swelling behavior on multi-ion irradiated F82H weldments up to 20 dpa.

The material used in this study was reduced activation ferritic/martensitic steel (F82H IEA; Fe-8Cr-2W-0.2V-0.04Ta-0.1C). The heat treatment was normalized at 1,040 °C for 0.63 h and the material was tempered at 750 °C for 1 h. TIG and EB weld metal (WM) were annealed at 720 °C for 1 h (PWHT; post weld heat treatment). Small coupon specimens ($6 \times 3 \times 0.8$ mm^3) were irradiated in the TIARA facility by 10.5 MeV Fe^{3+} ions with/without 1.05 MeV He^+ ions and 0.38 MeV H^+ ions. He^+ and H^+ ions implantation were performed using aluminum foil energy degraders. The irradiation was performed to 20 dpa at the depth of 1.0 μm and the damage rate was about 1.0×10^{-3} dpa/s at this depth. Post-irradiation experiments were performed at IFERC DEMO R&D building in Rokkasho. The microstructural examination was carried out using a JEOL JEM-2100F transmission electron microscope (TEM) operating at 200 kV. Micro-indentation tests were performed at loads to penetrate about 0.30 μm using an ENT-1100a (Elionix INC).

Figure 1 a)-c) show examples of microstructure images for F82H EB-WM and TIG-WM at 470 °C up to 20 dpa by dual and triple ion beam irradiation. For 470 °C irradiation in these F82H WMs, cavities are observed from about 0.7 to 1.6 μm from an irradiation surface. The void swelling in F82H EB-WM (dual beam), EB-WM (triple beam) and TIG-WM (triple beam) was ~0.6%, ~0.3% and ~0.4%, respectively. On the other hand, few cavities were observed in the same region as that at 400 °C irradiation.

The results of micro-hardness for F82H EB-WM and TIG-WM were shown in Fig. 2 a), b). For each F82H WMs, an irradiation hardening has a tendency to decrease at higher irradiation temperature. At 470 °C irradiation, many cavities were observed in each microstructure. However, these cavities did not strongly contribute to the irradiation hardening.

For this study, a temperature dependence of the void swelling for F82H EB WM and TIG WM could be roughly obtained. The peak of swelling arises at ~470 °C, and this result agrees with a behavior of high-dose irradiation (~50 dpa)[2]. Also, the void swelling of both WM microstructures was smaller than that of F82H IEA (base metal), slightly.

References

1) H. Tanigawa et. al., J. Nucl. Mater. 417 (2011) 9-15.
2) E. Wakai et. al., J. Nucl. Mater. 318 (2003) 27.

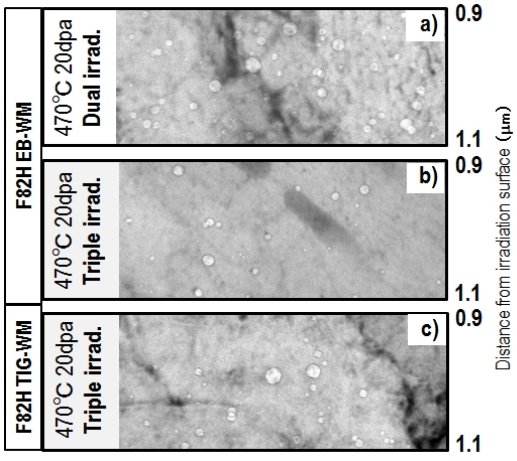

Fig. 1 Examples of microstructure images for F82H EB-WM and TIG-WM at 470 °C up to 20 dpa.

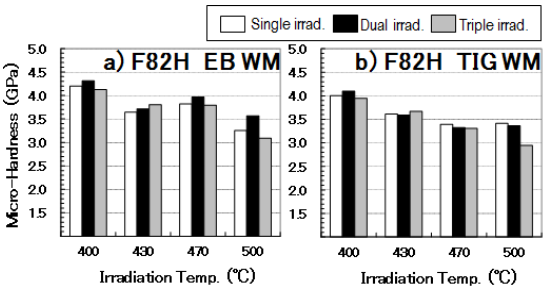

Fig. 2 Results of micro-hardness for F82H EB-WM and TIG-WM.

1 - 37 Influence of Irradiation Damages Produced by Heavy Ion on Hydrogen Isotope Dynamics for Plasma Facing Material

Y. Oya, L. Zhang, M. Kobayashi, H. Uchimura, K. Toda,
M. Sato and K. Okuno

Graduate School of Science, Shizuoka University

1. Introduction

For future fusion reactor, it is important to evaluate the fuel retention, especially tritium retention, for plasma facing W material under operation temperature. In especially, various energetic ions, like neutron, helium, and hydrogen isotopes will be dynamically implanted into W materials, which will introduce various trapping sites. We have already revealed that the D retention for 0.025 dpa neutron irradiated W is not reduced by D plasma exposure even at 800 K [1]. This indicates that the distribution of damages would control the D retention. In addition, the recovery of damages will proceed at the temperature above 800 K. Therefore, this study focuses on the elucidation of D retention behavior for damaged W at room temperature and accumulate the fundamental knowledge for hydrogen isotope retention in W exposed to complex circumstance at higher temperature.

2. Experimental

The mirror finished disk-type tungsten samples with the size of 10 mm in diameter and ~0.5 mm in thickness were exposed to 6 MeV Fe^{2+} to introduce the damages of 3.0×10^{-4} dpa to 1.0 dpa at TIARA facility in JAEA. Thereafter, the samples were picked up and transfer to Shizuoka University. The 1.0 keV deuterium ions (D^{2+}) were additionally implanted into these samples with the flux of 1.0×10^{18} D^+ m^{-2} s^{-1} up to the fluence of 1.0×10^{22} D^+ m^{-2} to evaluate the D retention behavior in W using TDS.

3. Results and discussion

Figure 1 shows the D_2 TDS spectra for W with various damage concentrations. The D desorption stages consisted of three stages, namely Stage 1 at ~400 K, Stage 2 at ~600 K and Stage 3 at above 700 K. Based on the previous reports, Stage 1 was assigned to be the desorption of D adsorbed on the surface or trapped by dislocation loops [2, 3]. The amount of D desorbed at Stage 1 was almost the same among all the damaged W with different damage concentration, although the D desorption of Stage 1 for the damaged W was higher than that for the undamaged W, indicating that the concentration of dislocation loops would be almost saturated at the damage concentration of 3.0×10^{-4} dpa. However, the D retention of Stage 2 was increased as the damage concentration increased. No large D desorption of Stage 2 for undamaged W was found, indicating that the Stage 2 should be the desorption of D trapped by vacancies, whose concentration was increased as the damages are accumulated. For Stage 3, no D desorption was found for the sample with the damage concentration less than 3.0×10^{-2} dpa, showing that the dense damage would initiate additional trapping site in W. In our previous study, the same desorption behavior was found for W with higher D fluence [4, 5]. The TEM observation showed that void was formed in W in this condition, leading the stable D trapping site. The accumulation of void in W would shift the D desorption temperature toward higher temperature side.

These desorption behavior was simulated using trapping & diffusion model. Figure 1 also show the simulation results. It was found that the experimental results were good agreement with the simulation results, especially Stages 2 & 3. The temperature shift of Stage 3 toward higher temperature side would be caused by the diffusion from bulk to surface. In future work, more detail evaluation of D trapping and diffusion behaviors will be elucidated.

References

1) M. Shimada et al., Fusion Eng. Des. 87 (2012) 1166.
2) H. Eleveld et al., J. Nucl. Mater. 191 (1992) 433-38.
3) H. Iwakiri et al., J. Nucl. Mater. 307 (2002) 135-38.
4) M. Kobayashi et al., Fusion Eng. Des. 88 (2013) 1749-52.
5) Y. Oya et al., Mater. Trans. 54 (2013) 430.

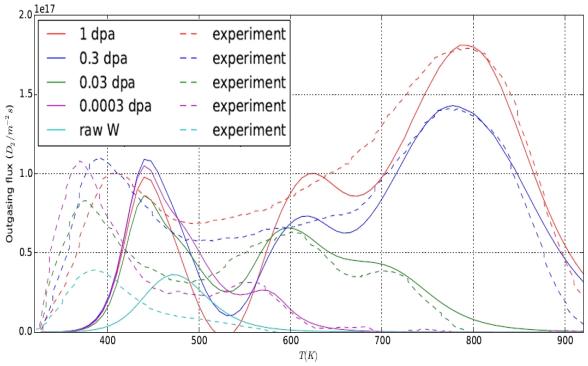

Fig. 1 D_2 TDS spectra for W with various damage concentrations. (The simulation results were also shown.)

1 - 38 Investigation of Microstructure in SiC Made by Nano-infiltration Transient Eutectic Process after Triple Ion Beam Bombardment

K. Ozawa [a)], T. Taguchi [b)], T. Nozawa [a)], M. Ando [a)] and H. Tanigawa [a)]

[a)] Division of Rokkasho BA Project, FRDD, JAEA,
[b)] Materials Science Research Division, QuBS, JAEA

Silicon carbide (SiC) and its composites (SiC/SiC) are attractive candidate materials for nuclear fusion energy application because of their superior irradiation performance and thermo-physical, -chemical, and -mechanical properties[1,2]. To realize the use of such composites, the effect of transmuted helium (He) and hydrogen (H) under fusion environment needs to be clarified in terms of dimensional stability of SiC. However, the information after irradiation is quite limited about SiC containing secondary phases composed of sintering additives as impurities, such as matrix of nano-infiltration transient eutectic (NITE) sintering process[3], in contrast to high purity SiC made by the chemical vapor infiltration method[4]. Therefore, the irradiation effect on dimensional stability of the NITE-SiC has been previously examined[5,6]. In this fiscal year, microstructural evolution of the NITE-SiC after ion irradiation to a relatively high-dose with a special emphasis on the transmuted H effects was investigated.

Monolithic SiC ceramics via the NITE method were irradiated at Takasaki Ion Accelerators for Advanced Radiation Application (TIARA) facility of Japan Atomic Energy Agency. Simultaneous dual or triple ion irradiation was conducted to ~30 dpa at 1,000 °C in order to simulate the synergistically transmuted He/H effects. Microstructure was evaluated with transmission electron microscopy (TEM) for a specimen thinned by focused ion beam.

After dual and triple ion irradiation to 10 dpa with 130 appmHe/dpa, small cavities (~2 nm) were formed in the SiC grains (Fig. 1), and larger ones (~15 nm) formed along yttrium-aluminum-garnet (YAG)/SiC grain boundaries. Based on the TEM micrograph analysis, under fusion environmental condition (40 appmH/dpa), no remarkable negative effects of hydrogen on cavity formation was found under the condition studied. Additionally, cavity swelling was also small even under the excessive H implanted condition (~0.06% for the cavities in grain interiors and ~ 0.05% for the ones at grain boundaries after 400 appmH/dpa (Triple×10) irradiation)[7].

Figure 2 represents typical low-mag TEM images of the monolithic NITE-SiC irradiated to 30 dpa, showing local cavity formation (i.e., bi-modal distribution of cavity size) seems to be more apparent in both cases. For example, in Fig. 2(a), 1) micro-cavity arrays (void swelling) were formed in Al_2O_3 grains, and 2) local coarsening cavity size was observed around on the GBs. In Fig. 2(b), cavities were also formed in YAG grains. Although cavities inherently exist even in unirradiated condition due to

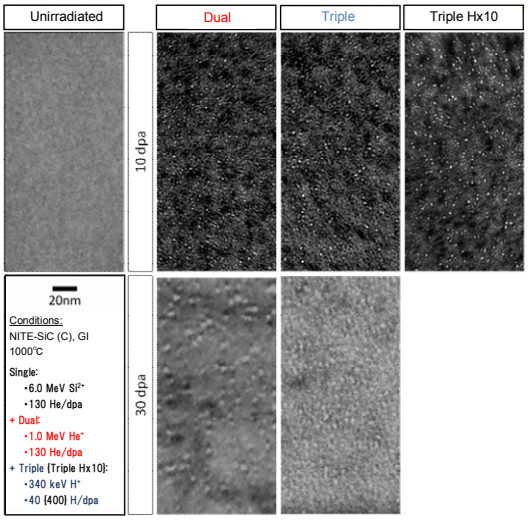

Fig. 1 TEM micrographs showing cavity formation after ion irradiation to 10 and 30 dpa at 1,000 °C with varied He/dpa and H/dpa conditions (Dual, Triple, Triple×10)[7].

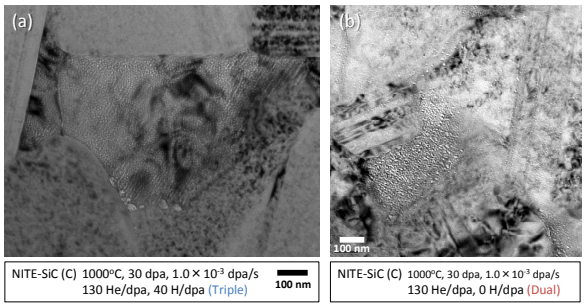

Fig. 2 Lower TEM micrographs of cavities after ion irradiation to 30 dpa at 1,000 °C.

possible reactant (CO, SiO, Al_2O and Al) gases when processing, He/H gases might enhance these cavity growth.

References

1) T. Nozawa et al., J. Nucl. Mater. 386-388 (2009) 622.
2) Y. Katoh et al., J. Nucl. Mater. 367-370 (2007) 659.
3) Y. Katoh et al, Fusion Eng. Des. 61-62 (2002) 723.
4) L. L. Snead et al., J. Nucl. Mater. (2007) 329.
5) T. Nozawa et al., JAEA Takasaki Annu. Rep. 2009 JAEA-Review 2010-065(2011) 138.
6) T. Nozawa et al., JAEA Takasaki Annu. Rep. 2010 JAEA-Review 2011-043 (2012) 131.
7) K. Ozawa et al., JAEA Takasaki Annu. Rep. 2012 JAEA-Review 2013-059 (2014) 39.

1 - 39 Ionizing Dose Dependences of Radiation-induced Conductivity and Radiation-induced Electrical Degradation of Chemical Vapor Deposited Silicon Carbides under Gamma-ray Irradiation

B. Tsuchiya [a)], T. Shikama [b)], S. Nagata [b)], K. Saito [b)] and S. Yamamoto [c)]

[a)] Department of General Education, Faculty of Science and Technology, Meijo University,
[b)] Institute for Materials Research, Tohoku University,
[c)] Environment and Industrial Materials Research Division, QuBS, JAEA

Silicon carbides (SiCs) are potential candidates as insulating materials in nuclear fusion systems such as separators or insulating flow channel inserts, between tritium breeding and neutron multiplier materials composing Li-Pb blanket modules. So far, for CVD-SiC materials with high purity and density, synthesized by the chemical vapor deposition technique, the radiation enhanced phenomena such as radiation induced conductivity (RIC) and radiation induced electrical conductivity (RIED)-like behavior has been observed by in situ radiation experiments under gamma-ray and fast neutron irradiations [1)].

Figure 1 show effects of dose on RIC, σ_{RIC}, under ^{60}Co gamma-ray irradiation (beam-on) and on the base conductivity, σ_{BC}, in the absence of radiation (beam-off) for the CVD-SiC at 3.4 Gy/s in He gas atmosphere, 3.6 Gy/s in vacuum, and 5.9 Gy/s in air at room temperature by the DC-electrical resistivity method. These relationships were determined from the Ohm's law using the increase in the currents when applied from 0 to +3 V and the volume of the CVD-SiC. The radiation-induced current was also proportional to the applied voltage under a constant irradiation intensity. A rapid increase in the electrical conductivities of the irradiated CVD-SiC; this is indicative of RIC, was observed at the beginning of the irradiation. The σ_{RIC} values gradually increased with an increase in the dose and subsequently became almost constant. Similarly, the σ_{BC} values also changed with rapid increases at initial doses below approximately 10 kGy, as compared with those that before irradiation, and hereafter with gradual increases at doses above approximately 10 kGy. These two kinds of rapid and gradual degradations in the insulating characteristics indicate the occurrence of RIED-like behavior [2)]. The radiation-induced phenomena in He and vacuum is similar to that in air. Therefore, the RIED-like behavior is not related to the reaction of radicals such as oxygen, nitrogen, water, and so on containing in air, produced by ionization, with the surface of the CVD-SiC. In addition, the diffusion of He into the CVD-SiC is not enhanced by ionization, either.

Figure 2 shows Cole-cole plots at various doses for the CVD-SiC, measured in vacuum under gamma-ray irradiation, by the AC impedance method, where Re and Im represent real and imaginary, respectively, parts of impedance. The Re and Im values decrease with an increase in the dose on gamma-ray beam-on, while those increase again on beam-off.

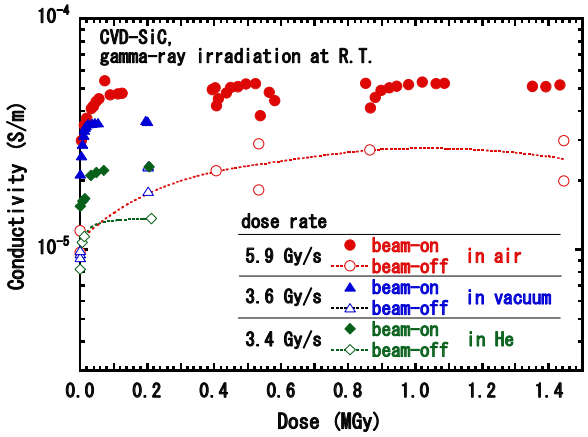

Fig. 1 Dose dependence of RIC, s_{RIC}, and base conductivity, s_{BC}, of CVD-SiC, where s_{RIC} and s_{BC} represent data on 1.17 and 1.33-MeV gamma-ray beam-on at approximately 5.9 Gy/s in air, 3.6 Gy/s in vacuum, and 3.4 Gy/s in He atomospheres, at 300 K and -off, respectively.

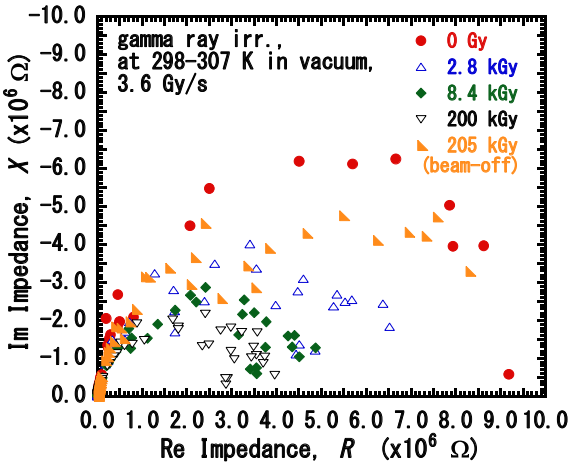

Fig. 2 Cole-cole plots at various doses for CVD-SiC samples, measured in vacuum at 298-307 K by AC impedance method on beam-on and -off.

References

1) B. Tsuchiya et al., Fusion Eng. Des. 86 (2011) 2487.
2) S. J. Zinkle et al., J. Nucl. Mater. 191-194 (1992) 58.

1 - 40 Preparation of CeO_2 Thin Film Containing Image Crystal by Precipitated Helium Injected by 400-keV Ion Implanter of TIARA

H. Serizawa [a], S. Yamamoto [b], K. Yasunaga [c], T. Hakoda [b] and Y. Kaji [a]

[a] Division of Fuels and Materials Engineering, NSED, JAEA,
[b] Environment and Industrial Materials Research Division, QuBS, JAEA,
[c] R&D Department, The Wakasa Wan Energy Research Center

JAEA's recent investigation has shown that a negative crystal is formed in UO_2 in a course of a precipitation of helium injected by HIP [1, 2]. The phenomena which has been attracting our interest is that the shape of the negative crystal changes drastically depending on the inner pressure, which implies that the shape can be transformed arbitrarily by controlling the condition of a helium release. The shape controllable negative crystal is named an image crystal. On the other hand, the study on the morphology of the facets on Wulff-shaped UO_2 cavity showed that the structure of (001) facet has complicated trench structure composed of {111} and {001} [3]. Based on this interesting information, we considered that a new photonics functional material might be developed by introducing image crystal into transparent single crystal since there should be difference in the reflexion between these facets. As an initiatory step toward the development, we examined formation of image crystal in CeO_2 thin film.

Pieces of CeO_2 (100) thin film (800 nm) formed on $SrTiO_3$ base were heat treated at 1,273 K for 2 h. Figure 1 shows the channeling effect of the film examined by RBS (Rutherford Backscattering Spectrometry). The

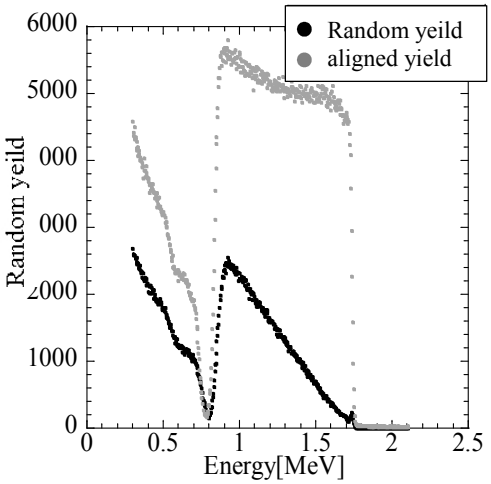

Fig. 1 Channeling effect of the film examined by RBS.

measurement showed that the minimum yield was as low as 2.3%. The oriented growth of the surface (100) was confirmed by X-ray diffraction. These results indicate that the film can be treated as a single crystal formed through an epitaxial growth. The films were irradiated with 130-keV He^{4+} ions from 400-keV ion implanter of TIARA. The helium ion doped film was heat treated at 1,673 K for 2 h. The sample was cut into rectangular slices for Transmission Electron Microscope (TEM); the abrasive cross section was formed with an ion slicer.

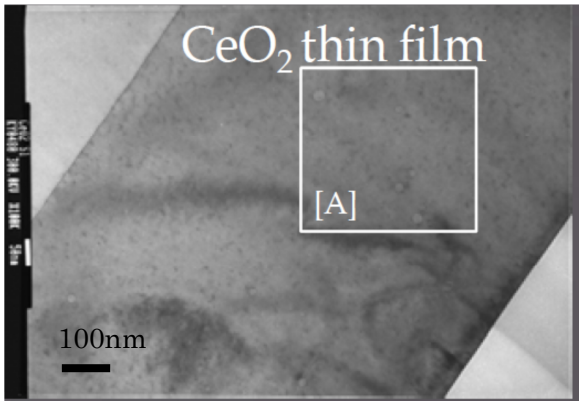

Fig. 2 TEM image of the cross section of helium precipitated CeO_2 thin film. The bright section (the lower right of the figure) is the $SrTiO_3$ base.

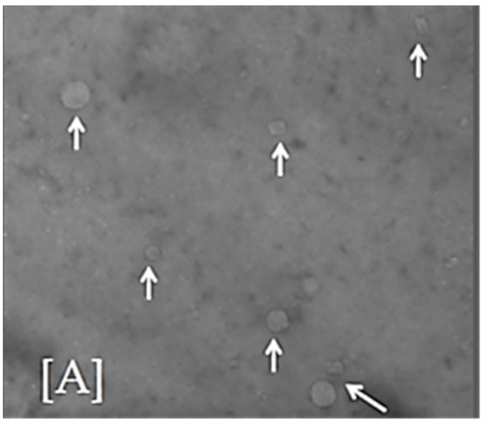

Fig. 3 High-magnification image of field of view [A] shown in Fig. 2.

As can be seen in Figs. 2 and 3, many gas bubbles are seen in the cross section. The largest diameter of the gas bubble is about 30 nm. It should be noted that the wall of the gas bubble marked with allow shows facet structure. However the shape is not complete polyhedron. We need to advance this investigation related to growth of the facet much more completely.

References

1) H. Serizawa et al., J. Asian Ceram. Soc. 1 (2013) 289.
2) H. Serizawa et al., Cryst. Growth Des. 13 (2013) 2815.
3) C. Muggelberg et al, Appl. Surf. Sci. 142 (1999) 124.
Grant-in-Aid for Young Scientists (B) 23760837.

1 - 41 Electronic and Chemical Interaction of Energetic Platinum Ions with Glassy Carbon Substrate

T. Yamaki [a)], S. Kato [a,b)], S. Yamamoto [a)], T. Hakoda [a)], K. Kawaguchi [a,c)], T. Kobayashi [d)], A. Suzuki [b)] and T. Terai [b)]

[a)] Environment and Industrial Materials Research Division, QuBS, JAEA,
[b)] Department of Nuclear Engineering and Management, The University of Tokyo,
[c)] Department of Chemistry and Materials Technology, Kyoto Institute of Technology,
[d)] Atomic Physics Laboratory, Advanced Science Institute, RIKEN

Synthesis of platinum (Pt) nanoparticles has been intensively studied for their applications to polymer electrolyte fuel cells. Quite recently, we have been trying to prepare Pt nanoparticles by ion implantation in a glassy carbon (GC) substrate for the first time. This contribution deals with a detailed investigation of the Pt implants in GC, emphasizing the importance of electronic and chemical interactions in determining the final properties of the implanted layer. Such information would be very important for us to precipitate Pt nanocrystal aggregates on GC by the subsequent electrochemical etching and thermal treatment[1,2].

The implantation of 100 keV Pt^+ was performed at nominal fluences up to 4×10^{16} ions/cm^2 in an IA1 chamber at the TIARA 400-kV ion implanter[1,2]. Sample analysis was performed mainly by transmission electron microscopy (TEM) and X-ray photoelectron spectroscopy (XPS).

Figure 1 shows a cross-sectional TEM image and the selected-area electron diffraction (SAED) pattern. The TEM image revealed that no nanoparticle aggregation occurred in the implanted layer at a depth of ca. 50 nm, which agreed with the projected ion range calculated by a SRIM code[3]. The SAED pattern exhibited only a diffuse halo, indicating an amorphous structure in the Pt and GC phases. The Pt implants would be well dispersed in the atomic state, and not be aggregated to form Pt nanocrystals.

Figure 2 shows Pt 4f XPS spectra after argon-ion sputtering for 150, 180 and 210 s. Interestingly, these indicated the formation of Pt-C bonds, suggesting some electronic interactions between Pt and the nearby carbon in GC. The depth profiling XPS also enabled us to understand the relationship between the Pt-C interactions and local Pt concentration (results not shown).

References

1) S. Kato et al., Trans. Mater. Res. Soc. Jpn. 38 (2013) 81.
2) S. Kato et al., Nucl. Instrum. Meth. Phys .Res. B 314 (2013) 149.
3) J. F. Ziegler et al., "The Stopping and Range of Ions in Solids", Pergamon, New York (1985) Chapter 8.

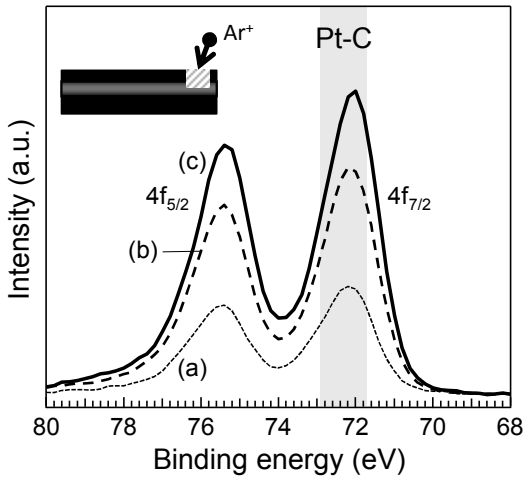

Fig. 2 Pt 4f XPS spectra after argon-ion sputtering for (a) 150, (b) 180 and (c) 210 s.

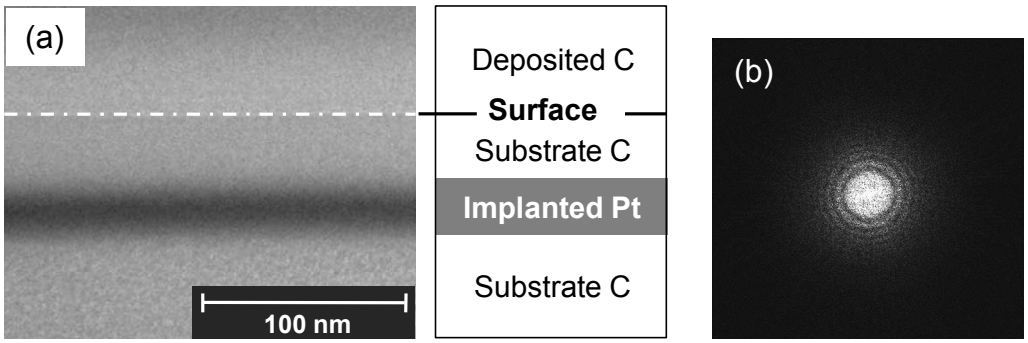

Fig. 1 (a) Cross-sectional TEM image showing the distribution of the Pt implants in GC and (b) the corresponding SAED pattern.

1 - 42 Alkaline Durable Vinylimidazolium-based Anion Conducting Polymer Electrolyte Membranes Prepared by Radiation-induced Grafting

K. Yoshimura [a)], H. Koshikawa [a)], T. Yamaki [a)], H. Shishitani [b)], S. Yamaguchi [b)], H. Tanaka [b)] and Y. Maekawa [a)]

[a)] Environment and Industrial Materials Research Division, QuBS, JAEA, [b)] Daihatsu Motor Co., Ltd.

An anion exchange membrane (AEM) is one of the key materials for alkaline-type fuel cells (AEMFC), which have potential advantages against proton exchange membrane fuel cells (PEMFC). In the AEMFC, electrochemical reactions are more facile than in acidic medium, and non-precious metals such as nickel, cobalt and iron can replace platinum as the catalyst [1, 2)]. Because of high temperature and strongly alkaline fuel cell operating condition, it is desirable to develop alkaline durable AEMs. In recent years, we have developed imidazolium-type AEMs by radiation-induced grafting for AEMFCs, especially in direct hydrazine fuel cells (DHFCs) and found that poly(1-vinylimidazolium (VIm))-grafted and copoly(VIm/styrene)-grafted AEMs (**AEM1** and **AEM2**) shows moderate alkaline stability; the AEMs degraded via the initial β-elimination and following ring opening reactions of the imidazolium unit [3,4)]. Therefore, we synthesized the AEM based on a poly(2-methyl-1-vinylimidazolium) grafts by radiation- induced grafting to improve long-term stability by suppressing β-elimination and ring opening reactions.

The poly(ethylene-co-tetrafluoroethylene) (ETFE) films were irradiated with a ^{60}Co γ-ray source (JAEA Takasaki, Gunma, Japan) at room temperature in argon atmosphere with an absorbed dose of 50 kGy. The pre-irradiated ETFE films were immediately immersed into the argon-purged monomer solution consisting of 50 wt% 2-methyl-1-vinylimidazole (MVIm) or a mixture of MVIm/stylene (8 : 2 weight ratio) in 1,4-dioxane. The imidazole groups in the grafted-ETFE were *N*-alkylated using methyl iodide. The resultant AEMs (an iodide form) were immersed in 1 M $NaHCO_3$ solution at 60 °C for 24 h to convert into a HCO_3^- form, followed by the ion-exchange reaction with OH^- in 1 M KOH solution at room temperature for 16 h to obtain the anion forms of the AEMs (**AEM3** and **AEM4**), as shown in Fig. 1. The ionic conductivity was measured by two-point probe AC impedance spectroscopy at 100% relative humidity in N_2-purged deionized water. The ion exchange capacity (IEC) was measured using standard back titration methods.

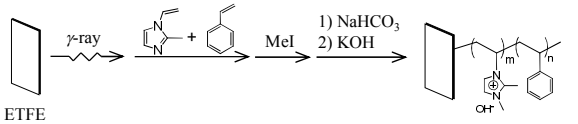

AEM3: GD = 36%, m = 100, n = 0
AEM4: GD = 55%, m = 42, n = 58

Fig. 1 Reaction scheme, grafting-degree (GD), and copolymerization ratio for **AEM3** and **AEM4**.

The alkaline stability of AEMs was evaluated by monitoring the change in conductivity of AEMs in 1 M KOH at 80 °C. Figure 2 shows the conductivities of the AEMs. The homopolymer-type **AEM1** and **AEM3** showed similar profiles in conductivity decreases, indicating the dominant β-elimination at an initial stage for homopolymer-type imidazolium grafts in the AEMs due to the steric and electrostatic repulsions. Copolymer-type **AEM2**, which had no 2-methyl group on the imidazolium group, showed a slower degradation rate after the fast decrease at the initial stage. Furthermore, copolymer-type **AEM4**, which had 2-methyl group on the imidazolium group, showed slower decreases at the initial stage and kept excellent long-term stability with keeping the conductivity of 12 mS cm^{-1} after 600 h immersion. The above results strongly indicate that the introduction of methyl group at 2-position of imidazolium unit drastically enhances the long-term durability in alkaline solutions at elevated temperatures due to the resistance to nucleophilic attack for the ring opening reactions of the imidazolium cations. Accordingly, the 2-methylimidazolium units in copolymer grafts in AEMs are an promising anion exchange unit for highly alkaline durable DHFCs.

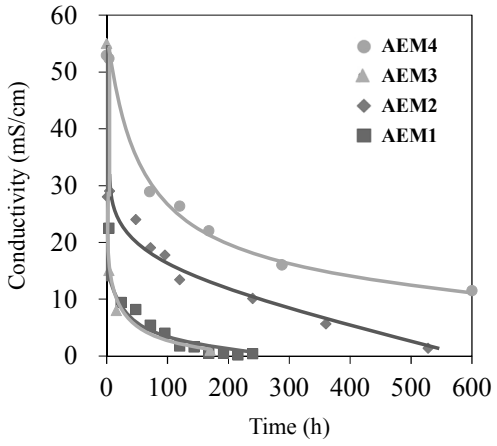

Fig. 2 The AEM conductivities after being immersed in 1 M KOH at 80 °C.

References

1) A. Serov et al., Appl. Catal. B-Environ. 98 (2010) 1.
2) K. Asazawa et al., Angew. Chem. Int. Ed. 46 (2007) 8024.
3) Y. Ye et al., Macromolecules 44 (2011) 8494.
4) K. Yoshimura et al., ECS Trans. 50 (2012) 2075.

1 - 43 Preparation of Anion-Exchange Membranes for Fuel Cell Applications by Radiation-induced Grafting: Effect of a Base Polymer

H. Koshikawa, K. Yoshimura, T. Yamaki, M. Asano and Y. Maekawa

Environment and Industrial Materials Research Division, QuBS, JAEA

Researchers have so far developed anion-exchange membrane fuel cells (AEMFCs), which do not need expensive platinum catalysts in the electrodes. Our recent focus has been the preparation of new hydroxide (OH)-conducting membranes for applications to "hydrazine-fueled" AEMFCs by radiation-induced grafting method [1-3]. Previously, we prepared the AEM consisting of poly(ethylene-*co*-tetrafluoroethylene) (ETFE) films and anion conducting group containing graft-polymers by radiation-induced grafting. However, the alkaline durability of the AEMs were still insufficient [4]. Thus, we investigated here to the preparation of novel graft-type AEMs from two aromatic hydrocarbon polymer substrates, polyether ether ketone (PEEK) and poly(phenylene sulfide) (PPS).

Figure 1 shows the preparation scheme of graft-type AEMs by the radiation-induced grafting of vinylimidazole (ViIm) into base polymer films and subsequent quaternization and ion exchange reactions (Fig. 1) [2-4]. We attempted two radiation-induced grafting methods; pre-irradiation and simultaneous grafting methods. For pre-irradiation method, 50 μm-thick ETFE, PEEK and PPS films were irradiated with ^{60}Co γ-rays dose of 50 kGy and then immersed in the ViIm/xylene 50/50 vol% solution under Ar at 60 °C for 24 h. For a simultaneous grafting method, those films were immersed in the ViIm/xylene 50/50 vol% solution and then irradiated with γ-rays dose rate of 10 kGy/h. The quaternization and anion exchange reactions of the grafted films were conducted in 1-iodopropane at 95 °C for 24 hand in a 1 M KOH solution at room temperature for 6 h, respectively.

By the pre-irradiation grafting, the grafting degree of PEEK and PPS, hardly proceeded (< 5%). In contrast, as shown in Fig. 2, which shows the grafting degree of ViIm *vs.* reaction time of simultaneous grafting, simultaneous grafting of ViIm into PPS and PEEK films proceeded and give poly(ViIm)-grafted PPS and PEEK with grafting degrees of 42% and 40%, respectively. By the quaternization and ion exchange reactions, the poly(ViIm)-grafted PPS and PEEK films were converted to the PPS- and PEEK-AEMs, which showed ion conductivities of 17.4 and 9.0 mS/cm, respectively. By taking advantage of the simultaneous grafting method, we successfully prepared the graft-type AEMs consisting of aromatic hydrocarbon base polymers with moderate ionic conductivity.

References

1) K. Asazawa et al., J. Electrochem. Soc. 156 (2009) B509.
2) H. Koshikawa et al., Proc. RadTech Asia 2011 (2011) 240.
3) T. Yamaki, Maku (Membrane) 36 (2011) 240.
4) H. Koshikawa et al., Macromol. Chem. Phys. 214 (2013) 1756.

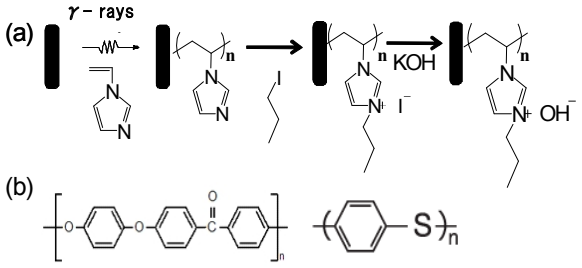

Fig. 1 Preparation scheme for graft-type AEMs. (a) Radiation-induced graft polymerization of ViIm into base polymer films and subsequent quaternization of the poly(ViIm) grafts. (b) Chemical structures of base polymers; PEEK and PPS.

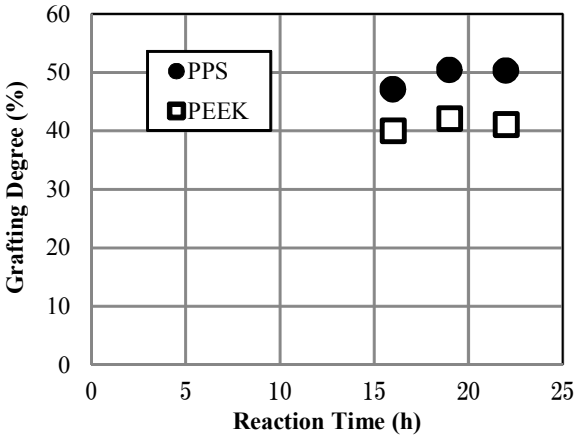

Fig. 2 The grafting degree of ViIm *vs.* reaction time of simultaneous grafting. ●:PPS and □:PEEK.

1 - 44 Chemical Modification in Fluoropolymers Irradiated with Uniform Beam in Oxygen Atmosphere

A. Kitamura [a)], T. Yamaki [b)], Y. Yuri [a)], H. Koshikawa [b)], S. Sawada [b)], T. Yuyama [a)] and T. Ishizaka [a)]

[a)] Department of Advanced Radiation Technology, TARRI, JAEA,
[b)] Environment and Industrial Materials Research Division, QuBS, JAEA

A uniform-beam formation/irradiation system using multipole magnets has been developed on the LB course of the TIARA cyclotron [1)]. For the evaluation of the beam uniformity, the relative intensity distribution is obtained from the optical density of a radiochromic film (Gafchromic HD-810, Ashland Inc). In our previous reports, the absolute particle fluence distribution was microscopically revealed using the track-etching technique, and the uniformity was in good agreement with that obtained from the Gafchromic film [2, 3)]. These results demonstrated that our uniform-beam system would give a useful technique for mass production and industrial materials. We have focused on poly(vinylidene fluoride) (PVDF, $(CH_2CF_2)_n$), one of fluoropolymers, because it has excellent properties as super-engineering plastic materials. This report deals with the chemical effect in PVDF films irradiated by our uniform-beam system.

Commercially-available PVDF films (25 μm in thickness) were irradiated in an oxygen atmosphere with a 520-MeV ^{40}Ar uniform beam using our system. The beam was extracted through a 30 μm-thick Ti foil window to reach the sample; the kinetic energy on the sample surface was estimated to be approximately 330 MeV by a SRIM code. For comparison, PVDF films were also irradiated in vacuum with 330 MeV ^{40}Ar scan beam using a conventional system on the LD course [4)]. The fluence was fixed at 6.0×10^{11} ions/cm^2. Fourier transform infrared (FT-IR) analysis was then performed in the transmission mode.

Figure 1 shows the FT-IR spectra of pristine and irradiated PVDF films. The irradiation in the two different ways gave spectra (a) and (b). The 1,754 and 1,712 cm^{-1} bands are attributed to -CF_2-HC=CF_2 and -HC=CF- produced by chain scission and dehydrofluorination, respectively [4, 5)]. The broad bands in the OH absorption region (3,660-3,480 cm^{-1}) are assigned to -CF_2-CF_2OH (3,650 cm^{-1}), -CF_2-CHOH-CF_2- (3,620 cm^{-1}) and -CF_2-CH_2OOH (3,540 cm^{-1}). The formation of -CH_2COF can also be suggested by the 1,850 cm^{-1} band [5)]. The difference spectra between (a) and (b) exhibited the absorption bands from oxygen-containing functional groups, indicating that the post-irradiation oxidation effect appeared more prominent for (a). It is well known that oxidation of ion tracks accelerates the etching rate [6)], and so the irradiation in oxygen using our uniform-beam system would promise to develop a rapid track-etching process. The investigation in this regard is now in progress. We believe that it is very important not only for future possible applications of the TIARA cyclotron but also for scientific or technical breakthrough in materials development using nanotechnology.

This work was supported by competitive research funds of JAEA in 2013.

References

1) Y. Yuri et al., Nucl. Instrum. Meth. A **642** (2011) 10-17.
2) A. Kitamura et al., JAEA Takasaki Annu. Rep. 2012 JAEA-Review 2013-059 (2014) 50.
3) A. Kitamura et al., Nucl. Instrum. Meth. B **314** (2013) 47-50.
4) T. Yamaki et al., Nucl. Instrum. Meth. B **314** (2013) 77-81.
5) M. -Cl. Clochard et al., Polymer **45** (2004) 8683-94.
6) W. T. Crawford et al., Nature **220** (1968) 1313-4.

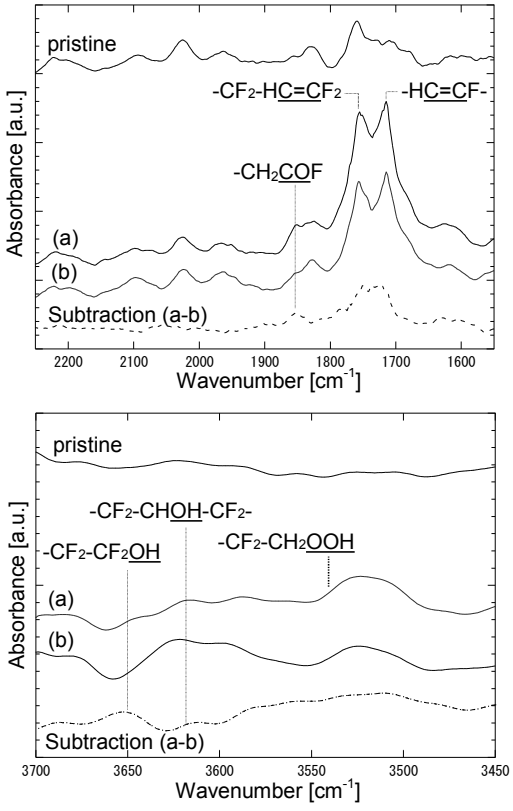

Fig. 1 FT-IR spectra of pristine and irradiated PVDF films by (a) our uniform-beam system and (b) a conventional scan-beam system, respectively. The dotted lines are difference spectra which subtracted (b) from (a).

1 - 45 Synthesis of Polymer Electrolyte Membranes with an Aromatic Hydrocarbon Polymer Using Radiation Living Graft Polymerization

S. Hasegawa, S. Sawada, J. Chen and Y. Maekawa

Environment and Industrial Materials Research Division, QuBS, JAEA

For the commercialization of fuel cells the development of polymer electrolyte membrane (PEM) showing two superior properties, high proton conductivity and mechanical strength at high temperatures under low (<30%RH) and high humidity (> 90%RH), respectively. It has been reported that the nano-ion channels work efficiently for high proton conductivity under low humidity and block-type structure consisting of hydrophobic and hydrophilic polymers can be expected to form well-organized continuous proton channels [1]. Thus, we have attempted the preparation of graft-type PEMs with hydrophobic and hydrophilic (ion-conducting) block-type graft-polymers by the combination of radiation-induced graft polymerization (RIGP) and atom transfer radical polymerization (ATRP) (Fig. 1). We previously reported the ethylene tetraethylene copolymer (ETFE)-based block-type PEMs prepared by RIGP/ATRP method [2]. Thus, we challenged the preparation of the RIGP/ATRP-PEMs using aromatic hydrocarbon polymer, poly (ether ether ketone) (PEEK), because the conventional graft-type PEEK-PEMs show both high conductivity and mechanical properties.

RIGP of chloromethylstyrene (CMS) was conducted by the ^{60}Co γ-rays irradiation of PEEK films (crystallinity: 11%) with 50 kGy, followed by the immersion in 50 wt% CMS in 1,4-dioxane (DOX) at 40 °C for 3 h to obtain CMS-grafted PEEK films (PEEK-g-CMS) with *GD*(grafting degree) of 2.3%. Next, ATRP of the PEEK-g-CMS were conducted in the ETSS solutions with 0.04 M CuBr and 0.08 M *N,N, N',N'',N''*-pentamethyldiethylenetriamine (PMDETA) as a catalyst as a previously reported [2]. The ATRP of ETSS hardly progressed in DOX (*GDs* < 10%), whereas it proceeded in acetonitrile to give the ATRP-grafted PEEK with a *GD* of 38% for 48 h.

When we replaced the ligand from PMDETA to Tris(2-pyridylmethyl) amine (TPMA) (CuBr:TPMA = 0.02:0.04 M), the ATRP of ETSS for PEEK-g-CMS in acetonitrile at 50 °C showed much higher polymerization rates to give the ATRP-grafted PEEK with a higher *GD* than 1,900%. Finally, by reducing the catalyst concentration (CuBr:TPMA 0.0032: 0.0064 M), the *GD* of ETSS in ATRP was controlled as a moderate value (186%) (Fig. 2).

References

1) K. Miyatake et al., J. Am. Chem. Soc. 129 (2007) 3879-87.
2) S. Sawada et al., JAEA Takasaki Annu. Rep. 2012 JAEA-Review 2013-059 (2014) 46.
3) K. Matyjaszewski, Macromolecules 45 (2013) 4015-38.

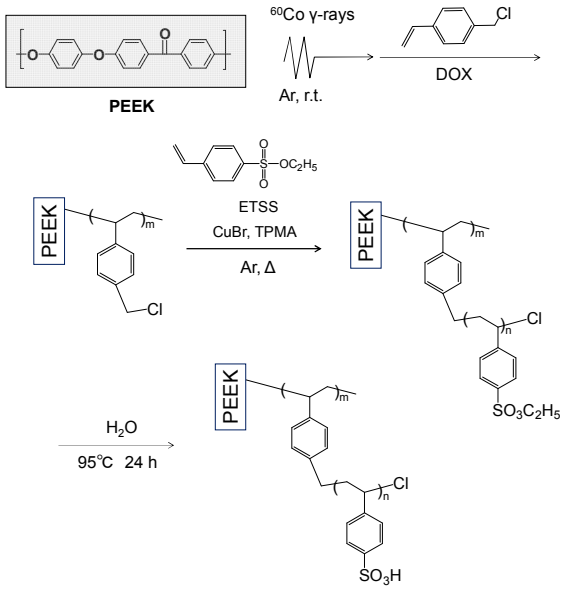

Fig. 1 Synthetic scheme of RIGP/ATRP-PEEK-PEMs by radiation-induced and living radical polymerizations.

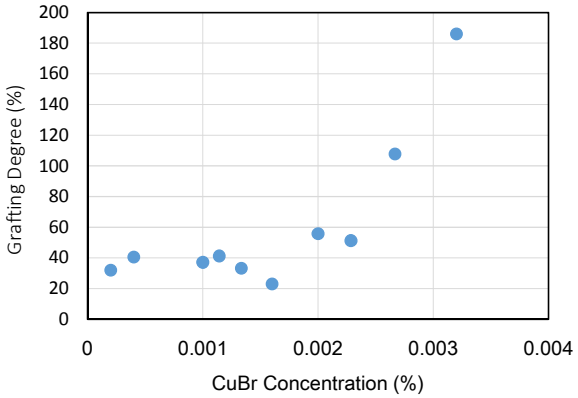

Fig. 2 Plots of *GD*s as a function of a catalyst concentration.

1 - 46 Proton Conductivity of Novel Polymer Electrolyte Membranes Prepared by RIGP and ATRP

S. Sawada, S. Hasegawa and Y. Maekawa

Environment and Industrial Materials Research Division, QuBS, JAEA

Polymer electrolyte membrane (PEM) fuel cells are expected as a promising power source for residential cogeneration, automobiles and mobile electric devices. A PEM, which transports protons from an anode to a cathode, is one of vital components in a fuel cell. Currently, perfluorinated PEMs such as Nafion™ is the most widely used PEM. However, the perfluorinated PEMs have the drawback: the proton conductivity, σ, dramatically decreases under the high temperature and low humidity condition. Therefore, many efforts have been devoted to develop alternative PEMs having higher σ.

Quite recently, our group successfully synthesized the novel PEMs by combination of radiation induced grafting polymerization (RIGP) and atom transfer radical polymerization (ATRP)[1]. At the first RIGP step, the base ethylene-co-tetrafluoroethylene (ETFE) film was irradiated with 15-kGy γ-rays, and then comonomers of styrene (St) and chloromethylstyrene (CMS) was grafted into the ETFE at 60 °C. At the second ATRP step, ethylstyrenesulfonate (ETSS) was grafted at 50 °C with CuBr and N,N,N',N'',N''-pentamethyl-diethylenetriamine as a catalyst and ligand, respectively. Finally, the grafted ETFE films were transformed to a PEM by the hydrolysis of ETSS.

For RIGP, the degree of St/CMS grafting (DOG_1) increased from 23 to 68% by changing the reaction time from 0.5 to 12 h. For the next ATRP, the films with DOG_1 of 60-65% were used. The degree of ETSS grafting increased from 9.3 to 170% for grafting time of 1-8 h. For hydrolysis, when the ETSS-grafted films were immersed in purified water at 95 °C, the ion exchange capacity (IEC) of the obtained PEMs was far lower than the theoretical IEC. The lower IEC would result from the degradation of the PEMs by the swelling induced detachment of ETSS graft chains[2]. Thus, the hydrolysis temperature was set at 80 °C, at which no degradation was observed.

The σ of the PEMs was measured by a two-probe AC impedance technique at the temperature of 80 °C and relative humidity of 30%. Figure 1 shows the σ as a function of IEC. The σ of Nafion and the conventional PEMs, which were prepared by RIGP of ETSS into ETFE films and hydrolysis of ETSS units, were plotted in Fig. 1 for the reference. The σ of the RIGP/ATRP-PEMs increased with the IEC, and reached the maximum value of 0.011 S/cm at 2.6 meq/g, being comparable to the σ of Nafion.

According to the Nernst–Einstein equation, the σ is expressed by:

$$\sigma = C_P D_P Z^2 F^2 / RT, \qquad (1)$$

where C_P is the proton concentration of the PEMs, D_P is the diffusion coefficient of protons, Z is the valence number of protons, F is the Faraday constant, R is the gas constant, and T is temperature. Equation (1) means that the σ is determined by the two factors: C_P and D_P. Therefore, the σ of the PEMs were re-plotted as a function of the C_P, instead of the IEC. The σ of the RIGP/ATRP-PEMs was higher than the corresponding σ of the conventional RIGP ones even at the same C_P (Fig.2). This result indicates that the RIGP/ATRP-PEMs exhibit the higher D_P, which may be related to their peculiar morphology of the block-type graft-copolymers consisting of poly(St(CMS)) and poly(styrenesulfonic acid). Our future work is to investigate the detailed structures of the RIGP/ATRP-PEMs for elucidation of the superior proton conduction mechanism.

References

1) S. Sawada et al., JAEA Takasaki Annu. Rep. 2011 JAEA-Review 2012-046 (2013) 46.
2) K. Enomoto et al., Macromol. Chem. Phys. 213 (2012) 72.

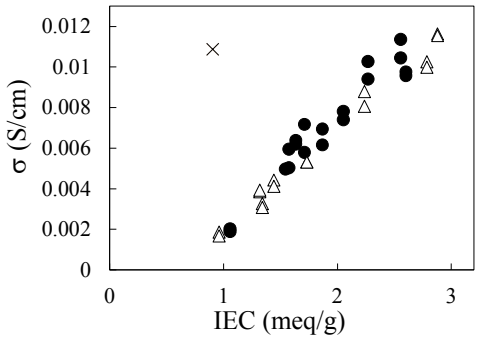

Fig. 1 The σ as a function of the IEC for (●) the RIGP/ATRP PEMs, (Δ) conventional RIGP PEMs, and (×) Nafion.

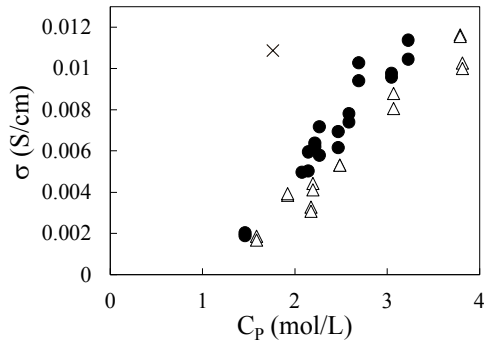

Fig. 2 The σ as a function of the C_P for (●) the RIGP/ATRP PEMs, (Δ) conventional RIGP PEMs, and (×) Nafion.

1 - 47 Ion-track Grafting of Vinylbenzyl Chloride into Poly(ethylene-*co*-tetrafluoroethylene) Films: Effect of Different Grafting Media

N. Nuryanthi [a,c], T. Yamaki [a], A. Kitamura [b], H. Koshikawa [a], K. Yoshimura [a], S. Sawada [a], S. Hasegawa [a], M. Asano [a], Y. Maekawa [a], A. Suzuki [c] and T. Terai [c]

[a] Environment and Industrial Materials Research Division, QuBS, JAEA,
[b] Department of Advanced Radiation Technology, TARRI, JAEA,
[c] Department of Nuclear Engineering and Management, The University of Tokyo

Our research focus is the preparation of anion exchange membranes for fuel cells by a direct ion-track grafting, which has so far been applied to the development of cation exchange membranes [1]. This grafting method involves irradiation of a base polymer film with swift heavy ions and the subsequent graft polymerization directly into the latent tracks. Anion-exchange functional groups were introduced by the grafting of a vinylbenzyl chloride (VBC) monomer into a poly(ethylene-*co*-tetrafluoroethylene) (ETFE) film and quaternization of the grafted polymer chains [2]. A key for success here is to obtain as high graft levels as possible (for higher conductivity) in a small number of tracks (for improving other membrane properties). To this end, therefore, the effect of reaction media was investigated toward optimization of the grafting conditions.

Twenty-five-μm-thick ETFE films were irradiated in a vacuum chamber of the LD beamline with 560 MeV ^{129}Xe at different fluences. In order to maintain their initiation sites, the irradiated films were then stored in air at −80 °C until just before the grafting. The grafting was performed by immersing the irradiated ETFE films in a mixture of water (H_2O) and isopropyl alcohol (*i*PrOH) containing 20 vol% VBC at 60 °C. The volume ratio of H_2O in the grafting media was varied from 0 to 1.0. The graft level or degree of grafting (DG) was calculated by $100(W_g - W_0)/W_0$, where W_0 and W_g are the weights of the film before and after the grafting, respectively.

Figure 1 shows the DGs obtained as a function of time at fluences of 3×10^8, 6×10^8, 1×10^9, and 3×10^9 ions/cm^2. The grafting medium was an H_2O/*i*PrOH mixture at an H_2O ratio of 0.5. The higher DGs at higher fluences would be reasonable as the number of the initiators for the graft polymerization, *i.e.*, alkyl radicals (-C•), their oxidized radicals (-COO•), and stabilized peroxide compounds (-COOH, -COOR), also increases with the fluence [3].

Figure 2 shows the DGs obtained at a reaction time of 24 h as a function of H_2O ratio. A fluence was fixed here at 3×10^9 ions/cm^2. When the H_2O ratio was zero, the DG exhibited a minimum, indicating the necessity of adding water to the grafting medium. The DG was enhanced by the addition of water and reached a maximum at a H_2O ratio of 1.0. We found that the poor-solvent system of H_2O/*i*PrOH could boost the reactivity of the VBC grafting very effectively. This is possibly because the formation of homopolymers was hindered in polar media, and thus a graft polymerization rate increased [4].

References

1) For review, T. Yamaki, J. Power Sources 195 (2010) 5848.
2) T. N. Danks et al. J. Mater. Chem. 13 (2002) 712.
3) N. Betz et al., Nucl. Instrum. Meth. Phys. Res. B 91 (1991) 151.
4) S. A. Gürsel et al., Nucl. Instrum. Meth. Phys. Res. B 265 (2007) 198.

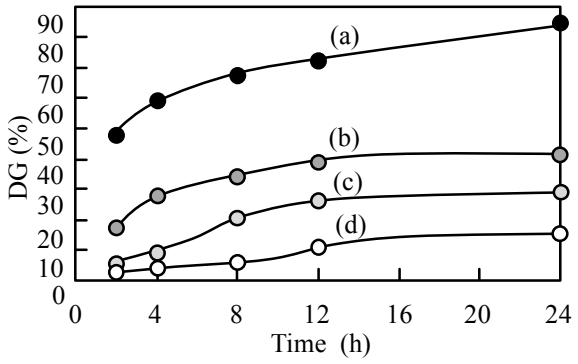

Fig. 1 Degree of grafting as a function of time at fluences of (a) 3×10^8, (b) 6×10^8, (c) 1×10^9, and (d) 3×10^9 ions/cm^2. The grafting medium was an H_2O/*i*PrOH mixture at an H_2O ratio of 0.5.

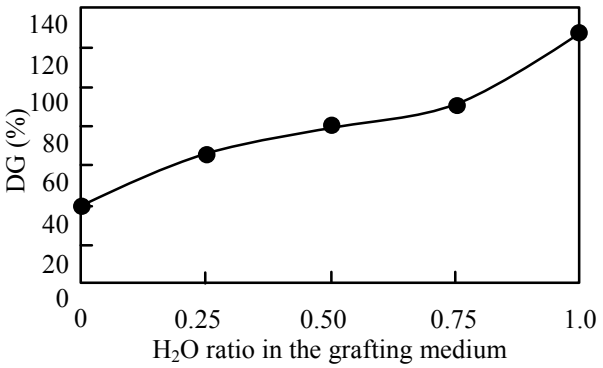

Fig. 2 Degree of grafting as a function of H_2O volume ratio in the grafting medium. A fluence was fixed here at 3×10^9 ions/cm^2.

1 - 48 Effect of HI Concentration on Proton Conductivity of Radiation-grafted Membrane in HIx Solution

N. Tanaka [a)], T. Yamaki [b)], M. Asano [b)] and T. Terai [c)]

[a)] Hydrogen Application Research and Development Division, NHARC, JAEA,
[b)] Environment and Industrial Materials Research Division, QuBS, JAEA,
[c)] Department of Nuclear Engineering and Management, The University of Tokyo

Hydrogen production thermochemical water-splitting Iodine-Sulfur (IS) process [1)] is the promising chemical process for the future hydrogen system. In the IS process, a new cation-exchange membrane prepared by the radiation-induced graft polymerization method has been applied to the electro-electrodialysis (EED) in order to enrich hydrogen iodide (HI) in HI-I_2-H_2O mixture (HIx solution) [2,3)]. Our particular interest would be in how the proton conductivity (σ) of the membrane immersed in the HIx solution changes at different HI concentrations from the standpoint of design requirements for the overall efficient IS process. Thus, we evaluated here the dependence of σ on the HI concentration experimentally for a styrene (St)-grafted and sulfonated poly(ethylene-*co*-tetrafluoroethylene) (ETFE-St) membrane. Based on our unique EED model [2)], the relationship between σ and the important membrane properties was also taken into account.

The ETFE-St membrane was prepared by the ^{60}Co γ-ray pre-irradiation of the ETFE film, the graft polymerization of St, and sulfonation. Its ion exchange capacity (IEC) and thickness were 1.1 mmol/g and 57 μm, respectively. The σ value measured using a filter-press type EED cell, to which a direct current of 200 mA/cm^2 was supplied at 373 K. The HI concentration in the feeding HIx solution was varied in 7, 10, 12 or 13 mol/kg while an I_2/HI molar ratio was fixed at 1.

Figure 1 shows the variation of σ as a function of HI molality in the feeding HIx solution. The σ value appeared to decrease with an increase in the HI molality. This means that the ions' permeation can be interfered at higher HI concentrations.

The EED model [2)] describes the transport of H^+ and I^- through ion exchange membrane immersed in the HIx solution using the Nernst-Planck equation, and so σ is given by:

$$\sigma = \frac{id}{E} = \frac{F^2}{TRV_0}\left(D_{H^+} n_{H^+} + D_{I^-} n_{I^-}\right), \quad (1)$$

where i [A/m^2], d [m], E [V], t_+ [-], T [K], R [J/mol•K], F [C/mol], V_0 [m^3/kg], n_i [mol/kg] and D_i [m^2/s] denote current density, thickness, cell voltage, transport number, temperature, gas constant, Faraday constant, volume per dry membrane weight, content of i (H^+ and I^-) component per dry membrane weight and diffusion coefficient of i component, respectively.

According to Eq. (1), D_i can be calculated from the measured and the previously-reported values [4)]. Figure 2 shows the calculated D_i as a function of HI molality. The D_{H+} value decreased with an increase in the HI molality, whereas D_{I-} increased. Because only cations are exchangeable in the ETFE-St membrane, n_{H+} is always much larger than n_{I-}; we previously found both of n_{H+} and n_{I-} almost stable irrespective of the HI molality [4)]. Therefore, the HI-molality dependence of D_{H+} could govern that of σ. In other words, σ is likely to become higher as the H^+ diffusivity in the membrane is enhanced.

References

1) S. Kubo et al., Nucl. Eng. Des. 233 (2004) 355.
2) N. Tanaka et al., J. Membr. Sci. 411-412 (2012) 99.
3) T. Yamaki et al., Polymer 45 (2004) 6569.
4) N. Tanaka et al., J. Membr. Sci. 456 (2014) 31.

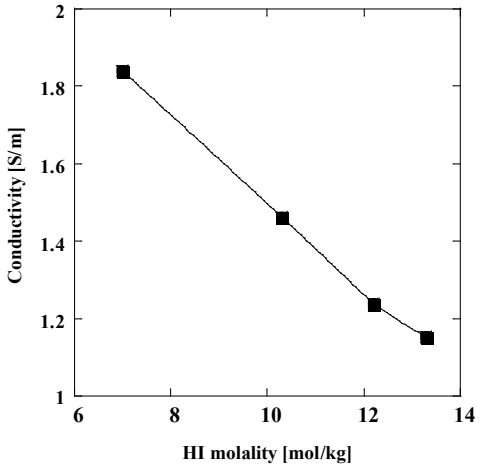

Fig. 1 HI-molality dependence of proton conductivity, σ (Plots: experimental values, Solid line: guide line).

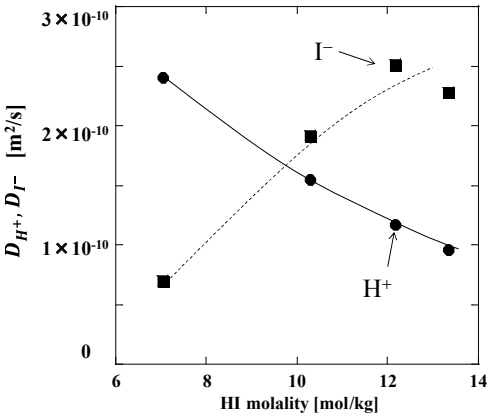

Fig. 2 HI-molality dependence of the diffusion coefficient of H^+ and I^- (Plots: calculated values, Solid and dashed lines: guide lines).

1 - 49 Water Permeation through Cation Exchange Membranes Prepared by a Radiation Graft Polymerization Method

T. Kodaira [a)], K. Oura [a)], A. Ikeda [a)], E. Matsuyama [a)],
S. Sawada [b)], T. Yamaki [b)] and M. Nomura [a)]

[a)] Department of Applied Chemistry, Shibaura Institute of Technology,
[b)] Environment and Industrial Materials Research Division, QuBS, JAEA

Thermochemical water splitting IS process is one of the hydrogen production methods. Hydrogen and oxygen are obtained from water through this process by using iodine and sulfur as catalysts in the Bunsen reaction ($I_2 + SO_2 + H_2O \rightarrow 2HI + H_2SO_4$). However, the amount of recycling I_2 must be reduced to improve the total thermal efficiency[1)]. In order to reduce I_2 in the Bunsen reaction, the reaction was conducted by using a cation exchange membrane [2)]. A main problem here was found to be SO_2 permeation through the membrane. The permeation of SO_2 might accompany that of water in the membrane. Thus, cation exchange membranes for the Bunsen reaction need an ability to suppress water permeation. In this report, cation exchange membranes were prepared by a radiation-graft polymerization method [3)]. The effect of crosslinking structures in the graft chain was evaluated in terms of water permeation in pervaporation (PV).

A poly(ethylene-co-tetrafluoroethylene) substrate (Asahi Glass Co., ϕ 50 μm) was irradiated with ^{60}Co γ-rays in Ar followed by graft polymerization and sulfonation. The irradiation period was 1 h at a dose rate of 15 kGy h^{-1}. The irradiated film was immersed in a monomer solution containing 95/5 vol% styrene/divinylbenzene (DVB) in toluene at 60 °C. The grafted film was sulfonated in the solution of chlorosulfonic acid at 50 °C. A water uptake and ion exchange capacity (IEC) were obtained in the established procedure[3)]. Water permeation was measured by a PV method at 25 or 60 °C.

Figure 1 shows the water flux through the membranes plotted as a function of water uptake. The water flux increased with increasing the water uptake. Two membranes prepared by styrene grafting with or without DVB and Nafion 212 possessed a similar water uptake of approximately 40%, and are used for comparison. The membrane grafted without DVB (referred to as a non-DVB membrane) and Nafion 212 had a water flux of >16 kg m^{-2} h^{-1} while, in contrast, the membrane grafted with DVB (referred to as a DVB membrane) exhibited 7.5 kg m^{-2} h^{-1}. The water permeation can be suppressed by adding DVB as a crosslinking agent.

Figure 2 shows the diffusion coefficients through the membranes assuming that the water uptake would be constant between 25 and 60 °C. The activation energies of the diffusion coefficients were 3.4, 5.6, and 16 kJ mol^{-1} for Nafion 212, the non-DVB and the DVB membranes, respectively. The activation energy increased with decreasing the water flux. The activation energy for the DVB membrane was about three times higher than that of the non-DVB membrane. These demonstrate that the DVB crosslinking would suppress the water diffusion in the membrane.

In conclusion, the membrane grafted with 95/5 vol% styrene/DVB showed lower water permeation with its IEC maintained. A water flux was as low as 7.5 kg m^{-2} h^{-1} even at a high IEC of 2 mmol g^{-1}.

References

1) S. Kasahara et al., J. Chem. Eng. Jpn. 36 (2003) 887.
2) M. Nomura et al., AIChE J. 50 (2004) 1991.
3) T. Yamaki, J. Power Sources 195 (2010) 5848.

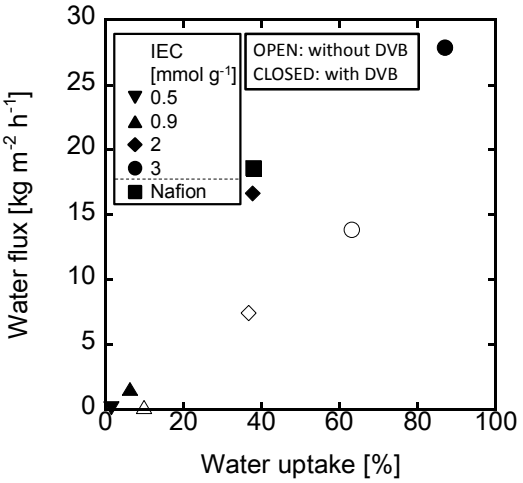

Fig. 1 The relationship between the water flux and water uptake.

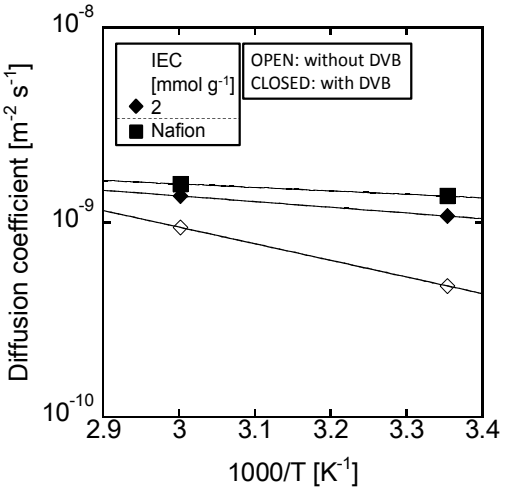

Fig. 2 Arrhenius plots for the three membranes.

This is a blank page.

2. Environmental Conservation and Resource Exploitation

This is a blank page.

2 - 01 Durability of Grafted Fibrous Catalyst for Biodiesel Fuel Production

Y. Ueki, S. Saiki and N. Seko

Environment and Industrial Materials Research Division, QuBS, JAEA

Grafted fibrous polymer has been attracting attention as a sophisticated adsorbent because its adsorption rate is 10 - 100 times higher than that of a commercial granular resin. Recently, we found that the grafted fibrous polymer could function as a highly-efficient heterogeneous basic catalyst for biodiesel fuel (BDF) production[1]. Durability and regeneration evaluation of the grafted fibrous catalyst (GFC) are important issues in order to achieve the practical use of GFC. The objective of this study is to investigate the durability of the GFC and to establish the regeneration process of the deactivated GFC.

The durability of the GFC was evaluated through the batch-wise transesterification of triglyceride (TG) in ethanol (EtOH) at 50 °C. The quaternary ammonium group density of the GFC was 3.6 mmol/g-catalyst, the molar ratio of TG to EtOH was fixed at 1:200, and the detailed transesterification procedures were described in our previous paper[1]. After each transesterification, the GFC was removed from the reaction solution, and the GFC was only washed with EtOH for the next run.

As shown in Fig. 1, the relative catalytic activity of the GFC gradually decreased with increasing number of transesterifications. In this study, the relative catalytic activity was defined as the ratio of the catalytic activity of each transesterification to the initial catalytic activity. There are two main reasons why this decay of catalytic activity is occurred: one is the removal of OH^- ions from the GFC, and the other one is a contamination of the quaternary ammonium groups by free fatty acid (FFA) anions, which are catalytically inactive. FFA anions were generated during the transesterification process by a direct ion-exchange reaction of the OH^- ions, which were immobilized onto the graft chains, with the fatty acid groups in the TG. In the presence of FFA anions, the counter ion of the quaternary ammonium group that was introduced into the graft chain is easily replaced with an FFA anion instead of the OH^- ion. Additionally, the rate of decrease of the catalytic activity was not steady: a rapid decrease was observed after the 8 time usage and subsequent transesterifications. At the 11th transesterification, the catalytic activity of the GFC was almost lost; thus, the conversion ratio of TG to BDF only reached 9%, even after 24 h of transesterification.

Next, in order to discuss the effect of the regeneration process on the catalytic activity, the deactivated GFC was treated with various combinations of the following three treatments: (Step 1) a washing with 0.25 M citric acid solution (solvent: EtOH) to desorb the FFA anions that cover the active sites, *i.e.*, the quaternary ammonium groups, of the GFC, (Step 2) a regenerating with 1 M NaOH aqueous solution to replace the citric acid ions, which formed ionic bonds with the quaternary ammonium groups, with OH^- ions and washing with deionized water, and (Step 3) a washing with EtOH to restore the initial swelled condition. When the deactivated GFC was treated with citric acid and EtOH (regeneration process: Step 1 and 3) and that was treated with only EtOH (regeneration process: Step 3), the catalytic activities of each GFC did not recover at all. The conversion ratios of each GFC were almost zero, even after 24 h of transesterification. When the deactivated GFC was treated with NaOH and EtOH (regeneration process: Step 2 and 3), the catalytic activity of the GFC partially recovered: the conversion ratio after 1 h of transesterification was 25%, which is equivalent to about one-fourth of the initial performance (90% after 1 h of transesterification). Also, the transesterification almost stopped after 4 h, and the conversion ratio after 4 h was about 43%. However, when the deactivated GFC was treated with all three steps (regeneration process: Step 1, 2 and 3), the catalytic activity of the GFC almost completely recovered to its initial catalytic activity, as shown in Fig. 1. The transesterification times required to convert 90% of the initial TG into BDF were 0.99 and 0.99 h for the 1st and 12th transesterifications, respectively. The conversion ratio and transesterification rate of the regenerated GFC almost overlapped with those of the unused GFC. Additionally, the regenerated GFC did not suffer significant physical or chemical damage, even after several transesterification-regeneration cycles. Based on the above results, it was found that the GFC had sufficiently durability, and furthermore the GFC could be used repeatedly by treatment with the three sequential regeneration processes, which involved organic acid, alkali and alcohol treatments.

Reference

1) Y. Ueki et al., Int. J. Org. Chem., **1(2)** (2011) 20-25.

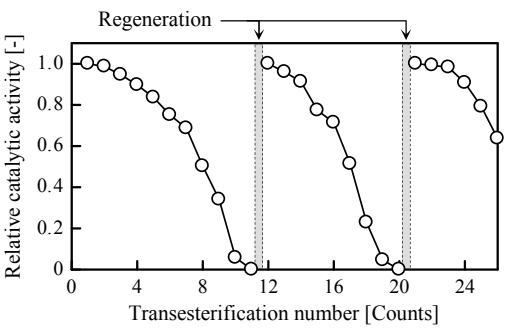

Fig. 1 Repeated-use durability and regeneration of GFC.

2 - 02 Synthesis of Highly-selective Adsorbent Containing 2-Ethylhexyl Hydrogen 2-Ethylhexylphosphonate for Scandium Adsorption

H. Hoshina, Y. Ueki, S. Saiki and N. Seko

Environment and Industrial Materials Research Division, QuBS, JAEA

Scandium (Sc) has been used for a fuel-cell electrolyte and a metal halide lamp. Even though a demand for Sc is increasing in recent years, it is difficult to ensure Sc, because Sc is produced as a byproduct of tungsten and uranium refining[1]. To ensure a stable supply of Sc, new supply method and resource are required. Therefore, recovering Sc with a fibrous graft adsorbent from hot spring water, which contains Sc at a low concentration, has been investigated[2].

2-ethylhexyl hydrogen 2-ethylhexylphosphonate (EHEP) is a superior metal extractant and has a high affinity for Sc especially in acid solutions. If EHEP can be introduced on a polymeric material without any loss of its performances, it is possible to use as a highly selective adsorbent for Sc.

In this study, the adsorbent for Sc was prepared by radiation-induced graft polymerization of dodecyl methacrylate (DMA), and subsequent introduction of EHEP as a functional group by hydrophobic interaction. Furthermore, the adsorption performance for Sc was investigated with an aqueous solution containing Sc and Fe.

A non-woven fabric composed of polyethylene coated polypropylene was used as a base material for the adsorbent for Sc recovery. The base fabric was irradiated at the maximum 500 kGy with an electron beam at a beam energy of 2 MeV and a current of 3 mA. The irradiated fabric was contacted with a deoxidized monomer solution, which was a mix of DMA, Tween 20, and pure water, at 60 °C for 6 hours. The concentrations of DMA and Tween 20 in the solution were 20% and 2%, respectively. The degree of grafting (Dg) was calculated by the following equation;

$$Dg\,[\%] = (W_1 - W_0)/W_0 \times 100\ ,$$

where W_0 and W_1 were the weight of fabrics before and after graft polymerization.

The effect of the absorbed dose on the Dg was shown in Fig. 1. The Dg increased with increment of the absorbed dose, and reached 120% at 500 kGy. The grafted fiber with Dg of 120% was chemically reacted by EHEP, which was used without diluting, for 12 hours at room temperature. The density of EHEP group was 1.0 mmol/g. The batch adsorption tests of Sc were carried out with an aqueous solution in the presence of Sc and Fe of 1 mg/L. The adsorbents were cut into approximately 7 mg and soaked in the 50 mL of Sc and Fe solution for 12 hours at room temperature. To know the effect of pH on Sc adsorption, the solutions were adjusted in the pH range from 0 to 3. After adsorption tests the adsorption ratio was calculated by the following equation,

$$Adsorption\ ratio\,[\%] = (C_0 - C_1) / C_0 \times 100\ ,$$

where C_0 and C_1 were the concentration of the Sc and Fe in solution before and after adsorption tests, respectively.

As a result, the developed new adsorbent had a high adsorption ratio more than 98% at the pH of 0 and 1 as shown Fig. 2. On the other hand, the adsorption ratio of Fe was affected on pH, and reached 2.8% at pH 0. As a result, it was found that the adsorbent of EHEP could recover Sc selectively from strongly acidic water media. The adsorbent of EHEP is expected to be applied for Sc recovery from hot spring water.

References

1) U. S. Geological Survey, Mineral Commodity Summaries 2012 (2012) 140.
2) N. Seko et al., J. Ion. Exchange. 21(3) (2010) 117.

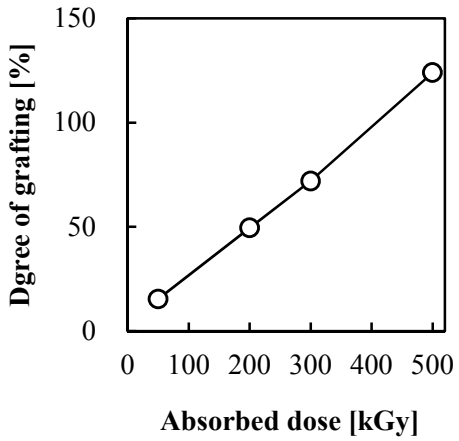

Fig. 1 Effect of the absorbed dose on degree of grafting.

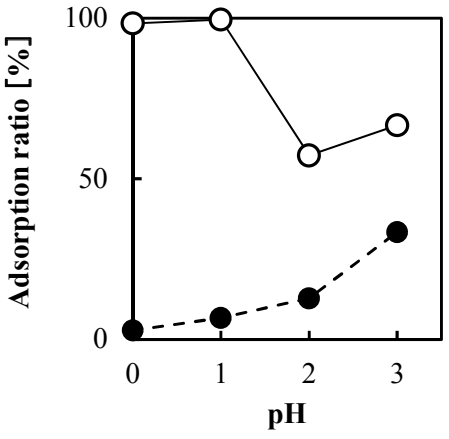

Fig. 2 Effect of pH on the adsorption of Sc (○) an Fe (●).

2 - 03 Decontamination of Leaching Water from Contaminated Plant Wastes

S. Saiki, T. Shibata, H. Hoshina, Y. Ueki, N. Kasai and N. Seko

Environment and Industrial Materials Research Unit, QuBS, JAEA

In 2011, the accidents of Fukushima Daiichi Nuclear Power Plant spread a large amount of radioactive species to surrounding circumstances around Fukushima Prefecture, Japan. To recover and ensure living environment at contaminated areas where people had ever lived, decontamination works has been executed promptly. With the progress of decontamination works, a lot of radioactively-contaminated wastes has been produced continuously at contaminated areas, and has been piled up at temporary storage sites. At some temporary storage sites, it was found that leaching water was accumulated under stacks of flexible container bags contaminated "plant" wastes such as branches, leaves and grasses and that the solution contained radioactive cesium. When these wastes will be transferred to interim storage facility in near future, the contaminated solution should be handled properly. In this topic, decontamination method of the leaching water with cesium adsorbents synthesized by radiation-induced graft polymerization was studied for handling the leaching water.

Cesium adsorbents were synthesized with immobilization of ammonium molybdophosphate on polyethylene /polypropylene nonwoven fabric by radiation-induced grafting method [1]. The nonwoven fabric irradiated with 2 MeV electron beam with the dose of 50 kGy at Takasaki Advanced Radiation Research Institute, JAEA, was soaked into a monomer solution under reduced pressure, which was mixed with glycidyl methacrylate, dimethyl sulfoxide, tween 80 and crosslinking agents. The grafting reaction proceeded at 40 °C for 2 hours, and the grafted samples taken out of the solution were rinsed and dried in vacuum oven.

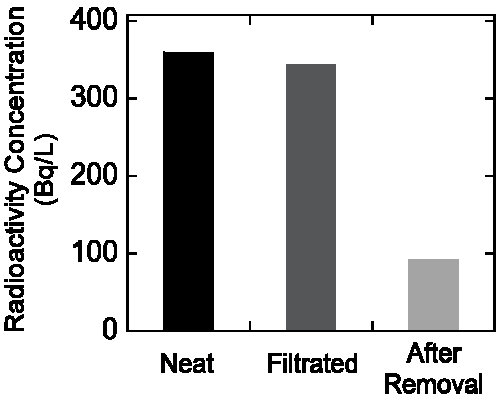

Fig. 1 Cesium radioactivity concentration of neat leaching water, filtrated solution through 0.45 μm membrane filter, and solution after cesium removal with grafted cesium adsorbents.

Before the batch adsorption test, the leaching water was filtrated by 0.45 μm membrane filter to separate insoluble components. Radioactivity concentration of the filtrated solution was almost the same as neat solution as shown in Fig. 1. This means that cesium exists in the solution at dissolved state.

At a batch cesium adsorption test, cesium adsorbents cut into 1 cm square were put into the leaching water with a weight ratio of 1:150 (adsorbent : solution) in a plastic bottle, which was shaken for 12 hours at room temperature. Then, the solution was transferred to U-8 type plastic container and radioactivity concentration of radioactive cesium (^{134}Cs+^{137}Cs) was measured by germanium semiconductor detector (SEIKO EG&G Co., Ltd). As a result of the batch adsorption test, 75% of radioactive cesium was succeeded to be removed.

In addition, to lower radioactivity concentration of the leaching water by the cesium adsorbents, repeat decontamination tests were examined. As well as above batch tests, cesium adsorbents were put into the leaching water with a weight ratio of 1:100 (adsorbent:solution) in a plastic bottle, which was shaken for 4 hours at room temperature. The removal process repeated three times, and radioactivity concentration after each removal process was shown as Fig. 2. After three times of removal process repeats, 97% of radioactive cesium could be removed.

These results showed that the leaching water could be decontaminated and the grafted cesium adsorbents were effective for the decontamination.

Reference

1) A. Iwanade et al., J. Radioanal. Nucl. Chem. 293 (2012) 703-09.

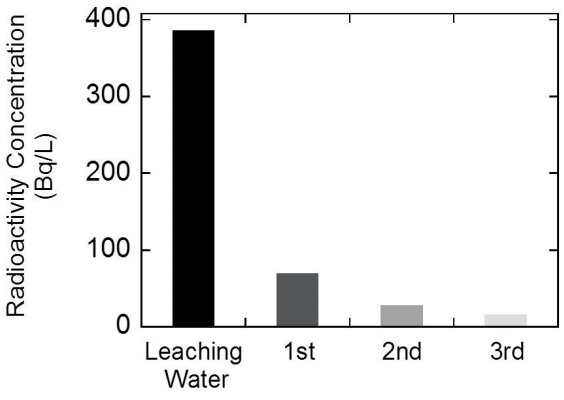

Fig. 2 Results of repeat decontamination tests by grafted cesium adsorbents from leaching water.

2 - 04 Development of Cs Adsorbent Synthesized by Radiation-induced Graft Polymerization for Drinking Water

T. Shibata, N. Seko, H. Amada, N. Kasai, S. Saiki, H. Hoshina and Y. Ueki

Environment and Industrial Materials Research Division, QuBS, JAEA

One of the important tasks for recovery of the disaster area by the accident of the Fukushima Daiichi Nuclear Power Plant is to secure safety life water. More than three years has passed since the accident, a most of dissolved radioisotopes such as ^{134}Cs and ^{137}Cs were not detected in the environment water. In the case of detected, the concentration of it below than 10 Bq/L which is the guideline for drinking water. However, there are some residents of the disaster area having uneasiness for water supply. Based on this background, we have developed Cs adsorbent for applicable to drinking water.

The Cs adsorbent has been developed by radiation-induced graft polymerization. The adsorbent was synthesized by following procedures; 1) polyethylene nonwoven fabric (NF) was irradiated with 50 kGy by electron beam or ^{60}Co γ-rays in N_2 atmosphere at dry ice temperature, 2) the irradiated NF was grafted with a monomer composed of 10 wt% glycidyl methacrylate (GMA), 90 wt% dimethyl sulfoxide, 0.8 wt% Tween 80, 0.4 mol% ammonium 12-molybdophosphate (AMP) against for GMA concentration. To stabilize the loaded AMP in the adsorbent, various kinds of polyethylene glycol dimethacrylate (PEGDM) or triallyl isocyanurate as the crosslinking reagent were mixed with the monomer solution at 40 °C for 2 or 3 h. The previous report showed that the crosslinked adsorbent synthesized by 1 mol% of 9G (G: dimethacrylate) type of PEGDM had not only high stability of the loaded AMP but also high adsorptivety for Cs, and satisfied the Food Sanitation Act[1].

The efficiency of adsorbent performance was investigated by batch and column adsorption test. The batch adsorption test that the adsorbent cut into 1 cm^2 (0.02 g) was immersed in 50 mL of 1 or 50 μg/L Cs solution and stirred for 24 h. Figure 1 shows the results of pH dependency in batch adsorption test which carried out by 50 μg/L Cs solution in the pH range from 3 to 9 for evaluation adaptively to various contaminated water. More than 60% of Cs was adsorbed in the all of pH range, and desorption of AMP moiety was less than 3% in the pH range from 5.8 to 8.6 for drinking water standard. AMP stability was evaluated by monitoring of molybdenum (Mo) concentration. Table 1 shows the results of Cs selectivity in batch adsorption test which carried out by 1 μg/L Cs solution added 1 mg/L of K, Ca, Mg and Na for evaluation adaptively to stream water used as life water. The developed fibrous adsorbent collected only Cs without any coexistence ions. The column adsorption were carried out 1 μg/L Cs solution at the flow rate of 1.3 mL/min (SV; space velocity: 400 h^{-1}) which packed the adsorbent with diameter of 7 mm and height of 5 mm (0.2 cm^3). The breakthrough point (BP) that determined 0.05 at C/C$_0$ [C: influent of Cs (μg/L), C$_0$: effuent of Cs (μg/L)] was 2,650 bed volume (Fig. 2), and the Cs adsorption capacity at BP was 1.4 mmol-Cs/kg-adsorbent.

Reference

1) T. Shibata et al., JAEA Takasaki Annu. Rep. 2012 JAEA-Review 2013-059 (2014) 55.

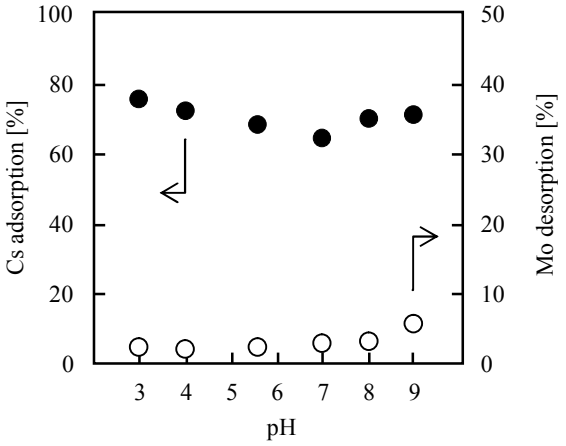

Fig. 1 pH dependency in batch adsorption test.

Table 1 Cs selectivity in batch adsorption test.

	Cs	K	Ca	Mg	Na
Adsorption [%]	83	0	0	0	0

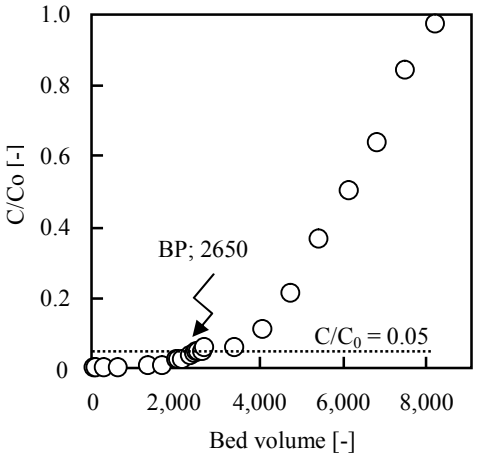

Fig. 2 Breakthrough curve in column adsorption test.

2 - 05 Development and Practical Use of Grafted Filter for Removal of Contaminative Metal Ions

T. Mikami [a)], T. Hosoe [a)], S. Muraki [a)], M. Nakano [a)], T. Takeda [a)], T. Nishino [a)], N. Chikaishi [a)] and N. Seko [b)]

[a)] Kurashiki Textile Manufacturing. Co., Ltd,
[b)] Environment and Industrial Material Research Division, QuBS, JAEA

The filtration media to remove metal ions dissolving in liquids has developed by radiation graft polymerization technology. In this study, various function groups were grafted onto nonwoven fabrics to be liquid filtration media. The media can rapidly adsorb metal ions dissolving in ultrapure water, various kind of enchant and organic solvents used in semi-conductor production. The performance is featured particularly when applied to purify such liquid into extremely low concentration level, i.e. analytical detection limit (< ppb). Based on the performance results, the filtration media is processed into a type of cartridge and capsule unit for practical application.

半導体用途に用いられている各種液体に溶存している有害金属イオンを除去する目的で、原子力機構との共同研究成果の一環として、放射線グラフト重合技術を用いた金属イオン捕集材（以下、「捕集材」という）の製造基礎技術を開発した。この捕集材は高密度ポリエチレン繊維からなる不織布を放射線グラフト重合によりイオン捕捉官能基を付与したもので、液中に存在する微量の金属イオンをきわめて高精度にかつ高速度で捕捉するものである。今回、クラボウ技術研究所の支援を得て、この捕集材を効率的に充填したフィルターカートリッジを開発することができ、商品名を“クラングラフト®”として上市するに至った。

この商品の応用先である半導体製造工程においては、エッチング液、研磨スラリー、フォトレジスト、現像液などの多種多様の液体および超純水が使用されているが、これらの薬液には微量ながら Na、Cu、Fe、Al、などの金属イオンが溶存しており、これが半導体の歩留り低下と高度の集積化を妨げている。このような不純物の除去において、微量金属イオン除去フィルター“クラングラフト”で対象薬液をろ過すると液体中の不純物の濃度をppmからpptレベルに引き下げることが可能であることを商品の特徴に挙げ、目下、販促中である。

ここで捕集材が持つ性能を示す例として、当該捕集材の金属イオン捕集性能を示す（Fig. 1）。同図は、スルホン基付与のグラフト重合不織布を充填カラムに収納し、各種金属イオンを予め調合した超純水を原体として通液試験を実施した結果である。また、有機溶剤やエッチング液についても、キレート基を付与したグラフト基材で同様の結果を得ている。この様に、捕集材を通過する液体中の金属イオンが、きわめて高精度に除去されることが判明している。

現在、捕集材としては、大別して強カチオン型交換基、弱アニオン型交換基、キレート型交換基を付与した 3 種類を準備した。ろ過フィルターの商品としては、この捕集材を充填したカートリッジそのものと、そのカートリッジをポリエチレン容器の中に封入したカプセルフィルターの 2 種類の形態をラインナップし、市場に紹介している（Fig. 2）。

また、これらの捕集材は、様々な金属イオンが精度よく捕集できていることに特徴があり、例えば、工業排水や生活用水に含まれるヒ素、六価クロム、鉛、カドミウムなどの除去が可能であるため、排水浄化、環境汚染対策などにも応用できるものと期待している。

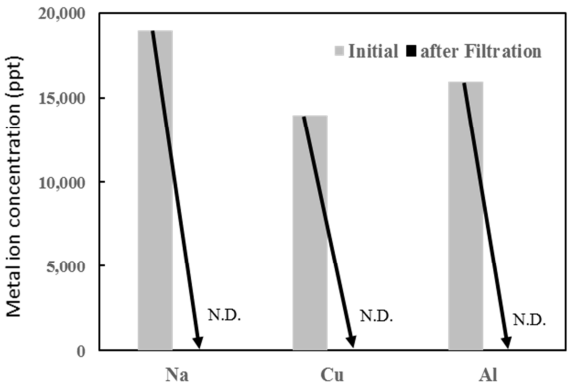

Fig. 1 The removal of contaminative metal ion from ultrapure water.

Fig. 2 The photograph of cartridge filter (left) and capsule filter (right).

2 - 06 Application Study of EB Grafted Water Seal Rubber in order to Improve Drive Efficiency of Water Feed Pump

H. Saito [a)], N. Mizote [a)], Y. Ueki [b)] and N. Seko [b)]

[a)] Mitsuba Corporation,
[b)] Environment and Industrial Materials Research Division, QuBS, JAEA

A hydrophilic monomer (methacrylic acid: MAA) was grafted on a water seal rubber by simultaneous radiation grafting followed by alkali treatment. We measured the friction coefficient of the grafted water seal rubber. From the measurement results, it was found that friction coefficient decreased significantly due to the grafting, compared to the initial rubber. Consequently, the drive efficiency of a water feed pump improved by means of applying the grafted water seal rubber.

我々はこれまでに放射線グラフト重合法を用いて、ゴムの表面改質に関する研究に取り組み、摩擦変動が少なく、かつ耐摩耗性に優れた新規表面改質ゴムの開発に成功した。さらにある条件下においては、表面改質ゴムの摩擦係数が初期値（未処理のゴムの摩擦係数）に対して 1/30 に低減するといった特異的な水潤滑摩擦特性を見出した[1)]。本研究では、特異的な摩擦傾向を発現させるグラフト重合技術をウォーターポンプのシール材に適用し、モータ効率への影響について検証した。

高温機材を冷却する手段の一つに水冷システムが挙げられ、ウォーターポンプはこのシステムにおいて冷却水を強制循環させる役割を担っている（Fig. 1）。ポンプに電流を流すとモータがインペラ（羽）を回転させて冷却水を循環させるが、モータとインペラの間にはモータへの水の浸入防止材としてシール材が組み込まれている。このシール材はインペラを回転させる際の大きな抵抗となり、モータ効率（入力したエネルギーに対するインペラの回転に使用されているエネルギーの割合）を低下させる大きな要因となっている。そのため、水の浸入を防止しつつ、インペラの回転を妨げない低摩擦なシール材の開発が求められている。本研究では、シール材の低摩擦化を図るためにシール材へのグラフト処理を試みた。

基材にはカーボンブラックを配合したアクリロニトリルーブタジエンゴム（NBR）製シート、及び、シール材（成形品）を用いた。電子線同時照射グラフト重合反応には、高崎量子応用研究所の電子線加速器（加速電圧: 2 MV, 電流値: 1 mA）を用いた。ポリエチレン袋にゴムサンプルと反応性モノマーであるメタクリル酸（MAA）溶液を入れ、ゴムが反応液に浸漬された状態で、照射線量30 kGyの条件でグラフト処理を施した。その後、水酸化カリウム水溶液を用いてアルカリ処理を行い、官能基末端にカリウムイオンを導入し、目的とする表面改質親水性ゴム材料を得た。

初めに、NBR 製シートに対するグラフト処理の有効性を検証するために、往復摺動試験機を用いた摩擦試験を実施した。本試験では、荷重を 100 gf、摩擦速度を 10 mm/s、摩擦相手として粒径 10 mm のステンレス球を用いた。Figure 2 は、未処理、及び、グラフト処理した NBR 製シートそれぞれに対する、乾燥環境下、及び、湿潤環境下における摩擦係数を示した図である。グラフト処理により、摩擦係数は乾燥環境下では、初期値（未処理のゴムの摩擦係数）の 1/6、湿潤環境下では初期値の 1/30 にそれぞれ低下した。以上の結果から、ゴムシートの低摩擦化にはグラフト処理が有効であることが分かった。

次に、シール材（成形品）に対してグラフト処理を施したところ、Fig. 3 に示すようにシール材表層にカリウムイオンが導入されていることを確認することができ、成形品に対してもグラフト処理が可能であることが分かった。グラフト処理したシール材をウォーターポンプに組み込み評価した結果、モータ効率が未処理のシール材と比較して 1.5%向上していることが確認された。今後は耐久性試験、並びに、更なるモータ効率の向上を目指し、グラフト率の最適化を図る。

Reference

1) H. Saito et al., JAEA Takasaki Annu. Rep. 2011 JAEA-Review 2012-046 (2013) 45.

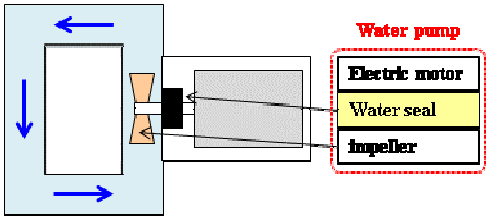

Fig. 1 Schematic of water circulation system by water pump.

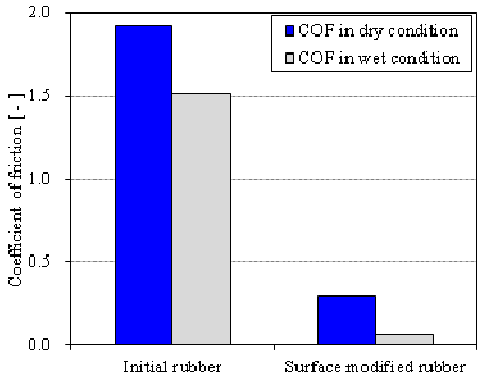

Fig. 2 Influence on a coefficient of friction by grafting.

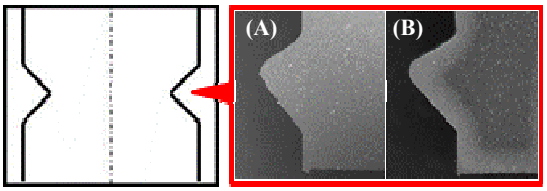

Fig. 3 Side cross-sectional view of a water seal rubber. (A) initial rubber, (B) grafted rubber.

2 - 07 Dose Response of Polymer Gel Dosimeters Based on Radiation-crosslinked Hydroxypropyl Cellulose Gels

A. Hiroki [a)], S. Yamashita [b)], A. Kimura [a)], N. Nagasawa [a)] and M. Taguchi [a)]

[a)] Environment and Industrial Materials Research Division, QuBS, JAEA,
[b)] School of Engineering, The University of Tokyo

Polymer gel dosimeters consisting of some monomers with gel matrix are drawing attention as a tool of three-dimensional dose distribution measurement [1)]. The monomers are polymerized by irradiation to form polymers, which in turn aggregate in the gel matrix, increasing the optical density of the gel. Absorbed dose in the gel is estimated by measuring the optical density. Recently, new polymer gel dosimeters consisting of 2-hydroxyethyl methacrylate (HEMA) and 9G as less toxic monomers and tetrakis (hydroxymethyl) phosphonium chloride (THPC) as an antioxidant with radiation-crosslinked hydroxypropyl cellulose (HPC) gel have been reported [2,3)]. The dosimeters became cloudy at 2 Gy with γ-irradiation and absorbance increased approximately linearly with an increase in the dose up to 10 Gy. The dose response depended on the composition ratio between HEMA and 9G. In this work, effects of THPC concentration and dose rate on the dose response of the dosimeters were investigated.

HPC was dissolved in ultrapure water at 20 wt%. HPC aqueous solution as a paste-state was formed to 1.0 mm thickness by pressing, and was irradiated to a dose of 10 kGy with electron beam to obtain the HPC gel membrane. The HPC gel membranes were washed with distilled water to remove uncrosslinked HPC, and then dried. The dried gels were immersed into aqueous monomer solutions that consist of 2 wt% HEMA, 3 wt% 9G, and 0.08-0.24 wt% THPC. The swollen gels were vacuum-packed to obtain polymer gel dosimeters. The prepared samples were irradiated up to 2 Gy by using a ^{60}Co γ-ray source. Dose rate was adjusted by varying the distance between the samples and the source. The irradiated dosimeters were optically analyzed by using an UV-Vis spectrophotometer. The EB- and γ-irradiations were carried out using Cockcroft Walton electron accelerator and ^{60}Co sources at Takasaki Advanced Radiation Research Institute, JAEA, respectively.

Figure 1 shows absorbance of the polymer gel dosimeters with various THPC concentrations as a function of dose. The absorbance of the polymer gel dosimeters at 660 nm increased with increasing dose. Dose response defined as the increment in absorbance per unit dose increased with an increase in THPC concentration, reached about 0.06 Abs. Gy^{-1} at the dosimeter with 0.24 wt% THPC. Conventional polymer gel dosimeter consisting of acrylamide and *N,N'*-methylene bis-acrylamide with gelatin gel matrix, optimum THPC concentration to maximize the dose response has been reported to be about 0.1 wt% THPC [4)]. However, in the prepared dosimeters, there was no maximum of the dose response until 0.24 wt% THPC.

Propagation and termination reactions compete with each other in the radical polymerization process, which affect the molecular weight of polymer. Figure 2 shows the relationship between dose rate and absorbance of the dosimeter irradiated to a dose of 2 Gy. The absorbance of the dosimeter consisting of 2 wt% HEMA, 3 wt% 9G, and 0.16 wt% THPC decreased with the dose rate. This dose rate effect would be due to the formation of the low-molecular weight polymers with increasing termination reaction of the radicals.

References

1) M. J. Maryanski et al., Phys. Med. Biol. 39 (1994) 1437.
2) A. Hiroki et al., J. Phys.: Conf. Ser. 444 (2013) 012028.
3) S. Yamashita et al., Radiat. Phys. Chem. 101 (2014) 53.
4) A. Jirasek et al., Phys. Med. Biol. 51 (2006) 1891.

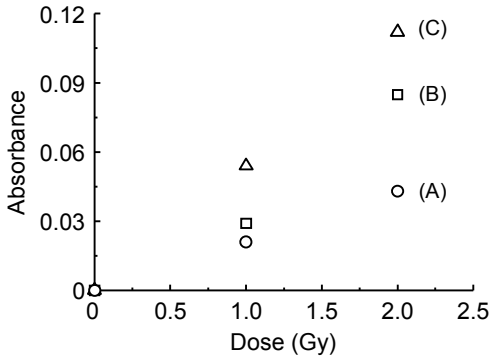

Fig. 1 Effect of the dose on the absorbance of the polymer gel dosimeters consisting of HEMA, 9G, and THPC. THPC concentrations are 0.08 wt% (A), 0.16 wt% (B), and 0.24 wt% (C), respectively.

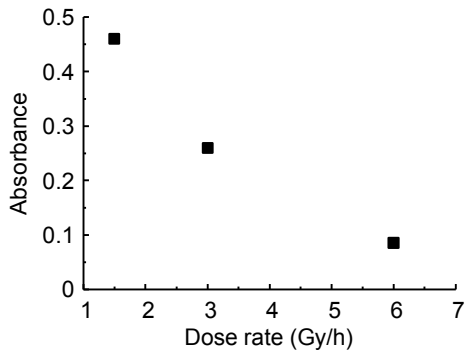

Fig. 2 Relationship between dose rate and absorbance of the polymer gel dosimeter with 2 wt% HEMA, 3 wt% 9G, and 0.16 wt% THPC. Total dose was 2 Gy.

2 - 08 Availability of HPC Gel as an Electron Donor in Denitrification

T. Tanaka [a)], T. Yanagisawa [a)], N. Nagasawa [b)] and M. Taguchi [b)]

[a)] Department of Civil and Environmental Engineering, Maebashi Institute of Technology,
[b)] Environment and Industrial Materials Research Division, QuBS, JAEA

Hydroxypropylcellulose (HPC) gel was prepared applying by the radiation crosslinking technique. The HPC hydrogel was packed into a carbon felt hollow cylinder, and then the carrier was immersed in the reactor. The continuous denitrification experiments were carried by using the carrier. In the experiment using the carrier without the hydrogel, total nitrogen concentration in the reactor was not decreased. On the other hand, a significant difference between influent and effluent TN concentrations was recognized in the experiment using the carrier with the hydrogel. The hydrogel could be used as an electron donor and/or carbon source in the denitrification.

【はじめに】硝酸性窒素および亜硝酸性窒素で汚染された地下水、河川水、排水などの浄化操作が原位置でかつ簡易的に実施可能な、電子供与体を添加する方式の生物学的脱窒技術の開発を目的として、電子線(EB)を照射して架橋した高分子ゲルを外部電子供与体として用いることを提案し、その可能性について検討した。EB 加工技術を適用することにより、薬剤を用いる従来の調製方法では困難であったゲルの成形と短時間量産が容易となる。加えて、照射条件により架橋密度を制御できるため、有機物の過剰溶出による二次汚染の抑制も比較的容易である。以上のことから、高分子材料として、有機炭素を含み、EB などを照射することによりゲル化することが見出されているヒドロキシプロピルセルロース(HPC)[1)]を選択し、生物親和性が高く、微生物保持能に優れた炭素繊維フェルト[2)]と組み合わせた担体を作製して、脱窒効果について検討した。

【実験】脱窒実験に用いた HPC ゲルは、そのペーストに EB を照射して調製した。HPC 濃度と EB の線量は、それぞれ 30%、20 kGy とした[1)]。EB 照射の後、完成したゲルを蒸留水に 48 時間浸漬して洗浄した。洗浄 HPC ゲルと炭素繊維フェルトとを組み合わせたものを担体として用いた。厚さ 1 cm の炭素繊維フェルトを縦:20 cm、横:10～12 cm にカットして筒状に丸め、その内部に HPC ゲルを挿入して担体を準備した。ここでは、担体の総比表面積が 40 m^2/m^3 程度[2)] となるように、上記の炭素繊維フェルト筒を 9 本準備した。脱窒実験に先立ち、ゲル充填なしの炭素繊維フェルト筒を用いて実験(対照実験)を行った。対照実験は攪拌を目的として緩やかに曝気を行い、被検水(硝酸カリウム水溶液)を連続的に供給して行った。被検水の供給量は、曝気槽での滞留時間が 24 時間[2)]となるように 4 mL/min とした。対照実験終了の後、担体をゲル充填炭素繊維フェルト筒に交換して連続方式の脱窒実験を行った。

【結果と考察】実験結果を Fig. 1(対照実験)および Fig. 2(脱窒実験)に示す。対照実験において、流入と流出の全窒素(TN)濃度はほぼ同レベルであった。炭素繊維フェルト筒のみでは脱窒反応の発現は期待できないことがわかった。一方、脱窒実験では、流出 TN 濃度の方が一貫して低かった。流出 TOC(全有機炭素)濃度に関しては、実験初期では 20 mg/L 程度と比較的高かったが、30 日以降では 5 mg/L 付近まで低下した。これは、炭素繊維フェルト筒内に挿入した HPC ゲルが脱窒細菌に利用され、同化・還元反応が同時に進行したためと推察される。なお、TP(全リン)については、対照実験の初期において検出が若干認められたものの、それ以降両実験ともに検出されなかった。以上の結果から HPC ゲルは、脱窒反応における電子供与体として利用可能と考えられる。

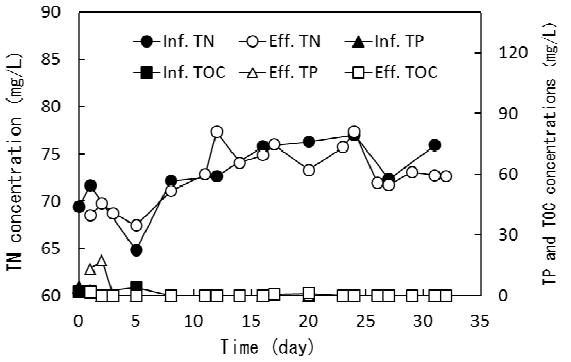

Fig. 1 Total contents of nitrogen, phosphorus and organic carbon at inflow and effluence in the control experiment. ●:total nitrogen at inflow, ○:total nitrogen at effluence, ▲;total phosphorus at inflow, △;total phosphorus at effluence, ■;total organic carbon at inflow, □;total organic carbon at effluence.

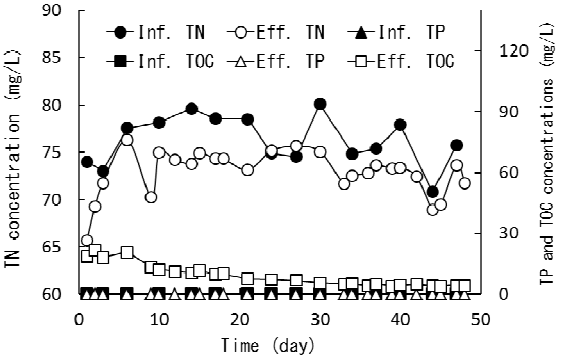

Fig. 2 Total contents of nitrogen, phosphorus and organic carbon at inflow and effluence in the denitrification experiment with gel as electron donor and carbon source. The symbols are the same as Fig. 1.

References

1) R. A. Wach et al., Macromol. Mater. Eng. 287 (2002) 285-95.
2) 田中ら、土木学会論文集、No.685 (2001)、115-22.

2 - 09 Preparation of Scaffold for Cell Culture Use from Silk Fibrous Protein by Gamma Ray-irradiation

T. Sekiguchi [a)], N. Nagasawa [b)], M. Taguchi [b)], Y. Tamada [c)] and Y. Kawahara [a)]

[a)] Division of Environmental Engineering Science, Faculty of Science & Technology, Gunma University,
[b)] Environment and Industrial Materials Research Division, QuBS, JAEA,
[c)] Division of Applied Biology, Faculty of Textile Science & Technology, Shinshu University

Silk aerogel has been prepared from liquid silk, and the influences of the gamma ray-irradiation on the mechanical properties and the adhesive properties against NIH3T3 cell were investigated. It was found that the formation of crosslinking in the sericin fractions induced by the gamma rays-irradiation will harden the aerogel and affect the cell adhesion and/or cultivation. Further investigations are needed for the practical use of silk aerogel.

【はじめに】iPS 細胞や ES 細胞技術によって患者自身の幹細胞を in vitro で分化誘導して、治療に用いる再生医療の試みが現実化している。幹細胞を増殖させながら、目的の臓器に分化させて生体に移植するには、異種細胞との接触の場や、臓器形状を保持する三次元構造の基材などの開発が必須と考えられている。再生医療要素技術の足場関連技術に不可欠なアイテムとして、細胞との親和性が高く増殖に適切な構造を有したスキャホールド材料の開発が求められている。最近、絹タンパク質由来のハイドロゲルが生体適合性に優れていることが示され[1)]、液状絹を用いればエアロゲル化した絹タンパク質由来のスキャホールド材料が製造可能であることが報告されている[2)]。本研究では、絹エアロゲルに対してγ線照射を行い、圧縮変形特性の変化や表面改質による細胞接着性への影響について検討した。

【実験】絹糸腺の中部から摘出した液状絹ゲルを超純水に展開し、約 3%の水溶液として-20 ℃で凍結・乾燥しエアロゲルを得た。このゲルをポリエチレン製の試料袋に入れ、原子力機構高崎量子応用研究所のコバルト照射施設において、^{60}Coγ線を空気雰囲気中、線量率 10 kGy/h で、線量 10, 25, 50 kGy 照射した。

接着性能は、調製したスポンジ試料を 6 mmϕに打ち抜き、リン酸バッファー（PBS）に浸漬した。浸漬した試料に NIH3T3 細胞分散液を 5×10^4 cells/sponge になるように播種し、37 ℃、5% CO_2 で 3 時間培養後、PBS で洗浄し、LDH 活性法で接着細胞数を測定することで評価した。

【結果と考察】絹タンパク質は結晶性のフィブロインと非晶性のセリシンの 2 成分から構成される。これらの複合体からなるスキャホールドは、フィブロインリッチな繊維状組織と、それを安定化させるセリシンリッチな皮膜構造からなるため、従来のフィブロイン単成分のものに比べ、エアロゲルの状態でも柔軟性が得られることを確認している。このエアロゲルのγ線照射後の繰り返し圧縮変形に対する力学特性の変化を調べたところ、セリシンにγ線照射で架橋結合が導入され、ゲルの硬さが高められることが分かった（Fig. 1）。

一方、NIH3T3 細胞の接着性について評価したところ、オートクレーブ処理をしてセリシンをある程度除去し、50 kGy のγ線照射後、再度、オートクレーブ滅菌した＃7 の試料が最も高い細胞接着性を示した（Fig. 2）。

さらに、細胞増殖性を調べたところ、＃7 ではなく、＃5 の倍加時間が 1.04 日と、＃7 の 1.21 日に比べ短く、増殖性が高かった。セリシン除去のために行った 1 回目のオートクレーブ処理での重量減少率を比較したところ、＃5 では 3 個のスポンジの重量減少率が、11.4, 11.6, 12.2%でほぼ一定あったのに対して、＃7 では、6.1、13.7、9.0%と不安定で、セリシンの皮膜の除去が＃7 では比較的進行しなかった。また、Fig. 2 において、セリシン除去処理を行っていない#1～4 のスポンジの細胞接着性が低かった。これらのことはセリシンの過剰な残留が細胞培養の障害となったことを示唆している。γ線照射による改質だけでなく、オートクレーブ処理でセリシンの適切な除去が再生医療に利用可能な液状絹由来スキャホールド材料開発に必要であることがわかった。

References

1) Y. Tamada, Biomacromolecules, 6 (2005) 3100-06.
2) Y. Kawahara et al., Asia & Africa Sci. Platf. Prog. Neo-Fiber Technol. Seminar Proc. (2013) 67.

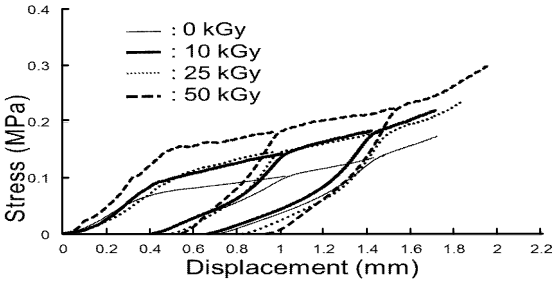

Fig. 1 Relationship between compressional stress and displacement for the γ-irradiated silk aerogel.

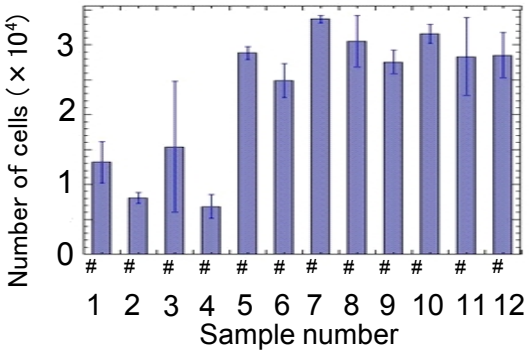

Fig. 2 Adhesive property against NIH3T3 cell for the γ-irradiated silk aerogel. #4,#8,#12: 0 kGy; #1,#5,#9: 10 kGy; #2, #6,#10: 25 kGy; #3,#7,#11: 50 kGy.

This is a blank page.

3. Medical and Biotechnological Application

This is a blank page.

3 - 01 Estimation of Damage Localization in DNA Irradiated with $^{4}He^{2+}$, $^{12}C^{5+}$ and ^{60}Co γ-rays in the Solid State

K. Akamatsu and N. Shikazono

Medical and Biotechnological Application Division, QuBS, JAEA

1. Introduction

DNA lesions induced by ionizing radiation can cause mutation and carcinogenesis. In particular, "clustered damage" or "multiply damaged site", that is a DNA region with two or more lesions within a few helical turns, is believed to be hardly repaired. This damage is considered to be frequently induced, especially around high-LET radiation tracks. However, detail of the distribution of damage is not fully known. We have already developed a method for estimating localization of abasic (AP) sites on DNA using Förster resonance energy transfer (FRET). The FRET efficiency (*E*) was calculated using the donor fluorescence intensities before/after enzymatic digestion of the labeled AP-DNA[1]. We applied the method to $^{4}He^{2+}$-, $^{12}C^{5+}$- and ^{60}Co γ-irradiated DNA in the solid state.

2. Experiments

●*Sample preparation and irradiation*

Plasmid DNA digested by Sma I was used (linear formed). The DNA aq. was dropped on a glass plate and dried in vacuum. The plate was irradiated with linear energy transfer (LET) of ~70 keV/μm of $^{4}He^{2+}$ and ~760 keV/μm of $^{12}C^{5+}$ beams (TC, TIARA), which was controlled by a depth-tunable cell irradiation equipment[2]. Moreover, ^{60}Co γ-rays were also used as a standard radiation source at Kyoto University Research Reactor Institute KURRI.

●*Preparation of fluorophore-labeled irradiated DNA and FRET observation*

The irradiated DNA (10 μL in water) and 10 μL of 100 mM Tris-HCl (pH 7.5) were mixed in a microtube. Two microliters of a mixture containing AF350 and AF488 with a given molar ratio was added to the DNA solution and was incubated 24 h at 35 °C. The fluorophore-labeled DNA was purified by ethanol precipitation. Ten microliters of water was added to the residue immediately after removal of the supernatant. Two hundreds microliters of 100 mM TrisHCl with 10 mM $MgCl_2$ (pH 8) was added to the purified labeled DNA sample. The fluorescence intensities were measured both at 449 nm (ex. 347 nm for AF350) and at 520 nm (ex. 460 nm for AF488). After the measurement, the enzyme cocktail containing DNase I and phosphodiesterase I was added to the solution, and the solution was incubated for 3 h at 37 °C. *E* values were calculated from the donor intensity before/after the digestion at 449 nm (ex. 347 nm).

3. Results and Discussion

The AP yields for He and C was similar to each other, and clearly higher than the AP yield for ^{60}Co γ-rays (Fig. 1)[3]. This result is consistent with the yields of base release[4].

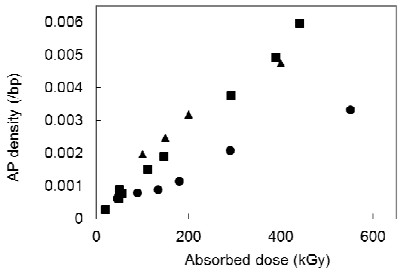

Fig. 1 AP densities (the number of APs per bp) for He (▲), C (■), and ^{60}Co γ-rays (●) as a function of absorbed dose. Revised from the submitted paper[3].

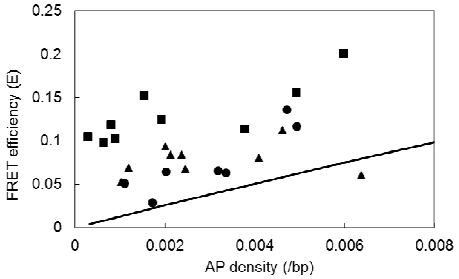

Fig. 2 FRET efficiency for He (▲), C (■), and ^{60}Co γ-rays (●) as a function of AP density. The line is that for random APs. Revised from the submitted paper[3].

Figure 2 shows the FRET efficiency (*E*) for these sources as a function of AP density. *E* values for He and ^{60}Co γ-rays were similar to or slightly higher than the E value for a randomly distributed APs, whereas the value for C was higher than the values for other sources. In addition, the *E* values for C, interestingly, seemed to be ~0.10 even at zero dose, implying that a single particle track of C produces more clustered APs than those for other sources[3]. The *E* value of 0.10 means that AP-AP distance at a clustered AP region is on average ~17 bp[3], which suggests that quite a few AP clusters with less than 17 bp apart can be produced within a track of C particle. Now we are applying the FRET method to an aqueous DNA sample with a cell-mimetic condition.

Acknowledgments

We would like to gratefully thank Dr. Takeshi Saito of KURRI for supporting ^{60}Co γ-ray irradiation and also thank Drs. Y. Sugo and H. Ohsawa for operating TC at TIARA.

References

1) K. Akamatsu and N. Shikazono, Anal. Biochem. **433** (2013) 171-180.
2) A. Tanaka et al., Nucl. Instr. Met. Phys. Res. **B129** (1997) 42.
3) K. Akamatsu et al., Radiat. Res., 183 (2015) pp.105-113.
4) K. Akamatsu, JAEA Takasaki Annu. Rep. 2008 JAEA-Review 2009-041 (2009) 63.

3 - 02 Isolation of Carbon Ions-Induced Mutants in *Arabidopsis thaliana* Exhibiting Different Anthocyanin Accumulation Patterns

S. Kitamura, Y. Oono and I. Narumi *

Medical and Biotechnological Application Division, QuBS, JAEA,
* Present affiliation: Faculty of Life Sciences, Toyo University

In plant kingdom, anthocyanins are the most popular and widespread group of pigments that can modify flower and fruit colors. Anthocyanins are categorized to flavonoid compounds, together with other subclasses such as flavonols and proanthocyanidins (PAs). These flavonoids are known to have several physiological functions, such as acting as ultraviolet-B absorbing compounds, anti-microbial agents, and antioxidants. It is known that anthocyanins are synthesized at cytoplasmic surface of the endoplasmic reticulum, whereas anthocyanins are accumulated within the vacuoles. In addition, to fulfill the physiological functions of anthocyanins such as pigments and ultraviolet-B absorbers, they must be accumulated in vacuoles after completion of their synthesis. Despite the prerequisite step for fulfilling their functions, the mechanisms by which anthocyanins are accumulated into vacuoles are poorly understood.

Ion beams have been used for isolation of novel mutants in a number of plant species in our laboratory. Re-mutagenesis by secondary irradiation of ion beams to already-established ion beam-induced mutants would be effective to modify plant characters step-by-step, because ion beams are likely to induce mutations at the limited regions of the genome. Here, we try to adapt the re-mutagenesis by secondary ion beam irradiation in model plant Arabidopsis, for obtaining flavonoid mutants that have not been found so far by standard mutagenesis and screening methods.

Arabidopsis thaliana L. was used in this experiment. An anthocyanin spotted testa (ast) mutant had been isolated as one showing spotted anthocyanin pigments in immature seed coat[1]. Dry seeds of ast were mutagenized with 150 Gy of 220 MeV carbon ion beams. Irradiated seeds were self-pollinated for obtaining M2 seeds. The M2 seedlings were grown individually and immature M3 seeds were dissected from young siliques. Because potted testa phenotype of ast is known to be dependent on its maternal genotype, immature seeds of M3 were screened with respect to anthocyanin pigmentation whether it could be different from that of ast.

Generally, immature seeds of wild-type Arabidopsis show pale-yellowish green phenotype (Fig. 1, left top). Although the seed coat at this stage accumulate a large amount of flavonoid compounds, they are colorless PA precursors. In contrast, immature seeds of ast show reddish phenotype, due to accumulation of anthocyanins instead of PA precursors (Fig. 1, left bottom). The reddish color gradually increases according to seed coat development (Fig. 1, right). This accumulation pattern of anthocyanins makes it possible to trace flavonoid accumulation levels during seed development by visual inspection (Fig. 1, right). Until now, approximately 5,000 M2 seedlings have been applied to screening for anthocyanin pigmentation mutants in immature seeds, and about 10 candidate M2 lines have been obtained. One of them was characterized and described below.

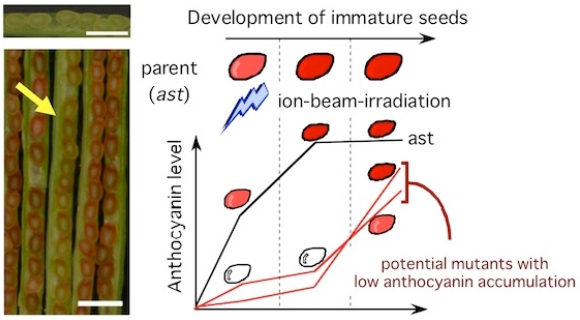

Fig. 1 Phenotypes of immature seeds of wild-type (left top) and *ast* (left bottom), and strategy for isolation of novel mutants using pigmentation in immature seeds of *ast* (right). Arrow in left panel indicates a anthocyanin-less phenotype. Bars in left panels indicate 1 mm.

The mutant (#62) shows a reduced level of anthocyanin pigmentation in immature seed coat at 6th day after flowering when it was compared to siblings showing ast phenotypes (Fig. 1, left bottom, arrow). Backcrossing of this mutant with ast plant showed the ast phenotype in all F1 plants, and ast and the mutant phenotypes were segregated at F2 with about 3:1 ratio, suggesting that mutation of #62 phenotype is single recessive. HPLC analysis suggested that the reduced level of #62 immature seeds was caused by less-accumulation of anthocyanin molecules. Map-based cloning of the responsible gene for the #62 phenotype indicated that the gene controlling the reduced level of anthocyanins in immature seed (#62 phenotype) was located on middle region of chromosome 4. Anthocyanin-less phenotype was limited in immature seed coats, and other tissues such as hypocotyl and cotyledon could accumulate anthocyanins. These results suggest that the gene responsible for #62 phenotype is involved in anthocyanin accumulation in tissue specific manner.

Reference

1) A. Tanaka et al., Genes Genet. Syst. 72 (1997) 141.

3 - 03 Target Irradiation of Individual Cells Using Focusing Heavy-ion Microbeam of JAEA-Takasaki (V): Irradiation of Individual Cells with Scanned Heavy-ion Microbeam

T. Funayama, Y. Yokota, M. Suzuki, T. Sakashita and Y. Kobayashi

Medical and Biotechnological Application Division, QuBS, JAEA

Heavy-ion irradiation has been employed in a wide range of biological applications, including heavy-ion radiotherapy and radiation breeding, because of its high and unique biological effectiveness. This property was considered to be caused by the non-uniform energy distribution along with heavy-ion tracks, and raised three major subjects to be studied in radiation biological field: bystander effect, single ion hit effect, and clustered DNA damage. To explore these three issues, a target irradiation of individual cells using heavy-ion microbeam is a useful means. Therefore, we have developed a collimating heavy-ion microbeam system under a vertical beam line of an AVF cyclotron of JAEA-Takasaki [1], and explored various effects of heavy-ion hit on biological materials [2]. However, there are limitations of the collimating system in the size of the microbeam spot and in the irradiation speed that cannot be overcome in principle. Thus, we started the development of a new focusing microbeam system for target-irradiating individual cells more precisely than the collimating system.

Using the system, we established a method to detect focusing beam spot under the microscopy, and carried out an irradiation of individual HeLa cells by moving cells to the position of focusing beam spot one by one [3]. However, according to the speed limitation of the mechanical stage, the throughput of the irradiation is still comparable with that of the collimating system. To improve the throughput, we next carried out a development of a method to irradiate cells with a scanned beam. We developed a method that can draw a cell distribution pattern, which was extracted from fluorescent microscopic image of cultured cells, on CR-39 film using scanned heavy-ion microbeam [4], and modified the irradiation-system control pathways to resolve the complicity of protocol for scanned beam irradiation [5]. By these developments, we concluded that the system now become able to irradiate individual cultured cells with scanned focusing microbeam, so that we start the establishment of the protocol for irradiating “actual” cell sample with scanned beam.

In the experiment, the HeLa cells stained with CellTracker Orange were used. The cells were inoculated on a CR-39 film, covered with a Kapton film, sealed with a petrolatum, then placed on the sample stage. The microscopic image of cells was analyzed, and the cells were irradiated with scanned neon microbeam of the 2 micron in diameter. After irradiation, the hit positions of the ion were visualized as the etched pit (Fig. 1a), and the cells were stained with the gamma-H2AX antibody (Fig. 1b). We found the correspondence of the distribution pattern of the etch pits, the cell positions and the gamma-H2AX foci. Thus we concluded that the developed method can irradiate cells rapidly and accurately with the focusing heavy-ion microbeam.

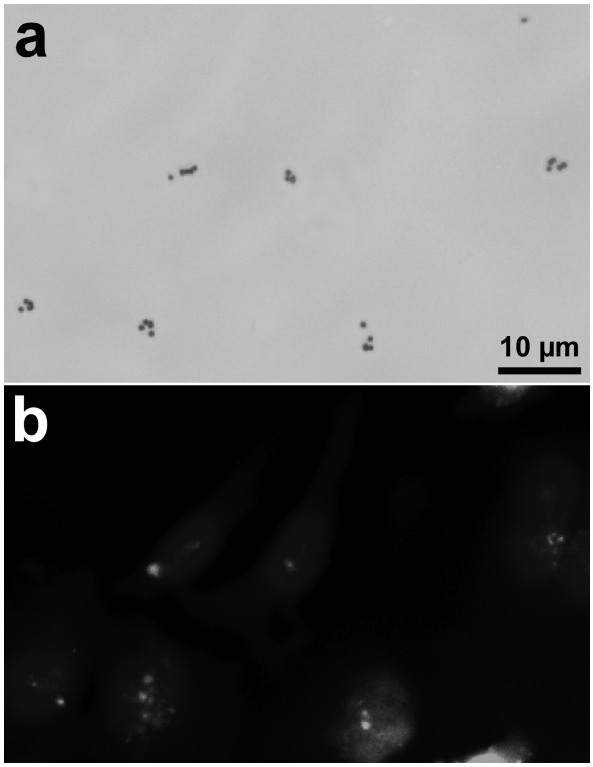

Fig. 1 Irradiation of individual cultured cells with scanned neon microbeam. (a) the distribution of etch pits on the CR-39 film, (b) the image of gamma-H2AX foci.

References

1) T. Funayama et al., J. Radiat. Res., 49 (2008) 71-82.
2) T. Funayama et al., IEEE Trans. Plasma. Sci. 36 (2008) 1432.
3) T. Funayama et al., JAEA Takasaki Annu. Rep. 2010 JAEA-Review 2011-043 (2012) 65.
4) T. Funayama et al., JAEA Takasaki Annu. Rep. 2011 JAEA-Review 2012-046 (2013) 63.
5) T. Funayama et al., JAEA Takasaki Annu. Rep. 2012 JAEA-Review 2013-059 (2014) 72.

3 - 04 Responses of the Salt Chemotaxis Learning in *C. elegans* Mutants to Microbeam Irradiation

T. Sakashita [a)], M. Suzuki [a)], Y. Hattori [a)], H. Ikeda [a)], Y. Mutou [a)], Y. Yokota [a)], T. Funayama [a)], N. Hamada [b)], K. Shirai [c)] and Y. Kobayashi [a)]

[a)] Medical and Biotechnological Application Division, QuBS, JAEA,
[b)] Radiation Safety Research Center, Central Research Institute of Electric Power Industry,
[c)] Faculty of Textile Science and Technology, Shinshu University

An increasing body of data indicates that ionizing radiation affects the nervous system and alters its function[1)]. Recently, we reported that chemotaxis of *C. elegans* during the salt chemotaxis learning (SCL), that is conditioned taste aversion to NaCl, was modulated by carbon ion irradiation, *i.e.* accelerated decrease in chemotaxis to NaCl during the SCL [2)]. However, we had no direct evidence for the interaction of ionizing radiation with the central neuronal tissue (nerve ring) in *C. elegans*. Microbeam irradiation is useful to analyze direct radiation effects at a cellular or tissue level. Thus, we applied the microbeam irradiation (^{12}C, 18.3 MeV/u, LET = 119 keV/μm) of the *C. elegans* nerve ring and examined the effect on the SCL. Our preliminary results obtained with wild-type animals showed the modulatory response of the SCL to targeted carbon-ion irradiation [3)]. Here, we present the effects of targeted carbon-ion irradiation on *gpc-1* [a heterotrimeric guanine nucleotide-binding protein gamma subunit, and this mutant defects in carbon ion induced modulatory responses during the SCL[2)]] and *daf-2* [a receptor tyrosine kinase that is the *C. elegans* insulin/insulin-like growth factor receptor ortholog and a well known mediator in response to oxidative stress[1)]] mutants of *C. elegans*.

Well-fed adults of *C. elegans* mutants grown at 20 °C on the plate spread with *E. coli* OP50 were used in all experiments. The areas of nerve ring (Head) and the counterpart (Tail) of mutants in a ditch filled with the S buffer including 100 mM NaCl of the micro device[4)] were irradiated with 12,000 carbon ions corresponding to 500 Gy at 20 μmφ micro-aperture area [3)]. On the other hand, whole-body carbon ion irradiation by the broad beam irradiation facility was carried out. Immediately after irradiation, chemotaxis to NaCl was measured. Using the assay plate with a gradient of NaCl concentration, we evaluated chemotaxis based on the chemotaxis index (CI; Fig. 1) [2)]. CI was expressed as mean ± 95% confidential interval, and a statistical test was carried out by the chi-square test with a Yates' correction. During the SCL, the CI is gradually decreased.

Figures 1a and 1b demonstrate the effects of target and broad beam irradiation on *gpc-1* and *daf-2* mutants. *gpc-1* mutants showed the significant accelerated decrease in CIs of head and tail targeted microbeam irradiations. On the other hand, microbeam irradiation did not significantly affect CIs of *daf-2* mutants, although broad beam irradiation significantly affected.

CI = {(number of animals at the high-concentration spot) – (number of animals at the control spot)} / (total number of animals in the assay plate)

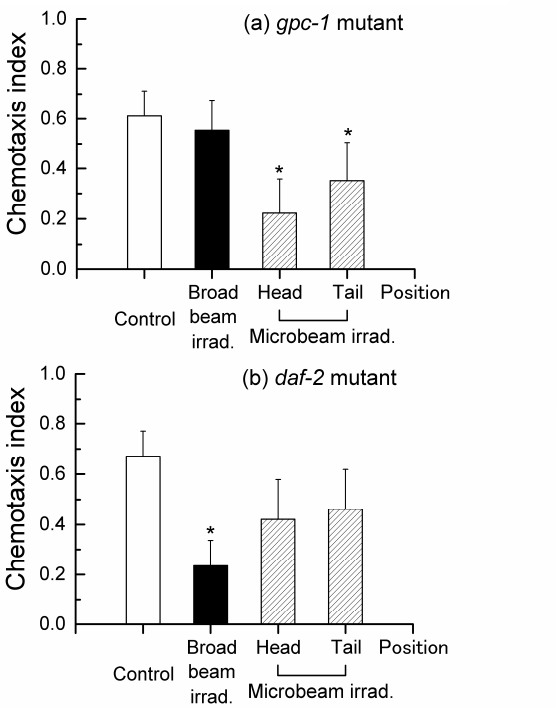

Fig. 1 Effects of carbon ion broad and microbeam irradiation on the salt chemotaxis of *gpc-1* (a) and *daf-2* (b) mutants. Error bars show the 95% confidence intervals, and asterisks indicate the significant differences (p <0.05) in CI.

Interestingly, the marked differences between *gpc-1* and *daf-2* mutants were demonstrated in broad beam and microbeam induced responses during the SCL. Although the detailed mechanism of the differences is unknown, it suggests that the signaling pathway in the chemotactic response of the SCL following ionizing irradiation related to the *gpc-1* gene differs from that of the *daf-2* gene in *C. elegans*.

References

1) T. Sakashita et al., J. Radiat. Res. 51 (2010) 107-21.
2) T. Sakashita et al., Biol. Sci. Space 26 (2012) 21-25.
3) T. Sakashita et al., JAEA Takasaki Annu. Rep. 2011 JAEA-Review 2012-046 (2013) 64.
4) S. R. Lockery et al., J. Neurophysiol. 99 (2008) 3136-43.

3 - 05 Bystander Effect Mediated by Nitric Oxide Depends on Irradiation Dose but not on Radiation Quality

Y. Yokota [a)], T. Funayama [a)], H. Ikeda [a,b)], T. Sakashita [a)], M. Suzuki [a)] and Y. Kobayashi [a)]

[a)] Medical and Biotechnological Application Division, QuBS, JAEA,
[b)] Gunma University Graduate School of Medicine

Radiation-induced bystander effect manifests cell killing and other effects in the non-irradiated cells that are close to irradiated cells[1]. It is necessary to elucidate the biological significance and molecular mechanism of bystander effect in order to estimate and to regulate the potential risks of low dose radiation accurately. The purpose of this study is to investigate the bystander cell-killing effect induced by varying doses of γ-rays or carbon ions and to analyze the role of nitric oxide (NO) in the effect. This study updates our reports[2] and sheds light on the molecular mechanism of bystander effect.

Normal human lung fibroblasts WI-38 cells were cultured in the minimum essential medium supplemented with fetal bovine serum and antibiotics. Cells inoculated in a porous membrane-based insert were irradiated with varying doses of ^{60}Co γ-rays (LET: 0.2 keV/μm) or carbon ions (108 keV/μm). Irradiated cells were then non-contact co-cultured with the non-irradiated cells that had been cultured in a companion plate. After co-culture of 24 h, the survival rates of non-irradiated bystander cells were measured with a conventional colony formation assay.

The survival rates of bystander cells co-cultured with the cells irradiated by γ-rays or carbon ions decreased with increasing dose and seemed to bottom out at 0.5 Gy or higher doses (Fig.1). This result indicates that the bystander cell-killing effect is dependent on irradiation dose in the lower dose range but is independent of radiation quality.

Next, to investigate the molecular mechanisms of the bystander cell killing, 20-μM of a specific NO scavenger 2-(4-Carboxyphenyl)-4,4,5,5-tetramethylimidazoline-1-oxyl -3-oxide (c-PTIO) was added to the culture medium of irradiated cells and non-irradiated cells during irradiation and co-culture. c-PTIO treatment prevented the reduction in survival rates of bystander cells co-cultured with the cells that had been irradiated with 0.5 Gy of γ-rays or carbon ions (Fig. 2). This clearly indicates that NO has an important role in the bystander cell-killing effect. Further analysis is now in progress to elucidate how NO kills the bystander cells.

References

1) W. F. Morgan et al., Radiat. Res. 159 (2003) 567-80.
2) Y. Yokota et al., JAEA Takasaki Annu. Rep. 2012 JAEA-Review 2013-059(2014) 74.

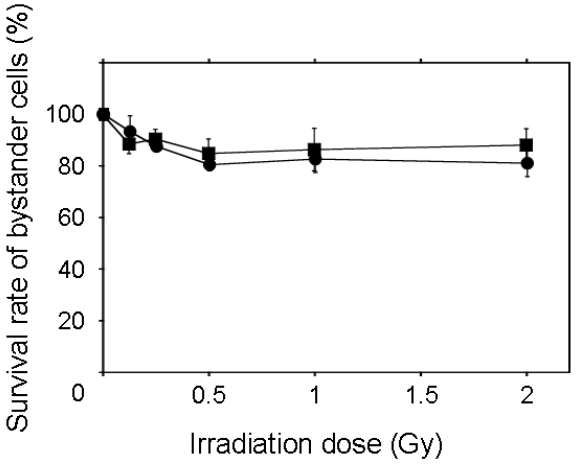

Fig. 1 Dose responses of the survival rates of non-irradiated bystander cells. Bystander cells were co-cultured with cells irradiated with graded doses of γ-rays (circle) or carbon ions (square). Survival data are presented as the mean ± standard error of the mean (SEM) of 3 or more independent beam times. Reductions in survival rates of bystander cells were dependent on irradiation dose in the lower dose range, but not on radiation quality.

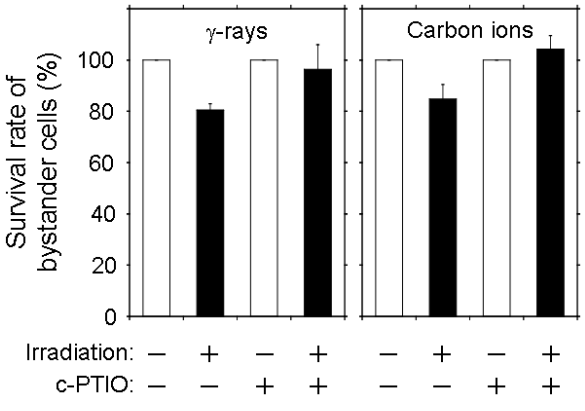

Fig. 2 Effects of the specific NO scavenger c-PTIO on the bystander cell-killing effect. Cells irradiated with 0.5 Gy of γ-rays or carbon ions were co-cultured with non-irradiated cells for 24 h. Irradiated cells and non-irradiated cells were treated with 20-μM c-PTIO or water during irradiation and co-culture. Survival data are presented as the mean ± SEM of 3 or more independent beam times. c-PTIO treatment prevented the reduction in survival rates of bystander cells.

3 - 06 Mechanisms for the Induction of Radioadaptive Response by Radiation-induced Bystander Response

H. Matsumoto [a)], M. Tomita [b)], K. Otsuka [b)], M. Hatashita [c)], M. Maeda [c)], T. Funayama [d)], Y. Yokota [d)], M. Suzuki [d)], T. Sakashita [d)], H. Ikeda [e)] and Y. Kobayashi [d)]

[a)] Biomedical Imaging Research Center, University of Fukui, [b)] Central Research Institute of Electric Power Industry, [c)] The Wakasa Wan Energy Research Center, [d)] Medical and Biotechnological Application Division, QuBS, JAEA, [e)] Gunma University Graduate School of Medicine

The objective of this project is to elucidate molecular mechanisms for the induction of radioadaptive response through radiation-induced bystander responses induced by irradiation with heavy ion microbeams in JAEA.

We found that the adaptive response was induced by Ar (520 MeV $^{40}Ar^{14+}$) microbeam-irradiation of a limited number of cells, followed by the broad beam-irradiation and that the adaptive response was almost completely suppressed by the addition of carboxy-PTIO, as a nitric oxide (NO) scavenger. In addition, we found several genes induced specifically and preferentially when radioadaptive response could be induced. We confirmed that *iNOS* expression was specifically induced only when radioadaptive response could be induced. Our findings strongly suggested that radioadaptive response can be induced by NO-mediated bystander responses evoked by irradiation with heavy ion microbeams.

低線量／低線量率放射線に対して生物が示す特異的な応答様式には、放射線適応応答、放射線誘発バイスタンダー応答、放射線超高感受性、遺伝的不安定性等がある[1)]。我々は、日本原子力研究開発機構において開発された細胞局部照射装置(HZ1)および深度制御種子照射装置(HY1)を用いて、放射線誘発バイスタンダー応答による放射線適応応答の誘導機構を明らかにすることを計画した。

1. 実験方法

(1) 細胞:*p53* 欠損ヒト非小細胞肺がん細胞(H1299 細胞)へ正常型 *p53* 遺伝子を導入した H1299/wt*p53* 細胞を用いた。

(2) 培養:35 mm ディッシュの内面中央に 2.0×10^6 cells/mL の細胞懸濁液 5 μL を 1 箇所スポットし(1.0×10^4 cells/colony)、15~20 時間培養したものを照射実験に供した。

(3) 照射:Funayama ら[2)]の方法に従って、中央にスポットしたコロニーの 1～50 個の細胞に 5 粒子の 520 MeV $^{40}Ar^{14+}$を HZ1 ポートにおいて照射した。一定時間(3～6 時間)培養後、520 MeV $^{40}Ar^{14+}$を HY1 ポートにおいて 1～5 Gy 照射した。実験群は下記の通りである。

(4) 細胞の生存率の測定:HY1 ポートでの照射から 6 時間後に、細胞を回収し、T25 フラスコへ 200～1,000 個の細胞を播種してコロニー形成させて生存率を求め、放射線適応応答の誘導を評価した。

(5) 全 RNA の抽出:各実験群において最終照射から 6 時間後に細胞を回収し、全 RNA をキット(RNeasy Plus Mini Kit、QIAGEN)を用いて抽出した。

(6) 各実験群の全 RNA を RT^2 First Strand Kit (QIAGEN)を用いて cDNA に変換し、RT^2 Profiler^{TM} PCR Array System の中の DNA Damage Signaling Pathway PCR Array および Nitric Oxide Signaling Pathway PCR Array を用いて、各実験群において特異的に発現誘導されている遺伝子を網羅的に解析した。

2. 結果および考察

(1) 中央にスポットしたコロニーの 1～50 個の細胞に 5 粒子の 520 MeV $^{40}Ar^{14+}$をマイクロビーム照射し、4～6 時間培養後に同 $^{40}Ar^{14+}$をブロードビーム照射(1～5 Gy)した場合、放射線適応応答が認められたのは、10 個以上の細胞に 5 粒子の同 $^{40}Ar^{14+}$を照射した時のみであり、この放射線適応応答の誘導は NO 特異的な捕捉剤である carboxy-PTIO(10 μM)の添加によりほぼ完全に抑制された。

(2) HZ1 照射のみの細胞では、*A*, *B* および *C* 遺伝子が特異的に発現誘導されていた。これらの遺伝子発現はバイスタンダー応答特異的であることが示唆される。これらの細胞では、*ATM*, *CHEK1/2*, *BRCA1* および *p53* 等の発現誘導も確認された。

(3) HZ1 照射→HY1 照射(適応応答誘導群)の細胞では、*D*, *E* および *F* 遺伝子が特異的に発現誘導されていた。これらの遺伝子発現は適応応答特異的であることが示唆される。これらの細胞では、*XRCC3*, *RAD1*, *iNOS* 等の発現誘導および *p53* の発現抑制も確認された[3)]。

※尚、見出された特異的発現誘導遺伝子の具体的な名称は現在精査中の為、伏せさせて戴く。

以上の結果より、放射線適応応答の誘導に必要と考えられる遺伝子が数種確認された。これらの遺伝子について、さらに精査することにより、放射線誘発バイスタンダー応答による放射線適応応答の誘導のメカニズム、特に NO を介したメカニズムの解明[4)]を目指す。

References

1) H. Matsumoto et al., J. Radiat. Res. 48 (2007) 97.
2) T. Funayama et al., J. Radiat. Res. 163 (2005) 241.
3) H. Matsumoto et al., Cancer Res. 67 (2007) 8574.
4) H. Matsumoto, Cell. Resp. Phys. Stress and Therap. Appl. Ed. T. Shimizu, T. Kondo (2013) 15.

3 - 07 Analysis of Bystander Response in 3D Cultured Tissue Induced by Heavy-ion Microbeam Irradiation

M. Tomita [a)], H. Matsumoto [b)], K. Otsuka [a)], T. Funayama [c)], Y. Yokota [c)], M. Suzuki [c)], T. Sakashita [c)] and Y. Kobayashi [c)]

[a)] Central Research Institute of Electric Power Industry, [b)] University of Fukui, [c)] Medical and Biotechnological Application Division, QuBS, JAEA

Radiation-induced bystander responses are defined as responses in cells that have not been directly targeted by radiation but are in the neighborhood of cells that have been directly exposed. In this study, we aim to clarify a role of bystander response to sustain the homeostasis of damaged tissue using heavy-ion microbeams. We established the heavy-ion microbeam irradiation method to a 3D cultured human epidermis. Using this method, a viable cell rate of the 3D cultured human epidermis irradiated with 260 MeV ^{20}Ne-ion microbeams or broadbeams was analyzed by the MTT method.

低粒子数の重イオン線による生物影響を解明する上で、DNA 初期損傷量に依存しない「非標的効果」が注目されている。特に、放射線に直接曝露された細胞の近傍に存在する全く放射線に曝露されていない細胞において観察される「放射線誘発バイスタンダー応答」は、最も特徴的な非標的効果である[1)]。その解明は放射線生物学のみならず、粒子線がん治療、宇宙放射線の生体影響評価においても重要である。我々は、ヒト正常線維芽細胞への重イオンマイクロビーム照射による研究から、高 LET 重イオン線によるバイスタンダー応答は、照射細胞から放出された一酸化窒素（NO）により、バイスタンダー細胞において転写因子である NF-κB、生存シグナル伝達に関与する Akt が活性化され、炎症反応に関与する COX-2 を誘導することによって生じることを明らかにした。一方、さまざまな細胞が密に積み重なった実際の生体組織内において、特に発がんの標的と考えられている組織幹細胞と分化細胞の間で、バイスタンダー応答のシグナル伝達機構が果たす役割には不明な点が多い。本研究は、これまでの 2 次元での培養細胞を用いた研究から、組織レベルでの生体応答研究への展開を図るため、分化誘導させたヒト3次元培養皮膚モデルを用い、原子力機構の細胞局部照射装置を利用し、放射線誘発バイスタンダー応答によって生じるシグナル伝達経路の変化を明らかにすることを目的とする。

試料には、3 次元培養したヒト表皮モデル（ラボサイト エピ・モデル 24、ジャパン・ティッシュ・エンジニアリング）を用いた。照射は、基底層側から角質層側にビームが抜ける方向に試料を配置して行った（Fig. 1）。マイクロビームの照射は、HZ1 ポートにおいて行い[2)]、15 粒子の 260 MeV $^{20}Ne^{7+}$ を直線状に 100 μm 間隔で 61 点照射し、影響を解析する方法を確立した。対照実験として、HY1 ポートにおいてブロードビーム 5 Gy を全体に照射した。照射 42 時間後の試料を用い、MTT 反応により生細胞率の測定を行うとともに、固定した試料のパラフィン切片を作成し、DNA 損傷の生成

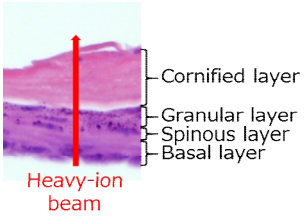

Fig. 1 Hematoxylin and eosin (HE) stained human epidermis model.

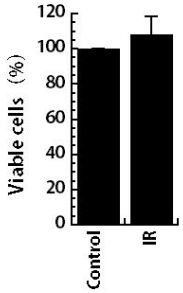

Fig. 2 Ratio of viable cells after Ne-ion microbeam irradiation. IR: Ne-ion microbeam irradiation.

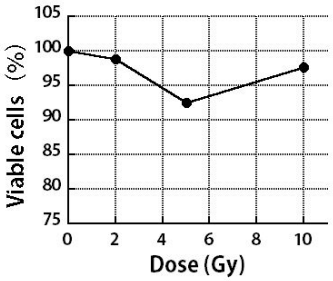

Fig. 3 Dose response of cell viability after Ne-ion broadbeam irradiation.

を観察した。

Ne イオンマイクロビーム照射 42 時間後の試料を用い、MTT 法により生細胞率を測定した（Fig. 2）。2 回の実験の結果、生細胞率の低下は認められなかった。また、Ne イオンブロードビーム照射後の生細胞率の変化を Fig. 3 に示した。5 Gy で生細胞率は低下するが、10 Gy では回復する傾向が見られた。高 LET 重イオン線を照射した場合、DNA 損傷が重篤なため、細胞死の誘導が遅延する可能性が考えられる。次年度は、再現性を確認するとともに、照射後の経過時間による変化についても解析する。また、Ne イオン照射後に生じた DNA2 重鎖切断を、γ-H2AX をマーカーとして蛍光観察することにも成功したが、現在条件の最適化を進めている。

References

1) H. Matsumoto et al., Curr. Mol. Pharmacol. 4 (2011) 126.
2) T. Funayama et al., Radiat. Res. 163 (2005) 241.

3 - 08 Ion-species Dependent Bystander Mutagenic Effect on *HPRT* Locus in Normal Human Fibroblasts Induced by C-, Ne- and Ar-ion Microbeams

M. Suzuki [a)], T. Funayama [b)], Y. Yokota [b)], Y. Mutou [b)], M. Suzuki [b)], H. Ikeda [b)], Y. Hattori [b)] and Y. Kobayashi [b)]

[a)] Research Center for Charged Particle Therapy, National Institute of Radiological Sciences,
[b)] Medical and Biotechnological Application Division, QuBS, JAEA

We have been studying the radiation-quality dependent bystander cellular effects, such as cell killing, mutation induction and chromosomal damage, using heavy-ion microbeams with different ion species. The bystander effects in cell killing was induced by C ions, but not Ne or Ar ions, via gap-junction mediated cell-cell communication [1]. On the other hand, the bystander effect in chromosomal damage was induced by C, Ne, and Ar ions and promoted by the two different mechanisms such as gap-junction mediated cell-cell communication and secreted factor(s) to culture medium from the irradiated cells [2]. Our results summarized that that bystander cellular effects depended on both biological endpoints and ion species. This year we focused on the ion-species dependent bystander mutagenic effect on *HPRT* locus in normal human fibroblasts induced by C-, Ne,- and Ar-ion microbeams.

Approximately 6×10^5 exponentially growing cells were inoculated into each of microbeam dish, which was made of acrylic resin ring with 36 mm diameter and attached 7.5 μm-thick polyimide film on the bottom of the ring, 2 days before microbeam irradiation. One day before irradiation, half of the sample dishes were treated with a specific inhibitor of gap-junction mediated cell-cell communication (40 μM of γ-isomer of hexachloro-cyclohexane). At the irradiation period, cultures were confluent. Gene mutation on *HPRT* locus mapped on the X chromosome was detected with 6-thioguanine resistant clones. Microbeam irradiations were carried out using a 256 (16 × 16)-cross-stripe method described previous report [3] using C ions ($^{12}C^{5+}$, 220 MeV), Ne ions ($^{20}Ne^{7+}$, 260 MeV), and Ar ions ($^{40}Ar^{13+}$, 460 MeV) at the HZ1 port. The values of linear energy transfer (LET) at the sample position were estimated to be 103 keV/μm for C ions, 380 keV/μm for Ne ions, and 1,260 keV/μm for Ar ions. The beam size of each ion microbeam was 20 μm in diameter and the irradiations in each point were carried out to deliver 8 ions for carbon, 2 ions for neon, and single ion for argon, respectively.

Figure 1 showed the results of mutation induction at *HPRT* locus in microbeam-irradiated cells (IR) and microbeam-irradiated cells with the specific inhibitor of gap-junction mediated cell-cell communication (L+IR). The mutation frequency in cells irradiated with C-ion microbeams was 6 times higher than that of non-irradiated control cells (Control). In our 256-cross-stripe irradiation method, only 0.04% of all cells on the dish was irradiated directly with the carbon ions and we could evaluate that the mutation frequency in the 0.04% microbeam-irradiated cells was the same level with non-irradiated control cells, based on the data using the 80 keV/μm-carbon-ion broadbeams at 0.4 Gy (data not shown). The result showed a higher mutation induction in the microbeam-irradiated cells than that of the expected frequency. Furthermore, the induced mutation returned to the control level, when using the gap-junction inhibitor. On the other hand, no enhanced mutation frequencies were observed in cells irradiated with either Ne- or Ar-ion microbeams. There is clear evidence that the bystander mutagenic effect via gap-junction mediated cell-cell communication depends on radiation quality.

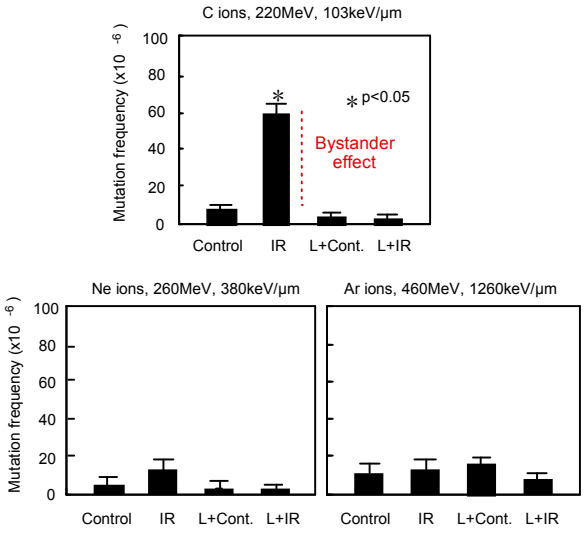

Fig. 1 Mutation induction in normal human fibroblasts irradiated with C-, Ne,- and Ar-ion microbeams (IR). Cells were treated with (L+IR) / without (IR) a specific inhibitor of gap-junction mediated cell-cell communication. The results were the means and standard errors from at least 4 independent beam times.

References

1) M. Suzuki et al., JAEA Talasaki Ann. Rep. 2010 JAEA-Review 2011-043 (2012) 72.
2) M. Suzuki et al., JAEA Talasaki Ann. Rep. 2012 JAEA-Review 2013-059 (2014) 77.
3) M. Suzuki et al., JAEA Talasaki Ann. Rep. 2006 JAEA-Review 2007-060 (2008) 107.

3 - 09 Analysis of Bystander Effect Induced by Cell Membrane Response in Glioma Cells

S. Wada [a)], T. Ando [a)], A. Wananabe [a)], T. Kakizaki [a)], M. Natsuhori [a)], T. Funayama [b)], T. Sakashita [b)], Y. Yokota [b)] and Y. Kobayashi [b)]

[a)] Department of Veterinary Medicine, Kitasato University,
[b)] Medical and Biotechnological Application Division, QuBS, JAEA

So far, we clarified that X-ray irradiation induced cell killing by bystander effect mediated-secreted factor. This phenomenon was related with sphingomyelinase (SMase). In this study we analyzed mechanism of secreted SMase from irradiated cells after irradiation. SMase was detected in the culture medium after irradiation by SDS-PAGE. Then, SMase was detected in the exosome of culture medium, but not out of exosome after irradiation. This result indicates that SMase was secreted as exosome from the irradiated cells.

1. はじめに

バイスタンダー効果とは、照射された細胞から何らかの液性因子が分泌され、非照射細胞はこの液性因子の作用によって細胞死が誘導される現象である。また、マイクロビームによる細胞の部分的な照射実験によりバイスタンダー効果の誘導には細胞核の損傷応答だけでなく細胞膜応答も重要であると考えられている。そこで、細胞膜応答分子であるスフィンゴミエリナーゼに着目し、スフィンゴミエリナーゼのバイスタンダー効果への関与を検証したところ、スフィンゴミエリナーゼノックダウン細胞を用いた培地交換実験では、バイスタンダー効果による細胞致死効果が誘導されなかった。このため、バイスタンダー効果の誘導にはスフィンゴミエリナーゼが関与すると考えられた。

しかしながら、この細胞膜応答分子であるスフィンゴミエリナーゼがどのようにバイスタンダー細胞にシグナル伝達をするかは詳細には明らかにされていない。一方、細胞間のシグナル伝達において、エクソソームによる伝達機構が重要と考えられている。このエクソソームは細胞から放出される膜小胞であり、このエクソソームは microRNA やタンパク質などシグナル伝達に重要な分子を含有しており、スフィンゴミエリナーゼもエクソソームの分泌やシグナル伝達に関与することが示唆されている。そこで本研究では、放射線照射により細胞外に分泌されるスフィンゴミエリナーゼを観察し、さらにこのスフィンゴミエリナーゼがエクソソーム内に含有されているかを解析した。

2. 実験方法

グリオーマ細胞（A172 細胞）を用い、X 線 6 Gy を照射し、細胞外に分泌されるスフィンゴミエリナーゼを解析するため、照射 5 分、30 分後に照射細胞の培養上清のみを回収し、抗スフィンゴミエリナーゼ抗体を用いて免疫沈降による濃縮を行い、SDS-PAGE によってスフィンゴミエリナーゼを検出した。さらに、エクソソーム中のスフィンゴミエリナーゼを解析するため、X 線 6 Gy 照射後経時的に培養上清を回収し、Exo Quick によるエクソソームの精製を行い、精製溶液を抗スフィンゴミエリナーゼ抗体による免疫沈降によって濃縮を行い、抗スフィンゴミエリナーゼ抗体を用いてウエスタンブロットを行った。

3. 結果および考察

Figure 1 は X 線 6 Gy 照射後の培養上清を抗スフィンゴミエリナーゼ抗体による濃縮後の SDS-PAGE の結果である。57 kDa のところにバンドが観察され、照射 5 分後に増加することが観察された。この結果は X 線照射によって細胞外にスフィンゴミエリナーゼが分泌されることを示唆している。Figure 2a は X 線照射後に培養上清を回収し、さらにエクソソーム成分を精製し、エクソソーム分画に対する抗スフィンゴミエリナーゼ抗体によるウエスタンブロットの結果である。スフィンゴミエリナーゼのバンドが観察され、X 線照射後 5 分には有意な増加が観察された。一方、Fig. 2b はエクソソーム外の分画に対する抗スフィンゴミエリナーゼ抗体によるウエスタンブロットの結果である。非照射および照射後においてもスフィンゴミエリナーゼのバンドは観察されなかった。この結果はスフィンゴミエリナーゼが X 線照射によって細胞外に分泌されるが、スフィンゴミエリナーゼは主にエクソソームの形態で細胞外に分泌されると考えられた。これらのことからバイスタンダー効果においてスフィンゴミエリナーゼ自身がバイスタンダー因子としてシグナル伝達に関与することが示唆された。

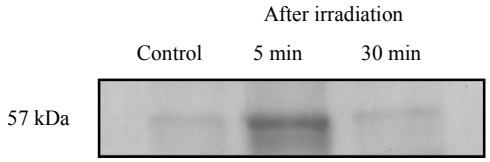

Fig. 1 Detection of 57 kDa protein from culture medium after irradiation by SDS-PAGE.

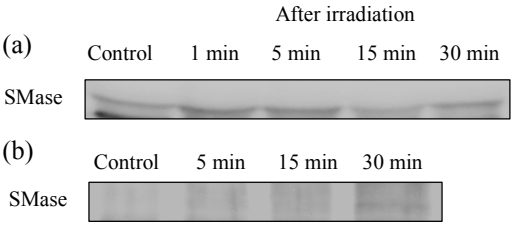

Fig. 2 Detection of SMase in the exosome (a) and out of exosome (b) by western blot.

3 - 10 Ion Beam Irradiation Has Different Influences on Superoxide Dismutase Activity in Cultured Human Retinal Vascular Endothelial Cells between ^{12}C and ^{4}He

K. Akeo [a,b], T. Funayama [c], Y. Kobayashi [c,d] and Y. Akeo [a]

[a] Akeo Eye Clinic, [b] Keio University School of Medicine, [c] Medical and Biotechnological Application Division, QuBS, JAEA, [d] Gunma University Graduate School of Medicine

It is known that superoxide dismutases (SOD) are a class of enzymes that catalyze the dismutation of superoxide into oxygen and hydrogen peroxide. Because superoxide is not very reactive biochemically or chemically, it has been suggested that the deleterious effects of superoxide are actually mediated by a cascade of oxidative events [1, 2]. Fridovich[2] describe that SOD does protect cells and damage to cells could be prevented by SOD but not by catalase. Cultivation of microvascular endothelial cells in 40% oxygen for week resulted in an inhibition of proliferation as compared to cells in 20% oxygen [3]. Freeman et al [4] showed that an oxygen-dependent injury to endothelial cells could be prevented with liposomal SOD. We reported that SOD activity of retinal pigment epithelial (RPE) cells was significantly related to ambient oxygen, and transfer of RPE cells growing 20% oxygen to 5% oxygen arrested the decrease in SOD and resulted in significantly higher SOD levels [5].

We reported that L-dopa acts in the same manner as free radicals under high oxidative stress conditions such as hyperoxia [6] or that induced by visible light [7]. Cultured bovine aortic vascular endothelial cells are more sensitive to oxidative damage by L-dopa, and/or light, than cultured porcine RPE cells. Damage to human retinal vascular endothelial (RE) cells is a characteristic feature of senile macular degeneration and diabetic retinopathy. In these studies, we used human RE cells, from retinal capillaries, a more suitable model than bovine aortic vascular endothelial cells, so that the results can be correlated to humans.

Ionizing radiation is known to induce oxidative stress through generation of reactive oxygen species (ROS) resulting in imbalance of the pro-oxidant and antioxidant in the cells, which is suggested to culminate in cell death. Srinivasan et al reported the evaluation of the radio-protective effect of curcumin, a yellow pigment of turmeric on γ-radiation-induced toxicity in primary cultures of isolated rat hepatocytes [8]. The increase in the severity of DNA damage was observed with the increase dose (1, 2 and 4 Gy) of γ-radiation in cultured hepatocytes. Thiobarbituric acid reactive substances were increased significantly, whereas the levels of antioxidant enzymes (SOD, catalase, glutathione peroxidase) were significantly decreased in γ-irradiated hepatocytes. Gamma-radiation is known to cause uniform ionization throughout an irradiated tissue. The use of ion beams might have the roles in oxidative stress production so as to have different irradiation energy, projectile range, and spot size of irradiation that influences the cytoplasm, membranes, and organelles (mitochondria and rough endoplasmic reticulum)[9].

It is possible that ion beam irradiation caused the induction of the oxidative stress by ROS, especially superoxide. We assayed SOD activity in order to investigate how ion beam irradiation influenced SOD in RE cells.

Human RE cells incubated were exposed to an ionization radiation (220 MeV C and 50 MeV He). We obtained the cells at 0, 4, 8, and 24 h after the irradiation and extracted. The SOD assay buffer (Tris-HCl buffer with diethylene-triaminepentaacetic acid) was added to the pellets, and the cells were lysed by several cycles of freezing and thawing. SOD was measured using a modification of the luminol assay described Bensinger et al [10]. This highly specific assay is based on the emission of a photon of light from luminol following interaction with the superoxide anion. A reaction mixture was prepared containing bovine serum albumin, hypoxanthine and luminol in the assay buffer. SOD standard solution and cell lysate were added to mini-scintillation vials containing reaction mixture. To start the assay, xanthine oxidase was added, rapidly mixed, and placed in the sample chamber of a luminometer. Photon emission was measured to determine the maximum emission rate, which was expressed as a percentage of the unsuppressed control. The nanogram equivalents of SOD were determined from a standard curve relating percent suppression of photon emission to the nanograms of bovine erythrocyte SOD added. Aliquots of each sample were assayed for protein measuring the absorbance spectrum by 260 nm wavelength of the spectrophotometry. Specific activity of SOD was expressed as nanogram equivalents of SOD/mg protein.

SOD activity in human RE cells in vitro decreased according to duration time after irradiation of 50 MeV He, and in case of 220 MeV C, SOD activity increased at 24 h after irradiation. It was possible that there were the differences of the effects by irradiation on SOD activity between 50 MeV He and 220 MeV C.

References

1) G. Czapski et al., In "Oxygen Radicals in Chemistry and Biology" (Eds. W., Bors et al.) Walter de Gruyter and Co., Berlin (1984) p. 225.
2) I. Fridovich, Arch. Biochem. Biophys. 247 (1986) 1.
3) P. A. D'more et al., In Vitro Cell Dev. Biol. 23 (1987) 123.
4) B. A. Freeman et al., J. Biol. Chem. 258 (1983) 12534.
5) K. Akeo et al., Curr. Eye Res. 7 (1988) 961.
6) K. Akeo et al., Exp. Eye Res. 49, (1989) 335.
7) C. K. Dorey et al., Curr. Eye Res. 9 (1990) 549.
8) M. Srinivasan et al., Environ. Toxicol. Pharmacol. 24 (2007) 98.
9) K. Akeo et al., Tiss. Cult. Res. Commun. 32 (2013) 195.
10) R. E. Bensinger et al., Anal. Biochem. 116 (1981) 142.

3 - 11 LET Dependency of Human Normal Dermal Cells Survival in Carbon Ion Irradiation

Y. Yoshida [a)], K. Mizohata [a)], A. Matsumura [a)], M. Isono [a)], T. Yakoh [a)], T. Nakano [a)], T. Funayama [b)], Y. Kobayashi [b)] and T. Kanai [a)]

[a)] Gunma University Heavy Ion Medical Center,
[b)] Medical and Biotechnological Application Division, QuBS, JAEA

In the clinical application of carbon-ion (C-ion) radiation therapy in Japan, different RBE values of carbons have been used for clinical and biological endpoints. The biological RBE (bRBE) was estimated by a method that is based on the linear-quadratic (LQ) model, and was defined *in vitro* at the 10% surviving fraction of human salivary gland (HSG) tumor cells. The clinical RBE (cRBE) was assumed to be 1.45 times of the bRBE, and it was determined to be 3.0 at the neutron-equivalent position of the carbon spread-out Bragg peak (SOBP)[1)]. Thus, the treatment planning for all of the tissues in patient is performed based on experimental data with radiosensitivity of human salivary gland (HSG) cells. However, many of biological parameters, that is, type of tissues, different sort of cells, oxygenation levels, and all, could affect radiosensitivity. It is therefore recommended that fundamental data other than HSG model be obtained for more effective radiotherapy.

One of the cell line models to be experimented is a normal tissue model with, generally speaking, radiation resistant characteristics compared to tumor tissues. First of all, we evaluated the linear energy transfer (LET) dependence of the radiosensitivity in normal skin cells using the normal human dermal fibroblast (NHDF). The skin is one of critical organs for C-ion radiation therapy.

The facility of Gunma University and TIARA was used for irradiation with C-ion beams of various LETs ranging from 10 to 200 keV/micrometer. At first, we performed dosimetry to evaluate difference of the dose and LET distribution of C-ion beam between the facility of Gunma University and TIARA. The difference of dose between the facility of Gunma University and TIARA was 1.0231% on average from the two sets of measurements (Table 1). The difference of LET distribution was not detected in both facilities when the doses measured in TIARA (measured dose) were compared with the dose in Gunma University, namely, calculated dose (Fig. 1). These results suggest that the biological data obtained from both facilities may treat equally.

NHDF cells were exposed to C-ion beams at Gunma University (10-80 keV/micrometer) and TIARA (108 and 158 keV/micrometer). The surviving fractions were analyzed with colony formation assays. The experimental RBE (eRBE) values were estimated from the radiation dose survival curve fitted by LQ model, and defined *in vitro* as follows.

$$eRBE = \frac{X\ ray\ dose\ (Gy)\ as\ reference\ giving\ 90\ \%\ cell\ killing}{Radiation\ dose\ (Gy)\ of\ interest\ giving\ 90\ \%\ cell\ killing}$$

The results of the biological experiment at TIARA have not been yet obtained, because we performed the dosimetry in this year.

Reference

1) T. Kanai et al., IJROBP. 44 (1999) 201-10.

Table 1 The comparison of dosimetry at two facilities.

Gunma University	TIARA	Ratio (Gunma Univ./TIARA)
1.0123±0.0144	1.0180±0.0150	0.9944±0.0025
1.0774±0.0133	1.0244±0.0107	1.0518±0.0175

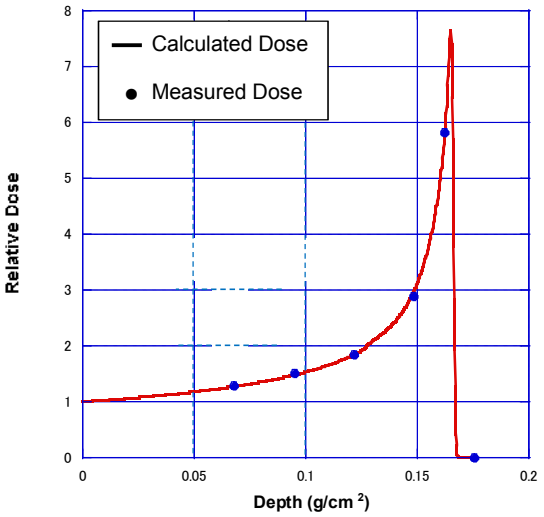

Fig. 1 LET and depth-dose-distribution at TIARA (18.33 MeV/u carbon) in Alminum.

3 - 12 NHEJ Repair Rather Than HR Repair is the Primary Function to Target to Enhance Radiosensitization at High LET Values

A. Takahashi [a,b], M. Kubo [b], C. Igarashi [a], Y. Yoshida [c], T. Funayama [d], Y. Kobayashi [d] and T. Nakano [b,c]

[a] Advanced Scientific Research Leaders Development Unit, Gunma University, [b] Department of Radiation Oncology, Gunma University, [c] Gunma University Heavy Ion Medical Center, [d] Medical and Biotechnological Application Division, QuBS, JAEA

DNA double-strand breaks (DSBs) induced by ionizing radiation pose a major threat to cell survival. The cell can respond to the presence of DSBs, through two major repair pathways: Homologous recombination (HR) and non-homologous end-joining (NHEJ). Higher levels of cell death are induced by high linear energy transfer (LET) radiation when compared to low LET radiation, even at the same doses because of less effective or more inefficient DNA repair. To clarify the question of whether high LET radiation inhibits all repair, or specifically one repair pathway, studies were designed to examine the effects of radiation with different LET values on DNA DSB repair and radiosensitivity.

The cell lines used in these studies were *p53*$^{-}$/$_{-}$ MEF *Lig4*$^{+}$/$_{+}$*Rad54*$^{-}$/$_{-}$ (*Rad54*-KO); *Lig4*$^{-}$/$_{-}$*Rad54*$^{+}$/$_{+}$ (*Lig4*-KO); *Lig4*$^{-}$/$_{-}$*Rad54*$^{-}$/$_{-}$ (double-KO); and *Lig4*$^{+}$/$^{+}$*Rad54*$^{+}$/$_{+}$ (wild type). These cell lines were kindly provided by Dr. Frederick W. Alt (Harvard Medical School, Boston, MA)[1]. Exponentially growing cells were irradiated at room temperature with X-rays, carbon ion beams (C-beams), neon ion beams (Ne-beams), and argon ion beams (Ar-beams). X-irradiation was performed through a 3.5 mm layer of culture medium and a 1 mm layer in a NuncTM flask (Thermo Fisher Scientific, Yokohama, Japan) using a 200-kVp X-ray generator (TITAN-225S, Shimadzu, Kyoto, Japan) with a total filtration of 0.5 mm aluminum plus 0.5-mm copper. The X-ray dose rate was about 1.3 Gy/min which was measured using a thimble ionization chamber (PTW FREIBURG, Freiburg, Germany) at the sample position. C-beam irradiation (18.3 MeV/nucleon, mono-beams: 108 keV/μm), Ne-beam irradiation (13 MeV/nucleon, mono-beams: 437 keV/μm), and Ar-beam irradiation (13 MeV/nucleon, mono-beams: 1,370 keV/μm) were performed through an 8 μm layer of Kapton® polyimide film (du Pont-Toray Co., Ltd., Tokyo, Japan) using the AVF cyclotron of the Takasaki Ion Accelerator for Advanced Radiation Application (TIARA) facilities in the Japan Atomic Energy Agency (JAEA, Gunma, Japan)[2]. Cell survival was measured with colony forming assays. The sensitization enhancement ratio (SER) values were calculated using the 10% survival dose (D10) of wild-type cells and repair-deficient cells.

Cellular radiosensitivity was listed in descending order: Double-KO cells > *Lig4*-KO cells > *Rad54*-KO cells > wild-type cells (Fig. 1). Wild-type cells and *Rad54*-KO cells, i.e. NHEJ proficient cells, exhibited the high RBE values at LET values of 108 keV/μm. The RBE value for each cell type decreased with increasing LET values over 200 keV/μm (Table 1). Although *Rad54*-KO cells had an almost constant SER value, *Lig4*-KO cells showed a high SER value when compared to *Rad54*-KO cells, even with increasing LET values (Table 1).

These results suggest that with carbon-ion therapy, targeting NHEJ repair yields higher radiosensitivity than targeting HR repair.

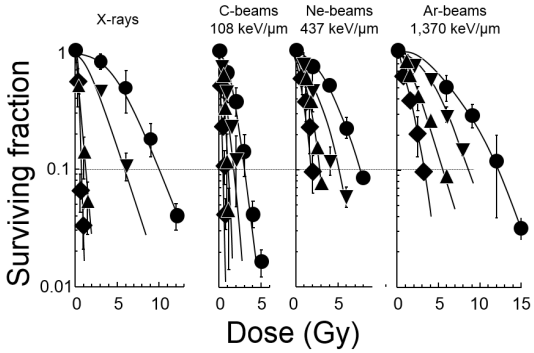

Fig. 1 Cell survival curves after exposure to radiation with different LET values in NHEJ and/or HR KO cells. ●, wild-type cells; ▲, *LIG4*-KO cells; ▼, *Rad54*-KO cells; ♦, double-KO cells.

Table 1 D10, RBE and SER values for different radiation types in NHEJ and/or HR KO cells.

	wild-type cells	*LIG4*-KO cells	*Rad54*-KO cells	double-KO cells
		D10 value		
X-rays	10.4 ± 1.2	1.1 ± 0.2	6.2 ± 0.3	0.6 ± 0.1
C-beams	3.4 ± 0.3	1.0 ± 0.1	2.0 ± 0.2	0.6 ± 0.1
Ne-beams	8.0 ± 0.6	2.8 ± 0.0	4.1 ± 0.2	2.0 ± 0.3
Ar-beams	13.2 ± 2.4	4.9 ± 0.7	9.1 ± 0.7	3.2 ± 0.4
		RBE		
X-rays	1.0 ± 0.1	1.0 ± 0.1	1.0 ± 0.1	1.0 ± 0.1
C-beams	3.1 ± 0.3	1.2 ± 0.2	3.1 ± 0.3	0.9 ± 0.1
Ne-beams	1.3 ± 0.1	0.4 ± 0.0	1.5 ± 0.1	0.3 ± 0.0
Ar-beams	0.8 ± 0.1	0.2 ± 0.0	0.7 ± 0.1	0.2 ± 0.0
		SER		
X-rays	-	9.3 ± 1.3	1.7 ± 0.1	18.8 ± 1.8
C-beams	-	3.5 ± 0.5	1.7 ± 0.2	5.7 ± 0.5
Ne-beams	-	2.9 ± 0.0	1.9 ± 0.1	4.1 ± 0.6
Ar-beams	-	2.7 ± 0.4	1.5 ± 0.1	4.2 ± 0.5

References

1) K. D. Mills *et al*., Genes Dev. 18 (2004) 1283-92.
2) T. Funayama *et al*., J. Radiat. Res. 49 (2008) 71-82.

3 - 13 Epigenetic Modifier as a Potential Radiosensitizer for Heavy-ion Therapy on Malignancy (II)

K. Saito [a,b,c], T. Funayama [b,c], Y. Kobayashi [b,c] and T. Murakami [a]

[a] Faculty of Pharmacy, Takasaki University of Health and Welfare, [b] Medical and Biotechnological Application Division, QuBS, JAEA, [c] Graduate School of Medicine, Gunma University

Introduction

Malignant melanoma is one of the most common cutaneous malignancies. Unfortunately, it resists often various authentic therapies including chemotherapy and radiation therapy, and it is well characterized by very low objective clinical responses, representing lethal disease.

Epigenetic modifiers, such as histone deacetylase inhibitors (HDACi) and DNA methyltransferase inhibitors, have emerged recently as promising anticancer agents and it has been expected that epigenetic modifiers may enhance the effect of other cancer therapeutics including radiotherapy [1]. In addition, the biological effects of the high linear energy transfer (LET) heavy-ion radiation are more pronounced than the low-LET radiation (e.g., γ-ray or X-ray). These accumulating evidences allowed us to investigate whether the use of epigenetic modifiers could sensitize melanoma cells for the heavy-ion therapy.

Materials and methods

Cells and cell culture

Murine B16F10 melanoma cells were purchased form the American Type Culture Collection (Manassas, VA, USA). Cells were cultured in Dulbecco's Modified Eagle Medium (Invitrogen, Carlsbad, CA, USA) supplemented with 10% fetal bovine serum (MP Biomedicals, Santa Ana, CA, USA) and 1% antibiotic-antimycotic (GIBCO, Carlsbad, CA, USA) at 37 °C in a humidified atmosphere with 5% CO_2.

Radiation exposure

The ^{60}Co γ-ray irradiation was performed in Room No.1 of the food irradiation facility at Takasaki Advanced Radiation Research Institute (TARRI), JAEA. The heavy-ion irradiation groups were exposed to carbon ions accelerated by the AVF cyclotron and generated with the HY1 port of TIARA at TARRI, JAEA. Control groups were sham-irradiated and handled in parallel with the test groups.

Clonogenic survival assay

Cells in exponential growth were seeded at a density 1×10^6 cells per 35 mm culture dish 20-24 h before irradiation. Cells were treated with investigational or comparator epigenetic modifier for 16.5 h and then irradiated. The concentration of modifier was selected that required to reduce colony formation by 10% or 20% alone. After irradiation, cells were trypsinized and plated after appropriate dilution onto 100 mm culture dishes. Cells (between 100 and 10,000) were seeded per dish in order to obtain between 30 and 100 single well-separated colonies per dish. After 9 (±1) days, colonies were fixed and stained. Colonies counting, data normalization and statistical evaluation were performed as described previously [2].

Results and discussion

In this study, we investigated several potential epigenetic modifiers before. Herein, this annual report will highlight the results of a HDACi trichostatin A (TSA). Treatment of B16F10 melanoma cells with TSA in combination with heavy-ion radiation provided enhanced inhibition of colony formation (Fig. 1). These data suggest that combination of an epigenetic modifier TSA together with heavy-ion therapy may provide improved therapeutic responses in melanoma patients.

References

1) L. S. Kristensen et al., Eur. J. Pharmacol. 625 (2009) 131-42.

2) K. Saito et al., JAEA Takasaki Annu. Rep. 2012 JAEA-Review 2013-059 (2014) 80.

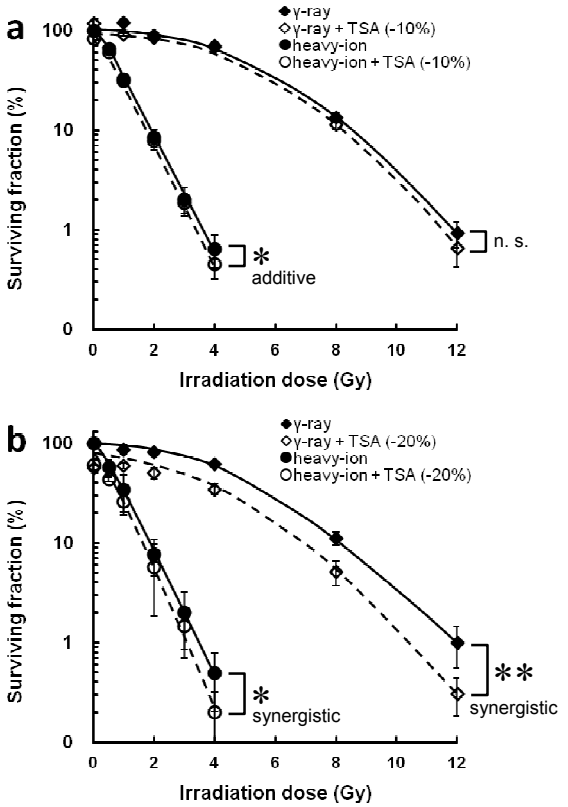

Fig. 1 The effect of TSA on radiosensitivity for B16F10 cells in the concentration that reduced colony formation by 10% alone (a) and by 20% alone (b). $*P < 0.05$; $**P < 0.01$; n.s., not significant.

3‐14 Effect of Heavy Ion Irradiation to the Silkworm Eggs at before Fertilization and at Nuclear Cleavage Stage

D. Ueda [a)], K. Shirai [a)], T. Funayama [b)], T. Sakashita [b)], Y. Yokota [b)] and Y. Kobayashi [b)]

[a)] Faculty of Textile Science and Technology, Shinshu University,
[b)] Medical and Biotechnological Application Division, QuBS, JAEA

We reported that the heavy ion-irradiated silkworm eggs (10 Gy of carbon ions) at just fertilization restart the development after short time delay, with imperfect repair of DNA damage. Then, the eggs having damaged DNA died at after cellular blastoderm stage by apoptosis. In this study, we investigated the effects of irradiation to the silkworm eggs at various developmental stages. First, we tried the irradiation to the unfertilized eggs (at 1.5 hour after oviposition). At this stage, the female pronucleus and the sperm nucleus are observed in the eggs, but not fertilized. After irradiation, the irradiated eggs stopped the development after fertilization. About 2 hours after, the egg restarted the nuclear cleavage. This result indicates the DNA damage on pronuleus cannot prevent the fertilization. We also investigated the effects of irradiation to the egg at the nuclear cleavage stage (at 6 hour after oviposition). The egg also stopped the development after irradiation, but the duration time of the developmental arrest was almost two times longer (about 4 hours) than that of the egg irradiated at fertilization.

昆虫およびその細胞は放射線に対し比較的耐性であるが、その詳細な機構は不明なままである。特に線量 10 Gy 程度の照射において、Sf9 や BmN4 などの昆虫培養細胞やカイコ幼虫造血気管内の血球前駆細胞などの比較的増殖の盛んな細胞においてすら、見かけ上、ほとんど影響が無いかのように増殖を続けるなど、哺乳類細胞と応答が異なり極めて興味深い。

著者らはこれまで産下 2 時間後のカイコ初期発生卵に 10 Gy の炭素イオンを照射すると短時間の発生停止の後に発生を再開するものの、傷害の修復は不完全であり、多くの卵が孵化することなく致死することを報告した。また昨年度は、これらの致死卵のうち、発生初期に致死する卵では傷害核が周辺細胞質において細胞化した直後に致死することを明らかにした。さらに昨年度、発生初期に致死する照射卵における傷害核の排除機構を追究した結果、産下 12~13 時間後の照射卵において多数の TUNEL 陽性が確認され、傷害核がアポトーシスにより排除されることを明らかにした。

本研究では、カイコ初期発生卵における放射線に対する応答の詳細をさらに明らかにすべく、受精直前と受精後卵黄内核分裂期に照射を行うことでその影響を調査した。

産下 2 時間後に炭素イオンを照射した場合、約半数の卵が胚帯形成前に致死する。産下 2 時間後はちょうど受精期であるため、発生初期に致死する約半数の卵では受精前の精前核と卵前核に炭素イオンが照射された可能性がある。そこで、確実に受精前である産下 1.5 時間後のカイコ卵へ炭素イオンを 10 Gy 照射し、その影響を確認した。しかし、照射卵における孵化率を調査した結果、発生初期の致死率は約 1/4 まで低下し、孵化率も約 20%であった。これらの値は産下 2 時間後に照射した場合より明らかに高い。このことより、卵前核および精前核への照射は受精にほとんど影響しないこと、孵化率は受精直後に照射された場合よりも高くなることが明らかになった。

孵化率の改善は受精前照射卵においても DNA 傷害の修復が行われることを示唆する。そこで DNA 修復と関連すると思われる照射卵の発生遅延を調査した。その結果、産下 1.5 時間後照射卵では非照射卵と比較すると平均して約 2 時間の発生遅延が認められた。よって、受精前照射卵においても、どこかのタイミングで傷害チェックポイントが働くと考えられる。

以前の研究において卵黄内核分裂期にある産下 8 時間後のカイコ卵の一部の核に 500 Gy という高線量の炭素イオンを局部照射し、その影響を調査した。その際、照射により傷害を受けた核は正常な分裂が阻害されつつも、周囲の細胞の周期と同調して DNA 複製を繰り返し、巨大な核となることとが観察されている。その際、発生遅延は認められていない。そこで、卵黄内核分裂期の卵において傷害チェックポイントが働くのかを確かめるため、卵黄内核分裂期である産下 6 時間後の卵に 10 Gy の炭素イオンによる全体照射を行い、その後の発生を調査した。その結果、非照射卵と比較して明らかな発生遅延が認められた。これは、卵黄内核分裂期においても受精期と同様に傷害チェックポイントが働くことを意味する。

卵黄内核分裂期の卵では、局部照射と全体照射でその後の応答に如実な違いが認められた。カイコ初期発生卵は一つの細胞（卵）内に多くの核が存在する「多核」状態にある。局部照射卵に発生遅延が認められない理由は、他に多くの正常な核が存在するためと考えられるが、その詳細には未だ不明な点があり、今後の研究課題と言える。

本研究により、カイコ初期発生卵においても様々なステージで放射線障害による発生遅延が存在することが確認された。一方で、発生を再開した卵の多くが致死することから、その修復と修復完了の認識機構には多くの疑問点が残る。また、細胞性胞胚期が傷害核排除の一つのタイミングであると考えられるが、その機構も不明なままである。今後はこの 2 点を中心に研究を進める予定である。

3 - 15 Medaka Blastoderm Cells Are Capable of Compensating the Injured Cells Irradiated by Carbon-ion Micro-beam

T. Yasuda [a)], S. Oda [a)], T. Watanabe-Asaka [a)], T. Funayama [b)], Y. Yokota [b)], Y. Mutou [b)], H. Ikeda [b)], Y. Kobayashi [b)] and H. Mitani [a)]

[a)] Graduated School of Frontier Sciences, The University of Tokyo,
[b)] Medical and Biotechnological Application Division, QuBS, JAEA

In this present study, we examined the effects of heavy carbon-ions on development in pre-implantation period utilizing medaka blastula stage embryos (st. 11: blastderm diameter is about 500 μm). We performed targeted irradiation by carbon-ion micro-beam (diameters of 120, 180 μm) to a central parts of blastoderm and observed the abnormalities during development compared with whole-body irradiated embryos. As a results, retardation and characteristic malformed eyes were observed during development when blastoderm cells were partially irradiated. However, more than half of 50 Gy-irradiated embryos (area size＝120 μm diameter) could hatch normally in contrast to all embryos with 2 Gy of whole-body irradiation being lethal before hutching.

1950 年代の Russel [1)] らが行ったマウス胚発生の異なる時期に放射線を被ばくさせた研究から、着床前期は “all or none”で催奇形性はない、とされてきたが 1990 年代後半、着床前期胚に放射線を照射した動物実験から、着床前期胚での被ばくにおいても奇形が誘発され、その影響は器官形成期被ばくよりも感受性が高いことが明らかになっている[2)]。着床前期の放射線被ばく影響研究はマウス胚を用いて多数行われているが、胚が子宮内で発生するため母親を殺して観察しなければならず、胚を生かしたまま発生の詳細を観察することは困難であった。そこで、胚が体外で発生し、かつ、卵殻が透明で発生までの全過程を生きたまま詳細に観察可能なメダカ胞胚期に照射を行い、その後の発生を詳細に観察した。

メダカ胞胚期に 2, 5, 10 Gy の炭素重粒子線をブロードビーム照射した結果、10 Gy では体軸形成不能、5 Gy では体軸形成異常、2 Gy では器官形成異常が観察され、全て早期胚死となり孵化には至らなかった。胚発生の詳細な観察の結果、最も高い線量である 10 Gy 照射胚においてのう胚期の細胞覆いかぶせ運動に遅れが見られたものの、胚形成前までは発生が進行することがわかった。これらの結果から、胞胚期に致命的な損傷を受けた細胞はすぐに死なずしばらく正常な細胞分裂を続け、その後体軸形成前までは進行することが示唆された（Fig. 1）。

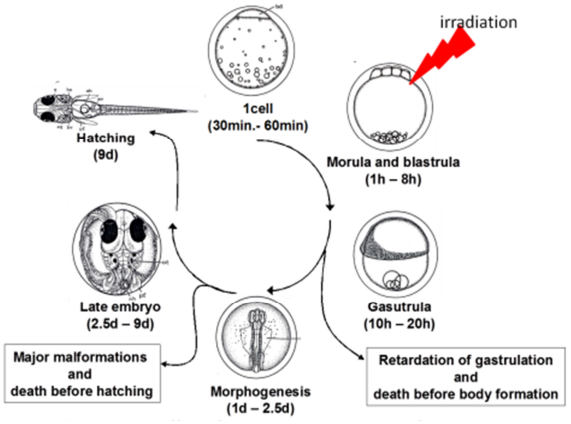

Fig. 1 Characteristic effect of whole-body irradiation of heavy carbon ions to blastrula stage of medaka embryo (st.11).

さらにブロードビーム照射では正常な体軸形成が不可能であった 5 Gy の重粒子線をφ180 μm に絞ったマイクロビームで胚盤（約 φ500 μm）中央に局部照射した結果、照射後 3 日までは発生進行に僅かな遅延が認められたものの、正常に孵化し成長することが判明した。これらの結果は、胚盤細胞の一部が致命的な損傷を受けても、残りの正常細胞がこれらの細胞損傷を補償し、胚は正常発生に至ることが可能であることを示唆する結果であった。

さらに、φ180 μm に絞った重粒子線を、線量 10 Gy に増加させて胚盤中央部へ照射したところ、照射 3 日後から明らかな発生遅延、および頭部、眼などの組織に明らかな器官形成異常が観察され、全ての胚は孵化に至らなかった。しかし、50 Gy の大線量をφ120 μm に絞って照射すると、照射胚の半数以上が孵化し正常に遊泳することから、胞胚期の細胞全てに全能性があり、被ばくした細胞の損傷を補償するのに必要な細胞数が残存していれば、正常発生できることが示唆された（Fig. 2）。本研究は、メダカ胚盤細胞の移植実験によって、この時期の胚盤細胞には全ての臓器に分化し得る万能性を有していることが示された最近の報告と一致する[3)]。

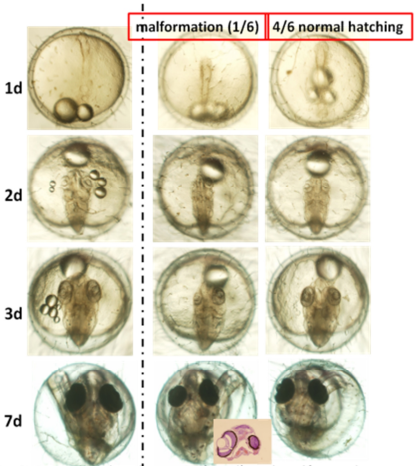

Fig. 2 Retarded development (2-4d) and malformed eyes were observed in irradiated with ϕ120 μm of C-ion 50 Gy to a central part of blastrula cells.

References

1) L. B. Russel et al., J. Cell Physiol. 43 (1954) 103.
2) Y. H. Gu et al., Radiat. Res. 147 (1997) 735.
3) N. Hong et al. , Stem Cells Dev. 22 (2013) 750-57.

3 - 16 Immunofluorescence Observation of Oxidative Damage of DNA Induced by Heavy Ions from TIARA

S. Kitabatake [a)], T. Ushiroda [a)], R. Hirayama [b)], Y. Furusawa [b)], T. Funayama [c)], Y. Yokota [c)], Y. Okahata [d)] and A. Ito [a)]

[a)] School of Engineering, Tokai University, [b)] National Institute of Radiological Sciences,
[c)] Medical and Biotechnological Application Division, QuBS, JAEA,
[d)] Graduate School of Science and Engineering, Yamagata University

Introduction

The track structure of high-LET radiation is generally recognized to consist of a core region with high ionization density and a penumbra region, where secondary electrons mainly contribute to energy deposition, with relatively low LET nature. Biological effects of high-LET radiation could be understood in terms of the track structure. Therefore the evaluation of the contribution of both regions to biological effects is an important issue for the study of high-LET effects. The significant contribution of the penumbra was strongly suggested by our study which claimed that indirect action mediated by OH radicals accounted for about 50% of cell killing by heavy ions with a high LET of 440 keV/μm[1)] and even at the very high LET of 2,106 keV/μm 32% of cell killing was attributed to indirect action[2)], in spite of decrease in G value of OH radical. To evaluate the contribution of OH radicals more directly, we measured the production of 8-hydroxydeoxyguanosine (8-OHdG), an oxidation product of guanine, in culture mammalian cells irradiated with high-LET ions. The results showed that the yield of 8-OHdG depended on ion species even with the same LET (unpublished observation). To confirm the production of OH radicals in the penumbra region whose size depends on ion species, an immunofluorescence method using 8-OHdG antibody is effective to visualize the area of OH radical production. In the present study, we developed a protocol to make a uniform DNA sheet with insoluble nature in aqueous solution, and explored the applicability to the detection of 8-OHdG distributions after heavy-ion irradiation.

Materials and Methods

Water-insoluble DNA sheet is formed in the presence of cationic lipid, dilauryldimethylammonium bromide[3)]. The DNA sheet was uniformly made on a cover glass as follows: The solution of DNA-lipid complex enters very narrow space between the cover glass and the attached Teflon® sheet by capillary phenomenon. After drying organic solvent, the Teflon® sheet can be easily detached from the DNA sheet[4)]. The DNA sheet is exposed to Bouin's fixative before irradiation, which possibly increases penetration of antibodies into the sheet.

Irradiation of heavy ions was performed in PBS solution at TIARA with 20 MeV protons with an LET of 2.77 keV/μm and with 260 MeV neon ions with an LET of 437 keV/μm. In addition, in the case of neon, microbeam irradiation was also carried out. After irradiation DNA samples were incubated with an 8-OHdG antibody followed by with a second antibody containing a fluorescence probe.

Results and Discussion

In advance of the experiments of ion exposure, X-rays of 20 Gy were irradiated to DNA sheet. Compared with non-irradiated sheet, uniformly increased fluorescence was observed, confirming the validity of the method we have developed. Figure 1 presents preliminary results of proton and neon irradiated samples. Upon ion irradiation randomly distributed dot-like fluorescence was observed, suggesting that these dots may be from incident ions. The sizes of the dots are in the range of a few microns, which is in accord with calculated penumbra region[5)]. Note that the outer parts in the dots seem to have more intense fluorescence, which may reflect that 8-OHdG was produced preferentially in the outer penumbra region. At present, any difference was not observed among ion species. Panel C shows the image for microbeam irradiation. Although the number of particles on each irradiation point was not identified, significant reduction of fluorescence in the center region and increase in the outer region of each hit area was apparent. The major problem is that dose dependence of the number of the dots was not clear, which remains for future study.

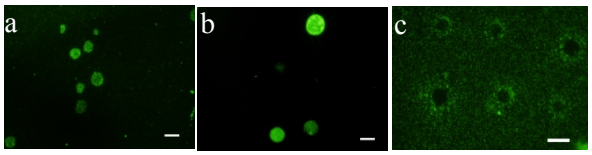

Fig. 1 Observation of DNA sheet with fluorescence microscope. (a) proton with 3.8 Gy, (b) Ne ion with 60 Gy, (c) Ne microbeam. Scale bar: 10 μm.

References

1) A. Ito et al., Radiat. Res. 165 (2006) 703-12.
2) R. Hirayama et al., Radiat. Res. 171 (2009) 212-18.
3) K. Tanaka and Y. Okahata, J. Am. Chem. Soc. 118 (1996) 10679-83.
4) S. Kitabatake, Master Thesis, Tokai University (2014).
5) A. Chatterjee and H. J. Schaefer, Radiat. Environ. Biophys. 13 (1976) 215-17.

3 - 17 Effect of Ionizing Radiation upon Dehydrated Pv11 Cultured Cells Originated from the Sleeping Chironomid

K. Watanabe [a)] , T. Akitsuki [a)], S. Shimura [a)], O. Gusev [a,c)], R. Cornette [a)], T. Kikawada [a)], T. Sakashita [b)], T. Funayama [b)], Y. Kobayashi [b)] and T. Okuda [a)]

[a)] Anhydrobiosis Research Group, National Institute of Agrobiological Sciences,
[b)] Medical and Biotechnological Application Division, QuBS, JAEA,
[c)] Department of Invertebrate Zoology, Kazan Federal University

The Sleeping Chironomid, *Polypedilum vanderplanki* can stand complete desiccation (anhydrobiosis) and also shows radio-resistance e.g. both larvae exposed to 9 kGy of ^{60}Co gamma rays and 4.5 kGy of high energetic He ions could revive for 2 days after rehydration[1,2]. However, a comet assay revealed that both desiccation and heavy ion irradiation cause severe DNA damage in cells of the larvae and that post-anhydrobiosis and post-irradiation recovery of nucleic acids takes at least for a few days [3]. Non-irradiated dry larvae after revival also possessed cells with severely damaged DNA, with a level of fragmentation comparable to those exposed to 70 Gy of He ions. ROS generated upon dehydration of cells are probably a major cause of the DNA fragmentation, as the ROS-elimination system, i.e. catalase, Cu/Zn-superoxide dismutase and glutathione peroxidase were abundantly expressed upon anhydrobiosis [3] and irradiation [4]. We also recognized the expression of two other genes involved in DNA-damage recognition and repair upon anhydrobiosis and irradiation, i.e. *Rad23* and *Rad51*.

We have generated cultured cell (Pv11) originated from *P. vanderplanki* embryo [5] which can also stand complete dehydration (Fig. 1). As it is of interest to know the radiation tolerance ability of Pv11 cells, we have exposed the dried Pv11 cells to different doses of He ions and followed by rehydration to see the viability rate (Fig. 2). At the present system, very low recovery rate less than 10% could be achieved after rehydration in anhydrobiotic Pv11 cells even without irradiation in contrast to slowly dehydrated larvae that can achieve almost 100% recovery after rehydration. Although irradiated dried Pv11 cells could recover after rehydration at slightly lower rate than control, even 480 Gy sample initiated proliferation. Pv11 samples exposed to 70 Gy and 160 Gy irradiation achieved proliferation as quick as the control within one week after rehydration. Pv11 cells exposed to 480 Gy showed a much slower recovery because of greater DNA damage so that normal proliferation started about 2 weeks after rehydration.

To clarify radiation tolerance mechanism at molecular level cultured cells are convenient as material samples due to its easy interpretation, as the cells are homogenous in characteristics. Moreover Pv11 cells can be handled much easier as it can be stored in a complete dried form at room temperature. In addition, it is possible to investigate the DSB repair mechanism of Pv11 cells that start proliferation even after expose of 480 Gy of He ions.

We believe that Pv11 cells would be a useful tool for studying not only radiation tolerance mechanism but also application, e.g. a biological monitor for radiation.

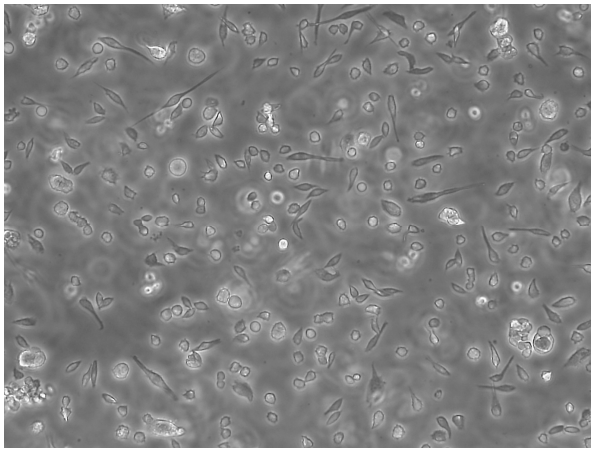

Fig. 1 Established Pv11 culture cells originated from anhydrobiotic *Polypedilum vanderplanki* embryo.

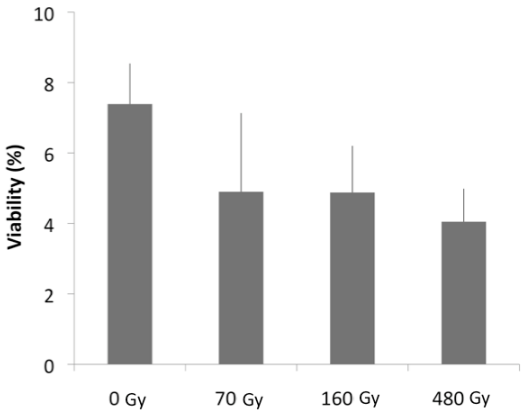

Fig. 2 Viability rate of dried Pv11 cells exposed to different doses of high energetic He ions at 1 day after rehydration.

References

1) M. Watanabe et al., Int. J. Radiat. Biol. 82 (2006) 587.
2) M. Watanabe et al., Int. J. Radiat. Biol. 82 (2006) 835.
3) O. Gusev et al., PLoS ONE 5 (2010) e14008.
4) R. Cornette et al., J. Biol. Chem. 285 (2010) 35889.
5) Y. Nakahara et al., Cryobiology 60 (2010) 138.

3 - 18 Effects of Carbon-ion Microbeam Irradiation on Locomotion and Pharyngeal Pumping Motion in *C. elegans*

M. Suzuki [a)], Y. Hattori [b)], T. Sakashita [a)], T. Funayama [a,c)], Y. Yokota [a)], H. Ikeda [a,c)] and Y. Kobayashi [a,c)]

[a)] Medical and Biotechnological Application Division, QuBS, JAEA,
[b)] Division of Environment and Radiation Sciences, NSED, JAEA,
[c)] Gunma University Graduate School of Medicine

The nematode *Caenorhabditis elegans* is a good *in vivo* model system to examine radiation effects on vital functions such as locomotion, feeding, learning and memory. Using *C. elegans*, we recently investigated the radiation effects on locomotion (snake-like crawling motion) and found that whole-body irradiation significantly reduced locomotion [1)]. Furthermore, we focused on the pharyngeal pumping motion (chewing and swallowing), which is a rapid periodic motion, and found that the proportion of pumping-motion arrest increased after whole-body irradiation. As the next step, we started to examine whether or not the effects observed after whole-body irradiation could be induced by microbeam irradiation to a very limited region [2,3)]. In this report, we summarize the results of microbeam irradiation experiments we carried out in the past few years.

Young adult wild-type *C. elegans* were used in all experiments. To investigate the effects of region-specific microbeam irradiation, we used energetic carbon ions ($^{12}C^{5+}$, 18.3 MeV/u, LET = 119 keV/μm) generated at the HZ1 port of TIARA. To inhibit free motion during irradiation an animal was enclosed in a ditch (approximately 60 μm in width) of a polydimethylsiloxane microfluidic device [4)] with buffer solution. The 'head' region including the pharynx, 'middle' region around the vulva and intestine, and 'tail' region were targeted independently; these regions were irradiated with 12,000 carbon ions corresponding to 500 Gy at a 20 μφ micro-aperture region. For comparison with microbeam irradiation, whole-body broad-beam irradiation with 500 Gy of carbon ions ($^{12}C^{5+}$, 18.3 MeV/u, LET = 113 keV/μm) was also carried out using HY1 port of TIARA. In the case of locomotion assay, an animal was placed on an agar dish without food immediately after irradiation. The locomotion was video-recorded and 'body bends' in locomotion, which is defined as the number of bends in the anterior body region at 20-sec intervals, was counted. In the case of pharyngeal pumping-motion assay, an animal was placed on an agar dish with a bacterial lawn (food) immediately after irradiation. Continuous shots of the pharyngeal pumping motion were obtained using a high-speed camera and the frequency of the pumping strokes per 1 sec duration was counted.

Locomotion reduced after whole-body irradiation, but did not change after either case of the region-specific microbeam irradiation (Fig. 1a). On the other hand, the proportion of pumping-motion arrest increased after head-irradiation, whereas the pumping motion after middle-irradiation or tail-irradiation did not change (Fig. 1b). This suggests that an increase of the proportion of pumping-motion arrest after whole-body irradiation reflects radiation effects on the head region.

Main findings in this study are the following: 1) Effects of the region-specific microbeam irradiation differ depending on types of motion, and 2) effects of whole-body irradiation tend to be more effective than those of the region-specific microbeam irradiation at the same irradiation dose. Further studies on the mechanisms underlying the radiation-induced changes of movements are required.

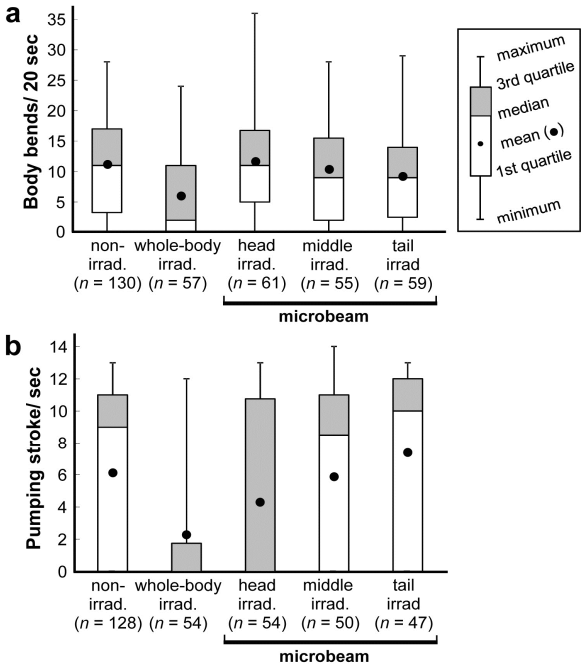

Fig. 1 Locomotion and pumping motion in *C. elegans*, immediately after whole-body or region-specific (head or middle or tail) irradiation with carbon ions. (a) Box plot of body bends in locomotion and (b) box plot of the frequency of pharyngeal pumping motion. *n* means the total number of animals that were tested.

References

1) T. Sakashita et al., Biol. Sci. Space 26 (2012) 7-11.
2) M. Suzuki et al., JAEA Takasaki Annu. Rep. 2011 JAEA-Review 2012-046 (2013) 77.
3) M. Suzuki et al., JAEA Takasaki Annu. Rep. 2012 JAEA-Review 2013-059 (2014) 84.
4) S. R. Lockery et al., J. Neurophysiol. 99 (2008) 3136-43.

3 - 19 Dose Responses of Irradiated Fresh Papaya Recorded on ESR at Different Temperature

M. Kikuchi [a], M. Ukai [b] and Y. Kobayashi [a]

[a] Medical and Biotechnological Application Division, QuBS, JAEA,
[b] Hokkaido University of Education

Electron spin resonance spectroscopy (ESR) has been utilized as a detection method of irradiated foods, measuring stable unpaired electrons induced by radiation. However, there is a problem on ESR measurement for the water-rich foods since the microwave input is absorbed to water molecules as of its vibration and rotation. We have examined two techniques to solve the water problem. One is direct measurement of the flesh at liquid nitrogen temperature in order to fix water-molecule's movement. When γ-induced long-lived radicals exist in the fleshes, those might be detected in liquid nitrogen. The other is measuring the powder of fruit fleshes at room temperature after freeze-drying. Additional radicals could be induced in the powder during the grinding of irradiated fleshes. In two ESR detection methods for fresh fruits, dose response curves of signal intensities were obtained independently[1,2]. Three responses show the direct proportional relationship (Fig. 1), except for main peak signals of freeze-dried powders (data not shown). In this study, we examined whether γ-induced radicals of papaya fleshes are changed after different sample preparations.

Fresh papayas were cut into 4 pieces and exposed to ^{60}Co γ-rays with the dose rate of 2 kGy/h at room temperature at Takasaki Advanced Radiation Research Institute of JAEA. The total absorbed dose was controlled by the irradiation period. After the irradiation, the papayas were kept at 4 °C for 0 to 14 days. To freeze-dry the papaya, fleshes were stored in -80 °C for at least 1 h and then kept under vacuum for about 15 h. The dried fleshes were powdered and put into an ESR tube. Otherwise, small piece of fresh papaya was directly put into an ESR tube to be measured in liquid nitrogen. ESR system of RE-3X and the substitute pulse-controlled magnetic field system (JEOL) were used. Those ESR parameters are summarized in Table 1.

Concerning ESR measurement, physical sensitivity increases at lower temperature since the ratio existing between α- and β-spins of electrons relates the excitation with the microwave input. To evaluate the physical sensitivity, a typical specimen was measured in liquid nitrogen (77 K) and the ambient temperature (297 K). As the result, signal intensity of central singlet line at 297 K was almost a half of the intensity at 77 K, despite of 10 times high microwave input (Fig. 2). Next, to estimate the signal intensity caused by a sample load, water content of papaya's fleshes was measured by the weight before and after a lyophilization, indicating that 87% of the fresh flesh was water. Therefore, 7.6 times much amount of wet flesh can be loaded into an ESR tube as dry specimen per weight. Based on the synergistic effect of the specimen's amount and the physical sensitivity, it was expected that the freeze-dried powder specimens give 3.7-fold higher signal intensity than the frozen flesh specimens do in liquid nitrogen. When this estimation is applied to a 3-kGy irradiated fresh papaya at 77 K (signal intensity: 12), the freeze-dried papaya specimen is calculated that the intensity becomes 44. As shown in Fig. 1, actual intensities of right and left side peaks were 43 and 30, respectively. Therefore, the right side peak intensity is good agreement with the estimation. This consideration suggests that the radicals of right side peak in the flesh's powder correspond to those of a side peak in the water-rich flesh. In other words, γ-induced radicals of the side peak are not affected by the sample preparations. This study indicates that the ESR detection methods for fresh fruits are reliable as a quantitative measurement.

References

1) M. Kikuchi et al., Spectrochim. Acta A 75 (2010) 310.
2) M. Kikuchi et al., RADIOISOTOPES 60 (2011) 163.

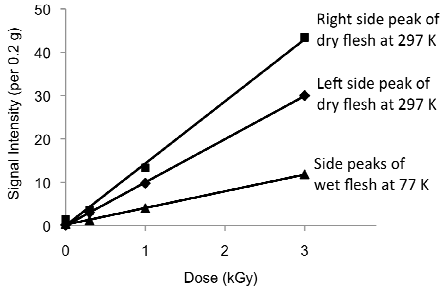

Fig. 1 Dose responses of side peaks measured from irradiated papaya fleshes at different temperatures. (Replot from ref. 2).

Table 1 ESR parameters used at 77 K and 297 K.

ESR Parameter	77 K	297 K
Microwave input (mW)	0.01	0.1
Center field (mT)	329	337
Sweep width (mT)	± 5	± 5
Sweep time (min)	1	1
Modulation width (mT)	0.5	0.5
Amplitude	1000	400

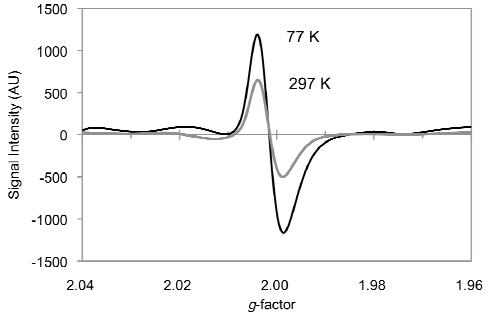

Fig. 2 ESR spectra of a 5-kGy irradiated waterless specimen recorded on each ESR parameter setting.

3 - 20 Analysis of Radicals Induced in Irradiated Amino Acid Using Pulse-ESR

K. Kishita [a)], M. Kikuchi [b)], H. Nakamura [a)], Y. Kobayashi [b)] and M. Ukai [a)]

[a)] Hokkaido University of Education,
[b)] Medical and Biotechnological Application Division, QuBS, JAEA

Radiation induced radicals in irradiated foods were analyzed with Pulse-ESR. The specimens were rice and wheat flour. We also analyzed 22 kinds of amino acids contained in foods to compare with the food specimens. Radiation dose level was 50, 100 and 200 kGy. We could not detect any signals in all specimens before irradiation treatment. Upon radiation treatment one broad signal was detected. Using Pulse-ESR, we succeeded to detect field swept echo signal in some irradiated amino acid specimens and to analyze the relaxation times (T_1 and T_2). It is concluded that ESR is very useful to analyze the radiation induced radicals in irradiated foods.

照射食品の Electron Spin Resonance Spectroscopy（以下、ESR）による検知を胡椒や乾燥野菜などのセルロースを主成分とする食品で検討してきたが、炭素由来のラジカルが、明瞭な singlet 信号として観測でき、放射線吸収線量に依存性を有することがわかった。照射誘導ラジカルは照射処理後 3 時間程度でほとんどが減衰し、その後は穏やかな減衰を示し、ほぼ一定値に収束することから、ESR による検知はこの安定なラジカルを計測に用いることになり、実用的な検知手法として有用である。

米や小麦のようなタンパク質含有量が高い食品での ESR による検知の導入を検討するため、小麦や米に照射し、Pulsed Wave-ESR（以下、Pulse-ESR）計測を行ったが、照射強力粉（50 kGy）のみで信号観測に成功した。他の照射試料でも Pulse-ESR 計測を試みたところ、echo 測定において、690 ns 付近に echo ではない信号が観測され、測定ができなかった。一方、Continuous Wave-ESR（以下 CW-ESR）では、信号観測が可能であったが、CW-ESR 信号は幅広の信号であった。そこで、本研究では幅広の信号とタンパク質との関連を検討するため、照射アミノ酸を試料とし、Pulse-ESR での測定を行った。

実験試料は和光純薬工業株式会社製及び関東化学株式会社製のアミノ酸 22 種である。試料は室温で保存し、ESR 測定に供した。照射処理は(独)日本原子力研究開発機構高崎量子応用研究所にてコバルト 60 を線源とするガンマ線を用い、室温で行った。吸収線量は 50，100，200 kGy である。

それぞれの試料を ESR 試料管に測定保証範囲に入るように詰め測定に用いた。Pulse-ESR 装置にセットするため、ESR 試料管のガラス部分の一部を切断して、試料管の長さ調節を行った。

ESR 測定では Pulse-ESR 機器は Bruker 社製の ESP-380E を用いた。正確な周波数及び磁場を求めるために、Anritsu MF 2412C，NMR FIELD METER EFM-2000AX を用いた。Echo 測定は $\pi/2 - \pi$ pulse sequence により計測した。測定パラメータは $\pi/2$-pulse width; 16 ns, π-pulse width; 24 ns, Pulse interval; 200 ns, Recycle delay; 1 ms とした。本来、$\pi/2$-pulse width が 16 ns のとき、π-pulse width は 32 ns となる。しかし、本実験に使用した pulse-ESR のピンダイオード性能では、16 ns のパルスから明瞭な矩形を得ることができないため、実験的に 16 ns, 24 ns を用いた。緩和時間は echo 測定パラメータに基づき、$\pi/2 - \tau - \pi$ sequence により計測した。測定パラメータは $\pi/2$-pulse width; 16 ns, π-pulse width; 24 ns, Pulse interval; 200 ns, Recycle delay; 1 ms とした。T_1 は π pulse $- \tau - \pi/2$ pulse $- \tau - \pi$ pulse $- \tau -$ (echo) の three pulse inversion recovery 法、T_2 は $\pi/2$ pulse $- \tau - \pi$ pulse $- \tau -$（echo）の two pulse spin echo 法を用いた。

未照射試料では Field swept 信号が得られなかった。20 種類の照射アミノ酸試料で Field swept 信号の観測に成功し、緩和時間 T_1, T_2 を求めることができた。Field swept 信号の観測ができなかった試料もあった。

Figure 1 に 50 kGy 照射グリシンの Field swept 信号を示した。4 本の信号が観測された。singlet 信号ではないことから米や小麦で観測された幅広の信号はアミノ酸による可能性があると推察した。

照射グリシンは吸収線量が変化してもピークの本数に変化はなかった。照射グリシンの他、いくつかの照射アミノ酸試料においても吸収線量の変化によるピーク数の変化は認められなかった。

緩和時間 T_1 は吸収線量が増加しても変化しなかったが、T_2 は吸収線量が上がるにつれ、減少していく傾向がみられた。

ESR は照射誘導ラジカルの検知に大変有用であることを再検証できたが、米や小麦のような食品での照射誘導ラジカルの解析をするには、今後更に Pulse-ESR 計測を詳細に行う必要があると考えた。

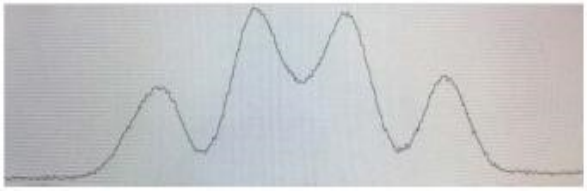

Fig. 1 Field-swept spectrum of irradiated glycine.

3 - 21 Characterization of Trace Element Distributions in LMECs Derived from ICR and C57BL/6 Strains of Mice

E. Sakurai [a,b], E. Sakurai [e], K. Yanai [b], K. Ishii [c], S. Koshio [c], S. Itoh [c], S. Matsuyama [c], M. Koka [d], T. Satoh [d] and T. Kamiya [d]

[a] Faculty of Pharmacy, Iwaki Meisei University,
[b] Department of Pharmacology, Tohoku University School of Medicine,
[c] Department of Quantum Science and Energy Engineering, Tohoku University,
[d] Department of Advanced Radiation Technology, TARRI, JAEA,
[e] Faculty of Pharmaceutical Sciences, Tokushima Bunnri University

Lung microvascular endothelial cells (LMECs) play an important role in preventing an injury by air pollutants through respiratory organs. We succeeded in isolation and culture of LMECs from C57BL/6J mice. However, LMECs from ICR mice were difficult to culture. We hypothesized that levels of some trace elements in LMECs from ICR mice might be less than those from C57BL/6J mice. To prove this hypothesis, we tried again to culture LMECs of the two kinds of mice strained on polycarbonate membranes. There is no report about distributions of trace elements in LMECs not only of mice but also of other animals. In this report, we searched what kind of element exits, and measured the amount of the trace elements in LMECs using an in air micro particle induced x-ray emission method. In addition, we observed change of trace element distributions in LMECs by nicotine treatment. In-air micro-PIXE was developed at the Takasaki Ion Accelerators for Advanced Radiation Application (TIARA), JAEA. Micro-PIXE allows analyzing the spatial distribution of the elements quantitatively.

Mice LMECs were isolated using a modification of the technique described by Magee et al [1]. The methods of the sample preparation for micro-PIXE analysis were described in a previous report[2]. This time, we tried to calculate the amount of trace elements in each cell which came from ICR mice or C57BL/6J mice. After stimulation of nicotine 0, 2, 20, 200 μM, levels of sodium, chloride and calcium in cells almost the same kinetic changes when we draw the comparison between the cell from ICR and the cell from C57BL/6J (Fig.1). However, the levels of phosphorus and sulfur in LMECs from C57BL/6J are higher than those in LMECs from ICR at normal condition (Fig. 3).

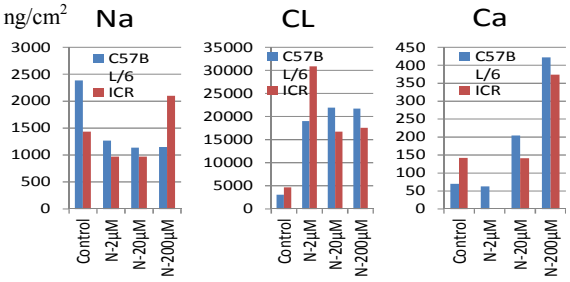

Fig. 1 Levels of sodium, chloride and calcium in LMEC s coming from ICR mice or C57BL/6J mice after treated with nicotine 2, 20 and 200 μM for 15 min.

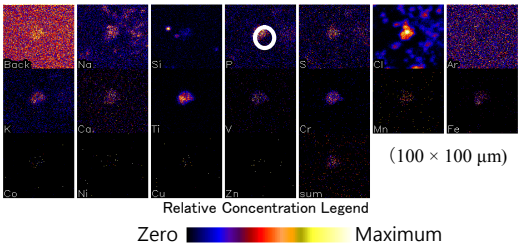

Fig. 2 Trace element images in a single LMEC from ICR which were treated with 2 μM nicotin for 15min.

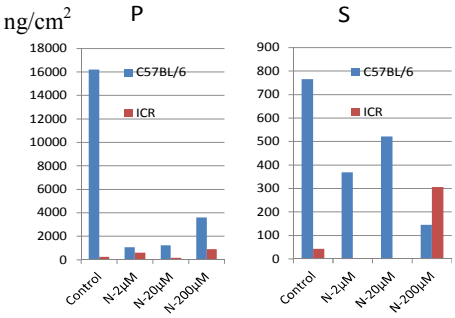

Fig. 3 Levels of phosphorus and sulfur in cells coming from ICR mice or C57BL/6J mice.

Figure 2 showed the images of all the elements in a cell that were detected in the micro-PIXE method. The cell was marked with a white circle in the phosphorus image in Fig. 2.

From these results, it is suggested that sulfur plays an important role in controlling LMECs proliferation. Sulfur is a component of heparin. C57BL/6J mice have a higher histamine level than that of ICR mice (unpublished study).

On the other hand, manganese was detected in both of LMECs which came from ICR mice and C57BL/6J mice treated 2 μM nicotine (data are not shown). These results seemed to suggest that the super oxide dismutase exists in LMECs, too. This report is a preliminary result of trace element levels and nicotine effects for mice LMECs. We will do further experiments and present results in near future.

References

1) E. Sakurai et al., Am. J. Physiol. Lung Cell Mol. Physiol. 282 (2002) L1192-7.
2) E. Sakurai et al., JAEA Takasaki Annu. Rep. 2012 JAEA-Review 2013-059 (2014) 88.

3 - 22 Distribution of Fluorine Penetrating from Fluoride-containing Filling Materials in Pre-demineralized Enamel

Y. Matsuda [a)], K. Okuyama [a)], H. Yamamoto [b)], H. Komatsu [a)], S. Oki [a)], N. Hashimoto [a)], Y. Iwami [b)], M. Hayashi [b)], H. Sano [a)], M. Nomachi [c)], K. Yasuda [d)], T. Satoh [e)] and M. Koka [e)]

[a)] Graduate School of Dental Medicine, Hokkaido University, [b)] Graduate School of Dentistry, Osaka University, [c)] Graduate School of Science, Osaka University, [d)] The Wakasa Wan Energy Research Center, [e)] Department of Advanced Radiation Technology, TARRI, JAEA

Introduction

Fluorine in fluoride-containing filling materials (FCFMs) can penetrate the tooth structure and produce a demineralization preventing effect, which is important from a clinical use point of view as the tooth structure is rendered spongy and sensitive to its environment by acid attack. The purpose of this study, therefore, is to evaluate the distribution of fluorine in pre-acid treated enamel under FCFMs by means of the in-air micro-PIGE/PIXE system at TIARA.

Materials and Methods

Class I surface cavities in extracted human molars were first drilled, and then the tooth surface was demineralized in a buffer solution (0.2 M lactic acid, 3.0 mM $CaCl_2$, 1.8 mM KH_2PO_4, 2% carboxymethyl cellulose, pH 4.5) at 37 °C for 72 hours. Three fluoride-containing materials, namely "Fuji IX extra (GC)" (EX), "Fuji IX (GC)" (FN) and "Fuji VII (GC)" (VII), were then used to fill the cavities, with a non-fluoride material, "Clearfil AP-X (KURARAY)", providing a control. The filled teeth were stored in a phosphate-buffered saline solution (pH 7.5) at 37 °C for 24 hours, after which 200 μm thick single sections incorporating the FCFMs were obtained from each tooth. The distribution of fluorine in the outer surface and cavity wall of each specimen was then evaluated using a proton induced gamma-ray emission (PIGE) technique[1)].

Results

Figure 1 shows the typical distribution of fluorine that was obtained in the outer surface and cavity wall of each FCFM, with all showing some evidence of fluorine in the tooth. The EX group shows more fluorine and a greater depth of penetration (~50 μm) at the outer surface than the FN and VII groups, but less fluorine than the other groups at the cavity wall. The FN group also shows fluorine at the outer surface, but only to a very limited depth, with the majority being present at the cavity wall. There is no evidence of fluorine in the outer surface of the VII group, but it does exist at the cavity wall. As expected, the control group did not show any evidence of fluorine, and thus its results were omitted.

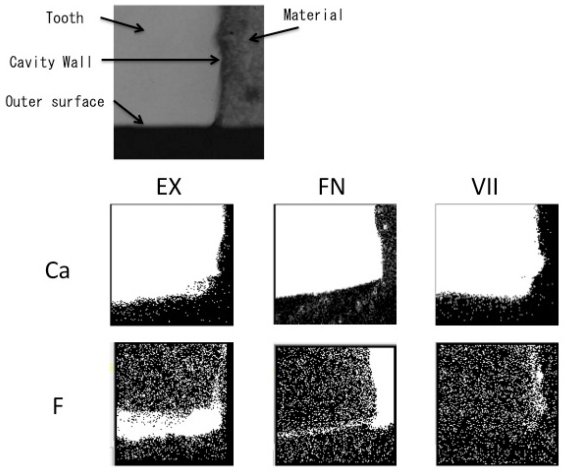

Fig. 1 Elemental PIGE maps of the teeth and fluoride-containing filling materials (FCFMs). The white dots represent PIGE signals from calcium fluorine.

Discussion

These results suggest that the distribution of fluorine is determined by two different pathways: direct to the enamel or through solution. By utilizing both pathways, EX can provide a wider area of fluorine distribution than other FCFMs. This variation in the distribution of fluorine will also directly influence the demineralization preventing effect.

Reference

1) H. Yamamoto et al., Nucl. Instrum. Meth. Phys. Res. B 210 (2003) 388.

3 - 23 Boron Imaging for Accelerator Based Neutron Capture Therapy

K. Nakai [a)], Y. Yamamoto [a)], E. Okamoto [a)], T. Yamamoto [a)], F. Yoshida [a)], A. Matsumura [a)], N. Yamada [b)], A. Kitamura [b)], M. Koka [b)] and T. Satoh [b)]

[a)] Department of Neurosurgery, Faculty of Medicine, University of Tsukuba,
[b)] Department of Advanced Radiation Technology, TARRI, JAEA

Introduction

The clinical trial of Boron Neutron Capture Therapy (BNCT) for glioblastoma and other malignant tumors was performed and the result is promising.[1)] We have been developing an accelerator based neutron source for BNCT. The patients dose has been determined by neutron flux and blood boron concentration during irradiation. The range of boron concentrations has been about 10 to 40μgB/g tissue. We could use prompt gamma ray analysis on nuclear reactor based BNCT, but boron measurement methods have not been established on accelerator based BNCT. We have already reported that the boron and gadolinium can be detected and that 2 dimensional images are taken using micro-PIXE/PIGE.[2)] To evaluate the possibility of PIGE for boron measurement at clinical BNCT, the boronophenylalanine(BPA) resolved within a cell culture medium was measured using PIGE. From the point of accuracy of clinical dose planning system, if this measurement has statistical precision of 5% and measurement time within 10-20 min, there is a possibility of application of PIGE to accelerator based BNCT.

Materials and methods

(1) Boronophenylalanine was resolved in a cell culture medium (Dulbecco's Modified Eagle's Medium containing 10% of Fatal Bovine Serum, 10 mg/L of penicillin streptomycin) and was dripped and dried on polycarbonate membranes. The boron concentrations were adjusted to 0, 18, 37.5, 75, 150, 300 μgB/mL. The samples were irradiated with a 1.7-MeV proton beam collimated to 1 μm in diameter and the emitted gamma rays were detected.

(2) U251 and CT26 cell lines were cultured on the polycarbonate membranes. These cells were treated with 0, 38, 300 μgB/mL of fructose-BPA complex (f-BPA) for 120min. with or without phosphate buffered saline washing. The samples were fixed with acute freeze-drying. These samples were analyzed using the micro-PIGE. Micro-PIXE/PIGE analysis was performed at Takasaki Ion Accelerators for Advanced Radiation Application (Takasaki, Japan).

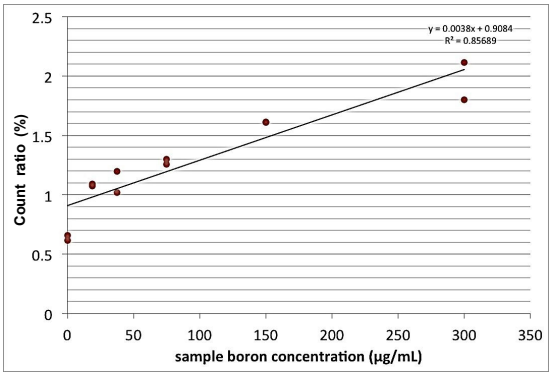

Fig.1 The count ratio of boron yields to total ones detected by PIGE in air measurement.

Results and Discussion

(1) 18 μgB/mL of f-BPA in the culture medium was detectable (Fig.1). The ratio of boron yields to total ones increased in a concentration-dependent manner. Though statistical precision within 5% was not accomplished in this experiment, PIGE has a potential to measure clinical concentration level of blood (10-40 μgB/mL). Further examination was needed. Measurement periods were 5 to 17min (data not shown). It meets the basic requirement for clinical application. (2) Two hours' f-BPA exposure makes a boron existing image by PIGE. A boron image revealed that boron remained at the cells (Fig 2). But we could not distinguish between boron on the cell membrane and boron in the cytoplasm, because the sample was dried and flattened. But boron cannot be detected for the saline wash group. It suggests that under the 2 hours' f-BPA exposure, boron atoms exist only on the surface of cell membrane and washing process removed the boron.

References

1) T. Yamamoto, K.Nakai, A. Matsumura Radiother Oncol. 91(2009) 80-4.
2) K. Endo et al., Oncol. Res. 16 (2006) 57-65.
3) Y. Yamamoto et al. Appl. Radiat. Isot.88 (2014) 114-117. doi: 10.1016/j.apradiso.2013.12.037.

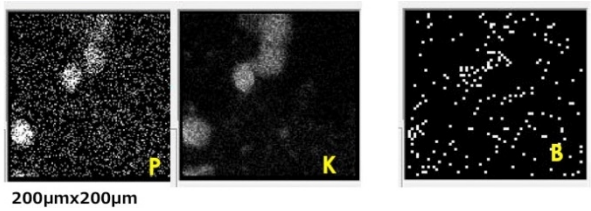

Fig. 2 (Left) The distribution of phosphorus atoms in human glioma cell line (U251) samples. Potassium (middle) and boron (right). Coexistence of phosphorus and potassium means the existence of a cell. Boron atoms were attached to the surface of the cell membrane and were solved in medium.

3 - 24 Analysis of Co-localization of Si and Fe in Lung Tissue of Silica-treated Mice by In-air Micro-PIXE

K. Dobashi [a)], Y. Shimizu [b)], H. Nagase [c)], S. Matsuzaki [b)], T. Satoh [d)], A. Yokoyama [d)], Y. Ishii [d)], T. Kamiya [d)], K. Ohta [e)], M. Mori [b)] and T. M. Yamada [b)]

[a)] Gunma University Faculty of Health Science,
[b)] Department of Medicine and Molecular Science, Gunma University Graduate School of Medicine,
[c)] Teikyo University School of Medicine, Department of Medicine,
[d)] Department of Advanced Radiation Technology, TARRI, JAEA,
[e)] National Hospital Organization, Tokyo National Hospital

The aim of this study is to prove the pathogenesis of lung injury induced by inhaled silica through the investigation of chemical change over time of inhaled silica in the lung. Silica particles were suspended in physiological saline and ultrasonicated prior to use. The suspension was transnasally administered to mice on days 0 and 1. Control mice were administered saline on the same days. On days 7 and 56 the animals were sacrificed. Specimens from mouse lung tissue were embedded in paraffin, and cut into sections 5 μm thick. Each section was dried, placed onto a 5-μm polyethylene terephthalate film, and fixed in the sample holder for in-air micro-PIXE analysis. Then the sample was irradiated with a proton microbeam. By the micro-PIXE analysis, the localization of much Fe was found to correspond with the sites of Si in the lung on days 56 in silica–treated mice, but not on days 7 in silica-treated mice. As a result of H-E staining and micro PIXE analysis, the localization of Fe deposited Si in silica-treated mouse was not found to correspond with the sites of prominent accumulation of macrophages. These findings suggest that the accumulation of Fe on inhaled silica is important to induce the chronic inflammation through reactive oxygen species and that the lung injury at the site of accumulation of macrophages is induced by other mechanism except apoptosis through Fas.

1. 背景と目的

アスベストの吸入は、肺線維症や肺ガンの原因となり、しかも発病まで数 10 年とかかることから、「静かな時限爆弾」とも言われ、大きな社会問題である。早期診断や病態解明には、肺内のアスベストの種類、量、分布などを、人肺組織内で特定する必要があるが、簡単でなかった。我々は、独立行政法人日本原子力研究開発機構との共同研究で、同機構が開発した大気マイクロ PIXE 分析技術を応用して、数 mg の肺組織の中のケイ素や金属元素の二次元分布を、1 μm の解像度で画像化する分析法を開発し、世界で初めて、吸入したアスベストを肺組織中に存在したままで画像化することに成功した。ケイ素（Si）の吸入は肺に炎症と線維化を引き起こす。Si によって誘導される肺線維症発症のメカニズムの一つに、Si 表層に鉄成分（Fe）が結合しオキシダントを発生させ、組織にアポトーシスを引き起こすことが提唱されている。我々は、肺内へ吸入されたシリカの化学変化を検討し肺組織像と比較することで、シリカによる肺障害の病態を明らかにしようとした。

2. 方法

シリカ粉末はリン酸緩衝生理食塩水（PBS）に懸濁し超音波粉砕し、1.5 mg/g Body weight を C57Bl/6 マウスに経鼻的に投与した。コントロールとして PBS を経鼻的に投与した。1 週目と 8 週目の肺組織中のシリカを大気マイクロ PIXE で解析した。肺組織は鉄染色（Belin blue stain）、抗 Fas 抗体で染色した。

3. 結果と考察

1 週目の肺組織中では、コントロール群に比較して Si 吸入群で有意な Si の沈着が認められたが（Fig. 1）、Fe の沈着は検出されなかった。8 週目の Si 吸入群では、1 週目に比較して、Si に一致して有意に Fe が多く検出された（Fig. 2）。

8 週目の肺組織中には、鉄染色で強い陽性を示す肺胞マクロファージの集積がみられたが同部位は必ずしも Fas 染色陽性と一致しない部位も存在した。以上から、Si による肺障害の機序として、Si に鉄が集積することで、活性酸素種を介し慢性炎症を進展させている可能性が示唆された。Si 肺のマクロファージ集積部位の肺障害には、必ずしも Fas を介したアポトーシスの関与だけでない可能性も示唆された。

Reference

1） Y. Shimizu et al., Respir. Res. 12:88 (2011).

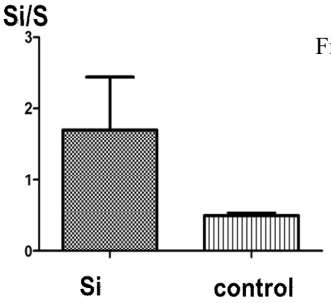

Fig. 1 Amount of Si in the lung tissue on day 7. The ratio of Si against S is significantly increased in the silica-inhaled mice. The amount of S is background of tissue.

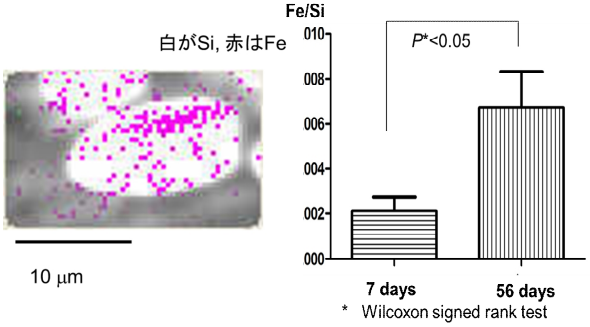

Fig. 2 Co-localization of Fe and Si in silica administrated mouse lung tissue on days 56 (Left). Deposition of Fe on Si proceeds with time (Right).

3 - 25 Analysis of Erythrocyte in Hepatitis C Patients Receiving Triple Therapy Using In-air Micro-PIXE

S. Tomioka [a)], T. Nagamine [a)], M. Koka [b)] T. Satoh [b)] and T. Kamiya [b)]

[a)] Graduate School of Health Sciences, Gunma University,
[b)] Department of Advanced Radiation Technology, TARRI, JAEA

1. Introduction

Chronic hepatitis C (CHC) patients treated with pegylated-interferon and ribavirin (Peg-IFN+RBV) and telaprevir (Peg-IFN+RBV+TPV) are frequently associated with anemia; however, the precise mechanism of anemia is not determined. In this study, we have analyzed the elemental changes in erythrocytes to investigate the pathogenesis of anemia caused by combination of Peg-IFN and anti-viral drugs.

2. Materials and Methods

Ten CHC patients (7 cases treated with Peg-IFN+RBV, 3 cases treated with Peg-IFN+RBV+TPV) and 4 healthy controls were enrolled in this study. Whole blood was collected via peripheral vein, and samples for PIXE analysis were prepared according to our method.[1)] Elemental levels in erythrocytes were determined by the method of Iwata et al.[2)] Elemental distributions in erythrocytes were analyzed by in-air micro-PIXE at JAEA-Takasaki.

3. Results and Discussion

1) Elemental maps of erythrocytes (Fig. 1)

The shape of erythrocyte, so-called the donut-like, fitted well with Cl, S, and K dots in healthy controls. Small-sized erythrocytes were shown in the Peg-IFN+RBV+TPV cases. In addition, Cl, S, and K dots tended to diffuse over the erythrocytes in the Peg-IFN+RBV+TPV cases. Na dots were increased in the Peg-IFN+RBV+TPV cases compared with the Peg-IFN+RBV cases. Fe dots in erythrocytes were distributed granularly divided into 3-4 particles in all the cases.

2) Elemental levels in erythrocytes (Fig. 2)

The Peg-IFN+RBV cases showed an increased level of Cu compared with the healthy controls. Ca, Fe, and Zn levels were higher in the Peg-IFN+RBV+TPV cases than in the Peg-IFN+RBV cases.

In conclusion, the spreading distributions of Cl, K and S dots over erythrocytes may reflect the alternation of erythrocyte membrane. Fe, Ca and Zn levels in erythrocytes were higher in the Peg-IFN+RBV+TPV cases than in the Peg-IFN+RBV cases, suggesting that the pathogenesis of anemia was different between Peg-IFN+RVB therapy and Peg-IFN+RBV+TPV therapy. Since Fe maps were similar among all the cases, iron deficiency dose not participate in anemia associated with Peg-IFN+RBV therapy and Peg-IFN+RBV+TPV therapy.

References

1) T. Nagamine et al., Int. J. PIXE (2012) 249-58.
2) Y. Iwata et al., JAEA Takasaki Annu. Rep. 2009 JAEA-Review 2010-065 (2011) 118.

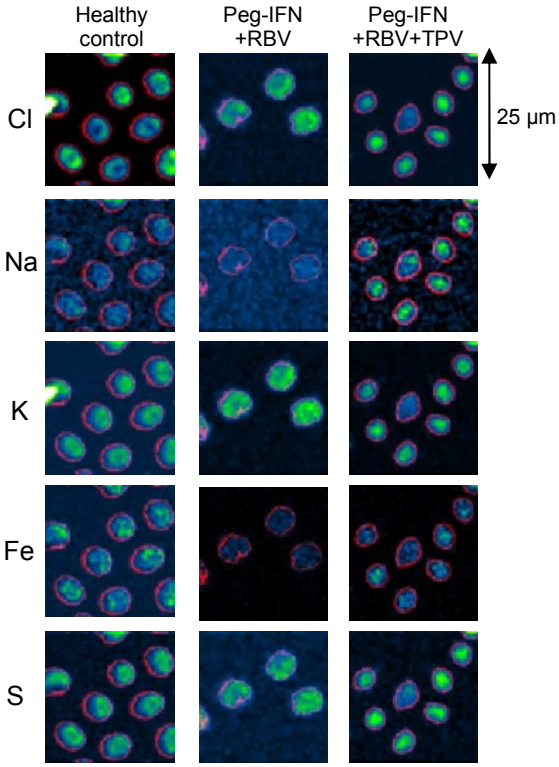

Fig. 1 Elemental maps of erythrocytes. Red and green show outlines of cells and relative concentration of each element, respectively.

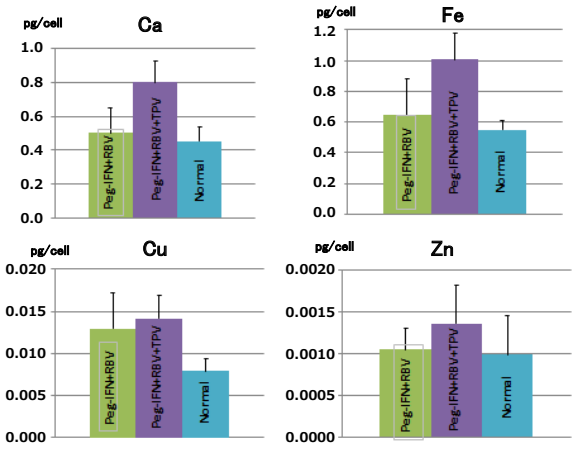

Fig. 2 Elemental levels in erythrocytes.

3 - 26 Targeted Radiation-sensitization by Inhibiting DNA Repair, Using Encapsulated AZD-2281

S. Harada [a)], S. Ehara [a)], K. Ishii [b)], T. Satoh [c)], T. Kamiya [c)] and N. Matsuyama [b)]

[a)] Iwate Medical University, School of Medicine, Department of Radiology,
[b)] Department of Quantum Science and Energy Engineering, Tohoku University,
[c)] Department of Advanced Radiation Technology, TARRI, JAEA

The induction and repair of DNA-double strand breaks (DSBs) are major determinants of cellular radiosensitivity. Poly [ADP-ribose] polymerase 1 (PARP-1) is 116-kDa nuclear protein that detects a broken strand of DSBs and initiates their repair. AZD-2281, a potential inhibitor of PARP-1, is a known radiation sensitizer.

We have been developing a targeted anticancer drug delivery system[1)], which uses microcapsules that release anticancer drugs in response to radiation. Irradiation-stimulated release of AZD-2281 from microcapsules subcutaneously injected around tumors inhibits repair of radiation-induced DNA damage and enhances the effects of radiation. In this study, we evaluated the efficacy of combined encapsulated AZD-2281 and radiation therapy for the in vivo treatment of CLAU-6 tumors in nu/nu CBA mice.

A mixture of 0.2% alginate and 0.1 % hyaluronic acid was prepared and 5 μmol AZD-2281 and 1 g L-ascorbic acid were added. A droplet of this mixture was sonicated using an ultrasound disintegrator and atomized using vibration to yield a 0.1-M solution of $CaCl_2$ and $FeCl_2$. Microcapsules were imaged using a micro-PIXE camera in TIARA and one of the images is shown in Fig. 1-A. Their mean diameter was 1.4 ± 0.6 μm. The capsules were subcutaneously injected around tumors that had been inoculated in the left hind legs of CBA mice. The tumors were then irradiated with 400-keV soft X-rays at 10 or 20 Gy at the Center for In Vivo Science, Iwate Medical University. The capsules around the tumors ruptured in response to the radiation (Fig. 1-B), and released AZD-2281. AZD-2281 kinetics measured in 5 tumors of the mice by using HPLC is shown in Fig. 2. Before injection, AZD-2281 was not detected in the tumors. Immediately after unencapsulated AZD-2281 injection (Fig. 2, ■) plus irradiation, the concentrations of AZD2291 were significantly increased, then rapidly decreased 2 weeks after the treatment (Fig. 2, ■). In contrast, encapsulated AZD-2281 exposed to 10 or 20 Gy

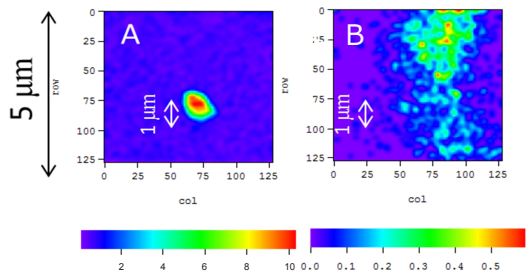

Fig. 1 Microcapsules imaged by Fe distributions using a micro PIXE camera. A: Unirradiated. B: Irradiated.

irradiation showed no immediate significant increase in the concentration of post-injection (Fig. 2, ■), but a significant increase was observed 2 weeks after injection (Fig. 2, ■). The antitumor effect was assessed by measuring tumor diameters in 5 mice, and their average and standard error were shown in Fig. 3. In combination with 10 or 20 Gy radiation, both unencapsulated and encapsulated AZD-2281 had enhanced antitumor effects.

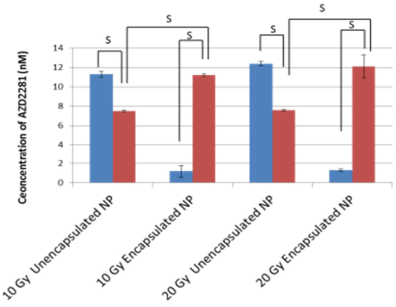

Fig. 2 Kinetics of AZD-2281 concentration. (n=5) ■: Immediately after irradiation. ■: 2 weeks after irradiation.

Tumor regression was delayed in mice receiving both

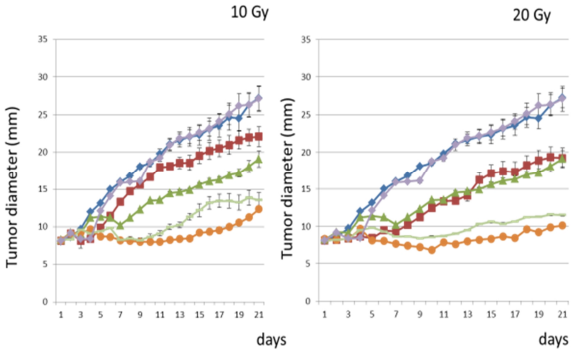

Fig. 3 Antitumor effect: ◆: control, ■: Radiation only, ▲ :Unencapsulated AZD-2281 only, ● Encapsulated AZD-2281 only. ─: Unencapsulated AZD-2281+Radiation. ●: encapsulated AZD-2281+Radiation.

encapsulated AZD-2281 and radiation compared to mice that received unencapsulated AZD228. Combined irradiation and encapsulated AZD-2281 treatment had the greatest antitumor effect 12 days after 10 or 20 Gy irradiation. We speculate that the continuous release of AZD-2281 from microcapsules resulted in an enhanced antitumor effect. However, the shrinkage of tumors by our treatment could not be observed. For better tumor control, addition of anticancer drug to our combined treatment are considered.

Reference

1) S. Harada et al., Int. J. Radiat. Oncol. Biol. Phys. 75(2) (2009) 455-62.

3 - 27 Development of Method for Plant Material Analysis by Micro-PIXE (Particle Induced X-ray Emission)

T. Yamamoto [a)], H. Noda [a)], J. Furukawa [a,b)], S. Satoh [a)], M. Koka [c)], T. Satoh [c)] and T. Kamiya [c)]

[a)] Life and Environmental Sciences, University of Tsukuba,
[b)] Center for Research in Isotope and Environmental Dynamics, University of Tsukuba,
[c)] Department of Advanced Radiation Technology, TARRI, JAEA

Plants need various trace elements. The measurement of their contents and their localization analysis in plant tissue is very important to identify their functions. Using micro-PIXE (Particle Induced X-ray Emission), multi-elements can be detected at the same time and visualized with high-resolution image, so it is very useful for identifying where the elements are localized. In micro-PIXE, especially samples are set on atmospheric pressure condition, so various types of sample preparations are acceptable for the analysis.

Previously, we analyzed a paraffin embedded section and a frozen section of plant sample to compare the difference of the sample preparations and to clarify the most suitable condition for micro-PIXE at TIARA [1)]. First, a paraffin section and a freeze section of a rice leaf blade were subjected for micro-PIXE. In rice leaf blades, it is known that silicon (Si) is highly accumulated at epidermis layer, so the silicon layer was observed by micro-PIXE, too.

In addition, Si was not only localized at the surface of the rice leaf blade, but in its mesophyll cell. About other elements, potassium (K), Calcium (Ca), Zinc (Zn) and Manganese (Mn) were detected as well. Localization of Si and Ca were not different between the paraffin section and the freeze section, but Mn and K were more detectable in the freeze section than the paraffin section. Such a difference might be caused by the chemical forms of the elements. In the paraffin section, the samples were fixed and dehydrate, so the soluble form elements were flowed out. While in the freeze section, the samples were not fixed and dehydrated, so soluble form elements were remained in tissue.

As above, we developed the method for imaging element localization in a rice leaf blade by a paraffin section and a freeze section[1)]. But, any other plant or tissue imaging was not performed, so we challenged to develop the method for imaging other plant and tissue by micro-PIXE, using hypocotyl and root tissues of *Lotus japonicus*. In the root, most elements may be soluble form to transport from a root to a shoot, so it was needed to use a freeze section. The freeze section did not adhere to polycarbonate film itself, so polyvinyl acetate was used for adhesive because it can make a very thin layer and contain only hydrogen, carbon and oxygen, such a trait is not detected in the measurement of trace elements by micro-PIXE.

Root and hypocotyl tissues of *Lotus japonicus* were embedded in compound for a freeze section and sliced at 20 μm by a cryo-microtome. The section was put on the polycarbonate film that was masked by diluted polyvinyl acetate and dried up. The film was exposed by 3 MeV H^+ beam. In the root, K, Ca and Mn were detected by the exposure for 40 min (Fig. 1). These elements mainly localized at outer layer of the pith of root. In the hypocotyl of two *Lotus japonicus* cultivars, MG-20 and B-129, K, Ca and Mn were detected. In B-129, K and Ca were localized at whole tissue of hypocotyl, while, K was localized in outer layer of pith and Ca was hardly detected in MG-20 (Fig. 2). Manganese was detected in the area that K was highly localized in both B-129 and MG-20.

In these studies, we developed the method that is extensively used for plant species and tissues. Especially, the freeze section can be applicable for the soluble form elements, such as K, and useful to analyze the element localization in the root tissue, in that element might mainly exist as a soluble form.

Reference

1) T. Yamamoto et al., JAEA Takasaki Annu. Rep. 2012 JAEA-Review 2013-059 (2014) 94.

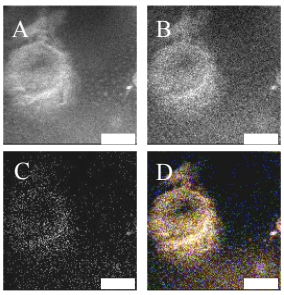

Fig. 1 Micro-PIXE images of *Lotus japonicus* root. Exposure time was 40 min. Each picture indicates K (A), Ca (B), Mn (C) and a merged image (D). In D, red, green and blue indicate K, Ca and Mn, respectively. Scale bar is 200 μm.

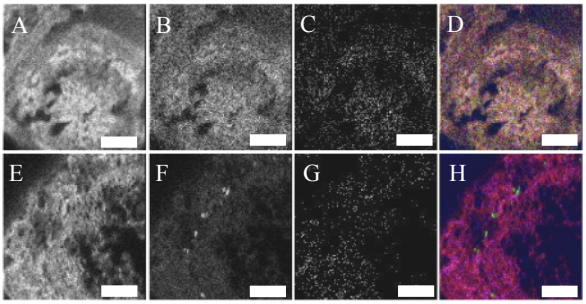

Fig. 2 Micro-PIXE images of *Lotus japonicus* hypocotyl tissues of B-129 (A, B, C, D) and MG-20 (E, F, G, H). Exposure time was 10 min. Each picture indicates K (A, E), Ca (B, F), Mn (C, G) and Merged (D, H). In merged image, red, green and blue indicate K, Ca and Mn, respectively. Scale bar is 200 μm.

3 - 28 Investigation of Elemental Distributions of Cesium and Rubidium in Rice Grains by Micro-PIXE

S. Koshio [a)], S. Itoh [a)], K. Ishii [a)], S. Matsuyama [a)], A. Terakawa [a)], S. Toyama [a)], K. Kasahara [a)], T. Kamiya [b)], M. Koka [b)] and T. Satoh [b)]

[a)] Department of Quantum Science and Energy Engineering, Tohoku University
[b)] Department of Advanced Radiation Technology, TARRI, JAEA

After the Great East Japan Earthquake and the accident at Fukushima Daiichi Nuclear Power Plant (F1) on March 11, 2011, a large amount of radioactive cesium (Cs) was diffused from F1 to all over Japan. Therefore many crops were banned to be exported. Moreover several agricultural spots have been hit by harmful rumors. This is how Japanese agriculture has suffered great losses. To avoid such losses and to develop efficient methods to decontaminate crops, we should investigate the way of Cs transition from soils to plants. For this purpose, we need efficient and ideal methods for measuring Cs distributions in plants' cells and microstructures. We applied a micro-PIXE method for analyzing Cs in crops. Additionally, we also analyzed rubidium (Rb) since the chemical properties of it are similar to those of Cs and detection efficiency of Rb characteristic X-ray is higher than that for Cs. For these reasons, we can use Rb as a substitute element of Cs.

We chose grains of rice as samples of this work because it is a major agricultural product consumed in Japan. At first, we prepared two soils: Cs_2CO_3 was added to one soil and Rb_2CO_3 was added to the other. With these soils, rice plants were cultivated under 8 conditions: Concentrations of added elements were 200 ppm and 300 ppm and cultivation terms were 14 days and 34 days. After cultivation, we picked grains from the plants to process them into samples for micro-PIXE analysis. In our previous work [1)], grains were simply cut with a knife (method A). In this case, they had thickness distributions. In contrast, samples processed with a microtome (method B) can enable us to analyze Cs and Rb quantitatively by the PIXE method. We prepared these two types of samples for micro-PIXE analysis and compared the results.

Then the experiment was carried out with the microbeam formation system and the micro-PIXE system attached to the 3 MV single-ended accelerator in TIARA. A 3 MeV H^+ beam was supplied as a microprobe for PIXE.

On the basis of experimental data, elemental concentrations were calculated and 2D elemental distributions were generated through GeoPIXE II [2)]. In most of the obtained elemental images distributions of Cs and Rb are similar (accumulating in brans and husks). We applied a digital image correlation method to these images to specify correlative elements with Cs and Rb. This method reveals the similarity between two images by calculating zero-mean normalized cross-correlation coefficients. The result says that Cs and Rb have strong relationships with K and P. Some of the results are shown in Fig. 1. Then we determined concentrations of Cs and Rb in rice, bran and husk separately by analyzing spectra extracted from regions of interest (ROI). In the case of the samples processed in the method A, values of concentrations of Cs and Rb vary widely in the same conditions. On the other hand, there is less variation in the results of samples processed in the method B. For this reason, thin and uniform samples sliced with a microtome seem to be more suitable for quantitative PIXE analysis. Next we investigated the effect coming from difference in cultivation terms and concentrations of Cs and Rb in the soils. Variation of the concentration ratios of Cs and Rb between the two cultivation terms (:14 days and 34 days) under each condition is 1.5 to 3.0. This is almost similar to the ratio of cultivation terms (34 days / 14 days). Comparing them in the two conditions (200 ppm and 300 ppm in the soils), the ratio vary 1.5 to 3.5 and it is larger than 1.5 (:300 ppm/ 200 ppm). Processed in the method A, the same tendency as the above is seen by dividing concentrations of added elements by those of K, which is a major and correlative element in every part.

We revealed that Cs and Rb accumulate in rice bran with K and P and distributions of Cs can be estimated by using substitute element Rb. In the future we should further investigate on the relationship Cs concentration in rice and that of soil or cultivation terms.

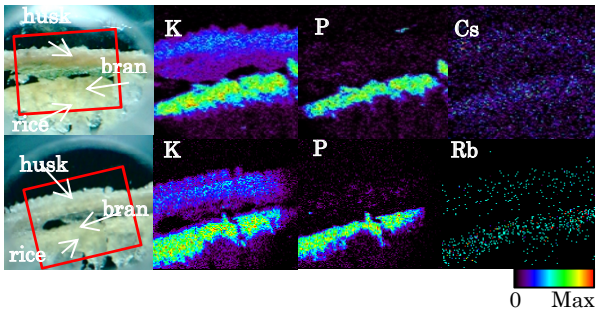

Fig. 1 Distributions of Cs, Rb and correlative elements in samples processed in method B. The areas surrounded by rectangles are scanned (800 μm each side). Behavior of Cs and Rb in samples seems similar. The part where they are the richest is bran and the second is husk. The digital image correlation method revealed the relationship between the added elements and K or P.

References

1) H. Sugai, Ph. D. Thesis, Tohoku University, (2012).
2) C. G. Ryan, Int. J. Imaging Syst. Technol., 11 (2000) 219-230.

3 - 29 Calibration of Several Detectors on Micro Beam PIXE System in TIARA by Standard Reference Material

Y. Iwata [a)], N. Yamada [b)], A. Kitamura [b)], M. Koka [b)], T. Satoh [b)] and T. Kamiya [b)]

[a)] Department of Chemistry, Faculty of Education and Human Studies, Akita University,
[b)] Department of Advanced Radiation Technology, TIARI, JAEA

Standard Reference Material (SRM) for determination of trace elements in biological materials was made by macro porous cation-exchange resin (Macro-Prep 25S). The resin was suspended in the standard solution containing the known amount of trace elements. The concentration of those elements in the resin was 0-270 ppmv. Sulfur is main inorganic element in the resin and its concentration was determined by dry digestion / volumetric titration by the standard Ba^{2+} solution as SO_4^{2-}. Individual particle of the resin was subjected to 3 MeV proton bombardments by micro beam system of TIARA. Several Si(Li) and PureGe detectors measured characteristic X-rays from the known amount of Al, S, Ca, Mn, Fe, Co, Ni, Cu, Zn, Sr and Pb. The Sensitivities for each detector were calculated by elemental abundance in the resin and does of proton. The Sensitivity was applied for calibration of micro beam PIXE system in TIARA.

1. PIXE分析における装置の校正や分析値の相互比較のために、イオン交換樹脂中に分析目的元素を正確量含有する標準物質（SRM）を開発している。これまでに、マクロポーラス型イオン交換樹脂に、生体関連元素のアルミニウム、カルシウム、マンガン、鉄、コバルト、ニッケル、銅、亜鉛、ストロンチウム、白金および鉛を一定量吸着させたSRMを調製した。PIXE分析に供し、特性X線強度と元素添加量から、TIARAマイクロビームシステムにおける分析感度を求めた[1-3]。本法で校正したTIARAマイクロビームシステムで、植物試料（地衣類）ならびに動物試料（ワムシ類）に含まれるpg以下の微少量元素の定量に成功した[3,4]。本研究では、TIARAマイクロビームシステムに新規導入された、X線検出器の校正をおこない、従来の検出器と比較したので報告する。

2. SRMの調製　純水中で懸濁させたマクロポーラス型陽イオン交換樹脂Macro Prep 25S（スルホン基型BIORAD）をメスシリンダー中で一昼夜放置し沈降させ、懸濁液中の樹脂体積を求めた。この懸濁液に、所定量のAl^{3+}、Ca^{2+}、Mn^{2+}、Fe^{3+}、Co^{2+}、Ni^{2+}、Cu^{2+}、Zn^{2+}、Sr^{2+}およびPb^{2+}の標準溶液を添加した。樹脂体積あたりの含有量は、AlとCaおよびPbで270 ppmv。Mn、Fe、Co、Ni、Cu、ZnおよびSrで135 ppmvとした[2]。原料の陽イオン交換樹脂にスルホン基として存在するSは、酸素フラスコ燃焼法/硫酸バリウム沈殿滴定法で求めた（2,056 ppmv）[4]。

PIXE分析　TIARAマイクロビームシステムにより3 MeVプロトンをサブミクロンにしぼり、スキャンエリア25 × 25 μmで、大気中200 - 600 nCの照射を行った。特性X線の測定は3種類の検出器を用いた（Table 1）。

3. 照射したSRMの樹脂はほぼ球形であり、半径は6 - 9 μmであった。この粒径から、樹脂一粒の元素量と照射電荷量を算出できる。検出器で検出した特性X線のカウントから、感度を求めた。測定器ごとの感度として、元素1 pgあたり1 nCのプロトン照射による特性X線のカウント数として求め、標準偏差とともに示した（Table 2）。検出器Aは従来から使用されており、軽元素に感度が高い。検出器Cはビームラインの下端に炭素膜を貼り付けて大気中に設置されている。Mnより原子番号の大きな元素に対して、検出器Aの約4倍の感度がある。検出器Bは、ポリマーウインドウを持ち、Naより軽い元素の検出が期待されている。加えて他の元素でも検出器Aよりも高感度が期待されたが、現在のところ、感度は同等か低かった。またピークの対称性も悪かった。今後、検出器のセットアップを進める必要がある。

References

1) Y. Iwata et al., JAEA Takasaki Annu. Rep. 2007 JAEA-Review 2008-055 (2008) 173.
2) Y. Iwata et al., JAEA Takasaki Annu. Rep. 2009 JAEA-Review 2010-065 (2011) 118.
3) Y. Iwata et al., JAEA Takasaki Annu. Rep. 2010 JAEA-Review 2011-043 (2012) 90.
4) Y. Iwata et al., JAEA Takasaki Annu. Rep. 2011 JAEA-Review 2012-046 (2013) 87.

Table 1　List of X-ray detector on microbeam system in TIARA.

Detector (SSD)	Model	Active Area / mm^2	Crystal Thickness /mm	FWHM @5.9keV /eV	Position
A (Si(Li))	PGT LS30135	30	5	135	Vacuum
B (PureGe)	CANBERRA GUL0110	100	10	118	Vacuum
C (PureGe)	PGT IGX100138	100	10	138	Air

Table 2　Analytical sensitivity for elements by several X-ray detectors on microbeam system in TIARA.

	Sensitivity/Count pg $^{-1}$nC $^{-1}$ (n)					
	A（Si(Li)）**		B（PureGe）*		C（PureGe）**	
Al	100 ± 16	(14)	101 ± 19	(6)	ND	
S	74 ± 13	(13)	77 ± 14	(6)	ND	
Ca	71 ± 14	(14)	58 ± 12	(6)	ND	
Mn	38 ± 5	(3)	23 ± 4	(3)	140 ± 22	(3)
Fe	33 ± 11	(7)	22 ± 8	(3)	130 ± 23	(7)
Co	24 ± 10	(6)	17 ± 7	(3)	91 ± 40	(6)
Ni	15 ± 6	(8)	9.1 ± 5	(3)	65 ± 11	(8)
Cu	18 ± 7	(6)	12 ± 5	(3)	65 ± 22	(6)
Zn	10 ± 2	(8)	6.9 ± 1.6	(3)	62 ± 11	(8)
Sr	1.2 ± 0.6	(8)	1.2± 0.9	(3)	4.7 ± 1.3	(8)
Pb	1.0±0.3	(14	0.7 ± 0.2	(6)	5.3 ± 1.5	(14)

*This work　**Measured at 2012.

3 - 30 Synthesis and *in vitro* Evaluation of ^{64}Cu-labeled Peptide for Tumor Imaging

Y. Sugo, I. Sasaki, S. Watanabe, Y. Ohshima and N. S. Ishioka

Medical and Biotechnological Application Division, QuBS, JAEA

1. Introduction

MARSGL peptide (H-Met-Ala-Arg-Ser-Gly-Leu-OH) has high affinity to the human epidermal growth factor receptor 2 (HER2) overexpressing in various tumor cells[1]. In the previous study, we have synthesized a novel radioiodinated MARSGL via electrophilic destannylation in high radiochemical yield[2].

Copper-64 (^{64}Cu) is a useful radionuclide in nuclear medicine, and can be produced by the cyclotron. In this study, we designed and synthesized ^{64}Cu-labeled MARSGL peptide conjugated with 1,4,7,10-tetraazacyclododecane-1,4,7,10-tetraacetic acid (DOTA) as a novel positron emission tomography (PET) imaging probe for HER2 overexpressing tumors.

2. Experimental

No-carrier-added ^{64}Cu was produced by the nuclear reaction of ^{64}Ni(p,n)^{64}Cu at high specific activity, using the AVF cyclotron of TIARA. An isotopically enriched ^{64}NiO (99.4%) target was irradiated with 11 MeV proton beam at a beam current of 5 μA. Radiochemical separation of ^{64}Cu was carried out by chelating ion-exchange method[3].

Protected MAR(Pbf)S(^{t}Bu)GL-Trt(2-Cl) resin was prepared by solid-phase peptide synthesis from 2-chlorotrityl chloride resin. Tri-*tert*-butyl 1,4,7,10-tetraazacyclododecane-1,4,7,10-tetraacetate was allowed to react with the peptide resin by 1-ethyl-3-(3-dimethylaminopropyl)carbodiimide hydrochloride and 1-hydroxy-1*H*-benzotriazole in dimethylformamide. And then the cleavage and the deprotection were performed at the same time using trifluoroacetic acid, 1,2-ethanedithiol, and triisopropylsilane.

To an aqueous solution of 0.1 mM DOTA-MARSGL, 0.1-1 MBq ^{64}CuCl$_2$ was added and the mixture was stirred at 40 °C for 60 min. The formation of ^{64}Cu-DOTA-MARSGL was determined by TLC and HPLC compared with a non-radioactive preparation.

3. Results and Discussion

TLC and LC/MS chromatogram of the non-radioactive preparation are shown in Fig. 1. A main peak in the chromatogram was assigned to non-radioactive Cu-DOTA-MARSGL (exact mass: 1,080.4) by ESI-MS spectra (positive: m/z = 1,081.4 $[M+H]^+$, negative: m/z = 1,079.5 $[M-H]^-$).

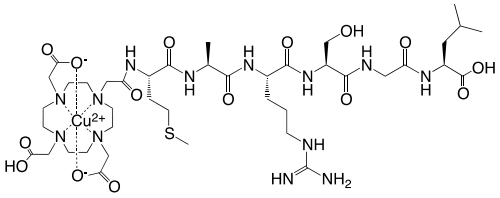

Cu-DOTA-MARSGL

Figure 2 indicates the changes in TLC and HPLC before and after radiolabeling. By comparison of the analytical data with those of non-radioactive preparation, it was confirmed that ^{64}Cu-DOTA-MARSGL was obtained in high radiochemical yield more than 94%.

We also examined a stability of ^{64}Cu-DOTA-MARSGL *in vitro*. The chromatogram was not changed after incubation in physiological saline at 37 °C overnight. In order to evaluate the usefulness as a PET imaging probe, further *in vitro* studies on the stability in human or mice plasma and the cellular uptake are in progress.

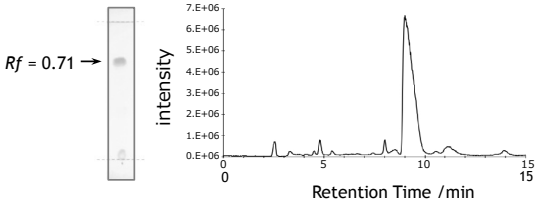

Fig. 1 TLC and LC/MS chromatogram of non-radioactive Cu-DOTA-MARSGL.

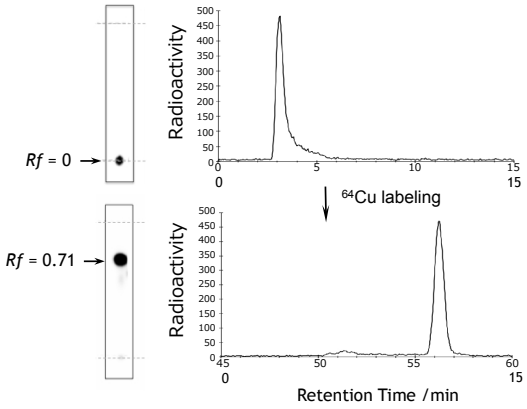

Fig. 2 TLC and radio-HPLC chromatograms of ^{64}CuCl$_2$ and ^{64}Cu-DOTA-MARSGL.

Acknowledgement

This study was supported in part by a Grant-in-Aid for Scientific Research (C) (No. 23591829) and a Funding Program for Next Generation World-Leading Researchers (No. LS124) from Japan Society for the Promotion of Science.

References

1) M. Houimel et al., Int. J. Cancer 92 (2001) 748.
2) I. Sasaki et al., Peptide Science 2012 (2013) 157.
3) S. Watanabe et al., Nucl. Med. Biol. 36 (2009) 587.

3 - 31 Medical Radioisotope Production with Accelerator Neutrons by Deuterons

K. Tsukada [a,b], N. Sato [a], S. Watanabe [c], N. S. Ishioka [c], Y. Hatsukawa [a,c], K. Hashimoto [a,c], T. Kin [d], M. Kawabata [a], H. Saeki [a] and Y. Nagai [a]

[a] Nuclear Engineering Research Collaboration Center, JAEA, [b] Advanced Science Research Center, JAEA, [c] Medical and Biotechnological Application Division, QuBS, JAEA, [d] Department of Engineering Science, Kyushu University

A new system has been proposed for the generation of radioisotopes with accelerator neutrons by deuterons [1], especially the production of ^{99}Mo ($T_{1/2}$ = 66 h), ^{90}Y ($T_{1/2}$ = 64 h), ^{67}Cu ($T_{1/2}$ = 61.8 h), and ^{64}Cu ($T_{1/2}$ = 12.7 h). Among various radioisotopes for medical use, ^{99m}Tc ($T_{1/2}$ = 6.0 h), the daughter nuclide of ^{99}Mo, is the most common radioisotope used in diagnosis, and its use accounts for 80% of all nuclear medicine procedures worldwide [2]. ^{90}Y-ibritumomab tiuxetan (Zevarin®), a radiopharmaceutical agent, a pure β^--ray emitter with a maximum energy of 2.28 MeV, has been used for cancer therapy. ^{67}Cu is believed to be a promising radionuclide to treat small distant metastases in radioimmunotherapy [3], since ^{67}Cu decays with their maximum β^- -ray energies of 0.377 MeV, 0.468 MeV, and 0.562 MeV. ^{67}Cu also emits low-energy γ-rays which can be readily detected by a gamma-camera. It can be used simultaneously for diagnostic imaging and internal therapy. ^{64}Cu is also expected for labeling many radio-pharmaceuticals for PET imaging, since it decays by positron (β^+) emission with a maximum energy of 0.653 MeV by 18%.

Enriched ^{100}Mo, ^{90}Zr, ^{68}Zn, and ^{64}Zn oxide samples with a radius of 10 mm and a weight of about 300 mg were irradiated with neutrons, which were obtained by the ^{nat}C(d,n) using 40 MeV deuterons provided from the TIARA cyclotron. After a bombardment we measured a γ-ray spectrum of the reaction products with a Ge detector.

^{99}Mo was successfully produced via the ^{100}Mo(n,$2n$) reaction, and we clearly observed the γ-rays from the internal transition of ^{99m}Tc (141 and 143 keV), ^{99}Mo (739 keV), ^{97}Zr (743 keV), and ^{97}Nb (658 keV). The radionuclides of ^{97}Zr ($T_{1/2}$ = 16.7 h) produced by ^{100}Mo(n,α) reaction, and its decay product ^{97}Nb ($T_{1/2}$ = 1.20 h), were impurity radionuclides. However, their yields were much smaller than that of ^{99}Mo, and therefore radioactive waste produced during chemical processing would be reduced compared with other proposed reaction systems.

We also measured a γ-ray spectrum of the reaction product produced by the ^{90}Zr(n,x) reaction. Since the activity of ^{90}Y was found to be comparable to that of impurity nuclide ^{89}Zr ($T_{1/2}$ =78.4 h)[4], ^{90}Y will be separated from ^{89}Zr by using an ion-exchange separation method and purified.

In Fig. 1, we show a γ-ray spectrum from the decay of ^{67}Cu (at 91, 93, 185, and 300 keV). ^{67}Cu was produced via the ^{68}Zn(n,pn) and ^{68}Zn(n,d) reactions. Relative production yields of impurity radionuclides of ^{69m}Zn ($T_{1/2}$ = 13.8 h), ^{65}Zn ($T_{1/2}$ = 243.7 d), ^{64}Cu ($T_{1/2}$ = 12.7 h), and ^{65}Ni ($T_{1/2}$ = 2.52 h) to ^{67}Cu are extremely low, which allow us to chemically separate ^{67}Cu from an irradiated ^{68}Zn sample with a few steps and to reuse high cost of an enriched ^{68}Zn sample. The present results strongly suggest that the ^{68}Zn(n, x)^{67}Cu reaction is the most promising route to produce high quality ^{67}Cu and could solve a longstanding problem of establishing an appropriate production method of ^{67}Cu [5].

^{64}Cu, ^{62}Zn ($T_{1/2}$ = 9.3 h), and ^{63}Zn ($T_{1/2}$ = 38.5 min) were found to be produced by the ^{64}Zn(n,x) reaction. Five hours after bombarding, however, the activity of the ^{63}Zn became negligible and the activity of ^{62}Zn was low. Hence, we can apply the same chemical procedure as that for ^{67}Cu to obtain high-quality ^{64}Cu.

The present results demonstrate that the medical radioisotopes, ^{99}Mo, ^{90}Y, ^{67}Cu, and ^{64}Cu, can be produced by using fast neutrons.

References

1) Y. Nagai et al., J. Phys. Soc. Jpn. 82 (2013) 064201.
2) F. F. Knapp, Jr. and S. Mirzadeh, Eur. J. Nucl. Med. 21 (1994) 1151.
3) I. Novak-Hofer and PA. Schubiger, Eur. J. Nucl. Med. 29 (2002) 821.
4) S. M. Qaim et al., Phys. Rev. C42 (1990) 363.
5) N. Sato et al., J. Phys. Soc. Jpn. 83 (2014) 073201.

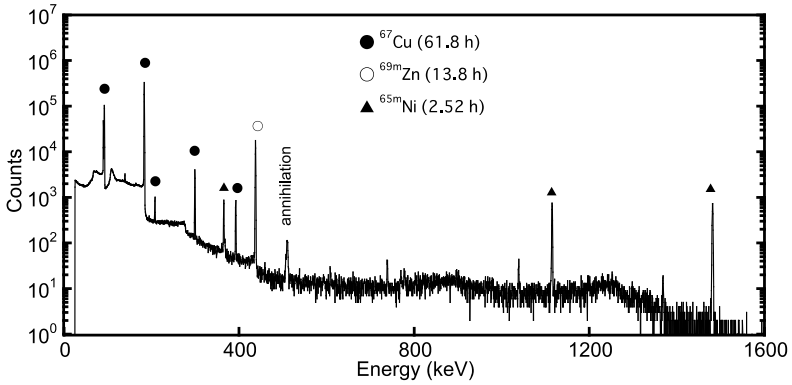

Fig. 1 A γ-ray spectrum of the ^{68}ZnO sample irradiated with neutrons, which was taken 15 hours after the end of irradiation.

3 - 32 Complexation of Lutetium-177 with Bifunctional Chelators in the Presence of Mg, Cu, and Yb

S. Watanabe , K. Hashimoto and N. S. Ishioka

Medical and Biotechnological Application Division, QuBS, JAEA

Introduction

The β^- emitter ^{177}Lu is a promising therapeutic radioisotope in radioimmunotherapy. In our early studies, the production of ^{177}Lu [^{176}Yb(n,γ)^{177}Yb→^{177}Lu] capable of labeling of ^{177}Lu-1,4,7,10-tetraazacyclododecan-N,N′,N′′, N′′′-tetraacetic acid (DOTA)-antibody (Fig. 1) [1] was developed, and the inhibition of the complexation of ^{177}Lu with DOTA and diethylenetriamine-N,N,N′, N′′,N′′-pentaacetic acid (DTPA) (Fig. 1) on the presence of the metallic impurities: Ca, Fe, and Zn was clarified[2]. In the present study, the inhibition of the complexation of ^{177}Lu with DOTA and DTPA on the presence of Mg, Cu, and Yb, which must be also included in the ^{177}Lu produced, was investigated. Moreover, the inhibition with Mg, Ca, Fe, Cu, Zn, and Yb was comprehensively discussed, and the knowledge to feed back into the production of ^{177}Lu was obtained.

Experimental

For the experiment of ^{177}Lu complexation with DOTA and DTPA, 1 μL of acetate buffer (3 M, pH=6.0) was added to a mixture of 5 μL of the ^{177}Lu solution (5.0×10^{-5} M as Lu) and 5 μL of solution of the competing metal (Mg, Cu, and Yb) from 2.5×10^{-5} M to 2.5×10^{-3} M. Then, 10 μL of 5.0×10^{-5} M DOTA and DTPA was added. After incubation for 1.5 h at 40 °C, the complexation yield, which was defined as the percentage of the radioactivity of ^{177}Lu-DOTA and ^{177}Lu-DTPA compared with that of ^{177}Lu used for the complexation, was determined by thin layer chromatography (TLC) on ITLC silica gel using aqueous ammonia:methanol:water (0.2 : 2 : 4) as the developing solvent. The unreactive ^{177}Lu remained at the origin point of the silica gel strip, while ^{177}Lu-DOTA and ^{177}Lu-DTPA moved with the solvent front.

Results and discussion

The ^{177}Lu complexation with DOTA and DTPA was not inhibited by Mg as well as Ca. The ^{177}Lu complexation yields of both DOTA and DTPA were highly inhibited by Cu, and the complexation with DOTA was more inhibited than that with DTPA as well as Fe and Zn. In the case of Yb, both DOTA and DTPA complexation of ^{177}Lu was highly inhibited by Yb.

Table 1 shows the order of the inhibition by metallic impurities in our experimental data and also the order of the ratios of the stability constants of metallic impurities to that of Lu, from which we can evaluate the ability of the inhibition by metallic impurities. By comparing our experimental data and the ratio of the stability constants, it was found that the order of Fe, Yb, Cu, and Zn for DOTA and that of Fe and Zn for DTPA were different. Therefore, we found that our experimental data could be partially explained by analyzing the stability constants. Lie et al.[3] reported that complexation between metal ions and chelating agents is related to both stability constants and kinetic stability. Therefore, to completely explain our experimental data, not only stability constants but also kinetic stability might be required.

In conclusion, the elimination of Mg and Ca from the ^{177}Lu final solution was not found to be necessary. In the case of Cu, Fe, and Zn, although the DTPA was found to be a better ^{177}Lu complexation agent than DOTA, the elimination of Cu, Fe, and Zn from the ^{177}Lu final solution was needed. Similarly, the elimination of Yb from the^{177}Lu final solution was found to be necessary.

References

1) S. Watanabe et al., Jpn. Patent Appl. 2010-223827.
2) S. Watanabe et al., JAEA Takasaki Annu. Rep. 2012 JAEA-Review 2013-059 (2014) 97.
3) S. Lie et al., Bioconjugate Chem. 12 (2001) 7.

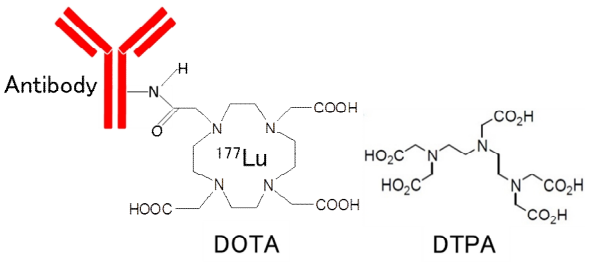

Fig. 1 Schematic diagram of ^{177}Lu-DOTA-antibody and structural formula of DTPA.

Table 1 The order of the inhibition by metallic impurities in our experimental data and the ratios of the stability constants of metallic impurities to that of Lu.

	Inhibition by metallic impurities in our experimental data	Ratio of stability constants of metallic impurities to that of Lu
DOTA	Mg, Ca < Fe < Yb < Cu, Zn	Mg < Ca < Zn < Fe < Cu < Yb
DTPA	Mg, Ca < Zn < Fe < Cu < Yb	Mg < Ca < Fe < Zn < Cu < Yb

3 - 33 Effect of Nutrient Elements to Cd Accumulation in a Cd Hyper-accumulator Fern

S. Ishii [a)], T. Yoshihara [b)], N. Suzui [a)], Y.-G. Yin [a)], N. Kawachi [a)] and S. Fujimaki [a)]

[a)] Medical and Biotechnological Application Division, QuBS, JAEA,
[b)] Laboratory for Environmental Science, Central Research Institute of Electric Power Industry

Cadmium (Cd) is an extremely toxic metal and should be eliminated from its pollutant soil to reduce that concentration in crops. Specialized plants are used to clean up contaminated soils. It is important to reveal the mechanism of Cd uptake and accumulation of these plants. Cd accumulation usually utilizes the same mechanism that other related elements such as Fe, Zn, Ca and Cu use, and the relationships with these elements is important for Cd accumulation. In this context, a positron-emitting tracer imaging system (PETIS) could be a strong tool. PETIS is a radiotracer-based imaging system that was specifically developed for a kinetic analysis of elements migration within the entire plant body at once. PETIS has already visualized the transport of several metals, including Fe, Zn, Mg and Cd, in intact plants.

Athyrium yokoscense (*Ay*), shows hyper-tolerance to multiple heavy metals, such as Cd, Zn and Pb, and accumulates them in the body at considerably higher concentrations than other plants. In this study, we subjected standardized intact plantlets of *Ay* to a time-course observation of Cd accumulation under two distinct medium conditions (basal and no-nutrient) using PETIS. Comparative analysis with these conditions eliminates the effects of nutrient elements other than Ca on Cd accumulation.

^{107}Cd was produced by bombarding silver foil with a 17 MeV energetic proton beam using a cyclotron at TIARA. Produced ^{107}Cd was purified as previously described [1)]. Finally, 4.8 to 10 MBq of ^{107}Cd was fed to *Ay* under the two conditions, basal and no-nutrient. The basal condition used 1/4 x MS medium with calcium further diluted to 0.25 mM. The no-nutrient condition used a solution of 0.25 mM $CaCl_2$. Each medium was adjusted containing Cd at the final concentration of 0.1 μM as $CdCl_2$ in addition to the ^{107}Cd tracer. PETIS images of the ^{107}Cd distribution were obtained every four minutes for 36 h.

Under the basal condition, PETIS imaging clearly demonstrated the real-time changes in Cd distribution from the culture solution to the entire plant body (Fig. 1). The amount of Cd in the culture solution decreased rapidly. The no-nutrient condition further accelerated the rapid decrease in the amount of Cd in the culture solution and the corresponding rapid increase in the distal roots compared with the basal conditions. In addition, the present work enabled to estimate physical and physiological Cd accumulation capacities in the distal roots, and demonstrated condition-dependent changes especially in *Ay*. These results clearly suggest Cd accumulation in *Ay* is regulated by nutrient condition. In addition, the present work enabled to estimate physical and physiological Cd accumulation capacities in the distal roots, and demonstrated condition-dependent changes especially in *Ay*. These results clearly suggested occurrences of species-/ condition-specific regulations in each observed parts.

It is probable that integration of these properties govern the specific Cd tolerance/accumulation in *Ay* [2)].

References

1) S. Fujimaki et al., Plant Physiol. 152 (2010) 1796-806.
2) T. Yoshihara et al., Plant Cell Environ. 37 (2014) 1086-96.

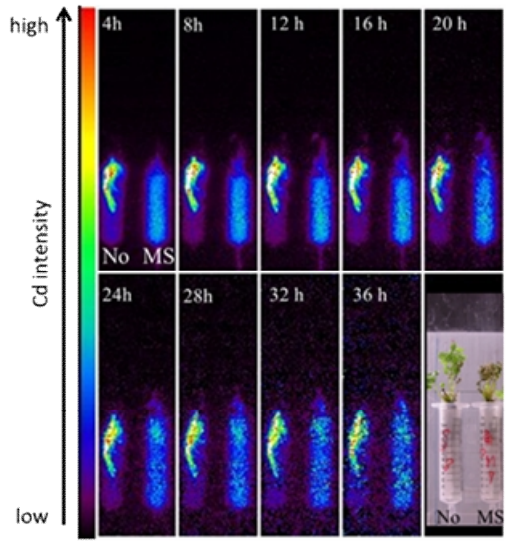

Fig. 1 Serial images of the Cd distribution within the plant bodies. Typical images of Cd distribution within the plant bodies are serially shown from 4 to 36 h after the Cd application. Each frame results from the integration of 240 original images collected every minute. Left and right plant was under no-nutrient condition and basal condition, respectively.

3 - 34 Feasibility Study of Using Cerenkov Light Imaging Technique for Plant Studies

N. Kawachi [a)], S. Yamamoto [b)], Y.-G. Yin [a)], N. Suzui [a)], S. Ishii [a)] and S. Fujimaki [a)]

[a)] Medical and Biotechnological Application Division, QuBS, JAEA,
[b)] Graduate School of Medicine, Nagoya University

Cerenkov light imaging is a relatively new non-contact radiotracer imaging technique that can image the distribution of radionuclides that emit beta rays (comprising electrons or positrons) by using a high-sensitivity optical camera. The electrons or positrons emit a small amount of blue light ($\lambda = 390$ nm) called Cerenkov light when their energies exceed a threshold level that is determined by the refractive index of the material in which they are traveling (260 keV in water). Figure 1 shows the schematic of the concept underlying Cerenkov light imaging. The originating point of Cerenkov light emission is close to that of beta radionuclides, and therefore, the theoretical spatial resolution achieved via Cerenkov imaging is better than those of other conventional imaging apparatus such as gamma cameras [1, 2)] and other beta detection methods. Since ^{137}Cs is a beta-emitting radionuclide (β^-: 512 keV), it is possible to image radiocesium distributions in plants using Cerenkov light imaging because plant tissues are sufficiently thin for Cerenkov light to penetrate them. In this paper, we report our feasibility study on the radiocesium imaging of a living plant in the light of developing a new Cerenkov imaging system, particularly for plant nutritional research.

For imaging the radiocesium distribution in a specimen plant, we used a high-sensitivity cooled charge-coupled device (CCD) camera (ORCA2-ER, Hamamatsu Photonics) for acquiring Cerenkov light. A bright lens (Xenon 0.95/25) was mounted on the camera, which was placed within a black box also containing the specimen plant. Figure 2 shows the photograph of our experimental setup with the CCD camera placed inside the black box installed in a plant growth chamber. Signals from the CCD camera were fed to the controller and a personal computer. An extension lens was inserted between the camera and lens to obtain magnified the images.

A solution containing ^{137}Cs with an activity of 4 MBq was mixed with a hydroponic culture solution into which the root of a soybean plant (*Glycine max* [L.] Merr.) was dipped. This soybean was exposed under light condition for seven days, after which we performed Cerenkov light imaging for 30 min. Figure 3 shows the Cerenkov light image of the soybean plant (a) and its optical photograph (b). While the stem and leaves appear to be clearly imaged with high spatial resolution, the image is also expected to indicate the ^{137}Cs distribution translocated from the root. However, signals acquired with the CCD camera from the plant include delayed fluorescence signals probably from chloroplasts, and therefore, the signals corresponding to the ^{137}Cs distribution are not clearly defined. Consequently, it is required to develop a method to identify the ^{137}Cs signals using certain optical filters when imaging living plants.

Developments are now in progress to improve the imaging system in terms of image quantitativeness and imaging acquisition of target plant specimens in their natural environmental conditions.

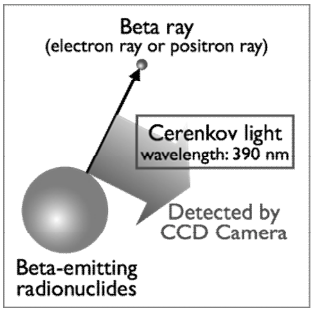

Fig. 1 Principle of Cerenkov light imaging for beta emitting radionuclide.

Fig. 2 Experimental setup.

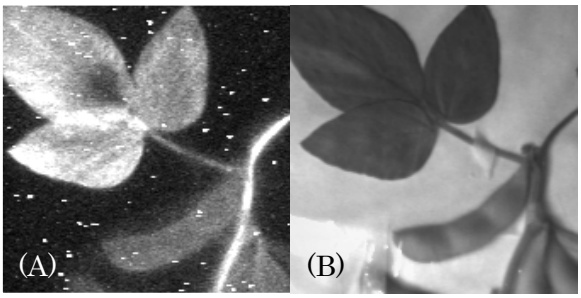

Fig. 3 Cerenkov light image of soybean (A) and its optical photograph (B).

References

1) S. Yamamoto et al., Nucl. Instrum. Meth. A 743 (2014) 124.
2) N. Kawachi, J. Vac. Soc. Jpn. 57 (2014) 27.

3 - 35 Evaluation of Velocity of ^{11}C-photoassimilate Flow Using Positron-emitting Tracer Imaging System

N. Suzui [a)], N. Kawachi [a)], S. Ishii [a)], Y.-G. Yin [a)], A. Hatano-Iwasaki [b, c)], K. Ogawa [b, c)] and S. Fujimaki [a)]

[a)] Medical and Biotechnological Application Division, QuBS, JAEA, [b)] RIBS Okayama, Okayama Prefectural Technology Center for Agriculture, Forestry and Fisheries, [c)] JST, CREST

Higher plants regulate photoassimilate flow from the "source" organs (e.g. mature leaves) to the "sink" organs (e.g. roots) in order to respond to environmental or developmental changes. An understanding of the source-sink interrelationship requires an experimental system which can measure the change of photoassimilate flow under various conditions. In this study, we developed an analytical method to evaluate velocity of photoassimilate flow using ^{11}C-tracer and the positron-emitting tracer imaging system (PETIS).

We conducted noninvasive imaging experiment using soybean (*Glycine max*) as described previously [1)]. $^{11}CO_2$ gas tracer was produced at TIARA, and fed to the compound leaves of the soybean plant. The dynamics of ^{11}C in an intact plant was monitored by PETIS every 10 s for 60 min.

Figure 1 shows serial images of ^{11}C distribution in the soybean plant. Regions of interests (ROIs) were set in the node of the first compound leaf (ROI-1) and the stem base (ROI-2). Time course of ^{11}C-radioactivity (Time-Activity Curve: TAC) in each ROI was generated from the serial images (Fig. 2). Initial slope of the rising ^{11}C-radioactivity was estimated by a linear least-square method using the TAC data. The value of the intercept of approximated line to the background line (X-intercept) was defined as "^{11}C-arrival time" to the ROIs.

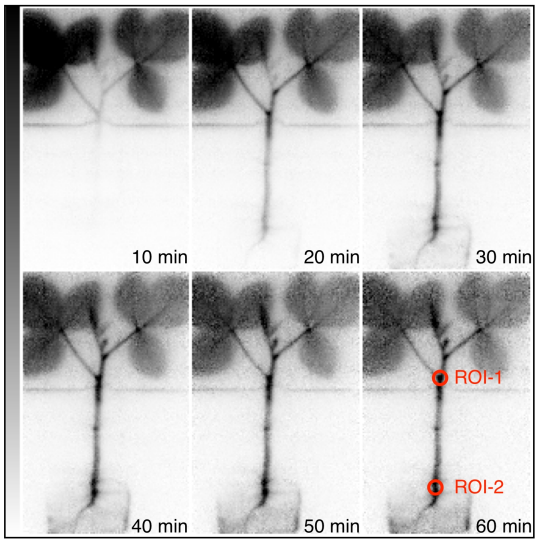

Fig. 1 Serial images of ^{11}C distribution in whole plant body. Each image comes from the integration of 60 original images collected every 10 s. Red circles indicate ROI-1 and ROI-2.

In order to determine X-intercept with a fair criterion, we developed an analytical program using the following algorithm; 1) draw a fitting line to consecutive 10 data points (100 s) and obtain a value of X-intercept, 2) execute this fitting sequentially in the range from 0 min to 20 min and obtain 120 values of X-intercept in total, 3) make a histogram for all of the X-intercept, 4) adopt the most frequent value as the representative X-intercept of the TAC.

The velocities of ^{11}C-photoassimilate flows of 18 individual soybean plants were estimated by the values of ^{11}C-arrival time and the distance between the ROIs. As a result, the average value of the velocity was 113 cm h^{-1} and the standard deviation was 20 cm h^{-1}. This result indicates the newly developed method is a reliable tool for the quantitative analysis of photoassimilate flow through the phloem.

Reference

1) N. Kawachi et al., Nucl. Instrum. Meth. Phys. Res. A 648 (2011) S317-20.

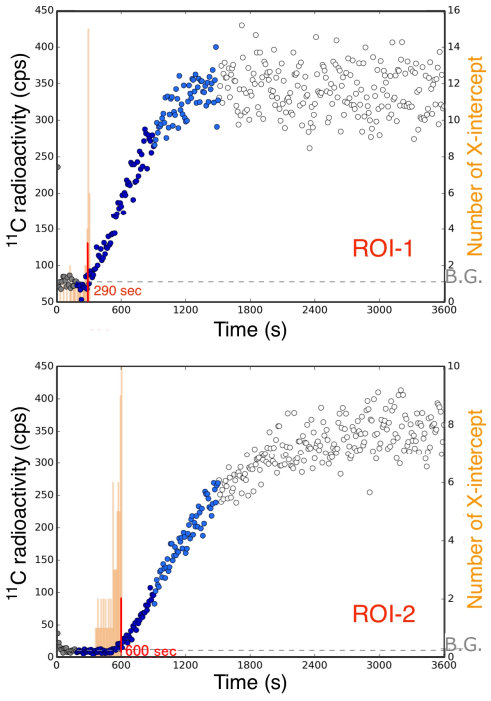

Fig. 2 Typical Time-Activity Curves (left Y-axis) and the histograms for X-intercept (right Y-axis) in ROI-1 and ROI-2. Dotted lines indicate the background levels determined from the average count rates from 0 s to 180 s. In this case, ^{11}C-arrival times to ROI-1 and ROI-2 were 290 s and 600 s, respectively.

3 - 36 Alteration of Segregation Ratio Suggests Complex Structural Alteration of DNA Induced by High-LET Ion Beams

Y. Hase and Y. Oono

Medical and Biotechnological Application Division, QuBS, JAEA

In the previous study, we showed that neon ions with a mean LET of 352 keV/μm [Ne (352)] and carbon ions with a mean LET of 425 keV/μm induced large deletions more frequently than carbon ions with a mean LET of 113 keV/μm [C (113)] in Arabidopsis [1]. Structural alteration of DNA including large deletions is supposed to cause the reduction of transmissibility to the progenies. Naito *et al*. showed that most of the mutations induced by C (113) and ^{60}Co gamma-rays in Arabidopsis pollen were large deletions and the majority of them were not transmitted to the progenies [2]. Shikazono *et al*. showed that Ne (352) and C (113) caused about two times higher level of sterility compared to electrons at a given level of lethality [3]. These results are consistent with the view that high-LET radiation frequently induces non-transmissible mutations. To further characterize the LET dependency of the transmissibility of mutations, we examined the segregation ratio of mutant plants in the progenies that were obtained by self-pollination of the mutagenized plants.

We used the Arabidopsis seeds obtained by crossing the wild type [ecotype: Columbia (Col)] with *gl1-1* mutant (background ecotype: Landsberg *erecta*). These material seeds are heterozygous for the *GL1* gene. The seeds were irradiated with helium ions with a mean LET of 30 keV/μm (He (30)), C (113), Ne (352) and gamma-rays. The doses that correspond to half of the shoulder dose of survival curves were employed for each radiation. Plants that harbored glabrous mutant sectors in rosette leaves were grown and the progeny seeds were independently harvested by self-pollination. More than fifty seeds were sown for each mutant line and the segregation ratio for the glabrous mutant plants was examined.

According to the Mendelian segregation, we expect one fourth of the progeny plants are glabrous mutants, i.e. the expected segregation ratio (the number of glabrous mutants / total number of plants) is 0.25. In the case of He (30) and C (113), the segregation ratio distributed with a mean of 0.25 and 0.23, respectively [Fig. 1(a) and (b)]. In the case of Ne (352), the mean segregation ratio was 0.28, which was still close to the expected ratio. However, the range of distribution was markedly wider than in the cases of He (30) and C (113) [Fig. 1(c)]. It is likely that the higher segregation ratio suggests the reduced transmissibility of wild-type *GL1* allele, and the lower segregation ratio suggests the reduced transmissibility of *gl1-1* allele. Although Ne (352) and C (113) were reported to show the similar level of sterility [3], our results suggest that the Ne (352) induces more complex types of structural alterations of chromosomes.

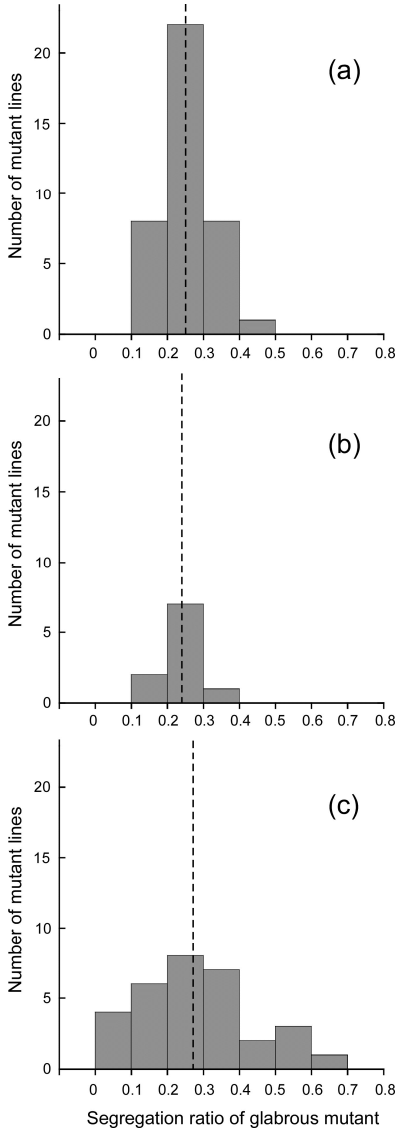

Fig. 1 Distribution of the segregation ratio for glabrous mutants in the progeny of the mutagenized *GL1*/*gl1-1* heterozygous plants. Number of mutant lines belongs to each class of segregation ratio is shown. The segregation ratio represents the number of glabrous mutants / total number of plants examined. (a) He (30), (b) C (113), (c) Ne (352). Dotted lines represent the mean of the data.

References

1) Y. Hase et al., Mutat. Res. 731 (2012) 41.
2) K. Naito et al., Genetics 169 (2005) 881.
3) N. Shikazono et al., Radiat. Environ. Biophys. 41 (2002) 159.

3 - 37 Ion Beam Breeding of Rice for the Mutation Breeding Project of the Forum for Nuclear Cooperation in Asia (FNCA)

A. Tanaka [a)], Y. Hase [a)], Y. Oono [a)], H. Ishikawa [b)] and A. Koike [b)]

[a)] Medical and Biotechnological Application Division, QuBS, JAEA,
[b)] Nuclear Safety Research Association

1. Introduction

Ion beams have been utilized for the Mutation Breeding Project of the Forum for Nuclear Cooperation in Asia (FNCA) of MEXT (Ministry of Education, Culture, Sports, Science and Technology) since 2009 [1)]. From fiscal year 2013, a new project 'Mutation Breeding of Rice for Sustainable Agriculture' has been launched, followed by the previous project on Composition or Quality in Rice (FY 2007-2012). This new project will contribute to the increase of food production and improvement of food quality in Asian countries by establishing mutant varieties such as high yielding varieties under low input conditions, new varieties tolerant to diseases, droughts, and other climate changes, according to participating country's demands by using gamma rays or ion beams. Ten countries, i.e., Bangladesh, China, Indonesia, Japan, Korea, Malaysia, Mongolia, The Philippines, Thailand, and Vietnam has been joined this project and most of these countries will irradiate seeds of their own rice varieties with ion beams. China will use its own ion beam facilities such as the facility in Institute of Modern Physics, Chinese Academy of Science. Korea will also use proton beams that are generated from 100 MeV proton beam linear accelerator (up to 20 MeV available at present) in Korea Atomic Energy Research Institute.

2. Materials and Methods

Hulled dry seeds of rice varieties of participating countries were exposed to 320 MeV carbon ions at TIARA with individual optimal doses to induce mutation. After irradiation, seeds were sent back to the participating countries and investigated for mutation induction.

At the FNCA workshop on Mutation Breeding held in Thailand in February 2012, we have deeply discussed the appropriate population size for mutation induction and concluded that at least several seeds from each 5 panicles from each 1,000 M_1 plants (5,000 initial mutated cells) should be harvested in order to obtain mutation efficiently.

3. Results and Discussion

From the previous project, some of the participating countries have already started to induce mutations in accordance with their countries' demands for sustainable agriculture. In Bangladesh, two mutants obtained from carbon irradiation with 40 Gy, produced higher yield and matured earlier at all locations than original variety, BRRI dhan29. These mutants also showed shorter in height and thus lodging resistant, and had similar grain quality as BRRI dhan29. This higher yield of this mutant was attributed to its considerably longer panicle length and significantly higher number of filled grains/panicle (Fig. 1: Bangladesh). In Indonesia, through ion-beam irradiation with 10 and 20 Gy, six promising mutant lines were obtained. One of the mutant line, IB-3, had the high grain yield, the short plant stature and short growth duration, therefore, were promising to be released (Fig. 1: Indonesia). In Malaysia, 31 selected mutant lines were obtained in M_3 derived from original variety, MR219, irradiated with 60 Gy. In these mutant lines, the differences in culm length, days to flowering, number of tiller, number of panicle, 1,000 grain weight, total grain yield, etc. were observed. Among them, several promising mutants which performed better in the agronomic traits as compared to MR219, these varieties are therefore suggested for further evaluation (Fig. 1: Malaysia). In Vietnam, carbon ion irradiation with 40 and 60 Gy on original varieties, Bacthom and Khangdan, have created many different phenotype mutants. In M_7 generation, two outstanding mutant lines from Bacthom for high grain potential yield and aroma trait have been chosen for location testing and national testing (Fig. 1: Vietnam).

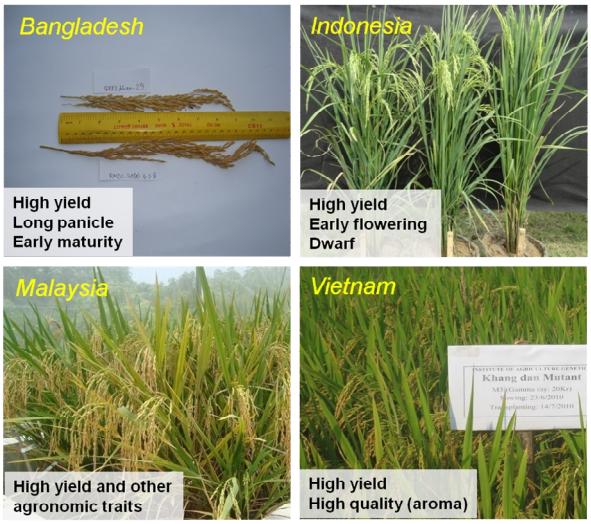

Fig. 1 Promising mutant lines selected from ion-beam irradiated rice seeds.

Reference

1) A. Tanaka et al., JAEA Takasaki Annu. Rep. 2012 JAEA-Review 2013-059 (2014) 103.

3 - 38 Development of New *Chrysanthemum Morifolium* Pink Mutants through Ion Beam Irradiation

A. Zaiton [a)], A.H. Affrida [a)], S. Shakinah [a)], M. Nurul Hidayah [a)], Y. Hase [b)] and Y. Oono [b)]

[a)] Agrotechnology and Biosciences Division, Malaysian Nuclear Agency,
[b)] Medical and Biotechnological Application Division, QuBS, JAEA

Developing new varieties of chrysanthemums is one of the emphases in Malaysian floriculture research as chrysanthemum is recognized as among the most important cut flower export for Malaysia [1)]. A combination of ion beam irradiation and *in vitro* organ culture techniques is very efficient in generating new ornamental varieties with novel traits and wider mutation spectrum [2)]. Therefore, in this project, ray floret cultures of pink chrysanthemum variety were irradiated at various doses with 320 MeV $^{12}C^{6+}$ ions, regenerated into plantlets and screened for morphological variations with an ultimate aim to produce mutants with useful horticultural traits.

This report highlights the development of new chrysanthemum Pink mutants from ray floret cultures. *In vitro* cultures of ray florets were cultured on MS [3)] regeneration medium, containing 2.0 mg/L BAP and 0.5 mg/L NAA. Irradiation was carried out at doses ranging from 0 to 30 Gy. Following irradiation, the cultures were transferred onto fresh MS regeneration medium and incubated at 25±2 °C under 16-h photoperiod for shoot regeneration. Data on callus formation and shoot regeneration after irradiation was discussed previously [4)]. Regenerated shoots were sub-cultured 4 times, before being hardened and planted in soils for morphological screening.

A series of screening was carried out at Nuclear Malaysia's glasshouse and MARDI Cameron Highlands (Fig. 1). The mutants were selected and characterized morphologically. Based on these screenings, three mutants were identified based on their distinct flower and/or plant characteristics (Fig. 2).

Fig. 1 Screening of mutants at MARDI Cameron Highlands.

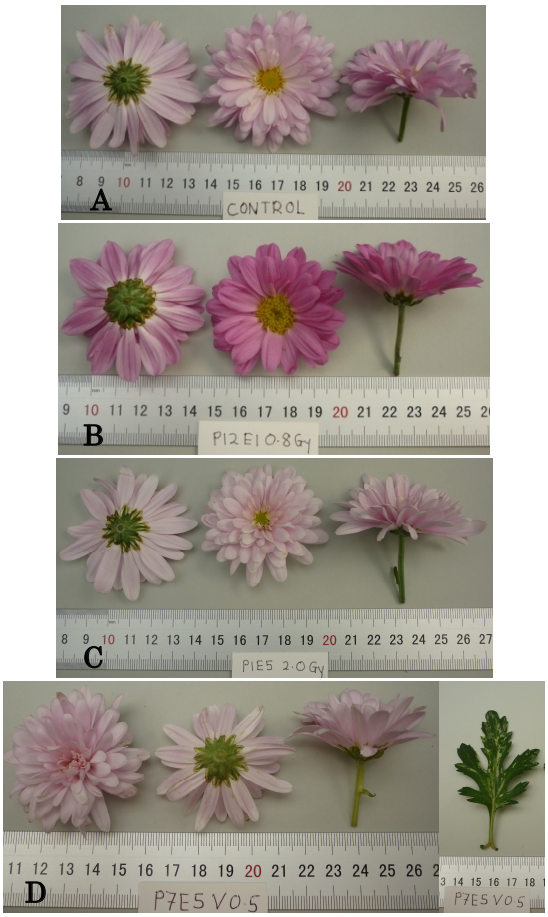

Fig. 2 Selected mutants from ion beam irradiated ray florets;
A: Control, pink (69B*), daisy-eyed double,
B: Mutant 1, 0.8 Gy, purple (74A*), semi double,
C: Mutant 2, 2.0 Gy, light pink (69C*), daisy-eyed double,
D: Mutant 3, 0.5 Gy, light pink (69C*), daisy-eyed double, variegated leaves.
*Based on The Royal Horticultural Society Colour Chart.

References

1) H. Noor Auni et al., Economic Technol. Management Rev. 3 (2008) 75.
2) S. Nagatomi et al., Inst. Radiat. Breeding Technical News No. 65 (2003).
3) T. Murashige et al., Physiol. Plant. 15 (1962) 473.
4) A. Zaiton et al., JAEA Takasaki Annu. Rep. 2011 JAEA-Review 2012-046 (2013) 97.

3 - 39 Breeding of Flower-color Mutation in Spray-mum by Ion Beam Irradiation

Y. Tanokashira [a)], S. Nagayoshi [a)], F. Tohjima [a)] and Y. Hase [b)]

[a)] Kagoshima Prefectural Institute for Agricultural Development,
[b)] Medical and Biotechnological Application Division, QuBS, JAEA

We performed ion beam irradiation on spray-mum cultivar 'Southern Chelsea (pink color)' to obtain white, deep-reddish yellow and yellow mutants. Although the white and deep reddish yellow mutants were obtained, yellow mutant was not obtained. It is likely that the white mutant is due to the loss of anthocyanin and the deep reddish yellow mutant is due to the increase of carotenoid content. These results suggest that the mutations on anthocyanin and carotenoid occur independently from each other, and therefore the yellow mutants could be obtained by re-irradiation of white or deep reddish yellow mutants.

1. はじめに

我々は、平成 14 年から鹿児島県の気候条件に適したスプレーギクの交配育種による品種育成を開始し、現在では 50 を超える品種を育成しており、県内に広く普及している。そこで当県育成スプレーギク品種へのイオンビーム照射による突然変異育種で花色のみが異なる、花色ファミリー品種の育成に取り組んだ。始めに、当県育成スプレーギクの花色変異スペクトルや変異率等の評価と、花色変異スクリーニングの結果を踏まえて、夏秋スプレーギク品種「サザンチェルシー」(Fig. 1)の桃色の花色から、白色、赤樺色、黄色を作出することとした。

2. 材料及び方法

材料には「サザンチェルシー」の無菌植物を用い、不定芽誘導培地(MS 培地, IAA 5 mg/L, BA 0.1 mg/L, sucrose 3%, gellangum 3 g/L, pH 5.8)に、2 mm×4 mm の葉片を置床後、原子力機構高崎研の AVF サイクロトロンにより発生させたイオンビーム(320 MeV・$^{12}C^{6+}$)を 0.5, 1, 2, 3 Gy 照射した。不定芽経由で再生した個体をバーミキュライト培地で順化後、2013 年 8 月開花試験を行った。

3. 結果及び考察

5,276 個体を供試し、376 個体の花色変異体が得られた(Table 1)。花色変異は、オリジナルの桃色(日本園芸植物標準色票:9211、紫ピンク)から、アントシアニンが減少した薄桃色(同 8903、紫ピンク)と白色、アントシアニンが増加した濃桃色(同 9213、濃紫ピンク)、カロテノイドが増加した赤樺色(同 0713、橙赤)、黄樺色(同 0704、黄ピンク)が得られた。

花色変異体のカロテノイドとアントシアニンの色素分析結果を踏まえた花色変異の方向と、変異誘発によって得られた花色変異率を Fig. 2 に示した。育種目標である白色の花色変異率は 0.6%、赤樺色は 1.4%であったが、黄色は 0%であった。

Fig. 1 'Southern Chelsea'.

「サザンチェルシー」の桃色から黄色を作出するには、アントシアニンが消失する変異と、カロテノイドが増加する2つの変異が必要だと考えられる。この 2 つの変異が独立して起こると仮定すると、1 回の変異誘発で黄色変異体が得られる確率は、計算上では約 12,000 分の 1(0.6%×1.4%)となるため、今回の供試個体数(計 5,276 個体)では得られなかったと推察される。今後は、得られた花色変異体への再照射(計 2 回の変異誘発)によって改良を図る予定である。

花色変異率は5.7～7.9%であり、線量別での変異率の差は見られなかった。3 Gy 照射区でも親株と同等な生育を示す花色変異体が得られたが、再照射による改良に用いる中間母本は、初回の照射線量ができるだけ低い方がダメージの蓄積が少ないため、0.5 Gy照射区で得られた花色変異体の利用が適切だと考えられる。

以上の結果から、「サザンチェルシー」の花色変異体を作出する場合、白色と赤樺色は 1 回の変異誘発で得られるが、黄色については、白色や赤樺色変異体への再照射で作出する方法が効率的であると推察された。

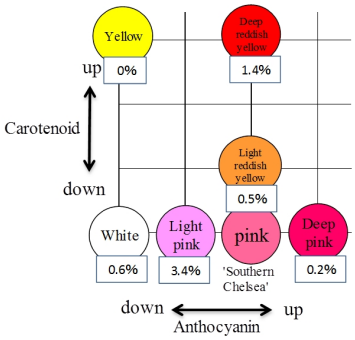

Fig. 2 Relationship between the amount of pigments and color variations in the mutants.

Table 1 Flower-color mutation induced by ion beam irradiation.

Variation source		Number of irradiated plants	Flower-color mutation						Number of mutants	Mutation rate(%)
Line class	Dose (Gy)		White	Light pink	Deep pink	Deep reddish yellow	Light reddish yellow	Other		
C	0.5	564	3	22	1	9	5	2	42	7.4
	1	1356	11	39	1	13	3	10	77	5.7
	2	1676	9	59	4	30	10	13	125	7.5
	3	1680	9	61	6	22	11	23	132	7.9
Total		5276	32	181	12	74	29	48	376	7.1
Mutation rate(%)			0.6	3.4	0.2	1.4	0.5	0.9	7.1	

3 - 40 Step-wise Improvement of Chrysanthemum by Ion Beam Irradiation

Y. Tanokashira [a)], S. Nagayoshi [a)], F. Tohjima [a)] and Y. Hase [b)]

[a)] Kagoshima Prefectural Institute for Agricultural Development,
[b)] Medical and Biotechnological Application Division, QuBS, JAEA

So far, we developed new chrysanthemum strains such as “Aladdin” and “C09-i-3” by step-wise improvement with ion beam irradiation. In this study, we tried to improve the efficiency of shoot production of “C09-i-3” by the third round of ion beam irradiation. We succeeded to obtain a promising line “C12-i-4”.

1. はじめに

我々は、白系秋輪ギクの主力品種「神馬」を材料とし、イオンビーム照射による特性改良によって、無側枝性、低温開花性、切り花のボリュームを併せ持つ品種の育成を進めている。現在までに、無側枝性で茎葉や花のボリュームの優れる「新神」を育成し、さらに「新神」へのイオンビーム再照射によって、低温開花性を併せ持つ「C09-i-3」等の新系統を育成した[1)]。しかしながらこれらの系統は、無側枝性が「新神」より更に強く、高温期の母株栽培では挿し穂の確保が困難で、自家増殖が可能である「新神」程度に萌芽性を回復させる必要がある。これまでの知見から、DNA 量と生育特性が低下していない変異体を照射材料とすることや[2)]、再照射線量は、不定芽再生率等から推定する適正線量よりも低い線量とすることで、不良変異を伴わずに複数の特性を段階的に改良できることが示されている。そこで、「新神」の再改良により作出した低温開花性系統へのイオンビーム再々照射を行い、母株採穂数が「新神」並に回復した個体の作出を図った。

2. 材料及び方法

供試系統には、「C09-i-3」の選抜系統「C10-g-46」の無菌植物を用い、不定芽誘導培地（MS 培地、IAA：5 mg/L、BA：1 mg/L、sucrose 3%、gellangum 3 g/L、pH 5.8）に、2 mm×4 mm の葉片を置床後、原子力機構高崎研の AVF サイクロトロンにより発生させたイオンビーム（320 MeV・$^{12}C^{6+}$）1 Gy を照射した。不定芽経由で再生した個体をバーミキュライト培地で順化後、ほ場で育苗した穂を用いて 2013 年 1 月開花試験を行い、生育および開花特性等について有望な個体を選抜した。また選抜した個体の切り下株をビニルハウス内で養成し、2013 年 6 月下旬に得られた芽を新母株として供試して、夏期高温期の露地母株栽培（定植：7 月 8 日、摘心：7 月 17 日、採穂：8 月 6 日、28 日、9 月 19 日）における採穂数を調査した。

3. 結果及び考察

2013 年 1 月開花の作型で 1,092 個体を供試して個体選抜試験を行い、低温開花性があり、花容、草姿や茎葉のボリュームが「新神」と同等以上の 13 個体を選抜した。供試系統は今回で 3 回目の炭素イオン照射による変異誘発となるが、集団全体では生育量はやや低下したものの極端に低下した個体は少なく、生育量が概ね「新神」と同等以上の個体が約 20%あった（データ省略）。

選抜した 13 個体は増殖後に系統として母株採穂数を調査した（Fig. 1）。1 株あたりの採穂数が、「新神」並に改善した系統は得られなかったが、「C10-g-46」より採穂数が約 20%以上改善した系統が 4 系統得られた。これらの系統では、葉の奇形やわい化等の不良変異は見られなかった。

また選抜した 4 系統は、2013 年 12 月と 2014 年 3 月開花で系統選抜試験を行ったが、この中でも「C12-i-4」は、「新神」と比べて茎葉のボリュームが同等かそれ以上であり、「C10-g-46」と同等の低温開花性を示したため、有望系統として選抜した（Fig. 2）。

以上のことから、生育特性や DNA 量が減少していない個体への低線量の照射を行うことで、通算 3 回のイオンビーム照射による変異誘発でも、不良変異を伴わずに段階的な特性改良が可能であることが示された。

References

1) 田之頭優樹ら、第6回高崎量子応用研究シンポジウム要旨集 (2011) 107.
2) 上野敬一郎ら、園芸学研究12 (2013) 245.

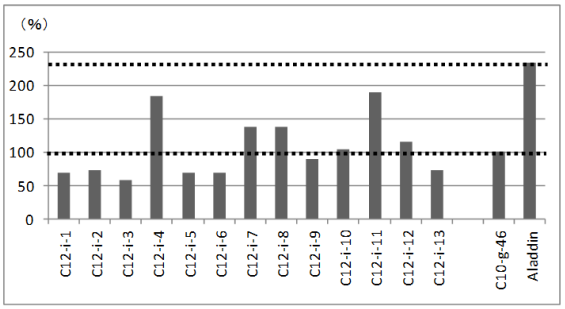

Fig. 1 Evaluation of the efficiency of shoot production in the mutant lines derived from the irradiated leaf tissues of “C10-g-46”. The data are relative number of shoots produced in each line, with that in “C10-g-46” being 100 percent. Dotted lines represent the data of “C10-g-46” and “Aladdin”.

Fig. 2 Selected mutant line “C12-i-4”.

3‐41 Study on the Sample Preparation Method for Ion Beam Irradiation in *Citrus unshiu*

Y. Matsuo [a)], Y. Hase [b)], H. Takeshita [a)] and A. Noutomi [a)]

[a)] Saga Prefectural Agricultural Fruit Tree Experiment Station,
[b)] Medical and Biotechnological Application Division, QuBS, JAEA

We examined the two preparation methods for ion beam irradiation to efficiently obtain the regenerated plants. Seeds of 'Kawada unshu' and 'Ohtsu 4 gou' were sown at 4 or 5 weeks before irradiation. Both hypocotyls and roots were cut with 20-mm length at 1 week before irradiation. Alternatively, only hypocotyls were cut with 60-mm length. The regeneration rates from the irradiated seedlings were generally higher in those prepared with the former method.

はじめに

ウンシュウミカンは、多胚性種子のために交雑育種による品種改良には多数の制約がある。このため新品種開発のほとんどは枝変わり若しくは珠心胚実生の中から突然変異個体を選抜することによって行われている。我々は、珠心胚実生へのイオンビーム照射により、突然変異個体の選抜を進めている。ここでは、より効率的に照射組織由来個体を獲得するために、照射試料の調整方法について検討した。

材料及び方法

供試材料として、中生ウンシュウミカン'川田温州'及び'大津4号'を用い、後述する2種類の方法で照射試料を調整し、発芽実生胚軸へイオンビームを照射した。高崎量子応用研究所のAVFサイクロトロンからの炭素イオンビーム($^{12}C^{6+}$ 320 MeV)を用いて2及び4 Gyの線量を照射した。

試験 1: ビーム照射 4 週間前に種子をシャーレに播種し、照射 1 週間前に発芽した幼実生の胚軸及び根部をそれぞれ約 20 mm の長さに切断してプラ壺(1/2 MS 培地)へ移植した(Table 1)。切断面より発生したカルスに照射を行った。照射後、プラントボックス(1/2 MS 培地)に移植し、出芽・伸長を開始した個体は馴化培地にて継代培養を行った。

試験 2: 組織の切断部位を少なくするため、ビーム照射4〜5 週間前に種子をシャーレに播種し、照射 1 週間前に発芽した幼実生の胚軸を約 60 mm の長さに切断した。根の切断は行わなかった。照射前にスチロールケースに配置した個体の胚軸切断面に照射した。乾燥防止のため、支持体には水分を十分に吸水させた。照射後の個体は育苗バットに移植した。さらに、乾燥防止のために照射部位をパラフィルムで巻き、ビニルにて育苗バットを覆った。

Table 1 Conditions of the sample preparation.

	Experiment 1	Experiment 2
Hypocotyl length	20 mm	60 mm
Cutting of roots	+	–
Root length	20 mm	> 50 mm
Medium	Gelrite	Cotton

結果及び考察

試験 1: '川田温州'の再分化率は、2 Gy 区では 61.9%、4 Gy 区では 39.7%となった。'大津 4 号'の再分化率は、2 Gy 区では 54.9%、4 Gy 区では 39.1%となった。4 Gy 区は両品種ともほぼ同様の再分化率となった(Table 2)。

試験 2: '川田温州'の再分化率は、2 Gy 区では 44.0%、4 Gy 区は 40.6%となった。'大津 4 号'の再分化率は、2 Gy 区は 43.1%となった。4 Gy 区は 33.3%となり、「試験1」の処理による照射個体よりも再分化率は低かった(Table 3)。

これらの結果から、切断部位を少なくすることによって植物体への影響を小さくすることを試みたが、'川田温州'の 4 Gy 区を除き、「試験 2」は「試験 1」よりも再分化率が低かったことから、調整が比較的容易な「試験 1」の方法で試料を調整する方が良いと考えられた。

Table 2 Number of regenerated plants (Experiment 1).

		0 Gy	2 Gy	4 Gy
Kawada -unshu	No. of irradiated plants	95	310	267
	No. of regenerated plants	74	192	106
	Regeneration rate (%)	77.9	61.9	39.7
Ohtsu 4 gou	No. of irradiated plants	97	852	957
	No. of regenerated plants	68	468	374
	Regeneration rate (%)	70.1	54.9	39.1

Table 3 Number of regenerated plants (Experiment 2).

		0 Gy	2 Gy	4 Gy
Kawada -unshu	No. of irradiated plants	95	134	138
	No. of regenerated plants	74	59	56
	Regeneration rate (%)	77.9	44.0	40.6
Ohtsu 4 gou	No. of irradiated plants	97	65	84
	No. of regenerated plants	68	28	28
	Regeneration rate (%)	70.1	43.1	33.3

3 - 42 A Study on Optimum Irradiation Dose of Gamma-ray and Carbon Ion Beams in Grain Amaranth

K. Nemoto [a)], A. Tsurukawa [a)], M. Minami [a)], K. Matsushima [a)] and Y. Hase [b)]

[a)] Graduate School of Agriculture, Shinshu University
[b)] Medical and Biotechnological Application Division, QuBS, JAEA

Grain amaranths (*Amaranthus* spp.) have excellent nutritional value and ample capacity for growth under drought, heat and soil nutrient deficiency. However, breeding works of the crop are very limited. In this study, as a first step to obtain new breeding materials by induced mutations, we decided the optimum irradiation dose of both gamma-ray and 320 MeV carbon ion beams using six strains of *A. cruentus*. As a result of survival curve, strains difference of the optimum irradiation dose was observed ranged from 200 to 500 Gy in gamma-ray and from 60 to 120 Gy in 320 MeV carbon ion beams, respectively.

アマランサス(*Amaranthus* spp.)は、中南米起源のヒユ科の作物で、子実中には必須アミノ酸のリジンや鉄分、カルシウム等のミネラルが豊富に含まれる。また、セシウム吸収能力の高い植物の一つとしても知られ、環境修復への利用の可能性を秘めている。しかしながら、これまでのアマランサス育種は既存の遺伝資源を系統選抜したものが多く、利用できる育種素材が限られているのが現状である。そこで本研究では、新たな有用変異体の獲得とその育種利用を目的とし、第一段階として変異原であるガンマ線および炭素イオンビームの最適照射線量を決定した。

＜材料および方法＞

信州大学が保有する *A. cruentus* の 6 系統・品種(GA5252、GA5252・4x、U-84、U-100、メキシコ系および伊那市桃色系統)を実験に供試した。

①^{60}Co ガンマ線照射:高崎量子応用研究所において、200、400、600、800、1,000、1,200、1,400、1,600、1,800、2,000 Gy の 10 線量区で照射した。照射した種子および無照射種子(各系統 50 粒)を 78 穴セルトレイに播種し、生育させた。

②イオンビーム照射:高崎量子応用研究所にて 320 MeV 炭素イオンビームを 60、90、120、150、180、210 Gy の 6 線量区で照射し、線量ごとに約 50 粒をセルトレイにて栽培した。

ガンマ線およびイオンビーム各処理区の出芽率および生存率を調査し、作成した生存率曲線のショルダー線量より最適線量を決定した。また、収穫期にランダムに各処理区 10 個体を選抜し、稔実率を算出した。

＜結果および考察＞

①ガンマ線の最適照射線量の検討:

1,200 Gy を超える線量では全系統で生存率が 0%となった。生存率曲線における各系統のショルダー線量には系統間差が認められ、GA5252 が 500～600 Gy と最も高く、GA5252・4x、伊那市桃色系統、U-100 およびメキシコ系が 400～500 Gy、U-84 が 200～400 Gy の順となった(Fig. 1)。この結果に稔実率の結果を合わせると、ガンマ線の最適照射線量は GA5252 が 500 Gy、GA5252・4x、U-100 およびメキシコ系が 400 Gy、伊那市桃色系統が 300 Gy、U-84 が 200 Gy であると考えられた。

他の作物では、イネ品種「ひとめぼれ」が約 200 Gy、オオムギ 400 Gy という線量が変異誘発に利用されており、今回供試した 6 系統の最適照射線量はこれら植物と同等もしくは高かった。

②320 MeV 炭素イオンビームの最適照射線量の検討:

生存率曲線より得られた各系統のショルダー線量にはガンマ線同様系統間差が認められ、GA5252 の 120～140 Gy が最も高く、続いてメキシコ系の 100～120 Gy、伊那市桃色系統の 90～120 Gy、GA5252・4x および U-100 の 60～90 Gy のであったが、U-84 では、明確なショルダーを得ることが出来なかった(Fig. 2)。しかしながら、0 から 120 Gy で照射した予備実験において、U-84 は 40～60 Gy でショルダーを示しており、この結果と稔実率を合わせた結果から、今回供試した各系統の 320 MeV 炭素イオンビームの最適照射線量は GA5252 が 120 Gy、メキシコ系が 100 Gy、伊那市桃色系統が 90 Gy、GA5252・4x および U-100 が 60 Gy であると考えられた。

今回用いた 2 つの変異原に対する放射線感受性には相関が認められ、U-84 または U-100 が最も高く、GA5252 が最も低かった。また、供試した系統の最適照射線量の生物学的効果比(RBE)は、3.3～4.2 となり、シロイヌナズナの約 5、イネ(ひとめぼれ)の約 3 の中間の値を示した。

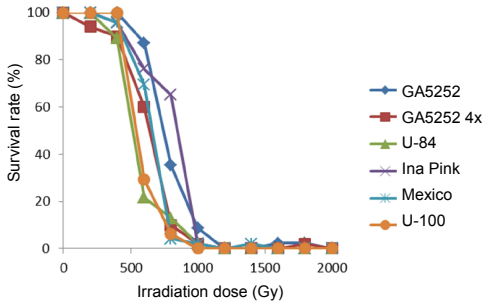

Fig. 1 Survival curves for gamma-ray.

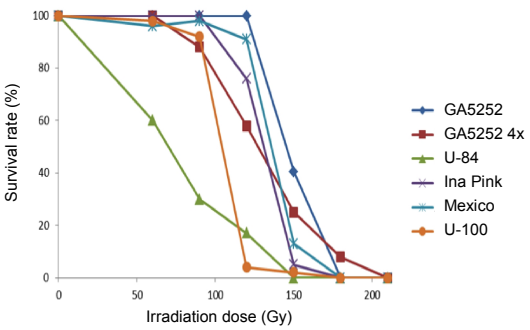

Fig. 2 Survival curves for carbon ion beams.

3 - 43 Screening of Salt Tolerant Mutants Regenerated from Irradiated Stem Segments of Lombardy Poplar (*Populus nigra*)

K. K. Biswas, Y. Hase and Y. Oono

Medical and Biotechnological Application Division, QuBS, JAEA

Species of the genus *Populus* are ecologically important trees and often serving as a vegetative pioneer species because of their fast growth rates. The rapid growth of poplar is dependent on access to sufficient water in plantation sites and this is problematic. To overcome this problem, a forward genetics approach has been taken for developing salt/drought tolerant mutants by combination of radiation mutagenesis and *in vitro* regeneration in *Populus*. There is evidence that induced mutation with radiation mutagenesis has a great potential to produce new cultivars with wider mutation spectrum[1].

As demonstrated in previous reports, we screened regenerated *Populus nigra* shoots regenerated from stems exposed with cobalt-60 source of gamma rays maintained in Food Irradiation Facility at JAEA (Takasaki, Japan) and found five candidates of salt tolerant mutant, named *gamma1* to *5*, which was able to develop root system in root inducing medium [RIM; Murashige and Skoog (MS) salts, 30 g/L sucrose (suc), 1 mL/L B5 vitamins (B5v), 4 g/L agar, 2 g/L Gelrite, 0.5 mg/L 4-indole-3-butyric acid and 0.02 mg/L 1-naphthaleneacetic acid, (pH 5.8)] supplemented with 75 mM NaCl in first screening [2]. However, only 2 of 5 lines, *gamma 1* (*g1*) and *gamma 5* (*g5*) developed from gamma-ray- (5 or 7 Gy, respectively) irradiated stem explants reproducibly generate roots in the medium mentioned above [2,3].

Detailed characterization, such as growth and salt tolerance of *g1* and *g5* in soil is under progress. Preliminary observation suggests root growth of *g1* is more vigorous than wild type (Table 1), whereas aerial parts of *g5* grow slower than wild type and *g1* (data not shown).

Although, *g1* and *g5*, might be candidates of putative salt tolerant mutants, only about 25% stem segments of both lines produced roots in RIM with 75 mM NaCl[2]. The low frequency in root production in NaCl medium may be attributed to that these plants are chimeric. The screening system we used is based on root induction ability in NaCl-supplemented RIM of the regenerated "shoots", and shoots themselves are not directly exposed to NaCl during selection. If shoots were regenerated from salt tolerant roots, the chimeric effects may remain in lower level. From this point of view, shoot regeneration system from "root explants" were developed (Table 2). Using this protocol, root induction ability of shoots from salt tolerant roots of *g1* and *g5* will be re-confirmed in NaCl-supplemented RIM.

We also successfully obtained at least 2 salt tolerant candidates regenerated from stem segments irradiated with 320 MeV $^{12}C^{6+}$ ion beams accelerated by the azimuthally varying field cyclotron in Takasaki Ion Accelerators for Advanced Radiation Application, JAEA. Propagation of these candidates is in progress and regenerated shoots from salt tolerant roots will be subjected to confirmation test in NaCl-supplemented RIM.

Table 1 Number of roots produced from stem segments.

Line	No. of stem tested	No. of roots (Days)						
		5	10	15	20	25	30	35
Wild type	30	0	0	7	32	54	59	61
g1	30	0	6	14	49	81	88	89

Stem segments (6 cm) were put in medium [MS salts, 30 g/L suc, 1 mL/L B5v, 4 g/L agar, 2 g/L Gelrite, (pH 5.8)] and total number of roots produced from all stems was collectively counted every 5 days. *g1* developed roots earlier and overall root number in *g1* is higher than that in wild type.

Table 2 Effect of various concentrations of indole-3-acetic acid (IAA) and 6-benzylaminopurine (BA) on shoot regeneration from roots.

Conc. (mg/L)		% shoot regeneration	No. of shoots/explants
IAA	BA		
0	0	0	-
0.05	0	0	-
0	0.25	0	-
0.02	0.12	45 ±3.2	2.1±0.2
0.05	0.25	95±2.5	3.2±0.1
0.1	0.5	78±3.7	1.3±0.2
0.2	1.0	77±3.6	1.1±0.1
0.5	2.5	23±5.1	n.a.

Regeneration ratio was monitored in medium (MS salts, 30 g/L suc, 1 mL/L B5v and 3 g/L Gelrite, pH 5.8) with IAA and BA. The best combination was 0.05 mg/L IAA and 0.25 mg/L BA. n.a.; data is not available.

References

1) S. Nagatomi et al., Acta Horticult. 508 (2000) 69.
2) K. K. Biswas et al., JAEA Takasaki Annu. Rep. 2012 JAEA-Review 2013-059 (2014) 107.
3) K. K. Biswas et al., Am. J. Plant Sci. 3 (2012) 1181.

3 - 44 Metabolome Analysis of Leaves of *Rumex obtusifolius* L. Irradiated with Ion Beams

A. Miyagi [a)], S. Kitano [a)], Y. Oono [b)], Y. Hase [b)] and M. Kawai-Yamada [a, c)]

[a)] Graduate School of Science and Engineering, Saitama University,
[b)] Medical and Biotechnological Application Division, QuBS, JAEA,
[c)] Institute for Environmental Science and Technology, Saitama University

Rumex obtusifolius (Polygonaceae) is a weed, which spreads all over the world. It contains amino acids and ascorbate (Vitamin C) more than other edible *Rumex* species (Miyagi et al., 2010). On the other hand, it highly accumulates soluble oxalate, which causes renal syndrome for vertebrates. Thus we aimed to lower oxalate contents in *R. obtusifolius* that can be used as a pasture by radiation breeding. In the present study, plant seeds irradiated with several doses of carbon ion beams ($^{12}C^{6+}$) were used to analyze effects of the radiation to oxalate contents and other metabolites using capillary electrophoresis-mass spectrometry (CE-MS). Results showed that the oxalate contents of leaves were increased by the irradiation of ion beams on the contrary to the case of the irradiation with gamma rays. High oxalate plants tended to contain high levels of organic acids. Amino acids and phosphorylated organic acids were decreased in these plants.

エゾノギシギシ（タデ科）はヨーロッパ原産の多年生草本である。他の近縁種よりもアミノ酸やビタミン C 等の有用成分を多く含み、繁殖力も強い。播種やバイオマス維持等のコスト削減が見込めるため、新規の牧草としての利用が期待できる。しかし、エゾノギシギシは腎結石の原因物質である可溶性シュウ酸を葉に高蓄積するため、牧草化のためには低シュウ酸系統の作出が必須である。これまでに、ガンマ線の種子照射により M1 世代の低シュウ酸化を見出した。本研究では、より大きな変異効果が期待できる高 LET 放射線である炭素イオンをエゾノギシギシの種子に照射し、低シュウ酸個体作出のためのメタボローム解析を行った。

まず、高崎量子応用研究所において 0-100 Gy のイオンビーム（$^{12}C^{6+}$, 320 MeV）を照射したエゾノギシギシの種子を発芽させ、第 3 葉を回収した。50%メタノールで葉の代謝物を抽出し、キャピラリ電気泳動-質量分析装置（CE-MS）を用いてシュウ酸含有量の測定を行った。その結果、イオンビーム照射個体におけるシュウ酸含有量が非照射個体に比べ増加することが明らかになった（Table 1）。

Table 1 Oxalate contents in leaves of *R.obtusifolius* irradiated by ion beams.

Ion beam (Gy)	Oxalate content (μmol/gFW)
0	40.9 ± 8.3
5	55.5 ± 9.8**
10	61.3 ± 12.1**
20	58.5 ± 19.0**
30	76.0 ± 11.3**
70	55.8 ± 12.0**
100	56.3 ± 7.3*

Seeds irradiated with 0-100 Gy of ion beams were germinated and third leaves were used for oxalate measurement. (*; p<0.05, **; p<0.01).

次に、シュウ酸含有量の違いがその他の代謝物に及ぼす影響を明らかにするため、シュウ酸含有量が多い個体（138-166 μg/FW）、平均的な個体（73-80 μg/FW）、少ない個体（34-42 μg/FW）をそれぞれ 10 サンプルずつ選抜し、計 30 個体の葉のメタボローム解析を行った。その結果、シュウ酸含有量の高い植物体ほど有機酸が増加し、アミノ酸および糖リン酸の減少傾向が見られた（Fig. 1）。イオンビーム照射により、アミノ酸合成が阻害され TCA サイクルの有機酸が蓄積し、結果としてシュウ酸が蓄積したと考えられる。

Reference

1) A. Miyagi et al., Metabolomics 6 (2010) 497-510.

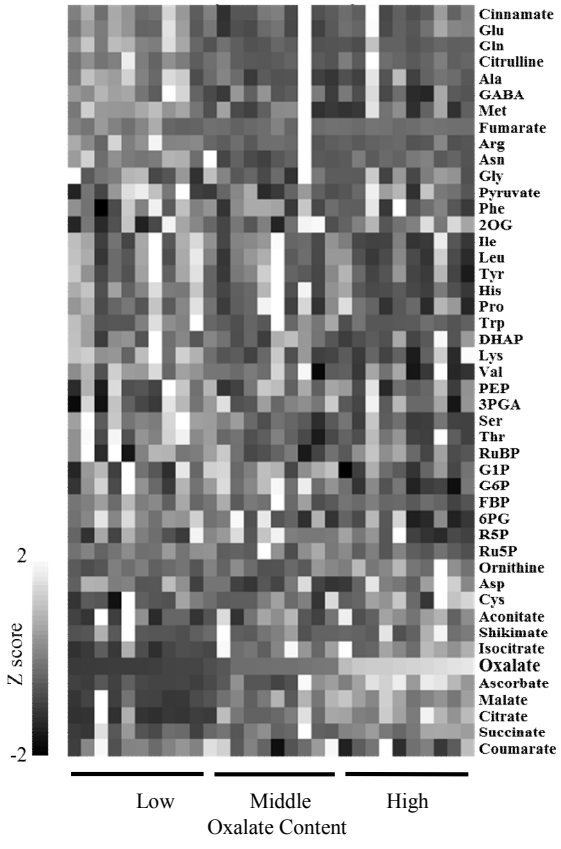

Fig. 1 Metabolome analysis of leaves of *R. obtusifolius* germinated from seeds irradiated by ion beams. Heatmap is based on Z scores of metabolite data.

3 - 45 Analysis of DNA Strand Breaks Induced by Carbon Ion Beams in *Arabidopsis*

M. Teranishi [a)], H. Yamaguchi [a)], A. N. Sakamoto [b)] and J. Hidema [a)]

[a)] Graduate School of Life Sciences, Tohoku University,
[b)] Medical and Biotechnological Application Division, QuBS, JAEA

Introduction

Ion beams induce DNA damage, such as strand breaks, possibly resulting in an increased mutation frequency. Thus, ion beams have been used as effective mutagens in plant breeding[1)]. To elucidate the mechanism of mutation induction in plants, it is important to know about which DNA damage converted into a mutation. However, little is known about the types and extent of DNA damage induced by ion beams in vigorous plant cells. It is known that DNA double-strand breaks are one of the critical lesion for inducing mutation. In this study, we examined the method for determining the number of DNA strand breaks induced by carbon ion beams in *Arabidopsis* seedlings.

Experimental procedures

Seeds of *Arabidopsis thaliana* (wild-type Colombia) were aseptically sown on Murashige and Skoog agar plates. The plants were grown at 23 °C under a 12-h light and 12-h dark cycle for 10 days. The seedlings were irradiated with carbon ion beams (320 MeV $^{12}C^{6+}$) from an AVF cyclotron. After irradiation, whole plants were harvested immediately in order to detect the induced DNA strand breaks. For determining the number of DNA strand breaks, we modified the method for detecting UV-induced DNA damage (CPD: cyclobutane pyrimidine dimer) described in Hidema et al[2)]. In brief, frozen plant samples were used for preparing an agarose plug. The agarose plugs were incubated in proteinase K containing buffer. After rinsing the plug with Tris-EDTA buffer, the DNA was denatured by treated with the alkaline mixture. The agarose plugs were subjected to alkaline agarose gel electrophoresis using static field electrophoresis and biased sinusoidal field gel electrophoresis. DNA molecules were dispersed according to their single-strand molecular lengths. The number of DNA strand breaks was calculated using the molecular length standard curve and the quantity of DNA at each migration position as shown by the quantitative image data. Using this method, the number of both single-strand and double-strand DNA breaks can be determined.

Results and discussion

Figure 1 represents dose response curve for DNA strand breaks induced by carbon ion beams. The number of DNA strand breaks increased with increasing dose of carbon ion beams (Fig. 1). This result indicates that the number of DNA strand breaks can be detected using our method. Irradiation of seedlings with 960 Gy of carbon ion beams resulted in up to 2.3 strand breaks per megabase (Mb). Given that the total size of the *Arabidopsis* genome is approximately 135 Mb, irradiation of seedlings with 960 Gy of carbon ion beams can theoretically induce approximately 310 strand breaks per genome.

In this study, we determined the number of strand breaks including single-strand and double-strand DNA breaks induced by carbon ion beams in *Arabidopsis* seedlings using the denatured agarose gel electrophoresis. It is thought that, only DNA double strand breaks can be detected using the non-denatured agarose gel electrophoresis. To elucidate the mechanism of mutation induction in plants, measurement of the extent of DNA damage other than DNA strand breaks should be needed. It is thought that DNA damage other than DNA strand breaks can be detected by modifying our method. In our previous method, we used the enzyme which specifically cleaves single DNA strands at sites of CPDs[2)]. Thus, it is thought that we can apply our method to oxidative DNA damage using the enzyme which specifically cleaves single DNA strands at sites of oxidative DNA damage. Further analysis is in progress.

References

1) A. Tanaka et al., J. Radiat. Res. 51 (2010) 223-33.
2) J. Hidema et al., Plant Cell 12 (2000) 1569-78.

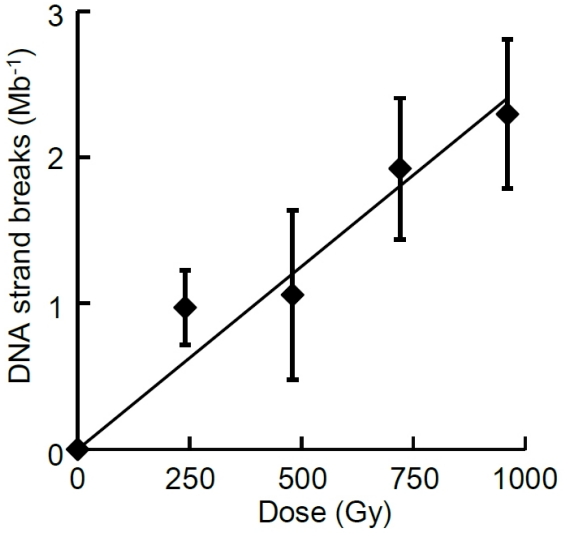

Fig. 1 Dose response curve for DNA strand breaks induced by 320 MeV $^{12}C^{6+}$ in *Arabidopsis* seedlings. The data points represent the mean ± SD of at least three experiments.

3 - 46 Mutation Breeding of New Horticultural Varieties by Irradiation of Ion Beams

K. Kawamura [a)], K. Yoshihira [a)] and Y. Hase [b)]

[a)] Kamitsuga Area Flower Production Promotion Liaison Conference,
[b)] Medical and Biotechnological Application Division, QuBS, JAEA

The optimal condition for irradiation of ion beams to five horticultural crops were examined. The optimum irradiation doses for Mandevilla seeds and Dahlia plantlets were 25-30 Gy (320 MeV $^{12}C^{6+}$) and 8-10 Gy (107 MeV $^{4}He^{2+}$), respectively. The survivability for irradiation of Calibrachoa seeds, Iberis cuttings and Marguerite cuttings were not able to evaluate because of technical problems on transportation and nurseries.

本研究では、カリブラコア(*Calibrachoa* spp.)、マンデビラ(*Mandevilla* spp.)、ダリア(*Dahlia* spp.)、イベリス(*Iberis* spp.)、マーガレット(*Argyranthemum* spp.)、等の園芸植物でイオンビーム照射による花色・花形、草姿等の突然変異体を作出し、実用性の高い花きの新品種育成を行うことを目的としている。今回は変異誘発に向けた照射条件の検討を行った。

【方法】

(1) 照射線種と試験線量

高崎量子応用研究所の AVF サイクロトロンを利用し、5種類の材料に対して以下の照射を実施した。

①カリブラコア種子:炭素イオン(320 MeV):10～120 Gy
②マンデビラ種子:炭素イオン(320 MeV):5～30 Gy
③ダリア植物体:ヘリウムイオン(107 MeV):4～16 Gy
④イベリス植物体:炭素イオン(320 MeV):3～4 Gy、およびヘリウムイオン(107 MeV):4～20 Gy
⑤マーガレット植物体:炭素イオン(320 MeV):2～12 Gy、およびヘリウムイオン(107 MeV):2～50 Gy

(2) 照射後の管理

照射後の種子は調整ピート等を混合した用土には種し、その後の生育にあわせてセルトレイやポリポットに移植して育成した。植物体はセルトレイ等に植付け、その後生育にあわせてポリポットに鉢上げし、育成した。

【結果及び考察】

(1) カリブラコア種子

炭素イオン(320 MeV)を 75 Gy 以上照射した区では発芽せず、50 Gy 照射区では発芽後に枯死する個体が多く生存率が低くなった。また、生存した個体についても葉色が淡く、生育不良のものが多いため、照射線量が高すぎることが考えられる。今後は10 Gy付近のより低い線量を中心に最適照射線量の検討を継続する必要がある。

(2) マンデビラ種子

炭素イオン(320 MeV)10～20 Gy 照射区の発芽率は90%を超えたが 25 Gy 以上照射した区では発芽率が低下する傾向が見られた(Fig. 1)。このため、変異誘発に適した照射線量は 25～30 Gy と考えられる。

(3) ダリア植物体

ヘリウムイオン(107 MeV)4～8 Gy 照射区の生存率は40%を超えたが、12 Gy照射区で40%を下回り、16 Gy照射区では 5%以下となった(Fig. 2)。このため、変異誘発に適した照射線量は 8～10 Gy と考えられる。

(4) イベリス植物体

炭素イオン(320 MeV)とヘリウムイオン(107 MeV)共に照射線量に関わらず低い生存率を示した。照射サンプルはセルトレイに挿し芽し発根させたものを使用したが、照射後の植え付けの際に発生する根痛みが原因で生存率が低下したと考えられる。今後、サンプルの作成方法の検討し、再調査を行う。

(5) マーガレット植物体

炭素イオン(320 MeV)とヘリウムイオン(107 MeV)共に照射線量に関わらず低い生存率を示した。照射サンプルはイベリス同様、セルトレイに挿し芽し発根させたものを使用したが、照射後に腐れが発生し枯死する個体が多くみられた。今後、サンプル調整方法や用土の検討を行う。

本研究成果は独立行政法人日本原子力研究開発機構の先端研究施設共用促進事業によるものである。

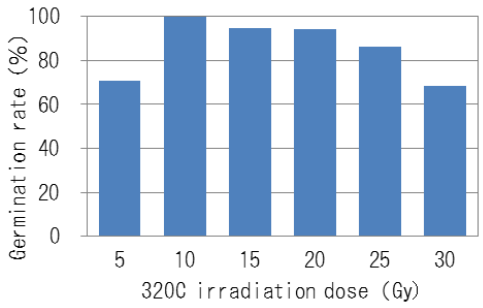

Fig. 1 The relationship between irradiation dose and germination rate of Mandevilla seedlings.

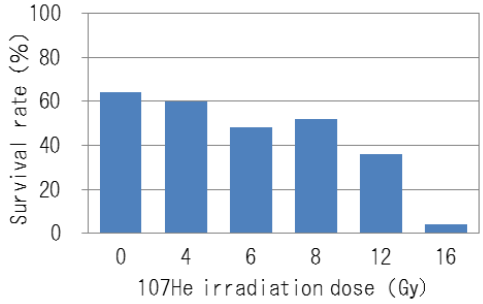

Fig. 2 The relationship between irradiation dose and survival rate of Dahlia plantlets.

3 - 47 Development of Cesium-accumulating Bacteria by Ion Beam Breeding Technology

K. Satoh [a)], R. Ueda [a,b)], Y. Hase [a)], I. Narumi [c)] and Y. Oono [a)]

[a)] Medical and Biotechnological Application Division, QuBS, JAEA,
[b)] Division of Biotechnology, Graduate School of Engineering, Maebashi Institute of Technology,
[c)] Department of Life Sciences, Faculty of Life Sciences, Toyo University

After the Great East Japan Earthquake on March 11, 2011, the accident at the Fukushima Daiichi Nuclear Power Plant of Tokyo Electric Power Company occurred a serious radioactive contamination at an extensive area. Therefore, it is an urgent issue to remove and recover the radioactive materials from contaminated environments. Especially, a long-term measures of cesium (Cs)-137 which has long physical half-life (approximately 30 years) is required for monitoring decontamination procedures. Bioremediation uses biological organisms to solve an environmental problem, which draws attention as a technology with a low environmental burden compared with physical and chemical technologies. Microorganisms were often used for developing a technology to remove and recover contaminated environments. However, microorganisms are sometimes not enough effective to achieve efficient recovery. Therefore, enhancing the functionality of microorganisms is needed to promote the active use of bioremediation. It is expected to generate useful mutants with enhanced functions by unlocking microorganisms' latent potential using ion beam breeding technology.

It is appropriate to use the radioresistant microorganism under the radioactive contaminated environment. The members of the genus *Deinococcus* exhibit extraordinary resistance to the lethal and mutagenic effects of ionizing radiations. This resistance is attributed to its highly proficient DNA repair capacity. In addition, genetically modified *Deinococcus radiodurans* strains had been generated to use for bioremediation under highly radioactive contaminated environments[1,2]. This study began with the purpose of development of Cs-accumulating bacteria by ion beam breeding technology. To accomplish this purpose, we investigated which members are better suited for Cs-accumulation in the genus *Deinococcus*.

The suitable deinococcal species was selected as follow. Six *Deinococcus* species (*D. radiodurans*, *D. grandis*, *D. proteolyticus*, *D. radiopugnans*, *D. geothermalis* and *D. murrayi*) were cultivated at 30 °C for 20 h in TGY broth (10 mL), added $CsNO_3$ (final concentration; 1 μg/mL) and cultivated for another 20 h with agitation. Cells were harvested, washed and resuspended in sterilized water (0.5 mL). Cell suspensions were frozen and dried *in vacuo*. Freeze-dried (FD) cells were subjected to acid digestion with 6.5 M HNO_3 (2 mL) at 110 °C for 1 h and 140 °C for 1 h, drying at 80 °C for 20 h and finally resuspended in 0.1 M HNO_3 (1 mL). The Cs concentration in the cell was measured with an atomic absorption spectrometer (AAS) (Thermo Scientific, iCE 3400).

The non-radioactive Cs concentration in the *Deinococcus* cells exhibited over 4-fold compared with that of the *E. coli* by AAS analysis (Fig. 1). The intracellular Cs concentration serves as an indicator of the Cs-accumulating ability. This result suggested that *D. radiodurans* and *D. grandis* are best two suitable species for the development of high Cs-accumulating bacteria by ion beam breeding technology.

D. radiodurans and *D. grandis* cells were began to irradiate with ion beams for mutagenesis as follows. Cells were grown, harvested, resuspended and frozen as described previously[3]. FD cells were irradiated with five kinds of ion beams ($^{4}He^{2+}$ [50 MeV; 19.4 keV/μm], $^{12}C^{6+}$ [320 MeV; 86.2 keV/μm], $^{12}C^{5+}$ [220 MeV; 121.8 keV/μm], $^{20}Ne^{8+}$ [350 MeV; 440.8 keV/μm] and $^{40}Ar^{13+}$ [460 MeV; 1649.6 keV/μm]) accelerated by an AVF cyclotron at TIARA. The irradiated cells were cultivated at 30 °C with agitation to fix mutation. Candidates of high Cs-accumulating bacteria may be screened from the population of mutagenized cells by measuring the intracellular Cs concentration.

References

1) C. C. Lange et al., Nat. Biotechnol. 16 (1998) 929.
2) H. Brim et al., Nat. Biotechnol. 18 (2000) 85.
3) K. Satoh et al., JAEA Takasaki Annu. Rep. 2011 JAEA-Review 2012-046 (2013) 103.

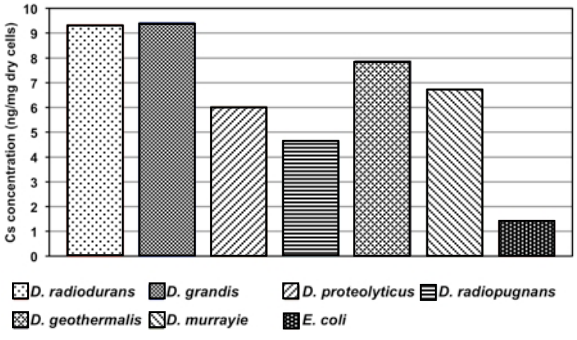

Fig. 1 The intracellular concentration of non-radioactive cesium in *Deinococcus* spp. and *Escherichia coli*.

3 - 48 Molecular Analysis of Polyphosphate Biosynthesis-related Genes in *Deinococcus radiodurans*

R. Ueda [a,b], K. Satoh [a], H. Hayashi [b], I. Narumi [c] and Y. Oono [a]

[a] Medical and Biotechnological Application Unit, QuBS, JAEA,
[b] Division of Biotechnology, Graduate School of Engineering, Maebashi Institute of Technology,
[c] Department of Life Sciences, Faculty of Life Sciences, Toyo University

Introduction

An enormous amount of radiocesium was released to the environment as a major radioactive contamination during the accident at the Fukushima Daiichi Nuclear Power Plant of Tokyo Electric Power Company after the Great East Japan Earthquake. Therefore, removing radiocesium from contaminated environment is an urgent issue. Polyphosphate is a linear polyanionic biopolymer of phosphate residues. The ability to store polyphosphate as granules in the cell was found to be widespread among microorganisms. Polyphosphate granules can be stabilized by the surrounding positive charged ions in cells, suggesting a possibility that the polyphosphate could accumulate harmful metal ions such as radiocesium to protect the cells from cytotoxicity[1]. Therefore, the highly accumulation of polyphosphate in microorganisms is important to improve bioremediation technology for removing radiocesium from contaminated environment. In general, polyphosphate kinase (PPK) and exopolyphosphatase (PPX) are responsible for polyphosphate synthesis and hydrolysis, respectively.

Deinococcus radiodurans exhibits extraordinary resistance to the lethal and mutagenic effects of ionizing radiations. In addition, *D. radiodurans* has been considered as a microorganism for bioremediation under highly radioactive contaminated environments[2,3]. In this study, we generated the polyphosphate biosynthesis-related genes (*ppk* and *ppx*) disruptant strains and characterized their disruption effect to clarify the role of polyphosphate in the accumulation of cesium in *D. radiodurans*.

Experimental procedures

D. radiodurans ppk and *ppx* disruptant strains were generated using a direct insertional mutagenesis technique. The *ppk* promoter region was replaced by the *groEL* promoter to generate a *D. radiodurans ppk* overexpressing strain. The intracellular level of polyphosphates was measured using a MicroMolar Polyphosphate Assay Kit (ProFoldin). *D. radiodurans* cells were cultivated at 30 ℃ in TGY broth (0.5% tryptone, 0.1% glucose, 0.3% yeast extract) until early stationary phase. The cells were harvested, washed twice with 10 mM HEPES (pH 7.4) and adjusted to an optical density at 600 nm of 0.5. Aliquots (30 μL) were mixed with 30 μL of fluorescent dye solution. Mixture was measured its fluorescence intensity at 550 nm (excitation 415 nm). The relative intracellular level of polyphosphate was normalized with the fluorescence intensity of wild-type strain.

Results and discussion

In order to characterize the disruption effects, we generated the *ppk* and *ppx* gene disruptant and *ppk* overexpressing strains in a wild-type background. To confirm gene disruption, the target allele of disruptant strains was amplified by genomic PCR. A single PCR product was observed in the *ppk* disruptant strain, indicating a complete disruption of the *ppk* gene. In contrast, the *ppx* gene disruptant strain invariably had heterozygous genomes, indicating that the *ppx* gene is essential for cell viability in *D. radiodurans*.

The intracellular level of polyphosphates in the disruptant and overexpressing strains was compared with that of the wild-type strain. The intracellular levels of polyphosphates in the *ppk* disruptant and overexpressing strains were almost same and slightly increased, respectively (Fig. 1). On other hand, the intracellular level of polyphosphates significantly increased in the *ppx* disruptant strains (Fig. 1). These results suggest that the *ppx* gene plays an important role in the accumulation of polyphosphate in *D. radiodurans*.

In the future, we will investigate the cesium accumulation and the sensitivity to gamma rays using the gene disruptant and overexpressing strains generated in this study.

References

1) C. Kuwahara et al., J. Environ. Radioact. 102 (2011) 138.
2) C. C. Lange et al., Nat. Biotechnol. 16 (1998) 929.
3) H. Brim et al., Nat. Biotechnol. 18 (2000) 85.

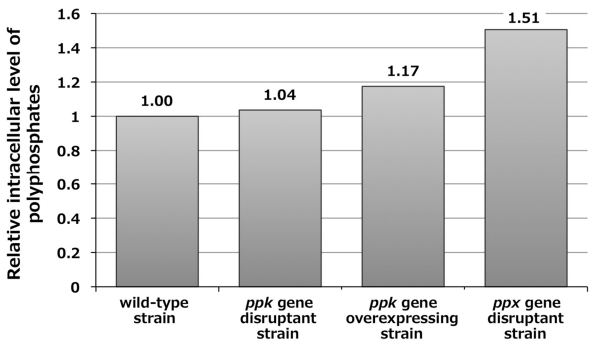

Fig. 1 Comparison of the intracellular polyphosphate level. Values represent the relative fluorescence intensity of signals normalized in relation to wild-type value of 1.

3 - 49 Molecular Analysis of Heavy Ion Induced Mutations in Budding Yeast *S. cerevisiae*

Y. Matuo [a)], Y. Izumi [a)], Y. Hase [b)], A. N. Sakamoto [b)] and K. Shimizu [c)]

[a)] Research Institute of Nuclear Engineering, University of Fukui,
[b)] Medical and Biotechnological Application Division, QuBS, JAEA,
[c)] Radioisotope Research Center, Osaka University

The ion beam has some outstanding characteristics in comparison with low LET radiations such as the gamma rays. An important characteristic of the ion beam is that it induces mutations with high frequency and through a broad range. Then the ion beam has been widely used as the mutagen for developing new varieties of plants and bacteria [1, 2]. To investigate the nature of mutations induced by accelerated ions in eukaryotic cells, the effects of carbon-ion irradiation were compared with those of gamma-ray irradiation in the budding yeast *Saccharomyces cerevisiae*. Carbon-ion irradiation at 100 Gy increased the mutation frequency in the *URA3* gene 100 times as compared to the spontaneous mutation frequency. The types of base changes consisted of transversion (68.7%), transition (13.7%) and deletion/insertion (17.6%). Most of the transversion mutations were G:C to T:A and all the transition mutations were G:C to A:T. We found that the base change mutations were often induced in 5'-ACA-3' and 5'-ACT-3' sequences. The most remarkable feature of the mutations induced by carbon ions was that the mutation sites were localized near the linker regions of nucleosomes, whereas mutations induced by gamma rays were located uniformly throughout the gene [3].

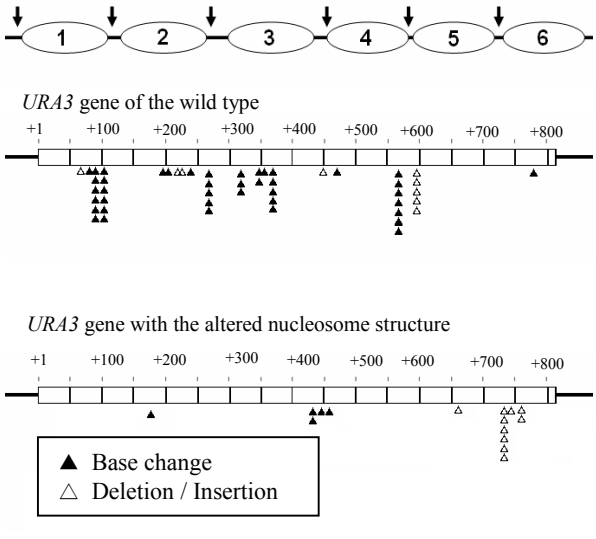

Fig. 1 Mutation spectrum induced by carbon-ion irradiation in yeast. Arrows indicate the position of linker DNA of the wild type [5]. Numbers refer to the nucleotide position of *URA3* gene. +1 is the A of the initiation codon ATG.

We hypothesized that the locus of mutations might be concerned with the nucleosome structure. Studies of the nucleotide excision repair and photorepair suggested that the DNA damage was repaired slowly on the nucleosomes but was repaired quickly on the linkers [4]. We designed new experiment to clarify this hypothesis. The yeast strain carrying the *URA3* gene on the altered nucleosome structure was generated by genetic manipulation using pAUR112 plasmid and Aureobasidin transformation system (TaKaRa). The yeast cells were irradiated with carbon ions (LET 107 keV/μm) with the dose of 100 Gy.

The frequency of the *URA3* mutation of the yeast strain that has the *URA3* gene with altered nucleosome was approximately 5 times of the wild strain (data not shown). Figure 1 shows the mutation spectrum in the *URA3* gene and Table 1 shows the summary of the sequence analyses. The mutation position in the wild strain was inconsistent with that in the yeast strain carrying the *URA3* gene with altered nucleosome. It is suggested that the locus of mutations depends on the nucleosome structure. We will accumulate the data further to examine the above hypothesis. Moreover, we are going to determine the nucleosome structure of *URA3* located on the altered nucleosome.

References

1) A. Tanaka et al., J. Radiat. Res. 51 (2010) 223.
2) T. Masubuchi et al., JAEA Takasaki Annu. Rep. 2011 JAEA-Review 2012-046 (2013) 110.
3) Y. Matuo et al., Mutat. Res. 602 (2006) 7.
4) R. E. Wellinger et al., EMBO. J. 16 (1997) 5046.
5) S. Tanaka et al., J. Mol. Biol. 257 (1996) 919.

Table 1 DNA sequence context of mutations in *URA3* caused by carbon ion beam.

Position	Change	Sequence context	Numbers
+167	G to A	AAT TTG TTT	1
+417	A to T	AGA AGT AGC	2
+419	T to A	AGA AGT AGC	1
+421	A to G	TGA AGC AAC	1
+662	Insert A	GGT GA↑T GAT	1
+718	Insert A	AAA ↑GGG AAG	6
+740	Insert A	TAG A↑GG GTG	1
+761	Insert C	AGC A↑GG CTG	2
Total			15

Arrow indicates the insertion site.

3 - 50 Genome Analysis of the High Temperature Tolerant Mutant of *Bradyrhizobium japonicum* USDA110 Generated by Ion-beam Irradiation

K. Takeda [a,b], K. Satoh [b], I. Narumi [c], Y. Oono [b], N. Ohkama-Ohtsu [d] and T. Yokoyama [d]

[a] United Graduate School of Agricultural Science, Tokyo University of Agriculture and Technology,
[b] Medical and Biotechnological Application Division, QuBS, JAEA,
[c] Department of Life Sciences, Faculty of Life Sciences, Toyo University,
[d] Institute of Agriculture, Tokyo University of Agriculture and Technology

Bradyrhizobium japonicum is a soybean-nodulating rhizobium that has an ability to elicit the formation of specialized organs called nodules on their leguminous host roots for the symbiotic nitrogen fixation. *B. japonicum* strain USDA110 is one of the most popular inoculants for soybean in the temperate area. The strain had been widely used in the fields of molecular genetics, physiology and ecology, largely because of its superior characteristics with respect to symbiotic nitrogen fixation.

Recently, many researchers in Asian agricultural institutes are trying to develop biofertilizers. However, several researchers point out constraints on application of biofertilizers. Major constraint of biofertilizer utilization in agricultural practice is a viability loss of beneficial microorganisms in biofertilizers by high temperature stress during both storage and transportation. Therefore, we have tried to improve high temperature tolerance of USDA110 using carbon-ion beams ($^{12}C^{5+}$, 220 MeV) accelerated by an AVF cyclotron at TIARA. Consequently, we have obtained a high temperature tolerant mutant that can maintain a high survival rate at 42 °C for at least 7 days in yeast-mannitol broth medium, and named it as M14.

The genome sequence of M14 was determined by a whole-genome shotgun strategy. The pyrosequencing data were accumulated using a GS Junior System (Roche Applied Science, Mannheim, Germany) according to the manufacture's protocol. Mutation sites were predicted by comparing these data to the reference sequence data of USDA110 (wild type) by a GS Reference Mapper software. Predicted mutation sites were confirmed using the Sanger sequencing method one by one. In consideration of spontaneous mutations in USDA110, the mutation sites were sequenced using the both strains' genome.

It was revealed that a large-scale structural change in the circular DNA genome was occurred in M14. Namely, a DNA region at the coordinates 4,029,225 - 5,299,697 (1,270,473 bp; 1.27 Mbp) was inverted (Fig. 1). This region contained 8 tRNAs and 1,139 genes with various functions. Interestingly, the inverted region was flanked by a certain sequence of 5'-TCAAA-3'. In addition to a large inversion, the GS Reference Mapper software predicted base mutations at 84 sites. However, it was found out that only 18 sites were unique to M14, and the remaining 66 sites existed in both M14 and parent USDA110. These 18 mutations were categorized into 16 single base substitutions (subdivided into 8 transitions and 8 transversions), 1 single base insertion and 1 single base deletion. Ten out of 18 mutation sites were distributed in individual structural genes, and the remaining 8 mutation sites were located in non-coding regions. Nine out of 10 structural genes were expected to have some influences resulting from amino acid substitutions at the translational level (Fig. 2).

The acquirement of high temperature tolerance in M14 could be attributed to these 18 base mutations and/or a large-scale inversion. In the future, we will conduct further analysis on these mutations in order to decipher the molecular mechanisms of high temperature tolerance of M14.

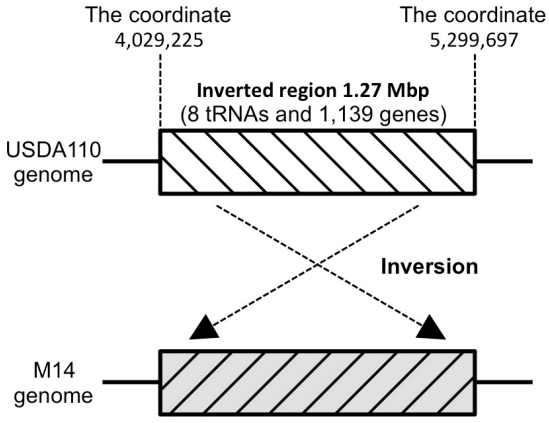

Fig. 1 Illustration of inverted region in the genomes of USDA110 and M14. Boxes represent inverted region (1.27 Mbp).

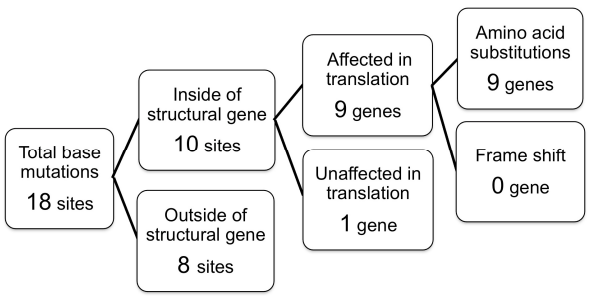

Fig. 2 Branching diagram of base mutations in M14.

3 - 51 Thermotolerant Mutants of Entomopathogenic Fungi Obtained by Ion Beam- and Gamma Ray-induced Mutagenesis

T. Saito [a)], Y. Fitriana [a)], K. Satoh [b)], Y. Oono [b)] and I. Narumi [c)]

[a)] Faculty of Agriculture, Shizuoka University, [b)] Medical and Biotechnological Application Division, QuBS, JAEA, [c)] Department of Life Sciences, Faculty of Life Sciences, Toyo University

Entomopathogenic fungi, such as *Metarhizium anisopliae*, are economically important agents for integrated pest management (IPM) programmes of insect pests. However, negative effects of temperature, such as heat stress that exceeds 35 °C, can have serious deleterious effects on conidial germination and persistence, vegetative growth, sporulation, and/or the infection process in these entomopathogenic fungi. This may result in reduced effectiveness of these fungi in biological control, especially in hot seasons, tropical and subtropical regions, or in glasshouses with elevated temperatures. In this study, we attempted to enhance thermotolerance in a model entomopathogenic fungus, *M. anisopliae*, by mutagenesis using ion beams or gamma rays and evaluated the relative virulence of the resulting mutants compared with the wild-type isolates.

Two isolates of *M. anisopliae* (AcMa5 and PaMa02) were used as the wild-type isolates. Conidia of each wild-type isolate were irradiated with either carbon-ion beams ($^{12}C^{5+}$, 121.8 keV μm^{-1}) accelerated by an AVF cyclotron at TIARA, or with gamma rays (^{60}Co, 0.2 keV μm^{-1}) at Food Irradiation Facility, JAEA. Irradiated conidia were cultured at 38±1 °C (a temperature high enough to prevent the growth of both wild-type isolates) for 2 weeks to select for thermotolerant mutants.

Four mutants were isolated from the wild-type isolate, AcMa5; one mutant (AcMa5-ib) was from ion-beam irradiation (300 Gy) and three mutants (AcMa5-gr-1, AcMa5-gr-2, and AcMa5-gr-3) were from gamma-ray irradiation (100 or 1,000 Gy). From another wild-type isolate, PaMa02, one mutant (PaMa02-ib) was isolated as a result of ion-beam irradiation (100 Gy) and no mutants were obtained from gamma-ray irradiation.

For vegetative growth, all the mutants derived from wild-type AcMa5 had an upper thermal limit of 38 °C which was higher than that (36 °C) of the wild-type by 2 °C (Table 1). By contrast, mutant PaMa02-ib derived from wild-type PaMa02 had an upper thermal limit of 39 °C which was higher than that (36 °C) of the wild-type by 3 °C (Table 1).

Thermotolerance in conidial germination was evaluated after exposure of conidia to 45±1 °C for 0, 0.5, 1, and 3 h (Table 2). Conidia of the wild-type AcMa5 were unable to germinate after 1 h exposure, whereas all the mutants derived from it germinated (5.6-19.3%). By contrast, the mutant PaMa02-ib derived from wild-type isolate PaMa02 was, like the wild-type, unable to germinate after 1 h exposure, and also, its germination rate was not significantly different to the wild-type after 0.5 h exposure.

At 25 and 30 °C, most mutants were as virulent to the maize weevil adults as the wild-type, however, one mutant (PaMa02-ib) almost lost virulence entirely (data not shown). All mutants had no mutations in the neutral trehalase gene, β-tubulin gene nor ABC transporter gene (ifT1) which were previously associated with thermotolerance and fungicide tolerance in entomopathogenic fungi (data not shown).

In conclusion, ion beams and gamma rays are useful tools for improving biological characteristics, such as thermotolerance and fungicide-tolerance[1)], in entomopathogenic fungi, but the mutants obtained in this study must be carefully evaluated for unpredictable negative side effects.

Reference

1) S. Shinohara et al., FEMS Microbiol. Lett. 349 (2013) 54.

Table 1 Colony diameter (mm, mean) of wild-type and mutant isolates at different temperatures.

Isolate	Temperature (°C)				
	30	33	36	38	39
AcMa5 (wild-type)	22.0	16.1	2.1	0	0
AcMa5-ib	27.9	18.9	4.9	0.7	0
AcMa5-gr-1	22.3	18.7	6.8	1.7	0
AcMa5-gr-2	25.2	16.0	6.1	2.3	0
AcMa5-gr-3	25.5	19.1	5.6	2.3	0
PaMa02 (wild-type)	26.0	15.7	0	0	0
PaMa02-ib	23.0	15.3	2.6	1.0	0

Table 2 Percent germination of wild-type and mutant isolates after exposure to heat stress of 45 °C.

Isolate	Hours of exposure to heat stress			
	0	0.5	1	3
AcMa5 (wild-type)	92.3	18.7	0	0
AcMa5-ib	93.0	66.1	19.3	0
AcMa5-gr-1	94.3	22.9	7.5	0
AcMa5-gr-2	96.0	45.9	5.6	0
AcMa5-gr-3	92.4	35.0	8.8	0
PaMa02 (wild-type)	91.6	16.0	0	0
PaMa02-ib	91.0	12.2	0	0

3 - 52 Screening of Yeast Strain for Ethanol Fermentation after Carbon Ion Beam Irradiation

C. Ogino [a], R. Yamada [a], K. Satoh [b] and Y. Oono [b]

[a] Department of Chemical Science and Engineering, Graduate School of Engineering, Kobe University, [b] Medical and Biotechnological Application Division, QuBS, JAEA

Ethanol fermentation from hydrolyzed lignocellulosic biomass with yeast is very important. However, in common sense, there are several chemical inhibitors for yeast from hydrolyzed biomass. Therefore, screening of yeast strain, possessing the tolerance properties against these chemical inhibitors, should be found from nature resources or mutant libraries. The several researchers tried to breed a tolerant yeast strain as a candidate by chemical mutation methodology or ultraviolet irradiation methodology. However, there was no report about the drastically alternation of yeast properties. In this research, by carbon ion beam irradiation, the screening of candidate yeast strains was performed.

The yeast strain was spread onto 40 mm agar plate, and this plate was irradiated with carbon ion beams ($^{12}C^{5+}$, 220 MeV) accelerated by an AVF cyclotron at TIARA. The irradiation dose ranged from 10 to 300 Gy. After irradiation, the colonies on the agar plate were suspended with 500 μL of SD medium, and the suspension was collected as master library. One hundred μL of this master library was inoculated 5 mL of liquid SD medium containing 50 mM acetic acid as model chemical inhibitor, and incubated 48 h at 30 °C. Then, the cultivated culture medium was also inoculated again into fresh liquid SD medium containing 50 mM acetic acid, again. Then, the culture medium was spread onto agar plate containing acetic acid, and incubated for several days at 30 °C. Then, the colony formation unit (CFU) of yeast was evaluated. As a result, the number of CFU was decreased depending on radiation dose (Fig. 1). In the case of 250 Gy over irradiation, the CFU number was decreased to less than 10% of total living cell, and it was assumed the good condition for mutation by carbon ion beam irradiation.

Next, the colony screening was performed with a 96-deep wells microplate. Each colony grown on agar plate was inoculated into 1.2 mL SD medium in each well by toothpick, and the cultivation was performed at 30 °C for 48 h. Then, the cultivated yeast was separated by centrifugation, and resuspended with 600 μL SD medium with 50 mM acetic acid. The fermentation was carried out at 30 °C for 48 h, and then the ethanol concentration was evaluated by spectrophotometric assay method. As a result, several stains exhibited high ethanol production profiling compared with that of wild type strain.

Finally, the detail cultivation profile was investigated in shaking flask scale. By using screened one colony strain, the cultivation profile was investigated from 20 mL liquid SD medium containing 50 mM acetic acid (Fig. 2). Compared with wild type strain (Fig. 2A), the ethanol production yield was improved in the case of selected strain (Fig. 2B). It was assumed that the carbon ion beam irradiation could be influence to yeast cell, and improve the metabolic pathway. In future, by using this selected yeast, the ethanol fermentation from hydrolyzed biomass with high efficiency would be performed.

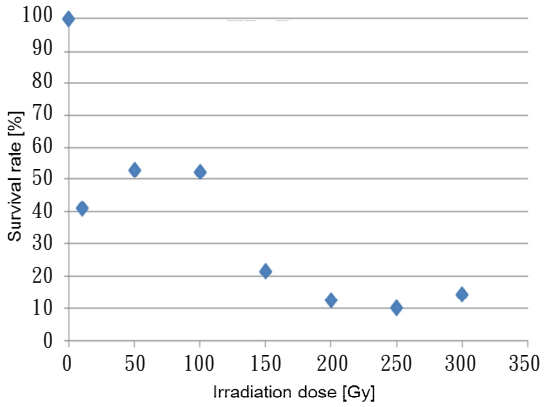

Fig. 1 Effect of carbon ion beam irradiation on colony formation units of yeast strain.

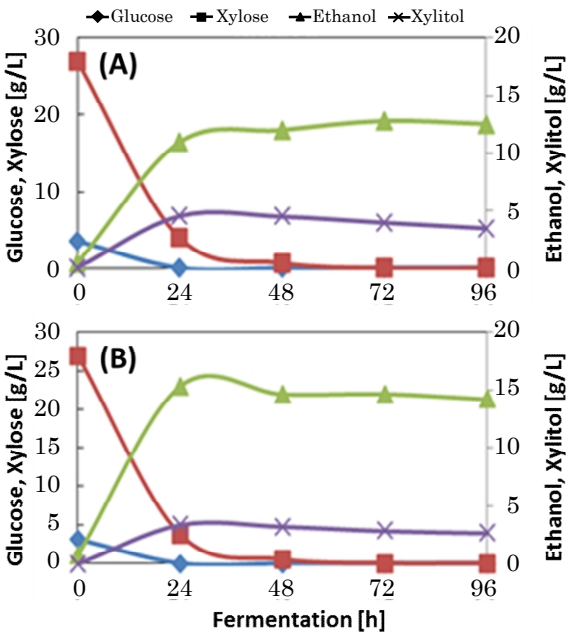

Fig. 2 Ethanol fermentation profile by wild type (A) and selected strain (B).

3 - 53 Genome Analysis of High Ethyl Caproate Producing Sake Yeasts Generated by Ion Beam Breeding

T. Masubuchi [a)], H. Hyuga [b,c)], R. Ueda [b,c)], H. Hidenori [b)], H. Ikenaga [b)], K. Satoh [c)] and Y. Oono [c)]

[a)] Gunma Industrial Technology Center, [b)] Maebashi Institute of Technology, [c)] Medical and Biotechnological Application Division, QuBS, JAEA

We analyzed genome sequence of the high ethyl caproate producing sake yeast mutant (No.227) generated by ion beam breeding in order to investigated factors contributing the reduced ability to alcohol fermentation. In the high ethyl caproate producing sake yeast, four pyruvate decarboxylase genes (*PDC*), six alcohol dehydrogenase genes (*ADH*), two biotin synthesis genes (*BIO*) and chitinase gene (*CTS1*) might be involved in the reduced ability to alcohol fermentation. The genome sequence of the strain No.227 was determined by a whole-genome shotgun strategy using pyrosequencing method and compared with the whole-genome sequence of the sake yeast strain Kyokai 7, which is characterized by the fermentation property, as a reference sequence. For the *PDC*, *ADH*, *BIO* and *CTS1* loci, no mutation was found in the strain No.227, suggesting that these genes did not involved in the reduced ability to alcohol fermentation.

群馬県では、オリジナルの吟醸用清酒酵母を開発するために、炭素イオンビーム照射（$^{12}C^{5+}$, 220 MeV, TIARA）による突然変異誘発で新たな吟醸用清酒酵母の開発を行っており、これまでに吟醸酒特有の香気成分であるカプロン酸エチルを高生産する優良清酒酵母（No.227）を作出した[1)]。しかし、カプロン酸エチル高生産酵母はアルコール発酵能が弱くなることがある。また、優良変異株の選抜・機能評価は多大な手数と時間を必要とし、研究の遂行を困難にする一因となっている。本研究では、イオンビーム突然変異育種により作出した清酒酵母の全ゲノム DNA 塩基配列を解読し、発酵特性等の機能とゲノム情報が既に明らかとなっている酵母と比較することで、酵母選抜のメルクマールとなる香気生成能・発酵能に関与する遺伝子群を特定することを目的とした。

イオンビーム突然変異育種により作出した優良清酒酵母 No.227 のゲノム DNA を抽出し、濃度と純度を確認した後、Roche 社の GS Junior システムを用いたパイロシークエンス法により全ゲノム DNA の塩基配列を決定した。得られた塩基配列は、GS *de novo* Assembler ソフトウェアによりゲノム再構築を行った。更に、GS Reference Mapper ソフトウェアを用いて、ゲノム情報が公開されている実験室酵母 S288C[2)]及び清酒酵母きょうかい 7 号（以下、Ky7 とする）[3)]をリファレンスとして DNA 塩基配列の比較を行った。また、アルコール発酵能の低下の要因を明らかにするために、アルコール発酵経路に関わる 4 種のピルビン酸デカルボキシラーゼ（PDC）及び 6 種のアルコールデヒドロゲナーゼ（ADH）をコードする遺伝子群に着目し、GENETYX-MAC ソフトウェア（Genetyx 社）を用いて変異の有無について解析を行った。更に、アルコール発酵能低下への関連が示唆されているビオチン前駆体取り組みに関与する BIO2 及び BIO5 や細胞質分裂に関与する CTS1 などをコードする遺伝子群についても併せて解析を行った。

GS Junior システムによって No.227 の DNA 塩基配列を決定した（Table 1）。決定した総塩基数約 219 Mb を用いてゲノムを再構築した結果、361 個の contig が得られ、ゲノムサイズが 14.6 Mb と推定された。S288C 及び Ky7 のゲノムサイズが約 12 Mb と推定されているのに比べ約 2.6 Mb 大きい値である。これは平均冗長度が 15 と低く、Contig 間にギャップを多く含むためと推測され、更なるシークエンスを行うことで、より精度が向上すると考えられた。

決定した No.227 の DNA 塩基配列について、塩基置換、小規模の挿入及び欠失を含む相違箇所は、S288C との比較は 68,853 箇所であったのに対し、同じ清酒酵母である Ky7 との比較では 1,254 箇所にとどまった（Table 2）。また、Ky7 と No.227 では、アルコール発酵能低下への関連が示唆されている *PDC*、*ADH*、*BIO* 及び *CTS1* 遺伝子領域には、相違箇所は見られなかった。従って、これらの遺伝子本体ではなく、プロモーター領域を含む上流領域に何らかの変異が起きている可能性が考えられた。

今後は、更にシークエンスを行うことで解読精度を向上させると共に、今回解析を行わなかった領域についても精査しなければならない。また、本研究ではゲノムデータが公開されている S288C および Ky7 との比較しか行わなかったが、No.227 の親株であるきょうかい 901 号のゲノム DNA 塩基配列を決定し、比較する必要がある。

References

1) T. Masubuchi et al, JAEA Takasaki Annu. Rep. 2010 JAEA-Review 2011-043 (2012) 113.
2) A. Goffeau et al, Science 274 (1996) 546.
3) T. Akao et al, DNA Res. 18 (2011) 423.

Table 1 Summary of sequencing and assemble.

Number of reads	497,772
Total bases (bp)	218,401,406
Average read length (bp)	439
Number of contigs	361
GC content (%)	38.11
Average sequencing redundancy	15
Estimated genome size (Mb)	14.6

Table 2 Differences between No.227 and other genome-sequenced strains.

References	S288C	Ky7
Estimated genome size (Mb)	12.07	11.88
Coverage (%)	94.02	96.59
Differences	68,853	1,254

3 - 54 Role of DNA Repair and Effect of Herbal Extract on LOH Induced by Ion Beam Radiations in *Saccharomyces cerevisiae*

T. Nunoshiba [a)], A. Yamauchi [a)], R. Iwata [a)], K. Satoh [b)], Y. Oono [b)] and I. Narumi [c)]

[a)] International Christian University, [b)] Medical and Biotechnological Application Division, QuBS, JAEA, [c)] Department of Life Sciences, Faculty of Life Sciences, Toyo University

The LOH (loss of heterozygosity) induction by various ion beam radiations was investigated in diploid *Saccharomyces cerevisiae*. The ion beams $^{12}C^{5+}$, $^{12}C^{6+}$, $^{4}He^{2+}$ and $^{40}Ar^{13+}$ at the lowest dose of 37.5 Gy, which had ~10% lethality, induced LOH with ~5-fold higher frequency, with dose-dependent manner until 150 Gy. The LOH induction was predominantly (~90%) resulted from homologous recombination. Polζ may be involved in the induction of LOH by ion beam radiations, because in the strain lacking Rev3, only slight induction of LOH was observed, whereas no remarkable effect of deletion for Polη was observed on ion beam induced LOH. In addition, the effects of *Eucalyptus regnans* extracts were examined on iron-beam radiation induced LOH, and ethanol extract of *Eucalyptus regnans* possessed inhibitory effect on LOH induced by $^{12}C^{6+}$, $^{4}He^{2+}$ and $^{40}Ar^{13+}$ ion-beam radiation.

DNA は常に細胞内的、あるいは外的要因によって損傷を被る環境に曝されているため、生命を維持することはそれらの損傷 DNA をいかなる仕組みで効率良く正確に修復し、ゲノム情報を維持するかに懸かっている。従って生命維持の根幹機能であるゲノム情報の維持機構を明らかにすることは、巧妙な生命現象を理解する上で非常に重要である。環境要因の微生物ゲノムへの影響を明らかにするため、我々は 2 倍体出芽酵母を用いたヘテロ接合性喪失(LOH: loss of heterozygosity)検出系を開発した。この 2 倍体菌株では LOH 誘発頻度とともに起こった LOH が 2 次的な突然変異、相同組換えに依存する遺伝子変換や交叉、または染色体の不均等な分配に起因する染色体喪失のいずれによるのかをも推定することができる。この検出系を用いて LOH を指標に、イオンビームによって出芽酵母のゲノムやゲノム維持機構への影響に関する基礎的知見を得、DNA 修復や損傷乗り越え DNA 合成酵素の役割について検討した。イオンビーム照射については、高崎量子応用研究所 TIARA において、4 種のイオンビーム($^{12}C^{5+}$; 220 MeV、$^{12}C^{6+}$; 320 MeV、$^{4}He^{2+}$; 50 MeV 及び $^{40}Ar^{13+}$; 460 MeV)を照射した(37.5～225 Gy)。

その結果、野生株の場合、非照射が概ね $2～5 \times 10^{-4}$ であるのに対し、$^{12}C^{5+}$及び $^{12}C^{6+}$は照射最小線量の 37.5 Gy でともに $1～2 \times 10^{-3}$ と 5 倍程度の頻度で LOH を誘発し、$^{4}He^{2+}$についても照射最小線量の 37.5 Gy で $1～2 \times 10^{-3}$ と約 5 倍、$^{40}Ar^{13+}$でも照射最小線量の 37.5 Gy で $1～3 \times 10^{-3}$ と 5 倍の頻度で LOH を誘発し、いずれの場合も線量依存的に $4～7 \times 10^{-3}$ 程度までおおむね量効果関係(75～150 Gy まで)が見られ、それ以上の線量による大きな LOH 誘発頻度の上昇は見られなかった(Fig. 1)。観察された LOH の 90%程度は、相同組換え依存の遺伝子変換や交叉によるもので、染色体の不均等分配によるものはわずか 10%程度で、非照射群との差は見られなかった。また、translesion DNA polymerase である Polη(Rad30)、Polζ(Rev3)欠損株そして二重欠損株についても、イオンビーム照射による LOH 誘導について検討した。その結果、Rad30 欠損株については、いずれの核種でも野生株と大きな差は見られなかったが、Rev3 欠損株では、非照射で $1～4 \times 10^{-3}$ と他の株より LOH が高頻度であるものの、照射によっても 37.5～150 Gy でそれぞれ 2～3 倍の LOH 誘発しか見られず、これらの LOH 誘発に translesion DNA polymerase Polζ の関与が伺え、特に核種による違いは見られなかった(Fig. 1)。Polη(Rad30)Polζ(Rev3)二重欠損株については、フィルターからの細胞回収率が悪く、変異体そのものが不安定で、明白な結果が得られなかった。

このイオンビームによる LOH 誘導が活性酸素に依存するかどうかを検討する目的で、O_2^-の消去系の Superoxide dismutase(SOD1)の欠損株を樹立し、O_2^-消去能の欠損や O_2^-に対する高感受性を確認するとともに、haploid における自然突然変異頻度および diploid における自然 LOH 誘発頻度を検討した。その結果、欠損株では haploid での自然突然変異頻度が野生株の 2.5 倍に、diploid における LOH 誘発頻度も 3 倍に上昇した。今後、この株を用いて、イオンビームのゲノム情報維持への影響を検討する予定である。

これまでに、$^{12}C^{5+}$照射による LOH 誘発に対して、ユーカリエキスが細胞増殖にはほぼ影響を与えず、添加量に伴う抑制効果を確認した。そこで同様の効果が他のイーンビームによる LOH 誘発にも見られるかどうかを調べた。その結果、無添加では $4～7 \times 10^{-3}$ であった LOH が、ユーカリ添加では $6～9 \times 10^{-4}$ にまで抑制した。今後、この抑制効果の機構について、組換えや損傷乗り越え DNA 合成、DNA 修復への影響を視野に検討したい。

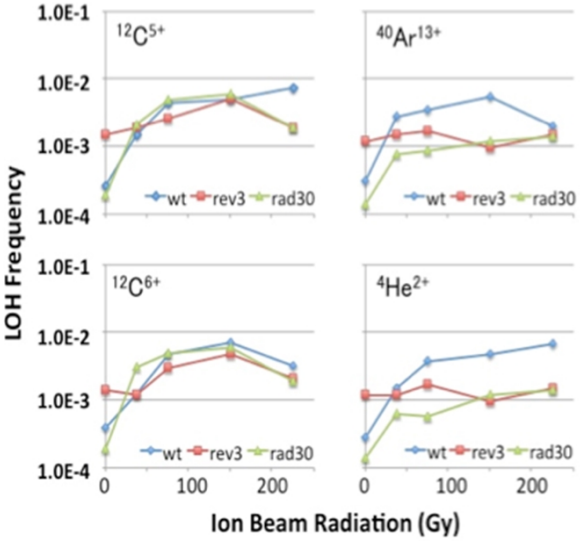

Fig. 1 LOH induced by ion beam radiations in wild type and translesion polymerase deficient *S. cerevisiae*.

4. Advanced Materials, Analysis and Novel Technology

This is a blank page.

4 - 01 Characterization of Pt and Pd Epitaxial Films on Sapphire Substrates by RBS/Channeling

S. Yamamoto, T. Hakoda and M. Yoshikawa

Environment and Industrial Materials Research Division, QuBS, JAEA

Platinum (Pt), Palladium (Pd) and Gold (Au) are typical industrial catalytic materials. The Pt is the most attractive catalyst for an oxygen reduction reaction in polymer electrode membrane fuel cells. The Pt and Pd are also used for hydrogen and organic-hydrides gas sensors as dehydrogenation catalysts. High quality epitaxial Pt, Pd and Au films were required to understand of catalytic processes and further improvement of their catalytic properties. Single-crystalline sapphire (α-Al_2O_3) substrate has excellent features suitable for thin film growth such as the good thermal stability and the chemical inertness. Especially epitaxial Pt and Pd films on α-Al_2O_3 substrates have been well studied by X-ray diffraction[1,2]. In order to characterize of grown epitaxial thin films, X-ray diffraction and ion beam channeling assessment are essential and complementary. In the present study, the orientation relationship between the epitaxial film and α-Al_2O_3 substrates was determined by X-ray diffraction analysis. The Rutherford backscattering spectroscopy (RBS)/ channeling analysis was performed to characterize the epitaxial films by employing $^4He^+$ ions with the energy of 2.0 MeV at JAEA Takasaki. Epitaxial Pt, Pd and Au films were grown on α-Al_2O_3 substrates by rf magnetron sputtering in an argon atmosphere from Pt, Pd, and Au targets.

Figure 1 illustrates typical RBS spectra from Pt on the α-Al_2O_3 (0001) substrate deposited at 600 °C taken under random and the <111> aligned conditions. The thickness of Pt film was approximately 100 nm. In the aligned spectra, one can recognize two peaks which are located at the surface and interface of Pt film. The peak at a lower energy side reflects possible imperfections in the Pt layer adjacent to the α-Al_2O_3 (0001) substrate. The ratio of the <111> to random spectrum yield (minimum yield) from Pt film is approximately 4.8% at just behind surface park, which demonstrates the excellent crystal quality. The results of RBS/channeling analysis on the Pd/α-Al_2O_3 (0001) indicated that epitaxial Pd (111) films were grown on the α-Al_2O_3 (0001) substrate deposited at 500 °C. Figure 2 shows typical RBS spectra from the Au (250 nm) and Pt (1 nm) layers on the α-Al_2O_3 (0001) substrate measured under the random and the Au<111> aligned condition. The substrate temperature for the Pt (111) buffer layer on the α-Al_2O_3 (0001) was 600 °C, and that for the Au (111) film on the Pt (111) buffer layer was 300 °C. In the aligned spectra, the yield degrease with increasing from the interface to the surface region. It indicates that the crystal quality of Au (111) layer was improved with the increase of the layer thickness. The minimum yield for the Au <111> axis goes down to about 10% at just behind the surface peak of the Au film even if the Pt buffer layer thickness is only 1 nm. However, the Au deposition directly on the α-Al_2O_3 (0001) substrate did not induce any good channeling behavior even if thin films were prepared at substrate temperature of 300 °C.

In summary, epitaxial Pt (111) and Pd (111) films were grown on α-Al_2O_3 (0001) substrates at substrate temperature of 600 °C and 500 °C, respectively. Furthermore, epitaxial Au (111) films were successfully grown on α-Al_2O_3 (0001) substrates with a high quality Pt (111) buffer layer. For the growth of Au (111) film, approximately 1 nm thick Pt layer is good enough as a buffer layer. Epitaxial Pt (111) films have a potential to use as a buffer layer to adjust the lattice mismatches with α-Al_2O_3 substrates for further growth of different materials.

References

1) G. R. Harp et al., Thin Solid Films 288(1996) 315.
2) H. Zhou et al., J. Crystal Growth 234 (2002) 561.

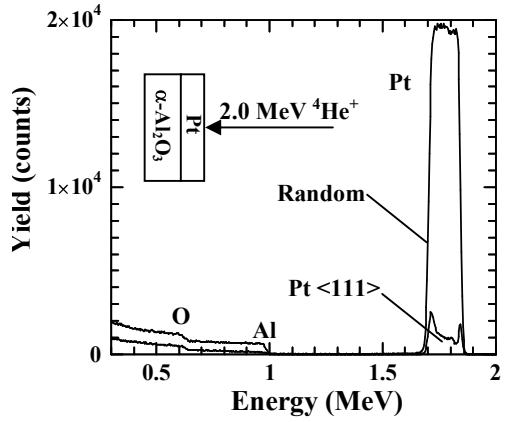

Fig. 1 Two MeV $^4He^+$ RBS/channeling spectra from the deposited Pt (111) film on the α-Al_2O_3 (0001) substrate. The thickness of the Pt film was 100 nm. The aligned spectrum was taken along the <111> axis of the Pt film.

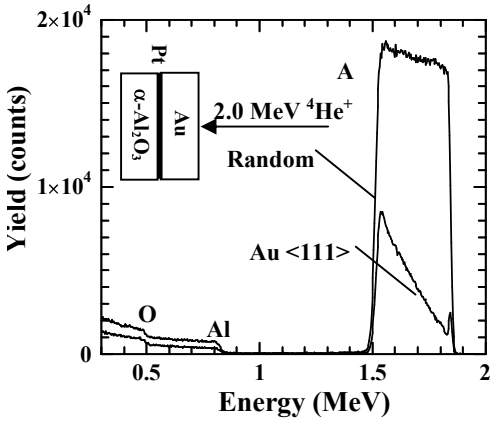

Fig. 2 RBS/channeling spectra from the deposited Au (111) film on the Pt (111)/α-Al_2O_3 (0001) substrate. The thicknesses of the Au film and Pt layer were 250 nm and 1 nm, respectively.

4 - 02 Formation of Poly(vinylpyrrolidone) Nanowires Decorated with Au Nanoparticles

S. Tsukuda [a)], M. Sugimoto [c)], A. Idesaki [c)], M. Yoshikawa [c)], S. Seki [b)] and S.-I. Tanaka [a)]

[a)] Institute of Multidisciplinary Research for Advanced Materials, Tohoku University,
[b)] Division of Applied Chemistry, Graduate School of Engineering, Osaka University,
[c)] Environment and Industrial Materials Research Division, QuBS, JAEA

A high energy single ion can induce local cross-linking reactions of polymers along the ion path and produce a cylindrical nanostructure (nanowire) in the film [1,2]. Developing irradiated samples using a solvent to remove a non-cross-linked polymer affords isolated nanowires with controlled size and number density. This direct fabrication technique of polymer nanowire is called a single particle nanofabrication technique (SPNT). In this study, hydrogel poly(vinylpyrrolidone) (PVP) nanowires were formed using SPNT, and the surface of the nanowires were decorated with Au nanoparticles by photo-reduction treatment. The number and size of Au nanoparticles can be also controlled by changing the reduction conditions.

PVP was dissolved in isopropanol (IPA) at 5 wt% with N,N'-Methylene-bisacrylamide (MBA) as cross linking agents. These solutions were spin coated onto Si substrates. The thin films were exposed to beams of 490 MeV $^{192}Os^{30+}$ at the TIARA cyclotron accelerator facility of the Japan Atomic Energy Agency (JAEA). After irradiation and development, the substrates were immersed into a methanol containing $HAuCl_4$ and PVP as capping reagents. The reduction of $HAuCl_4$ was carried out by UV irradiation for 5, 7.5, 10, and 15 minutes. After UV irradiation, the samples were rinsed with pure water to stop the reduction reaction and dried. Observation of nanowires and measurement of sizes of Au nanoparticles were subsequently carried out using SEM and TEM.

The PVP nanowires decorated with Au nanoparticles were successfully fabricated by SPNT and photo-reduction treatment as shown in Fig 1. The Au nanoparticles were selectively formed on PVP nanowires. This result indicates Au nanoparticles were rapidly formed on PVP compared with that in the solution. Therefore, it might be suggest that the PVP nanowires, which consist of cross-linked network structures, promoted the nucleation and growth of Au particles. In order to measure the number and size of Au particles, TEM observation was also carried out. The number of Au nanoparticles on one nanowire were increased with an increase in the reduction time as shown in Fig. 2. Especially, the PVP nanowires were completely covered with Au nanoparticles after reduction for 15 minutes [Fig. 1 (c)]. The size of Au particles was also measured for each reduction time. The values were 9.3, 11.7, 13.9, and 17.5 nm for 5, 7.5, 10 and 15 minutes, respectively. Therefore, the reduction time is very important factor to control the size and number of Au nanoparticles on PVP nanowires.

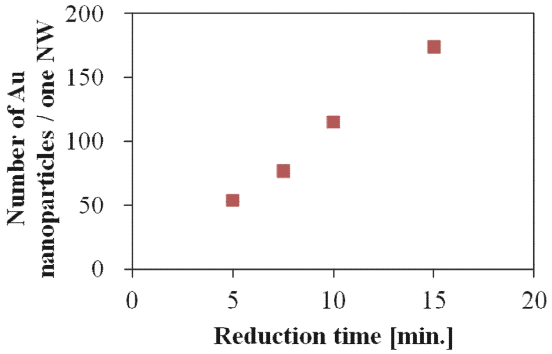

Fig. 2 Relationship between number of Au particles and reduction time. The particles were counted on one nanowire by TEM observation.

References

1) S. Seki et al., Adv. Master. 13 (2001) 1663-65.
2) S. Tsukuda et al., Appl. Phys. Lett. 87 (2005) 233119-1-3.
3) S. Tsukuda et al., Radiat. Phys. Chem. 84 (2013) 39-41.

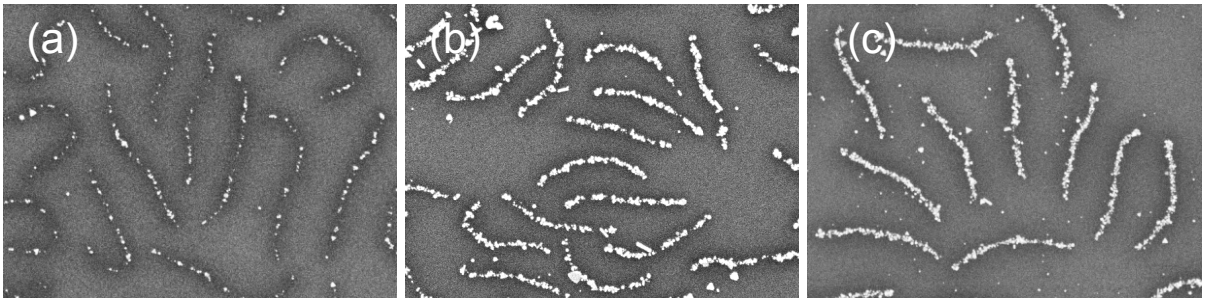

Fig. 1 SEM micrographs of PVP nanowires decorated with Au nanoparticles. The PVP nanowires were prepared by SPNT on Si substrates. The formation of Ag nanoparticles on surface of PVP nanowires was carried out by photo-reduction in a methanol containing $HAuCl_4$ for (a)5, (b)10, and (c)15 minutes.

4 - 03 Formation of Hybrid Polymer Nanofiber Including Metal Nanoparticles by High Energy Ion Beam Irradiation

M. Sugimoto [a)], S. Tsukuda [b)], M. Yoshikawa [a)], S. Seki [c)] and S. Tanaka [b)]

[a)] Environment and Industrial Materials Research Division, QuBS, JAEA,
[b)] Institute of Multidisciplinary Research for Advanced Materials, Tohoku University,
[c)] Department of Applied Chemistry, Osaka University

A nanofiber with a quite large specific surface shows excellent catalyst and absorption activity compared with bulk materials[1)]. In the present work, we succeeded in obtaining nanofiber containing platinum (Pt) nano particles synthesized from poly(vinylpyrrolidone) (PVP) and hexachloroplatinic(IV)acid (H_2PtCl_6) [2)]. However, the nanofiber was discontinuous in the case of over 7.5 mass% concentration of H_2PtCl_6, because the Pt nanoparticles prevent the cross-linking reactions between each PVP polymer chain. In this research, to stabilize the nanofiber with continuous shapes, we tried to introduce many active intermediates within an ion track by addition of the cross-linking agent or additional electron beam (EB) irradiation.

Poly(vinylpyrrolidone) was dissolved in 2-propanol at 5 mass%, then H_2PtCl_6 was also dissolved at 1.0~7.5 mass% as against PVP. Methylenebisacrylamide (MBA) was added to each solution as the cross-linking agent. These solutions were spin coated on a Si substrate to make the polymer thin films, then they were irradiated in vacuum at ambient temperature using 490 MeV $^{192}Os^{30+}$ beams at an ion fluence of $1.0\times10^7\sim1.0\times10^9$ ions/cm^2. Subsequently, some films were irradiated by EB with total dose up to 40 kGy. The irradiated films were treated using 2-propanol and then the insoluble irradiated part of the film was developed as nanofibers. The sizes of the nanofibers were estimated using scanning probe microscopy (SPM).

The PVP nanofiber including Pt nanoparticles was successfully fabricated by irradiation to thin films of PVP / H_2PtCl_6 with the concentration of 1.0~7.5 mass%. The radii of nanofiber also decreased with an increase of concentration of H_2PtCl_6 as shown in Fig. 1. These results indicate a decrease in the cross-linking efficiency of PVP. Addition of MBA as cross-linking agent, nanofibers were observed as continuous shapes with an increase in concentration of cross-linking agent at 20 and 30 mass%. Besides, the radii of nanofibers increased from at 15 to 30 mass% of cross-linking agent. These results indicate the high concentration of the cross-linking agent promotes the high crosslink density of the polymer in the ion track. Radii of the PVP nanofiber containing 7.5 mass% H_2PtCl_6 formed by the additional EB irradiation are presented in Fig. 2. The radii of the nanofibers also increased by additional EB irradiation and the nanofibers were observed as continuous shapes. It is suggested that EB introduced additional cross-linking points in an ion track resulting in stabilization of the fiber structure.

These synthesis methods using addition of cross-linking agent or additional EB irradiation will enable to fabricate the continuous nanofiber including metal nanoparticles with high concentration.

Acknowledgment We thank Mr. Hiroyuki Kikuma for technical advice of irradiation.

References

1) M. Sugimoto et al., Ceramic Trans. **213** (2010) 105-11.
2) S. Tsukuda et al., Rad. Phys. Chem. **84** (2013) 39-41.

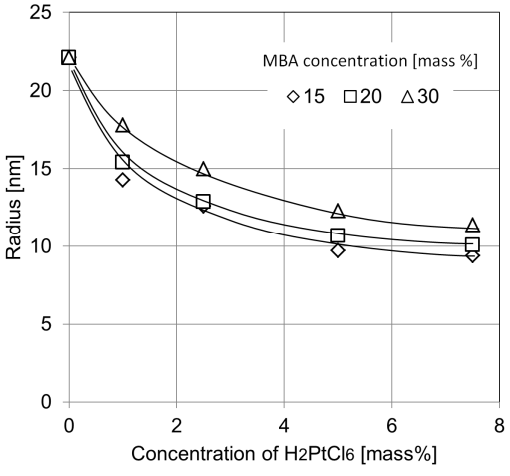

Fig. 1 Dependence of the radii of the PVP nano fibers on concentration of H_2PtCl_6 with concentration of cross-linking agent 15 (◇), 20 (□), 30 (△).

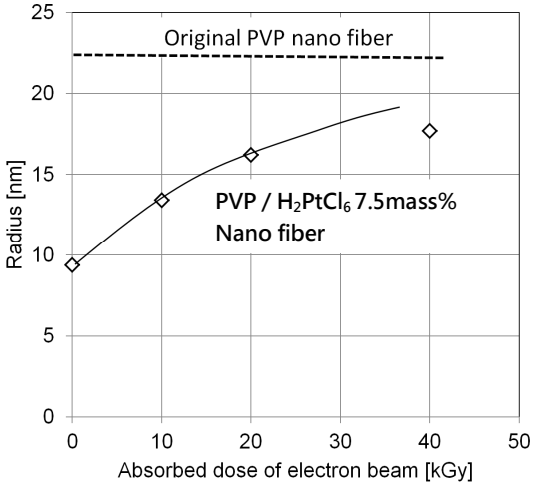

Fig. 2 Dependence of the radii of the PVP nano fiber on absorbed dose of electron beam.

4 - 04 Swelling of Radiation-cured Polycarbosilane during Pyrolysis

A. Takeyama, M. Sugimoto and M. Yoshikawa

Environment and Industrial Materials Research Division, QuBS, JAEA

Use of carbon dioxide (CO_2) separation membrane consisted of CO_2 absorb/desorbent such as lithium silicate (Li_4SiO_4) have been paid attention for CO_2 capture and storage (CCS) [1]. In order to improve gas permeation property of the membrane, plugging pinholes formed between crystal grains of Li_4SiO_4 by chemically inert precursor-derived silicon carbide (SiC) is of interest. In this viewpoint, volume shrinkage of polymer precursor, polycarbosilane (PCS) should be as small as possible during pyrolysis. This research aims at revealing mechanism for prevention of the volume shrinkage of PCS when it is converted into SiC by pyrolysis.

PCS powder was cured by electron beam irradiation with the dose of 12 MGy in helium at room temperature. Radiation-cured PCS powder was annealed at 673 K in argon, in order to kill the radical formed in PCS by irradiation. Annealed powder was pyrolyzed at 773, 823, 873, 973 and 1,073 K in argon to convert it into SiC powder. Weight change of as-annealed PCS powder before/after the pylorisys (ceramic yield) and densities of powders were measured. For each pyrolysis temperature, densities were measured for five small rumps of pyrolyzed PCS powder using Archimedes method. Estimated average density and ceramic yield were used to calculate volume change of pyrolyzed PCS powder. Nitrogen isotherm was measured at 77 K to obtain total volume of pores formed in the powder and to calculate surface area.

Figure 1 shows density and volume change of pyrolyzed PCS powder. At 773 K, there is subtle but certainly decrease of average density from 1.08 g/cm^3 to 1.05 g/cm^3. Over 773 K, average density is monotonically increased until 1,073 K. While, little increase of volume change from 1 up to 1.02 is observed at 773 K, indicating the powder was swelled. For the pyrolysis temperature over 773 K, monotonically decrease of volume change is observed. During the pyrolysis, the weight of PCS powder was continuously decreased with increasing the pyrolysis temperature, as it was converted into SiC powder. Therefore, it is interesting PCS powder was swelled and did not continuously shrink proportionally to the weight decrease, despite progress of the conversion.

Total pore volume and surface area are shown in Fig. 2. Total pore volume means total volume of pores whose diameter is less than about 60 nm formed in as-annealed or pyrolysed PCS powder. Both total pore volume and surface area increased with increasing the pyrolysis temperature and reached maximum at 823 K. Total pore volume at 823 K is approximately three times larger than that of as-annealed powder. It indicates numbers of pores were formed in PCS powder during pyrolysis. Increase of total pore volume and surface area attributed to volume swelling as well as decrease of density of PCS powder shown in Fig. 1. With increasing the temperature over 823 K, total pore volume and surface area are decreased to almost 0 at 923 K. Decrease of total pore volume and surface area in this temperature range corresponds with volume shrinkage shown in Fig. 1. In summary, volume shrinkage of PCS powder during pyrolysis was prevented by swelling by formation of pores. So as to use PCS for plugging pinholes of CO_2 separation membrane, further optimization of curing and pyrolysis condition is required to relieve the shrinkage by high temperature pyrolysis.

Reference

1) J. L. Wade et al., J. Membr. Sci. 369 (2011) 20.

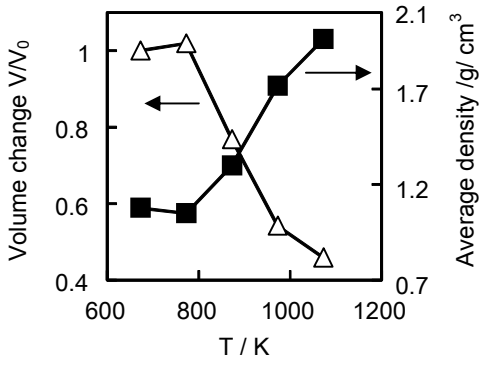

Fig. 1 Plots of density and volume change of pyloryzed PCS powder. At 673 K, density and volume change for as-annealed powder are plotted.

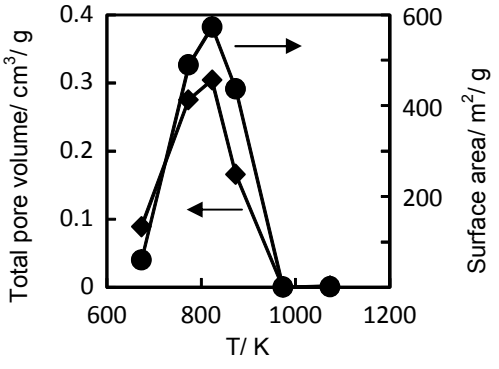

Fig. 2 Total pore volume and surface area of pyloryzed PCS powder. At 673 K, total pore volume and surface area for as-annealed powder are plotted.

4 - 05 Ion Beam Treatment for a Sodalite Zeolite Membrane

M. Nomura [a)], M. Kitajima [a)], A. Ikeda [a)], E. Matsuyama [a)] and M. Sugimoto [b)]

[a)] Department of Applied Chemistry, Shibaura Institute of Technology,
[b)] Environment and Industrial Materials Research Division, QuBS, JAEA

Sodalite zeolite membranes have been developed as hydrophilic water permselective membranes [1)]. Sodalite zeolite is one of the 6 membered ring zeolites, and water diffusion through 6 membered rings is slow due to the small size of the 6 membered ring. Water considered to pass through the intercrystalline pathways of polycrystalline sodalite membranes. However, the permeation mechanism through sodalite membranes is not clear. In this study, the permeation properties through sodalite membranes was discussed by using post treatments such as ion beam treatments. The effects of the post treatments can be investigated by comparing the permeation properties before and after the post treatments.

Sodalite zeolite membranes were synthesized with sodalite seed crystals on porous α-alumina tube substrates (ϕ: 10 mm, 150 nm of the pore size: Noritake Co.) based on the recipe described in the former literature [1)]. Sodalite seed crystals were coated on the alumina substrates by changing the pH of the seed slurry between 3 and 12. Hydrothermal synthesis was carried out in the parent gel of SiO_2: Al_2O_3: Na_2O: H_2O= 5: 1: 50: 1,005 at 140 °C for 3.5 h. There were two kinds of post treatments for the sodalite membranes. One was the ion beam irradiation. Ion beam irradiation was carried out using $^{192}Os^{30+}$ ion at 490 MeV by using a cyclotron. The irradiation fluence was at 3.0×10^{10} ions cm^{-2}. The other was the alkaline treatment [2)]. The sodalite membrane was immersed in 0.1 N of NaOH at 75 °C for 5 or 10 min. The permeation properties through the obtained membranes were evaluated by isopropyl alcohol (IPA)/water pervaporation (PV) and single gas permeation tests. IPA/water PV was employed for 80 wt% of IPA at 75 °C. Single gas permeation tests were conducted for He and N_2 at room temperature.

First, effects of the pH of the seed slurry were tested. Figure 1 shows N_2 permeances through the sodalite zeolite membrane plotted as a function of the pH of the slurry.

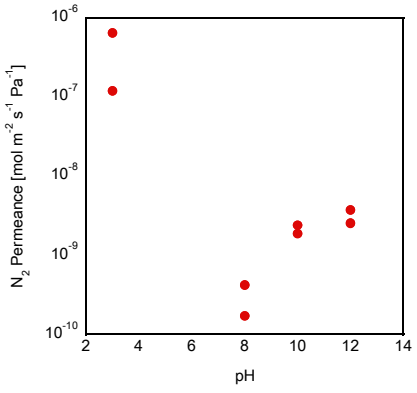

Fig. 1 N_2 permeances through the membranes prepared by changing the pH of the slurry coating.

Lower N_2 permeance indicates the compactness of the membrane. The minimum N_2 permeance was 1.72×10^{-10} mol m^{-2} s^{-1} Pa^{-1} for the slurry pH of 8. This can be explained by the ζ-potential difference for the sodalite seed crystals. ζ-potential of the sodalite seed crystals was measured by changing the pH of the slurry. ζ-potential of the sodalite seed crystals was positive for the pH of the slurry between 4.2 and 6.8, the potential was negative or the pH of the slurry between 9.0 and 12.0. The potential was 0.10 mV (almost neutral) for the pH of 8. ζ-potential is important for MFI zeolite seed coating [3)]. The optimum slurry pH was 2 for the MFI seeds that ζ-potential of the MFI seeds was neutral. ζ-potential for the sodalite seeds is also important for the coating.

Next, the post treatments were tested for the sodalite zeolite membrane prepared from the slurry pH of 8. Figure 2 shows the single gas permeation results and PV results through the soldalite membrane after the ion beam treatment and the alkaline treatments. The water selectivity over IPA was 158 through the as-made membrane. After the ion beam treatment, water permeance improved from 1.38×10^{-8} mol m^{-2} s^{-1} Pa^{-1} to 3.66×10^{-8} mol m^{-2} s^{-1} Pa^{-1} keeping the IPA permeances at approximately 8.7×10^{-11} mol m^{-2} s^{-1} Pa^{-1}. As a result, water selectivity increased to 423. N_2 permeance was also increased from 1.29×10^{-10} mol m^{-2} s^{-1} Pa^{-1} to 2.84×10^{-9} mol m^{-2} s^{-1} Pa^{-1}. The pathways created by the ion beam treatment showed water permselectivity. The irradiated membrane was treated in alkaline for 5 min. IPA permeance increased sharply, and water selectivity decreased to 4 showing that the membrane was damaged by the treatment.

References

1) S. Khajavi et al., J. Membr. Sci. 299 (2007) 63.
2) M. Ogura et al., Applied Catal. A 219 (2001) 33.
3) M. Nomura et al., Membrane 39(3) (2014) 162.

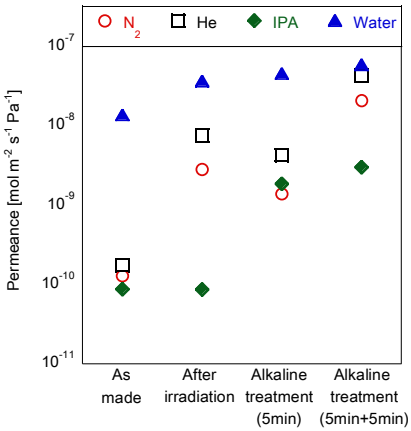

Fig. 2 Gas permeation and water/IPA PV results.

4 - 06 Formation of Poly(vinylpyrrolidone) Nanowires by Ion and Electron Beam Irradiation

S. Tsukuda [a)], M. Sugimoto [c)], A. Idesaki [c)], M. Yoshikawa [c)], S. Seki [b)] and S.-I. Tanaka [a)]

[a)] Institute of Multidisciplinary Research for Advanced Materials, Tohoku University,
[b)] Division of Applied Chemistry, Graduate School of Engineering, Osaka University,
[c)] Environment and Industrial Materials Research Division, QuBS, JAEA

The radiation sensitivity of polymers has been studied for many polymers and types of ionizing radiations. The main chemical effects are chain scission and crosslinking reactions resulting in enhanced or reduced solubility. Heavy-ion beams are used for high-density energy deposition in polymeric materials, and the effects of ion beams differ markedly from those for low-energy ionizing radiation such as γ-ray and electron beams. In heavy-ion beam processes, the ionization and excitation processes that occur in ion tracks result in the generation of active intermediates at high density, leading to chemical reactions. Thus, the ion irradiation of cross-linked type polymers produced 1-d nano-gel (nanowires) by local cross-linking reactions along in an ion track[1,2]. Hydrogel nanowires of poly(vinylpyrrolidone) (PVP) was also formed by SPNT. However, the formation needs addition of crosslinking agents because of low crosslinking efficiency of solid state PVP. Actually, in the case of no addition of crosslinking agent to PVP film, the nanowires were not observed on the Si substrate after wet-development procedure, because the irradiated parts were also dissolved during development procedure. In this study, additional electron beam irradiation to PVP film without crosslinking agent was carried out in order to form PVP nanowires which did not contain a crosslinking agent.

PVP films were prepared on Si substrates by spin coating technique. The thin films were firstly exposed to beams of 490 MeV $^{192}Os^{30+}$ at the TIARA cyclotron accelerator facility of the Japan Atomic Energy Agency (JAEA). After ion irradiation the films were also exposed to electron beam with doses of 240 and 710 kGy (dose rate: 0.40 kGy/s). After irradiation, a non-crosslinked polymer was removed by development using IPA. At the dose of electron beam more than 1 MGy, the films could not developed because of gelation throughout the film. The direct observation of the surface of the substrates were performed using an atomic force microscope (AFM Seiko Instruments Inc.(SII) SPI-4000).

Figure 1 shows results of ion beam and additional electron beam irradiation with 0, 240, and 710 kGy, respectively. The ion beam irradiation did not give the nanowires [Fig. 1(a)], because the irradiated parts dissolved during development procedure. It means that ion irradiation of PVP film could not induced enough crosslinking points inner ion tracks to achieve gelation. After the electron beam irradiation, PVP nanowires were successfully observed on the Si substrate. The nanowires formed by electron beam irradiation with 240 kGy were partially dissolved and separated in the structures [Fig. 1(b)]. In contrast, the continuous structures were observed with increase of radiation dose as shown in Fig. 1(c). These results indicate that electron beam irradiation form the additional crosslinking points inner nanowires. Therefore, the increase of density of crosslinking points prevented from disolving during wet development procedures. It is suggested that ion and electron beam irradiation is very useful to control the local crosslinking reaction along the latent track.

References

1) S. Seki et al., Adv. Mater. 13 (2001) 1663-65.
2) S. Tsukuda et al., Appl. Phys. Lett. 87 (2005) 233119-1-3.

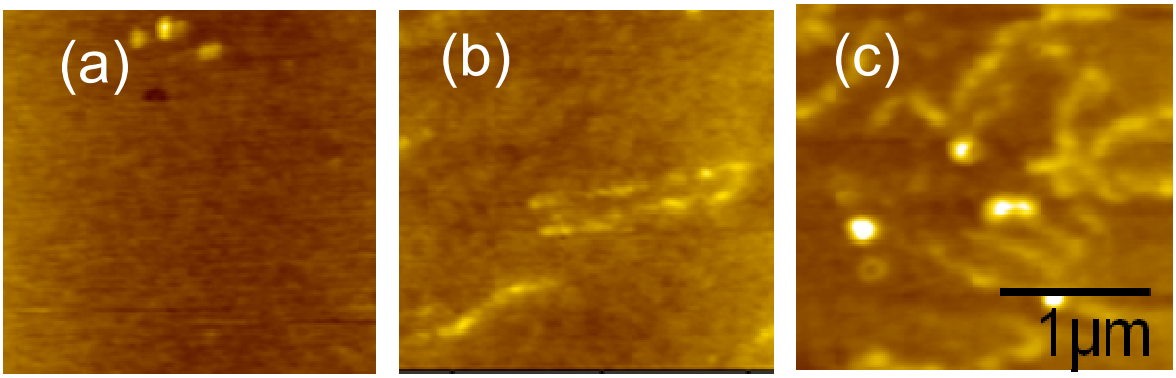

Fig. 1 AFM micrographs of nanowires based on PVP. The nanowires were formed by 490 MeV Os ion beam irradiation at 1.0×10^8 ions/cm^2, and additional electron beam irradiation with the dose of (a) 0 kGy, (b) 240 kGy, and (c) 710 kGy, respectively.

4 - 07 Effect of Atomic Weight on Critical Ion Fluence of Amorphization of Polycrystalline SiC Nanotubes

T. Taguchi [a], S. Yamamoto [b] and H. Asaoka [a]

[a] Materials Science Research Division, QuBS, JAEA,
[b] Environment and Industrial Materials Research Division, QuBS, JAEA

Since the discovery of carbon nanotubes (CNTs) in 1991, many researchers have synthesized a lot of new one-dimensional nanostructured materials such as nanotubes, nanorods and nanowhiskers for potential applications. Some of them have reported that many nanomaterials such as TiC, NbC, BN, SiO_2 and GaN nanostructures are fabricated from CNTs as the template. SiC is one of the most important wide-band-gap semiconducting materials for high temperature and high power. And SiC is also one of the most important structural materials at high temperature. Therefore, SiC offers exciting opportunities in electronic devices and in structural materials at high temperature. We have reported that the polycrystalline C-SiC coaxial nanotubes, which were CNTs sheathed with SiC layer, and that polycrystalline single-phase SiC nanotubes were synthesized [1,2]. Furthermore, the amorphous SiC nanotubes were successfully synthesized by the ion irradiation of the polycrystalline SiC nanotubes at 100 °C [3]. However, the critical ion fluence and displacement per atom of amorphization of polycrystalline SiC nanotubes has not been investigated yet. The purpose of this study is, therefore, to investigate the effect of atomic weight of irradiation ions on the critical dose of changing to amorphous SiC nanotubes from polycrystalline SiC nanotubes.

Carbon nanotubes (GSI Creos Corporation, Tokyo, Japan) were used as the template. The C-SiC coaxial nanotubes were synthesized by heating CNTs with Si powder (The Nilaco Corporation, Tokyo, Japan) at 1,200 °C for 100 h in a vacuum. Single-phase SiC nanotubes were formed by the heat treatment of C-SiC coaxial nanotubes at 600 °C for 2 h in air. The single-phase SiC nanotubes dispersed in ethanol were deposited on nickel grid sample holder for transmission electron microscope (TEM) observation. These nickel grid sample holders deposited with single-phase SiC nanotubes were irradiated with 3-MeV Ni^{2+}, Zr^{2+} or Au^{2+} ions at 100 °C. The ion fluence ranges of Ni, Zr or Au ions were 1.7×10^{19}-7.4×10^{19}, 2.2×10^{18}-6.3×10^{19} or 2.9×10^{17}-1.5×10^{19} ions/m^2, respectively.

Figure 1 showed the typical TEM image and the corresponding electron diffraction patterns of amorphous SiC nanotubes. The results of TEM observations indicated that polycrystalline SiC nanotubes were completely transformed to amorphous SiC nanotubes by Ni, Zr or Au ions irradiation. Figure 2 showed the critical Ni, Zr or Au ion fluence and displacement damage of complete amorphization of polycrystalline SiC nanotubes. Both critical ion fluence and displacement per atom decreased with increasing the atomic weight of irradiation ions. The reason may be that the damage area induced by one irradiated ion increased with increasing the atomic weight of irradiation ion. These results indicate that the irradiation with heavier ions causes the amorphization of polycrystalline SiC nanotubes at the lower fluence and displacement damage.

References

1) T. Taguchi et al., J. Am. Ceram. Soc. 88[2] (2005) 459-61.
2) T. Taguchi et al., Physica E 28[4] (2005) 431-38.
3) T. Taguchi et al., JAEA Takasaki Annu. Rep. 2009 JAEA-Review 2010-065 (2011) 127.

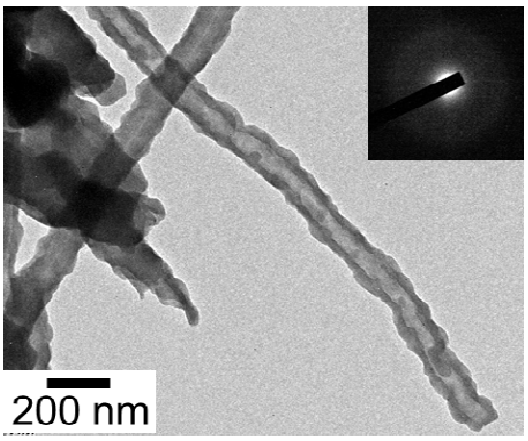

Fig. 1 Typical TEM image and the corresponding electron diffraction pattern of amorphous SiC nanotubes.

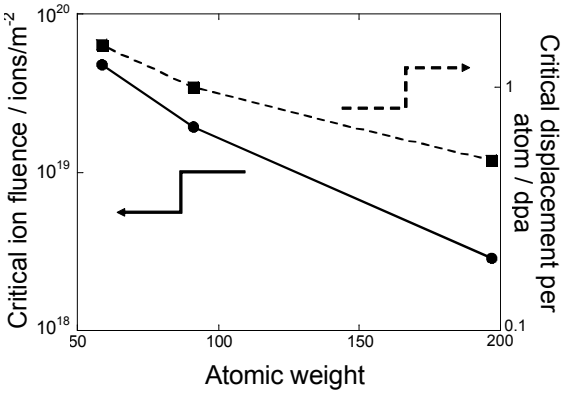

Fig. 2 Critical ion fluence and displacement per atom of amorphization of polycrystalline SiC nanotubes.

4 - 08 Effect of Impurities in Charge Stripper Foils for the 3-GeV Rapid Cycling Synchrotron of J-PARC

Y. Yamazaki [a)], M. Yoshimoto [a)], P.K. Saha [a)], M. Kinsho [a)], T. Taguchi [b)], S. Yamamoto [c)] and I. Sugai [d)]

[a)] Accelerator Division, J-PARC, JAEA, [b)] Material Science Research Division, QuBS, JAEA, [c)] Environment and Industrial Materials Research Division, QuBS, JAEA, [d)] High Energy Accelerator Research Organization, KEK

A charge stripper foil is one of the key technologies to keep high operating rate for multi-turn injection of high power proton synchrotron. Typically carbon-based material is used to strip two electrons off the incident H^-. J-PARC also requires carbon stripper foils to strip electrons from H^- supplied by the linac in order to inject H^+ into the Rapid Cycling Synchrotron (RCS). It is important for a charge stripper foil to endure heat load by energy deposition from the beam. For a charge stripper foil in the RCS, we applied the Hybrid type thick Boron-doped Carbon (HBC : Boron 20%) foil which is developed with the arc-discharge method by Sugai and has toughness for standing against heavy irradiation. For the beam operation in RCS, the foil thickness is about 1 μm (200 μg/cm^2) corresponding to conversion efficiency of 99.7% for 181 MeV injection from linac.

We have investigated the characteristics of HBC foils to develop much more long-lifetime foil about for five years with TEM, Ion-irradiating machine, RBS, PIXE, XPS and so on in Tokai and TIARA (Takasaki Ion Accelerators for Advanced Radiation Application). Although typical foil thickness is 200 μg/cm^2 for the practical usage, in this study we used foil thickness of 15 μg/cm^2 for the sake of ease for TEM observation. We selected Ar^+ as irradiated ion instead of H^+ in order to examine damage in a short period of time. Ar^+ of 300 keV, which we use as irradiated ion from ion implanter in TIARA, can only deliver the energy deposition by the ion beam into the foil and pass through without ion implantation.

In this research, we found that impurity contents such as Fe, Cu, Na, Al are different for each foil. HBC is generally in amorphous phase, but they involved a lot of micro graphite grains of a few nanometer and many boron-rich micro grains before irradiation of ions. In impurities, we observed that metals such as Fe and Cu were grown to crystallize micro grains from atoms, as shown by Fig. 1. This phenomenon is one of the destructive mechanisms of the HBC foil. Such metals also contribute a large-angle scattering and neutrons' generation by nuclear reaction against the injecting beam. As a result, residual radioactivity was increased around the foil.

On the other hand, though we actually have never exchanged a HBC foil for the reason of distraction by the beam operation, we have a big problem with residual radioactivity of foil itself and components around it. By energy upgrade of linac from 181 MeV to 400 MeV, the problem get more serious to increase residual radioactive dose. By nuclear reaction with the proton beam, long half-life radioactive isotopes such as Na-22 and Be-7 were mainly detected from the irradiated foils. Be-7 is generated from Boron including as the basic component in HBC. Na-22 is generated from impurities such as Na and Al contained in charge stripper foils. Especially, Na-22 has year-order long half-life and workers must be exposed to radiation while treating the irradiated foils.

We found that these impurities got mixed from components in the arc-discharge rod material and during the evaporative process. So, we made possible efforts in order to improve of production control not to contain impurities into foils and could get rid of impurities in HBC foils.

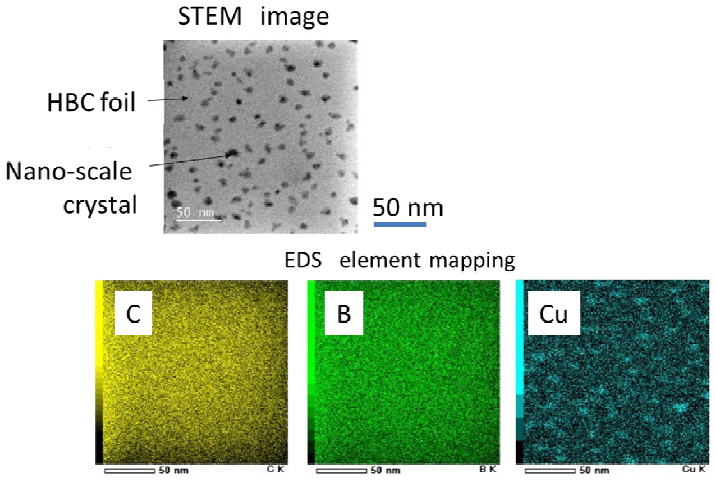

Fig. 1 STEM image and element mapping (C, B, Cu) of HBC foil after 5 hours irradiation of 300 keV Ar ion beam. Nano-scale crystals were generated by Cu atoms.

4 - 09 Development of an Embedded Structure of Polymer-based Mach-Zehnder Waveguide Drawn by Proton Beam Writing

W. Kada [a)], K. Miura [a)], R. Saruya [a)], A. Kubota [a)], T. Satoh [b)], Y. Ishii [b)], M. Koka [b)], T. Ohkubo [b)], A. Yokoyama [b)], T. Kamiya [b)] and O. Hanaizumi [a)]

[a)] Graduate School of Science and Technology, Gunma University,
[b)] Department of Advanced Radiation Technology, TARRI, JAEA

Proton beam writing (PBW) technique has a capability to fabricate next-generation micro-optical devices which will be required in high-speed optical communications [1)]. In the previous study, we had demonstrated the direct fabrication of Mach-Zehnder (MZ) type optical waveguides in PMMA (poly-methyl-methacrylate) [2)]. Optical switching functions were successfully accomplished with this PMMA-based MZ waveguides working at $\lambda = 1.55$ μm. A switching power of 43.9 mW were obtained for the operation of PMMA-based optical switch [3)], however, results indicated that enhancement in optical transmittance of the MZ waveguide structures is strongly required for the practical applications.

In this study, we demonstrated the modification of MZ optical waveguide. An embedded structure of optical waveguide was firstly demonstrated by decreasing the proton microbeam energy down to 750 keV. Also the base material of polymer waveguide was changed with PDMS (poly-dimethyl-siloxane), which attracts many researches as a potential candidate of a material with enhanced optical properties for such micro-optical devices.

A 30-μm-thick PDMS film (Toray Dow Corning SYLGARD184) was formed on a plane silicon substrate (40 mm × 20 mm × 0.5 mm) by spin-coat process. An MZ waveguide, as shown in Fig. 1, was drawn inside of the PDMS film using a 750 keV H^+ beam from 3-MV single-ended accelerator. The H^+ beam energy was selected to fabricate embedded optical waveguide structures with the depth of approximately 18 μm in the PDMS films. Whole waveguide were drawn using the combination of a proton beam scanner with maximum area of 800 μm × 800 μm and a mechanical stage with the position accuracy of 10 nm. The beam diameter was focused to approximately around 1 μmϕ with the beam current up to 50 pA. The symmetrically-coupling of two Y junctions with a core with $w = 8$ μm were used to fabricate a single-mode MZ waveguide structures in PDMS.

The several irradiations were performed with different beam fluence from 40 nC/mm² to 100 nC/mm² and evaluated by 1.55-μm fiber-laser irradiation with different light propagation conditions. Optical transmittance images were obtained by Infrared vidicon camera Hamamatsu C2741-03. Figure 2 shows the optical transmittance images of the PDMS MZ waveguides drawn by different beam fluences. Two different incident angles of fiber-laser-light were examined for each waveguide to generate different excitation conditions for simple estimation of light propagation mode. As shown in the Fig. 2, the light propagation through the MZ waveguide was observed in both PDMS waveguides fabricated by proton microbeam with comparably-low-beam fluence of 40 nC/mm² and 100 nC/mm². Comparing the transmittance images with different excitation conditions, the results indicated that single-mode light propagation was successfully accomplished by the embedded PDMS waveguide fabricated with beam fluence of 100 nC/mm².

References

1) M. C. Wu, et al., 19-Microelectromechanical systems for lightwave communication, Optics and Photonics, Academic Press, Burlington, (2008)713-58.
2) K. Miura et al., Key Eng. Mater. 534 (2013) 158.
3) K. Miura et al., Key Eng. Mater. 596 (2014) 134.

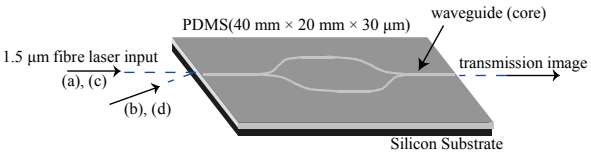

Fig. 1 Schematic drawing of PDMS-based MZ waveguide. Different excitation conditions were generated by changing incident angle of 1.5 μm-fibre-laser.

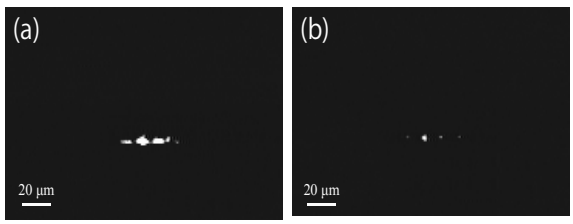

750 keV H^+ with beam fluence of 40 nC/mm²

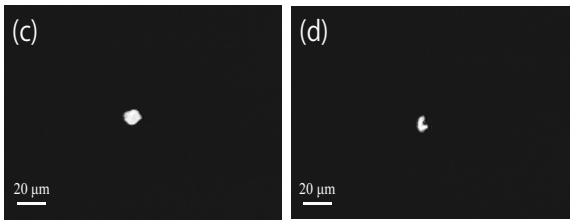

750 keV H^+ with beam fluence of 100 nC/mm²

Fig. 2 Optical transmittance images of PDMS MZ waveguides. (a) and (b) were obtained with sample fabricated with beam fluence of 40 nC/mm² while (c) and (d) were obtained that with fluence of 100 nC/mm². Single-mode operation was evaluated for single light spot in the image of (d) with alternated excitation condition of (a).

4 - 10 Synergic Effects of Ion Irradiations and Alkaline Pretreatment on Property of Hydrogen Storage Alloy

H. Abe [a)], S. Aone [b)], R. Morimoto [b)], H. Uchida [c)] and T. Ohshima [a)]

[a)] Environment and Industrial Materials Research Division, QuBS, JAEA,
[b)] Course of Applied Science, Graduate School of Engineering, Tokai University,
[c)] Department of Energy Science and Engineering, School of Engineering, Tokai University

In this study, we examined synergic effects of both surface modification of ion irradiations [1, 2)] and alkaline treatment on the initial hydriding rate of a Mm-Ni based alloy. The irradiations by lanthanum (La) and cerium (Ce) ions combined with an alkaline KOH pretreatment were found much more effective in the enhancement of the initial hydriding rate compared with irradiations with other ions. This report describes the synergic effects of the surface modifications by the both the surface irradiations with rare earth ions of La and Ce, and an alkaline surface treatment on the hydriding knetics. An alkaline atoms in the surface oxide layers effectively reduce the work function of electrons of the metal surface, and this leads to the acceleration of the dissociation of H_2O molecules, resulting in the enhancement of the initial hydriding rate[3,4)].

A powder sample of the Mm-$Ni_{3.48}Co_{0.73}Mn_{0.45}Al_{0.34}$ (Mm= $La_{0.35}Ce_{0.65}$) (expressed as Mm-Ni in this paper) alloy was used. The particle size was smaller than 38 μm in diameter. The alloy powder was pressed at 7 t/cm^2 to form a pellet with a diameter 12.3 mm and a thickness 1.3 mm as an electrode for electrochemical hydrogen absorption measurement. Before electrochemical process, the pellet sample was subjected to ion irradiations. Surface modifications were made by ion irradiations and alkaline treatment. Ion irradiations such as proton (H^+), magnesium (Mg^+), potassium (K^+), lanthanum (La^+), cerium (Ce^+) and bismuth (Bi^+) using a 400 kV ion implanter. These ion irradiations onto the sample surface was made in an acceleration energy of 350 keV, and a dose from 3.8×10^{15} to 5×10^{16} cm^{-2} at room temperature. For the electrochemical measurements of initial hydrogen absorption reaction rate, before this process, these samples were heated at 373 K for 30 min in 6M-KOH as an alkaline surface pretreatment in this study, after ion irradiated and un-irradiated samples.

Figure 1(a) and (b) show typical hydriding curves for irradiated samples without and with the KOH alkaline surface pretreatment, respectively. Irradiations were made using H^+, Mg^+, K^+, La^+, Ce^+ or Bi^+ ions before the alkaline pretreatment. The irradiation pretreatment enhanced slightly the initial hydriding rate compared with those without irradiation pretreatments [Fig. 1(a)]. However, samples with the both pretreatments of the irradiations and the subsequent alkaline treatment exhibited much higher initial hydriding rates than that without the pretreatment [Fig. 1(b)]. Apparently, a synergetic effect by the both pretreatments can be seen in the enhancement of the hydriding rate.

Generally, the ion irradiation induces high concentrations of vacancy type defects in the surface region of a metal. Since the vacancy type defects in the surface act as active sites for ambient molecules like O_2 or H_2O, surface oxidation/hydroxidation proceeds vigorously in the exposure of a sample to air. In this study, after the irradiations, samples were exposed to air, and then subjected to the alkaline pretreatment before electrochemical process. Therefore, the surface of samples shown in Fig. 1(a) exhibited retarded hydriding rates because of the formation of surface oxide layers in air exposure.

On the other hand, the alkaline treatment of the alloy surface induces the penetration of alkaline atoms in the surface oxide layers, and this reduces the work function of electrons of the surface, resulting in the enhancement of the rates of the H_2O dissociation and subsequent hydriding[3,4)]. By the additional alkaline treatment of samples, the irradiation effects became more distinct. After the alkaline treatment, samples irradiated with La^+ and Ce^+ ions exhibited much higher hydriding rates than the other samples irradiated with the other ions [Fig. 1(b)]. These results may be explained by the formation and distribution of vacancy type defects where the hydride nucleation and growth easily proceed in the surface of samples.

Among the irradiations by H^+, Mg^+, K^+, La^+, Ce^+ and Bi^+, the irradiation by La^+ or Ce^+ ions into the surface of a Mm-Ni based alloy combined with the KOH alkaline pretreatment was very effective in the enhancement of the initial hydriding rate by electrochemical process at room temperature. These ions induce vacancy type defects with very high concentrations over 10^{24} cm^{-3} in the shallow area of the alloy surface. With a combination of the KOH alkaline surface treatment, the irradiation treatment by La^+ or Ce^+ ions were found very effective in the enhancement of the initial hydriding rate of a Mm-Ni based alloy. Further investigation is required needed to confirm the relation among ion species, vacancy distributions and hydriding rate.

References

1) H. Abe et al., J. Alloy. Comp. 404-406 (2005) 288.
2) H. Abe et al.. J. Alloy. Comp. 408-412 (2006) 348.
3) H. Uchida et al., J. Alloy. Comp. 293-295 (1999) 751.
4) H. Uchida et al., J. Alloy. Comp. 330-332 (2002) 622.

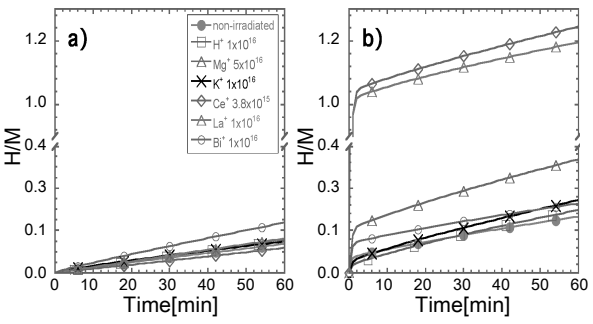

Fig. 1 Typical hydrding curves of samples irradiated by H^+, M^+, K^+, La^+, Ce^+ and Bi^+ ions at 350 keV; (a) without and (b) with alkaline 6M-KOH pretreatment, respectively. Each ion dose was in the range from 3.8×10^{15} to 1×10^{16} cm^{-2}.

4‐11 Application of a Removable Negative Resist for PB LIGA

J. Takahashi [a)], H. Nishikawa [a)], Y. Ishii [b)] and T. Kamiya [b)]

[a)] Department of Electrical Engineering, Shibaura Institute of Technology,
[b)] Department of Advanced Radiation Technology, TARRI, JAEA

We have studied application of a commercially available resist, KMPR from Kayaku MicroChem for proton beam writing. The microstructures on the KMPR surface can be used as a mother for Ni electroplating, which can be used as a mold for the LIGA process. The KMPR resist was found to be suitable for the PB-LIGA process, since it shows six times higher sensitivity than a typical negative resist, SU-8.

本研究では、陽子線を用いた集束プロトンビーム描画（Proton Beam Writing：PBW）とLIGA（Lithographie, Galvanoformung, Abformung）の利用を提案する。モールドを用いた転写法の一種である、Nanoimprint（NIL）は熱や光による成型が一般的だが、近年では電子線を用いた成型法（EB-NIL）[1)]や、PTFE [2)]のモールド活用など、様々な材料、方式が報告されている。

PBWは、マスクレスの直接描画方式による自由度の高い微細加工が可能であり、多品種の試作に有用である[3)]。電子線と比較して物質中で直進性が高く、高アスペクト比加工が可能である。このことから、バイオチップやMEMSに要求されるモールド作製に活用できる。これまで我々はPBWを用いたアスペクト比30程度のNi金属構造の作製[4)]やマイクロレンズアレイの作製[5)]を報告している。

本報告では、PBWを、LIGAと組み合わせ、パターン作製と転写を含む一連の工程をPB-LIGAプロセスとして展開し、フレキシブル性と生産性を兼ね備えた3次元微細加工技術としての応用を検討した。

PBWによる高アスペクト比電鋳パターン作製を検討する上で、ネガ型レジストを使用することは、加工に必要な照射面積が小さくスループットが高いため、ピラーや導波路、ニードルなど細長い構造の形成に有用である。従来我々がネガ型パターンのPB照射をする際には、エポキシ系樹脂であるSU-8（化薬Micro Chem社製）を使用していたが、永久膜として利用されるSU-8はエッチングが非常に困難であり、Niパターン内に残存したSU-8の除去が出来なくなる。

そこで同じくネガ型レジストである KMPR（化薬Micro-chem 社製）の使用を検討した。KMPR は 6~120 μm の厚膜成膜が可能で PBW を用いた垂直性の良好な加工により、高アスペクト比構造の形成に適する。化学的耐性があり、専用除去液を用いて、めっき後のレジスト除去も可能である。

芝浦工大フレキシブル実装工学研究センターにおける、1.0 MeV-PBW 装置による予備的実験の結果、その感度は 4.0 nC/mm^2 で、SU8 における 60 nC/mm^2 に比べて高い感度を示した。より高いアスペクト比を有する構造の形成には、JAEA 高崎量子応用研究所 TIARA にて 3.0 MV シングルエンド加速器の PBW 装置を使用した。スピンコートによる成膜後 100 °C、15 分間のベイク処理を行った。また、PBW 後、PEB 処理を 100 °C、3 分間行い、現像は、SU-8 現像液を用いた。PBW の条件は、ビームエネルギー3.0 MeV、電流値 10 pA、ビームサイズ 1.0 μm、照射量 5.0 nC/mm^2 にて膜厚 60 μm の KMPR 膜に照射した。照射パターンはライン、サークル、ドットの複合パターン、線幅 1~10 μm のラインパターン、ドットパターンを照射した。

現像により得られた KMPR パターンの SEM 像を Fig. 1 に示す。各形状に対応した低ラフネスかつ垂直性の高い構造を確認した。Figure 1 (b)に示すように倒壊なく得られたラインのパターン幅は最小 2.1 μm、アスペクト比は最大 29 であった。ドットパターンに対応するピラー構造として Fig. 1 (c)および(d)に示すアスペクト比約 10 の構造を得た。今後、これらを母型とする Ni 電鋳とその肩を用いたプロセスを確立する必要がある。予備的実験にて Ni 電鋳によるモールドは得られた。しかしながら、UV インプリントによる転写時に充填性、離型性の課題が生じた。転写時の圧力、UV 照射条件、離型剤の添加などにより、課題を解決する必要がある。

References

1) S. Okubo et al., Appl. Phys. Express 5 (2012) 027303-1.
2) H. Nishikawa, T. Hozumi, J. Vac. Sci. Technol. B 31, 06F403 (2013).
3) F. Watt et al., Mater. Today 10 (2007) 20-29.
4) N. Uchiya et al., Microsyst. Technol., 14 (2008) 1537-40.
5) K. Saito, et al., Nucl. Instrum. Meth. Phys. Res. B 306 (2013) 284-87.

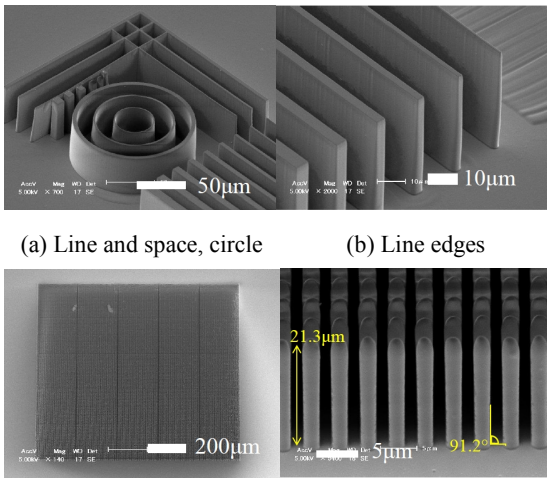

(a) Line and space, circle (b) Line edges

(c) Pillar arrays (d) Magnified pillar arrays

Fig. 1 SEM images obtained for patterns of lines and circles (a), lines with different width (b), and pillar arrays (c) and (d), which were written and developed respectively on 60-μm and 21-μm thick KMPR layers on Si by PBW at 3.0 MeV at a fluence of 5.0 nC/mm^2.

4 - 12 Ion Beam Analysis on Relaxation of Li Distributions in Li Ion Battery Electrodes

K. Mima [a)], K. Fujita [a)], A. Yamazaki [b)], Y. Orikasa [c)], Y. Uchimoto [c)], C. Okuda [d)], H. Sawada [d)], T. Satoh [e)], M. Koka [e)] T. Kamiya [e)], T. Saito [f)] and Y. Kato [a)]

[a)] The Graduate School for the Creation of New Photonics Industries, [b)]Research Facility Center for Science and Technology, Univ. of Tsukuba, [c)] The Graduate School of Human and Environment Science, Kyoto Univ., [d)] Toyota Central R&D Labs. Inc., [e)] Department of Advanced Radiation Technology, TARRI, JAEA, [f)] Battery Research Division, Toyota Motor Corp.

The lithium concentration distribution in the lithium ion battery (LIB) material was investigated using ion beam analysis (IBA) technique in the microbeam system at TIARA. It was found that the Li distribution was non-uniform for thicker samples or fast charge samples [1)]. In this work, the relaxation of the non-uniformity of Li concentration was investigated for fast charge and thick positive electrodes made by two typical active materials: $LiNi_{0.8}Co_{0.15}Al_{0.05}O_2$, (LNO) and $LiFePO_4$ (LFP).

The electrode (positive electrode) was fabricated from the mixture of active material, $LiNi_{0.8}Co_{0.15}Al_{0.05}O_2$, (LNO) or $LiFePO_4$ (LFP), carbon black as conductive carbon and binder (PVdF) on 25 μm thick Al. The composition of these materials was 85:10:5 in weight and the average particle diameter of active material was about 5~10 μm. The thickness of the positive electrode was 100 μm for LNO and 50 μm for LFP and the area density was about 2.1 mg/cm^2 for LNO and 1.0 mg/cm^2 for LFP. The current densities for charging were 6 mA/cm^2 for LNO and 45 mA/cm^2 for LFP. The charging times were determined as 15 minutes for LNO and 1 minute for LFP. The average compositions of positive material after charging corresponded to $Li_{0.75}Ni_{0.80}Co_{0.15}Al_{0.05}O_2$ and $Li_{0.5}FePO_4$. The IBA was applied for the fast charged electrodes made by LNO and LFP. The specifications of the samples are shown in Table 1. The electrolyte of the charged electrodes was washed out to quench the battery reaction after the relaxation period. The relaxation periods are selected to be 3 minutes, 60 minutes and 600 minutes for the present experiments. As shown in the Fig. 1, the non-uniformity of Li distributions disappeared for the LNO electrode within 1 hour, but it remains in the LFP electrodes. It was found that the potential distribution inside the LFP electrode was quite flat since Li concentrations were kept constant for long time.

This means that the electro-chemical potential of secondary particles inside the LFP electrode does not depend upon the particle position. Namely, electric potential does not depend upon the Li concentration of the secondary particles. This characteristics of LFP will prevent the localized Joule heating caused by the current localization. This is expected to be the advantage from the point of safety issue of the LIB. On the other hand, the energy capacity of the LIB made by LFP will be degraded because of the slow relaxation of non-uniform Li distribution.

Table 1 Parameters of samples.

Sample number	LN01	LN02	LN03	LFP1	LFP2	LFP3
Active material	$Li_xNi_{0.8}Co_{0.15}Al_{0.05}O_2$			Li_xFePO_4		
Charge rate	2 C/15 min			30 C/1 min		
Thickness	100 μm			30 μm		
Relaxation time (min)	3	60	600	3	60	600

Reference

1) K. Mima et al., Nucl. Instrum. Meth. Rhys. Res. B 290 (2012) 79.

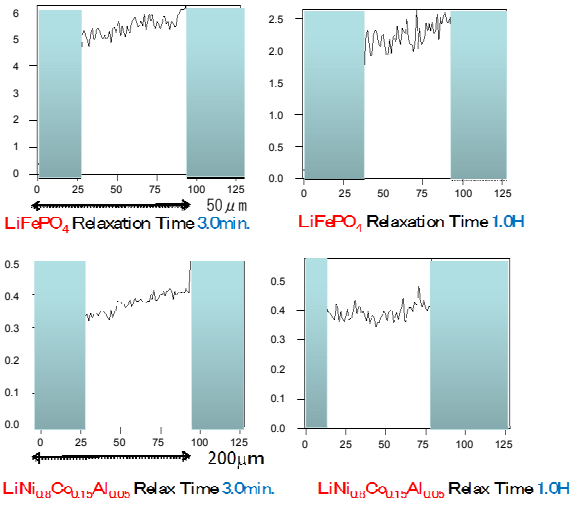

Fig. 1 Relaxation of Li distribution non-uniformity of $LiNi_{0.8}Co_{0.15}Al_{0.05}O_2$ (charging 20 C/30 μm-thick) vs. $LiFePO_4$ (charging 30 C/100 μm-thick) from 3 minutes (left two) to 1 hour (right two).

4 - 13 Evolution of Transformation Processes due to the Correlation of Implanted N-ions with Ti Thin Films

Y. Kasukabe [a,b], H. Shimoda [b], S. Yamamoto [c] and M. Yoshikawa [c]

[a] Center for International Exchange, Tohoku University, [b] Department of Metallurgy, Tohoku University, [c] Environment and Industrial Materials Research Division, QuBS, JAEA

Non-stoichiometric titanium nitrides, TiN_y, have covalent properties as well as metallic and ionic properties, which make them fascinating for both fundamental research and technological applications. Recently, it has been revealed that the interesting physical properties are related to the crystallographic (preferred oriented) and electronic structures[1]. However, atomistic transformation processes of deposited Ti films due to ion implantation, especially correlations between implanted ions and Ti films in the early N-implantation stage, have not been sufficiently studied. In order to clarify atomistic transformation processes of Ti films, in-situ observations by using transmission electron microscope (TEM) and electron energy loss spectroscope (EELS) have been carried out.

The as-deposited Ti films on thermally cleaned NaCl substrates consisted of both TiH_x and hcp-Ti with some preferred orientations at RT. The N_2^+ ions with 62 keV were implanted into hcp-Ti and TiH_x with preferred orientations in the 400 kV analytic high resolution TEM combined with ion accelerators at JAEA-Takasaki[2].

In-situ TEM observations have revealed that the (110)-oriented TiN_y is formed by nitriding the (110)-oriented TiH_x in the band-like TEM contrast region of the as-deposited Ti film, whereas the (001)-oriented TiN_y is mainly formed by the transformation of the $(03\cdot5)$-oriented hcp-Ti to (001)-oriented fcc-Ti. In-situ EELS observations have elucidated that the release of H atoms in TiH_x proceeds preferentially in the early N-implantation stage, and that in the subsequent N-implantation stage the electron density in the hybridized band by N 2p and Ti 3d-Ti 4p states increases gradually with increasing N-concentration, which means that the number of N atoms bonding to Ti atoms increases gradually. By comparison of the net areas of the energy loss peaks concerning N 1s (K) and Ti 2p ($L_{2,3}$) electrons in electron energy loss spectra for TiH_x and hcp-Ti regions, it can be seen that at the initial implantation stage (less than N/Ti = 0.25) there are more N atoms invading into the octahedral sites in the fcc-Ti sublattice of H-released TiH_x than those invading into the octahedral sites in hcp-Ti sublattice. Since, in the equilibrium, the amount of octahedral sites occupied by N atoms in hcp-Ti lattice is limited to the lesser amount than that in H-released fcc-Ti sublattice by the solubility limit of N in hcp-Ti [~20 at.%, which corresponds to N/Ti=0.25[3]], the subsequent invasion of N atoms in the hcp-Ti lattice can be promoted only after the transformation of hcp-Ti to fcc-Ti sublattices (TiN_y). This hcp-fcc transformation is energetically not easy to occur in the very early N-implantation stage. Further invasion of N atoms into the hcp-Ti become difficult, which leads to fewer N content in the hcp-Ti region compared with that in TiH_x region. On the other hand, when the N/Ti ratio exceeds ~0.25, the amount of N atoms bonded to Ti atoms in hcp-Ti region becomes the same as that in TiH_x region. Here, we define N/Ti, 0.25 as a critical concentration ratio. It was found that the explanation of critical concentration ratio N/Ti=0.25 can be done by using the model in Fig. 1, as follows. Since there are four Ti atoms in the two unit cells of hcp-Ti such as those indicated by the two parallelogram prisms BKFE-LMNO and JPKB-RQML with atoms indicated by C and I in Fig. 1, the critical number of nitrogen atoms at the critical concentration ratio N/Ti=0.25 is one. As one nitrogen atom (indicated by G) has already occupied one octahedral site (indicated by ABCDEF in the model) at N/Ti> ~ 0.25, the transformation could occur collectively when another N atom invades the neighboring octahedral site (indicated by HJICBK). This is because the invasion of N atom to the unoccupied octahedral site next to the occupied one induces the evolution of nucleus of the hcp-fcc transformation. Thus, the hcp-fcc transformation should collectively occur by this evolution in order to reduce the lattice strain due to the occupation by N atoms.

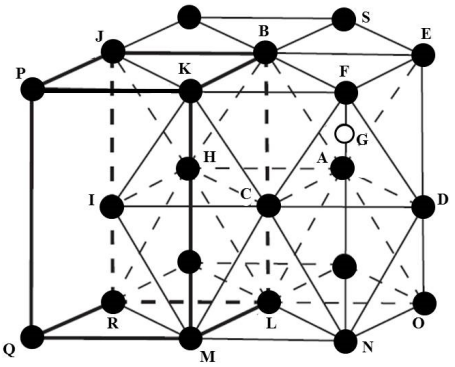

Fig. 1 The parallelogram prisms BKFE-LMNO and JPKB-RQML are a unit cell of hcp-Ti with two Ti atoms, respectively. Solid circles and an open circle represent Ti atoms and a N atom, respectively.

References

1) S. Hao, B. Delley and C. Stampfl, Phys. Rev. B 74 (2006) 035424-1.
2) H. Abe et al., JAERI-Research 96-047 (1996) 1.
3) Phase Diagram of Binary Titanium Alloys, edited by Joanne L. Murray, Metals Park, ASM International, (1990) p. 176.

4 - 14 Ion Channeling Analysis of Disordering Behavior at $Fe_3Si(111)/Si(111)$ Heteroepitaxial Interfaces

Y. Maeda [a, c)], Y. Kawakubo [c)], Y. Noguchi [c)], T. Hirata [c)], K. Narumi [a, b)] and S. Sakai [a)]

[a)] Advanced Science Research Center, JAEA, [b)] Department of Advanced Radiation Technology, TARRI, JAEA, [c)] Department of Computer Science and Electronics, Kyushu Institute of Technology

Iron-based Heusler alloy Fe_3Si is promising for a spin injector into Si since high quality epitaxial growth of DO_3 type ordered Fe_3Si on Si(111) or Ge(111) has been succeeded by low temperature molecular beam epitaxy (MBE). In the $Fe_3Si(111)/Ge(111)$ heterointerface with little lattice mismatch, thermally activated interdiffusion between Fe and Ge atoms caused significant disordering of atomic raw along Ge<111> axial directions [1)]. On the other hand, the $Fe_3Si(111)/Si(111)$ heterointerface has large lattice mismatch by ~ 4%. This elastic condition at the heterointerface may give a considerable effect on epitaxial quality. In this study, under such a concerned situation, we have applied axial ion channeling (AXIC) to evaluate thermal stability of thermally activated disordering at the $Fe_3Si/Si(111)$ interface.

The $Fe_3Si(111)/Si(111)$ hybrid structure was prepared by a low temperature MBE and annealed at 373-573 K for 2 h in vacuum in order to cause thermally activated atomic disordering. The AXIC was carried out in BL-SC1. The incident beam of 2.0 MeV $^4He^+$ and the angle of incidence of 165 degrees were employed. We computed channeling parameters (χ_{min}, $\Psi_{1/2}$) from channeling dip curves. Furthermore, we can compute the total atomic displacement $\langle u \rangle$ from the parameters. One-dimensional *rms* thermal vibration amplitude $\langle u_{th} \rangle$ is computed from Debye theory. We can obtain the $\langle u_s \rangle$ from $\langle u \rangle$ and $\langle u_{th} \rangle$ [2,3)]. This static displacement comes mainly from inperfect crystal growth or plastic displacement due to lattice mismatch.

Figure 1 shows channeling dip curves for (a) Si and (b) Fe channels. In the Fe_3Si/Si heterointerface, we can measure independently either Fe or Si channel, so that both $\langle u_s \rangle$ of Fe and Si atoms can be obtained. The $\langle u_s \rangle$ at each anneal temperature were shown in Fig. 2. The $\langle u_s \rangle$ and its temperature dependence of Fe atoms were larger than those of Si atoms. This result indicates that atomic disordering is associated to randomness of Fe atoms.

Vacancy migration models [4)] have suggested that in the DO_3 lattice nearest neighbor jump of Fe atoms along the <111> axis is much easier than that of Si atoms. However, below 573 K we did not observed any diffusion behavior in the RBS spectra. Next we discuss atomic displacement caused by difference in thermal expansion between Fe_3Si and Si. It is found that the $\langle u_s \rangle$ of Fe atoms at each anneal temperature obeys to thermal expansion. This result shows that the $\langle u_s \rangle$ of Fe atoms may be dominated by plastic displacement due to thermal expansion, and that such thermal expansion at each temperature can be quenched into room temperature and remains as the $\langle u_s \rangle$.

References

1) Y. Maeda et al., Appl. Phys. Lett. **91** (2007) 171910.
2) Y. Maeda et al., Thin Solid Films **519** (2011) 8461.
3) Y. Kawakubo et al., Phys. Stat. Sol. C **10** (2013) 1828.
4) S. Dennler, Phys. Rev. B**73** (2006) 174303.

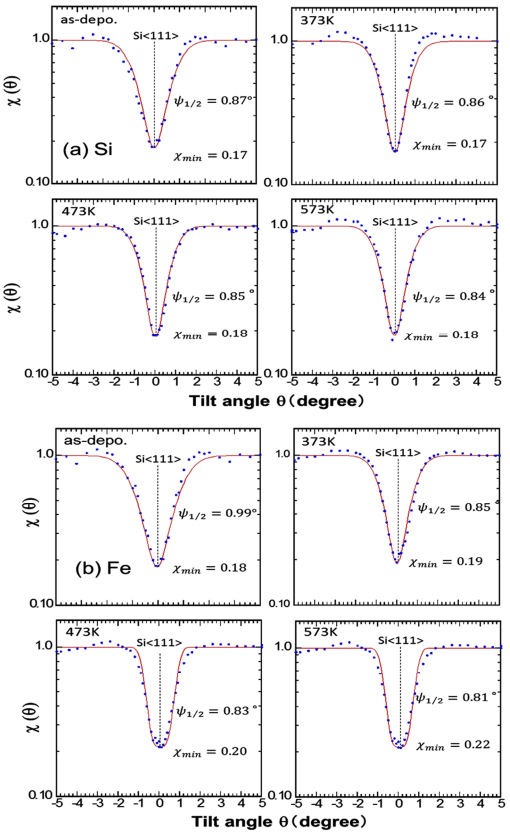

Fig. 1 Channel dip curves for (a) Si and (b) Fe channels at each anneal temperature.

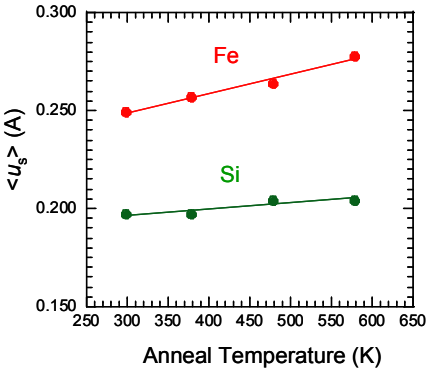

Fig. 2 Static displacements $\langle u_s \rangle$ for Si and Fe atoms at each anneal temperature.

4 - 15 Ion-beam Effect on Mechanical Property and Lattice Structure of Ni_3Al

H. Yoshizaki [a], A. Hashimoto [a], Y. Kaneno [a], S. Semboshi [b], F. Hori [a], Y. Saitoh [c] and A. Iwase [a]

[a] Department of Materials Science, Osaka Prefecture University,
[b] Institute for Materials Research, Tohoku University (Kansai Center),
[c] Department of Advanced Radiation Technology, TARRI, JAEA

In our previous study, the effect of ion irradiation on mechanical property and lattice structure of Fe - 45 at.% Rh intermetallic alloy was investigated [1]. The disordered A1(fcc) phase, which is intrinsically the high temperature phase, appeared even at room temperature in Fe - 45 at.% Rh by the ion irradiation. The ordered $L1_0$ structure, which has been obtained by the high speed deformation[2], was also observed. In this report, the effect of ion irradiation on mechanical property and lattice structure of Ni_3Al was studied. This alloy shows the $L1_2$ ordered lattice structure at room temperature and keeps it even just below the melting temperature.

Ni_3Al bulk ingot was thermally annealed at 1,323 K for 48 h. After the annealing, the ingot was cut into the sheets with the dimension of $10 \times 10 \times 1$ mm^3. They were irradiated with 16 MeV Au^{5+} ions by using the 3 MV tandem accelerator of TIARA. The ion fluences were 5×10^{13} /cm^2 and 5×10^{14} /cm^2. After the ion irradiation, the crystal structure analysis was carried out by surface X-ray diffraction(SXRD). The mechanical property change was also estimated by using Vickers hardness tester.

The SXRD spectra for unirradiated and irradiated specimens are shown in Fig. 1. In order to estimate the effect of the irradiation on the lattice structure, we have used the relative degree of order, which is given by,

$$(Relative\ Degree\ of\ order) = \frac{I_{110}/I_{220}}{U_{110}/U_{220}} \quad ,$$

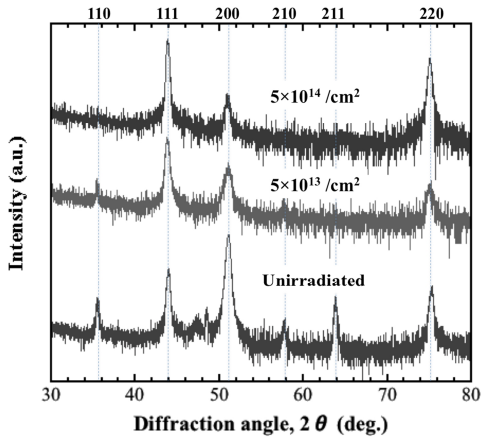

Fig. 1 SXRD spectra of Ni_3Al specimens before and after 16 MeV Au ion irradiation.

where I_{hkl} is the hkl peak intensity in irradiated specimen, U_{hkl} is the hkl peak intensity in unirradiated specimen. The ion fluence dependence of the relative degree of order is shown in Fig. 2. This result indicates that the lattice structure of Ni_3Al changes from the ordered $L1_0$ structure to the disordered A1(fcc) structure by the ion irradiation.

The result of Vickers hardness testing is shown in Fig. 3. The Vickers hardness decreases with increasing ion fluence. This hardness change is possibly due to the irradiation induced lattice structure transformation from the ordered $L1_0$ phase to the disordered A1(fcc) phase. As the Burger's vector of the $L1_0$ lattice structure is larger than that of the A1(fcc) lattice structure, the irradiated Ni_3Al is more deformable than the unirradiated Ni_3Al.

References

1) A. Hashimoto et al., Trans. Mater. Res. Soc. Jpn. 38 [2] (2013) 329-31.
2) R. Oshima et al., Mater. Sci. Eng. A350 (2003) 139-44.

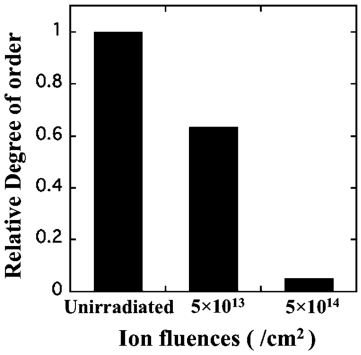

Fig. 2 Relative degree of order as a function of ion fluence.

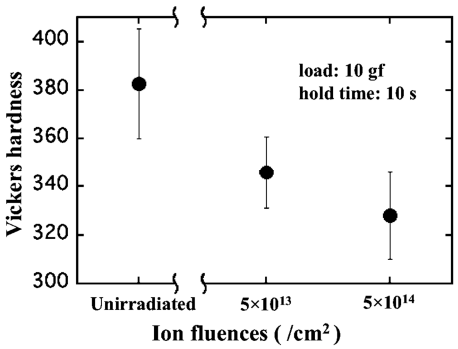

Fig. 3 Vickers hardness as a function of ion fluence.

4 - 16 Hardness Modification of Al-Mg-Si Alloy by Means of Energetic Ion Beam Irradiation

D. Ueyama [a)], Y. Saitoh [b)], F. Hori [a)], K. Nishida [c)], N. Soneda [c)],
S. Semboshi [d)] and A. Iwase [a)]

[a)] Department of Materials Science, Osaka Prefecture University,
[b)] Department of Advanced Radiation Technology, TARRI, JAEA,
[c)] Materials Science Research Labortory, Central Resarch Institute of Electric Power Industry,
[d)] Kansai-Center,Institute of Materials Research, Tohoku University

In supersaturated alloys, irradiation produced point defects such as interstitial atoms and vacancies enhance the diffusion of some solute elements, concentration of which is larger than that under the thermal equilibrium condition, and lead to their segregation [1)]. In our previous studies, we have found that ion beam irradiation caused a remarkable change in hardness in Al-Cu-Mg alloys (a typical duralumin)[2)]. Therefore we are interested in whether this method is also effective for the hardness modification of other aluminum alloys. In the present experiment, we measured hardness of ion-irradiated Al-Mg-Si alloys.

We prepared supersaturated Al-Mg-Si alloys as specimens. We irradiated the specimens at room temperature with 5.4 MeV Al ions (Al^{2+}), 7.3 MeV Fe ions (Fe^{2+}), 10 MeV I ions (I^{3+}) and 16 MeV Au ions (Au^{5+}) using a tandem accelerator at Takasaki Advanced Radiation Research Institute, Japan Atomic Energy Agency. The ion-fluences were from 3×10^{12} /cm^2 to 3×10^{15}/cm^2. The beam current was less than 260 particle nA/cm^2 (1.6×10^{12} /cm^2) in order to avoid the beam heating. After the irradiation, the Vickers hardness was measured at room temperature.

Figure 1 shows the change in Vickers hardness measured with the load of 10 gf as a function of ion fluence. For the irradiations with all kinds of ions, the Vickers hardness increases with increasing ion fluence at room temperature and tends to be saturated at higher fluences.

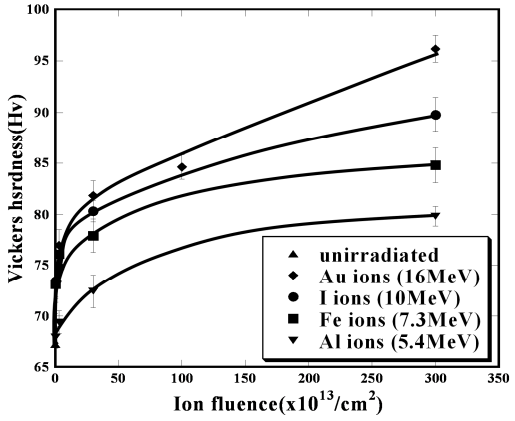

Fig. 1 Change in Vickers hardness as a function of ion fluence for 5.4 MeV Al ions, 7.3 MeV Fe ions, 10 MeV I ions and 16 MeV Au ions.

To evaluate the effects of the ion irradiation more quantitatively, we discuss the change in Vickers hardness in term of the energy deposited in the specimen by the irradiation. It is well known that there are two processes of energy transfer from energetic ions to targets. One is the energy transfer through the electronic excitation. The other is the energy deposited through the elastic collisions. Figure 2 shows the change in Vickers hardness as a function of the density of energy deposited through the elastic collisions. The figure clearly shows that in spite of the irradiation with different ion species and energies, the change in Vickers hardness is well scaled by the elastically deposited energy density. This means that the elastically deposited energy leads to the increase in hardness.

The present result shows that the energetic ion irradiation can systematically control the hardness of Al-Mg-Si alloys as well as Al-Cu-Mg alloys.

References

1) G. S. Was, Fundamental of Radiation Materials Science, Springer, (2007) Chapter 6.
2) T. Mitsuda et al., J. Nucl. Mater. 408 (2011) 201.

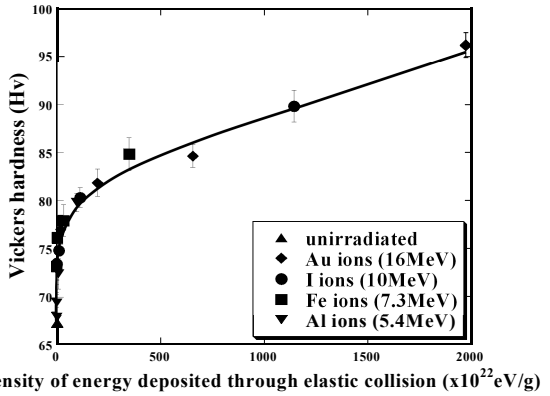

Fig. 2 Change in Vickers hardness as a function of density of energy deposited through the elastic collision [i.e., the energy deposited per unit mass of the specimen (gram)].

4 - 17 A Comparative Study on Transmission Properties of 4-MeV C^+ and C^{4+} Ion Beams Entering a Curved Insulating Channel

K. Motohashi [a,b], Y. Saitoh [c], N. Miyawaki [c], S. Matoba [c] and Y. Suzuki [b]

[a] Department of Biomedical Engineering, Toyo University,
[b] Department of Intelligent Material and Mechatronics Systems, Graduate School of Engineering, Toyo University,
[c] Department of Advanced Radiation Technology, TARRI, JAEA

The efficient reflection of both fast singly-charged light ions and slow highly-charged heavy ions by solid surfaces has attracted attention. Nebiki et al.[1] found that about 2% of the 2-MeV-He^+ ions exited the outlet of the tapered-glass capillary without significant energy loss. The binary collisions with small scattering angle may act an important role in this phenomenon. On one hand, charging on the surface is considered vital for the transmission of slow, highly charged ions through capillaries with inner insulating walls[2]. It may be possible to guide fast heavy ions like C, N, O, and other ions by combination of charging and small-angle scattering on insulating walls. In our previous study[3], we first investigated the transmission properties of a 4-MeV C^+-ion beam entering a gap between a pair of cylindrical convex and concave glass lenses. It was found in the study that the transmission of the ion beam was larger than that of He–Ne laser-beam at tilt angles $|\theta| \geq 2°$ by a factor of 2 - 100 and further there was no significant energy loss. In the present study, we have measured transmission and energy of 4-MeV C^{4+} ion beam entering the same curved insulating channel to investigate charging effect.

A pair of cylindrical glass lenses was used as the walls of the curved insulating channel[3], as shown in Fig. 1. The setup basically consists of three parts: an aluminum electrode with an entrance hole, a cylindrical convex borosilicate-crownglass lens, and a cylindrical concave borosilicate-crown glass lens. The diameter of the entrance hole was 1.5 mm. The curvature of both lenses was 155.70 mm. The convex and concave lenses face each other across a gap of 1.2 mm. The entire setup can be tilted around the axis, which passes through the center of the entrance hole. The tilt angle θ was defined to be positive for clockwise rotation. The depth and height of both cylindrical lenses were 20 mm. The entire setup was connected to a manipulator with three linear (x, y, and z) motions and one rotational (θ) motion. The transmission and energy of the 4-MeV C^{4+}-ion beam as a function of the tilt angle θ were measured by a silicon surface barrier detector (SBD).

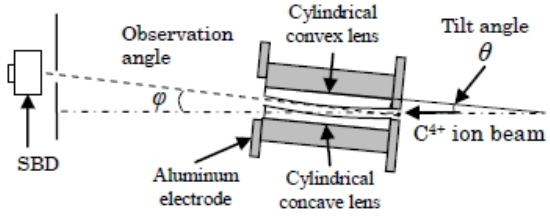

Fig. 1 Schematic illustration of the experimental setup.

Figure 2 shows the transmission probabilities of C^+ and C^{4+} ion beams as a function of tilt angle (θ) observed at the angle of φ=0°. The transmission of C^{4+} was slightly higher than that of C^+ around $|\theta| = 1°$. Figure 3 shows the peak energies of transmitted ions observed at φ=0° as a function of tilt angle. The peak energies of C^{4+} ions are slightly larger than those of C^+ over all tilt angles by 3~24 keV. Although these results strongly suggest that charging on the glass surfaces acts a main role in the ion transmission, further expermental efforts are necessary to clarify the details.

References

1) T. Nebiki et al., J. Vac. Sci. Tech. A **21** (2003) 167.
2) N. Stolterfoht et al., Phys. Rev. Lett. **88** (2002) 133201.
3) K. Motohashi et al., Jpn. J. Appl. Phys. **52** (2013) 076301.

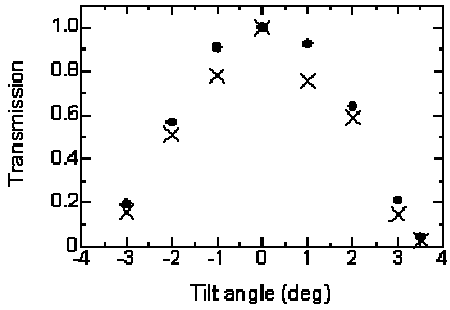

Fig. 2 Transmission probabilities of C^+ (×) and C^{4+} (●) ion beams at the observation angle of φ = 0°.

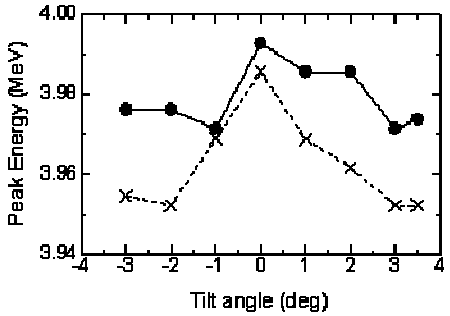

Fig. 3 Peak energies of transmitted C^+ (×) and C^{4+} (●) ions at the observation angle of φ = 0°.

4 - 18 In-situ Monitoring of Photo Emission of White Si–O–C(–H) Ceramics under Irradiation of Proton Beam

M. Narisawa [a)], A. Iwase [a)], M. Sugimoto [b)], A. Idesaki [b)], A. Takeyama [b)] and T. Satoh [b)]

[a)] Graduate School of Engineering, Osaka Prefecture University,
[b)] Environment and Industrial Materials Research Division, TARRI, JAEA

Si–O–C ceramics synthesized by pyrolysis of densely cross-linked silicone resins or condensates of Si alkoxides have been investigated mainly in the field of Ceramics Matrix Composites (CMC), because of their low costs and high creep resistance at high temperature region. Pyrolysis in an inert atmosphere, however, yields black ceramics including many defects. In particular, excess carbon is considered to be main origin of the black color. Recently, our group in Osaka Prefecture University succeeded in synthesizing white Si–O–C(–H) ceramics, which show PL under UV light, by using hydrogen for the pyrolysis atmosphere [1)]. The samples obtained beyond 1000 °C possess high oxidation resistance, and PL properties are also maintained after the oxidation [2)]. On the other hand, the samples obtained around 800 °C have large specific surface area, and are oxidized easily beyond 400 °C. This means that properties of the white Si–O–C(–H) ceramics depend on heat treatment conditions. In this study, the samples decarbonized at 800 °C (S800) and 1100 °C (S1100) are exposed to proton beam irradiation and photo emission under proton beam irradiation is analyzed.

The precursor is silicon resin particles with a diameter of 2 μm. Synthesis process of the Si–O–C(–H) ceramics has been reported in various previous studies. Obtained particles, S800 or S1100, were mixed with 5 wt% of PVA, and water was added to control viscosity. The prepared slurries were painted and dried on Si substrates. The proton beam in an energy range of 1-3 eV was irradiated on the painted layers, and resulting photo emission was monitored. The beam irradiation was conducted by a 3MV Single-ended Accelerator in Takasaki Ion Accelerators for Advanced Radiation Application (TIARA) and the "in-situ" monitoring of photo emission was conducted by Solid Lambda CCD UV-NIR (Spectra Co-op).

Under vacuum (10^{-3} Pa), the S800 layer shows broad emission peaking at 520 nm, whereas the S1100 layer shows emission peaking at 540 nm (Fig. 1). As the irradiation dose increases up to 1.2×10^{14} cm^{-2} with the dose rate of 6.25×10^{10} cm^{-2} s^{-1} intensity of the emission decreases logarithmically (Fig. 2). Under fixing the irradiation time at 1 min, apparent emission intensity is monitored at various conditions (Table 1). The intensity is high at a large irradiation current and at a high acceleration voltage. Emission intensity of the S800 layer is, however, always far lower than that of S1100.

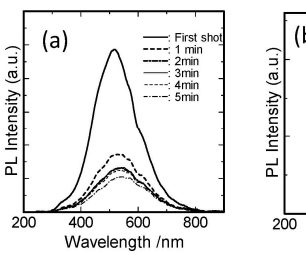

Fig. 1 Photo emission spectra under 1 MeV proton beam; (a) S800 in vacuum, (b) S1100 in vacuum.

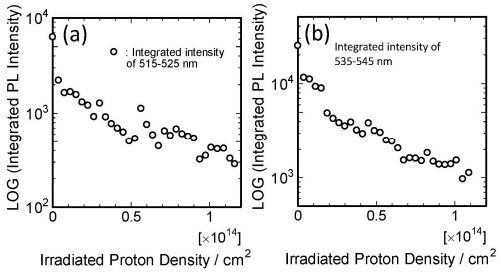

Fig. 2 Decrease of photo emission during 1 MeV proton beam irradiation; (a) S800 in vacuum, (b) S1100 in vacuum.

Table 1 Apparent peak intensity (a.u.) of photo emission from the layer under the beam irradiation.

Sample	1 MeV, 10 pA ($1\ mm^2$)	1 MeV, 100 pA ($1\ mm^2$)	3 MeV, 100 pA ($0.64\ mm^2$)
S800 (515-525 nm)	588 (counts)	2220 (counts)	2866 (counts)
S1100 (535-545 nm)	2773 (counts)	11587 (counts)	24471 (counts)

On the other hand, the emission from the layer in air was also monitored. The experiments were done by using thin carbonate films to separate the samples from a vacuum chamber. In such oxidation atmosphere, a new sharp emission peaking at 310 nm appeared besides the main broad peak. Intensity of this sharp peak was strong in S800 and was weak in S1100. The intensity of the peak, however, decreased during irradiation, and decreasing rate seemed to be rapid as compared with the main broad emission. This sharp peak is possibly assigned to ODC (II), which is widely known as a major PL center in defect-introduced silica.[3)] Under existence of oxygen, proton beam irradiation may cause partial decomposition of Si–O–C(–H) ceramics to yield SiO_x phase temporally, which is remarkable in S800 having a high specific surface area.

References

1) M. Narisawa et al., Bull. Chem. Soc. Jpn. **85** (2012) 724.
2) M. Narisawa et al., J. Non-Cryst. Solids **391** (2014) 1.
3) L. Skuja, J. Non-Cryst. Solids **239** (1998) 16.

4 - 19 Estimating Mixing Ratio of the Sediments Discharged from Yangtze River Based on ESR Signal Intensity

K. Saito [a)], R. Tada [a)], H. Zheng [b)], T. Irino [c)], C. Luo [d)], M. He [d)], K. Wang [c)] and Y. Suzuki [a)]

[a)] Department of Earth and Planetary Science, The University of Tokyo,
[b)] Nanjing Normal University,
[c)] Graduate School of Environmental Science, Hokkaido University,
[d)] Nanjing University

The drainage of Yangtze river, China, has been strongly effected by East Asia Summer Monsoon (EASM). The position of EASM has changed, also effecting the spatial variation of sediment yields from each part of Yangtze. To reconstruct the past spatial variation of EASM as the provenance change of sediment from Yangtze, we tried to use ESR (Electron Spin Resonance) and CI (Crystallinity Index) of quartz as a proxy to distinguish sediments from each tributary of Yangtze.

中国を流れる揚子江は全長 6,300 km、流域面積は約 200 万平方キロメートルにおよぶ東アジア最大の河川である。流域の雨季は東アジア夏季モンスーンの発達に伴う前線によりもたらされ、前線が流域のどこで停滞するかにより降水域が変化する。従って、夏季モンスーン降水の長期的な挙動を明らかにするには、1 地点での降水の時系列変動だけではなく、空間分布の変動も知る必要がある。

気象観測記録以前の降水量の時空変動を復元するには、古気候記録を用いることとなる。揚子江においては流出する堆積物の 95%以上は懸濁粒子であり、流域の降水量と水流出量、水流出量と堆積物流出量の間には、それぞれ正の相関がある。そこで、河口部における堆積物の供給源変化は降雨地域の変動を反映しており、堆積物中の砕屑物の供給源とその変動の復元から、流域内での降水分布とその変動が推定できると期待される。そして、そのためには供給源を推定する指標が必要となる。

そこで本研究では、石英の電子スピン共鳴（ESR; Electron Spin Resonance; ESR）信号強度および結晶化度（Crystallinity Index; CI）に着目し、揚子江の各流域に由来する砕屑粒子の区別を試みた。石英の E1'中心の ESR 信号強度は、石英中の酸素空格子量、すなわち母岩の形成年代におおまかに比例するとされている。また、石英の結晶化度は、母岩の形成過程における温度や速度等を反映するとされている。石英の酸素空格子を E1'中心として検出するためには、試料中の石英に対し、事前にγ線の照射および加熱（300 ℃）を行う必要がある。これはγ線の照射により正孔を生成し、加熱によって生成した正孔を酸素空孔と結合させ、E1'中心へと変換するためである。そのため本研究では、高崎量子応用研究所において 2.5 kGy の ^{60}Co-γ線照射を行い、加熱した後、ESR 分析を行った。

本研究の目的は、揚子江流域における過去の降水分布の時間・空間変動を石英の ESR 信号強度を用いて復元するための基礎として、1) 主要な支流から流出する石英粒子の ESR 信号強度を分析して、それが流域の基盤岩の年代を反映することを確認すること、2) これらの値が現在の本流における懸濁物の混合を説明しうるか、3) 特定の支流域での増水を仮定し、どの程度の規模の増水であれば河口における ESR 値の変化として検出可能であるか、という 3 点である。

まず、揚子江の主要な支流から河床堆積物を採取し、ESR および CI の分析を行った。その結果、石英の ESR 信号強度により各支流に由来する砕屑物粒子が区別され、流域の基盤年代から推定される ESR 信号強度と整合的であることが示された（Fig.1）。

この結果を基に、支流の ESR 信号強度を端成分とし、現世における各支流から本流への堆積物流出量の観測値を元に、本流上流部から河口にかけての ESR 信号強度の変化河口部の堆積物における ESR 信号強度の理論値を推定したところ、実際に本流の堆積物を分析して得られた値と整合的な結果が得られた。よって石英の ESR 信号強度は堆積物の混合比を推定するための指標として用いうること考えられる。

次に、モンスーンの変動により降水フロントが移動した上流部または中流部の特定の支流での堆積物流出量の増加を仮定して河口部の ESR 値を計算し、河口における ESR 値の変化として検出しうる増水の規模を推定した。その結果、少なくとも中流域について、平常時の 3 倍に相当する降水があった場合、河口部で採取される懸濁物の ESR 信号強度の変化としてその供給源の検出が可能であると考えられる。

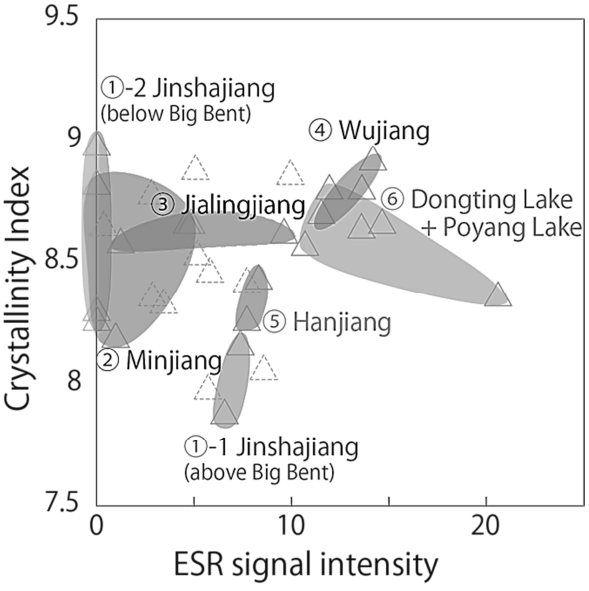

Fig. 1 The relationship between ESR signal intensity and Crystallinity Index of sediments from each tributary of Yangtze.

4 - 20 Development of Spin-polarized Positron Beam and Its Application to Spintronics Study

A. Kawasuso, M. Maekawa, Y. Fukaya, H. J. Zhang and H. Li

Advanced Science Research Center, JAEA

Spintronics is promising to go beyond the traditional electronics. Current-induced spin polarization (CISP) at surface and interface plays a critical role in spintronics. The spin Hall effect (SHE) and the Rashba effect are the representative phenomena producing CISP due to spin-orbit coupling (SOC). In the last fiscal year, we studied the CISP on the outermost metal surfaces using a spin-polarized positron beam [1-3].

Positrons implanted into a sample diffuse back to the surface and emitted into vacuum as positronium which is the positron-electron bound state like hydrogen. Two spin states, singlet (S=0) and triplet (S=1), are possible. These decay into two and three gamma quanta, respectively. The annihilation probability shows asymmetry upon flipping the mutual polarization vector of positrons and electrons. From this, the electron spin polarization at the outermost surface can be determined. Since two-gamma annihilation of positronium overlaps the free positron-electron annihilation, three-gamma annihilation event is used for observing the surface electron spin polarization.

Figure 1 shows the three-gamma annihilation probability of positronium observed for the Au, Cu, Pt, Pd, α, β-Ta and α, β-W surfaces as a function of successive current reversal. The Au and Cu surfaces show no significant CISP. In contrast, the Pt, Pd, Ta, and W surfaces exhibit large CISP and the CISP of Ta and W are opposite to those of Pt and Pd. The sign of the CISP obeys the same rule in SHE suggesting that SOC is mainly responsible for the CISP. Figure 2 shows the spin polarizations of the above surfaces per input charge current density of j_c=10^5 A/cm^2.

According to the spin diffusion theory, the energy width of polarized electrons in the density of states is given by the shift of chemical potential: $\Delta\mu = 2\theta_{SH}\lambda_S j_c \rho$, where λ_S is the spin diffusion length, θ_{SH} is the SHE angle and ρ is the resistivity. For θ_{SH}=10%, λ_S=10 nm, ρ=50 μΩcm and j_c=10^5 A/cm^2, one finds $\Delta\mu$=1 eV. The typical density of states at the Fermi level (E_F) is 10^{23} cm^{-3}eV^{-1}, and hence the excess spin density will be 10^{17} cm^{-3}. Assuming that positrons pick up electrons located from E_F to E_F-1 eV, the observable electron spin polarization will be 10^{-4}%. The above huge CISP is hardly explained as the diffusive SHE.

The spin density induced by the Rashba effect is given by $\langle \delta s_y \rangle = 4\pi e D_{2D} E \tau \alpha_R / \hbar$, where e is the elementary charge, D_{2D} is the two-dimensional density of states, E is the applied electric field, τ is the electron relaxation time and α_R is the Rashba parameter. Assuming $\alpha_R = 3 \times 10^{-10}$ eVm, D_{2D} = 10^{14} cm^{-2}eV^{-1}, τ=10 ps, E=1 kV/m, one finds the spin polarization of the order of 5%. Thus, if the relaxation time is long enough, the above-observed huge CISP can be explained by the Rashba mechanism rather than the diffusive SHE. This settles a controversy, that which of these two mechanisms dominates the large CISP on metal surfaces.

References

1) M. Maekawa et al., Nucl. Instrum. Meth. Phys. Res. B **308** (2013) 9-14.
2) A. Kawasuso et al., J. Magn. Magn. Mater. **342** (2013) 139-43.
3) H. J. Zhang et al., Scientific Reports 4, (2014) 04844.

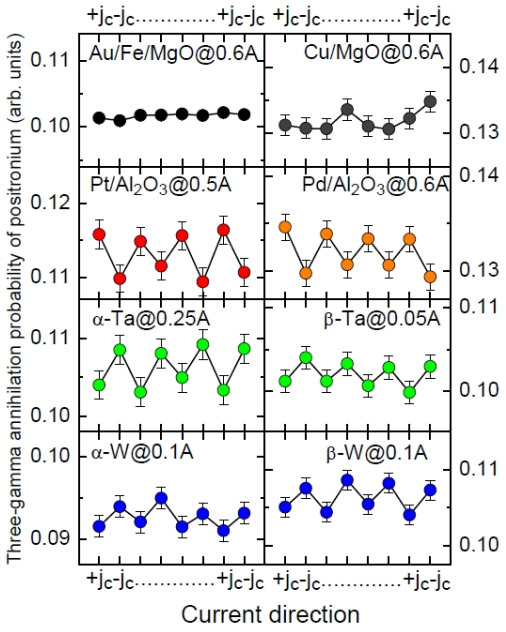

Fig. 1 Three-gamma annihilation probability of positronium upon successive current reversal observed for the Au, Cu, Pt, Pd, α-Ta, β-Ta, α-W and β-W surfaces. (+j_C) and (-j_C) denote the direction of current applied for the sample.

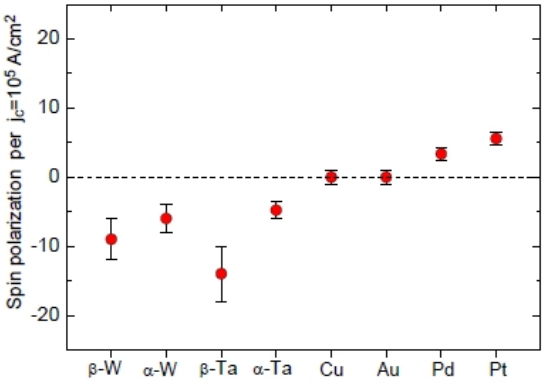

Fig. 2 Spin polarizations per input charge current density of 10^5 A/cm^2 obtained for the Au, Cu, Pt, Pd, α-Ta, β-Ta, α-W and β-W surfaces.

4 - 21 Ovserbation of Spatial Distributins of Vacancy Defects in Si Substrates by Using Scanning Positron Microprobe

M. Maekawa and A. Kawasuso

Advanced Science Research Center, JAEA

Scanning positron microscope (SPM) is a powerful tool for observing spatial distribution of vacancy defects near the subsurface region. We have constructed a SPM by using a specially fabricated small source and a solid neon moderator [1]. Using this apparatus, it is expected that the diffusion process of vacancies in semiconductor materials can be observed directly. This means that it is also expected that detailed information for the controlling of intrinsic defects, which are difficult to observe by conventional methods, is obtained. The diffusion process of vacancy defects in silicon has been estimated from its thermal characteristics [2]. In this work, we attempted to observe directly the two-dimensional diffusion process of vacancy-type defects introduced by partially ion implantation.

Figure 1 shows the schematics of sample preparation. Samples used in this work was *n*-type Si crystals (10 × 10 mm). Silicon ion implantation was carried out to the half area of the sample by using an aluminum mask with thickness of 50 μm. Implantation dose was set to 1×10^{16} cm^{-2}. After irradiation, sample was annealed at 573 K for 30 minutes. At the boundary region, a focused positron beam was scanned to obtain a special distribution of positron annihilation parameter (S-parameter). Scan area was 1,200 × 1,000 μm and scan step was 50 μm.

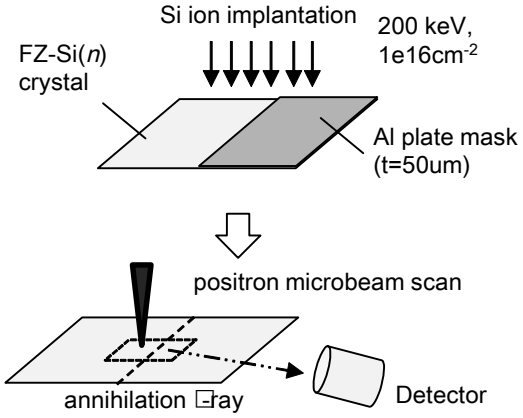

Fig. 1 Sample preparation and observation of vacancy-type defects by a scanning positron microbeam.

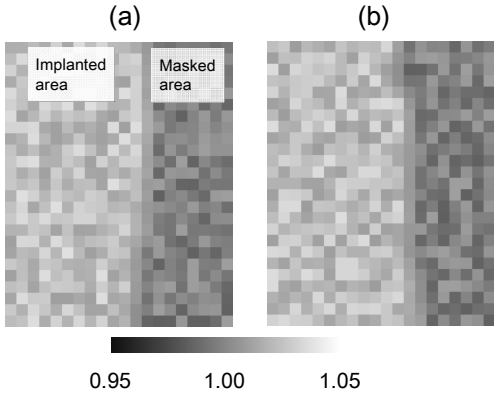

Fig. 2 Spatial distributions of S parameter for the (a) as-implanted sample and (b) annealed sample. Scan step was set to 50 mm.

Figure 2 shows the obtained spatial distributions. All the S parameters are normalized to the value of un-implanted Si. For the as-implanted state, S parameters at only implanted area were increased. This is due to the vacancy-type defects created by ion implantation. S parameter was increased 2%, which is attributed to the positron trapping at divacancies [3]. It is reported that such vacancies starts to disappear at around 600 K [2]. The difference was not observed in S parameter distribution of the sample which was annealed at that temperature. Figure 3 shows the line profiles of S parameter across the border. Planer diffusion of S parameter in the edge was not observed. The defect migration might not happen up to a temperature that is almost equal to the defect annealing temperature.

References

1) M. Maekawa and A. Kawasuso, Appl. Surf. Sci. 255 (2008) 39-41.
2) A. Polity et al., Phys. Rev. B 58 (1998) 10363-77.
3) R. Krause-Rehberg, "Positron Annihilation in Semiconductors", Springer (1998).

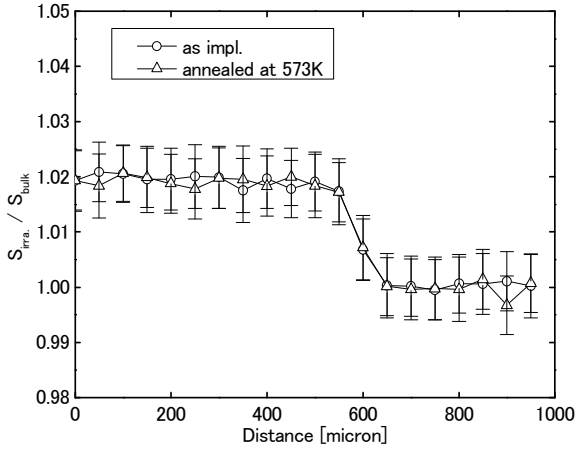

Fig. 3 Position dependences of S parameter for the as-implanted sample and annealed sample.

4 - 22 Chemical Yield of Transient Species in NaBr Aqueous Solution Using Ion Pulse Radiolysis Method

K. Iwamatsu [a,b], S. Yamashita [b], M. Taguchi [a], A. Kimura [a], S. Kurashima [c] and Y. Katsumura [b]

[a] Environment and Industrial Materials Research Division, QuBS, JAEA,
[b] The University of Tokyo, [c] Department of Advanced Radiation Technology, TARRI, JAEA

Nowadays a heavy ion beam, one of the high linear energy transfer (LET) radiations, is applied to various fields because of its specific irradiation effects being different from those of low LET radiations such as electron beam, X-rays and γ-rays. The specific irradiation effects of the ions are attributed to dense energy depositions along their trajectories leading to heterogeneous distributions of the transient species, so called a "track structure". Water was selected as target in this study because it is a main component of our body and more data exist for radiolysis than any other material. A hydroxyl radical (•OH), one of the most important water decomposition species, was investigated by the ion beam pulse radiolysis system [1].

Reactions of radicals have been observed by electron pulse radiolysis. •OH has a small molar absorption coefficient (ε: 540 $M^{-1}cm^{-1}$ at 200 nm) so that probe agents for scavenging of •OH can be used. NaBr was selected as a probe reagent since the reactions of •OH in NaBr aqueous solution are well known, and $Br_2^{\bullet-}$, reaction intermediate of •OH with Br^-, has a large ε (9,000 $M^{-1}cm^{-1}$ at 375 nm) [2]. Ninety mM NaBr aqueous solution saturated with N_2O gas was irradiated with 10-μs pulsed beam of 11.4 MeV/u He^{2+}, 15.8 MeV/u C^{5+} and 12.8 MeV/u Ne^{8+} ions provided from AVF cyclotron in TIARA facility. N_2O converts hydrated electron (e^-_{aq}) to •OH in aqueous samples. Transient absorbance of NaBr aqueous solution was observed at 375 nm by the pulse radiolysis technique [2]. Dose distribution in the optical analyzing region was estimated from beam current value and GAF film dosimeter. The beam currents were 3.0, 1.75 and 1.1 μA, and after pulsing their dose rate were 13.3, 39.4 and 139 Gy/pulse for $^4He^{2+}$, $^{12}C^{5+}$ and $^{20}Ne^{8+}$ ions, respectively. Track averaged LET values for each ion were calculated by TRIM code [3] as shown in Table 1.

The absorbance of $Br_2^{\bullet-}$ increased within ion pulse and decreased as time. The peak absorbance values were almost the same at 0.007 in all the ions in spite of different doses. Chemical yield of $Br_2^{\bullet-}$ per absorbed energy were estimated from the absorbance using the Lambert-Beer law, absorbance = $\varepsilon c \ell$, c:concentration, ℓ:optical path. ℓ was obtained from ion's range in the sample solution as shown in Table 1. Chemical yields of $Br_2^{\bullet-}$ by the ion irradiations decreased with elapsed time as shown in Fig 1 The chemical yields of $Br_2^{\bullet-}$ decreased with the increase in atomic mass of the incident ion. Reactive radicals, for example •OH and e^-_{aq}, are produced in the track. Recombination reactions, such as •OH + •OH and •OH + e^-_{aq}, occur easier by higher LET, in other words heavier ions, because of denser radical formations. Thus the yield of $Br_2^{\bullet-}$ decreased because the amount of •OH scavenged by Br^- decreased in the track of heavier ion. The concentrations of $Br_2^{\bullet-}$ at the pulse end were estimated at 2.4, 3.8 and 8.7 μM for $^4He^{2+}$, $^{12}C^{5+}$ and $^{20}Ne^{8+}$ ions, respectively. The concentrations increased as the atomic mass of the ions increased even though chemical yields of $Br_2^{\bullet-}$ decreased as mentioned above. The decay rates of the concentrations increased with the atomic mass of the ions, and are well fitted to a second-order-reaction kinetics, disproportionation reaction of $Br_2^{\bullet-}$. Diffusion kinetics analysis based on track structure model in order to understand of chemical reactions of •OH in the track is in progress.

References

1) M. Taguchi et al., Radiat. Phys. Chem. 78 (2009) 1169.
2) K. Iwamatsu et al., Trans. Mater. Res. Soc. Jpn. 36 (2011) 32.
3) J. F. Ziegler et al., The Stopping Power and Range of Ions in Solids, Vol. 1, Pergamon Press, New York. (1985).

Table 1 Track averaged LET and range of each ion.

	$LET_{Track\ averaged}$ /eV/nm	Range of ion / mm
He	28.7	1.58
C	205	0.92
Ne	624	0.41

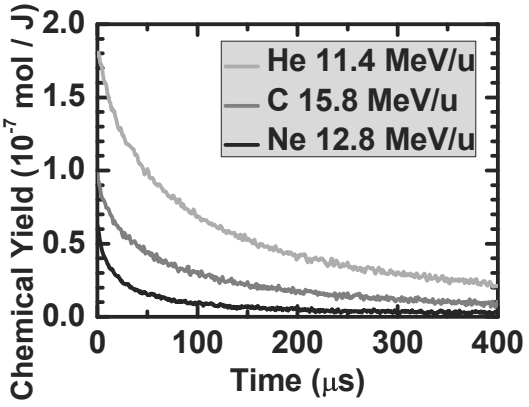

Fig. 1 Time profile of chemical yield of $Br_2^{\bullet-}$ in N_2O saturated 90 mM NaBr aqueous solution from the pulse end, 11.4 MeV/u $^4He^{2+}$, 15.8 MeV/u $^{12}C^{5+}$ and 12.8 MeV/u $^{20}Ne^{8+}$ ion.

4 - 23 Microsecond Ion Pulse Radiolysis of Biphenyl-dodecane Solution by Scavenging Experiment

T. Kondoh [a)], K. Iwamatsu [b)], M. Taguchi [b)], S. Kurashima [c)], J. Yang [a)], K. Kan [a)], M. Gohdo [a)], H. Shibata [a)] and Y. Yoshida [a)]

[a)] The Institute of Scientific and Industrial Research, Osaka University,
[b)] Eenvironment and Industrial Materials Research Division, QuBS, JAEA,
[c)] Department of Advanced Radiation Technology, TARRI, JAEA

To disclose ion beam induced track reactions in dodecane, a microsecond time-resolved ion-pulse radiolysis system was developed at the TIARA facility. Absorbance at 375 nm increased with a biphenyl concentration. Transient absorption was measured in biphenyl-dodecane solutions with electron or cation scavengers irradiated by 220 MeV C^{5+} ions. The species measured at 375 nm was suppressed by electron scavenger and enhanced by a cation scavenger, but the decay rate did not change.

イオンビームは高LET放射線であり、高密度イオン化効果により、がん治療や植物の品種改良、材料改質などの応用技術が注目されている。イオンビームの高密度イオン化状態における活性種反応の初期過程は、イオントラック構造の複雑さと反応の速さから直接観測が困難なために詳細には理解されていない。イオントラック内の活性種の時間挙動を解明するために、チョッパーのゲート幅を変化させることにより、数千のパルス列をマクロパルスとして試料に照射し、マクロパルスのパルス幅より長い時間領域で活性種の光吸収時間挙動を観測できるマイクロ秒重イオンパルスラジオリシスを田口らは開発した[1)]。核燃料サイクルにおいて抽出溶媒として用いられるドデカンの分解及び水素発生の基礎過程の解明を目指して、重イオンを照射した場合の高密度イオン化効果を解明するために、TIARAで開発された国内で唯一のマイクロ秒重イオンパルスラジオリシスシステムを用いた。前年度は、高密度イオン化による活性種反応の速度を遅くして、反応を観測するためのプローブ分子としてビフェニルを加えたドデカン溶液中で、重イオンが誘起した過渡吸収時間挙動とスペクトルを測定したが、活性種の同定には至らなかった。そこで今年度は、ビフェニル-ドデカン溶液に電子捕捉剤としてジクロロメタン（CH_2Cl_2）、カチオン捕捉剤としてトリエチルアミン（TEA）、電子及びラジカル捕捉剤として酸素を用いて、活性種の同定を目的とした。

約1,000個のマイクロパルスを持つマクロパルスをHYポートに輸送し、試料に入射して溶媒の活性種や溶質との反応を誘起した。吸光度は10^{-3}程度であることが多く、これを観測するために分析光には高安定な半導体レーザーを用いた。220 MeV C^{5+}イオンビームをビフェニル-ドデカン溶液に照射し、375 nmで測定した。ビフェニル-ドデカン溶液の375 nmの吸光度は、ビフェニル濃度増加に伴い増大した（Fig. 1）。このことから375 nmで観測されるのはビフェニルに関連した活性種と考えられる。次に、ビフェニル-ドデカン溶液中に1 Mジクロロメタンまたは TEA、飽和量の酸素を溶かした場合の過渡吸収をFig. 2に示した。375 nmでは、パルス幅50 μsの重イオンマクロパルスにより吸光度が増加し、パルスエンド直後から吸光度の減衰が観測された。電子捕捉剤であるジクロロメタンを1 M加えた場合、ビフェニル-ドデカン溶液よりも初期収量が減少した。一方、カチオン捕捉剤であるTEAを1 M加えた場合、初期収量は増加した。このことから、観測している活性種の前駆体は電子と反応し、カチオン種ではないことが分かった。しかしながら、観測している活性種の減衰速度は、ジクロロメタンを加えてもTEAを加えてもビフェニル-ドデカン溶液と変化しなかった。次に酸素を飽和量溶解した結果、著しく収量が減少した。以上のことから観測した活性種は、ビフェニルラジカルアニオンもしくは高密度イオン化状態での再結合を経た長寿命のビフェニル励起3重項状態と考えられる。

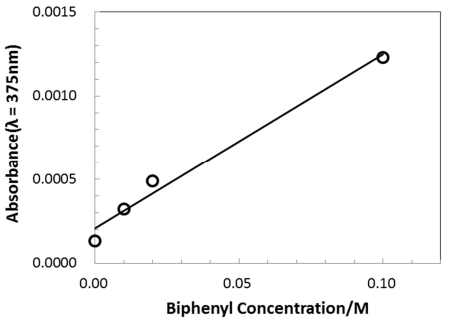

Fig. 1 Absorbance at 375 nm vs biphenyl concentration in dodecane.

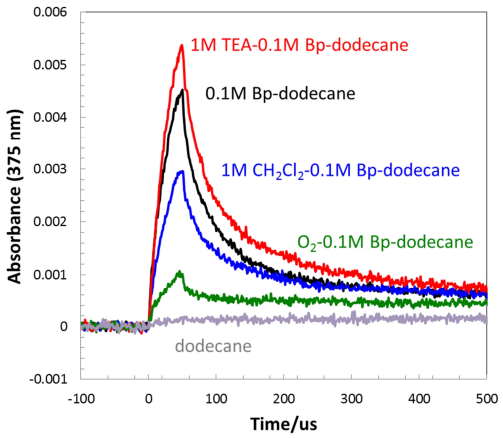

Fig. 2 Transient absorption of 0.1 M biphenyl (Bp) dodecane solution with electron scavenger, cation scavenger or oxygen at 375 nm.

Reference

1) M. Taguchi et al., Radiat. Phys. Chem. 78 (2009) 1169-74.

4 - 24 Effects of Excitation Density on Scintillation Properties of a Li-glass Scintillator

M. Koshimizu [a)], K. Iwamatsu [b, c)], M. Taguchi [c)], S. Kurashima [d)], A. Kimura [c)], T. Yanagida [e)], Y. Fujimoto [e)], K. Watanabe [f)] and K. Asai [a)]

[a)] Department of Applied Chemistry, Tohoku University, [b)] Graduate School of Engineering, The University of Tokyo, [c)] Environment and Industrial Materials Research Division, QuBS, JAEA, [d)] Department of Advanced Radiation Technology, TARRI, JAEA, [e)] Graduate School of Life Science and Systems Engineering, Kyushu Institute of Technology, [f)] Graduate School of Engineering, Nagoya University

Excitation density, or linear energy transfer (LET), caused by impinged ionizing radiation influences scintillation properties because the interaction among excited states cannot be ignored in the case of high excitation density. This is particularly true in the case of high-energy ions or alpha particles. LET effects appear in neutron detection events in which a (n, α) reaction occurs. In this case, detection events for neutrons and gamma-ray photons may be discriminated based on the difference in scintillation properties between gamma-ray photons and alpha particles produced by the (n,α) reaction. Thus, analysis of scintillation properties dependent on LET is essential in understanding the responses of conventional scintillators for high-LET particles and acquiring knowledge about the basic scintillation processes in the case of high LET. In this study, we analyzed scintillation properties of a Li-glass scintillator, GS20, using pulsed ion beams with varying LET values.

Scintillation time profiles were collected using pulsed ion beams in the AVF cyclotron at the TIARA facility, JAEA, Japan. Scintillation was detected using a photomultiplier tube (PMT, Hamamatsu, R7400), and detection signals were recorded using a digital oscilloscope. Time profiles were obtained by averaging 1,000 detection signals. The time resolution of the measurement system was several ns. A sample was irradiated with pulsed beams of 20 MeV H^+, 50 MeV He^{2+}, and 220 MeV C^{5+}. In this measurement, LET was higher for beams with heavier ions.

Figure 1 shows scintillation time profiles. The inset shows the scintillation spectrum with irradiation of 50 MeV He^{2+}. This scintillation spectrum is consistent with that obtained with X-ray irradiation, which indicates that scintillation in both irradiation cases originates from the same excited state: the excited state at Ce^{3+} centers. In contrast to the spectra, the time profiles are significantly different for different LET values. The rise in the time profiles was more gradual for the pulsed beam of 20 MeV H^+, which had the lowest LET among the investigated ions. The rise reflects the process of energy transfer from the host glass matrix to emitting Ce^{3+} centers. In general, light yield is lower for higher LET. The α/β ratio (the ratio of light yield for alpha particles and beta particles) of light yield in GS20 is far lower than unity; thus, the difference in time profiles among different LET values is ascribed to quenching of excited states with high LET. The fast rise in the time profiles for higher LET ions, therefore, indicates that quenching occurs in competition with the energy transfer process. Figure 2 shows the scintillation time profiles at long time scale. Decay behaviour was quite similar for irradiations of different ions. Thus, the LET effects in GS20 originate from quenching owing to the interaction among excited states in the glass matrix, and quenching occurs on the time scale of several ns.

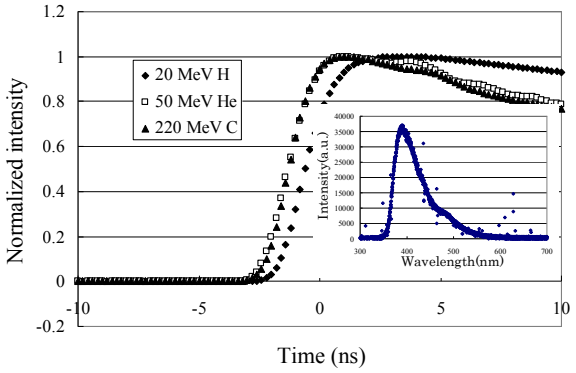

Fig. 1 Scintillation time profiles of GS20 under irradiations of different ions. Inset: Scintillation spectrum of GS20 under 50 MeV He^{2+} irradiation.

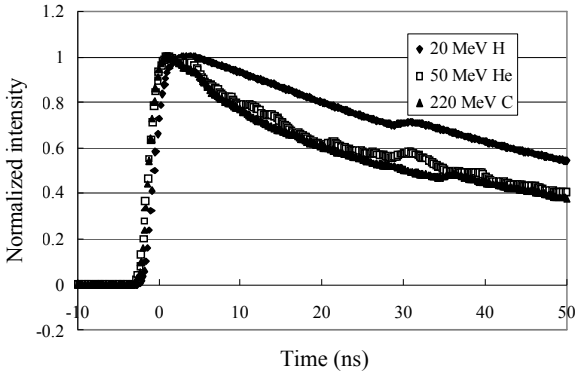

Fig. 2 Scintillation time profiles of GS20 under irradiations of different ions at long time scale.

4 - 25 LET and Dose Rate Effect on Radiation Induced Copolymerization in Physical Gel

S. Nakagawa [a)], M. Taguchi [b)], A. Kimura [b)], N. Nagasawa [b)] and A. Hiroki [b)]

[a)] Tokyo Metropolitan Industrial Research Institute,
[b)] Environment and Industrial Materials Research Division, QuBS, JAEA

N_2-saturated 2-propanol solutions containing styrene and maleimide gelated by the addition of hydroxypropylcellulose and irradiated by proton, He and C-ion beams. The trend in the dose rate and LET effects on the yield and molecular weight distribution of the polymer produced in the gel was almost the same in the solution. On the contrary, the relative values between lower and higher dose rate in the gel were higher than those in the solution. This effect was enhanced for irradiations by proton as well as heavier ion with a higher LET value.

2-プロパノール中でマレイミド($C_2H_2(CO)_2NH$)とスチレンを放射線共重合したところ、平均分子量およびポリマー生成量は線量率(電流値)が減少するほど増加し、この効果はLETの大きい重イオンビームほど顕著であった[1)]。さらに、溶媒ラジカルのマレイミドへの付加反応が遅いメタノール中では、線量率効果やLET効果が2-プロパノール中より顕著に現れることがわかった[2)]。ラジカルの反応速度も放射線重合反応制御の要素であるためと推測される。そこで、ラジカルの拡散が抑制されるゲル中での放射線重合反応の効率について検討することとした。

マレイミドおよびスチレンを 2-プロパノールに溶かし(各 0.5 mol/L)、窒素雰囲気中でヒドロキシプロピルセルロース(HPC)を 5 mg/100 μL の割合で添加してゲル状試料を作成した。試料に TIARA でイオンビーム(C-320 MeV, He-50, 107 MeV, H-20 MeV)を照射した。試料の厚さは、各イオンビームの飛程より十分長かった。照射により、ビームの飛程に沿って白色微粒子が生成した。分光光度計で、生成物の透過スペクトルを測定した。また、生成物をテトラヒドロフラン(THF)に溶解し、ゲルパーミエーションクロマトグラフ(GPC)で分子量分布を測定した。

Figure 1 に、He-107 MeV を照射した際の生成物の 700 nm における吸光度を平均吸収線量(=エネルギー×フルエンス/(飛程×密度))に対してプロットした。照射線量の増加に伴って吸光度が増加することがわかる。得られたポリマー生成効率を Table 1 に示す。低線量率照射および軽イオンでの照射において、ポリマー生成効率が大きいことがわかる。これは、溶液中での結果とほぼ同じ傾向である。一方、高線量率に対する低線量率照射におけるポリマー生成効率の比は、すべてのイオン種において溶液中よりゲル中で大きい。この線量率効果は、高 LET 照射である炭素イオンのみならず、プロトン照射においても大きいことがわかる。また、生成物の平均分子量 M_n(Table 1)においても、プロトン照射における線量率効果は He-107 MeV 照射より大きい。LET の大きいビームによる高線量率照射においては、溶媒ラジカルが再結合により消失するためポリマー生成効率が低下すると考えられ[1)]、ラジカルの拡散が抑制されるゲル中において、この効果がより大きくなると推測される。一方、プロトン照射では多くの溶媒ラジカルが重合の開始剤となるため、高線量率照射では重合ラジカルが十分に成長する前にターミネーションしてしまう。溶媒中と比較するとゲル中では、重合ラジカルの拡散が抑制されやすいため、プロトン照射においても大きな線量率効果が現れたものと考えられる。

References

1) S. Nakagawa et al., Radiat. Phys. Chem. 80 (2011) 1199-202.
2) S. Nakagawa et al., Radiat. Phys. Chem. 91 (2013) 143-47.

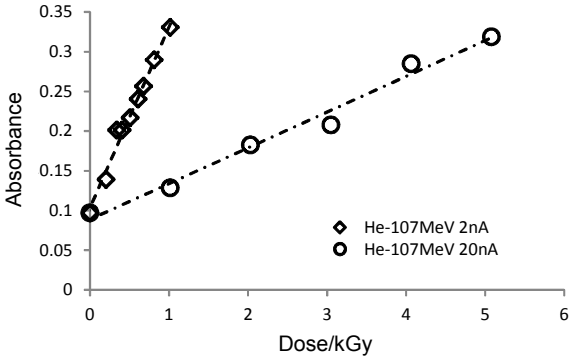

Fig. 1 Dose dependence of the absorbance at 700 nm of the polymer obtained by irradiation of He-107 MeV.

Table 1 The yield of polymer by 1 kGy irradiation of ion beams and the number average molecular weight (M_n).

irradiation source	LET eV/nm	polymer yield solution (mg/mL/kGy)[a]	gel(absorbance/depth/kGy)	M_n
H-20 MeV(20 nA)	2.2-13	3.7	0.11	25,500
H-20 MeV (2 nA)	2.2-13	13.0 (3.5)[b]	0.94 (8.5)[b]	40,500 (1.59)[b]
He-107 MeV (20 nA)	7.1-60	2.2	0.06	32,100
He-107 MeV (2 nA)	7.1-60	9.1 (4.1)[b]	0.31 (5.1)[b]	43,000 (1.34)[b]
He-50 MeV (20 nA)	13-100	1.1	0.05	25,340
He-50 MeV (2 nA)	13-100	4.4 (4.0)[b]	0.33 (7.0)[b]	43,000 (1.70)[b]
C-320 MeV (20 nA)	75-600	0.7	0.015	24,650
C-320 MeV (2 nA)	75-600	3.7 (5.3)[b]	0.14 (9.5)[b]	45,300 (1.84)[b]

a) Data from reference 1,

b) The ratio of the dose rate effect on each irradiation source.

4 - 26 Evaluation of Quasi-monoenergetic Neutron Fields at TIARA for Calibration of a Neutron Detector

T. Matsumoto [a)], A. Masuda [a)], H. Harano [a)], Y. Tanimura [b)], H. Yoshitomi [b)], M. Yoshizawa [b)], H. Seito [c)] and Y. Haruyama [c)]

[a)] National Metrology Institute of Japan, National Institute of Advanced Industrial Science and Technology, [b)] Department of Radiation Protection, NSRI, JAEA, [c)] Department of Advanced Radiation Technology, TARRI, JAEA

Precise measurements for high-energy neutrons are important in studies on neutron dose estimation around large accelerator facilities such as J-PARC, nuclear data, exposure in aircrafts and neutron induced soft error rate in semiconductor devices. Research has proceeded to use high energy quasi-monoenergetic neutron fields at peak neutron energies of 45 MeV and 60 MeV at the AVF cyclotron in TIARA facility as neutron standards in order to calibrate high energy neutron detectors[1,2]. It is important to determine the neutron energy distributions and neutron fluence for the calibration. It is also necessary to investigate reliability of a neutron monitor to determine the neutron fluence at a place of calibration instrument.

Neutron energy distributions were measured with a liquid scintillation detector (BC501A, 7.62 cm diameter × 7.62 cm thickness) and a ^{6}Li-glass scintillation detector (GS20, 50 mm diameter × 5 mm thickness) by means of the time-of-flight (TOF) method. The liquid scintillator and the ^{6}Li-glass scintillator were placed 6.5 m away from the target. The detection efficiency of the liquid scintillator was determined by calculation with the SCINFUL-QMD code [3] as well as by calibration with mono-energetic neutrons at AIST. The detection efficiency of the ^{6}Li-glass scintillator was obtained from calibration using mono-energetic neutrons at AIST. In the TOF measurements, the neutron energy from 20 keV to a full energy peak was observed by using s- and p- chopper systems developed by Kurashima et al[4].

Neutron fluence was determined using a proton recoil telescope composed of a silicon surface barrier detector (sensitive area of 28.3 cm^2, depletion depth of 500 μm) and the liquid scintillation detector that was used in the TOF measurements. Figure 1 shows a two-dimensional plot of proton energy loss measured with the Si detector and proton energy measured with the liquid scintillation detector for 45 MeV neutrons. The detection efficiency was determined using the Monte-Carlo code MCNPX[5]. A high density polyethylene disc with a 100-mm diameter and a 2-mm thickness was used as an n-p converter. A graphite disc with a 100-mm diameter and a 1-mm thickness was used to subtract contributions due to nuclear reactions with graphite in the polyethylene disc. Measurements without the polyethylene disc and the graphite disc were performed to obtain background.

A thin plastic scintillation detector (BC400) with a 0.5 mm thickness developed by Y. Shikaze[6] was used as a neutron fluence monitor. In the present experiments, measurements with the liquid scintillation detector were performed for neutron beams with and without the chopper. Ratios of count rate from the monitor and count rate from the liquid scintillation detector for the measurements are in agreement within 1 % as shown in Fig. 2.

Uncertainty for calibration will be determined and the reliability of the results obtained from the TOF and neutron fluence measurements will be confirmed by measurements in the partial different conditions in future.

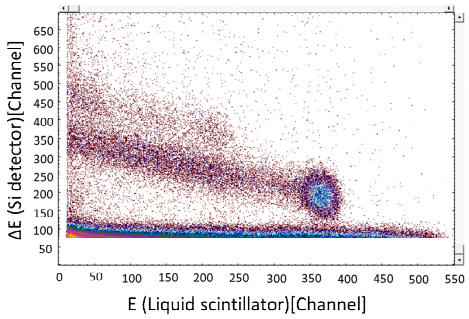

Fig. 1 Two-dimensional plot of proton energy loss measured with the Si detector and proton energy measured with the liquid scintillation detector for 45 MeV neutrons.

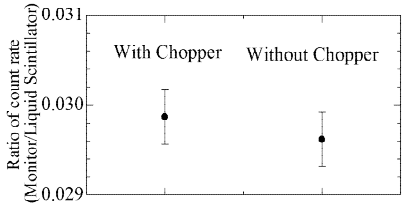

Fig. 2 Ratios of count rate from the monitor and count rate from the liquid scintillation detector for the measurements with and without the chopper.

References

1) H. Harano et al., Radiat. Meas. 45 (2010) 1076.
2) Y. Shikaze et al., Nucl. Instrum. Meth. Phys. Res. A 615 (2010) 211.
3) D. Satoh et al., JAEA-Data/Code 2006-023 (2006).
4) S. Kurashima et al., Proc. CYCLOTRONS 2010, MOPCP090 (2010).
5) D. B. Pelowitz, MCNPX user's manual Ver 2.5.0, Los Alamos National Laboratory, LA-CP-05-0369 (2005).
6) Y. Shikaze et al., Prog. Nucl. Sci. Technol. 1 (2011) 166.

4 - 27 Measurement of Lineal Energy Distributions for Energetic Ion Beams Using a Wall-less Tissue Equivalent Proportional Counter

S. Tsuda, T. Sato and T. Ogawa

Division of Environment and Radiation Sciences, NSED, JAEA

The biological effects of ion beams have attracted attention, particularly in particle therapies and space activity. Deposit energy distribution in a microscopic site is basic information for evaluating the biological effects of energetic ion beams. In microdosimetry, lineal energy (y) is defined and used in the index of energy deposition in micrometer scale. Lineal energy can express each energy deposition in a microdosimetric scale by a single event of both incident primary heavy ions and secondary particles.

Microdosimetric deposit energy spectra have been measured for various energetic heavy ion beams using a wall-less tissue equivalent proportional counter (wall-less TEPC) and used for the verification of the Monte Carlo simulation codes with microdosimetric function for calculating y distributions, such as the PHITS code. In the previous studies, the measured deposit energy spectra include the contribution of both incident heavy ion beams and secondarily produced electrons (delta rays), since uniformly spread beams were used to simulate a uniform irradiation to cells. In this study, to investigate the radial dependence of y distributions, y distributions are measured in radial direction using the wall-less TEPC[1,2].

Figure 1 shows the schematic view of the experiment in the HB1 course. The wall-less TEPC and the beam monitors are irradiated with the 30 MeV proton beam through a collimator with 1 mm in diameter. The beam width at the center of the wall-less TEPC is estimated to be 2~3 mm in diameter. The wall-less TEPC has a transparent detection part composed of thin wires, the size of which is 3 mm in diameter and 3mm high. The gas pressure inside the wall-less TEPC is kept at 50, 100 and 200 Torr so as to simulate a site in tissue measuring 0.36, 0.72 and 1.44 μm, respectively. The centers of the detection part in the wall-less TEPC and the beam monitor are set in a straight line on the trajectory of the incident ion beam (z = 0.0). The vertical positions of the wall-less TEPC are changed to measure the y distributions apart from the incident ion beam. The adjustment of height is performed using a lab jack with precision of 1 mm in the range of z up to 35 mm.

In Fig. 1, beam monitor 1 is a bundle of plastic scintillation fiber arrays (PSF) to detect the positions of the trajectory of each proton beam passing the sensitive region of the wall-less TEPC. Beam monitor 2 is a plastic scintillation detector to obtain total incident ions on the wall-less TEPC, since protons cannot be detected by beam monitor 1 when beam passes through the gaps between arranged PSFs.

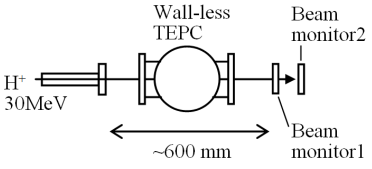

Fig. 1 Schematic view of the experimental setup.

Measured radial doses are shown in Fig. 2, along with the calculation by RITRACKS[3]. The measured radial doses agree with the calculated doses fairly well, though those over approximately 3 μm are larger than the calculated one. The result shows the experimental method is reasonable.

Figure 3 shows the y distributions measured at z = 0.0, 1.2 and 8.2 μm [$yf(y)$], shown in microdosimetric scale unit. In the distribution at z = 0.0 μm, on the beam path, the peak of the primary protons is clearly seen in the range of y from 1 to 2 keV/μm. The counts obtained away from the beam path are much smaller than that at 0.0 μm and decrease with increasing the radial distance. Radially integrated y distribution will be obtained using the y distributions obtained at several radial distances and be compared with the calculated y distribution using the PHITS code which includes the energy deposition of delta rays in microscopic-scale region.

References

1) S. Tsuda et al., JAEA Takasaki Annu. Rep. 2012 JAEA-Review 2013-059 (2014) 153.
2) S. Tsuda et al., HITSRS2013 (2013).
3) RITRACKS, NASA Space Radiation Program Element.

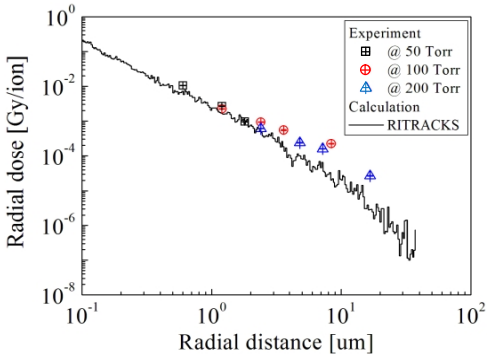

Fig. 2 Radial dose distributions for 30 MeV H^+ beam.

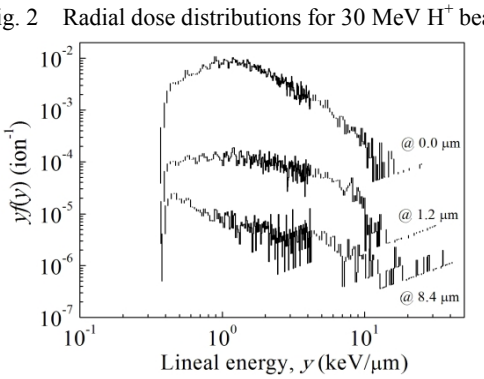

Fig. 3 Measured y distributions for 30 MeV H^+ beam.

4 - 28 Fabrication of Novel Fluorescent Plates Made from a UV/EB Curable Resin Using PBW Technique

T. Sakai [a)], R. Yasuda [a)], H. Iikura [a)], T. Nojima [a)], M. Koka [b)], T. Satoh [b)], Y. Ishii [b)] and A. Oshima [c)]

[a)] Materials Science Research Division, QuBS, JAEA,
[b)] Department of Advanced Radiation Technology, TARRI, JAEA,
[c)] The Institute of Scientific and Industrial Research, Osaka University

We report on the application of a UV/EB curable resin, in proton beam writing (PBW) for the production of micro-structured fluorescent plates [1)]. PBW is a unique technique used for the fabrication of micro- and nano-structures with high aspect ratios from polymeric and inorganic materials [2)]. On the other hand, UV/EB curable resin is a photo-curable polymer that rapidly cures in three dimensions by radical polymerization that occurs with ultraviolet (UV) light or electron beam (EB) irradiation. This resin has been widely used for various industrial applications, such as printings, paintings, material coatings and so on [3)]. The resin is a liquid at room temperature; therefore, it mixes easily with functional materials, such as phosphor grains. The fabrication process is similar to lithography.

The base materials used in this work are UV/EB curable resin and phosphor grains. The utilized resin is Bis-A ethylene oxide modified acrylate (ARAKAWA CHEMICAL INDUSTRIES, LTD.)[3)]. The resin is a pale yellow, transparent, and viscous liquid. The phosphor grains are sifted silver-activated zinc sulfide (ZnS(Ag)). The mean particle size is approximately 7 μm. A negative honeycomb pattern exposures are performed using 2 MeV or 3 MeV proton beams approximately 1 μm in diameter. The pixel resolution of the beam scanning is approximately 0.7 μm. The beam fluence is of the order of 100 pC/mm^2 with a beam current of 1~2 pA. The irradiated areas are quickly cured by polymerization. Then the samples are developed and treated with a chemical etching.

The fabricated fluorescent plates were observed using an optical microscope. The samples were illuminated using both visible and UV lights. The micrograph of a negative honeycomb structure is shown in Fig. 1. In addition, several samples were observed using the scanning electron microscope (SEM). These samples were tilted at 45 degrees and the height of each micro-pillar was measured to be 107 μm. The visible microscopic images show that the patterns of the fabricated structures agree well with the original ones.

In conclusion, we have demonstrated the fabrication of the micro-structured fluorescent plates, successfully. The UV-illuminated microscopic images revealed that each micro-pillar works well as a microcolumnar fluorescent material. The fabricated fluorescent plates are expected to be high efficiency imaging devices with good spatial resolution and they are promising as detectors for single ion hitting experiments [4)]. The results also proved that the UV/EB curable resin is very promising material for use in PBW micromachining.

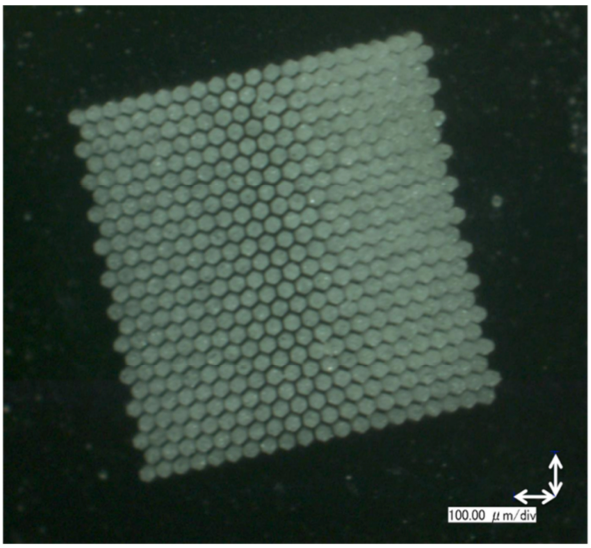

Fig. 1 Micrograph of the fabricated negative honeycomb-structured fluorescent plate.

References

1) T. Sakai et al., Nucl. Instrum. Meth. Phys. Res. B 332 (2014) 238-41.
2) S. V. Springham et al., Nucl. Instrum. Meth. Phys. Res. B 130 (1997) 155.
3) ARAKAWA CHEMICAL INDUSTRIES, LTD. website:http://www.arakawachem.co.jp/en/business/photo/03.html.
4) M. Folkard et al., Int. J. Radiat. Biol. 72 (4) (1997) 375.

4 - 29 Research and Development of an Ultra-high-energy Neutrino Detector Using Radar Reflection

M. Chiba [a)], T. Kamijo [a)], F. Yabuki [a)], H. Yano [a)], M. Utsumi [b)] and M. Fujii [c)]

[a)] Graduate School of Science and Engineering, Tokyo Metropolitan University,
[b)] Department of Applied Science and Energy Engineering, School of Engineering, Tokai University,
[c)] School of Medicine, Shimane University

Ultra-high-energy neutrinos (UHEν's) would be produced at collisions of UHE-cosmic ray against the cosmic-microwave-radiation background in the universe. A gigantic detector is needed for the detection due to the expected ultra-low flux of about 1 $km^{-2} \cdot d^{-1}$. When an UHEν interacts with rock salt or ice as a detection medium, a shower is generated which is composed of hadronic and electromagnetic avalanche processes. The energy of the UHEν converts to thermal energy through ionization processes. Consequently, the temperature rises along the shower produced by the UHEν. The refractive index rises as a function of the temperature. The irregularity of the refractive index in the medium for radio waves causes reflection. We have found a radio-wave-reflection effect in rock salt. Details of the experimental equipment with readout electronics and results were described in a list of references [1)]. Increases of the reflection fraction and the temperature with time were similar in shape. Therefore the reflection mechanism was conjectured that the temperature rise would give rise to radio-wave reflection. This reflection effect combined with long attenuation length of radio waves in rock salt and ice would yield a new method to detect UHEν's.

We report on an experiment and a simulation to study reflection mechanism of 435 MHz radio wave. Ice was filled in a coaxial tube of 20 mm in diameter and 100 mm in length. An open end of the tube where the electric field of radio wave were the maximum, was exposed by an electron beam of 4.2 J/s for 60 s at the 2-MV Cockcroft-Walton accelerator facility in the Takasaki Advanced Radiation Research Institute. During the exposure, the tube was put in a dry-ice box and its temperatures were measured using chromel-alumel thermocouples at six points (z, r); z=2, 7 and 12 mm from the open end along the axis and r=6 and 9 mm radially from the axis.

The reflection effect from ice was observed as "Experiment" shown in Fig. 1. The energy deposit in ice was simulated by Geant4 (CERN) using Monte Carlo method. The thermal energy distribution was fed into Multiphysics (COMSOL AB Co Ltd.) which utilizes 3-dimensional finite-element method. The thermal transport and the radio wave reflection inside the coaxial tube were simulated against the time from start of the electron beam to 120 s using a coupled analysis method. During the irradiation, the temperature of the ice increased from -67 to -56 °C at the position of z=2 and r=9 mm. The largest discrepancy between the measured temperatures of the 6 points and those of the simulation was 50 %. But shapes of the simulation with respect the irradiation time were similar to those of the experiment. The differences are estimated due to imperfect agreement of the thermal conductivity, thermal contact between different materials, etc. between the experiment and the simulation.

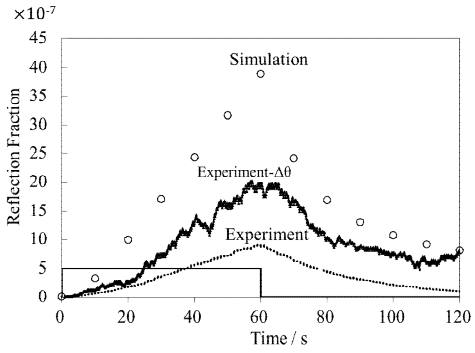

Fig. 1 The power reflection fraction measured by a real time spectrum analyzer is plotted as "Experiment" and increased from 0 to 8.9×10^{-7}. "Experiment-Δθ" and "Simulation" were deduced from a vector rotation: $2(1 - \cos\Delta\theta)$ where Δθ's were a measured phase shift and that of the simulation, respectively.

"Experiment-Δθ" and "Simulation" are 2.4 and 4.6 times larger than "Experiment" as shown in Fig. 1. The source of the larger "Experiment-Δθ" compared to "Experiment" is conjectured that the measured phase shift Δθ was disturbed by a signal in the readout electronics. Cause of the larger "Simulation" than "Experiment" is estimated that the reflection fraction increases square of the temperature, and the difference is exaggerated. Although the discrepancies exist in the absolute values, the shapes of the temperatures and the reflection fractions with time are similar between the experiment and the simulation. Therefore we regard that the reflection mechanism is verified to be the local rise of the refraction index caused by the temperature rise.

The radar reflection effect is applicable to not only for radiation detection but also for all dielectric media, e.g. solid, liquid, gas and plasma with inhomogeneous refractive indices. Among them, an imaging of a human body is intriguing.

References

1) M. Chiba et al., AIP Conf. Proc. 1535, 45-50 (2013); http://dx.doi.org/10.1063/1.4807519; http://arxiv.org/abs/1307.1767.

4 - 30 Development of Micro-optics for High-resolution Ionoluminescence Spectroscopy with a Proton Microbeam

W. Kada [a)], T. Satoh [b)], A. Yokoyama [b)], M. Koka [b)] and T. Kamiya [b)]

[a)] Faculty of Science and Technology, Gunma University,
[b)] Department of Advanced Radiation Technology, TARRI, JAEA

Introduction

An analysis system of Ion Luminescence (IL) using external proton microbeam was developed on the same beam line of in-air micro-PIXE analysis system to analyze the chemical composition of micrometer-sized targets. IL images of micrometer-sized particulate aerosol targets were successfully obtained from IL measurement. However, the experimental results suggested that the detection efficiency of IL for high-sensitivity spectroscopy and microscopic imaging needed to be improved by introducing high-efficiency optics[1)]. In this study, an improvement of micro-optics for external microbeam driven IL analysis was reported. The confocal micro-optics was newly designed for the IL spectroscopy and the microscopic imaging simultaneously obtained with that of in-air micro-PIXE.

Materials and Methods

Figure 1 shows a schematic drawing of the newly developed IL confocal optics setup on the external micro PIXE analysis system. Biconvex lens assembly with effective wavelengths ranging from the UV to the near IR regions was placed inside the vacuum chamber at an angle of 40° to the microbeam axis at a distance of 110 mm from the irradiation target point. An 800-μm-diameter optical fiber was installed at the opposite focal point of the same biconvex lens[2)]. ILs collected by the confocal optics were transmitted to a photon counting unit or UV-Vis spectrometer (Spectra Co-op, Solid Lambda).

Results and discussion

Figure 2 shows a comparison of the IL spectra obtained from a microscopic target through conventional and newly designed confocal optics. The result suggests that the detection efficiency of IL was much improved as it recognized as the intensity of IL peaks in the spectra. Simultaneous PIXE and IL imaging of microscopic targets were also accomplished as shown in Fig. 3.

Conclusion

Confocal micro-optics were developed and successfully installed on an ion microbeam line for precise IL spectroscopy and microscopic imaging. Our IL system was more sensitive than conventional IL analysis, as the results demonstrated the advantages of the continuous observation of the IL spectroscopy and microscopic imaging of targets.

References

1) W. Kada et al., Nucl. Instrum. Meth. B 306 (2013) 299-301.
2) W. Kada et al., Nucl. Instrum. Meth. B 318(2013)42-46.

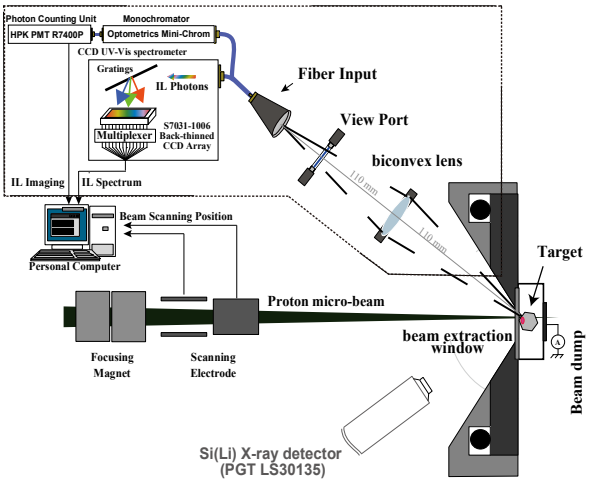

Fig. 1 Schematic drawing of micro-confocal system of IL analysis. It has been combined with in-air micro-PIXE system and was capable to detect IL from the sample set in air[2)].

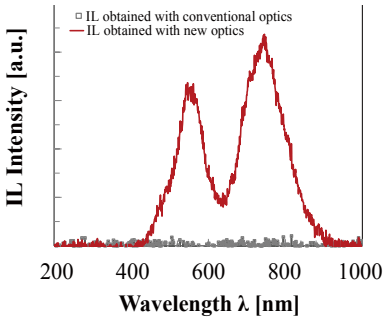

Fig. 2 Comparison of IL spectra obtained using general micro-optics and using confocal micro-optics designed for IL spectroscopy[2)].

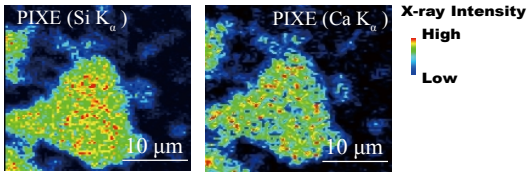

(a) PIXE imaging

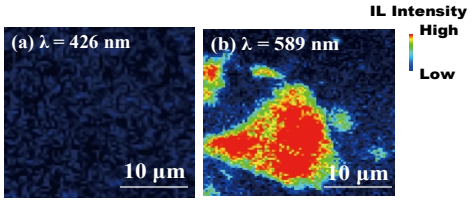

(b) IL imaging

Fig. 3 Examples of an IL and a PIXE image of the particulate aerosol samples obtained by the external microbeam analysis system[2)].

4 - 31 Element Analysis by Fiber-coupled Laser-induced Breakdown Spectroscopy under γ-ray Irradiation

H. Ohba, M. Saeki and A. Iwanade

Laser Application Technology Division, QuBS, JAEA

Focusing of powerful laser pulses onto a material generates ablation plasma that is composed of excited atoms. Analysis of emission from the excited atoms gives us information on the elemental compositions of the ablated material. This technique is called laser induced breakdown spectroscopy (LIBS), and is attractive as elemental analysis method because real-time, in-situ and remote observation is possible without any sample preparation. These advantages are available in elemental analysis involving a high-radiation field, such as the post-accident environment inside the TEPCO Fukushima Daiichi nuclear power plant (F1- NPP), which was seriously damaged by the tsunami on 11 March 2011. In the present work, the performance of our fiber-coupled LIBS apparatus under high radiation dose has been investigated to demonstrate the applicability for monitoring the debris materials inside of the F1- NPP.

The influence of the radiation dose on the optical transmittance of the laser delivery fiber was investigated using the ^{60}Co gamma irradiation facility number-1. The optical fiber was a commercially available product: Fiberguide industries Inc., Type Low-OH (FG, 15 m), Mitsubishi Cable Industries, Ltd., Low-OH (ST, 20 m) and High-OH (STU, 20 m). The ^{60}Co gamma-ray irradiation was performed at room temperature at a dose rate of 15 kGy/h. The radiological dosage in air of the F1-NPP is reported to be ~73 Gy/h in Unit 2 [1)] and is speculated to increase near the nuclear fuel debris. Thus, the dose rate in this work was sufficient to verify the radiation resistivity of the fiber for the inspection in the F1-NPP. Figure 1 shows the spectra of the white light through the optical fiber before (black lines) and during (blue lines) the ^{60}Co gamma-ray dose. The upper figures indicate the spectra in the visible wavelength region and the lower ones are those in the near infrared wavelength region. The spectral intensity in the region of 400-730 nm drastically decreased after the radiation dose. However, we confirmed that there was a little damage in the near infrared region. Especially, STU has no radiation damage in the region of 800-1,150 nm. A small amount of recovery on the optical transmittance was observed for Low-OH type fibers after the irradiation was stopped, as shown in red lines of Fig. 1, whereas the High-OH type fiber (STU) has not recovered without any thermal treatments.

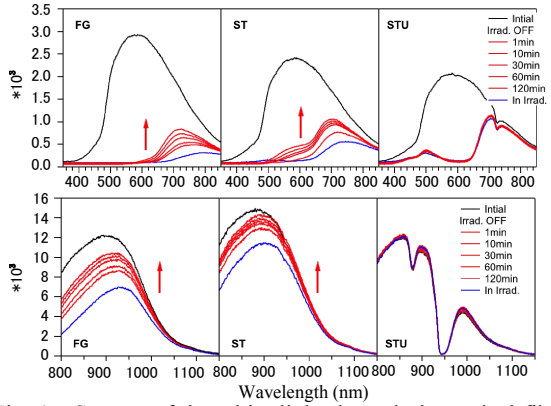

Fig. 1 Spectra of the white light through the optical fiber both before (black lines) and during (blue lines) the ^{60}Co gamma-ray dose.

Figure 2 shows the LIBS emission spectra from the simulated debris, which was prepared with a weight ratio of Ce:Zr:Fe being 1:1:1, by using fiber-coupled LIBS apparatus that was developed in our group [2)]. Cerium was used as a surrogate of uranium. The spectrum was measured in the region of 830-840 nm, where the emission lines was not strongly affected by the radiation dose, as shown in Fig. 1. The spectral assignment was based on the NIST database [3)]. The blue line indicates the spectra obtained through the FG fiber (5 m) under non-radiation field, while the red line shows the spectra through the FG fiber (15 m) under a radiation dose rate of 15 kGy/h. Comparison of the blue and red spectra suggests that our fiber-coupled LIBS apparatus works well even under high radiation field, although the emission intensity under radiation field was 1/10 compared to that under no-radiation field. In addition, the calibration curves for Zr/Ce, Fe/Ce during the irradiation agreed with those of the non-irradiation field except in higher weight ratio (not shown). These results guarantee that our fiber-coupled LIBS system is applicable for the analysis of the debris materials in the F1-NPP.

References

1) http://www.irid.or.jp/reports/20140307/.
2) M. Saeki et al., J. Nucl. Sci. Technol.51(2014) 930.
3) http://www.nist.gov/pml/data/asd.cfm.

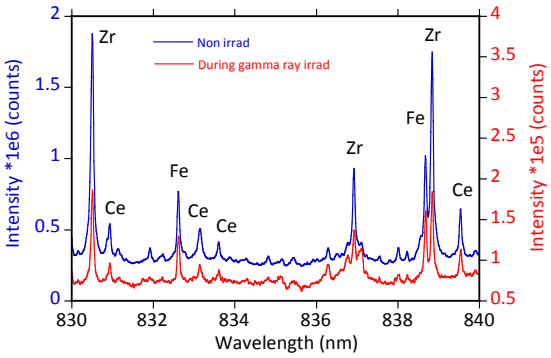

Fig. 2 Emission spectra from the simulated debris in the breakdown through the optical fiber cable. The assignments of the major emission lines are indicated.

4 - 32 Microbeam Irradiation Effect on Thin CVD Diamond Detector

W. Kada [a)], N. Iwamoto [b)], T. Satoh [c)], S. Onoda [b)], T. Makino [b)], V. Grilj [d)], N. Skukan [d)], M. Koka [c)], T. Ohshima [b)], M. Jakšić [d)] and T. Kamiya [c)]

[a)] Faculty of Science and Technology, Gunma University,
[b)] Environment and Industrial Materials Research Division, QuBS, JAEA,
[c)] Department of Advanced Radiation Technology, TARRI, JAEA,
[d)] Division of Experimental Physics, Ruđer Bošković Institute

Introduction

High purity Chemical Vapor Deposition (CVD) diamonds have excellent electrical properties and detectors based on such CVD diamonds have been already demonstrated for the measurement of high-energy particles or X-ray photons. Although CVD diamonds have been employed for spectroscopic uses of highly energetic particles, there are only a few experimental results evaluating the reliability/stability of their characteristics under various irradiation conditions [1, 2]. In a previous study[3], it was reported that the temporal signal degradation during the irradiation, so called polarization effect occurred during intense heavy-ion microbeam irradiations. In this study, we investigate the effects of irradiation conditions (fluence rate and bias voltage) on the characteristics of CVD diamond detectors.

Materials and Methods

A 50-μm-thick Single Crystal (SC)-CVD diamond was employed for the irradiation experiment of 15 MeV oxygen (O), 15 MeV nickel (Ni), and 8 MeV carbon (C) focused heavy ion microbeams. The SC-CVD diamond detector was fixed on the movable stage to control the irradiation position. An electrode on the diamond film directed to the beam entrance was used as signal electrode. The bias voltage of ±50 V was applied through a charge sensitive amplifier (CSA), whereas the other side of the SC-CVD diamond detector was grounded. The output of the CSA was transmitted to a chain of gate and trigger electrical circuits to consecutively obtain the Ion Beam Induced Charge (IBIC) signals.

Results and Discussion

Figure 1 shows the IBIC spectra obtained at 8 MeV C ion irradiation with different fluence rate. The biases of (upper) +50 V and (lower) -50 V were applied to the samples during the measurement. In the case of the negative bias, the sharp single peak is observed and no significant difference in peak position among fluence rates is obtained. On the contrary, broad peaks are obtained for samples applied with positive biases and the peak position depends on fluence rate. Thus, peak position changes during measurements (irradiation), and as a result, the degradation of IBIC characteristics is observed (polarization effect). Similar results were observed when other ions were used.

Since the polarization effect disappeared by changing bias polarity, there might be an effect caused by defects which is caused by trapping holes or electrons during their travel in the diamond. Also, we can say that the polarization effect depends on the amounts of charge generated in diamond because the decrease of the IBIC peak increases with increasing fluence rate. So far, the detailed mechanism of the polarization effects has not yet been revealed. However, the IBIC peak degradation observed in the SC-CVD diamond can be interpreted in terms of defects that have longer de-trapping time for holes since higher fluence rate induces larger effect.

References

1) R. S. Sussmann, John Wiley & Sons Ltd Press (2009).
2) V. Grilj et al., Nucl. Instrum. Meth. B 161 (2013) 446.
3) W. Kada et al., Trans. Mater. Res. Jpn. 38 (2013) 279.

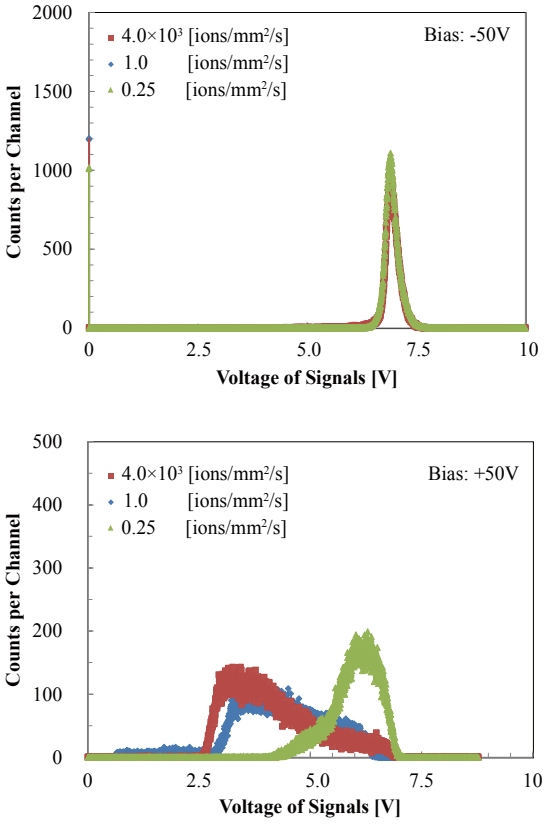

Fig. 1 Comparison of the IBIC spectra of 8 MeV carbon obtained with different fluence rates with (upper) negative and (lower) positive bias voltage of 50 V.

4 - 33 Energy Losses of MeV C_2^+ Ions Transmitted through a Nanoporous Film

S. Matoba, K. Narumi, Y. Saitoh, K. Yamada and A. Chiba

Department of Advanced Radiation Technology, TARRI, JAEA

Experiments under the condition of spatial orientation of molecular ions are very important to improve the understanding of molecular physics, such as a chemical reaction with a molecular ion. Friedrich and Herschbach have realized the alignment control of a diatomic molecule with a strong electric field.[1] In contrast, spatial orientation of molecular ions has not been reported yet. In the past research, Susuki *et al.* observed angular and energy distributions of molecular fragments after the scattering of MeV HeH^+ ions from a SnTe crystal surface at a grazing angle of incidence of several mrad[2]. The angular distributions of H^+ from dissociated HeH^+ are narrower than that derived from Coulomb explosions in free space, whereas the energy distributions are almost equal to that derived from Coulomb explosions in free space. They concluded that the results were explained by alignment of the vector connecting the dissociated fragments under an influence of a surface planar potential after the Coulomb explosion. These results can be interpreted differently. It states that the axial direction of the molecular ion which moves along the surface are aligned parallel to the surface plane and the reflecting plane before the Coulomb explosion. In this case, it is supposed that this alinement is caused by a surface wake induced by the molecular ion. It is difficult, however, to produce oriented molecular ions by colliding molecular ions to a surface because little molecular ions survive at small angle scattering from a surface.

The dissociation of a molecular ion at a surface can be avoided by making the target a capillary instead of a surface. A dissociation probability of a molecular ion moving near a surface decreases exponentially with the distance from a surface. On the other hand, the surface-wake potential decreases with the power of the distance from the surface[3]. A molecular ion passing through a straight capillary of submicron in diameter can undergo the surface-wake potential without dissociation at the inner-wall surface of the capillary. It is, therefore, expected that the axial direction of the molecular ion which passes through the capillary are aligned. The surface wake decreases a kinetic energy of the moving molecular ion because the slope of the surface-wake potential at the molecular ion is a negative to the travel direction of the molecular ion. In our present study, we have measured the energy of C_2^+ ions transmitted through a nanoporous kapton film with a number of capillaries in order to confirm whether the C_2^+ ions undergo the surface wake of the inner wall of a capillary in the nanoporous kapton film.

A nanoporous kapton film was prepared by an ion-track technique, which involved 490-MeV Os ion irradiation and subsequent alkaline etching. The diameters of the holes on the entrance and exit sides were 210 ± 60 and 50 ± 10 nm, respectivery. The thickness of the kapton film was 7.5 μm. The 6-MeV C_2^+ ions produced by the 3-MV tandem accelerator were injected into the nanoporous kapton film, which was mounted on a goniometer. The energies of the ions were measured with a silicon surface barrier detector (SSD) with an acceptance angle of 9.2 mrad. The incident angle of the moleclar ion beam to the kapton film was adjusted so that the current of the beam transmitted through the film would be maximized.

Figure 1 shows the energy distributions of the primary C_2^+ ions and the transmitted ions. Note that the energy distribution of the transmitted ions can contain both intact C_2 ions/neutrals and two dissociated C ions/neutrals entering into the SSD simultaneously. The energy at the peak of the Gaussian fitting for the transmmitted ions is 21 keV lower than that for the primary C_2^+ ions. This result suggests that the transmitted ions are scattered at the inner wall of the capillary. It is not determined, however, whether the kinetic energy of the C_2^+ ions are lost since the trancmitted ions contain two compornents. In future experiments, the component of the transmitted ions will be clarified and the direction of the moleclar axis of transmitted C_2^+ ions will be observed in the case that C_2^+ ions exist in the transmitted ions.

References

1) B. Friedrich and D. R. Herschbach, Nature 353 (1991) 412.
2) Y. Susuki et al., Nucl. Instrum. Meth. B 48 (1990) 347.
3) Y. Susuki, "Studies on interactions of fast molecular ions with single crystal surfaces", Doctoral Thesis, Kyoto univ., 1996.

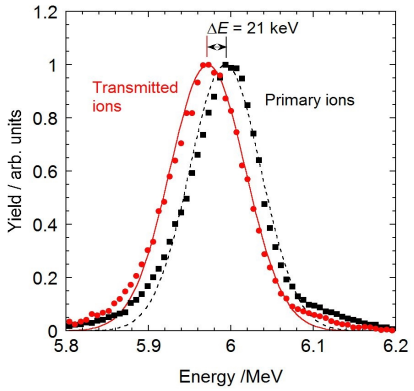

Fig. 1 Energy distributions of primary C_2^+ ions (squares) and transmitted ions (circles). The dashed and solid lines are Gaussian fitting for the primary C_2^+ ions and the transmitted ions, respectively.

4 - 34 Evaluation of Dose Rate in ^{60}Co Gamma-ray Irradiation Fields: Comparison of Results from an Ionization Chamber, Alanine Dosimeters and Monte Carlo Simulation

H. Seito, Y. Nagao, R. Yamagata, H. Hanaya, T. Agematsu and H. Kaneko

Department of Advanced Radiation Technology, TARRI, JAEA

Chemical dosimeters such as polymethylmethacrylate (PMMA) dosimeter, alanine dosimeter and cellulose triacetate (CTA) film dosimeter, are commonly used for radiation monitoring in the irradiation process. These dosimeters measure the integral dose but give no information on the dose rate variation during the irradiation. It is important to have knowledge of the dose received at each point in the irradiation field. Such information is invaluable when planning a board radiation source arrangement, configuring the radiation source and designing irradiation facility. It also enables the facility operator to optimize the scheduling of irradiation of products with different densities or dose requirements. We have been engaged in the development of simulation technique on dose rate evaluation in a ^{60}Co gamma-ray irradiation field, using Monte Carlo simulation code EGS4-SPG[1]. The simulation technique is routinely used to calculate the instantaneous dose rates in gamma irradiation field. This study aims to examine the effectiveness of the simulation technique by means of the direct comparison to different methods to measure the dose rates in a ^{60}Co gamma-ray irradiation field.

The gamma-ray irradiation in this study was conducted using a ^{60}Co board source (8.89 PBq), which was fixed at a position used for irradiation. The some points on irradiation table in the irradiation room were selected for measurement. Plane view of the irradiation room used in this study is shown in Fig. 1. An ionization chamber (2 mm thick aluminum wall, 20 mm in diameter, 3 mm gap) was used as a reference dosimeter to measure dose rate[2]. It was calibrated in terms of current per unit dose rate at National Institute of Advanced Industrial Science and Technology (AIST), the Japanese primary standard laboratory. The JAEA-alanine dosimeters were also used, which were 3 mm in diameter and 30 mm in length, and were enclosed in a cylindrical polystyrene holder[3]. At first, the measurement by the ionization chamber was conducted, then the irradiation of alanine dosimeters was done, replacing the ionization chamber with alanine dosimeters. The irradiation time for the alanine dosimeters was 1 hour to estimate dose rate [Gy/h]. The dose rate under the same irradiation geometry was calculated, using EGS4-SPG code. To simplify input of the code, the board radiation source which has uniform radioactive intensity was modeled.

The results of the simulation and two ways of real measurement are shown in Table 1. They are generally in good agreements within 0.3%, at positions of X = 30 and X = 170 cm from ^{60}Co source. On the other hand, there are difference as large as 5 ~ 14% between the simulation and experimental results at the positions closer to the source. The input of the simulation code does not include specification of individual pencil source, which has an effect of the scattering in radioactive intensity of each pencil source on simulation results in region closer to the source.

These results imply that the dose rate distribution can be estimated at high accuracy within 0.3% using the simulation technique, at distances of 30 cm or more from the radiation source. This enables us to save the number of the dosimeters and measurement time for the evaluation of dose rate after the radiation source arrangement.

References

1) H. Kaneko et al., RADIOISOTOPES. 59 (2010) 11.
2) T. Kojima et al., RADIOISOTOPES. 50 (2001) 291.
3) T. Kojima et al., Appl. Radiat. Isot. 40 (1989) 851.

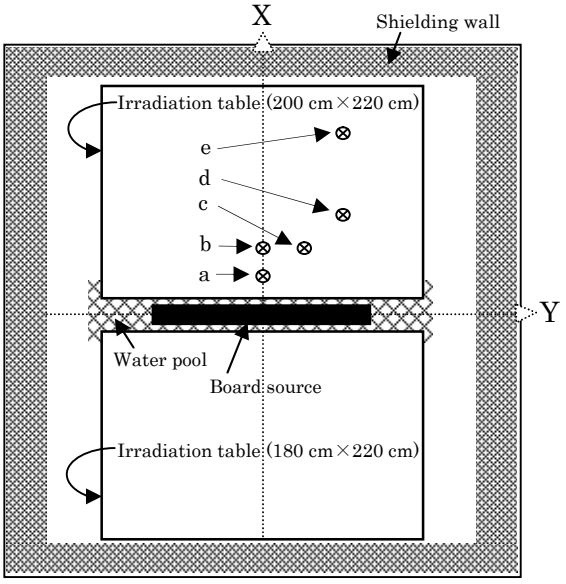

Fig. 1 Geometry of irradiation field where a board source was arranged. The marks '⊗' show measurement positions.

Table 1 Calculated and measured dose rates [Gy/h] at each position of a - e in Fig. 1.

Measurement position [cm]	Simulation (Calculation)	Ionization chamber	Alanine
a) X=10, Y=0	1.52E+04	1.34E+04	1.37E+04
b) X=20, Y=0	1.04E+04	9.84E+03	9.93E+03
c) X=20, Y=20	1.02E+04	9.94E+03	1.01E+04
d) X=30, Y=40	7.22E+03	7.23E+03	7.24E+03
e) X=170, Y=40	8.22E+02	8.23E+02	8.23E+02

4 - 35 Improvement of the Focusing Microbeam System at TIARA Cyclotron

S. Kurashima, M. Koka, T. Satoh, A. Kitamura, A. Yokoyama, N. Miyawaki, H. Kashiwagi and K. Yoshida

Department of Advanced Radiation Technology, TARRI, JAEA

The fast single-ion hit system on the HX course of the TIARA cyclotron[1] was continuously improved for higher quality of microbeam and single-ion hit. A technique of real-time detection of single-ion-hit position was realized and a microbeam of 320 MeV $^{12}C^{6+}$ is being developed using this technique[2,3].

A beam size of the microbeam must be precisely estimated before irradiation of target samples. The size is obtained by analyzing a secondary electron (SE) image of a copper grid with 1,000 lines/in. irradiated with scanned microbeam. The beam size is defined as a full width at half maximum value of a one-dimensional fitting curve to the contrast near the edge of the copper grid for horizontal and vertical direction, respectively. This technique requires high signal-to-noise ratio (S/N) of the SE image for precise estimation of the bean size. In order to improve the S/N, a beam intensity of the microbeam and/or an efficiency of the SE collection have to be increased. However it is difficult to drastically increase the beam intensity since the performance of an ion source and the transmission efficiency from the source to the upstream point of the microbeam system will not be improved further, i.e. the ion source and cyclotron system are already tuned well. We therefore tried to improve the efficiency of the SE collection using a plastic scintillator. The surface of the scintillator is coated by a metallic thin film to apply high voltage of 5 kV for the SE collection. The metallic thin film was changed from Al of 500 nm in thickness to Au of about 20 nm so that more electrons reach the surface of the scintillator through the metallic thin film layer than before. Secondary, a distance between the copper grid and the scintillator was reduced from 15 mm to 6 mm to capture more SEs before dispersion.

Figure 1 shows SE images of the copper grid obtained by using a microbeam of 260 MeV $^{20}Ne^{7+}$ before and after modification of the SE collection efficiency. Beam intensities upstream of the microbeam system were about 500 enA for both cases. The S/N of the SE image was obviously improved as shown in Fig. 1. Although the beam sizes were estimated to be about 3 μm for both cases shown in Fig. 1, higher reliability of the estimation is guaranteed for the case with better S/N of the image. It was so hard and took time to form the microbeam by tuning lens parameters of the microbeam system in the case of bad S/N of the image; tuning time of the microbeam was reduced as a result of improvement of the S/N of the SE image.

References

1) W. Yokota et al., JAEA Takasaki Annu. Rep. 2011 JAEA-Review 2012-046 (2013) 156.
2) W. Yokota et al., JAEA Takasaki Annu. Rep. 2012 JAEA-Review 2013-059 (2014) 160.
3) T. Satoh et al., Nucl. Instrum. Meth. B 332 (2014) 242-244.

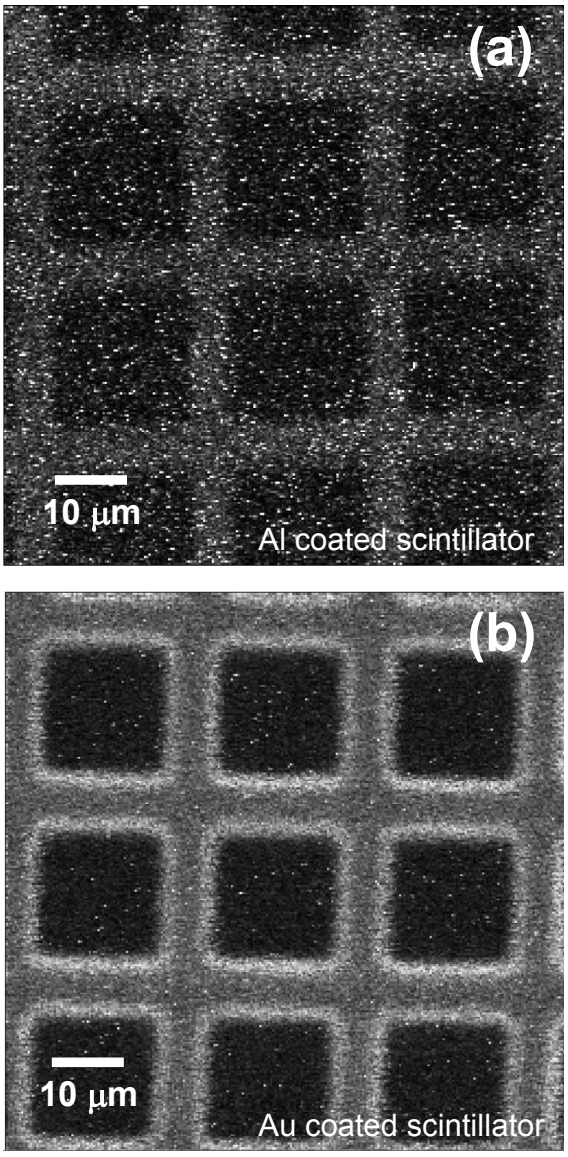

Fig. 1 Comparison of the SE images of a copper grid irradiated with scanned 260 MeV $^{20}Ne^{7+}$ microbeam: (a) before and (b) after improvement of the efficiency of the SE collection.

4 - 36 Formation of Large-area Uniform Heavy-ion Beams by Means of Multipole-magnet Nonlinear Focusing

Y. Yuri, T. Yuyama, T. Ishizaka, I. Ishibori and S. Okumura

Department of Advanced Radiation Technology, TARRI, JAEA

A large-area uniform-beam formation/irradiation system based on nonlinear focusing of multipole magnets is being developed continuously at the TIARA cyclotron for ion-beam applications in the field of materials science. It is required to efficiently adjust a uniform beam profile on a target to irradiation conditions. We, therefore, developed the adjustment method of the uniform beam using a real-time beam tuning system [1] toward the establishment of the uniform-beam irradiation technique.

There are 25 quadrupole magnets along the high-energy beam transport line from the cyclotron down to the LB target. According to the design of the beam optics and the tracking simulation result, the procedure of beam tuning was determined as follows; the first quadrupole triplet is tuned to make the beam waist at the first diagnostic station TS1. Then, a metallic thin foil for multiple Coulomb scattering is inserted onto the beam path so that the transverse intensity distribution is smoothed into a Gaussian-like distribution, prerequisite to the formation of a uniform beam with multipole magnets. The foil material is chosen among Al, Cu, and Ta, depending on the ion species and its energy. The parameters of the next 20 quadrupole magnets are usually fixed both for the beam transport through two narrow-gap bending magnets and a long drift space, and for the suppression of undesirable coupling of the betatron oscillation at multipole magnets. The cross-sectional profile of the uniform beam on the target is adjusted using the last quadrupole doublet and multipole magnets under real-time monitoring with a fluorescent screen. The beam misalignment, which distorts the on-target profile and thus deteriorates the beam uniformity, is corrected using steering dipole magnets also with the real-time monitoring system. Now, this procedure to form a uniform beam takes about one hour.

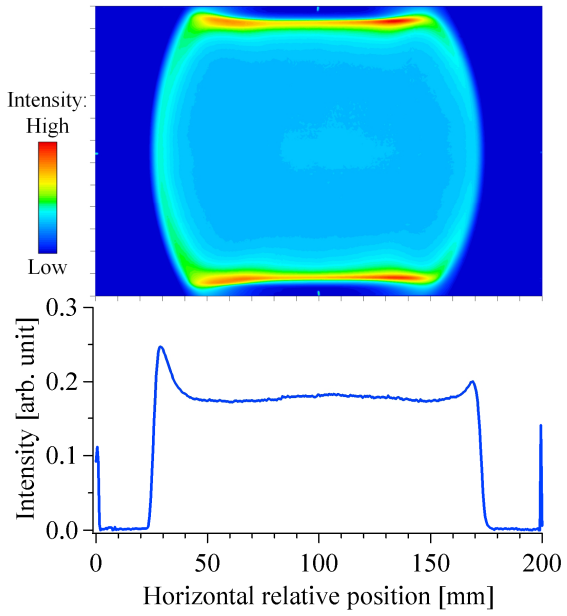

Fig. 1 On-target intensity distribution of a 520 MeV ^{40}Ar large-area beam focused by multipole magnets. It was obtained by irradiating a Gafchromic film HD-810 with the 0.1-μA beam for 0.5 s.

A typical intensity profile of a two-dimensional uniform beam is shown in Fig. 1, measured with a radiochromic film on the target. A large-area uniform beam over 100 cm^2 can be regularly produced with a root-mean-square uniformity below 10% [2-4]. By tuning only the last two quadrupole and multipole magnets, the beam profile can be changed into a ribbon-like elongated one [4], as displayed in Fig. 2. The high-intensity peak at the edge of the uniform beam profile as seen in Fig. 1 was removed with slits installed in the beam line.

Such heavy-ion beams tailored by nonlinear focusing for uniform beam irradiation are applied to the production of functional polymer films and related research [5].

References

1) T. Yuyama et al., JAEA Takasaki Annu. Rep. 2012 (2014) 162.
2) Y. Yuri et al., Nucl. Instrum. Meth. Phys. Res. A 727 (2013) 40.
3) Y. Yuri et al., Proc. North Am. Part. Accel. Conf., NA-PAC'13 (2013) 1388.
4) Y. Yuri et al., Plasma Fusion Res. 9 (2014) 4406106.
5) A. Kitamura et al., JAEA Takasaki Annu. Rep. 2013 JAEA-Review 2014-050 (2015) 48.

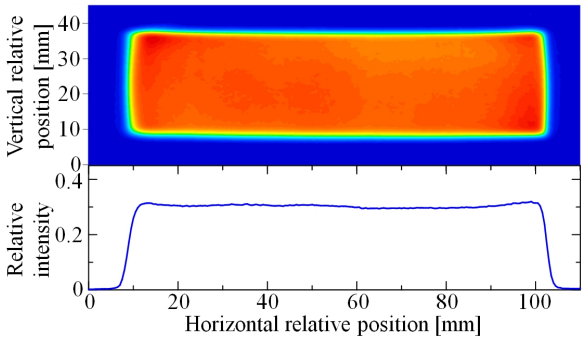

Fig. 2 On-target intensity distribution of a 520 MeV ^{40}Ar ribbon-like beam focused by multipole magnets. It was obtained by irradiating a Gafchromic film HD-810 in air with the 3-nA beam extracted through a thin-foil window for 3 s.

4 - 37 ^{60}Co Gamma-ray Irradiation Response of Gafchromic Films, HD-V2 and EBT3

T. Ishizaka, Y. Yuri, H. Seito, T. Agematsu and S. Okumura

Department of Advanced Radiation Technology, TARRI, JAEA

Recently, we developed a method of evaluating the charateristics of large-area ion beams using Gafchromic radiochromic films, HD-810 and EBT2 (Ashland), and general-purpose image scanners [1]. However, the films were discontinued and recently renewed to HD-V2 and EBT3, respectively. Before testing the new films with ion beams, we, therefore, studied the basic irradiation response characteristics of the films using ^{60}Co gamma rays in advance since gamma-ray uniform irradiation can be easily accomplished compared to ion-beam irradiation.

According to the available dose ranges of the films, HD-V2 and EBT3 films were irradiated with gamma rays up to 5 kGy at the second cobalt irradiation facility and up to 120 Gy at the food irradiation facility, respectively. Then, the spectroscopic characteristics of the irradiated films were analyzed using a spectrophotometer U-3310 (Hitachi High-Tec). Moreover, they were digitized into 16-bit RGB, 127-dpi TIFF images at a transmission mode of a flatbed image scanner ES-10000G (EPSON) toward the large-area evaluation. The optical density (OD) was obtained from the RGB intensity values I in all three color channels by the equation: $OD = \log_{10}(65535/I)$. An analysis software was developed to extract the 16-bit RGB intensity values and the OD from the TIFF image.

The response of the HD-V2 is shown in Fig. 1 as a function of the wavelength of the U-3310. The OD of the un-irradiated film (0 Gy) is relatively high below 500 nm because of the yellow fundamental color of the film. On the other hand, the absorption due to irradiation is dominant around 670 and 610 nm, and the peak locations slightly shift to the short-wavelength side with dose. The dose-dependence of the films scanned by the ES-10000G is shown in Fig. 2. The tendency of the three-color response curves reflects the result in Fig. 1. The OD increment of the HD-V2 is not proportional to the dose, unlike HD-810.

Similarly, the irradiation responses of the EBT3 were also analyzed. As shown in Fig. 3, two dominant peaks of the absorption are located at 633 and 585 nm and the locations are almost insensitive to the dose. The nonlinear response of the OD is shown in Fig. 4.

The dependences of the response characteristics on scanning conditions were also investigated.

On the basis of these results, HD-V2 and EBT3 films will be applied to the evaluation of the size and uniformity of large-area uniform ion beams, which are under development in the TIARA cyclotron [2].

References

1) Y. Yuri et al., Nucl. Instrum. Meth. Phys. Res. A 727 (2013) 40.
2) Y. Yuri et al., JAEA Takasaki Annu. Rep. 2013 JAEA-Review 2014-050 (2015) 164.

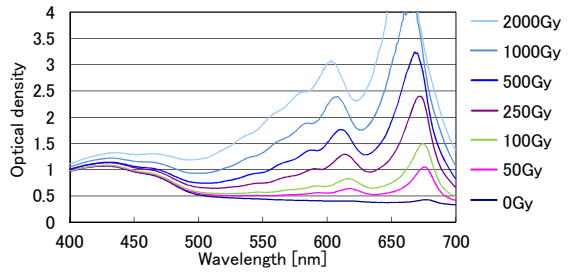

Fig. 1 ^{60}Co gamma-ray irradiation response of HD-V2, measured with the spectrophotometer U-3310.

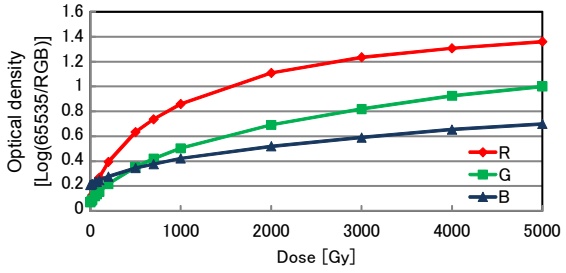

Fig. 2 ^{60}Co gamma-ray irradiation response of HD-V2, measured with the scanner ES-10000G.

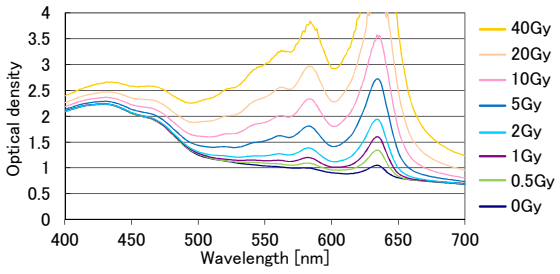

Fig. 3 ^{60}Co gamma-ray irradiation response of EBT3, measured with the spectrophotometer U-3310.

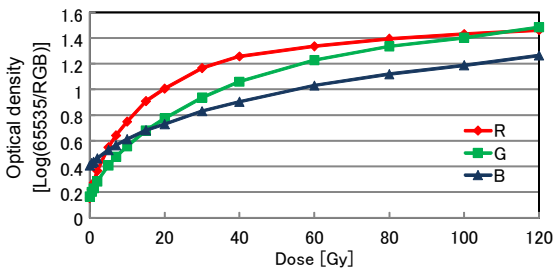

Fig. 4 ^{60}Co gamma-ray irradiation response of EBT3, measured with the scanner ES-10000G.

4 - 38 Emittance-expansion Technique for Transverse Acceptance Measurement

H. Kashiwagi, N. Miyawaki, S. Kurashima and S. Okumura

Department of Advanced Radiation Technology, TARRI, JAEA

In the TIARA cyclotron, various kinds of ion beams are used for research in biotechnology and material sciences, etc. Changes of particle and/or energy are performed frequently (e.g. a few times a day) according to the beam time required for experiments. With respect to each change, parameters of magnets in the low energy beam transport line are adjusted to accelerate the beam with good transmission through the cyclotron. However, it is not easy to find out the optimum condition because there are many parameters for the emittance matching to the acceptance of the cyclotron. To provide a tool for the optimization, a transverse emittance and acceptance measurement system has been developed [1]. The system visualizes the relationship between the injected beam emittance and the acceptance of a cyclotron.

In acceptance measurement, every small beamlet at various positions in phase-plane is injected into the cyclotron and then detected by a current probe in the cyclotron to clarify whether it is in the acceptance. The beamlets are formed by a pair of slits, in the low energy beam transport line, which admits an arbitrarily small portion of the beam from an ion source. However, only a part of acceptance was able to be measured because the region of emittance of the injection beam did not cover the whole acceptance in phase space[2].

To enable measurements outside the region covered by the emittance of the beam, we have developed a technique for effectively expanding the emittance. The system and method of the expansion is illustrated in Fig. 1. The beam from an ion source is enlarged in the position direction as necessary using solenoid magnets placed upstream of the phase space collimator. The enlarged beam is then scanned in the angular direction by the steering magnet in accordance with change in the region defined by the slits during the measurement. Consequently, the emittance is effectively expanded to a large parallelogram in the phase-plane. To accurately move the beam to a time varying position of the region defined by the slits, the current applied to the steering magnet is repeatedly changed to the value calculated from the measurement data of the emittance shape and the coordinates of the region.

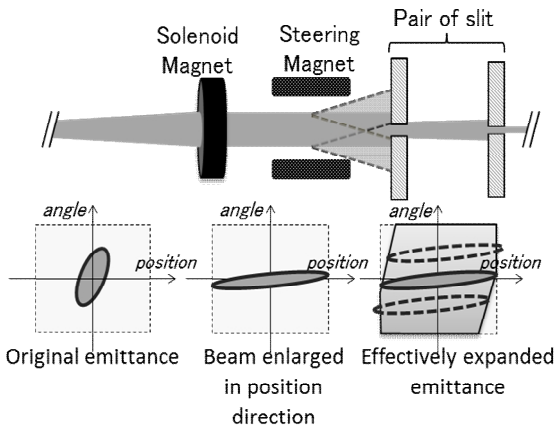

Fig. 1 Method of the effective emittance expansion.

An experimental demonstration was performed under the 160 MeV $^{16}O^{6+}$ accelerating condition. In the condition, a beam with 50.2 keV from a 14.5 GHz ECR ion source (Hypernanogan) is injected to the cyclotron and accelerated to 160 MeV. The emittance of the injection beam [Fig. 2(a)] was effectively expanded to large parallelograms [Fig. 2(b)]. The emittance and the expanded emittance are 59π mm mrad and 1,049π mm mrad, respectively. We have succeeded to expand emittance more than 17 times. Figure 2(c) shows the acceptance measured using the expanded emittance. We have confirmed that the measurement of whole acceptance was achieved using the emittance-expansion technique.

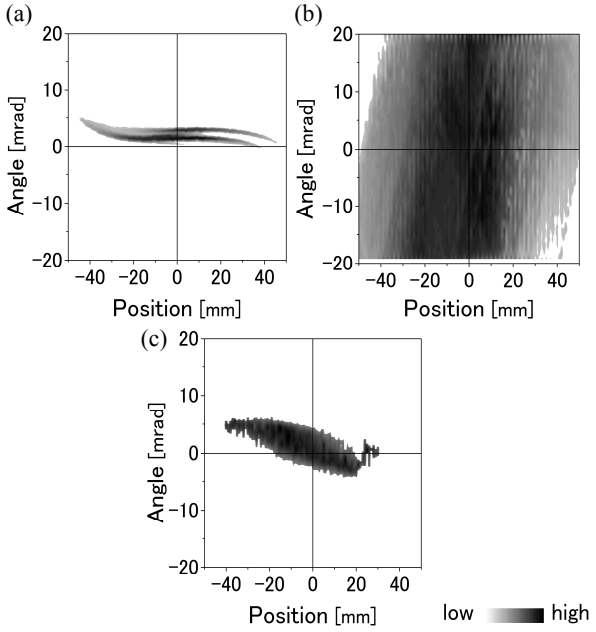

Fig. 2 Measurement results of the $^{16}O^{6+}$ beam (a) Original emittance, (b) expanded emittance, (c) acceptance.

References

1) H. Kashiwagi et al, Rev. Sci. Instrum. 85 (2014) 02A735.
2) H. Kashiwagi et al., Proc. 8th Annu. Meet. Part. Accel. Soc. Jpn. 8 (2011) MOPS079.

4 - 39 Status Report on Technical Developments of Electrostatic Accelerators

K. Yamada, Y. Saitoh, Y. Ishii, S. Matoba, A. Chiba, A. Yokoyama, A. Usui, T. Satoh, T. Ohkubo, K. Narumi and S. Uno

Department of Advanced Radiation Technology, TARRI, JAEA

Transmission ratios of C_{60} cluster ions through a tandem accelerator

One of the key points in accelerating cluster ions using a tandem accelerator is a transmission, which is defined as a ratio of a beam current of incident negative cluster ions upon the tandem to that of accelerated intact positive cluster ions without destruction. Most negative cluster ions injected into a tandem are destructed in collisions with a charge exchange gas at a high voltage terminal in the tandem, thus making the transmission of cluster ions much lower than that of mono-atomic ions. The transmissions are strongly dependent on a charge exchange gas pressure. So, the transmission measurement as a function of the gas pressure is important to obtain a higher beam current of cluster ions. In this year, we have measured the transmission of C_{60} ions as a function of the charge exchanging gas (helium) pressure in the terminal voltage of 2.5 MV. The pressure was monitored with a cold cathode gauge that the beam line is equipped with just downstream of the tandem. As a result, we obtain typical transmission ratios of 2.6% for C_{60}^{1+} and 1.4% for C_{60}^{2+} shown in Fig. 1. The suitable pressures which provides maximum transmissions for C_{60} ions (C_{60}^{1+}: 1.2×10^{-6} Pa, C_{60}^{2+}: 1.1×10^{-6} Pa) are lower than those for small carbon clusters. The C_{60} beam current of several tens pA on a target can be available by fine tuning of gas pressure.

Measurement of cluster ion beam current

A fullerene ion beam current is usually measured using a high-aspect-ratio Faraday Cup (FC) because a bombardment of a fullerene ion generates not only secondary electrons but also secondary positive ions more than those of a monoatomic ion. However, it is unknown how much aspect ratio of a FC is needed to measure a correct current of a cluster ion beam. We measured the ion beam currents of Ar^{+}, Ar^{2+}, C_{60}^{+}, and C_{60}^{2+} ions generated by the 400 kV Ion Implanter using the FCs with aspect ratios of 5, 10, 15, and 20. Figure 2 shows the measured ion currents normalized by another FC with aspect ratio 15 at the end of beam line. Each measured current using the FCs with aspect ratio of 10, 15, and 20 is independent of the aspect ratio and less than that using the FC with aspect ratio of 5 for every ion shown in Fig. 2. We found that the FC with 10 or more-aspect ratio should be used to measure the beam current of cluster ions.

Measurement of beam energy shift at 3 MV single-ended accelerator using resonance nuclear reaction

The shifts of trace elements distribution depending on time are observed in a sample in the μ-PIXE analysis. The main reason of the shift is considered as a slight beam energy shift of several keV at Single-ended Accelerator. In this study, the beam energy shift is estimated by the yield of the γ-ray from the resonance nuclear reaction of $^{27}Al(p,\gamma)^{28}Si$. The beam energy was selected to obtain a large cross section in the reaction. The γ-rays of 1.77 MeV from the reaction between 992 keV protons and an Al target, were measured using a Ge detector. The results showed that the γ-rays were successfully observed by the nano-ampere beam current. We will study the beam energy shift using the resonance nuclear reaction in the next fiscal year.

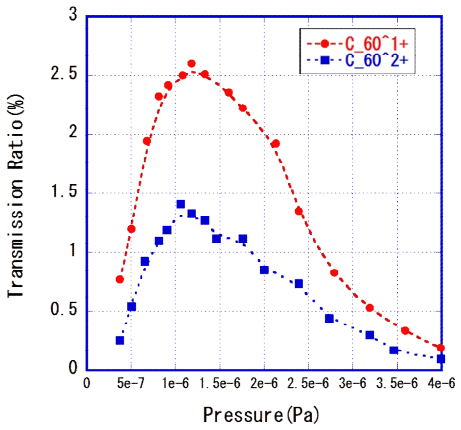

Fig. 1 Transmission ratios of C_{60} ions as the function of stripper gas pressure. Dotted lines are guides for the eyes.

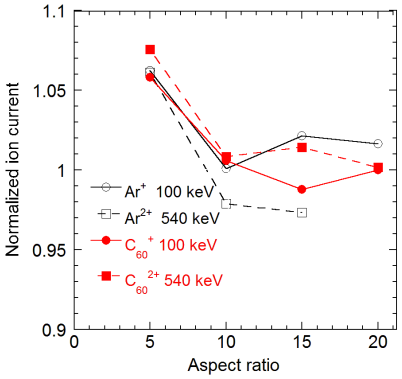

Fig. 2 Ion current as the function of aspect ratio of FCs. y-axis represents the ion current normalized another FC at the end of the beam line.

4 - 40 Development of a Scintillator for Single-ion Detection

A. Yokoyama [a)], W. Kada [b)], T. Satoh [a)], M. Koka [a)], S. Yamamoto [c)], T. Kamiya [a)] and W. Yokota [a)]

[a)] Department of Advanced Radiation Technology, TARRI, JAEA,
[b)] Division of Electronics and Informatics Faculty of Science and Technology, Gunma University,
[c)] Environment and Industrial Materials Research Division, QuBS, JAEA

A real-time position detection of single-ion hit with high spatial accuracy is essential in irradiation experiments of biological cells. A CR-39 plastic track detector placed under the cell targets is currently used to detect hit position. Off-line observation of ion tracks in the CR-39 using a microscope after chemical etching takes more than an hour. Real-time detection is therefore strongly required, which will be realized by using a scintillator that has both a spatial resolution of 1 μm and a strong luminescence intensity. It is known that Al_2O_3:C exhibits photostimulated luminescence (PSL) with high dose sensitivity. Photostimulable phosphe̲r can be prepared by adjusting implantation fluence of activators using the TIARA ion implanter. Ion implantation is a good method for forming luminescence layers with nanometer-order in the samples to obtain high spatial resolution.

The intensity of PSL correlates with that of Photoluminescence (PL) and Ion luminescnece (IL), which accompanies with electronic excitation [1)]. Based on this nature, preparation of samples for strong IL or PL was tried instead of PSL, since construction of the measurement devices were newly needed for PSL detection. Al_2O_3:Eu, which was prepared by implanting Eu into Al_2O_3, was selected. Al_2O_3:Eu has strong IL and can be thinned due to single crystal. Preparation conditions, such as implantation fluence, were studied to increase the maximum IL intensity for Al_2O_3:Eu [2)].

The dependence of the PL intensity on the annealing temperature and annealing time was observed for the Al_2O_3:Eu with an implantation fluence of 3.0×10^{16} cm^{-2} in fiscal 2012 [3)]. The annealing temperature for maximum PL intensity was obtained at 600 °C as shown in Fig. 1. The PL spectra of the samples annealed below 700 °C differ significantly from those above 800 °C. For 700 °C or lower, a broad peak appeared with a maximum in the intensity at around 590 nm, whereas for 800 °C or higher, a sharp peak centered at 620 nm occurred. The following two subjects were carried out in fiscal 2013 based on those results. (1) The PL spectra of prepared Al_2O_3:Eu were compared to that of Al_2O_3:Ar to identify the origin of the peaks in the PL spectra. Al_2O_3:Ar was prepared by irradiating with Ar beam to Al_2O_3, since Ar do not contribute to luminescence. (2) The IL measurements of the prepared Al_2O_3:Eu were carried out to examine sensitivity for 260 MeV-Ne^{7+}.

In the subject (1), the Al_2O_3:Ar and Al_2O_3:Eu were annealed at 600 °C for 0.5 h. PL signal was not appeared for Al_2O_3:Ar, which confirmed that the luminescence peaks observed for Al_2O_3:Eu all originated from the implanted Eu. This may be attributed to the temperature dependent behavior of Eu in annealing; during low-temperatures annealing, diffusion is a major process, whereas at high temperatures, aggregation is significant.

In the subject (2), the IL measurement to examine the sensitivity of the prepared Al_2O_3:Eu having maximum PL intensity was carried out by irradiating with 260 MeV- Ne^{7+}. A system for IL detection consisted of confocal microscope with 10 times magnification objective lens and an electron-multiplier charge-coupled device (EM-CCD) camera. The EM-CCD camera had 512 × 512 light sensitive pixels, each of which were 16×6 μm^2 in size and had maximum linear gain of 8×10^5 electron. With this configuration the system had a spatial resolution of 1 μm, the same as the resolution of a single-ion hit. The system detected scintillation from the prepared Al_2O_3:Eu at a hit rate of two hundreds ions per second that was measured with a silicon charged particle detector after irradiation. PSL is not yet able to be observed from the prepared Al_2O_3:Eu and Al_2O_3:C. However, a real-time detection system of single-ion using IL will be able to be realized by enhancing the IL intensity of Al_2O_3:Eu with two hundred times thicker implantation layer.

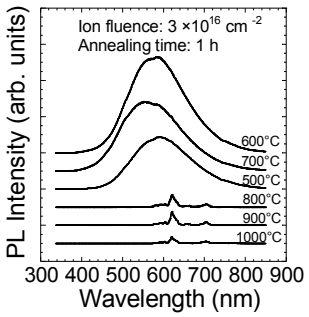

Fig. 1 Effects of annealing temperature for PL intensity of Al_2O_3:Eu. The implantation fluence and annealing time of the samples were fixed at 3.0×10^{16} cm^{-2} and 1 h, respectively. The 600-°C-annealed sample emitted the maximum PL intensity.

Acknowledgment

We would like to gratefully thank Dr. Miura in Graduate School of Engineering, Gunma University for PL measurement. This work was supported by KAKENHI, Grant-in-Aid for Young Scientists (B) 23760837.

References

1) M. Takebe, Radiation 23 (2) (1995) 3.
2) K. Aono et al., Nucl. Instrum. Meth. Phys. Res. B 141 (1998) 518.
3) A. Yokoyama et al., JAEA Takasaki Annu. Rep. 2012 JAEA-Review 2013-059 (2014) 164.

4 - 41 Novel Approach to Intensification and Stabilization of Negative Fullerene Ion Beam Using a Cesium Sputter Type Ion Source

A. Chiba, A. Usui and K. Yamada

Department of Advanced Radiation Technology, TARRI, JAEA

The rate of utilization of the cluster ion beams are increasing and currently occupies more than 20% of an annual beam time of the electrostatics accelerators at TIARA. The characteristic physical phenomena resulting from the ultrahigh-density excitation formed by the interaction between a cluster ion and a solid cannot be fully explained by a superposition model of the interaction between an atomic ion and a solid. The irradiation effects caused by the collective behavior of the cluster constituent ions in the solid, which are called here "cluster effects", tend to increase with increasing the cluster size; therefore, it is very interesting to research the cluster effect caused by collision of the fullerene ions, e.g. C_{60} and C_{70}, which have the largest size of the cluster ions accelerated in the MeV energy range. On the other hand, there are few facilities which supply the MeV energy fullerene ion beams available to experimental users, because it is not easy to produce the negative fullerene ions using a general ion source corresponding for tandem accelerators; therefore, so far the study on interaction with MeV fullerene ions is superficial to date. This report presents an unconventional method for stable production of the higher-intensity C_{60}^- ion beam using a general ion source.

A schematic view of a Cs sputter negative ion source commonly used for many tandem accelerators is shown in Fig. 1(a), and the usual ions are produced through next process. Cs vaporized in the oven ionize at surface of an ionizer heated over 1,000 degrees C. The Cs ions are accelerated towards to the cathode equipped with a solid sample by an electric field between ionizer and cathode. Some of the sputtered particles from the sample are converted to negative ions as they pass through the condensed cesium layer, and are extracted from the ionizer chamber. The negative fullerene ion beam is also produced by the above method. However, intensity of the fullerene beam is rapidly reduced from a few nano-amperes to a few pico-amperes, because the fragments dissociated from the fullerenes by collision with the Cs^+ ions are deposited on the surface of the sample.

A novel proposal on the negative fullerene beam production is making use of a strong electron affinity of the fullerene. The production method is described in Fig. 1(b). The micro-oven which is similar in shape to the cathode is set in the ionizer chamber instead of the cathode. The fullerene sublimed in the micro-oven comes out to the ionizer chamber and converts into negative ion by attachment of the thermal electrons emitted from the surface of the ionizer.

This production method has three advantages as follows: 1) the beam intensity more than a thousand-fold compared with that produced by the sputtering method is preserved for a long time, 2) this technique of using a usual ion source is very easy to build for many tandem accelerators, 3) the source is possible to be used as a Cs sputter ion source by just replacing the micro-oven with the cathode.

Finally, the changes with time of beam intensity of the negative fullerene ions and temperature of the micro-oven are shown in Fig. 2. The beam intensity was measured with a Faraday cup located downstream of an analyzing magnet. The availability of the fullerene beam produced by the new method was demonstrated through a continuous running test for more than 12 hours.

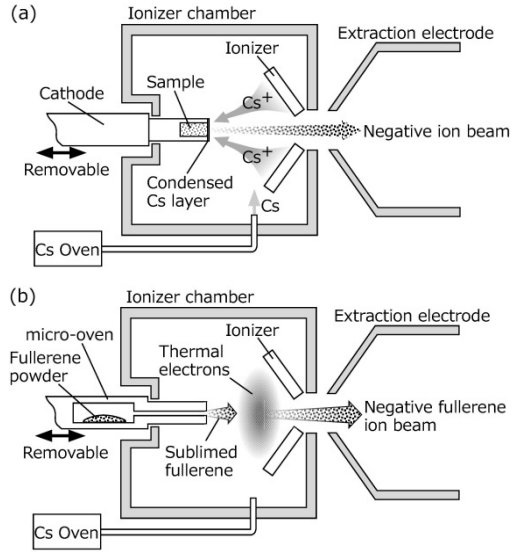

Fig. 1 Schematic views of the production method for negative ion beam; (a) sputtering method; (b) sublimation method for negative fullerene ions.

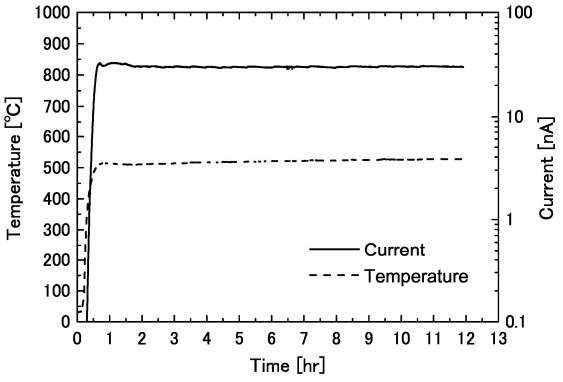

Fig. 2 Results of the stability testing of the C_{60}^- ion beam current and the micro-oven temperature.

4 - 42 Performance Test of a Three-stage Acceleration Lens in a 300 keV Compact Microbeam System

Y. Ishii, T. Ohkubo and T. Kamiya

Department of Advanced Radiation Technology, TARRI, JAEA

A 300-keV compact ion microbeam system with a three-stage acceleration lens and a duoplasmatron-type ion source[1], hereafter called the compact microbeam system, is being developed step-by-step. The system, which is placed in air, is designed to produce ion microbeams of several hundred keV.

The preliminary studies on performance of the three-stage acceleration lens in the constructed compact microbeam system was reported by comparing theoretically calculated and experimentally measured hydrogen ion microbeam sizes for beam energies below 150 keV.

As shown in Fig. 1, the three-stage acceleration lens is composed of a two-stage acceleration lens plus a third acceleration lens. The two-stage acceleration lens was developed at the JAEA; it has a demagnification of over 1000, as demonstrated by forming a 160-nm hydrogen ion beam at about 50 keV[2]. The third acceleration lens, with a high-voltage gradient of over 3 keV/mm, was designed because an image point was formed at the outside of its lens and demagnification of over 1 was obtained[3].

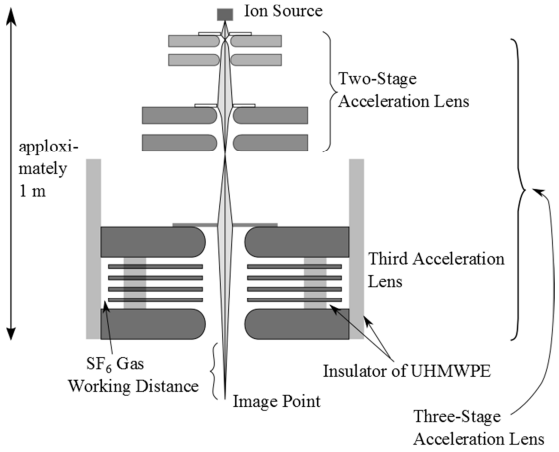

Fig. 1 Schematic of the three-acceleration lens system.

Experimental formation of the microbeam was designed for an acceleration voltage of the third acceleration lens below 150 keV; at these voltages the compact microbeam system operated stably without electric discharges. Using the Munro code to compute lens parameters of the acceleration lenses, the position of images at around 145 keV was found to be 83 mm (the so-called working distance) downstream of the third acceleration lens.

To obtain theoretical beam sizes before starting experiments of microbeam formation, parameters for theoretical beam sizes, such as no-aberration beam size, divergence angle, working distance, and spherical and chromatic aberrations, were calculated using the lens parameters for the acceleration lenses obtained from the Munro code between 140 keV and 150 keV. In these calculations, we used the geometric arrangement of lenses in the three-stage acceleration lens as shown in Fig. 1.

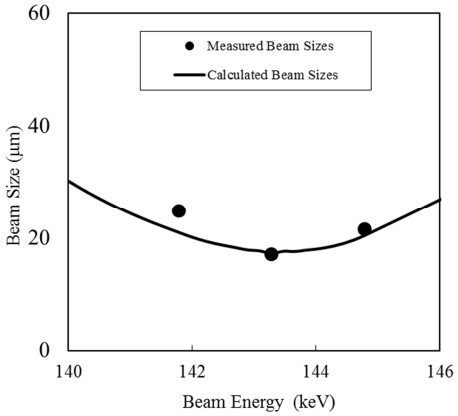

Fig. 2 Compassion of beam sizes which were obtained by the experiments and theoretical calculation.

Hydrogen ion microbeams were experimentally formed at acceleration voltages below 150 keV. The minimum ion beam size in this study was experimentally obtained at 143.28 keV from repetitive measurements of ion beam sizes by finely changing the voltage of the third acceleration lens between 140 keV and 150 keV. By fitting the experimentally measured beam currents to the error function, the minimu ion beam size was estimated to be 17.2 μm ± 0.5 μm at 143.28 keV, which corresponds to FWHM of its error function. Two other beam sizes of 25.0 μm ± 0.4 μm and 21.7 μm ± 0.4 μm were also experimentally obtained at 141.78 and 144.78 keV, respectively. These were obtained by changing the acceleration voltages of the third acceleration lens relative to the minimum beam size. These three beam sizes are plotted, with error bars based on the fittings, in Fig. 2 (filled circles) as a function of the acceleration voltage of the acceleration tube. Therefore, from Fig. 2, estimated and calculated beam sizes were consistent within 10% for the range 17-25 μm[4]. This demonstrates that the three-stage acceleration lens performed as designed for a focusing lens.

References

1) Y. Ishii et al., Nucl. Instrum. Meth. B 113 (1995) 75.
2) Y. Ishii et al., Nucl. Instrum. Meth. B 210 (2003) 702.
3) Y. Ishii et al., Nucl. Instrum. Meth. B 269 (2011) 2193.
4) Y. Ishii et al., Nucl. Instrum. Meth. B 332 (2014) 156-59.

4 - 43 Secondary Electron Emission at 0-degree from Carbon Foil under Swift Ion Bombardment

T. Kaneko [a)], K. Ihara [a)], H. Ogawa [b)], Y. Saitoh [c)], A. Chiba [c)] and K. Narumi [c)]

[a)] Graduate School of Science, Okayama University of Science, [b)] Department of Physics, Nara Women's University, [c)] Department of Advanced Radiation Technology, TARRI, JAEA

Cluster-ion-solid interaction has attracted attention in that the irradiation effects are different from those expected in single-ion irradiation. The so-called cluster effects have been found in the average charge [1-4)], energy-loss [1-2)], and secondary electron emission [5)] under MeV/atom carbon cluster impacts. In order to investigate the cluster effect in secondary electron (SE) emission, first we studied the energy spectra of SE's emitted at 0-degree (the incident direction of a projectile) from a thin carbon foil under MeV ion bombardment.

The present theoretical research is based on the impact-paramach shell-electron in a target carbon-atom are obtained by the absolute square of the transition amplitude, where the initial state wave-functions are described by the Hartree-Fock wave-functions and the final states are assumed a plane wave.

In addition to the above direct ionization process, we take into account the transportation process of excited electrons to the exit surface via the inelastic energy-loss Δ. We use the convolution method to estimate the energy-loss spectre $f(ndx,\Delta)$ for a projectile penetratina layer of $n\,dx$ by a convolution of $f(dx,\Delta)$ for one penetrating a layer of dx. To determine the characteristic quantities there, i.e., the inelastic mean-free-path, the stopping power, and the energy straggling are estimated for the excited electrons moving in an electron-gas described by the dielectric function.

Figure 1 shows the calculated energy spectra of SE's emitted directly at 0-degree (the incident direction) by a point-charge projectile as a function of impact parameter. $b = 0.1 \sim 0.5\,a_0$ where a_0 is the Bohr radius. The energy of the binary peak is located around 2.1 keV, which is contributed from the 2s and 2p state electrons, but not the 1s state one. The dip structure appearing around several ten eV originates from the wave function of the 2s state, that has a node in radial distribution. As increasing impact parameter, the yield of secondary electron with kinetic energy ranging 0.1 to 2 keV decreases seriously. This is mainly due to suppression of the 1s state contribution. The present result will be compared with a recent experimental result shown in Fig. 2. In this figure, there is the convoy electron cusp around at 0.5 keV, which was not considered in Fig. 1. This figure shows a qualitative agreement with Fig. 1. Comparison with the theoretical result that contains the energy-loss of the electrons and the emergent-angle dependences of the projectile will be prepared. As the next step, we will perform a similar calculation for a di-atom cluster in order to investigate the alignment effect. Finally we are grateful for useful discussion of project members in collaboration.

References

1) T. Kaneko, Phys. Rev. A66, 052901 (2002).
2) T. Kaneko et al., Nucl. Instrum. Meth. B 315 (2013) 76.
3) A. Chiba et al., Phys. Rev. A76 (2007) 063201.
4) A. Chiba et al., Nucl. Instrum. Meth. B 315 (2013) 81.
5) S. Tomita et al., Phys. Rev. A73 (2006) 060901(R).
6) H. Ogawa et al, Nucl. Instrum. Meth. B 315 (2013) 291.

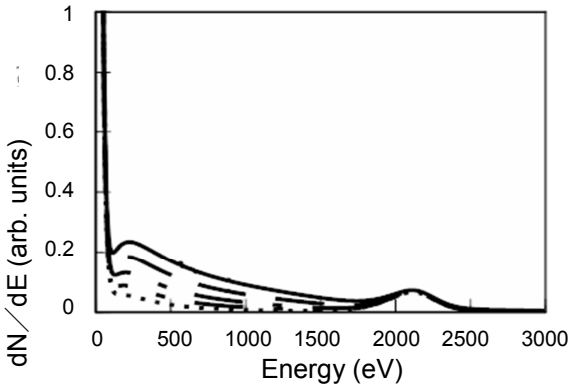

Fig. 1 Energy spectra of SE's emitted from carbon induced by 1 MeV/u He+ ion with b=0.1(solid), 0.2 (broken), 0.3 (dot-dash), 0.4 (dot-dot-dash) and 0.5 a_0 (dot-line).

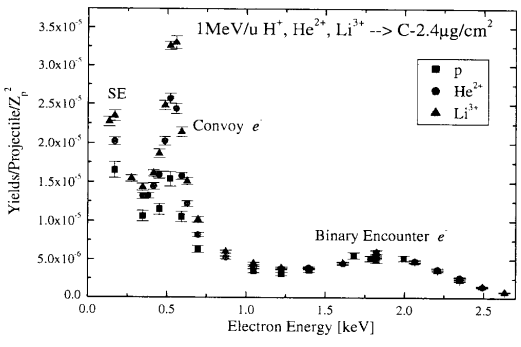

Fig. 2 Experimentally obtained energy spectra [6)] of SE's emitted from carbon induced by 1 MeV/u He^{2+} ion traversing 2.4 μg/cm^2.

4 - 44 TOF Mass Spectra of Secondary Ions Induced by Energetic Cluster Transmission of a Foil Target

K. Hirata [a)], A. Chiba [b)], K. Yamada [b)], S. Matoba [b)], K. Narumi [b)] and Y. Saitoh [b)]

[a)] National Institute of Advanced Industrial Science and Technology (AIST),
[b)] Department of Advanced Radiation Technology, TARRI, JAEA

Time-of-flight (TOF) secondary ion (SI) mass spectrometry is a very powerful surface analysis technique as it allows sensitive detection of SIs over a wide range of mass-to-charge ratios (m/z) and gives chemical-specific information. In addition, use of a cluster ion instead of a monoatomic ion as a primary ion with the same speed provides higher emission yields of SIs originating from target surfaces, showing that use of cluster primary ions is advantageous for further sensitive surface analysis in TOF SI mass analysis [1)]. The TOF SI measurements require timing signals for both the primary ion incidence on the target (the start signal) and the SI detection (the stop signal). Although the stop signal is simply obtained from an SI detector placed at the end of the flight path, the start signal measurements require more sophisticated methods. We developed the transmission type of TOF SI mass spectrometer with energetic cluster ion impacts that provides SI ion mass spectra without sophisticated methods such as ion beam pulsing [2)].

The SI mass spectra were obtained using a TOF SI mass spectrometer along with primary ions produced by a 3 MV tandem accelerator at the Japan Atomic Energy Agency/Takasaki. Primary cluster ions were injected into a thin foil target at an angle of 45° to the target surface, then transmitted through the target. Detection signals of transmitted constituent particles originating from the primary cluster from a solid-state detector (SSD) were used for the start signals. SIs emitted from the front surface of the target were accelerated between the target and a TOF mass spectrometer. The stop signals were obtained from a microchannel plate placed at the end of the flight path in the TOF drift tube. The details of the experimental setup have been described elsewhere [2)].

Figure 1 shows a pulse-height spectrum of the SSD detector for 4.0 MeV C_8^+ transmitted through a silicon nitride membrane with a thickness of 20 nm (Silison Ltd.). The relative intensity was obtained by dividing the count for each channel by the total count. The intense peak around channel 425 is attributed to detection of all the constituent atoms of the primary C_8 cluster (N = 8: N is the number of detected C atoms). Interaction of a constituent with target atoms and/or the other constituents makes the velocity direction of the constituent deviate from that of the primary cluster, resulting that a fraction of the constituents miss the detector. Depending on the number of the detected constituents, the peaks for N = 7, 6 observed in the spectrum. The relatively higher peaks for N = 3 and 5 are primarily due to C_3 and C_5, produced by preferential decomposition of C_8 into C_3 and C_5 before injection into the target [2)]. Figure 2 shows a positive SI TOF mass spectrum under the same condition as Fig. 1. The timing signals, simultaneously provided with the pulse-height signals by the pre-amplifier, were used as the start signals. The major peaks observed in Fig. 2 can be assigned to ions of singly charged atomic and molecular hydrogen H_p^+ (p:1-3), hydrocarbon $C_qH_r^+$ (q:1-4) originating from surface contaminants. The peak at m/z= 57 can be partially attributed to $SiC_2H_5^+$ and/or $NC_3H_7^+$ originating from the target surface.

In conclusion, TOF SI mass spectra were successfully obtained by the transmission type of TOF SI mass spectrometer with energetic primary cluster ions without sophisticated methods such as ion beam pulsing.

References

1) K. Hirata et al., Appl. Phys. Lett. **86** (2005) 044105.
2) K. Hirata et al., Rev. Sci. Instrum. **85** (2014) 033107.

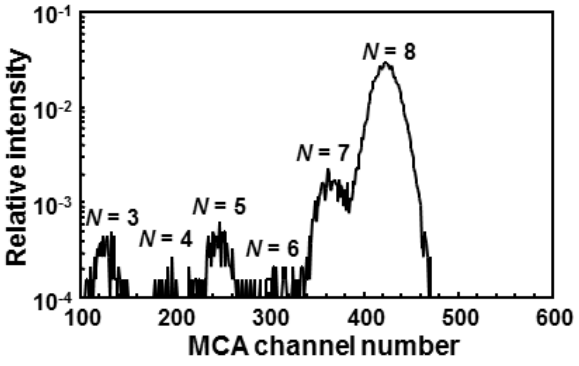

Fig. 1 Pulse-height spectrum for 4 MeV C_8^+ transmitted through a silicon nitride membrane with 20 nm thickness.

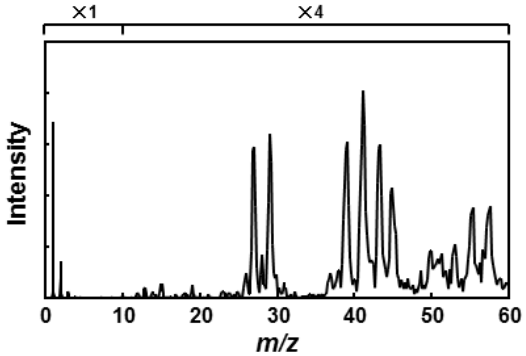

Fig. 2 Positive SI TOF mass spectrum under the same condition as Fig. 1.

4 - 45 Cluster-size Dependence of Secondary-electron Yields Emitted from Carbon Foils Bombarded with 62.5-keV/u C_n^+ Ions

K. Narumi, A. Chiba, K. Yamada, S. Matoba and Y. Saitoh

Department of Advanced Radiation Technology, TARRI, JAEA

A vicinage effect on secondary-electron (SE) emissions from a solid induced by swift molecular/cluster ions is one of the unresolved problems of atomic collisions in solids[1]. In the previous report, we have observed thickness dependence of SE yields in the forward emission from amorphous carbon foils bombarded with 62.5-250-keV/u H_2^+ and C_2^+ ions[2]. Internuclear-distance analysis of the vicinage effect has demonstrated that the effect consists of two contributions: One depends on the internuclear distance and the other hardly depends on it. We have concluded that the former can be attributed to the *production* process of the three-step model of SE emissions from a solid[3], which is closely related to the energy deposition by a projectile. On the other hand, the latter could originate from the *transport* process. However, the vicinage effect which originates from other processes except the *production* process has not been demonstrated experimentally yet. In the present study, we have observed cluster-size dependence of SE yields emitted in the forward direction from amorphous carbon foils bombarded with C_n^+ ions. It demonstrates the vicinage effect attributed to other processes except the *production* process.

62.5-keV/u C_n^+ ions (n = 1-4) were incident on self-supporting amorphous carbon foils of 1-80 μg/cm^2 thicknesses, which were tilted by 45° to the beam axis. C_n^+ ions were supplied with the 3-MV tandem accelerator of JAEA/Takasaki. SEs emitted in the forward direction from a carbon foil were detected with a microchannel-plate (MCP) detector placed at the lower side of the target holder in parallel with the foil. Bias voltage of +0.7 kV was applied to the entrance of the MCP detector in order to collect all SEs emitted in the forward direction. The pulse height of the MCP-detector signal is proportional to the number of the detected SEs. Projectiles transmitted through the foil were detected with a solid-state detector (SSD) placed on the beam axis in the forward direction, which made it possible to measure the energy and the number of the transmitted particles. The acceptance angle of the SSD was 7.6°. The signal from each detector was stored in a PC in a list mode. In order to evaluate the vicinage effect correctly, only MCP-detector signals coinciding with the two-carbon signals from the SSD were selected, and the pulse-height distributions of the MCP-detector were measured. The SE yield per incident projectile was defined as the most probable number of the SEs. The vicinage effect was evaluated with the ratio of the SE yields $R_n = \gamma_n / n\gamma_1$, where γ_n and γ_1 were SE yields induced by bombardment with C_n-cluster and monatomic ions with the same velocity, respectively; then, the effect is shown to be observed in the case that $R_n \neq 1$.

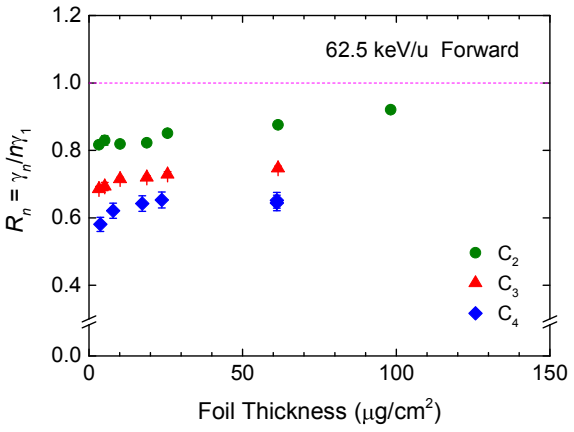

Fig. 1 Dependences of the ratio of the SE yields R_n on the foil thickness.

Figure 1 shows that $R_n < 1$ in all the cases measured, *i.e.*, suppression of SE emission has been observed. The ratio R_n approaches 1 gradually as the target is thicker, whereas it never reaches 1 within the thickness used in the present experiments. Figure 1 also represents that the larger the cluster size n is, the smaller the ratio R_n is. This cluster-size dependence of R_n has been observed for at least 60 μg/cm^2 as obvious in Fig. 1.

Our previous internuclear-distance analysis has revealed that the vicinage effect attributed to the *production* process dominates at thin foils, and could diminish at approximately 30 μg/cm^2 [2]. Thus, the contribution of the *production* process to the effect could be excluded at the thicker foils. On the other hand, the observed cluster-size dependence of R_n indicates that the vicinage effect originating from some physical mechanism exists even at the thicker foils. This supports our conclusion that the vicinage effect which originates from other processes except the *production* process is demonstrated experimentally. For further confirmation, theoretical study is necessary.

References

1) R. A. Baragiola, Nucl. Instrum. Meth. Phys. Res. B **237** (2005) 520.
2) K. Narumi et al., JAEA Takasaki Annu. Rep. 2012 JAEA-Review 2013-059 (2014) 171.
3) E. J. Sternglass, Phys. Rev. **108** (1957) 1.

4 - 46 Visualization of Interactions between Cluster Ion Beams and Soft Organic Materials by Single Particle Nanofabrication Technique

T. Sakurai [a)], Y. Takeshita [a)], A. Chiba [b)], A. Asano [a)], Y. Saitoh [b)], M. Omichi [c)] and S. Seki [a)]

[a)] Department of Applied Chemistry, Graduate School of Engineering, Osaka University,
[b)] Department of Advanced Radiation Technology, TARRI, JAEA,
[c)] Center for Collaborative Research, Anan National College of Technology

We have so far found that high-energy particles penetrating into materials give their kinetic energy to a limited nm-sized spatial area along their trajectories, affording insoluble nanogels (nanowires) via cross-linking of the materials. The resulting nanowires can be isolated on the substrate by the subsequent development using organic solvent and visualized by atomic force microscopy (AFM). This methodology motivated us to visualize cluster ion beam tracks by investigating the shape and size of the obtained nanowires. Here we found that some of ethynyl-substituted π-systems provide nanowires by Al cluster beam irradiation, where interactions between Al cluster ions and organic materials are clearly visualized.

クラスターイオンとは、数個から数万個の原子が結合した状態で、一個のイオンとして振る舞うが、高速に加速して物質に照射した場合、以下のような特徴があることが知られている。①複数のイオンが数 Å 間隔で結合した状態で物質内に突入すると、原子間距離程度の空間的相関を持って、あるいは数フェムト秒の時間相関を持って物質内で高密度の電離、電子励起、格子励起を誘起する。このような高密度・高励起状態においては様々な反応場が形成され、物質の構造変化や化学反応を起こす。②低速クラスターイオンが物質の表面近傍にのみ作用するのに対し、高速クラスターイオンでは表面より内部への効果も期待できる。このような MeV エネルギーに加速された高速クラスターイオンは新しい放射線源としての有用性・将来の産業応用への可能性が考えられ、そのさらなる理解が不可欠である。

我々の研究グループでは『単一粒子ナノ加工法』と呼ばれる手法を展開してきた[1–6]。この手法では、高エネルギーの粒子線を基板上の有機材料薄膜に照射することで、粒子の飛跡に沿って有機分子の架橋反応が引き起こされ、その部位のみが選択的に不溶化する。そのため、有機溶媒を用いた現像過程によりワイヤー状のナノゲルを単離することが可能である。この手法を高速クラスターイオンビーム照射にも適用することで、ソフトマテリアルとクラスタービームとの相互作用による化学反応を引き起こし、得られるナノワイヤーを観察することでその相互作用の可視化を行うことを研究目的とした。

過去の検討により、高エネルギー重イオン照射の場合では、エチニル基が架橋反応を誘起するのに適していることがわかっているため[4]、本課題においてもエチニル基を多数有し、溶解性の比較的高い低分子材料である tetrakis(2,5-ethynylphenyl)porphyrin を用いた。低分子であることのメリットとして、現像過程を迅速に行うことができ、ナノワイヤーを破壊することなく単離可能という特徴がある。この化合物をテトラヒドロフラン（THF）溶媒に溶解させ、シリコン基板上にスピンコートすることで厚さ約 350 nm のフィルムを作製した。これに対しアルミニウムを核種としたクラスタービーム Al_1（1.5 MeV）, Al_2（3.0 MeV）, Al_3（4.5 MeV）, Al_4（6.0 MeV）をそれぞれ照射し、照射後にクロロホルム溶媒で現像したのち、原子間力顕微鏡（AFM）により観察を行った。その結果、Al_1 の照射では 3.5 nm 程度の細いナノワイヤーが得られたのに対し、Al_2 の照射ではその 2 倍程度の太さ（6.3 nm）のナノワイヤーが得られ、さらにその一部においては末端で 2 分岐した様子が観察された（Fig.1）。この分岐部分のナノワイヤーの太さ（4.3 nm）は Al_1 照射で得られたものの太さに近いものであった。したがって、Al_2 照射においてはクラスタービームがそのエネルギーを材料薄膜に与えていく過程で有機化合物の架橋反応を誘起すると同時に、多重散乱によって粒子の直進性が低下していき、ある地点で Al_1 イオン 2 つとして振る舞うということが示唆された。詳細については今後検討する予定である。

References

1) S. Seki et al, Adv. Mater. 13 (2001) 1663-65.
2) S. Seki et al, Phys. Rev. B 70 (2004) 144203/1-8.
3) S. Seki et al, J. Phys. Chem. B 116 (2012) 12857-63.
4) A. Asano et al, J. Phys. Chem. C 116 (2012) 17274-79.
5) Y. Maeyoshi et al, Sci. Rep. 2 (2012) 600/1-6.
6) M. Omichi et al, Nature Commun. 5 (2014) 3718. (doi:10.1038/ncomms4718).

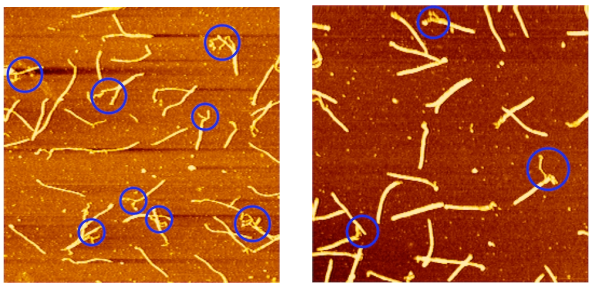

Fig. 1 AFM topographic images of nanowires by SPNT of 350-nm thick tetrakis(2,5-ethynylphenyl)porphyrin films. The left and right images were obtained by irradiation of Al_2 (3.0 MeV) and Al_3 (4.5 MeV) ion cluster beams, respectively. The films were prepared by spin coating from THF solutions. Benzene was used for the development. Blue circles indicate a sign of split ion tracks.

4 - 47 Change in Magnetic and Structural Properties of FeRh Thin Films by Gold Cluster Ion Beam Irradiation

T. Koide [a)], Y. Saitoh [b)], M. Sakamaki [c)], K. Amemiya [c)], A. Iwase [a)] and T. Matsui [d)]

[a)] Department of Materials Science, Osaka Prefecture University,
[b)] Department of Advanced Radiation Technology, TARRI, JAEA,
[c)] Institute of Materials Structure Science, KEK,
[d)] Research Organization for the 21st Century, Osaka Prefecture University

Ordered FeRh alloy with B2 (CsCl-type) crystal structure has considerably attracted scientific interests because of its unique magnetic behavior of a first order phase transition from antiferromagnetic (AF) to ferromagnetic (FM) near room temperature [1)]. Hereby, we revealed that the ion beam irradiation induced the FM state in FeRh bulk and film samples below room temperature where they were originally in the AF state.

In the present studies, we have investigated the effect of energetic cluster ion beam irradiation on magnetic and structural properties of FeRh thin films. When a couple of atoms constituting a cluster ion impinge on a very small volume simultaneously, high-density energy deposition and multiple-collision processes can be realized [2)]. Hence, lattice defects, which are ascribed to the change in the magnetic natures of FeRh, will be introduced in the FeRh films in a different way from the case in the irradiation with the conventional single ion beam.

FeRh thin films were deposited on the MgO (001) substrate at 973 K by ion beam sputtering from a FeRh target. The FeRh thin films were subsequently irradiated with 5 MeV Au_3 cluster ion as well as 1.67 MeV Au_1 ion beam at Japan Atomic Energy Agency (JAEA) -Takasaki by using a 3 MV tandem accelerator. The irradiation was performed at room temperature with the ion fluence of 3×10^{12} Au/cm^2. After the irradiation, the magnetic properties of the films were evaluated by X-ray magnetic circular dichroism (XMCD) at the synchrotron radiation facility (KEK-PF), as well as by a superconducting quantum interference device (SQUID) magnetometer.

Figure 1 shows the magnetic-hysteresis loops measured at 5 K for the unirradiated films and irradiated ones with the Au_3 cluster ion and Au_1 ion with the ion fluence of 3×10^{12} Au/cm^2. Even in the films irradiated with the same ion fluence, the saturation magnetization of the film irradiated with the Au_3 cluster ion (280 emu/cc) is larger than that of the film irradiated with Au_1 ion (240 emu/cc).

Similar results have also been confirmed by the XMCD measurement. Figure 2 shows the XMCD spectra at the Fe $L_{2,3}$-edge for the unirradiated and irradiated films. The Fe $L_{2,3}$-edge spectrum for the film irradiated with Au_3 cluster ion with the fluence of 3×10^{12} Au/cm^2 shows a larger XMCD signal than that of the film irradiated with Au_1 ion with the same fluence. This fact suggests that the surface magnetization of the film irradiated with Au_3 cluster ion is larger than that of the film irradiated with Au_1 ion. Cluster ions can leave many displaced atoms on the surface compared to a single ion because cluster ion irradiation can realize the processes of high-density energy deposition and multiple-collision. This is because cluster ion is composed of a few atoms in a distance of a few angstroms.

These results show that cluster ion irradiation is better than the single ion irradiation from the viewpoint of the saturation magnetization, even if the same irradiation energy is deposited in the films.

References

1) M. Fallot et al., Rev. Sci. 77 (1939) 498.
2) T. Aoki et al., Nucl. Instrum. Meth. Phys. Res. B 121 (1997) 49-52.

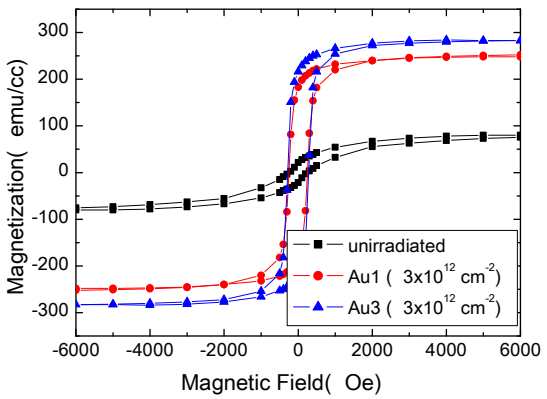

Fig. 1 M-H curves for the unirradiated and irradiated with Au_3 cluster ion and Au_1 ion.

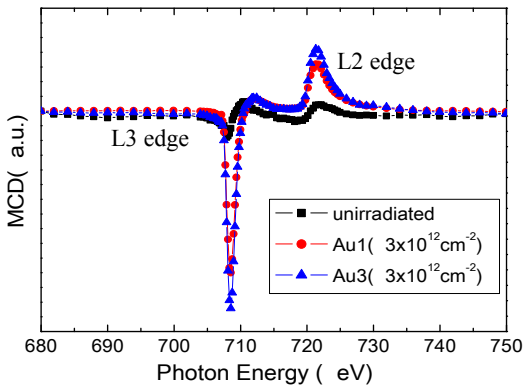

Fig. 2 XMCD spectra for the unirradiated and irradiated with Au_3 cluster ion and Au_1 ion.

4 - 48 Secondary Ion Emission from Amino Acid Films Irradiated with 5 MeV C_{60} Ions

K. Nakajima [a], K. Nagano [a], M. Suzuki [a], K. Narumi [b], Y. Saitoh [b], K. Hirata [c] and K. Kimura [a]

[a] Department of Micro Engineering, Kyoto University, [b] Department of Advanced Radiation Technology, TARRI, JAEA, [c] National Metrology Institute of Japan, National Institute of Advanced Industrial Science and Technology

There has been an increasing demand to extend accessible mass range in secondary ion mass spectrometry (SIMS) particularly for biological and biomedical molecular imaging[1]. During the past two decades, various kinds of large clusters, such as C_{60} ions, argon gas cluster ions, water cluster ions, and metal cluster ions have been used as primary ions. It was shown that these cluster ions enhance emission of intact large molecular ions compared to monatomic ion bombardment. In the present study, we employ 5 MeV C_{60}^+ ions to measure secondary ions emitted in the forward direction from phenylalanine amino acid films deposited on self-supporting amorphous Si_3N_4 (a-Si_3N_4) films. We found significant enhancement of the intact phenylalanine ion yield and suppression of fragment ions in the forward direction compared to the backward direction.

Phenylalanine amino acid was purchased from Nacalai Tesque (Japan) and used without further purification. Self-supporting a-Si_3N_4 films (1.5×1.5 mm^2) of thickness 20 - 50 nm made by low pressure chemical vapor deposition were purchased from Silson Ltd (Northampton, UK). Thin films of phenylalanine (20 - 100 nm) were prepared on the a-Si_3N_4 films using vacuum evaporation.

A beam of 5 MeV C_{60}^+ ions was produced by a 3 MV tandem accelerator at JAEA/Takasaki. The beam was collimated by an aperture (diameter 1mm) and incident on the phenylalanine/a-Si_3N_4 film from the a-Si_3N_4 side at 45° with respect to the surface normal. The ions passing through the film were detected by a silicon surface barrier detector of 20 mm diameter which was placed about 110 mm downstream from the specimen. Positive secondary ions emitted in the forward direction from the phenylalanine films were accelerated by a mesh electrode biased at -0.7 kV and detected by a micro-channel plate (MCP) after traveling through a drift tube of 930 mm length. The timing of the projectile and secondary ion signals were measured by a 4ch TDC (WE7521: Yokogawa Electric Corp., time resolution 5 ns) and the data was stored in a list mode. We also measured the secondary ions emitted in the backward direction from the phenylalanine film. In the backward measurement, the drift tube and MCP were moved behind the sample (135° with respect to the beam direction) and the phenylalanine/a-Si_3N_4 film was rotated by 180° so that the secondary ions emitted from the entrance surface of the phenylalanine film can be measured.

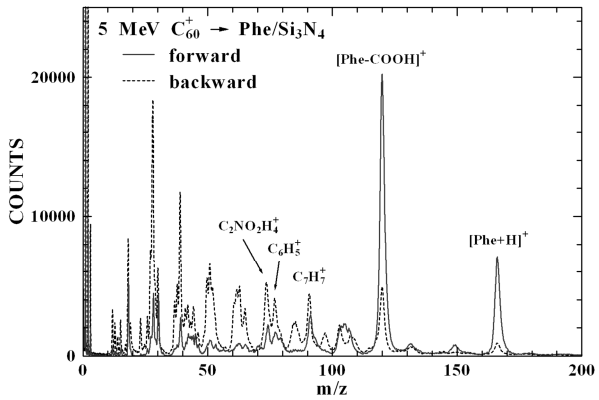

Fig. 1 Mass spectra for positive ions from phenylalanine films on a-Si_3N_4 films under 5 MeV C_{60}^+ ion bombardment. The spectra observed in the forward direction (solid line) and the backward direction (dashed line) are shown.

Figure 1 shows the observed mass spectra of positive secondary ions emitted in the forward (solid line) and backward (dashed line) directions. In addition to a peak of the protonated phenylalanine ions at m/z = 166, there are many ions corresponding to the fragment ions. The yield of the intact phenylalanine ion is 4.7×10^{-3} ions/incident ion in the backward direction. In the forward direction, the yield is almost one order of magnitude larger than the backward direction. It is also noteworthy that the yield of the fragment ions are suppressed in the forward direction compared to the backward direction. The forward to backward yield ratio is about 0.2 for smaller fragment ions and increases very rapidly with mass number. This behavior can be qualitatively understood in terms of the distribution of the deposited energy at the entrance and exit surfaces [2]. The present result demonstrates a large advantage of the transmission SIMS using MeV C_{60} ions for the analysis of biological materials.

References

1) L. A. McDonnell et al., Mass Spectrom. Rev. **26** (2007) 606.
2) K. Nakajima et al., Appl. Phys. Lett. **104** (2014) 114103.

5. Present Status of Irradiation Facilities 2013

This is a blank page.

5 - 01 Utilization Status at TIARA Facility

K. Hirota [a)], H. Takizawa [a)], M. Hosono [a)], Y. Haruyama [a)],
Y. Nakamura [b)], S. Kaneya [b)], T. Asai [b)], M. Kawabata [b)], S. Nozawa [b)] and K. Watanabe [b)]

[a)] Department of Advanced Radiation Technology, TARRI, JAEA,
[b)] Takasaski Establishment, Radiation Application Development Association

1. Research & Industrial Uses

There are four accelerators, cyclotron, tandem, single-ended accelerators, and ion implanter, in the TIARA to meet various research needs. Research activities for the cyclotron for the past 5 years are shown in Fig. 1. Total utilization time is ranging from 2,200 to 2,500 hours. This time is equal to more than 95% of available time of the cyclotron. Researches on "biotechnology and medical application" account for the largest portion of total utilization time each year. The trend of research activities in the TIARA are slowly changing recently, where "base technology" is in high demand. In contrast, researches on "RI production and nuclear science" are decreased for the past 3 years.

When we see the research activities for the three electrostatic accelerators, the profile of total utilization time is different from that of the cyclotron, as shown in Fig. 2. The utilization time of "base technology" is increased year by year and reached to about 50% of the total time. Relatively lower energy irradiation probably meets demand of researchers who study the fundamental phenomena of materials under irradiation, elemental analysis and so on. An increasing trend is also the case with "nuclear and fusion materials".

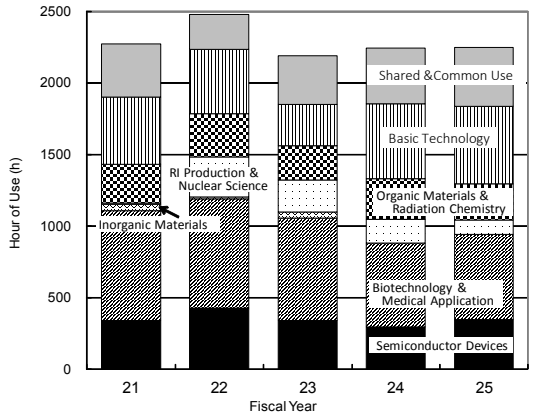

Fig. 1 Status of utilization for cyclotron for recent 5 years.

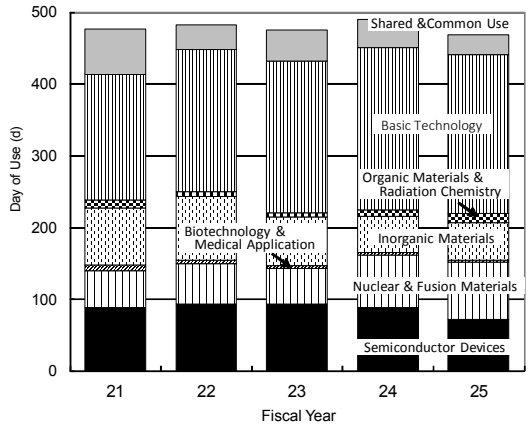

Fig. 2 Status of utilization for three electrostatic accelerators for recent 5 years.

2. Fukushima Recovery

The TIARA facility contributes to Fukushima recovery in a variety of fields through in-house researches as follows;

- Research on breakdown events of wide band gap semiconductor in the space environment,
- Study of radiation effects on anti-radiation microbes,
- Study of nitride layer effect on breakdown of zircaloy oxide layer.

Cyclotron is one of the key radiation-source machines to understand radiation effects on semiconductor and to develop robots for reactor decommissioning of Fukushima Daiichi Nuclear Power Station. This research is also carried out using the tandem accelerator and the ion implanter. Researches on anti-radiation microbes using the cyclotron are expected to create microbes which are able to enrich cesium in the environment.

In addition to the in-house researches, collaboration researches are progressing. For example, basic RI imaging technology is studied to observe real-time phenomena of cesium dynamics in plants. Positron-emitting isotope of cesium-129 generated using the cyclotron through reaction of $^{127}I(\alpha, 2n)^{129}Cs$ was used for this imaging study.

3. The others

Eighth Takasaki Advanced Radiation Research Symposium was held on 11th to 12th in October, 2013 at Takasaki City Gallery. Special session on the fiftieth anniversary of the Takasaki Institute was programmed in the symposium. More than 500 participants discussed about research topics such as radiation effect on organic and inorganic materials, radiation-induced mutation, and radiation degradation of pollutants.

Furthermore, the JAEA Takasaki annual report 2012 included in 164 research papers was issued the same as before. About 600 books were distributed to relevant departments.

The second five-year plan for our institute covers the period from 2010 to 2014. We continue to provide user-friendly environment for researchers' demand at the TIARA facility.

5 - 02 Operation of the AVF Cyclotron

I. Ishibori [a)], S. Kurashima [a)], K. Yoshida [a)], T. Yuyama [a)], T. Ishizaka [a)], N. Miyawaki [a)], H. Kashiwagi [a)], Y. Yuri [a)], S. Okumura [a)], T. Nara [a)], To. Yoshida [b)], Tu. Yoshida [b)], K. Akaiwa [b)], S. Ishiro [b)], S. Kanou [b)], A. Ihara [b)], K. Takano [b)] and T. Saitoh [b)]

[a)] Department of Advanced Radiation Technology, TARRI, JAEA, [b)] Beam Operation Service, Co., Ltd.

Operation

The AVF cyclotron was smoothly operated in fiscal 2013. The accumulative operation time was 72,097.9 hours and the total number of experiments was 10,336 from the first beam extraction in 1991 to March 2014.

Table 1 shows the statistics of the cyclotron operation of fiscal 2013. For comparison, it includes the data in fiscal 2012. The total operation time amounted to 3,005.6 hours, and monthly operation times are shown in Fig. 1. The percentages of operation time of the year used for regular experiments, facility use program and promotion of shared use program, beam tuning, and beam development are 62.9%, 13.0%, 22.4%, and 1.6%, respectively. There was only one cancellation of the experiments, which was caused by a machine trouble.

Table 2 shows the operation time of the multi-cusp ion source for H^+ and D^+ production and two ECR ion sources for heavier ions. The ECR ion sources are used alternatively. The Operation time of the OCTOPUS ion source decreased, and the operation time of the HYPERNANOGAN ion source and the multi-cusp ion source increased compared to fiscal 2012. Fractional distribution of major ions used for experiments is shown in Fig. 2. The ratios of D, Ne and Metal increase compared to fiscal 2012.

Table 1 Statistics for cyclotron operation.

	2012	2013
Beam service time (h)	2398.5	2282.7
Machine tuning (h)	714.9	674.5
Beam development (h)	62.2	48.4
Total operation time (h)	3175.6	3005.6
Change of particle and/or energy	225 times	251 times
Change of beam course	273 times	267 times
Change of harmonic number	72 times	76 times
The number of experiments	547	548
Experiment cancelled due to machine trouble	0	1

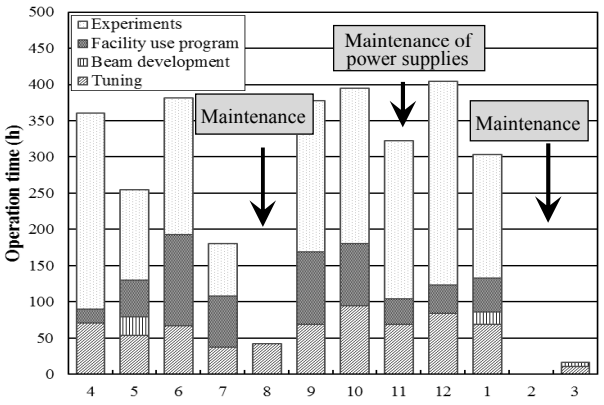

Fig. 1 Monthly operation times in fiscal 2013.

Table 2 Operation times of ion sources.

Ion source	Operation time 2012 (h)	Operation time 2013 (h)
Multi-cusp	821.3	848.1
ECR (OCTOPUS)	1170.4	646.3
ECR(HYPERNANOGAN)	1833.9	2084.4

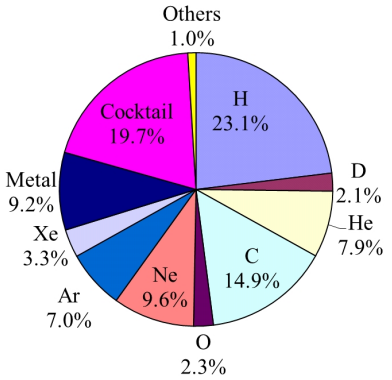

Fig. 2 Ion species used for experiments in fiscal 2013.

Maintenance

The regular yearly overhaul and maintenance were carried out. The major items were as follows: 1) Installation of a differential pumping port to guide bush in order to drive the shorting plate of the RF system without deteriorating the vacuum level, 2) Inspection of the cryogenic pumps in the injections system, 3) Exchange of cooling fans for power supplies, 4) Exchange of the evacuation control sequencer units for the beam transport system, 5) Routine maintenance of the power supplies, 6) Additional installation of the inverter control unit to the secondary water cooling system for the ion sources and injections system, 7) Exchange of HC rotary shutter in the beam transport system, 8) Exchange of radiation monitor system.

Technical Development

New beam acceleration tests were carried out for 40 MeV D^+ and 385 MeV $^{40}Ar^{12+}$, which were needed for experiments. Moreover, the current and energy of $^{129}Xe^{28+}$ are significantly improved; 30 nA and 660 MeV were obtained. Low contamination rate was confirmed in the HYPERNANOGAN ion source; 0.2 percent Cu ion for 520 MeV $^{84}Kr^{20+}$ and none of the other ions for 400 MeV $^{84}Kr^{18+}$.

In order to increase the transmission of heavy-ion beams for uniform irradiation in the LB course, a vacuum pipe with a large square section was installed. The detail is described elsewhere in this annual report.

5 - 03 Operation of Electrostatic Accelerators

A. Chiba [a)], S. Uno [a)], K. Yamada [a)], A. Yokoyama [a)], A. Usui [a)], Y. Ishii [a)], K, Narumi [a)], T. Satoh [a)], T. Ohkubo [a)], T. Nara [a)], T. Kitano [b)], T. Takayama [b)], S. Kanai [b)], T. Orimo [b)], Y. Aoki [b)] and M. Hashizume [b)]

[a)] Department of Advanced Radiation Technology, TARRI, JAEA,
[b)] Beam Operation Service, Co., Ltd

1. Operations and Status

The operating ratio of 100% with respect to the research utilization in fiscal year 2013 had been achieved, because the serious troubles in any electrostatic accelerators were avoided due to the appropriate repairs and maintenance. The fiscal operating times of the 3-MV tandem accelerator, the 400-kV ion implanter and the 3-MV single-ended accelerator were 2,062, 1,866 and 2,320, respectively, in the same levels with usual years. The monthly operating times of these accelerators are shown in Fig. 1. The scheduled maintenances for about two weeks were carried out in August, December and March, respectively. The accumulated operating time since starting the operation of the tandem accelerator at 1991 had been achieved at 40,000 hours in October, following the single-ended accelerator in fiscal year 2011.

2. New Beam

There are few facilities in which the fullerene ion beams, e.g., C_{60}^{+} and C_{70}^{+}, are usable in a MeV energy region through use of a tandem accelerator[1)]. One of the reasons for not popularizing the MeV energy fullerene ion beams is difficulty in generating the negative fullerene ions using a Cs sputter type ion source which is generally installed on many tandem accelerators.

In the tandem accelerator in TIARA, a generation technique of C_{60}^{-} ions on the electron attachment basis is being developed using the existing Cs sputter type ion source (SNICS Ⅱ, National Electrostatics Corp.). At the current stage, intensity of the C_{60}^{+} ion beam which was charge-exchanged by collision with the stripper gas and which was accelerated by the tandem accelerator has increased 1,000-fold as compared with that generated by a conventional method. The provision of the enhanced fullerene beam to several users has already been started.

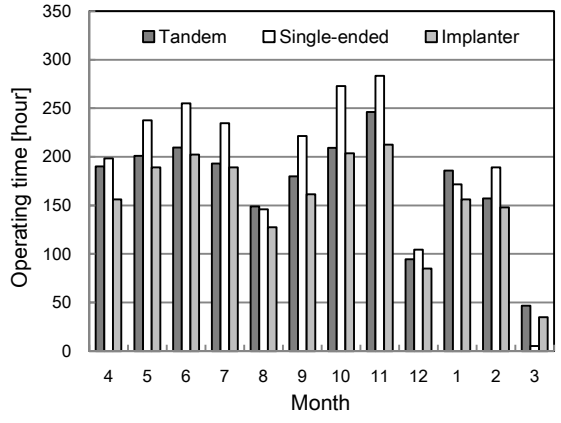

Fig. 1 Monthly operating times of electrostatics accelerators in FY 2013.

3. Maintenance and Improvement

The renewal of incidental equipment and devices for the electrostatic accelerators had been carried out in line with the schedule of the governmental supplementary budget for fiscal year 2013.

A SF_6 gas-recovery unit for the tandem accelerator was fully-refurbished. The dilapidated unit, which had been operating more than two-decade, had fears that the deterioration of a compressor or a vacuum pump impairs the gas-recovery ability and that the SF_6 gas, which is greenhouse gas, leaks due to the deterioration of the packing in the pipe joints. The new unit without the use of lubricating oil for the compressor and the vacuum pump will contribute to more stable operation of the accelerator, because of keeping a high purity of SF_6 gas. In the ion implanter, a booster power supply, an acceleration tube (see Fig. 2), and sequence modules in a control system were renewed. In the single-ended accelerator, an acceleration tube and sequence modules in a control system were exchanged for new ones; moreover, some instruments installed on a SF_6 gas-recovery unit: a compressor, a vacuum pump, solenoid valves, and a console, were renewed. It is expected that the renewals of these equipment lead to more stably providing the ion beams and to safer operation.

Reference

1) B. Waast et al., Nucl. Instrum. Meth. Phys. Res. A 382 (1996) 348-56.

Fig. 2 Exchanging process of the acceleration tube on the ion implanter.

5 - 04 Operation of the Electron Accelerator and the Gamma-ray Irradiation Facilities

T. Agematsu [a)], H. Hanaya [a)], R. Yamagata [a)], H. Seito [a)], Y. Nagao [a)], H. Kaneko [a)], T. Yamaguchi [b)], I. Kawashima [b)], N. Yagi [b)], M. Takagi [b)] and S. Matsuzaki [b)]

[a)] Department of Advanced Radiation Technology, TARRI, JAEA,
[b)] Takasaki Establishment, Radiation Application Development Association (RADA)

1. Operation

The electron accelerator and the gamma-ray irradiation facilities were operated approximately smoothly.

The electron accelerator was on service as scheduled 9:00-17:30 on Monday and Friday, and 8:30-23:00 from Tuesday to Thursday, to satisfy users' demand for operation time; however, the service time on Thursday was shortened to 9:00-17:30 since June 2013 for effective operation in consideration of users' demand. As shown in Fig. 1, the annual operation time of the electron accelerator in FY 2013 has increased to 1,242 h as compared with that in FY 2012 because longer-time irradiation increased in the materials-for-space research field.

The ^{60}Co gamma-ray irradiation facilities consisting of three buildings with eight irradiation rooms cover a wide dose-rate range from 10^{-1} to 10^{4} Gy/h. The annual operation times for the first, the second cobalt irradiation facilities and the food irradiation facility are 18,900 h, 11,804 h and 6,587 h, respectively, as shown in Fig. 2.

2. Maintenance

2.1 Electron accelerator

The SF_6 gas withdrawal system, which broke down in October 2012, was renewed in February 2014. This renewal enabled to open the accelerator vessel, and damaged coupling part of the Motor-Generator rod in the accelerator vessel was replaced to new one. The PLC (Programmable Logic Controller) of the accelerator's control system was renewed in February 2014. A cooling tower of the water cooling system for the accelerator was renewed in June 2013. The air-conditioning system for the accelerator's building was renewed in January-March 2014.

2.2 Gamma-ray irradiation facilities

The periodical maintenance check mainly on mechanical system for radiation source transportation is performed every year on one of three gamma-ray irradiation facilities in turn. The maintenance check of the food irradiation facility was done in November 2013 with suspension of operation for fifteen days.

The new ^{60}Co sources, whose total radioactivity was 4.44 PBq, were loaded into the irradiation room No.2 in the first irradiation facility and the irradiation rooms No.5 and No.6 in the second irradiation facility to increase the area of high dose-rate fields.

The 600-m^3 water storage tank was installed on the south side of the first irradiation facility in November 2013. Before the maintenance check of each facility, the water pool of the each facility has to be evacuated. This tank enabled to store the evacuated water without drainage and to re-store the water quickly to the pool without production of newly refined water, and furthermore, to shorten the suspension period of operation. This storage tank will be used for three gamma-ray irradiation facilities.

The air-conditioning systems for the first and the second irradiation facilities were renewed with the intermittent suspension period of operation between January and March 2014.

Following jobs were carried out using mainly the intermittent suspension periods of operation in January and February 2014. The PLCs of the irradiation control system in the first and the food irradiation facilities were renewed. The radiation monitoring systems for irradiation rooms in the first and the food irradiation facilities were renewed. Large-sized LEDs of the radiation monitoring system for the controlled areas were repaired. The water treatment system was renewed partly.

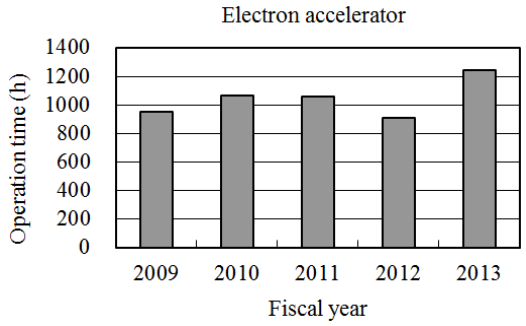

Fig. 1 Annual operation time of the electron accelerator.

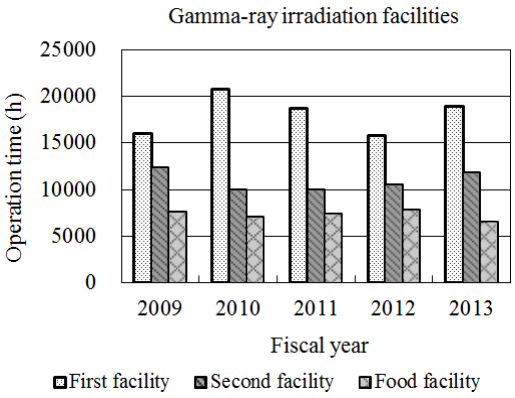

Fig. 2 Annual operation times of the ^{60}Co gamma-ray irradiation facilities.

5 - 05 Utilization Status of the Electron Accelerator and the Gamma-ray Irradiation Facilities

T. Agematsu [a)], H. Hanaya [a)], R. Yamagata [a)], H. Seito [a)], Y. Nagao [a)], H. Kaneko [a)], T. Yamaguchi [b)], I. Kawashima [b)], N. Yagi [b)], M. Takagi [b)] and S. Matsuzaki [b)]

[a)] Department of Advanced Radiation Technology, TARRI, JAEA,
[b)] Takasaki Establishment, Radiation Application Development Association (RADA)

The electron accelerator and the three gamma-ray irradiation facilities were operated for various research subjects according to the operation plan in FY 2013.

The irradiation time and the number of research subjects for each facility in FY 2013 are shown in Table 1. The accelerator mainly served for graft-polymerization for new material development, radiation effect study on semiconductors and various experiments of visiting users. The first cobalt irradiation facility mainly served for radiation-resistance testing of cables used in nuclear power plants and nuclear reactor facilities with a long irradiation period. The second cobalt irradiation facility, involving the irradiation room No.6 operated on hourly schedule, mainly served for development of new functional materials and other research subjects of visiting users. The food irradiation facility mainly served for development of detection method for irradiated foods and radiation resistance testing at lower dose rates.

Figure 1 shows the number of research subjects for each research field in each facility in FY 2009-2013. The number of research subjects in FY 2013 is kept constant from FY 2012 for each facility.

Among these research subjects, 47 and 91 ones respectively performed at the electron accelerator and the gamma-ray irradiation facilities were relevant to recovery from the Fukushima Daiichi nuclear disaster.

Table 1 The irradiation time and the number of research subjects for each facility in FY 2013.

Facility / Research fields	Electron accelerator		Gamma-ray irradiation facilities	
	Irradiation time (h)	Research subjects	Irradiation time (h)	Research subjects
Material processing	104.1	149	4991.5	303
Heat-resist material	119.5	36	0.0	0
Materials for space	843.9	145	1526.3	40
Nuclear facilities	17.4	5	55436.2	126
Environment	0.0	0	0.0	0
Resources & Bio-technology	0.0	0	293.8	112
Basic technology	92.6	5	1048.0	23
Joint use	64.3	22	27123.4	194
Total	1241.7	362	90419.3	798

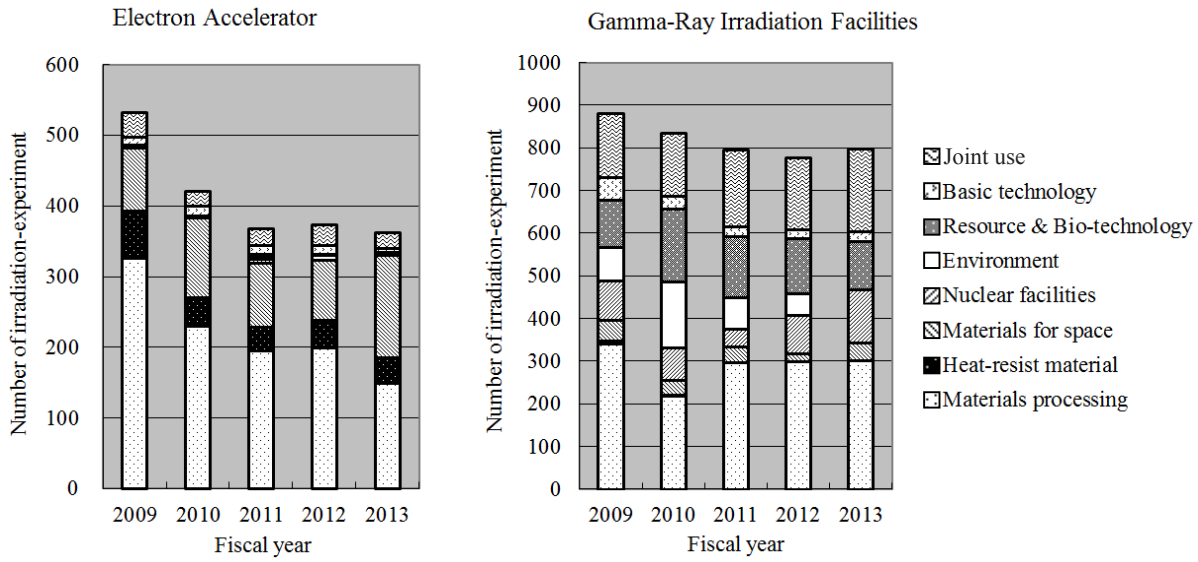

Fig. 1 The number of research subjects (FY 2009-2013).

5 - 06 Radiation Control in TIARA

Safety Section

Department of Administrative Services, TARRI, JAEA

1. Individual monitoring

(1) Individual monitoring for the radiation workers

Table 1 shows a distribution of effective dose of the radiation workers in FY 2013. The effective dose values of almost all radiation workers were below the detection limit (0.1 mSv).

The maximum dose was 0.3 mSv/y due to the overhaul of the TIARA AVF cyclotron.

Table 1 Distributions of the effective dose of the radiation workers in FY 2013.

Items		Number of persons in each period				
		1st quarter	2nd quarter	3rd quarter	4th quarter	Annual
Distribution range of effective dose	HE < 0.1	610	578	588	624	779
	0.1 ≦ HE ≦ 1.0	1	5	2	1	8
	1.0 < HE ≦ 5.0	0	0	0	0	0
HE:Effective dose *1 (mSv)	5.0 < HE ≦ 15.0	0	0	0	0	0
	15.0 < HE	0	0	0	0	0
Total number of persons (A)		611	583	590	625	787
Exposure above 1 mSv	Number of persons (B)	0	0	0	0	0
	(B)/(A)×100(%)	0	0	0	0	0
Mass effective dose (Person･mSv)		0.1	0.8	0.2	0.1	1.2
Mean dose (mSv)		0.00	0.00	0.00	0.00	0.00
Maximum dose (mSv)		0.1	0.3	0.1	0.1	0.3

*1 The dose by the internal exposure was not detected.

(2) Individual monitoring for the visitors and others

Table 2 shows the number of persons who temporary entered the radiation controlled areas. The effective dose of all persons was less than 0.1 mSv.

Table 2 The number of persons who temporary entered the radiation controlled areas in FY 2013.

Periods	1st quarter	2nd quarter	3rd quarter	4th quarter	Total
Number of persons	764	946	1379	1936	5025

2. Monitoring of radioactive gas and dust

Table 3 shows the maximum radioactive concentrations and total activities for radioactive gases released from the stack of TIARA, during each quarter of FY 2013.

Small amount of ^{41}Ar, ^{11}C and ^{13}N were detected for some time during operation of the cyclotron or experiment, but the particulate substances (^{65}Zn, etc.) were not detected.

Table 3 Monitoring results of released radioactive gases and dust in FY 2013.

Nuclide	Items \ Periods	1st quarter	2nd quarter	3rd quarter	4th quarter	Total
^{41}Ar	Maximum concentration	$<1.4\times10^{-4}$	$<1.4\times10^{-4}$	$<1.4\times10^{-4}$	$<1.5\times10^{-4}$	
	Activity	2.1×10^{7}	0	2.1×10^{8}	2.0×10^{8}	4.3×10^{8}
^{11}C	Maximum concentration	$<1.4\times10^{-4}$	$<1.4\times10^{-4}$	$<1.4\times10^{-4}$	$<1.5\times10^{-4}$	
	Activity	2.0×10^{8}	4.6×10^{7}	8.4×10^{7}	4.4×10^{7}	3.7×10^{8}
^{13}N	Maximum concentration	$<1.4\times10^{-4}$	——	$<1.4\times10^{-4}$	——	
	Activity	5.3×10^{7}	——	1.8×10^{7}	——	7.1×10^{7}
^{65}Zn	Maximum concentration	$<6.2\times10^{-10}$	$<5.9\times10^{-10}$	$<5.9\times10^{-10}$	$<5.3\times10^{-10}$	
	Activity	0	0	0	0	0

Unit : Bq/cm^{-3} for Maximum concentration, Bq for Activity.

3. Monitoring for external radiation and surface contamination

External radiation monitoring was routinely carried out in/around the radiation controlled areas and surface contamination monitoring was also carried out. Neither unusual value of dose equivalent rate nor surface contamination was detected.

Figure 1 shows a typical example of distribution of the dose equivalent rate in the radiation controlled area of the cyclotron building.

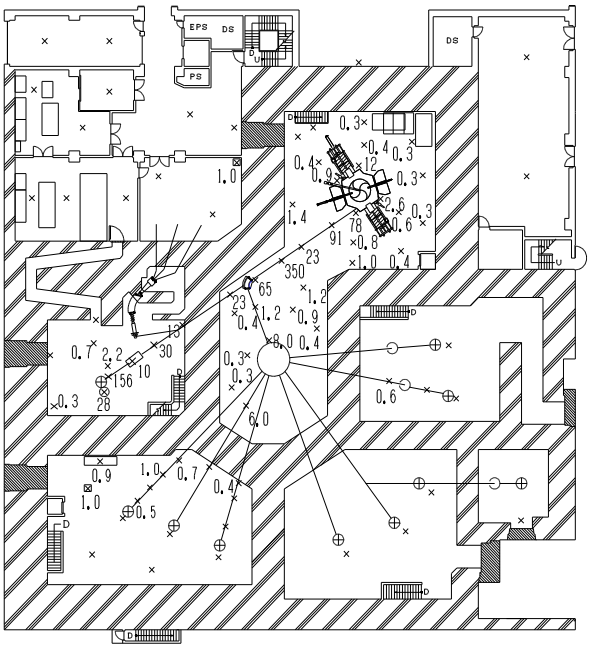

Fig. 1 Dose equivalent rate distribution in the radiation controlled area of the cyclotron building.
Measurement date : 20th ,25th and 26th March 2014,
Measuring position : Indicated with × (1 m above floor),
Unit : μSv/h.
(The values are not indicated if less than 0.2 μSv/h.)

5 - 07 Radioactive Waste Management in TIARA

M. Nabatame and T. Hosoi

Department of Administrative Services, TARRI, JAEA

1. Radioactive wastes management

The radioactive wastes generated in TIARA are managed by Utilities and Maintenance Section. The main radioactive wastes are the solid ones generated from research experiments and the maintenance of the cyclotron. Other radioactive wastes are the liquid ones, which is mainly inorganic waste fluids generated from research experiments and the air-conditioning machines in the controlled area. The wastes are managed according to their properties.

2. Solid radioactive waste

Table 1 shows the amounts of solid wastes at various properties and kinds generated in each quarter of FY 2013. The main solid waste is generated from research experiments and the maintenance of the cyclotron.

Combustible wastes are rubber gloves, paper, clothes, etc. Incombustible wastes are metal pieces, the glasses, and contaminated parts.

3. Liquid radioactive waste

Table 2 shows the amounts of liquid wastes generated in each quarter of FY 2013. Most of liquid waste was inorganic waste water generated from chemical experiments and condensed water from operation of air conditioning units installed in each room of the first class controlled area. The largest quantity of waste water in summer season (2nd quarter) is mainly due to condensed water. After treatment by evaporation of liquid residue, inorganic water is reused in the radiation controlled area. Only small amounts of concentrated liquid are generated from the evaporation.

Table 1 Radioactive solid wastes generated in FY 2013.

Amounts / Items	Amounts of generation in each period (m^3)					Number of package /drum
	1st quarter	2nd quarter	3rd quarter	4th quarter	Total	
Category A*	0.06	0.44	0.42	0.36	1.28	
1)Combustible	0.06	0.30	0.24	0.16	0.76	5**
2)Incombustible	0	0.14	0.18	0.20	0.52	0
Compressible	0	0.14	0.18	0.20	0.52	3**
Filters	0	0	0	0	0	0
Incompressible	0	0	0	0	0	0
Ion exchange resin	0	0	0	0	0	0
Category B*	0	0	0	0	0	0

* defined by dose at the outer surface of container : (A) $<$ 2 mSv/h $\leqq$ (B),
** 200-liter drum.

Table 2 Radioactive liquid waste generated in FY 2013.

Amounts / Items	Amounts of generation in each period (m^3)					Number of package /drum
	1st quarter	2nd quarter	3rd quarter	4th quarter	Total	
Category A*	8.65	22.99	4.38	3.79	39.81	
1)Inorganic	8.65	22.99	4.38	3.79	39.81	treatment
2)Organic	0	0	0	0	0	0
Organic	0	0	0	0	0	0
Oil	0	0	0	0	0	0
3)Sludge	0	0	0	0.1	0.1	1
4)Evaporation residue	0	0	0	0.1	0.1	1
Category B*	0	0	0	0	0	0

* defined by concentrations in Bq/cm^3 (β, γ) : (A) $< 3.7 \times 10 \leqq$ (B) $< 3.7 \times 10^4$.

5 - 08 FACILITY USE PROGRAM in Takasaki Advanced Radiation Research Institute

H. Yoshida, D. Ushijima and K. Shidomi

Department of Advanced Radiation Technology, TARRI, JAEA

1. Introduction

The facilities of JAEA are widely opened to users in universities, public institutes, industries, etc. FACILITY USE PROGRAM started in 2006, which is the system of facility use for the user's service on fee-charging basis. The open used facilities in Takasaki are Co-60 Gamma-ray Irradiation Facilities, Electron Accelerator, TIARA (Takasaki Ion Accelerators for Advanced Radiation Application), and some of the off-line analysis instruments.

In this program, the Research Proposals are examined carefully every half year from the standpoint of the availability and the validity of the experimental plan by the special committee. The facility usage fee has revised in FY2013. The details of the fee consist of handling fees, the irradiation fee, the expendables fee, radioactive waste disposal expenses and the additional charge. In case of Non-proprietary research, the users, who are exempted from the irradiation fee, should report the experimental results to JAEA. The reports are opend to the public by the annual report. Users of universities can also apply to the facility usage through another program operated by The University of Tokyo. Such applications are accepted as priority case. Table 1 shows main classification of FACILITY USE PROGRAM.

Table 1 Main Classification of FACILITY USE PROGRAM.

Purpose	Research and Development		Except R&D
Classification	General	Priority case	Commercial
Result	Non-proprietary	Proprietary	
Referee	Yes	No	
Charge*	A	B	C

*A = handling fees + the expendables fee + radioactive waste disposal expenses,
B = handling fees + the irradiation fee,
C = handling fees + the irradiation fee + depreciation.

2. Use in FY2013

There were 21 applications of Research Proposals in FY2013 at Takasaki Institute, and 17 of them were as Non-proprietary use. Including the users from priority case and others, 310 applications from 76 users are accepted. Table 2 and Fig. 1 show user's classification for each facility and distribution of classification for FACILITY USE PROGRAM.

Table 2 User's classification for each facility.

Facility \ User		University	Public Institute	Indsutries and others	Total
TIARA	AVF cyclotron	7	3	14	24
	3MV tandem accelerator	4	0	1	5
	3MVsingle-ended accelerator	1	0	1	2
	400kV ion implanter	1	0	0	1
Co-60 gamma-ray irradiation facilities		4	4	30	38
Electron accelerator		1	0	5	6
Total for each classification		18	7	51	76

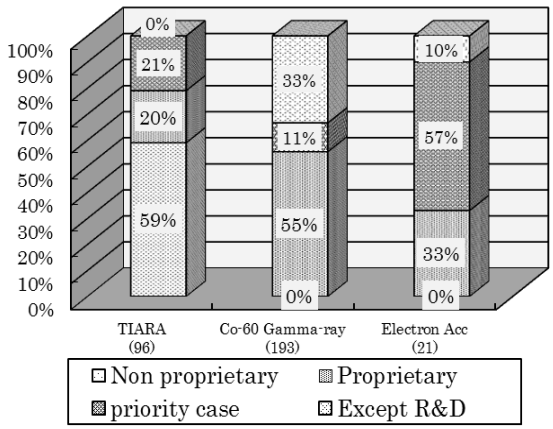

Fig. 1 Distribution of classification for FACILITY USE PROGRAM. The number of theme for each facility is shown in parentheses.

3. Public Relations

The information, such as an outline of this system, guidelines for applicants, format of download etc. can be found on JAEA website as follows:
http://sangaku.jaea.go.jp/3-facility/01-intro/index-02.html.

The "Advanced-research base common use and a platform formation enterprise", which is one of the subsidiary project of Ministry of Education, Culture, Sports, Science and Technology (MEXT) has been cooperated from FY2013. This project intends that industrial users promote shared use of facilities, which accelerates the whole activity of science technology from basic research to innovation creation.

An outline of this project can be seen on website as follows: http://www.taka.jaea.go.jp/innovation/index.html

5 - 09 Project for Creation of Research Platforms and Sharing of Advanced Research Infrastructure at TARRI

S. Nozawa, M. Koka, H. Ohsawa, K. Shidomi, K. Hirota and Y. Haruyama

Department of Advanced Radiation Technology, TARRI, JAEA

"Project for Creation of Research Platforms and Sharing of Advanced Research Infrastructure" which is subsidized by the Ministry of Education, Culture, Sports, Science and Technology (MEXT) has been started in FY2013. The aim of this project is to promote utilization of irradiation facilities in Takasaki Advanced Radiation Research Institute (TARRI) with providing technical support and reasonable irradiation charges for external users. Four irradiation facilities having some irradiation sources are applicable to various commercial purpose (Table 1).

Outline of user support

New users and users who are not familiar to irradiation facilities frequently face various problems at an early stage such as operation of equipment, experimental plan, evaluation of results, schedules and so on. On this project, we clear these problems and provide technical support for all irradiation facilities practically. We help users to prepare samples, operate equipment, and evaluate results. These services are provided to meet user's demands.

There are two plans for irradiation on this project. A trial use is available free of charge to applicants which use our facilities for the first time. The other is non-proprietary use. Users of companies and institutes can use our facilities with the reduction of charge on condition of opening their experimental reports on website within two years after the project is over. The charge is about 10% of proprietary-use charge for external users in case of AVF cyclotron. For example, the engineer who plans to process the novel materials by irradiation can check the possibility of processing on the trial use. After the effectiveness of irradiation is confirmed, investigation under appropriate conditions might be continued on non-proprietary use.

In FY2014, we will start the new irradiation plan that applicants can use our facilities confidentially. The companies whose targets are research and development of new materials, electronic devices and biological resources are expected in this plan.

Public relations

As one of the publicity activities for this project, we introduced the irradiation facilities of TARRI at some exhibitions to be held in Japan. In addition, we visited 11 public exhibitions for gathering information about demands in public companies. As a result of these public relations, the nine applicants had contacted to this project and we consulted them about using irradiation facilities.

Table 1 List of irradiation facilities covered by Project for Creation of Research Platforms and Sharing of Advanced Research Infrastructure at TARRI.

Irradiation sources	Examples for application by commercial users
TIARA AVF cyclotron, 3MV tandem accelerator 3MV single-ended accelerator 400kV ion implanter	● Ion-beam mutagenesis for plant and microbial ● PIXE (particle induced X-ray emission) and PIGE (particle induced gamma-ray emission) analysis in the micrometer range ● Development of functional materials ● Micro processing by proton beam writing ● Evaluation of electronic devices under radiation environment
Electron accelerator	● Development of functional polymers ● Processing of organic materials
Cobalt-60 gamma-ray irradiation facility	● Evaluation of radiation resistance ● Sterilization
Positron beam facilities	● Detection of voids inside material

This is a blank page.

Appendices

Appendix 1. List of Publication

A 1.1 Publications in Journal

13J001 1-01 E
R. Hoheisel, M. González, M. P. Lumb,
D. A. Schiman, S. R. Messenger, C. G. Bailey,
J. Lorentzen, T. N. D. Tibbits, M. Imaizumi,
T. Ohshima, S. Sato,
P. P. Jenkins and R. J. Walters
"Quantum-Well Solar Cells for Space: The Impact of Carrier Removal on End-of-Life Device Performance"
IEEE J. Photovoltaics 4(1) (2014) 253-59.

13J002 1-02 C, T, S, I
T. Ohshima, S. Sato, M. Imaizumi, T. Nakamura,
T. Sugaya, K. Matsubara and S. Niki
"Change in the Electrical Performance of GaAs Solar Cells with InGaAs Quantum Dot Layers by Electron Irradiation"
Sol. Energ. Mater. Sol. Cell. 108 (2013) 263-68.

13J003 1-03 C
E. Mizuta, S. Kuboyama, H. Abe,
Y. Iwata and T. Tamura
"Investigation of Single-Event Damages on Silicon Carbide (SiC) power MOSFETs"
Radiat. Eff. Compon. Syst. 2013 (RADECS 2013).

13J004 1-05 T
S. Onoda, A. Hasuike, Y. Nabeshima, H. Sasaki,
K. Yajima, S.-i. Sato and T. Ohshima
"Enhanced Charge Collection by Single Ion Strike in AlGaN/GaN HEMTs"
IEEE Trans. Nucl. Sci. 60 (2013) 4446-50.

13J005 1-07 I
A. Abderrahmane, S. Koide, H. Okada,
H. Takahashi, S. Sato,
T. Ohshima and A. Sandhu
"Effect of proton irradiation on AlGaN/GaN micro-Hall sensors"
Appl. Phys. Lett. 102 (2013) 193510.

13J006 1-07 I
A. Abderrahmane, T. Tashiro, H. Takahashi,
P. J. Ko, H. Okada, S. Sato,
T. Ohshima and A. Sandhu
"Partial recovery of the magnetoelectrical properties of AlGaN/GaN-based micro-Hall sensors irradiated with protons"
Appl. Phys. Lett. 104 (2014) 023508.

13J007 1-07
A. Abderrahmane, H. Takahashi, T. Tashiro,
P. J. Ko, H. Okada, S. Sato,
T. Ohshima and A. Sandhu
"Effect of Proton Irradiation on 2DEG in AlGaN/GaN Heterostructures"
J. Phys.: Conf. Ser. 433 (2013) 012011.

13J008 1-08 T
T. Yamamoto, T. Umeda, K. Watanabe,
S. Onoda, M. L. Markham, D. J. Twitchen,
B. Naydenov, L. P. McGuinness, T. Teraji,
S. Koizumi, F. Dolde, H. Fedder, J. Honert,
J. Wrachtrup, T. Ohshima,
F. Jelezko and J. Isoya,
"Extending spin coherence times of diamond qubits by high-temperature annealing"
Phys. Rev. B 88 (2013) 075206

13J009 1-08 I

T. Yamamoto, C. Müller, L. P. McGuinness,
T. Teraji, B. Naydenov, S. Onoda, T. Ohshima,
J. Wrachtrup, F. Jelezko and J. Isoya
"Strongly Coupled Diamond Spin Qubits by Molecular Nitrogen Implantation"
Phys. Rev. B. 88 (R) (2013) 201201.

13J010 1-08 E

G. Waldherr, Y. Wang, S. Zaiser, M. Jamali,
T. Schulte-Herbrüggen, H. Abe, T. Ohshima,
J. Isoya, J. F. Du, P. Neumann and J. Wrachtrup
"Quantum error correction in a solid-state hybrid spin register"
Nature 506 (2014) 204-07.

13J011 1-10 G

M. Arisaka, M. Watanabe, M. Ishizaki,
M. Kurihara, R. Chen and H. Tanaka
"Cesium adsorption ability and stability of metal hexacyanoferrate irradiated with gamma-rays"
J. Radioanal. Nucl. Chem. 2013-57th (2013) 294 .(Proc. APSORC2013)

13J012 1-14 G

T. Motooka, A. Komatsu,
T. Tsukada and M. Yamamoto
"Pitting Potential of Zircaloy-2 in Artificial Seawater under Gamma-ray Irradiation"
ECS Trans. 53 (21) (2013) 25-32.

13J013 1-14 G

T. Motooka, A. Komatsu,
T.Tsukada and M. Yamamoto
"Effect of gamma radiolysis on pit initiation of zircaloy-2 in water containing sea salt"
J. Nucl. Sci. Tech. 51 (7-8) (2014) 987-95.

13J014 1-16 G

中野 純一、山本 正弘、塚田 隆
"ガンマ線照射下におけるヒドラジン添加希釈海水中での炭素鋼および低合金鋼の腐食"
日本原子力学会和文論文誌 13 (2014) 1-6.

13J015 1-16 G

J. Nakano, Y. Kaji,
M. Yamamoto and T. Tsukada
"Effects of hydrazine addition and N_2 atmosphere on the corrosion of reactor vessel steels in diluted seawater under gamma-rays irradiation"
J. Nucl. Sci. Tech. 51 (7-8) (2014) 977-86.

13J016 1-24 G

T. Ito, S.-Y. Kim, Y. Xu, K. Hitomi, K. Ishii,
R. Nagaishi and T. Kimura
"Adsorption Behaviors of Platinum Group Metals in Simulated High Level Liquid Waste Using Macroporous (MOTDGA-TOA)/SiO_2-P Silica-based Absorbent"
Separ. Sci. Tech. 48 (2013) 2616-25.

13J017 1-24 G, E

I. Yamagishi, R. Nagaishi, C. Kato, K. Morita, A.
Terada, Y. Kamiji, R. Hino, H. Sato,
K. Nishihara, Y. Tsubata, S. Tashiro, R. Saito,
T. Satoh, J. Nakano, W. Ji, H. Fukushima,
S. Sato and M. Denton
"Characterization and Storage of Radioactive Zeolite Waste"
J. Nucl. Sci. Tech. 51 (7-8) (2014) 1044-53.

13J018 1-24 G

T. Ito, S.-Y. Kim, R. Nagaishi and T. Kimura
"Study on Radiation Effects and Radiation Resistance of (MOTDGA-TOA)/SiO_2-P

Adsorbent for Separation of Platinum Group Metals from High Level Radioactive Waste"
to be accepted in Journal of Radioanalytical and Nuclear Chemistry.

13J019 1-25 G
A. Idesaki, H. Uechi, Y. Hakura and H. Kishi
"Effects of gamma-ray irradiation on a cyanate ester/epoxy resin"
Radiat. Phys. Chem. 98 (2014) 1-6.

13J020 1-26 G
A. Shimada, M. Sugimoto, H. Kudoh,
K. Tamura and T. Seguchi
"Degradation distribution in insulation materials of cables by accelerated thermal and radiation ageing"
IEEE Trans. Dielectr. Electr. Insul. 20 (2013) 2107-16.

13J021 1-26 G
A. Shimada, M. Sugimoto, H. Kudoh,
K. Tamura and T. Seguchi
"Degradation mechanisms of silicone rubber (SiR) by accelerated ageing for cables of nuclear power plant"
IEEE Trans. Dielectr. Electr. Insul. 21 (2014) 16-23.

13J022 1-41 C
S. Kato, T. Yamaki, S. Yamamoto, T. Hakoda, K. Kawaguchi, T. Kobayashi,
A. Suzuki and T. Terai
"Preparation of Tungsten Carbide Nanoparticles by Ion Implantation and Electrochemical Etching"
Nucl. Instrum. Meth. Phys. Res. B 314 (2013) 149-52.

13J023 1-43 G
H. Koshikawa, K. Yoshimura, W. Sinnananchi,
T. Yamaki, M. Asano, K. Yamamoto,
S. Yamaguchi, H. Tanaka and Y. Maekawa
"Counter Anion Effect on the Properties of Anion-Conducting Polymer Electrolyte Membranes Prepared by Radiation-induced Graft Polymerization"
Macromol. Chem. Phys. 214 (2013) 1756.

13J024 1-44, 1-45 C
T. Yamaki, M. Asano, H. Koshikawa,
Y. Maekawa, D. Severin,
T. Seidl and C. Trautmann
"Analysis of Ion-Beam Induced Degradation of Poly(vinylidene fluoride) and Post-Irradiation Treatment for Efficient Track Etching"
GSI Sci. Rep. 2012 (2013) 402.

13J025 1-44, 1-45, 1-46 C
T. Yamaki, N. Nuryanthi, H. Koshikawa,
M. Asano, S. Sawada, T. Hakoda, Y. Maekawa,
K.-O. Voss, D. Severin, T. Seidl,
C. Trautmann and R. Neumann
"Ion-Track Membranes of Fluoropolymers: Toward Controlling the Pore Size and Shape"
Nucl. Instrum. Meth. Phys. Res. B 314 (2013) 77-81.

13J026 1-44, 1-45, 1-46 C
N. Nuryanthi, T. Yamaki, H. Koshikawa,
M. Asano, S. Sawada, S. Hasegawa,
Y. Maekawa and Y. Katsumura
"Applied-Voltage Dependence on Conductometric Track Etching of Poly(vinylidene fluoride) Films"
Nucl. Instrum. Meth. Phys. Res. B 314 (2013) 95-98.

13J027 1-44, 1-45, 4-37 C
A. Kitamura (Ogawa), T. Yamaki, Y. Yuri,
S. Sawada and T. Yuyama
"Microscopic Evaluation of the Absolute Fluence Distribution of a Large-Area Uniform Ion Beam Using the Track-Etching Technique"
Nucl. Instrum. Meth. Phys. Res. B 314 (2013) 47-50.

13J028 1-45 C
S. Hasegawa, S. Takahashi, H. Iwase,
S. Koizumi, M. Ohnuma and Y. Maekawa
"Crystal Morphology-Dependent Graft Polymerization in Poly(ether ether ketone) films"
Polymer 54 (2013) 2895.

13J029 1-46 G
S. Sawada, D. Yamaguchi, A. Putra,
S. Koizumi and Y. Maekawa
"Nanoscale structures of radiation-grafted polymer electrolyte membranes investigated via a small-angle neutron scattering technique"
Polymer J. 45 (2013) 797.

13J030 1-46 G
S. Sawada, A. Yabuuchi, M. Maekawa,
A. Kawasuso and Y. Maekawa
"Location and size of nanoscale free-volume holes in crosslinked-polytetrafluoroethylene-based graft-type polymer electrolyte membranes determined by positron annihilation lifetime spectroscopy"
Radiat. Phys. Chem. 87 (2013) 46.

13J031 1-46 G
K. Sano, A. Yamada, A. Matsui, H. Tsuji,
S. Hasegawa, S. Sawada and Y. Maekawa
"Effect of salt-containing filter paper attached to osmotic membrane"
Desalination 324 (2013) 34.

13J032 1-46 G
T. D. Tran, S. Sawada, S. Hasegawa,
Y. Katsumura and Y. Maekawa
"Poly(ethylene-co-tetrafluoroethylene) (ETFE)-based graft-type polymer electrolyte membranes with different ion exchange capacities: Relative humidity dependence for fuel cell applications"
J. Membr. Sci. 447 (2013) 19.

13J033 1-46 G
N. Nuryanthi, T. Yamaki, H. Koshikawa,
M. Asano, S. Sawada, S. Hasegawa,
Y. Maekawa and Y. Katsumura
"Ion-track Membranes of Poly(vinyliden fluoride):Etching Characteristic During Conductomeric Analysis"
Trans. Mater. Res. Soc. Jpn. 38 (2013) 105.

13J034 1-48 G
N. Tanaka, T. Yamaki, M. Asano,
T. Terai and K. Onuki
"Membrane Performance on Electro-Electrodialysis of HI-I_2-H_2O Mixture for IS Process"
Nucl. Eng. Des. 271 (2014) 51-54.

13J035 1-48 G
N. Tanaka, T. Yamaki, M. Asano,
T. Terai and K. Onuki
"Affinity of Ion-exchange Membrane for HI-I_2-H_2O Mixture"
J. Membr. Sci. 456 (2014) 31-41.

13J036 2-01 E
J.F. Madrid, Y. Ueki and N. Seko
“Abaca/polyester nonwoven fabric functionalization for metal ion adsorbent synthesis via electron beam-induced emulsion grafting”
Radiat. Phys. Chem. 90 (2013) 104-10.

13J037 2-01 E
植木 悠二
“放射線グラフト技術を用いたバイオディーゼル燃料製造用触媒の開発について”
放射線と産業 135 号 (2013) 10-14.

13J038 2-03 G
笠井 昇、岩撫 暁生、植木 悠二、佐伯 誠一、保科 宏行、瀬古 典明
“放射線グラフト重合装置を用いたセシウム吸着材の作製とフィールド試験”
JAEA-Technology. 2013-046 (2013).

13J039 2-03 E
H. Ma, H. Chi, J. Wu, M. Wang, J. Li, H. Hoshina, S. Saiki and N. Seko
“A Novel Avenue to Gold Nanostructured Microtubes Using Functionalized Fiber as the Ligand, the Reductant, and the Template”
ACS Appl. Mater. Interfaces 5 (2013) 8761-65.

13J040 2-07 G
S. Yamashita, A. Hiroki and M. Taguchi
“Radiation-induced Change of Optical Property of Hydroxypropyl Cellulose Hydrogel Containing Methacrylate Compounds: As a Basis for Development of a New Type of Radiation Dosimeter”
Radiat. Phys. Chem. 101 (2014) 53-58.

13J041 2-07 G
A. Hiroki, Y. Sato, N. Nagasawa, A. Ohta, H. Seito, H. Yamabayashi, T. Yamamoto, M. Taguchi, M. Tamada and T. Kojima
“Preparation of Polymer Gel Dosimeters Based on Less Toxic Monomers and Gellan Gum.
Phys. Med. Biol. 58 (2013) 7131-41.

13J042 2-07 G
A. Hiroki, S. Yamashita, Y. Sato, N. Nagasawa and M. Taguchi
“New Polymer Gel Dosimeters Consisting of Less Toxic Monomers with Radiation-crosslinked Gel Matrix”
J. Phys.: Conf. Series 444 (2013) 012028.

13J043 2-07 G
廣木 章博
“放射線橋かけ技術を用いたゲルの創生研究とゲル線量計への展開”
放射線と産業 135 号 (2013) 15-18.

13J044 3-01 C
K. Akamatsu and N. Shikazono
“A methodology for estimating localization of apurinic/apyrimidinic sites in DNA using fluorescence resonance energy transfer”
Anal. Biochem. 433(2) (2013) 171-80.

13J045 3-06 C
H. Matsumoto
“Nitric oxide-mediated signal transduction induced by ionizing radiation. in Cellular Response to Physical Stress and Therapeutic Applications”
Ed. T. Shimizu, T. Kondo, NOVA publishers. (2013) 15-36.

13J046 3-08 C
N. Autsavapromporn, M. Suzuki, T. Funayama, N. Usami, Y. Yokota, Y. Mutou, H. Ikeda, K. Kobayashi, Y. Kobayashi, Y. Uchihori, T. K. Hei, E. I. Azzam, T. Murakami and G. junction
"communication in the propagation of bystander effects induced by microbeam irradiation in human fibroblast cultures : The impact of radiation quality"
Radiat. Res. 180 (2013) 367-75.

13J047 3-11 C
K. Murata, SE. Noda, T. Oike, A. Takahashi, Y. Yoshida, Y. Suzuki, T. Ohno, T. Funayama, Y. Kobayashi, T. Takahashi and T. Nakano
"Increase in cell motility by carbon ion irradiation via the Rho signaling pathway and its inhibition by the ROCK inhibitor Y-27632 in lung adenocarcinoma A549 cells"
J. Radiat. Res. 55 (2014) 658-64.

13J048 3-20 G
鵜飼 光子、川村 翔栄、岸田 敬吾、亀谷 宏美
"ESR スピントラップ法による緑茶のスーパーオキシドラジカル捕捉活性計測方法"
日本調理科学会誌 46 (2013) 45-49.

13J049 3-20 G
伊藤 友美、川村 翔栄、原田 栄津子、亀谷 宏美、鵜飼 光子、大澤 俊彦
"キノコ熱水抽出物の ESR スピントラップ法によるラジカル捕捉活性評価と ORAC 法"
食品科学工学会誌 60 (2013) 173-78.

13J050 3-20 G
H. Kameya and M. Ukai
"Photochemical Method to Evaluate Oxidation Levels in Heat-Treated Vegetable Oil: Comparison with Peroxide-Value and Acid-Value"
J. Food Sci. Eng. 3 (2013) 299-308.

13J051 3-20 G
H. Kameya and M. Ukai
"Analysis of Relaxation Behavior of Free Radicals in Irradiated Cellulose Using Pulse and Continuous-Wave Electron Spin Resonance"
In Ven T. & Godbout L. (Eds.), Cellulose-Fundamental Aspects, Croatia, INTECH (2013) 285-302.

13J052 3-20 G
川村 翔栄、岸田 敬吾、菊地 正博、小林 泰彦、鵜飼 光子
"照射穀類粉に誘導されるラジカルの ESR による解析"
食品照射 48 (2013) 3-10.

13J053 3-20 G
岸田 敬吾、川村 翔栄、中村 秀夫、菊地 正博、小林 泰彦、鵜飼 光子
"長期保存中の照射食品に誘導されるラジカルの減衰挙動"
食品照射 48 (2013) 11-18.

13J054 3-20 G
H. Kameya and M. Ukai
"Fat and Oil Oxidation by Electron Spin Resonance (ESR) Spin-Trapping Method"
J. Food Sci. Eng. 3 (2013) 584-91.

13J055 3-20 G
岸田 敬吾、川村 翔栄、亀谷 宏美、中村 秀夫、菊地 正博、小林 泰彦、

鵜飼 光子
“放射線照射食品に誘導されるラジカルの Pulse-ESR と CW-ESR による緩和時間の計測”
RADIOISOTOPES 63 (2014) 131-37.

13J056 3-20 G
太多 由依、川村 翔栄、菊地 正博、
小林 泰彦、鵜飼 光子、中村 秀夫
“ESR スピントラップ法による放射線照射漢方エキス剤のラジカル捕捉活性評価”
RADIOISOTOPES 63 (2014) 119-29.

13J057 3-20 G
菅野 友美、山本 久美子、原田 栄津子、
亀谷 宏美、鵜飼光子、大澤 俊彦
“数種のきのこ粉末の ESR による分析”
日本きのこ学会誌 22 (2014) 19-23.

13J058 3-21 S
E. Sakurai, Y. Ueda, Y. Mori,
Y. Shinmyouzu and E. Sakurai
“Flavin-Containing Monooxygenase (FMO) Protein Expression and Its Activity in Rat Brain Microvascular Endothelial Cells”
Pharmacol. Pharm. 4 (2013) 1-6.

13J059 3-23 S
Y. Yamamoto, T. Yamamoto, Y. Horiguchi,
M. Shirakawa, T. Satoh, M. Koka, Y. Nagasaki,
K. Nakai and A. Matsumura
“Intra-tumor distribution of metallofullerene using micro-particle induced X-ray emission (PIXE)”
Appl. Radiat. Isot. 88 (2014) 114–117.

13J060 3-24 S
Y. Shimizu and K. Dobashi
“Proton ion-microbeam elemental analysis for inhaled particle-induced pulmonary diseases: application for diagnosis and assessment of progression”
Curr. Med. Chem. 20 (6) (2013) 789-93.

13J061 3-26 S
S. Harada, S. Ehara, K. Ishii, H. Yamazaki,
S. Matsuyama, Y. Sato, M. koka,
K. Sera and S. Goto
“Imaging and treatment of malignant metastatic tumors by using radiation-sensitive, immunolabeled liquid-core microcapsules”
Nucl. Instrum. Meth. Phys. Res. B 318 (2014) 173-77.

13J062 3-26 S
S. Harada, S. Ehara, K. Ishii, H. Yamazaki,
S. Matsuyama, Y. Sato, M. koka,
K. Sera and S. Goto
“Enhanced radiation effect on tumor growth using oxygn rich microcapsules”
Int. J. PIXE 23 (1-2) (2013) 39-45.

13J063 3-26 S
S. Harada, S. Ehara, K. Ishii, H. Yamazaki,
S. Matsuyama, Y. Sato, M. koka,
K. Sera and S. Goto
“Micronizing radiosensitive microcapsules by adding carbonated water to their core material”
Int. J. PIXE (2014), in press.

13J064 3-28 S
K. Ishii, A. Terakawa, S. Matsuyama,
A. Ishizaki, H. Arai, N. Osada, H. Sugai,
H. Takahashi, K. Sera, H. Sasaki,
K. Sasaki and T. Sawamura
“Application of PIXE analysis to investigation of plants cultivated with contaminated soil of

Fukushima”
Nucl. Instrum. Meth. Phys. Res. B 332 (2014) 46-49.

13J065 3-28 S
K. Ishii, A. Terakawa, S. Matsuyama, Y. Kikuchi, F. Fujishiro, A. Ishizaki, N. Osada, H. Arai, H. Sugai, H. Takahashi, K. Nagakubo, T. Sakurada, H. Yamazaki and S. Kim
“Reducing logistical barriers to radioactive soil remediation after the Fukushima No. 1 nuclear power plant accident”
Nucl. Instrum. Meth. Phys. Res. B 318 (2014) 70-75.

13J066 3-28 S
A. Ishizaki, K. Ishii, S. Matsuyama, F. Fujishiro, H. Arai, N. Osada, H. Sugai, S. Koshio, S. Yamauchi, K. Kusano, Y. Nozawa, M. Karahashi, S. Oshikawa, K. Kikuchi, K. Watanabe, S. Itoh, K. Kasahara, S. Toyama and Y. Suzuki
“Concentration of Cs in plants and water resulting from radioactive pollution”
Nucl. Instrum. Meth. Phys. Res. B 318 (2014) 105-08.

13J067 3-28 S
F. Fujishiro, K. Ishii, S. Matsuyama, H. Arai, A. Ishizaki, N. Osada, H. Sugai, K. Kusano, Y. Nozawa, S. Yamauchi, M. Karahashi, S. Oshikawa, K. Kikuchi, S. Koshio, K. Watanabe and Y. Suzuki
“Micro-PIXE evaluation of radioactive cesium transfer in contaminated soil samples”
Nucl. Instrum. Meth. Phys. Res. B 318 (2014) 99-101.

13J068 3-28 S
H. Sugai, K. Ishii, S. Matsuyama, A. Terakawa, Y. Kikuchi, H. Takahashi, A. Ishizaki, F. Fujishiro, H. Arai, N. Osada, M. Karahashi, Y. Nozawa, S. Yamauchi, K. Kikuchi, S. Koshio and K. Watanabe
“PIXE analyses of cesium in rice grains”
Nucl. Instrum. Meth. Phys. Res. B 318 (2014) 191-93.

13J069 3-30 C
Y. Ohshima, H. Hanaoka, H. Tominaga, Y. Kanai, K. Kaira, A. Yamaguchi, S. Nagamori, N. Oriuchi, Y. Tsushima, K. Endo and N. S. Ishioka
“Biological and evaluation of 3-[^{18}F]fluoro-α-methyl-D-tyrosine (D-[^{18}F]FAMT) as a novel amino acid tracer for positron emission tomography”
Annu. Nucl. Med. 27 (2013) 314-24.

13J070 3-30 C
K. Kaira, Y. Sunose, Y. Ohshima, N. S. Ishioka, K. Arakawa, T. Ogawa, N. Sunaga, K. Shimizu, H. Tominaga, N. Oriuchi, H. Itoh, S. Nagamori, Y. Kanai, A. Yamaguchi, A. Segawa, M. Ide, M. Mori, T. Oyama and I. Takeyoshi
“Clinical significance of L-type amino acid transporter 1 expression as a prognostic marker and potential of new targeting therapy in biliary tract cancer”
BMC Cancer 13 (2013) 482.

13J071 3-30 C
Y. Sugo, I. Sasaki, S. Watanabe, Y. Ohshima and N. S. Ishioka
“Synthesis and *in vitro* evaluation of ^{64}Cu-labeled peptide for tumor imaging”

Pept. Sci. 2013 (2014) 355-58.

13J072 3-31 C

N. Sato, K. Tsukada, S. Watanabe, N. S. Ishioka, M. Kawabata, H. Saeki, Y. Nagai, T. Kin, F. Minato, N. Iwamoto and O. Iwamoto

"First Measurement of the Radionuclide Purity of the Therapeutic Isotope ^{67}Cu Produced by ^{68}Zn(n,x) Reaction Using ^{nat}C(d,n) Neutrons"

J. Phys. Soc. Jpn. 83 (2014) 073201.

13J073 3-32 C

E. R. Balkin, D. K. Hamlin, K. Gagnon, M.-K. Chyan, S. Pal, S. Watanabe and D. S. Wilbur

"Evaluation of a Wet Chemistry Method for Isolation of Cyclotron Produced [^{211}At] Astatine"

Appl. Sci. 3 (2013) 636-55.

13J074 3-34 C

S. Yamamoto, H. Watabe, N. Kawachi, S. Fujimaki, K. Kato and J. Hatazawa

"Three-layer GSO depth-of-interaction detector for high-energy gamma camera"

Nucl. Instrum. Meth. Phys. Res. A 743 (2014) 124-29.

13J075 3-34 C

N. Kawachi

"Recent Developments in Plant Science Involving Use of Gamma-ray Imaging Technology"

J. Vac. Soc. Jpn. 57 (2014) 37-44

13J076 3-35 C

T. Yoshihara, N. Suzui, S. Ishii, M. Kitazaki, H. Yamazaki, K. Kitazaki, N. Kawachi, Y.-G. Yin, S. Ito-Tanabata, S.-N. Hashida, K. Shoji, H. Shimada, F. Goto and S. Fujimaki.

"A kinetic analysis of cadmium accumulation in a Cd Hyper-accumulator Fern, Athyrium Yokoscense and tobacco plants"

Plant Cell Environ. 37 (2014) 1086-96.

13J077 3-39, 3-40 C

上野 敬一郎、永吉 実考、今給黎 征朗、郡山 啓作、南 公宗、田中 淳、長谷 純宏、松本 敏一

"イオンビームの再照射によって秋輪ギク'神馬'の複数形質を改良した新品種'新神2'の育成"

園芸学研究 12 (2013) 245-54.

13J078 3-47 C

鳴海 一成、佐藤 勝也

"放射線抵抗性細菌を用いた基礎研究とその応用への展開"

工業技術 36 (2014) 78-83.

13J079 3-51 C, G

S. Shinohara, Y. Fitriana, K. Satoh, I. Narumi and T. Saito

"Enhanced fungicide resistance in Isaria fumosorosea following ionizing radiation-induced mutagenesis"

FEMS Microbiol. Lett. 349 (2013) 54-60.

13J080 4-01 S

S. Kato, T. Yamaki, S. Yamamoto, T. Hakoda, K. Kawaguchi, T. Kobayashi, A. Suzuki and T. Terai

"Preparation of Tungsten Carbide Nanoparticles by Ion Implantation and Electrochemical Etching,"

Nucl. Instrum. Meth. Phys. Res. B 314 (2013) 149-52.

13J081 4-03 C
S. Tsukuda, M. Sugimoto, A. Idesaki, A. Asano, S. Seki and S. Tanaka
"Poly(vinylphenol) nanowires including Au nanoparticles formed by single particle nano fabrication technique"
Radiat. Phys. Chem. 84 (2013) 39-41.

13J082 4-05 C
M. Nomura, D. Tamashiro, S. Sakai, R. Ono, A. Bukhari, M. Sugimoto, M. Yoshikawa and Y. Sasaki
"Improvement of MOR zeolite membranes by using ion beam irradiation"
Trans. Mater. Res. Soc. Jpn. 38 (3) (2013) 481-84.

13J083 4-07 E
T. Taguchi, A. K. M. Fazle Kibria and S. Shamoto
"Morphology change of multi-walled carbon nanotubes with SiC coating by electron irradiation"
J. Phys.: Conf. Series 417 (2013) 012037.

13J084 4-07 O
T. Taguchi, T. Miyazaki, S. Iikubo and K. Yamaguchi
"Deposition of hydroxyapatite on SiC nanotubes in simulated body fluid"
Mater. Sci. Eng. C 34 (2014) 29-34.

13J085 4-09 S
K. Miura, H. Kiryu, Y. Ozawa, A. Kubota, Y. Hiratani, O. Hanaizumi, T. Satoh, Y. Ishii, M. Kohka, K. Takano, T. Ohkubo, A. Yamazaki, W. Kada, A. Yokoyama and T. Kamiya
"Demonstration of Thermo-Optic Switch Consisting of Mach-Zehnder Polymer Waveguide Drawn Using Focused Proton Beam"
Key Eng. Mater. 596 (2014) 134-38.

13J086 4-10 I
H. Abe, S. Orimo, M. Kishimoto, S. Aone, H. Uchida, H. Daido and T. Ohshima
"Effects of an Ultra-Intence Laser Driven Proton Beam on the Hydriding Property of a Hydorgen Storage Alloy"
Nucl. Instrum. Meth. Phys. Res. B. 307 (2013) 218-20.

13J087 4-10 I
H. Abe, S. Aone, R. Morimoto, H. Uchida and T. Ohshima
"Synergic Effects of Ion Irradiations (La, Ce) and Alkaline Pretreatment (KOH) on Hydriding Kinetic Property of a Mm-Ni Based Alloy"
J. Alloy. Comp. 580 (2013) S219-21.

13J088 4-11, 4-42 S
H. Nishikawa and T. Hozumi
"Application of proton beam writing for the direct etching of polytetrafluoroethylene for polydimethylsiloxane replica molding"
J. Vac. Sci. Tech.
B 31 (2013) 06F403.

13J089 4-13 I
Y. Kasukabe, H. Shimoda, Yu. Chen, S. Yamamoto, M. Yoshikawa and Y. Fujino
"Characterization of Epitaxial Transformation Phenomena Induced by the Interaction of Implanted N-Ions with Ti Thin Films"
Nucl. Instrum. Meth. Phys. Res. B 315 (2013) 131-35.

13J090 4-13 I

Yu. Chen, X. Feng, Y. Kasukabe, S. Yamamoto, M. Yoshikawa and Y. Fujino
"Epitaxial Transformation of hcp-fcc Ti sublattices during Nitriding Processes of Evaporated-Ti Thin Films due to Nitrogen-Implantation"
J. Alloy. Comp. 577S (2013) S18-24.

13J091 4-14 S

Y. Noguchi, T. Hirata, Y. Kawakubo, K. Narumi, S. Sakai and Y. Maeda
"RBS study of disordering of $Fe_{3-x}Mn_xSi$/Ge(111) heteroepitaxial interfaces"
Phys. Status Solidi C 10 (2013) 1732-34.

13J092 4-14 S

Y. Kawakubo, Y. Noguchi, T. Hirata, K. Narumi, S. Sakai, S. Yamada, K. Hamaya, M. Miyao and Y. Maeda
"Ion beam analysis of quaternary Heusler alloy $Co_2(Mn_{1-x}Fe_x)Si$(111) epitaxially grown on Ge(111)"
Phys. Status Solidi C 10 (2013) 1828-31.

13J093 4-15, 4-16 T

D. Ueyama, Y. Saitoh, F. Hori, Y. Kaneno, K. Nishida, K. Dohi, N. Soneda, S. Semboshi and A. Iwase
"Effects of energetic heavy ion irradiation on hardness of Al‐Mg‐Si alloys"
Nucl. Instrum. Meth. Phys. Res. B 314 (2013) 107-11.

13J094 4-15 T

A. Hashimoto, Y. Kaneno, T. Matsui, Y. Saitoh and A. Iwase
"Non-thermal equilibrium crystal structure and Vickers hardness of FeRh intermetallic compound irradiated with energetic heavy ions"
Trans. Mater. Res. Soc. Jpn. 38 (2013) 329-31.

13J095 4-16 T

D. Ueyama, S. Semboshi, Y. Saitoh, N. ishikawa, K. Nishida, N. Soneda, F. Hori and A. Iwase
"Hardening induced by energetic electron beam for Cu-Ti alloys"
Jpn. J. Appl. Phys. 05FC04 (2014).

13J096 4-25 C, T

S. Nakagawa, M. Taguchi and A. Kimura
"Solvent Effect on Copolymerization of Maleimide with Styrene Induced by Irradiation of Ion and Electron Beams"
Radiat. Phys. Chem. 91 (2013) 143-47.

13J097 4-25 C, T

S. Nakagawa, M. Taguchi, A. Kimura, N. Nagasawa and A. Hiroki
"LET and Dose Rate Effect on Radiation-induced Copolymerization in Physical Gel"
Nucl. Instrum. Meth. Phys. Res. B 334(2014) 64-68.

13J098 4-28 S

T. Sakai, R. Yasuda, H. Iikura, T. Nojima, M. Kohka ,T. Satoh, Y. Ishii and A. Oshima
"Fabrication of fine imaging devices using an external proton microbeam"
Nucl. Instrum. Meth. Phys. Res. B 332 (2014) 238-41.

13J099 4-30 S

W. Kada, T. Satoh, A. Yokoyama, M. Koka and T. Kamiya

"Determining Aerosol Particles by In-air Micro-IL Analysis Combined with Micro-PIXE"
Nucl. Instrum. Meth. Phys. Res. B 306 (2013) 299-301.

13J100 4-30 S
W. Kada, T. Satoh, A. Yokoyama,
M. Koka and T. Kamiya,
"Development of a New Scanning Ion Microbeam Analysis and Imaging Technique: Ion-Luminescence Microscopic Spectroscopy (ILUMIS)"
Trans. Mater. Res. Soc. Jpn. 38 (2013) 443-46.

13J101 4-30 S
W. Kada, T. Satoh, A. Yokoyama,
M. Koka and T. Kamiya
"Development of microscopic optics for high-resolution IL spectroscopy with proton microbeam probe"
Nucl. Instrum. Meth. Phys. Res. B. 318 (2013) 42-46.

13J102 4-35,4-40 C
A. Yokoyama, W. Kada, T. Satoh, M. Koka,
S. Yamamoto, T. Kamiya and W. Yokota
"Development of real-time position detection system for single-ion hit"
Nucl. Instrum. Meth. Phys. Res. B 332 (2014) 334-36.

13J103 4-35 C
T. Satoh, M. Koka, W. Kada,
A. Yokoyama and T. Kamiya
"Real-time single-ion hit position detecting system for cell irradiation"
Nucl. Instrum. Meth. Phys. Res. B 332 (2014) 242–244.

13J104 4-36 C, G
Y. Yuri, T. Ishizaka, T. Yuyama,
I. Ishibori and S. Okumura
"Study on ion irradiation response of Gafchromic films for the intensity distribution measurement of a large-area beam"
Nucl. Instrum. Meth. Phys. Res. A 727 (2013) 40-45.

13J105 4-38 C
S. Kurashima, H. Kashiwagi, N. Miyawaki,
K. Yoshida and S. Okumura
"Influence of injection beam emittance on beam transmission efficiencyin a cyclotron"
Rev. Sci. Instrum. 85 (2014) 02A725.

13J106 4-38 C
H. Kashiwagi, N. Miyawaki,
S. Kurashima and S. Okumura
"A transverse emittance and acceptance measurement system in a low-energy beam transport line"
Rev. Sci. Instrum. 85 (2014) 02A735.

13J107 4-42 O
Y. Ishii, T. Ohkubo, T. Kojima and K. Kamiya
"Construction of a 300-keV Compact Ion Microbeam System with a Three-Stage Acceleration Lens"
Nucl. Instrum. Meth. Phys. Res. B 332 (2014) 156–159.

13J108 4-43 T
H. Ogawa, K. Sorai, S. Amano,
K. Ishii and T. Kaneko
"Forward-backward correlated secondaryy electron emission dependning on the angle of emergence of protons transmitted through a thin

carbon foil"
J. Phys. B : Atom. Mol. Opt. Phys. 47 (2014) 085201.

13J109 4-44 T, I
K. Hirata, Y. Saitoh, A. Chiba,
K. Yamada and K. Narumi
"Time-of-flight secondary ion mass spectrometry with energetic cluster ion impact ionization for highly sensitive chemical structure characterization"
Nucl. Instrum. Meth. Phys. Res. B 314 (2013) 39-42.

13J110 4-44 T, I
K. Hirata, Y. Saitoh, A. Chiba, K. Yamada,
S. Matoba and K. Narumi
"Time-of-flight secondary ion mass spectrometry with transmission of energetic primary cluster ions through foil targets"
Rev. Sci. Instrum. 85 (2014) 033107.

13J111 4-47
T. Koide, Y. Saitoh, M. Sakamaki, K. Amemiya,
A. Iwase and T. Matsui
"Change in magnetic and structural properties of FeRh thin films by gold cluster ion beam irradiation with the energy of 1.67MeV/atom"
J. Appl. Phys. 115 (2014) 17B722.

13J112 4-47 T
K. Aikoh, A. Tohki, S. Okuda, Y. Saitoh,
T. Kamiya, T. Nakamura, T. Kinoshita,
A. Iwase and T. Matsui
"Study on ferromagnetic ordering of FeRh thin films induced by energetic heavy ion irradiation by means of X-ray Magnetic Circular Dichroism"
Nucl. Instrum. Meth. Phys. Res. B 314 (2013) 99-102.

13J113 4-48 T
Y. Morita, K. Nakajima, M. Suzuki, K. Narumi,
Y. Saitoh, N. Ishikawa, K. Hojou, M. Tsujimoto,
S. Isoda and K. Kimura
"Surface effect on ion track formation in amorphous Si_3N_4 films"
Nucl. Instrum. Meth. Phys. Res. B 315 (2013) 142-45.

13J114 4-48 T
K. Nakajima, K. Nagano, M. Suzuki, K. Narumi,
Y. Saitoh, K. Hirata and K. Kimura
"Transmission secondary ion mass spectrometry using 5 MeV C60+ ions"
Appl. Phys. Lett. 104 (2014) 114103 1-4.

13J115 4-48 T
K. Nakajima, Y. Morita, T. Kitayama,
M. Suzuki, K. Narumi, Y. Saitoh, M. Tsujimoto,
S. Isoda, Y. Fujii and K. Kimura
"Sputtering of SiN films by 540 keV C_{60}^{2+} ions observed using high-resolution Rutherford backscattering spectroscopy"
Nucl. Instrum. Meth. Phys. Res. B 332 (2014) 117-21.

A 1.2 Publication in Proceedings

13C001 1-01 E
M. González, R. Hoheisel, M. P. Lumb,
D. A. Scheiman, C. G. Bailey, J. Lorentzen,
S. Maximenko, S. R. Messenger, P. P. Jenkins,
T. N. D. Tibbits, M. Imaizumi, T. Ohshima,
S. Sato and R. J. Walters
"Radiation Study in Quantum Well III-V Multi-Junction Solar Cells"
Proc. 39th IEEE Photovoltaic Specialists Conf. [Tampa, USA] (2013) 3233-36.

13C002 1-01 C, T, I, E
M. Sugai, J. Harada, M. Imaizumi,
S.-i. Sato and T. Ohshima
"A study on the artifact external quantum efficiency of Ge bottom subcells in triple-junction solar cells"
Proc. 39th IEEE Photovoltaic Specialists Conf. [Tampa, USA] (2013) 0715-20.

13C003 1-01 C, T, I, E
M. Imaizumi, T. Nakamura, M. Tajima,
S.-i. Sato and T. Ohshima
"Comparative study on degradation characteristics of component subcells in IMM triple-junction solar cells irradiated with high-energy electrons and protons"
Proc. 39th IEEE Photovoltaic Specialists Conf. [Tampa, USA] (2013) 3243-48.

13C004 1-01 C, T, I, E
T. Nakamura, M. Imaizumi,
S.-i. Sato and T. Ohshima
"Estimation of subcell photocurrent in IMM3J using LED bias light"
Proc. 39th IEEE Photovoltaic Specialists Conf. [Tampa, USA] (2013) 0696-700.

13C005 1-01 C, T, I, E
M. Imaizumi and T. Ohshima
"Radiation Effects in Solar Cells"
Proc. SPIE 8725 (2013) 872515-1-8.

13C006 1-02 C, T, S, I
T. Ohshima, S.-i. Sato, T. Nakamura,
M. Imaizumi, T. Sugaya, K. Matsubara,
S. Niki, A. Takeda and Y. Okano
"Electrical Performance Degradation of GaAs Solar Cells with InGaAs Quantum Dot layers due to Proton Irradiation"
Proc. 39th IEEE Photovoltaic Specialists Conf. [Tampa, USA] (2013) 2779-83.

13C007 1-07 C
A. Abderrahmane, H. Takahashi, T. Tashiro,
P. J. Ko, H. Okada, S. Sato,
T. Ohshima and A. Sandhu
"Effect of annealing on proton irradiated AlGaN/GaN based micro-Hall sensors"
AIP Conf. Proc. 1585 (2014) 123.

13C008 1-16 G
T. Tsukada and J. Nakano
"Effects of seawater injection and radiation on corrosion of PCV/RPV steels for Fukushima Daiichi NPP"
Proc. Water Chemistry and Corrosion in Nuclear Power Plants in Asia (2013) 1-4.

13C009 1-18 G
K. Hata et al.,
"Radiolysis calculation and gamma-ray

irradiation experiment of aqueous solutions containing seawater components”
Proc. Water Chemistry and Corrosion in Nuclear Power Plants in Asia”
[Taichung, Taiwan] (2013/10).

13C010 1-24 G
T.-M.-D. Do, Y. Matsumoto, R. Nagaishi, H. Suematsu and T. Ogawa
“Research and education on nuclear system safety in nagaoka university of technology including post‐accident management research”
10 th Int. Conf. Nucl. Sci. Tech. (VINANST10) [Vietnam] (2013).

13C011 1-24 G
T. Ito, S.-Y. Kim, Y. Xu, K. Hitomi, K. Ishii, R. Nagaishi and T. Kimura
“Study on Separation of Platinum Group Metals from High Level Liquid Waste Using Macroporous (MOTDGA-TOA)/SiO_2-P Silica-based Absorbent”
Int. Nucl. Fuel Cycle Conf. (GLOBAL 2013) [Salt Lake City, USA] (2013).

13C012 1-29 G
T. Takeuchi, S. Ueno, H. Komanome, N. Ohtsuka, H. Shibata, N. Kimura, Y. Matsui, K. Tsuchiya and M. Araki
“Research and Development of High-Performance Instruments for Safety Measure of LWRs”
Proc. 6th Int. Symp. Mater. Testing Reactors [Bariloche, Argentina] (2013).

13C013 1-30 G
上川 将章、泉 敬介、武本 純平、川崎 正治、岡 潔、山縣 諒平
“核融合環境における電気設備（その 53） 耐放射線性 LED 照明の開発“
2014 年（第 32 回）電気設備学会全国大会 講演論文集 (2014).

13C014 2-01 E
植木 悠二、佐伯 誠一、笠井 昇、保科 宏行、柴田 卓弥、瀬古 典明
“放射線グラフト重合技術を利用したバイオディーゼル燃料用繊維状固体触媒の作製とその性能評価”
第 29 回日本イオン交換研究発表会要旨集 (2013) O104.

13C015 2-01 E
植木 悠二
“量子ビームを用いた繊維状高分子捕集材の開発”
高分子学会関東支部 第25回埼玉地区懇話会講演要旨集 (2013) O104.

13C016 2-04 E
柴田 卓弥、瀬古 典明、岩撫 暁生、鈴井 伸郎、藤巻 秀、笠井 昇、佐伯 誠一、保科 宏行、植木 悠二
“放射線グラフト重合技術を活用したセシウム捕集材の開発”
第 29 回日本イオン交換研究発表会 (2013/10).

13C017 3-07 C
M. Tomita, H. Matsumoto, T. Funayama, Y. Yokota, K. Otsuka, M. Maeda and Y. Kobayashi
“Mechanisms of activation of signal transductions by bystander responses induced after heavy-ion microbeam irradiation.”
The 59th Annual Meeting of the Radiation Research Society.
[New Orleans, USA] (2013) 135.

13C018 3-12 C
高橋 昭久、久保 誠、馬 洪玉、中川 彰子、
吉田 由香里、磯野 真由、古澤 佳也、
小林 泰彦、舟山 知夫、金井 達明、
大野 達也、中野 隆史
“殺細胞効果におよぼす DNA 二本鎖切断修復の LET 依存性”
第 51 回日本放射線腫瘍学会生物部会学術大会 [仙台] (2013/07).

13C019 3-12 C
A. Takahashi, M. Kubo, H. Ma, A. Nakagawa,
Y. Yoshida, T. Kanai, T. Ohno, T. Funayama,
Y. Kobayashi, Y. Furusawa and T. Nakano
“LET-dependent biological effect of DNA double-strand break repair on radiosensitivity”
52nd Annu. Meet. Part. Ther. Co-operative Group (PTCOG52)
[Essen, Germany] (2013/06).

13C020 3-12 C
A. Takahashi, M. Kubo, H. Ma, A. Nakagawa,
Y. Yoshida, T. Funayama, Y. Kobayashi,
Y. Furusawa and T. Nakano
“LET-dependent biological effect of DNA DSB repair on cell killing”
Heavy Ion Ther. Space Radiat. Symp. 2013 (HITSRS2013) [千葉] (2013/05).

13C021 3-12 C
A. Takahashi
“Recent advances in the biology of carbon-ion cancer therapy”
KHIMA Seminar on Heavy-ion Radiotherapy [Seoul, Korea] (2012/08).

13C022 3-12 C
久保 誠、高橋 昭久、馬 洪玉、中川 彰子、
吉田 由香里、磯野 真由、古澤 佳也、
小林 泰彦、舟山 知夫、金井 達明、
大野 達也、中野 隆史
“LET 依存的な標的増感候補としての NHEJ 修復および HR 修復”
第 19 回癌治療増感研究会 [東京] (2013/06).

13C023 3-12, 3-10 C
高橋 昭久、吉田 由香里、古澤 佳也、
大野 達也、中野 隆史
“放射線感受性におよぼす DNA 二本鎖切断修復の LET 依存的な効果”
第 72 回日本癌学会学術総会 [横浜] (2013/10).

13C024 3-12 C
久保 誠、高橋 昭久、馬 洪玉、中川 彰子、
吉田 由香里、磯野 真由、古澤 佳也、
小林 泰彦、舟山 知夫、金井 達明、
大野 達也、中野 隆史
“放射線増感剤の標的候補としての DNA 二本鎖切断修復による LET 依存的感受性”
第 4 回国際放射線神経生物学会大会 [高崎] (2014/01).

13C025 3-12 C
久保 誠、高橋 昭久、馬 洪玉、中川 彰子、
吉田 由香里、磯野 真由、金井 達明、
大野 達也、中野 隆史
“炭素線治療における放射線増感剤の標的候補としての HR および NHEJ”
第 16 回癌治療増感研究シンポジウム [奈良] (2014/02).

13C026 3-25 S
富岡 智、長嶺 竹明、佐藤 博隆、江夏 昌志、
神谷 冨裕
“マイクロPIXEによる赤血球元素分析の臨床応用”
第 29 回 PIXE シンポジウム抄録集 (2013) 33.

13C027 3-32 C
S. Watanabe, K. Hashimoto and N.S. Ishioka
“Lutetium-177 complexation of DOTA and DTPA in the presence of competing metals”
Proc. APSORC2013 [Kanazawa, Japan].

13C028 3-37 C, G
A. Tanaka
“Development of ion beam breeding”
Int. Symp. New Trend Tech. Mutat. Breeding [Jeongeup, Korea] (2014).

13C029 3-41 C
松尾 洋一、石地 耕太郎、竹下 大樹、
納富 麻子、長谷 純宏、野澤 樹
“カンキツ類における量子ビーム照射による突然変異育種法の検討”
第 7 回九州シンクロトロン光研究センター研究成果報告会 予稿集 [鳥栖、日本] (2013).

13C030 3-41 C
松尾 洋一、長谷 純宏、野澤 樹、竹下 大樹、
納富 麻子
“ウンシュウミカンにおける量子ビーム感受性の品種間差異及び‘今村温州’わい化変異体の作出”
園芸学研究 第 13 巻 別冊 1 (2014) 248,
園芸学会平成 26 年度春季大会[つくば、日本].

13C031 3-45 C, G
寺西 美佳、山口 弘子、坂本 綾子、
土岐 精一、日出間 純
“植物における放射線誘発 DNA 損傷の定量解析”
日本宇宙生物科学会第 27 回大会予稿集
(2013) 39.

13C032 3-49 C
Y. Matsuo, Y. Izumi, N. Sato,
T. Yamamoto and K. Shimizu
“Dosimetric application of biological technique evaluating DNA lesions caused by radiation exposure”
9th Int. Workshop Ionizing Radiat. Monit. [Oarai, Japan] (2013).

13C033 3-50 C
武田 喜代子、佐藤 勝也、鳴海 一成、
大津 直子、横山 正
“イオンビーム照射誘導性ダイズ根粒菌高温耐性変異株の DNA 変異部位の特定”
日本土壌微生物学会 2013 年度大会講演要旨集 (2013) 55.

13C034 3-50 C
武田 喜代子、佐藤 勝也、鳴海 一成、
大津 直子、横山 正
“イオンビーム突然変異育種法により作出したダイズ根粒菌高温耐性変異株のゲノム解析”
植物微生物研究会第 23 回研究交流会講演要旨集 (2013) 47-48.

13C035 3-50 C
K. Takeda, K. Satoh, I. Narumi,
O. Ohtsu and T. Yokoyama
“Genome analysis of a high temperature tolerant mutant of Bradyrhizobium japonicum USDA110 generated by ion-beam irradiation”
18th Int. Cong. Nitrogen Fixation (2013) 181.

13C036 3-53 C
佐藤 勝也、上田 涼史郎、増渕 隆、上山 修、
林 秀謙、池永 裕、鳴海 一成、田中 淳
“イオンビーム育種により作出したカプロン酸エチル高生産清酒酵母の変異解析”
第 9 回イオンビーム育種研究会大会要旨集
(2013) 23-24.

13C037 3-53 C
佐藤 勝也、上田 涼史郎、増渕 隆、上山 修、林 秀謙、池永 裕、鳴海 一成
“イオンビーム育種技術による香りの良い日本酒”
第 3 回 CSJ 化学フェスタ 2013 講演予稿集
(2013) 13.

13C038 4-05 C
M. Nomura, D. Tamashiro, A. Bukhari, R. Ono, M. Kitajima, E. Matsuyama, M. Sugimoto, M. Yoshikawa and Y. Sasaki
“Effects of high energy ion beam irradiation on permeation properties through MOR membranes”
Proc. 6th Int. Zeolite Membr. Meet. (IZMM-6) PP07 [Jeju Island, Korea] (2013).

13C039 4-05 C
D. Tamashiro, R. Ono, A. Bukhari, M. Kitajima, M. Sugimoto, M. Yoshikawa, Y. Sasaki, E. Matsuyama and M. Nomura
“MOR zeolite membranes for efficient biomass energy conversion”
Proc. Int. Symp. Innovat. Mater. Process. Energ. Syst. 2013 (IMPRES2013) [Fukuoka, Japan] (2013) IIIC-P8.

13C040 4-05 C
M. Kitajima, D. Tamashiro, E. Matsuyama, M. Sugimoto, M. Yoshikawa, Y. Sasaki and M. Nomura
“Permeation improvements of SOD membranes by using ion beams”
Proc. 23rd Annu. Meet. Mater. Res. Soc. Jpn. Symp. Q-P10-001 [Yokohama, Japan] (2013)

13C041 4-05
M. Nomura, M. Kitajima, I. Uduki, E. Matsuyama, M. Sugimoto, M. Yoshikawa and Y. Sasaki
“High energy ion beam irradiation on MOR zeolite membranes”
Proc. 13th Int. Conf. Inorg. Membr. ICIM2014_0090 [Brisbane, Australia] (2014).

13C042 4-09 S
K. Miura, T. Satoh, Y. Ishii, M. Koka, K. Takano, T. Ohkubo, A. Yamazaki, W. Kada, A. Yokoyama, T. Kamiya, H. Kiryu, Y. Ozawa, A. Kubota and O. Hanaizumi
“Prototype of Thermo-Optic Switch Consisting of Mach-Zehnder Polymer Waveguide Drawn by Focused Proton Beam”
Conf. Lasers and Electro-Optics Eur. & Int. Quant. Electron. Conf. [Munich, Germany)] (2013) CK-P.29 MON.

13C043 4-09 I
K. Miura, T. Suzuki, T. Osawa and O. Hanaizumi
“Visible Photoluminescence Properties of Eu-doped Ta_2O_5 Sputtered Thin Films”
Optics & Photonics Taiwan, Int. Conf. [Zhongli (Taiwan)] (2013) 2013-FRI-S1002-O006.

13C044 4-09 S
A. Kubota, R. Saruya, K. Noguchi, W. Kada, K. Miura, O. Hanaizumi, T. Satoh, Y. Ishii, M. Koka, T. Ohkubo, A. Yokoyama and T. Kamiya
“Fabrication of Mach-Zehnder Type Optical Waveguides in Flexible Acrylic Sheets Using Proton Beam Writing”
5th Int. Conf. Adv. Micro-Device Eng. [Kiryu, Japan] (2013) 59.

13C045 4-09 I
A. Kawashima, K. Kano, K. Noguchi, W. Kada, K. Miura, S. Yamamoto, M. Yoshikawa and O. Hanaizumi
“Visible-Light Emission Properties of Carbon-Doped Silica Glasses after Silicon-Ion Implantation”
5th Int. Conf. Adv. Micro-Device Eng. [Kiryu, Japan] (2013) 62.

13C046 4-09 S
猿谷 良太、加藤 聖、久保田 篤志、三浦 健太、加田 渉、佐藤 隆博、江夏 昌志、石井 保行、神谷 富裕、西川 宏之、花泉 修
“PBW 微細加工による PDMS を基材としたフレキシブル光導波路の開発”
第 61 回応用物理学会春季学術講演会 (2014/03) 19a-PA1-28.

13C047 4-11 S
H. Nishikawa and T. Hozumi
“Application of Proton Beam Writing to a Direct Etching of PTFE for PDMS Replica Molding”
57th Int. Conf. Electron, Ion, and Photon Beam Tech. & Nanofabrication (2013/05) P01-02.

13C048 4-11 S
Y. Koike, H. Hagiwara, T. Ogura, D. Aoki, Y. Anzai, K. Seki and H. Nishikawa
“Micro fabrication of Poly L Lacid using PBW and Piezoelectric application”
39th Int. Conf. Micro & Nano Eng. (2013/09) P-Fab-58.

13C049 4-11 S
H. Nishikawa, Y. Takeno, H. Hayashi and Y. Maekawa
“Micro‐fabrication of polyimide films by proton beam writing”
39th Int. Conf. Micro & Nano Eng. (2013/09) P-Fab-59.

13C050 4-11 S
G. Ayugase, H. Nishikawa, T. Sato, Y. Ishii, T. Kamiya, H. Tokita and S. Uchida
“Effects of the Height of Pillar Arrays Fabricated by Proton Beam writing on the Trapping Capability of Bacteria by 3-D Dielectrophoresis”
27th Int. Microprocesses &Nanotechnology Conf. (MNC2013) (2013/11) 7P-7-112.

13C051 4-11 S
加藤 聖、林 秀臣、西川 宏之
“集束陽子線による PET フィルム上のマイクロレンズアレイ作製”
日本機械学会マイクロ・ナノ工学部門主催第 5 回マイクロ・ナノ工学シンポジウム (2013/11) 7PM1-D-3.

13C052 4-11 S
山口 正樹、渡辺 和貴、西川 宏之
“強誘電体厚膜形成におけるクラック抑制”
第 74 回応用物理学会秋季学術講演会 (2013/09) 18a-P1-2.

13C053 4-11 S
高橋 潤一、加藤 聖、林 秀臣、西川 宏之
“集束プロトンビーム描画を利用した微細構造形成と転写プロセスの開発”
2013 年放電学会年次大会 (2013/11) P-11.

13C054 4-11 S
渡辺 和貴、山口 正樹、西川 宏之
“プロトンビームによる誘電体厚膜への直接パターニング”
第 61 回応用物理学会春季学術講演会

(2014/03) 17p-PG1-8.

13C055 4-11 S
時田 寛也、内田 諭、鮎瀬 銀也、西川 宏之
“ピラー構造誘電泳動デバイスの菌捕集分布における流量及びピラー高さの影響”
第 61 回応用物理学会春季学術講演会
(2014/03) 19p-E15-8.

13C056 4-25 C, T
S. Nakagawa, M. Taguchi, A. Kimura,
N. Nagasawa and A. Hiroki
“LET effect on radiation induced polymerization in gel”
Proc. 94th Spring Meet. Chem. Soc. Jpn.
[Nagoya, Japan] (2014/03).

13C057 4-26 C
A. Masuda, T. Matsumoto, H. Harano,
Y. Tanimura, Y. Shikaze, S. Kurashima,
M. Hagiwara, Y. Unnno, J. Nishiyama,
M. Yoshizawa and H. Seito
“Time-of-flight measurement of low-energy components of quasi-monoenergetic high-energy neutron field”
2013 IEEE Nucl. Sci. Symp. Conf. Rec.
[Seoul, Korea] (2013).

13C058 4-32 S
W. Kada, Y. Kanbayashi, K. Miura, R. Saruya,
A. Kubota,T. Satoh, M. Koka, T. Ohkubo,
Y. Ishii, T. Kamiya and O. Hanaizumi
“Fabrication of microstructures embedded in SC-CVD diamond by focused ion microbeam”
5th Int. Conf. Adv. Micro-Device Eng.
[Kiryu, Japan] (2013) 60.

13C059 4-35 C
倉島 俊、宮脇 信正、奥村 進
“サイクロトロンにおけるパルスビーム形成技術の開発”
2013 年秋季第 74 回応用物理学会学術講演会
講演予稿集 (2013) 42.

13C060 4-35 C
N. Miyawaki, S. Kurashima, H. Kashiwagi,
S. Okumura and M. Fukuda
“Analysis of phase bunching in the central region of the JAEA AVF cyclotron”
Proc. 20th Int. Conf. Cyclo. Their Appl.
(2013) 350-52.

13C061 4-35 C
N. Miyawaki, M. Fukuda, S. Kurashima,
H. Kashiwagi, S. Okumura,
K. Arakawa and T. Kamiya
“Analysis of phase bunching in a central region of a cyclotron”
10th Annu. Meet. Part. Accel. Soc. Jpn. (2014),
500-02.

13C062 4-36 C
Y. Yuri, T. Ishizaka, T. Yuyama, K. Yoshida,
I. Ishibori and S. Okumura
“Formation of large-area heavy-ion uniform beams using multipole magnets in TIARA, JAEA”
10th Annu. Meet. Part. Accel. Soc. Jpn. (2014)
138-42 [in Japanese].

13C063 4-36, 4-37 C
Y. Yuri, T. Ishizaka, T. Yuyama,
I. Ishibori and S. Okumura
“Ion-Irradiation Response of Gafchromic Films and their Application to the Measurement of the

Transverse Beam Intensity Distribution”
Proc. North Am. Part. Accel. Conf.
NA-PAC’13 [Pasadena, USA] (2013/09-10)
1388-90.

13C064 5-03 T, S, I
宇野 定則、千葉 敦也、山田 圭介、
横山 彰人、薄井 絢、北野 敏彦、高山 輝充、
織茂 貴雄、金井 信二、青木 勇希、
山田 尚人、石井 保行、鳴海 一雅、
佐藤 隆博、大久保 猛、奈良 孝幸
“TIARA 静電加速器の現状”
第 26 回「タンデム加速器及びその周辺技術の
研究会」報告集 [山形] (2013/07) 79-81.

Appendix 2

List of Related Patents

13PAT001 1-03
久保山 智司 、新藤 浩之 、飯出 芳弥 、
槙原 亜紀子（JAXA）
「シングルイベント耐性のラッチ回路」
特許番号：特許第 5339282 号
登録日：2013 年 8 月 16 日

13PAT002 1-24
永石 隆二、吉田 善行、山田 禮司、青柳 登（原子力機構・原子力基礎工）
「貴金属の回収方法と機能材料の製造方法、並びに機能材料を用いた強酸化性金属イオン含有水溶液の処理方法」
登録番号：特許第 5424297 号
登録日：2013 年 12 月 6 日

13PAT003 1-42
吉村 公男、越川 博、八巻 徹也、前川 康成（原子力機構・量子ビーム）、
猪谷 秀幸、田中 裕久、山口 進、山本 和矢（㈱ダイハツ工業）
「アニオン伝導電解質膜及びその製造方法」
出願番号：特願 2013-269281 号
出願日：2013 年 12 月 26 日

13PAT004 1-42
吉村 公男、越川 博、八巻 徹也、浅野 雅春、前川 康成（原子力機構・量子ビーム）、
猪谷 秀幸、田中 裕久、山口 進、山本 和矢（㈱ダイハツ工業）
「ANION CONDUCTING ELECTROLYTE MEMBRANE AND MANUFACTURING METHOD THEREOF」
出願番号：US 2013/0280626 A1
出願日：2013 年 10 月 24 日

13PAT005 2-03
鈴木 太郎、瀬古 典明、玉田 正男、
佐伯 誠一、稲富 直彦（原子力機構・量子ビーム）
「金属捕集材」
出願番号：特願 2013-065992 号
出願日：2013 年 3 月 27 日

13PAT006 2-03
岩撫 暁生、瀬古 典明、保科 宏行、
植木 悠二、佐伯 誠一（原子力機構・量子ビーム）
「布状の放射性物質吸着材及びその製造方法」
登録番号：特許第 8476188 号
登録日：2013 年 7 月 2 日

13PAT007 3-32
渡辺 智、橋本 和幸（原子力機構・量子ビーム）、飯田 康彦、花岡 宏史、遠藤 啓吾（群馬大）
「抗体標識が可能な無担体 ^{177}Lu の分離精製法」
特許番号：特許第 5376130 号
取得日：2013 年 10 月 4 日

13PAT008 4-03
杉本 雅樹、出崎 亮、吉川 正人、（原子力機構・量子ビーム）関 修平、渡辺 省伍（大阪大院）
「ナノファイバー及びその製造法」
特許番号：特許第 5419001 号
取得日：2013 年 11 月 29 日

13PAT009　4-07
田口 富嗣、樹神 克明、社本 真一（原子力機構・量子ビーム）
「アモルファス炭化ケイ素ナノチューブの製造方法」
特許番号：特許第 5322054 号
取得日：2013 年 7 月 26 日

13PAT010　4-09
花泉 修、三浦 健太（群馬大・理工学）、
吉川 正人、山本 春也、杉本 雅樹（原子力機構・量子ビーム）
「青色発光部材の製造方法」
特許番号：特許第 5331961 号
登録日：2013 年 8 月 9 日

13PAT011　4-28
酒井 卓郎、飯倉 寛、野島 健大、山本 博之、
松林 政仁、安田 良（原子力機構・量子ビーム）
「放射線検出用蛍光板の製造方法」
出願番号：特願 2014-036368 号
出願日：2014 年年 2 月 27 日

13PAT012　4-37
百合 庸介、湯山 貴裕、石坂 知久、
石堀 郁夫、奥村 進（原子力機構・高崎研）、
前川 康成、越川 博、八巻 徹也、浅野 雅春(原子力機構・量子ビーム）、古山 了、
森山 順一、長井 陽三（日東電工㈱）、
「多孔性高分子フィルムの製造方法および多孔性高分子フィルム」
公開番号：特開 2013-227548 号
公開日：2013 年 11 月 7 日

13PAT013　4-39
千葉 敦也、薄井 絢、山田 圭介（原子力機構・高崎研）
「フラーレン及び有機高分子の負イオンビーム生成方法」
出願番号：特願 2014-058079 号
出願日：2014 年 3 月 20 日

13PAT014　4-44
平田 浩一（産総研）、斎藤 勇一、鳴海 一雅、
千葉 敦也、山田 圭介（原子力機構・高崎研）
「粒子分析法および粒子分析装置」
出願番号：特願 2013-104507 号
出願日：2013 年 5 月 16 日

Appendix 3

List of Related Press-release and Television Broadcasting

13NP001　1-08
ダイヤモンドを用いて量子コンピュータの実現に不可欠な量子エラー訂正に成功～量子情報デバイスの実用化・量子コンピューティングの実現に前進～
2014 年 1 月 29 日プレス発表。
経産業新聞、毎日新聞に掲載。

13NP002　2-03
倉敷繊維加工株式会社と共同でプレス発表
「被災地域の復興の推進に向けた水の安心の確保　－福島県双葉郡川内村で実施したセシウム除去用給水器のモニター試験結果について」
2014 年 3 月 27 日プレス発表。

13NP003　2-04
原子力機構・倉敷繊維加工
（給水器の用いた吸着材の開発者）（共同開発者）
「被災地域の復興の推進に向けた給水器の開発」
2014 年 3 月 27 日プレス発表
原子力産業新聞、上毛新聞、日刊工業新聞、繊維ニュース（新聞）に掲載。
NHK 福島で放映。

13NP004　4-03
大阪大学、原子力機構、阿南工業高等専門学校、東北大学
「莫大な表面積を持つ世界一細いタンパク質の紐の形成に成功」
2014 年 4 月 25 日（プレス投げ込み）、
報道解禁 4 月 28 日。

Symbol used in the Appendix 1 to 3

An example of symbol expression is written as following.

13 J 116 4-48 T

① ② ③ ④-⑤ ⑥

① Number of last two orders in fiscal year

② Kind of publication

- **J** : Publication in Journal
- **C** : Publication as Proceedings
- **NP** : Press-Release (Newspaper)
- **TV** : Television Broadcasting
- **PA** : Patent

③ Consecutive numbers for the kind of publication

④-⑤ Paper number

④ Classification number of research field

- **1** : Space, nuclear and energy engineering
- **2** : Environment conservation and resource exploitation
- **3** : Medical and biotechnological application
- **4** : Advanced materials, analysis and novel technology

⑤ Consecutive number every research field

⑥ Accelerators or irradiation facilities utilized for the research

- **C** : AVF Cyclotron
- **T** : 3 MV Tandem Electrostatic Accelerator
- **S** : 3 MV Single-ended Electrostatic Accelerator
- **I** : 400 kV Ion Implanter
- **E** : 2 MV Electron Accelerator
- **G** : Co-60 Gamma-ray Irradiation Facilities
- **O** : Off-line (Research without the utilization of irradiation facilities)

Appendix 4 Type of Research Collaboration and Facilities Used for Research

Paper No.	Type of Research Collaboration[*1]					Irradiation Facilites[*2]						Paper No.	Type of Research Collaboration[*1]					Irradiation Facilites[*2]					
	Joint Res.	Entr. Res.	Coop. Res.	JAEA Inter.	Ext. Use	C	T	S	I	E	G		Joint Res.	Entr. Res.	Coop. Res.	JAEA Inter.	Ext. Use	C	T	S	I	E	G
1-01	●					◎	◎	◎	◎			1-48				●						◎	◎
1-02				●		◎	◎	◎	◎			1-49				●						◎	◎
1-03	●					◎																	
1-04				●		◎	◎		◎			2-01				●						◎	
1-05	●						◎					2-02				●						◎	
1-06					●	◎						2-03				●						◎	
1-07	●								◎			2-04				●						◎	◎
1-08	●									◎		2-05	●									◎	
1-09	●					◎	◎					2-06	●									◎	
1-10		●									◎	2-07				●						◎	◎
1-11				●							◎	2-08	●									◎	
1-12				●						◎		2-09	●										◎
1-13			●					◎															
1-14				●							◎	3-01				●		◎	◎				
1-15				●							◎	3-02				●		◎					
1-16				●							◎	3-03				●		◎					
1-17				●							◎	3-04	●					◎					
1-18				●							◎	3-05				●		◎					◎
1-19				●							◎	3-06	●					◎					
1-20				●							◎	3-07	●					◎					
1-21				●							◎	3-08	●					◎					
1-22				●							◎	3-09	●					◎					
1-23				●			◎					3-10	●					◎					
1-24		●									◎	3-11	●					◎					
1-25				●							◎	3-12	●					◎					
1-26				●							◎	3-13	●					◎					
1-27				●							◎	3-14	●					◎					
1-28				●							◎	3-15	●					◎					
1-29				●							◎	3-16	●					◎					
1-30	●										◎	3-17	●					◎					
1-31				●			◎	◎	◎			3-18				●		◎					
1-32				●			◎	◎	◎			3-19	●									◎	◎
1-33				●			◎	◎	◎			3-20	●									◎	◎
1-34			●				◎	◎	◎			3-21			●					◎			
1-35				●			◎	◎	◎			3-22			●					◎			
1-36				●			◎	◎	◎			3-23			●					◎			
1-37					●		◎					3-24			●					◎			
1-38				●			◎	◎	◎			3-25			●					◎			
1-39					●						◎	3-26			●					◎			
1-40				●					◎			3-27			●					◎			
1-41				●		◎			◎			3-28			●					◎			
1-42	●										◎	3-29			●					◎			
1-43	●										◎	3-30	●					◎					
1-44				●		◎						3-31				●		◎					
1-45				●						◎	◎	3-32	●					◎					
1-46	●										◎	3-33	●					◎					
1-47	●					◎			◎			3-34	●					◎					

Paper No.	Type of Research Collaboration[*1]					Irradiation Facilites[*2]						Paper No.	Type of Research Collaboration[*1]					Irradiation Facilites[*2]					
	Joint Res.	Entr. Res.	Coop. Res.	JAEA Inter.	Ext. Use	C	T	S	I	E	G		Joint Res.	Entr. Res.	Coop. Res.	JAEA Inter.	Ext. Use	C	T	S	I	E	G
3-35	●					◎						4-20				●		◎					
3-36				●		◎					◎	4-21				●			◎			◎	
3-37	●					◎						4-22				●		◎					
3-38				●		◎						4-23	●					◎					
3-39	●					◎						4-24	●					◎					
3-40	●					◎						4-25	●					◎				◎	◎
3-41	●					◎						4-26	●					◎					
3-42	●					◎					◎	4-27				●		◎					
3-43				●		◎					◎	4-28				●				◎			
3-44	●					◎					◎	4-29					●					◎	
3-45	●					◎					◎	4-30			●					◎			
3-46					●	◎						4-31				●							◎
3-47				●		◎						4-32	●					◎	◎				
3-48				●							◎	4-33				●		◎	◎				
3-49	●					◎						4-34				●						◎	◎
3-50	●					◎					◎	4-35				●		◎					
3-51	●					◎					◎	4-36				●		◎					
3-52	●					◎						4-37				●							◎
3-53	●					◎						4-38				●		◎					
3-54	●					◎						4-39				●			◎	◎	◎		
												4-40				●		◎		◎	◎		
4-01				●				◎	◎			4-41				●OL			◎				
4-02					●	◎						4-42				●OL							
4-03	●					◎						4-43			●				◎				
4-04				●						◎		4-44			●				◎		◎		
4-05					●	◎						4-45			●				◎				
4-06					●	◎				◎		4-46			●				◎				
4-07				●			◎		◎			4-47			●				◎				
4-08	●							◎	◎			4-48	●						◎				
4-09	●							◎	◎														
4-10	●								◎	◎		5-01						◎	◎	◎	◎		
4-11	●						◎					5-02						◎					
4-12	●							◎				5-03							◎	◎	◎		
4-13					●				◎			5-04										◎	◎
4-14	●							◎				5-05										◎	◎
4-15	●						◎					5-06						◎	◎	◎	◎		
4-16	●						◎					5-07						◎	◎	◎	◎		
4-17	●						◎					5-08						◎	◎	◎	◎	◎	◎
4-18					●			◎				5-09						◎	◎	◎	◎	◎	◎
4-19					●						◎	Total	64	2	17	66	11	74	37	35	29	26	48

[*1] Type of Research Collaboration

Joint Res. : Joint research with external users

Entr. Res. : Research entrusted to JAEA

Coop. Res. : Cooperative research with plural universities through The University of Tokyo

JAEA Inter. : JAEA internal use

Ext. Use : Common use based on two programs of "JAEA-facility-use" and "Creation of Research Platforms and Sharing of Advanced Research Infrastructure" supported from MEXT

[*2] Utilization of Irradiation Facilities

C : AVF Cyclotron

T : 3 MV Tandem Electrostatic Accelerator

S : 3 MV Single-ended Electrostatic Accelerator

I : 400 kV Ion Implanter

E : 2 MV Electron Accelerator

G : Co-60 Gamma-ray Irradiation Facilities

OL : Off line (Research without the use of irradiation facilities)

Appendix 5 Examples of Typical Abbreviation Name for Organizations in Japan Atomic Energy Agency (JAEA)

◆Directorate, Center, Institute, etc.

QuBS（量子ビーム応用研究部門）: Quantum Beam Science Directorate

NSED（原子力基礎工学研究部門）: Nuclear Science and Engineering Directorate

FRDD（核融合研究開発部門）: Fusion Research and Development Directorate

GIRDD（地層処分研究開発部門）: Geological Isolation Research and Development Directorate

ANSRD（次世代原子力システム研究開発部門）: Advanced Nuclear System Research and Development Directorate

NCBD（バックエンド推進部門）: Nuclear Cycle Backend Directorate

NSRC（安全研究センター）: Nuclear Safety Research Center

NFCEL（核燃料サイクル工学研究所）: Nuclear Fuel Cycle Engineering Laboratories

NERCC（原子力エネルギー基盤連携センター）: Nuclear Engineering Research Collaboration Center

NHARC（原子力水素・熱利用研究センター）: Nuclear Hydrogen and Heat Application Research Center

J-PARC（J-PARC センター）: J-PARC Center

TARRI（高崎量子応用研究所）: Takasaki Advanced Radiation Research Institute

NSRI（原子力科学研究所）: Nuclear Science Research Institute

ORDC（大洗研究開発センター）: Oarai Research and Development Center

KPSI（関西光科学研究所）: Kansai Photon Science Institute

◆Division, Unit, Department, etc.

・量子ビーム応用研究部門、環境・産業応用量子ビーム技術研究ユニット
⇒ Environment and Industrial Materials Research Division, QuBS, JAEA

・量子ビーム応用研究部門、医療・バイオ応用量子ビーム技術研究ユニット
⇒ Medical and Biotechnological Application Division, QuBS, JAEA

・量子ビーム応用研究部門、量子ビーム材料評価・構造制御技術研究ユニット
⇒ Materials Science Research Division, QuBS, JAEA

・量子ビーム応用研究部門、レーザー応用技術研究ユニット
⇒ Laser Application Technology Division, QuBS, JAEA

・原子力基礎工学研究部門、環境・放射線科学ユニット
⇒ Division of Environment and Radiation Sciences, NSED, JAEA

・原子力基礎工学研究部門、燃料・材料工学ユニット
⇒ Division of Fuels and Materials Engineering, NSED, JAEA

・原子力基礎工学研究部門、原子力化学ユニット
⇒ Division of Chemistry for Nuclear Engineering, NSED, JAEA

・核融合研究開発部門、ITER プロジェクトユニット
⇒ ITER Project Unit, FRDD, JAEA

・核融合研究開発部門、トカマクシステム技術開発ユニット
⇒ Tokamak System Technology Unit, FRDD, JAEA
・核融合研究開発部門、六ヶ所 BA プロジェクトユニット
⇒ Rokkasho BA Project Unit, FRDD, JAEA
・先端基礎研究センター
⇒ Advanced Science Research Center, JAEA
・原子力科学研究所、放射線管理部
⇒ Department of Radiation Protection, NSRI, JAEA
・原子力科学研究所、福島技術開発特別チーム
⇒ Fukushima Project Team, NSRI, JAEA
・大洗研究開発センター、高速実験炉部
⇒ Experimental Fast Reactor Department, ORDC, JAEA
・大洗研究開発センター、福島燃料材料試験部
⇒ Fukushima Fuels and Materials Department, ORDC, JAEA
・原子力水素・熱利用研究センター、水素利用研究開発ユニット
⇒ Hydrogen Application Research and Development Division, NHARC, JAEA
・高崎量子応用研究所、放射線高度利用施設部
⇒ Department of Advanced Radiation Technology, TARRI, JAEA
・J-PARC センター、加速器ディビジョン
⇒ Accelerator Division, J-PARC, JAEA
・J-PARC センター、安全ディビジョン
⇒ Safety Division, J-PARC, JAEA
・安全研究センター、軽水炉長期化対応研究ユニット
⇒ LWR Long-term Reliability Research Unit, NSRC, JAEA
・地層処分研究開発部門、地層処分基盤研究開発ユニット
⇒ Geological Isolation Research Unit, GIRDD, JAEA
・核燃料サイクル工学研究所、サイクル工学試験部
⇒ Nuclear Cycle Engineering Department, NFCEL, JAEA
・核燃料サイクル工学研究所、プルトニウム燃料技術開発センター
⇒ Plutonium Fuel Development Center, NFCEL, JAEA
・核燃料サイクル工学研究所、再処理技術開発センター
⇒ Tokai Reprocessing Technology Development Center, NFCEL, JAEA
・核燃料サイクル工学研究所、福島技術開発試験部
⇒ Department of Fukushima Technology Development, NFCEL, JAEA
・次世代原子力システム研究開発部門、燃料材料技術開発ユニット
⇒ Fast Reactor Fuels and Materials Technology Development Unit, ANSRD, JAEA
・バックエンド推進部門、バックエンド技術開発ユニット
⇒ Nuclear Cycle Backend Technology Development Unit, NCBD, JAEA
・産学連携推進部
⇒ Industrial Collaboration Promotion Department, JAEA

国際単位系（SI）

表１．SI 基本単位

基本量	SI 基本単位	
	名称	記号
長さ	メートル	m
質量	キログラム	kg
時間	秒	s
電流	アンペア	A
熱力学温度	ケルビン	K
物質量	モル	mol
光度	カンデラ	cd

表２．基本単位を用いて表されるSI組立単位の例

組立量	SI 基本単位	
	名称	記号
面積	平方メートル	m^2
体積	立法メートル	m^3
速さ，速度	メートル毎秒	m/s
加速度	メートル毎秒毎秒	m/s^2
波数	毎メートル	m^{-1}
密度，質量密度	キログラム毎立方メートル	kg/m^3
面積密度	キログラム毎平方メートル	kg/m^2
比体積	立方メートル毎キログラム	m^3/kg
電流密度	アンペア毎平方メートル	A/m^2
磁界の強さ	アンペア毎メートル	A/m
量濃度(a)，濃度	モル毎立方メートル	mol/m^3
質量濃度	キログラム毎立法メートル	kg/m^3
輝度	カンデラ毎平方メートル	cd/m^2
屈折率(b)	（数字の） 1	1
比透磁率(b)	（数字の） 1	1

(a) 量濃度（amount concentration）は臨床化学の分野では物質濃度（substance concentration）ともよばれる。
(b) これらは無次元量あるいは次元１をもつ量であるが、そのことを表す単位記号である数字の１は通常は表記しない。

表３．固有の名称と記号で表されるSI組立単位

組立量	SI 組立単位			
	名称	記号	他のSI単位による表し方	SI基本単位による表し方
平面角	ラジアン(b)	rad	1 (b)	m/m
立体角	ステラジアン(b)	sr(c)	1 (b)	m^2/m^2
周波数	ヘルツ(d)	Hz		s^{-1}
力	ニュートン	N		m kg s^{-2}
圧力，応力	パスカル	Pa	N/m^2	m^{-1} kg s^{-2}
エネルギー，仕事，熱量	ジュール	J	N m	m^2 kg s^{-2}
仕事率，工率，放射束	ワット	W	J/s	m^2 kg s^{-3}
電荷，電気量	クーロン	C		s A
電位差（電圧），起電力	ボルト	V	W/A	m^2 kg s^{-3} A^{-1}
静電容量	ファラド	F	C/V	m^{-2} kg^{-1} s^4 A^2
電気抵抗	オーム	Ω	V/A	m^2 kg s^{-3} A^{-2}
コンダクタンス	ジーメンス	S	A/V	m^{-2} kg^{-1} s^3 A^2
磁束	ウエーバ	Wb	Vs	m^2 kg s^{-2} A^{-1}
磁束密度	テスラ	T	Wb/m^2	kg s^{-2} A^{-1}
インダクタンス	ヘンリー	H	Wb/A	m^2 kg s^{-2} A^{-2}
セルシウス温度	セルシウス度(e)	℃		K
光束	ルーメン	lm	cd sr(c)	cd
照度	ルクス	lx	lm/m^2	m^{-2} cd
放射性核種の放射能(f)	ベクレル(d)	Bq		s^{-1}
吸収線量，比エネルギー分与，カーマ	グレイ	Gy	J/kg	m^2 s^{-2}
線量当量，周辺線量当量，方向性線量当量，個人線量当量	シーベルト(g)	Sv	J/kg	m^2 s^{-2}
酸素活性	カタール	kat		s^{-1} mol

(a)SI接頭語は固有の名称と記号を持つ組立単位と組み合わせても使用できる。しかし接頭語を付した単位はもはやコヒーレントではない。
(b)ラジアンとステラジアンは数字の１に対する単位の特別な名称で、量についての情報をつたえるために使われる。実際には、使用する時には記号rad及びsrが用いられるが、習慣として組立単位としての記号である数字の１は明示されない。
(c)測光学ではステラジアンという名称と記号srを単位の表し方の中に、そのまま維持している。
(d)ヘルツは周期現象についてのみ、ベクレルは放射性核種の統計的過程についてのみ使用される。
(e)セルシウス度はケルビンの特別な名称で、セルシウス温度を表すために使用される。セルシウス度とケルビンの単位の大きさは同一である。したがって、温度差や温度間隔を表す数値はどちらの単位で表しても同じである。
(f)放射性核種の放射能（activity referred to a radionuclide）は、しばしば誤った用語で"radioactivity"と記される。
(g)単位シーベルト（PV,2002,70,205）についてはCIPM勧告2（CI-2002）を参照。

表４．単位の中に固有の名称と記号を含むSI組立単位の例

組立量	SI 組立単位		
	名称	記号	SI 基本単位による表し方
粘度	パスカル秒	Pa s	m^{-1} kg s^{-1}
力のモーメント	ニュートンメートル	N m	m^2 kg s^{-2}
表面張力	ニュートン毎メートル	N/m	kg s^{-2}
角速度	ラジアン毎秒	rad/s	m m^{-1} s^{-1}=s^{-1}
角加速度	ラジアン毎秒毎秒	rad/s^2	m m^{-1} s^{-2}=s^{-2}
熱流密度，放射照度	ワット毎平方メートル	W/m^2	kg s^{-3}
熱容量，エントロピー	ジュール毎ケルビン	J/K	m^2 kg s^{-2} K^{-1}
比熱容量，比エントロピー	ジュール毎キログラム毎ケルビン	J/(kg K)	m^2 s^{-2} K^{-1}
比エネルギー	ジュール毎キログラム	J/kg	m^2 s^{-2}
熱伝導率	ワット毎メートル毎ケルビン	W/(m K)	m kg s^{-3} K^{-1}
体積エネルギー	ジュール毎立方メートル	J/m^3	m^{-1} kg s^{-2}
電界の強さ	ボルト毎メートル	V/m	m kg s^{-3} A^{-1}
電荷密度	クーロン毎立方メートル	C/m^3	m^{-3} sA
表面電荷	クーロン毎平方メートル	C/m^2	m^{-2} sA
電束密度，電気変位	クーロン毎平方メートル	C/m^2	m^{-2} sA
誘電率	ファラド毎メートル	F/m	m^{-3} kg^{-1} s^4 A^2
透磁率	ヘンリー毎メートル	H/m	m kg s^{-2} A^{-2}
モルエネルギー	ジュール毎モル	J/mol	m^2 kg s^{-2} mol^{-1}
モルエントロピー，モル熱容量	ジュール毎モル毎ケルビン	J/(mol K)	m^2 kg s^{-2} K^{-1} mol^{-1}
照射線量（X線及びγ線）	クーロン毎キログラム	C/kg	kg^{-1} sA
吸収線量率	グレイ毎秒	Gy/s	m^2 s^{-3}
放射強度	ワット毎ステラジアン	W/sr	m^4 m^{-2} kg s^{-3}=m^2 kg s^{-3}
放射輝度	ワット毎平方メートル毎ステラジアン	$W/(m^2$ sr)	m^2 m^{-2} kg s^{-3}=kg s^{-3}
酵素活性濃度	カタール毎立方メートル	kat/m^3	m^{-3} s^{-1} mol

表５．SI 接頭語

乗数	接頭語	記号	乗数	接頭語	記号
10^{24}	ヨタ	Y	10^{-1}	デシ	d
10^{21}	ゼタ	Z	10^{-2}	センチ	c
10^{18}	エクサ	E	10^{-3}	ミリ	m
10^{15}	ペタ	P	10^{-6}	マイクロ	μ
10^{12}	テラ	T	10^{-9}	ナノ	n
10^{9}	ギガ	G	10^{-12}	ピコ	p
10^{6}	メガ	M	10^{-15}	フェムト	f
10^{3}	キロ	k	10^{-18}	アト	a
10^{2}	ヘクト	h	10^{-21}	ゼプト	z
10^{1}	デカ	da	10^{-24}	ヨクト	y

表６．SIに属さないが、SIと併用される単位

名称	記号	SI 単位による値
分	min	1 min=60s
時	h	1h =60 min=3600 s
日	d	1 d=24 h=86 400 s
度	°	1°=(π/180) rad
分	’	1’=(1/60)°=(π/10800) rad
秒	”	1”=(1/60)’=(π/648000) rad
ヘクタール	ha	$1ha=1hm^2=10^4m^2$
リットル	L, l	$1L=1l=1dm^3=10^3cm^3=10^{-3}m^3$
トン	t	$1t=10^3$ kg

表７．SIに属さないが、SIと併用される単位で、SI単位で表される数値が実験的に得られるもの

名称	記号	SI 単位で表される数値
電子ボルト	eV	$1eV=1.602\ 176\ 53(14)\times10^{-19}J$
ダルトン	Da	$1Da=1.660\ 538\ 86(28)\times10^{-27}kg$
統一原子質量単位	u	1u=1 Da
天文単位	ua	$1ua=1.495\ 978\ 706\ 91(6)\times10^{11}m$

表８．SIに属さないが、SIと併用されるその他の単位

名称	記号	SI 単位で表される数値
バール	bar	1 bar=0.1MPa=100kPa=10^5Pa
水銀柱ミリメートル	mmHg	1mmHg=133.322Pa
オングストローム	Å	1 Å=0.1nm=100pm=10^{-10}m
海里	M	1 M=1852m
バーン	b	$1\ b=100fm^2=(10^{-12}cm)2=10^{-28}m^2$
ノット	kn	1 kn=(1852/3600)m/s
ネーパ	Np	SI単位との数値的な関係は、対数量の定義に依存。
ベル	B	
デシベル	dB	

表９．固有の名称をもつCGS組立単位

名称	記号	SI 単位で表される数値
エルグ	erg	$1\ erg=10^{-7}$ J
ダイン	dyn	$1\ dyn=10^{-5}$N
ポアズ	P	1 P=1 dyn s cm^{-2}=0.1Pa s
ストークス	St	1 St =$1cm^2$ s^{-1}=$10^{-4}m^2$ s^{-1}
スチルブ	sb	1 sb =1cd cm^{-2}=10^4cd m^{-2}
フォト	ph	1 ph=1cd sr cm^{-2} 10^4lx
ガル	Gal	1 Gal =1cm s^{-2}=$10^{-2}ms^{-2}$
マクスウェル	Mx	1 Mx = 1G cm^2=10^{-8}Wb
ガウス	G	1 G =1Mx cm^{-2} =10^{-4}T
エルステッド(c)	Oe	1 Oe≙ $(10^3/4\pi)$A m^{-1}

(c) ３元系のCGS単位系とSIでは直接比較できないため、等号「 ≙ 」は対応関係を示すものである。

表10．SIに属さないその他の単位の例

名称	記号	SI 単位で表される数値
キュリー	Ci	$1\ Ci=3.7\times10^{10}Bq$
レントゲン	R	$1\ R = 2.58\times10^{-4}C/kg$
ラド	rad	$1\ rad=1cGy=10^{-2}Gy$
レム	rem	$1\ rem=1\ cSv=10^{-2}Sv$
ガンマ	γ	1 γ =1 nT=10-9T
フェルミ		1フェルミ=1 fm=10-15m
メートル系カラット		1メートル系カラット = 200 mg = 2×10-4kg
トル	Torr	1 Torr = (101 325/760) Pa
標準大気圧	atm	1 atm = 101 325 Pa
カロリー	cal	1cal=4.1858J（「15℃」カロリー），4.1868J（「IT」カロリー）4.184J（「熱化学」カロリー）
ミクロン	μ	1 μ =1μm=10^{-6}m

（第8版，2006年改訂）